

H 24/3704

MONASH UNIVERSITY
THESIS ACCEPTED IN SATISFACTION OF THE
REQUIREMENTS FOR THE DEGREE OF
DOCTOR OF PHILOSOPHY
ON..... 11 November 2003

Sec. Research Graduate School Committee

Under the Copyright Act 1968, this thesis must be used only under the normal conditions of scholarly fair dealing for the purposes of research, criticism or review. In particular no results or conclusions should be extracted from it, nor should it be copied or closely paraphrased in whole or in part without the written consent of the author. Proper written acknowledgement should be made for any assistance obtained from this thesis.

**DIRECT SHEAR TESTING OF
JOINTED SOFT ROCK MASSES**

JERRY SZYMAKOWSKI, B.E., BSc

**A THESIS SUBMITTED FOR THE DEGREE OF
DOCTOR OF PHILOSOPHY IN THE
DEPARTMENT OF CIVIL ENGINEERING,
MONASH UNIVERSITY**

JULY, 2003

SYNOPSIS

Most current practical methods of assessing the strength of jointed rock masses are empirically based. While these empirical criteria usually provide workable solutions for designs involving rock masses, they do not explicitly model the failure processes occurring within the rock mass or provide a basis for accounting for anisotropic behaviour. They also provide no real indication of the level of conservatism of the design unless correlated with previous, site-specific experience.

Previous studies aimed at improving our understanding of rock mass behaviour have incorporated laboratory techniques, case studies or numerical methods. This study extends the laboratory based data by examining the behaviour of jointed, soft rock mass samples in direct shear. The rock mass samples tested in this study were fabricated by cutting smooth joint sets into a soft, synthetic siltstone. This investigation required the development of new procedures and equipment for fabricating and testing the rock mass samples.

The data recovered from this testing were used to identify and model the displacement and failure mechanisms occurring within the samples. The observed pre-peak behaviour of the rock masses was found to comprise either sliding along one or more of the joint sets or rotation of a portion of the rock mass defined by the jointing pattern. All samples ultimately failed by shearing through intact rock coincident with the shear plane defined by the testing apparatus. Mechanistic models of the sliding and rotation mechanisms were developed.

The direct shear tests were modelled using the distinct element code, UDEC. The UDEC simulations replicated the displacement and failure mechanisms observed in the laboratory tests. The shear stress at failure calculated by the UDEC model also compared favourably with those measured in the tests. However, the calculated displacement and dilation at failure did not agree as well with the test results. Nevertheless, it was judged that UDEC satisfactorily replicated the mechanisms occurring within rock masses undergoing shear and therefore had the potential to provide accurate simulations of more complex rock mass behaviour with the appropriate choice of properties.

TABLE OF CONTENTS

SYNOPSIS	i
TABLE OF CONTENTS.....	iii
STATEMENT.....	xi
ACKNOWLEDGEMENTS.....	xiii
NOTATION	xv
1 INTRODUCTION.....	1
1.1 General.....	1
1.2 Background.....	2
1.3 Significance of this study.....	6
1.4 Aims of this thesis.....	6
1.5 Outline of this dissertation.....	7
2 REVIEW OF ROCK MASS STRENGTH.....	9
2.1 Introduction.....	9
2.2 Analytical studies.....	9
2.3 Empirical studies.....	13
2.3.1 Rock mass classification systems.....	13
2.3.1.1 The Rock Mass Rating (RMR) system.....	14
2.3.1.2 The Q system.....	15
2.3.1.3 GSI System.....	16
2.3.2 Rock mass strength criteria.....	16
2.3.2.1 The original Hoek-Brown criterion.....	16
2.3.2.2 The modified Hoek-Brown criterion.....	18
2.3.2.3 The Hoek-Brown Geological Strength Index (GSI).....	20
2.3.2.4 Rock Mass Index (RMi).....	26

2.4	Laboratory studies.....	27
2.4.1	Introduction.....	27
2.4.2	Triaxial and UCS testing.....	28
2.4.3	Direct shear testing.....	33
2.5	Numerical modelling studies	37
2.5.1	Numerical methods	38
2.5.1.1	Continuum methods.....	38
2.5.1.2	Discontinuum methods	39
2.5.1.3	Reviews of numerical methods.....	40
2.5.1.4	Numerical modelling of direct shear tests.....	43
2.6	Summary	45
3	DIRECT SHEAR TESTING.....	47
3.1	Introduction.....	47
3.2	Field conditions.....	48
3.3	Previous studies using direct shear tests	49
3.4	CNS and CNL conditions	51
3.5	Monash University direct shear apparatus.....	53
3.6	Shear boxes.....	55
3.6.1	Type "A" shear box	55
3.6.2	Type "B" shear Box	56
3.7	Summary	59
4	LABORATORY TESTING PROGRAM.....	61
4.1	Program objectives.....	61
4.2	Test configuration	61
4.3	Jointed rock mass tests.....	63
4.3.1	Type "A" tests.....	63
4.3.2	Type "B" tests.....	64
4.4	Summary of laboratory testing.....	65

5	SAMPLE PREPARATION.....	67
5.1	Introduction	67
5.2	Sample material.....	68
5.3	Johnstone manufacture.....	69
5.3.1	Johnstone ingredients	69
5.3.2	Johnstone batching process	71
5.3.3	Johnstone block production.....	71
5.4	Johnstone properties.....	75
5.4.1	Saturated moisture content.....	75
5.4.2	UCS and modulus testing.....	75
5.4.3	Brazilian testing.....	78
5.4.4	Rock triaxial testing.....	78
5.4.5	Rock joint properties	81
5.5	Jointed rock mass sample fabrication.....	82
5.5.1	Cutting apparatus.....	82
5.5.1.1	Brick saw	82
5.5.1.2	Block saw	82
5.5.2	Cutting procedure-Type "A" blocks.....	83
5.5.3	Cutting procedure-Type "B" blocks.....	83
5.5.4	Rock mass sample assembly	88
5.5.5	Shear test procedure-preparation.....	92
5.5.5.1	Type "A" shear tests.....	92
5.5.5.2	Type "B" shear tests.....	93
5.5.6	Shear test procedure-execution	94
5.5.7	Shear test-tidy up.....	95
5.6	Summary	95
6	RESULTS OF DIRECT SHEAR TESTS	97
6.1	Introduction.....	97
6.2	Consolidation phase	97
6.2.1	Introduction	97
6.2.2	Application of initial normal stress	98
6.2.3	Vertical displacement resulting from normal stress	98

P
t
c
e
p
1

6.2.4	Vertical displacement with time	99
6.3	Shear behaviour	103
6.3.1	Initial phase (A-B)	105
6.3.1.1	Shear stress versus normal stress	105
6.3.1.2	Shear stress versus shear displacement	105
6.3.1.3	Dilation versus shear displacement	105
6.3.1.4	Normal stress versus shear displacement	108
6.3.2	Pre-peak phase (B-C)	108
6.3.2.1	Shear stress versus normal stress	108
6.3.2.2	Shear stress versus shear displacement	113
6.3.2.3	Dilation versus shear displacement	114
6.3.2.4	Normal stress versus shear displacement	116
6.3.3	Peak phase (C-D)	116
6.3.3.1	Shear stress versus normal stress	116
6.3.3.2	Shear stress versus shear displacement	116
6.3.3.3	Dilation versus shear displacement	116
6.3.4	Post-peak phase (D-E)	116
6.3.4.1	Shear stress versus normal stress	116
	Shear stress versus shear displacement	117
6.3.4.3	Dilation versus shear displacement	118
6.3.5	Progressive failure	119
6.3.6	Summary of rock mass behaviour	122
6.4	Observation of pre-peak and failure mechanisms	123
6.4.1	Introduction	123
6.4.2	Sliding followed by asperity shear	123
6.4.3	Rotation followed by shear	125
6.4.3.1	Strut shear	126
6.4.3.2	Block shear	127
6.5	Influence of parameters on sample behaviour	128
6.5.1	Joint inclination	131
6.5.2	Intact rock strength	140
6.5.2.1	Type "B" tests	140
6.5.2.2	Type "A" tests	145
6.5.3	Sub-Parallel Jointing	146
6.5.4	Number of joint sets	151

6.5.4.1	Type "B" tests	151
6.5.4.2	Type "A" tests	153
6.5.5	Joint spacing	154
6.5.5.1	Type "B" tests	154
6.5.5.2	Type "A" tests	158
6.5.6	Initial normal stress	159
6.5.6.1	Type "B" tests	159
6.5.6.2	Type "A" tests	162
6.5.7	Rock mass geometry	163
6.5.8	Summary of the effects of rock mass parameters on rock mass behaviour	167
7	ANALYSIS OF DIRECT SHEAR TESTS	169
7.1	Introduction	169
7.2	Analysis of pre-peak and failure mechanisms	170
7.2.1	Failure by sliding / asperity shear	170
7.2.1.1	Shear strength for sliding	172
7.2.1.2	Shear strength for asperity shear	172
7.2.2	Rotational behaviour	178
7.2.2.1	Pre-peak behaviour of rock masses containing three joint sets	185
7.2.2.2	Dilation	186
7.2.2.3	Pre-peak behaviour for samples with $\theta_2=45^\circ$	187
7.2.2.3.1	Pre-peak behaviour for samples with $\theta_2=45^\circ$ and closely spaced joints	188
7.2.2.3.2	Pre-peak behaviour for samples with $\theta_2=45^\circ$ and widely spaced joints	189
7.2.2.4	Pre-peak behaviour—sliding or rotation?	190
7.2.3	Shear failure through a strut or block	192
7.3	Comparison with Hoek-Brown GSI criterion	196
7.4	Failure in Type "A" tests	199
7.5	Summary	201
8	UDEC MODELLING OF DIRECT SHEAR TESTS	203
8.1	Introduction	203
8.2	Development of the UDEC model	203
8.2.1	Model geometry	204
8.2.2	Material and joint constitutive models and properties	207

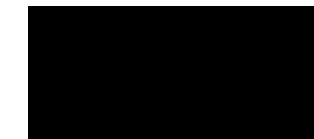
P
t
c
e
p
1

8.2.3	Boundary conditions	209
8.2.3.1	Initial horizontal stress, σ_{hi}	210
8.2.3.2	Initial normal stress, σ_{ni}	210
8.2.3.3	Horizontal velocity, x_{vel}	213
8.2.4	FISH routines	214
8.2.4.1	FISH routines to set up gridpoint arrays	214
8.2.4.2	FISH routines to measure displacements and stresses	216
8.2.4.3	FISH routines to apply CNS conditions.....	217
8.2.4.4	FISH routines controlling the program	218
8.2.5	Output of results.....	218
8.3	Comparison of test and UDEC outputs.....	219
8.3.1	Pre-Peak and failure behaviour	221
8.3.1.1	Sliding / asperity shear	222
8.3.1.2	Rotation / strut shear	226
8.3.1.3	Rotation / block shear	228
8.4	Overall predictions.....	230
8.5	Parametric study using UDEC model	231
8.5.1	Effect of joint spacing	231
8.6	Extrapolation of UDEC model to hard rock masses	234
8.7	Summary	239
9	SUMMARY AND CONCLUSIONS	241
9.1	Development of equipment and techniques	241
9.2	Observation and modelling of rock mass behaviour	241
9.3	Effects of varying sample parameters	242
9.4	UDEC modelling	242
9.5	Limitations and further research	243
9.5.1	Rock mass geometry	243
9.5.2	Joint inclination and spacing.....	243
9.5.3	Joint properties.....	244
9.5.4	Refinement of strength criteria	244
9.5.5	Improvement of numerical model.....	244
9.5.6	Application to field studies	245

10	REFERENCES.....	247
	APPENDIX A.....	A-1
	APPENDIX B.....	B-1
	APPENDIX C.....	C-1

STATEMENT

This thesis contains no material that has been previously submitted for any other degree or diploma in any university. To the best of my knowledge, this thesis contains no material published or written by others, except where due reference has been made in the text.



Jerry Szymakowski

ACKNOWLEDGEMENTS

I would like to extend my sincerest thanks to the people that have assisted me during this project.

Firstly, I would like to thank my supervisor, Associate Professor Chris Haberfield, for his support, patience and understanding. His practical attitude and keen intellect to all matters were appreciated.

I would also like to thank the staff at Monash University who assisted me during the experimental program. In particular, I'd like to acknowledge the prompt assistance provided Graeme Rundle, Jeff Dodrell, Len Dodrell, Roger Doulis and Don McCarthy. Special mention must be made of the skills of Roy Goswell, who did an outstanding job of building the Type "B" shear box.

I would also like to thank the postgraduates and staff at Monash University with whom I was able to discuss and get feedback from my work, especially Sarah Richards and Bernard Francis. Other people that provided useful feedback were Mike Coulthard, who provided assistance with developing the UDEC model, and Professor Erling Nordlund, with whom I had many fruitful discussions during my visit to Luleå University of Technology.

I am grateful for the financial support provided by Monash University and the financial assistance from the Australian Research Council for the funding of this project.

Finally, I would like to express my deepest love and gratitude to my family in Perth and in Melbourne, especially to my wife Katie and daughter Jasmine, for all of the love, support and encouragement they have given me, in particular over the course of this project.

NOTATION

a	empirical Hoek-Brown constant depending on composition, structure and joint surface conditions of rock mass (Hoek et al., 1992)
Λ	included angle between joint sets
B	constant used in Johnston criterion (Johnston, 1985)
BEM	Boundary Element Method
c	constant used to calculate K_{max} (Skinas et al., 1990)
c	cohesion
C	a mobilisation factor between 0 and 1 (Lajtai, 1969b)
c'	effective cohesion
$CaCl_2$	calcium chloride
c_d	cohesion of discontinuity (Priest, 1993)
CD	consolidated, drained condition in triaxial tests
c_i	cohesion of intact rock
CI	Confidence Interval
c_m	cohesion of intact rock (Priest, 1993)
CNL	Constant Normal Load
CNS	Constant Normal Stress
DBEM	Dual Boundary Element Method
DDA	Discontinuous Deformation Analysis
de	displacement due to elastic deformation

DEM	Discrete Element Method
dx	incremental shear displacement
dy	dilation
E	Young's modulus
E_{50}	secant modulus
FDM	Finite Difference Method
FEM	Finite Element Method
FISH	inbuilt UDEC programming language
FLAC	Finite Lagrangian Analysis of Continua
G	shear modulus
gen edge	UDEC command to form zones within model
GSI	Geological Strength Index (Hoek et al., 1995)
i	angle of inclination of saw tooth joints (Patton, 1966)
ISRM	International Society for Rock Mechanics
J_a	joint alteration number (Barton et al., 1974)
J_n	joint set number (Barton et al., 1974)
JP	jointing parameter (Palmstrom, 1996)
J_r	joint roughness number (Barton et al., 1974)
J_w	joint water reduction factor (Barton et al., 1974)
k	normal stiffness
K	bulk modulus
K_{max}	maximum stiffness (Skinas et al., 1990)

L	length of rock mass (Skinas et al., 1990)
L	length of shear surface through an asperity
L_a	contact length of asperity
LHS_zones	FISH function to identify zones within load cell in lower left end of shear box
L_N	lever arm between normal forces
L_{NB}	lever arm between normal forces for block rotation
L_S	lever arm between shear forces
L_{SB}	lever arm between shear forces for block rotation
LVDT	Linear Variable Displacement Transducer
M	constant used in Johnston criterion (Johnston, 1985)
m	empirical Hoek-Brown constant depending on rock type (Hoek and Brown, 1980a)
m	mass of smallest block in UDEC model
m/c	saturated moisture content
m_b	empirical Hoek-Brown constant depending on composition, structure and joint surface conditions of rock mass (Hoek et al., 1992)
m_i	empirical Hoek-Brown constant depending on composition, structure and joint surface conditions of rock mass (Hoek et al., 1992)
MOVIE	UDEC function that captures screen dump
MRMR	Modified Rock Mass Rating (Meyers, 1994)
N	normal force
\bar{N}	normal force acting on shear plane
N_s	global normal force
p	mean stress in triaxial test

P axial load within a strut

PFC parallel flange channel

Q rock quality as estimated from rock mass classification system (Barton et al., 1974)

q deviator stress in triaxial test

q_u intact rock strength (Johnston, 1985)

r radius

RMi Rock Mass Index (Palmstrom, 1996)

RMR Rock Mass Rating (Bieniawski, 1973)

rpm revolutions per minute

RQD Rock Quality Designation (Deere, 1963)

RSR Rock Structure Rating (Wickham et al., 1972)

s empirical Hoek-Brown constant depending on joint spacing (Hoek and Brown, 1980a)

S shear force

\bar{S} shear force acting on shear plane

side_disp FISH function to calculate x direction displacement of side gridpoints

side_gridpoints FISH function to identify gridpoints at interface between shear box and lower left end of sample

side_stress FISH function to calculate x direction stress on load cell

S_0 Cohesion of intact rock (Lajtai, 1969b)

SPW Single Plane of Weakness (Jaeger, 1960)

SRF Stress Reduction Factor (Barton et al., 1974)

S_x global shear force

supsolve FISH function to call supstep routine

supstep FISH function to call routines to calculate stresses and displacements

szz out of plane stress (UDEC)

top_array FISH function to calculate dilation of top of shear box and additional of normal stress

top_disp FISH function to calculate y direction displacement of top gridpoints

top_gridpoints FISH function to identify gridpoints at interface between shear box and top of sample

T_t tensile strength of intact rock (Lajtai, 1969b)

UCS Unconfined Compressive Strength or Uniaxial Compressive Strength

UDEC Universal Distinct Element Method

UDL Uniformly Distributed Load

w water content

xvel x direction velocity (UDEC)

β inclination of failure plane through an asperity from the horizontal

$\delta\theta_r$ change in rotation angle

$\Delta\sigma, \Delta\sigma_n$ change in normal stress

$\Delta\sigma_{n(de)}$ change in normal stress due to elastic deformation

$\Delta\sigma_{n(dy)}$ change in normal stress due to dilation

Δr change in radius

Δt timestep (UDEC)

Δx shear displacement calculated by UDEC using timestep and xvel

Δy	dilation
ϕ	friction angle
ϕ'	effective friction angle
ϕ_d	friction angle of discontinuity (Priest, 1993)
ϕ_i	friction angle of intact rock
ϕ_j	joint friction angle
ϕ_m	friction angle of intact rock (Priest, 1993)
ϕ_p	Angle of joint friction (Lajtai, 1969b)
ϕ_{pp}	apparent friction angle (gradient of τ - σ curve)
ϕ_{res}	residual friction angle
ϕ_u	residual (ultimate) friction angle (Lajtai, 1969b)
κ	degree of joint separation (Lajtai, 1969b)
ν	Poisson's ratio
θ	the acute angle between the major principle stress axis and the unit vector normal to the discontinuity (Jaeger, 1960)
θ_1	inclination of first joint set in the rock mass sample
θ_2	inclination of second joint set in the rock mass sample
θ_3	inclination of third joint set in the rock mass sample
θ_d	angle of diagonal of the sample
θ_r	angle about which rotation occurs
σ	normal stress

σ_1	major principal stress
σ'_1	major effective principal stress at failure (Hoek and Brown, 1980a)
σ_{1d}	peak stress required to fail a rock mass along a discontinuity (Priest, 1993)
σ_{1f}	peak stress at failure
σ_{1m}	peak stress required to fail a rock mass through the intact rock (Priest, 1993)
σ_2	intermediate principal stress
σ_3	minor principal stress
σ'_3	minor effective principal stress at failure (Hoek and Brown, 1980a)
σ_s	normal stress acting on shear plane (Lajtai, 1969b)
σ_c	uniaxial compressive strength of the intact rock within the rock mass (Hoek and Brown, 1980a)
σ_{ci}	uniaxial compressive strength of the intact rock within the rock mass (Hoek et al., 1995)
σ_{hi}	initial horizontal stress
σ_n	normal stress
$\bar{\sigma}_n$	normalised normal stress
σ'_n	effective normal stress
σ_{ni}	initial normal stress
$\bar{\sigma}_{ni}$	normalised initial normal stress
σ_p	peak normal stress
$\bar{\sigma}_p$	normalised peak normal stress
σ_t	tensile strength

τ	shear stress
$\bar{\tau}$	normalised shear stress
τ_a	shear strength of intact rock (Lajtai, 1969b)
τ_p	peak shear stress
$\bar{\tau}_p$	normalised peak shear stress
ω	included angle formed between θ_1 and θ_2
ψ	dilation angle

Metric units and effective stresses have been used in this dissertation unless otherwise noted.

1 INTRODUCTION

1.1 General

Civil infrastructure as a means of providing the basic needs of shelter and access to food and water has always been of vital importance to society. As the human race has developed and living standards improved, the methods of providing these needs have become more sophisticated. Adequate shelter was once considered to be a cave, now modern multi-storey structures are common. Water that was once drawn from a spring or well must now be available on tap. Increasing populations need more housing, transport, water supply and wastewater disposal. Business requires more accommodation and better road, rail, air and shipping access. The construction of this infrastructure results in interaction between the built environment and the ground on or in which it is located. In many places throughout the world, this ground will comprise rock masses of variable quality. Rarely will civil projects be located in or on what can be considered to be intact rock. It is more likely that the ground encountered will be a jointed rock mass, where the intact rock is intersected by discontinuities such as joints, bedding planes and/or faults.

The interaction between infrastructure and the jointed rock mass that supports it is of paramount importance to the design, construction and maintenance of many civil infrastructure projects. This interaction occurs in many forms and results in a wide variety of loads and stress paths being applied to the rock mass. The behaviour of the rock mass needs to be assessed during the design process so that a safe and economical design can be achieved. Over-estimating the strength of the rock mass may lead to excessive settlements or even failure of the foundation or tunnel, with the associated costs and risks of possible injury or loss of human life. Under-estimating these properties can add significant unnecessary costs to the project.

The strength of intact rock and of rock joints is relatively well understood. However, the strength of jointed rock masses is often far more complex than exhibited by the superposition of the intact rock and joint strengths acting in isolation. As stated by Hoek (1983);

"The strength of such rock masses depends on the strength of the intact pieces and on their freedom of movement which, in turn, depends on the number, orientation, spacing and shear

strength of the discontinuities. A complete understanding of this problem presents formidable theoretical and experimental problems..."

This statement still holds true today despite the significant advancements in rock mass modelling, testing and analysis (outlined in Chapter 2) made over the last 20 years.

The theoretical and experimental problems referred to by Hoek are perhaps the reason why many research investigations into the strength of rock masses have relied upon simple laboratory techniques or assessment of field performance to develop (usually) empirical correlations to quantify behaviour. While such correlations may allow successful predictions of rock mass strength to be made, they also provide little detailed information on the interactions occurring within the rock masses as they are loaded and the mechanisms by which they fail.

One way of further developing our understanding of rock mass behaviour is by conducting appropriate laboratory tests on rock mass samples, where the intact rock and joint properties are known and can be closely controlled. The strength of the rock mass can be observed and measured directly and provide valuable data that may allow the development of analytical and numerical models that capture the interactions and failure mechanisms that occur within the rock mass.

This thesis aims to investigate the behaviour of carefully constructed rock mass samples in direct shear and to develop basic models of the behaviour and failure mechanisms observed during the tests. The direct shear tests are also modelled using the distinct element code, UDEC, to assess if UDEC can replicate the rock mass sample behaviour and assess it's potential for application to more complex rock mechanics problems.

1.2 Background

The bedrock below the city of Melbourne, Australia, which comprises interbedded siltstones and sandstones (with minor claystones) of Silurian/Devonian age, is referred to locally as Melbourne Mudstone. Melbourne Mudstone displays the full weathering profile, from fresh rock with widely spaced joints at depth, to highly weathered, soft, heavily jointed rock at shallow depth to extremely weathered rock and residual soil at the surface. Similar weathering profiles are present in Melbourne Mudstone whether it outcrops at the ground surface or is buried under tens of metres of alluvial deposits. Given that civil infrastructure is typically located at or near the ground surface,

much of the Melbourne Mudstone encountered can be considered to be very weak rock containing widely to very closely spaced joints. The intact rock strength can vary from that of a hard soil to in excess of 80 MPa.

As with rock masses in general, the behaviour of Melbourne Mudstone is complicated by significant scale dependence. Figure 1-1 illustrates the effect of scale on rock mass behaviour. Depending on the scale selected, the rock mass sample can be considered to be anything from an intact piece of rock to a heavily jointed rock mass.

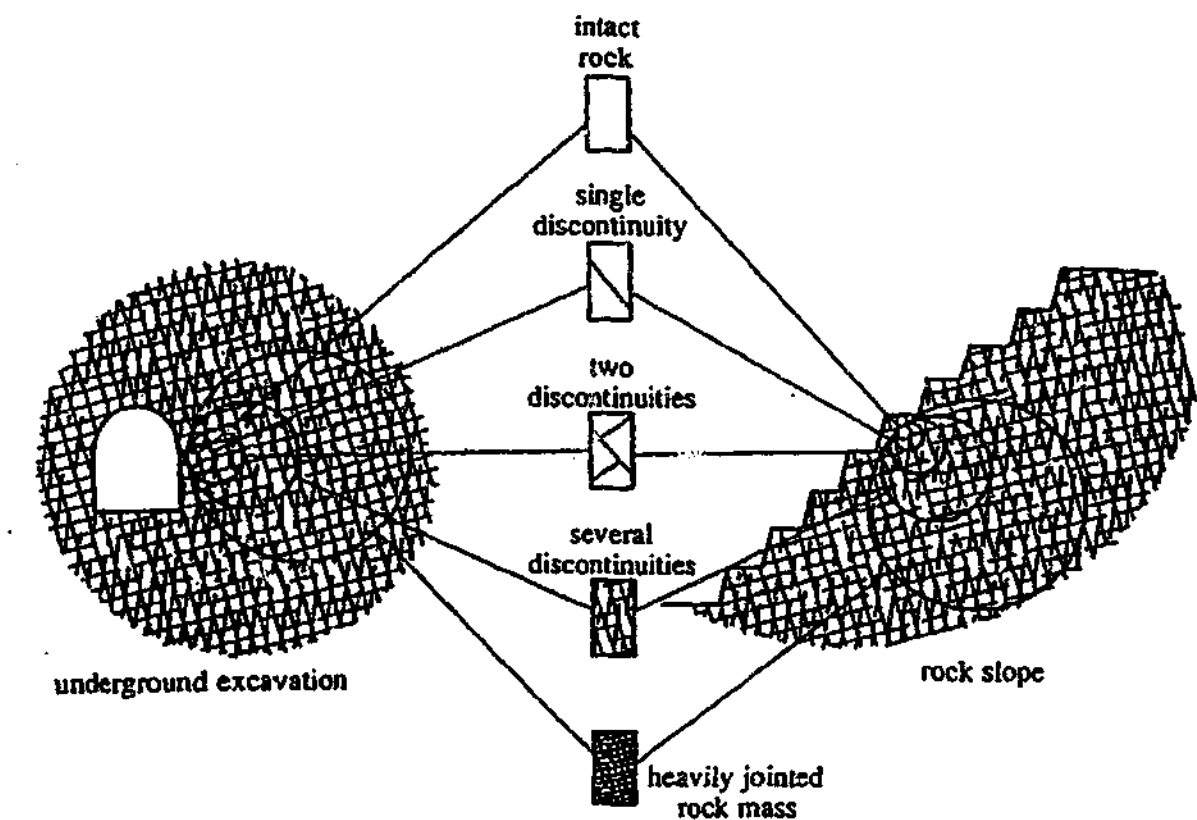


Figure 1-1: Effect of scale on definition of rock mass (after Hoek, 1983).

The influence of scale on the level of understanding of rock mass behaviour has been summarised by Hoek (1983) and included here as Figure 1-2. The poor understanding of the behaviour of jointed rock masses described as either massive rock containing a few sets of discontinuities or as heavily jointed rock are highlighted in Figure 1-2. In the 20 years since this table was published, there appears to have been little improvement in the level of understanding of the behaviour of these types of rock masses. This may be due to the difficulties of carrying out and analysing laboratory and field testing in rock masses, their anisotropic nature and/or the complex behaviour

they exhibit. The intact rock pieces that make up the rock mass can rotate, crush, slide or translate, depending on the loading configuration, block geometry and intact rock strength.

	Description	Strength characteristics	Strength testing	Theoretical considerations
	Hard intact rock	Brittle, elastic and generally isotropic	Triaxial testing of core specimens in laboratory relatively simple and inexpensive and results usually reliable	Theoretical behaviour of isotropic elastic brittle rock adequately understood for most practical applications
	Intact rock with single inclined discontinuity	Highly anisotropic, depending on shear strength and inclination of discontinuity	Triaxial testing of core with inclined joints difficult and expensive but results reliable. Direct shear testing of joints simple and inexpensive but results require careful interpretation	Theoretical behaviour of individual joints and of schistose rock adequately understood for most practical applications
	Massive rock with a few sets of discontinuities	Anisotropic, depending on number, shear strength and continuity of discontinuities	Laboratory testing very difficult because of sample disturbance and equipment size limitations	Behaviour of jointed rock poorly understood because of complex interaction of interlocking blocks
	Heavily jointed rock	Reasonably isotropic. Highly dilatant at low normal stress levels with particle breakage at high normal stress	Triaxial testing of undisturbed core samples extremely difficult due to sample disturbance and preparation problems	Behaviour of heavily jointed rock very poorly understood because of interaction of interlocking angular pieces
	Compacted rockfill	Reasonably isotropic. Less dilatant and lower shear strength than in situ jointed rock but overall behaviour generally similar	Triaxial testing simple but expensive because of large equipment size required to accommodate representative samples	Behaviour of compacted rockfill reasonably well understood from soil mechanics studies on granular materials
	Loose waste rock	Poor compaction and grading allow particle rotation and movement resulting in mobility of waste rock dumps	Triaxial or direct shear testing relatively simple but expensive because of large equipment size required	Behaviour of waste rock adequately understood for most applications

Figure 1-2: Summary of understanding of rock mass behaviour and testing (after Hoek, 1983).

If the behaviour of a rock mass during construction, while in service and at failure could be better understood and modelled, significant cost savings may be possible, as well as greater confidence in the design.

The current practical methods of assessing the strength of rock masses are generally empirically based. These empirical criteria have usually provided workable solutions for designs involving rock masses without capturing the processes occurring within the rock mass or providing any significant guidance on the level of conservatism of the design.

Previous studies have attempted to improve our understanding by testing rock mass samples and observing the outcomes. The test methods utilised have included field tests, laboratory tests on samples recovered from the field, laboratory tests on full scale or reduced scale synthetic samples.

The selection of a test method to assess rock mass behaviour may depend on such constraints as practicality, equipment availability and cost. Ideally, the test method selected should, as practically as possible, reflect the conditions that occur in the field.

Some studies have used back-analysis of full-scale failures or tests conducted *in-situ* to measure rock mass strength. This approach can be expensive and may suffer from the disadvantage that the properties of the intact rock and joints may not be known accurately. Numerical techniques are often used in these studies to model the failure or test. In such cases, the rock and joint properties are usually selected to produce similar outcomes to those observed.

Several studies, documented in the literature, have comprised laboratory testing of synthetic samples. Such techniques can reduce the scatter resulting from variations in properties of the intact rock and joints inherent to natural rock masses. The test conditions and sample manufacture can also be tightly controlled, allowing the results of parametric studies to be more easily identified and the pre-peak behaviour and failure mechanisms to be observed, measured and recorded.

The most widely reported laboratory techniques adopted for testing rock masses have been triaxial tests and uniaxial compressive strength (UCS) tests. The use of direct shear testing has not been as widely adopted. This may be due to a lack of suitably configured shear equipment, difficulty in preparing samples or a belief that this technique is not suitable. However, as demonstrated in this

thesis, the use of direct shear testing on rock masses is both appropriate and relatively straightforward to perform and can provide a valuable insight into the behaviour of rock masses.

1.3 Significance of this study

This dissertation examines the behaviour of jointed, soft rock masses undergoing direct shear under relatively low confining stresses (up to 400 kPa). In particular, it investigates the shear strength of synthetic siltstone samples used to model the very weak, closely jointed siltstone commonly found at shallow depth around the Melbourne area. This investigation was carried out using rock mass samples fabricated by cutting joint sets into the synthetic siltstone and shearing these samples in a direct shear apparatus. The intact uniaxial compressive strength of the synthetic siltstone ranged between 1 MPa and 5 MPa and the rock masses were intersected by up to three major joint sets, with joints spaced at about 30 mm to 70 mm. Direct shear testing of samples made from stronger rock or with more widely spaced joints was not considered in this study due to limitations imposed by the capacity of the shear box. The samples were produced at a scale that was thought would allow the interactions between the intact rock and the joints to fully develop.

As discussed in Section 1.2, the behaviour of rock masses is complicated by the inherent variability of the intact rock, joint characteristics and the interactions between the intact rock and the joints. Numerical techniques are often used to model rock mass behaviour, but the results obtained from these models are of little value unless correlated with measured behaviour. The lack of quality data makes it difficult to correlate the models and assess the accuracy of estimates of rock mass strength and deformation. If the mechanisms observed and measured during physical testing of rock mass samples can be replicated by the numerical model, there will be greater confidence in the output from the model for problems of more practical significance.

1.4 Aims of this thesis

The specific aims of this thesis are:

- To develop procedures and testing equipment to carry out laboratory direct shear testing of relatively large scale jointed rock mass samples. Fabrication and testing of such samples have not been widely reported in the literature.

- To observe, document and model the pre-peak and failure mechanisms in a rock mass undergoing direct shear. This will help to improve our knowledge and understanding of the processes occurring within the rock mass as shear displacement increases.
- To develop simple mechanistic models that model the pre-peak and failure mechanisms occurring within the rock mass and can be used to calculate the peak shear strength of a rock mass. These models would ideally be based on the geometry and basic properties of the intact rock blocks and the characteristics of the joints within the rock mass.
- To assess the ability of the distinct element code UDEC to model the behaviour observed during the direct shear tests. In particular, to assess the ability of UDEC to capture the pre-peak and failure mechanisms observed in the rock mass during the direct shear tests.

It should be emphasised that this study concentrates on the shear strength of jointed rock masses. However, from time to time, comments on the deformation response have been included where it is judged that this behaviour would be of potential interest or has an impact on strength.

1.5 Outline of this dissertation

This dissertation is set out as follows:

Chapter 2 Review of rock mass behaviour

This chapter reviews the evolution of existing criteria used for estimating the strength of rock masses. A summary of the analytical, empirical and numerical approaches used in earlier studies is presented. The laboratory testing techniques used in earlier studies are also described.

Chapter 3 Direct shear testing

This chapter discusses the suitability, advantages and disadvantages of direct shear testing techniques for assessing rock mass strength. The application of constant normal load and constant normal stiffness conditions are also discussed. Previous studies involving direct shear testing of rock masses are reviewed. A description of the Monash direct shear apparatus and the two shear boxes used in this study are also provided.

Chapter 4 Laboratory testing program

The laboratory testing program is outlined in this chapter. The testing program was divided into several stages, wherein each stage a different rock mass parameter was varied. The aim of each stage of testing is discussed.

Chapter 5 Sample preparation

This chapter outlines the reasons for the choice of modelling material used in this project. The manufacture of the synthetic rock is outlined and the engineering properties of the intact rock and the rock joints are described. The fabrication of samples by cutting joints into the synthetic rock blocks and reassembling the rock mass pieces is described. The placement of the sample in the shear box and then into the shear apparatus is also described.

Chapter 6 Results of direct shear tests

The behaviour of the rock mass as observed during each phase of the shear test is discussed in this chapter. The pre-peak and failure mechanisms that were observed during the shear tests are introduced. Results from each stage of testing are presented and the effects of varying each of the parameters on the behaviour and strength of the rock mass are discussed.

Chapter 7 Analysis of direct shear tests

This chapter presents the development of simple mechanistic models of the pre-peak mechanisms observed in the direct shear tests. Comparisons between calculated and measured values of peak shear strength are made.

Chapter 8 UDEC modelling of direct shear tests

This chapter describes the application of the distinct element code, UDEC, to the modelling of the direct shear tests. The model is also used to conduct a preliminary investigation into the effects of varying intact rock strength and joint spacing on rock mass strength.

Chapter 9 Summary and Conclusions

The outcomes of this project are summarised. Directions for future work are also provided.

2 REVIEW OF ROCK MASS STRENGTH

2.1 Introduction

The majority of civil and infrastructure projects will apply loads to the rock masses in or on which they are located. It is therefore important to be able to assess the likely response of the rock mass to these loads, in particular, the maximum load that can safely be applied and the deformations that may occur.

A jointed rock mass comprises intact rock intersected by discontinuities, such as joints. The behaviour of intact rock and rock joints have been the subject of much research and individually are relatively well understood. The behaviour of a rock mass, however, is more complex than the superposition of the behaviour of the intact rock and the rock joints (Amadei, 1988). This has made the accurate prediction of rock mass behaviour difficult.

Much of the previous research into the behaviour of rock masses has been empirically based, with only relatively limited success being obtained using analytical approaches. Many studies into the behaviour of rock masses have incorporated laboratory investigations, mostly to develop new strength criteria or refine existing ones. There has also been a recent increase in the application of numerical modelling techniques to investigate rock mass behaviour. The improved processing speed of computers and increasing sophistication of the software have made numerical modelling more attractive, particularly for projects where meaningful laboratory or field testing is not possible or practical.

A review of the major contributions made by earlier analytical, empirical and numerical studies conducted by others into the strength of rock masses follows.

2.2 Analytical studies

The origins of the various analytical strength criteria for rock masses are based on the Mohr-Coulomb failure criterion, which basically defines the shear strength of a frictional interface by:

$$\tau = c + \sigma_n \tan \phi$$

Equation 2-1

where:

- τ is the shear strength of the frictional surface
- c is the cohesive strength of the surface,
- ϕ is the frictional angle of the surface, and
- σ_n is the normal stress acting on the frictional surface.

Jaeger (1960) introduced the Single Plane of Weakness (SPW) theory. Consider the rock mass containing a single discontinuity shown in Figure 2-1.

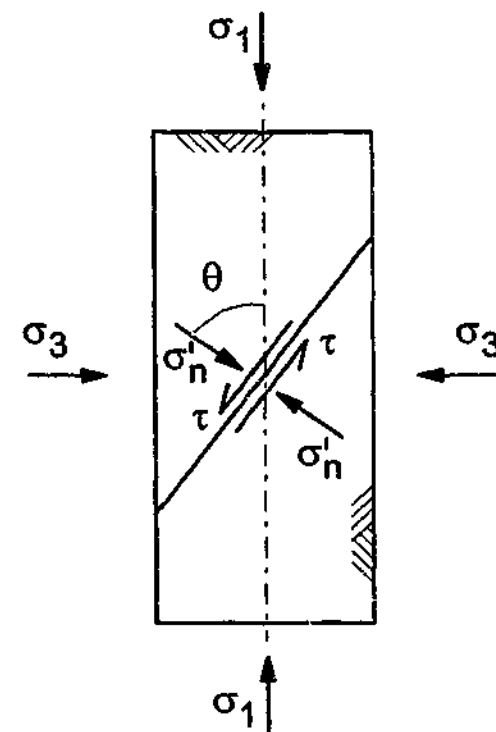


Figure 2-1: Stresses acting on an inclined plane.

Jaeger calculated that for a rock mass containing one or more parallel planar discontinuities at any inclination and subjected to uniaxial compression, failure through the intact rock or along the discontinuities would depend on the angle θ formed between the dip vector of the discontinuity and the direction of the major principal stress, σ_1 . Using two dimensional stress transformation equations, major and minor principal stresses could be included. As shown by Priest (1993),

amongst others, the peak stress required to fail the rock mass along a discontinuity (ignoring porewater pressure) can be calculated from:

$$\sigma_{1d} = \sigma_3 + \frac{2[c_d + \sigma_3 \tan \phi_d]}{\sin 2\theta [1 - \tan \phi_d \tan \theta]}$$

Equation 2-2

where:

- σ_{1d} is the major principal stress along the discontinuity at failure,
- σ_3 is the minor principal stress acting on the rock mass,
- c_d and ϕ_d are the cohesion and friction angle of the discontinuity,
- θ is the acute angle between the unit vector normal to the discontinuity and the major principal axis.

However, there are values of θ for which sliding cannot physically occur. This leads to failure through the intact material. The minimum major principal stress for which shearing through the intact material occurs is given by:

$$\sigma_{1m} = \sigma_3 + \frac{2[c_m + \sigma_3 \tan \phi_m]}{\tan \phi_m + \sqrt{1 + \tan^2 \phi_m}}$$

Equation 2-3

where:

- σ_{1m} is the major principal stress requires to initiate failure through the intact rock,
- σ_3 is the minor principal stress acting on the rock mass, and
- c_m and ϕ_m are the cohesion and friction angle of the intact rock.

The failure stress though the intact rock is independent of joint inclination and defined by a straight horizontal line. The failure stress along a joint varies with inclination of the joint. Therefore, the failure envelope produced by these two equations is the minimum value obtained from equations

2.2 and 2.3 and has the form shown in Figure 2-2, which clearly shows the anisotropic strength of a rock mass containing one joint set.

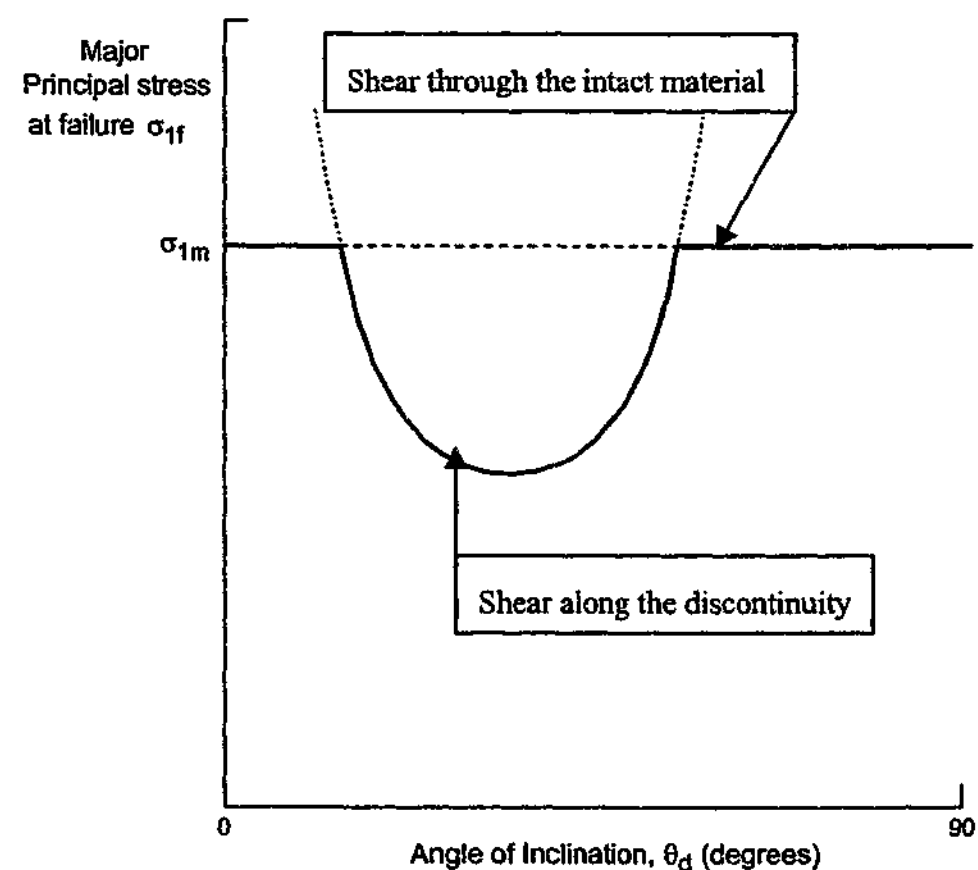


Figure 2-2: Typical failure envelope of a rock mass containing one joint set

Amadei (1988) extended Jaeger's two-dimensional solution to include the intermediate principal stress, σ_2 . The result was a stereographical approach to calculate slip along the joint surface and an analytical solution to the inverse problem, where the range of loading conditions to induce slip along the plane was calculated.

This work, however, covers only rock masses cut by a single joint set. As stated by Amadei, the use of superposition to model the effect of several joint sets on rock mass strength is not mechanically correct. The strength of a rock mass is affected by not only the behaviour of the intact rock and the joints, but also by the interaction between them.

There have been a number of analytical criteria developed to define the modulus of rock masses containing multiple joint sets (e.g. Kulhawy, 1978; Kulhawy and Goodman, 1980; Gerrard, 1982b; Gerrard, 1982a; Fossum, 1985; Yoshinaka et al., 1986; Peres-Rodrigues, 1990; Li, 2000).

However, the deformation of jointed rock masses is not of prime interest to this study and will not be considered further.

2.3 Empirical studies

The development of analytical approaches for the analysis of the strength of rock masses containing multiple joint sets has proven to be difficult. However, the development of rock mass classification systems and empirically based criteria to predict the strength of rock masses is well advanced.

2.3.1 Rock mass classification systems

The development of rock mass classification systems has evolved as a means of identifying, in a qualitative manner, categories of rock that behave in a similar manner in a particular engineering environment. The systems have been largely derived from tunnelling projects in rock masses, where the properties of the rock mass and the successful support systems were recorded. From this, rock mass classification systems were developed to provide details of the support required for similarly classified rock masses in tunnelling operations elsewhere. However, they generally provide little or no guidance on the strength of rock masses for assessment of the performance of foundations, retaining walls and other non-tunnelling related structures. Some of the earlier classification systems are briefly outlined below.

One of the earliest rock mass classification systems was introduced by Terzaghi (1946). He suggested classifying the rock mass into one of a number of groups, so that when the loads in the tunnel were evaluated, suitable steel sets could be selected to support the rock.

Deere (1963) proposed a rock mass classification system using the rock quality designation (RQD). The lengths of the sections of core recovered from drilling into a rock mass that are over 100 mm long are summed and divided by the total length of the core. The RQD is expressed as a percentage of the original core length, and provides an indication of the degree of fracturing.

Wickham et al. (1972) proposed the Rock Structure Rating (RSR) System. This system described the quality of the rock in which a tunnel was to be constructed and was derived empirically from historical data, reviews and evaluations made from published papers. The RSR was used to assess

the support requirements of a tunnel driven through fair to good rock. This method acknowledged the impact of joint inclination with respect to the tunnel direction on the stability of the rock mass. It also considered the rock type and condition and impact of anticipated water inflow.

The above systems provided a basis from which major developments in rock mass classification systems could be made, such as those provided by Bieniawski (1973) and Barton et al. (1974). These systems are widely used and are discussed in greater detail.

There have been more recently proposed classification systems (e.g. Ramamurthy and Arora, 1993). These schemes, in general, have not been widely adopted.

2.3.1.1 The Rock Mass Rating (RMR) system

The Rock Mass Rating (RMR) system was developed by Bieniawski (1973) from the analysis of a number of case studies featuring shallow tunnels in sedimentary rock. Subsequently, the system has been modified to include additional case studies and to conform to international standards and procedures (Bieniawski (1979). The RMR value of a rock mass is obtained by assigning a rating to the following parameters:

- rock quality designation (RQD)
- UCS of the intact rock material
- spacing of discontinuities
- condition of discontinuities
- inclination of discontinuities and
- groundwater conditions

These ratings are summed to give a value out of 100, with better quality rock masses having a higher rating.

The RMR system suffers from the subjectivity, common to all classification systems, in deciding the values of each of the input parameters. RQD can be of limited value in describing rock masses.

For example, a rock mass may have joints spaced at 98 mm, inferring the RQD value is low. However, if the joint spacing is 102 mm, the RQD value is much higher.

Meyers (1994) proposed a modified RMR (MRMR) system. In this system, the RQD rating was replaced with additional points for joint inclination. Meyers found that this system produced better agreement with results from triaxial tests on rock mass samples made from a gypsum cement based material.

An important factor considered by the RMR system is the influence of joint inclination with respect to the inclination of the construction, (as did the RSR system). This acknowledges the potentially anisotropic behaviour of rock masses.

2.3.1.2 The Q system

The Q system was originally developed by Barton et al. (1974) based on the review of around 200 tunnelling case studies. The Q system classifies rock masses as follows:

$$Q = \frac{RQD}{J_n} \times \frac{J_r}{J_a} \times \frac{J_w}{SRF}$$

Equation 2-4

where:

- *RQD* = rock quality designation
- *J_n* = joint set number
- *J_r* = joint roughness number
- *J_a* = joint alteration number
- *J_w* = joint water reduction factor and
- *SRF* = stress reduction factor

Barton provides charts and tables that allow the assessment of the parameters listed above to be made from observations of the rock mass. The Q value calculated from the above parameters is

then used to designate an appropriate tunnel support system found to be successful based on the case studies.

The Q system has been expanded for use in predicting P-wave seismic velocity, static modulus of deformation and joint fluid movement, as described in Barton (2002).

2.3.1.3 GSI System

The use of a classification scheme as a basis of selecting parameters for input into a rock mass strength criterion has been incorporated in the Geological Strength Index (GSI) proposed by Hoek et al. (1995). This criterion is discussed in Section 2.3.2.3.

2.3.2 Rock mass strength criteria

Empirically based rock mass strength criteria have generally been developed from observing rock mass behaviour during *in-situ* or laboratory testing and fitting a curve to the measured behaviour. Several such criteria have been developed for intact rock (e.g. Fairhurst, 1964; Hoek and Brown, 1980a; Johnston, 1985). The main contributions in the development of rock mass strength criteria have come from Hoek and Brown (1980a), Hoek et al. (1992), Palmstrom (1996) and Hoek and Brown (1997), with subsequent refinements by Marinos and Hoek (2000).

2.3.2.1 The original Hoek-Brown criterion

Hoek and Brown (1980a) proposed an empirical criterion to estimate the strength of a rock mass based on the results of tests on intact rock and rockfill. They proposed that strength could be assessed from:

$$\sigma_1' = \sigma_3' + \sigma_c \left(m \frac{\sigma_3'}{\sigma_c} + s \right)^2 \tag{Equation 2-5}$$

where:

- σ_1' is the major principal effective stress at failure

- σ_3' is the minor principal effective stress at failure
- σ_c is the uniaxial compressive strength of the intact rock within the mass
- m is an empirical constant dependent on rock type and
- s is an empirical constant that varies between 0 to 1 depending on joint spacing

The values selected for the empirical constants, m and s , were tabulated in accordance with the type of rock and the quality of the rock mass. To assist users of this criterion, the rock mass classification values obtained using the RMR or Q system could also be used in selection of the empirical constants. The suggested values for the empirical constants based on the rock type and rock mass quality are presented in Figure 2-3.

Empirical failure criterion $\sigma_1' = \sigma_3' + (m\sigma_3' + s\sigma_c)^2$ σ_1' = major principal stress σ_3' = minor principal stress σ_c = uniaxial compressive strength of intact rock m, s = empirical constants	Carbonate rocks with well developed crystal cleavage, e.g. dolomite, limestone and marble	Lithified argillaceous rocks, e.g. mudstone, siltstone, shale and slate (tested normal to cleavage)	Arenaceous rocks with strong crystals and poorly developed crystal cleavage, e.g. sandstone and quartzite	Fine grained polymineralic igneous crystalline rocks, e.g. andesite, diorite, diorite and rhyolite	Coarse grained polymineralic igneous and metamorphic crystalline rocks, e.g. amphibolite, gabbro, gneiss, granite, noritic and quartzite
Intact rock samples Laboratory size samples free from pre-existing fractures Bieniawski, 1974b (CSIR)* rating 100 Barton et al., 1974 (NGI)† rating 500	$m = 7$ $s = 1$	$m = 10$ $s = 1$	$m = 15$ $s = 1$	$m = 17$ $s = 1$	$m = 25$ $s = 1$
Very good quality rock mass Tightly interlocking undisturbed rock with rough unweathered joints spaced at 1 to 3 m Bieniawski, 1974b (CSIR) rating 85 Barton et al., 1974 (NGI) rating 100	$m = 3.5$ $s = 0.1$	$m = 5$ $s = 0.1$	$m = 7.5$ $s = 0.1$	$m = 8.5$ $s = 0.1$	$m = 12.5$ $s = 0.1$
Good quality rock mass Fresh to slightly weathered rock, slightly disturbed with joints spaced at 1 to 3 m Bieniawski, 1974b (CSIR) rating 65 Barton et al., 1974 (NGI) rating 10	$m = 0.7$ $s = 0.004$	$m = 1$ $s = 0.004$	$m = 1.5$ $s = 0.004$	$m = 1.7$ $s = 0.004$	$m = 2.5$ $s = 0.004$
Fair quality rock mass Several sets of moderately weathered joints spaced at 0.3 to 1 m, disturbed Bieniawski, 1974b (CSIR) rating 44 Barton et al., 1974 (NGI) rating 1	$m = 0.14$ $s = 0.0001$	$m = 0.20$ $s = 0.0001$	$m = 0.30$ $s = 0.0001$	$m = 0.34$ $s = 0.0001$	$m = 0.50$ $s = 0.0001$
Poor quality rock mass Numerous weathered joints at 30 to 500 mm with some gouge. Clean, compacted rockfill Bieniawski, 1974b (CSIR) rating 23 Barton et al., 1974 (NGI) rating 0.1	$m = 0.04$ $s = 0.00001$	$m = 0.05$ $s = 0.00001$	$m = 0.08$ $s = 0.00001$	$m = 0.09$ $s = 0.00001$	$m = 0.13$ $s = 0.00001$
Very poor quality rock mass Numerous heavily weathered joints spaced at 50 mm with gouge. Waste rock Bieniawski, 1974b (CSIR) rating 3 Barton et al., 1974 (NGI) rating 0.01	$m = 0.007$ $s = 0$	$m = 0.010$ $s = 0$	$m = 0.015$ $s = 0$	$m = 0.017$ $s = 0$	$m = 0.025$ $s = 0$

* CSIR Commonwealth Scientific and Industrial Research Organization.
† NGI Norway Geotechnical Institute.

Figure 2-3: Relationship between rock mass quality and empirical constants (after Hoek, 1983).

Hoek (1983) found that this criterion consistently under predicted rock mass strength. He therefore suggested that the results obtained could be considered to be lower bound values.

The strength of intact rock can be estimated using the Hoek-Brown criterion in equation 2-5 by setting $s=1$. The strength envelope has a parabolic form, and models the strength of hard rocks reasonably well. This contrasts with the Mohr-Coulomb criterion for soils, which predicts a strength envelope with a linear form. It would seem reasonable to expect the strength envelope for hard soils/soft rocks would lie between these two extremes (Johnston, 1985).

Johnston (1985) proposed the following criterion for intact rock strength following work carried out on soft rock:

$$\sigma_1 = \left[\frac{M}{B} \sigma_3 + 1 \right]^B \quad \text{Equation 2-6}$$

where:

- the constant $B=1-0.0172(\log q_u)^2$, where q_u is the intact rock strength in kPa and
- the constant $M=2.065+0.170(\log q_u)^2$ for lithified argillaceous rocks

The intact rock strengths typical for weathered Melbourne Mudstone range between 1 MPa and 10 MPa. The value of B therefore ranges between 0.85 and 0.72, which produces a flatter strength envelope than that suggested in the original Hoek-Brown equation, which produces a parabolic envelope.

2.3.2.2 The modified Hoek-Brown criterion

The historical development of the Hoek-Brown criterion is summarised in Hoek and Brown (1997). Modifications were made to the original Hoek-Brown criterion as it gained widespread acceptance in industry. These modifications were required so the Hoek-Brown equation could be applied to a wider range of rock mass qualities. An early modification was presented in Hoek and Brown (1988) where relationships between m and s and a modified form of RMR were established. The distinction between disturbed and undisturbed rock masses was introduced, as was a means of estimating the deformation modulus of rock masses.

One of the deficiencies of the original Hoek-Brown criterion was that the criterion indicated a non-zero tensile strength for heavily fractured rock masses that should have none. This prompted the introduction of equation 2-7 by Hoek et al. (1992).

$$\sigma_1' = \sigma_3' + \sigma_c \left(m_b \frac{\sigma_3'}{\sigma_c} \right)^a \quad \text{Equation 2-7}$$

where:

- σ_1' is the major principal effective stress at failure,
- σ_3' is the minor principal effective stress at failure,
- σ_c is the uniaxial compressive strength of the intact rock within the mass, and
- m_b and a are constants, which depend on the composition, structure and surface conditions of the rock mass.

This version of the Hoek-Brown criterion set the joint spacing variable, s , to zero and also provided a simpler means of selecting the empirical constants based on the composition, structure and surface conditions of the rock mass as shown in Figure 2-4 and Figure 2-5.

Grain size	Sedimentary			Metamorphic		Igneous		
	Carbonate	Detrital	Chemical	Carbonate	Silicate	Felsic	Mafic	Mafic
Coarse	Dolomite 10.1	Conglomerate (20)		Marble 9.3	Gneiss 29.2	Granite 32.7	Gabbro 25.8	Norite 21.7
Medium	Chalk 7.2	Sandstone 18.8	Chert 19.3		Amphibolite 31.2		Dolerite 15.2	
Fine	Limestone 8.4	Siltstone 9.6	Gypstone 15.5		Quartzite 23.7	Rhyolite (20)	Andesite 13.9	Basalt (17)
Very fine		Claystone 3.4	Anhydrite 13.2		Slate 11.4			

Values shown were derived from statistical analysis of triaxial test data for each rock type. Values in parenthesis have been estimated.

Figure 2-4: Values for empirical constant, m_b (after Hoek et al., 1992).

MODIFIED HOEK-BROWN FAILURE CRITERION		SURFACE CONDITION				
$\sigma_1 = \sigma_3 + \sigma_c \left(m_b \frac{\sigma_3}{\sigma_c} \right)^a$ <p> σ_1 = major principal effective stress at failure σ_3 = minor principal effective stress at failure σ_c = uniaxial compressive strength of <i>intact</i> pieces in the rock mass m_b and a are constants which depend on the composition, structure and surface conditions of the rock mass </p>		VERY GOOD	GOOD	FAIR	POOR	VERY POOR
		Unweathered, discontinuous, very tight aperture, very rough surface, no infilling	Slightly weathered, continuous, tight aperture, rough surface, iron staining to no infilling	Moderately weathered, continuous, extremely narrow, smooth surfaces, hard infilling	Highly weathered, continuous, very narrow, polished/slickensided surfaces, hard infilling	Highly weathered, continuous, narrow, polished/slickensided surfaces, soft infilling
STRUCTURE						
	BLOCKY - well interlocked, undisturbed rock mass; large to very block size	m_b/m_i a	0.7 0.8	0.5 0.35	0.3 0.4	0.1 0.45
	VERY BLOCKY - interlocked, partially disturbed rock mass; medium block sizes	m_b/m_i a	0.3 0.4	0.2 0.45	0.1 0.5	0.04 0.5
	BLOCKY/SEAMY - folded and faulted, many intersecting joints; small blocks	m_b/m_i a		0.08 0.5	0.04 0.5	0.01 0.55
	CRUSHED - poorly interlocked, highly broken rock mass; very small blocks	m_b/m_i a		0.03 0.5	0.015 0.55	0.003 0.6
						0.001 0.65

Figure 2-5: Table showing values of m_b/m_i and a (after Hoek et al., 1992).

2.3.2.3 The Hoek-Brown Geological Strength Index (GSI)

The Hoek-Brown criterion was modified further with the concept of the Geological Strength Index (GSI) introduced by Hoek et al. (1995). A range of GSI values appropriate for a particular rock mass could be estimated from the chart shown in Figure 2-6, based on the rock mass structure and joint surface conditions. The selected values of GSI were used to calculate the input values for the generalised criterion shown in equation 2-8.

$$\sigma_1 = \sigma_3 + \sigma_{ci} \left(m_b \frac{\sigma_3}{\sigma_{ci}} + s \right)^a \quad \text{Equation 2-8}$$

where:

- σ_1 is the major principal effective stress at failure,
- σ_3 is the minor principal effective stress at failure,
- σ_{ci} is the uniaxial compressive strength of the intact rock within the mass,
- m_b is the value of the Hoek-Brown constant, m , for the rock mass, and
- s and a are constants, which depend on the characteristics of the rock mass.

A suitable range of GSI values for the rock mass are selected from Figure 2-6 and used to calculate m_b and s using equations 2-9 and 2-10.

$$m_b = m_i \exp\left(\frac{GSI - 100}{28}\right) \quad \text{Equation 2-9}$$

$$s = \exp\left(\frac{GSI - 100}{9}\right) \quad \text{Equation 2-10}$$

For poor quality rock (arbitrarily chosen where $GSI < 25$):

$$s = 0 \quad \text{Equation 2-11}$$

$$a = 0.65 - \frac{GSI}{200} \quad \text{Equation 2-12}$$

The maximum value of a remains at 0.65, with this increased value of a acknowledging the more linear behaviour of 'scil-like' rock masses. However, this value of a is still less than the 0.72 to 0.85 suggested using the Johnston criterion for siltstones. The GSI criterion may therefore have difficulty replicating the strength envelope for softer, argillaceous rocks.

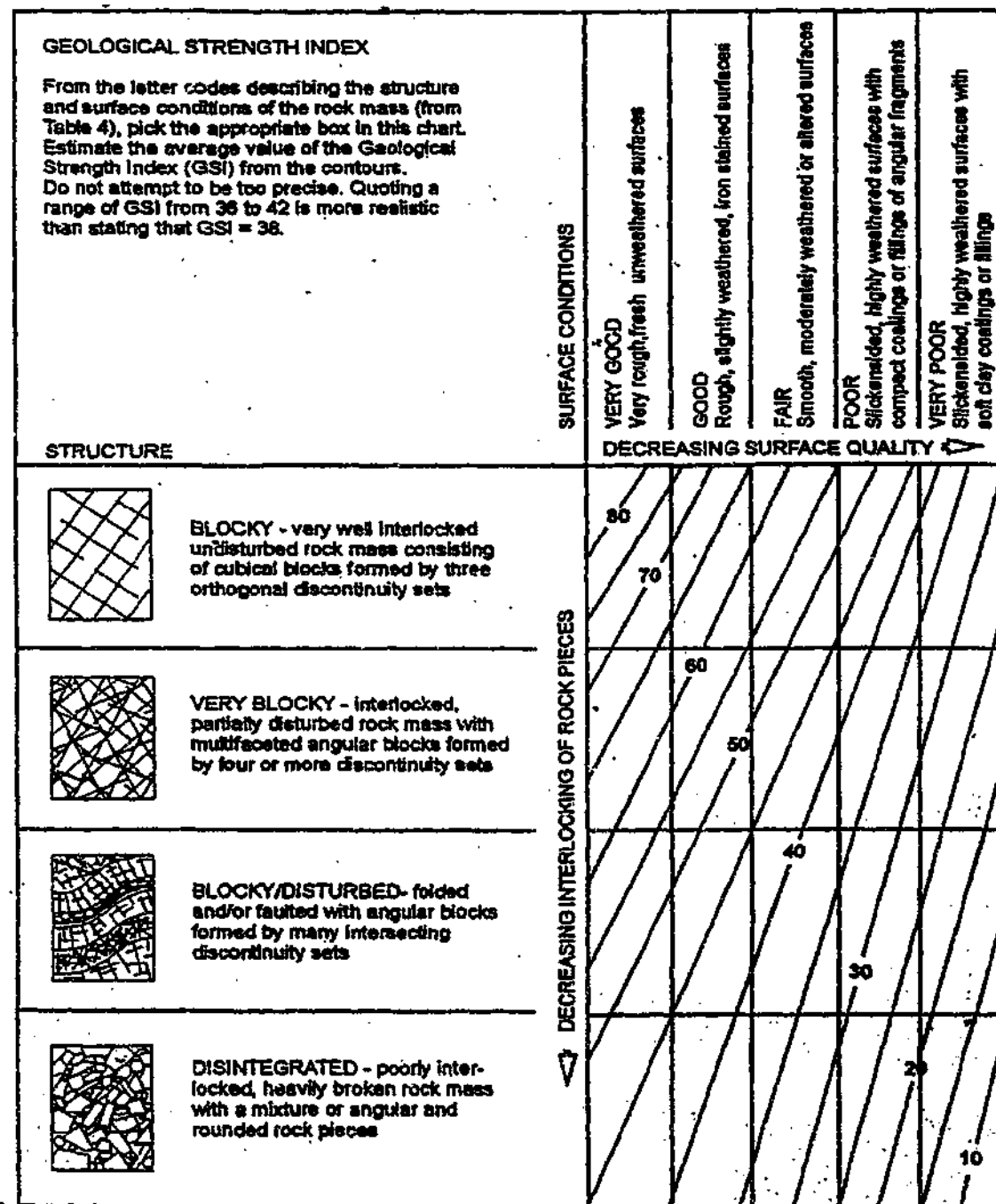


Figure 2-6: Chart showing GSI values based on rock mass structure and joint surface conditions (after Hoek and Brown, 1997).

There is still a degree of subjectivity associated with using the GSI system. This author carried out a very limited survey to assess the subjectivity of the estimation of GSI values. Five members of the Geomechanics group at Monash University were provided with the chart in Figure 2-6 and asked to estimate the GSI value of 13 rock masses from photos. These photos were of outcrops of sedimentary rocks containing a number of discontinuities, an example of which is shown in Figure 2-7.

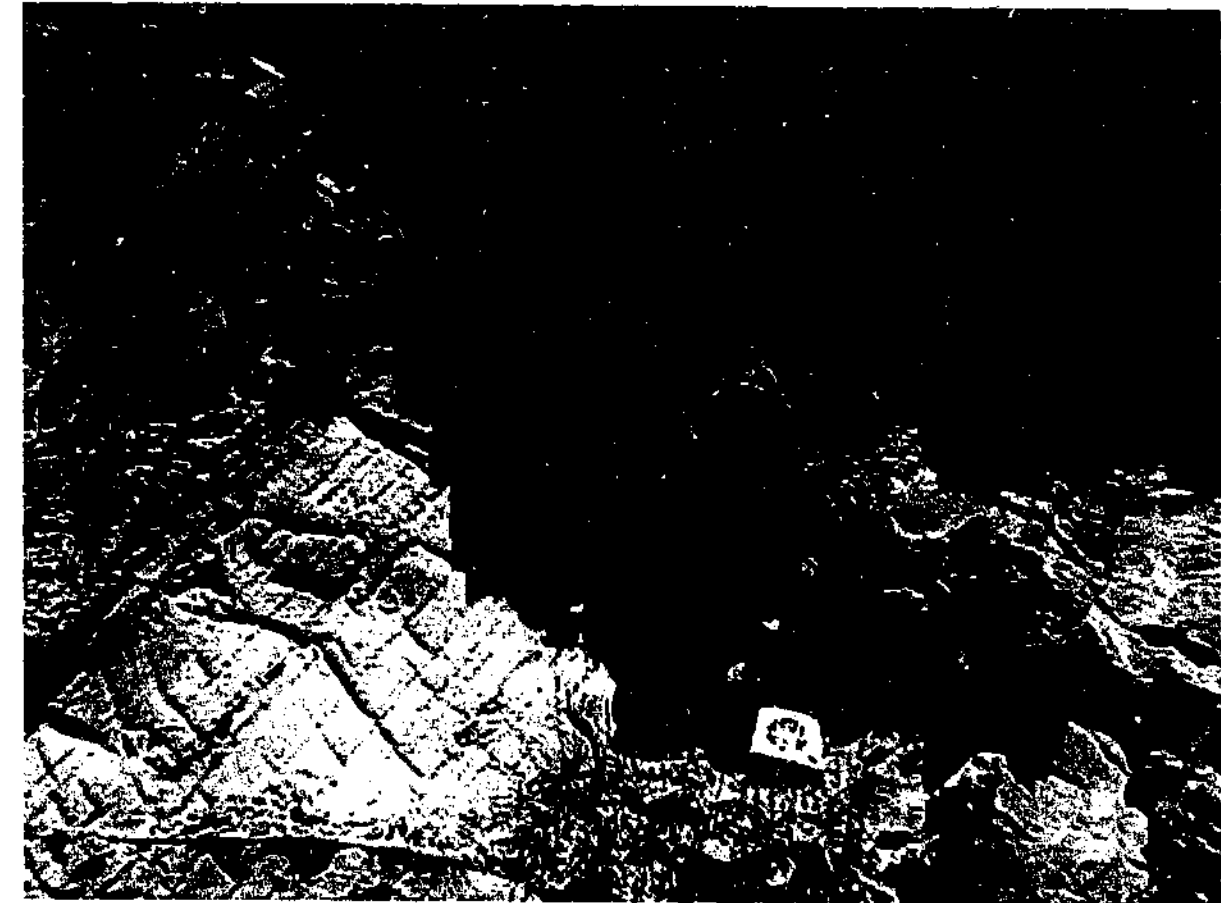


Figure 2-7: Sample photo of rock mass used in survey.

The experience of the survey participants ranged from new postgraduates with no working experience to members of staff with a high level of understanding of rock mass classification. It was found the difference in estimated GSI values for each rock mass varied, on average, by between 10 and 40. For example, the estimated GSI values for the rock mass shown in Figure 2-7 ranged between 40 and 75. It is acknowledged that the classification of rock masses from photographs is not ideal. However, this survey demonstrated the same photograph could produce a wide range of GSI values from people with a wide range of experience.

One attempt to provide a more quantitative basis for evaluating GSI was proposed by Sonmez and Ulusay (1999), based on the back-analysis of slope instability case histories. They introduced a structure rating based on the volumetric joint count to take account of the influence of scale. They also introduced a surface condition rating, based on joint roughness, weathering and infilling in an attempt to make the selection of joint surface conditions more rigorous. The modified GSI chart is presented in Figure 2-8.

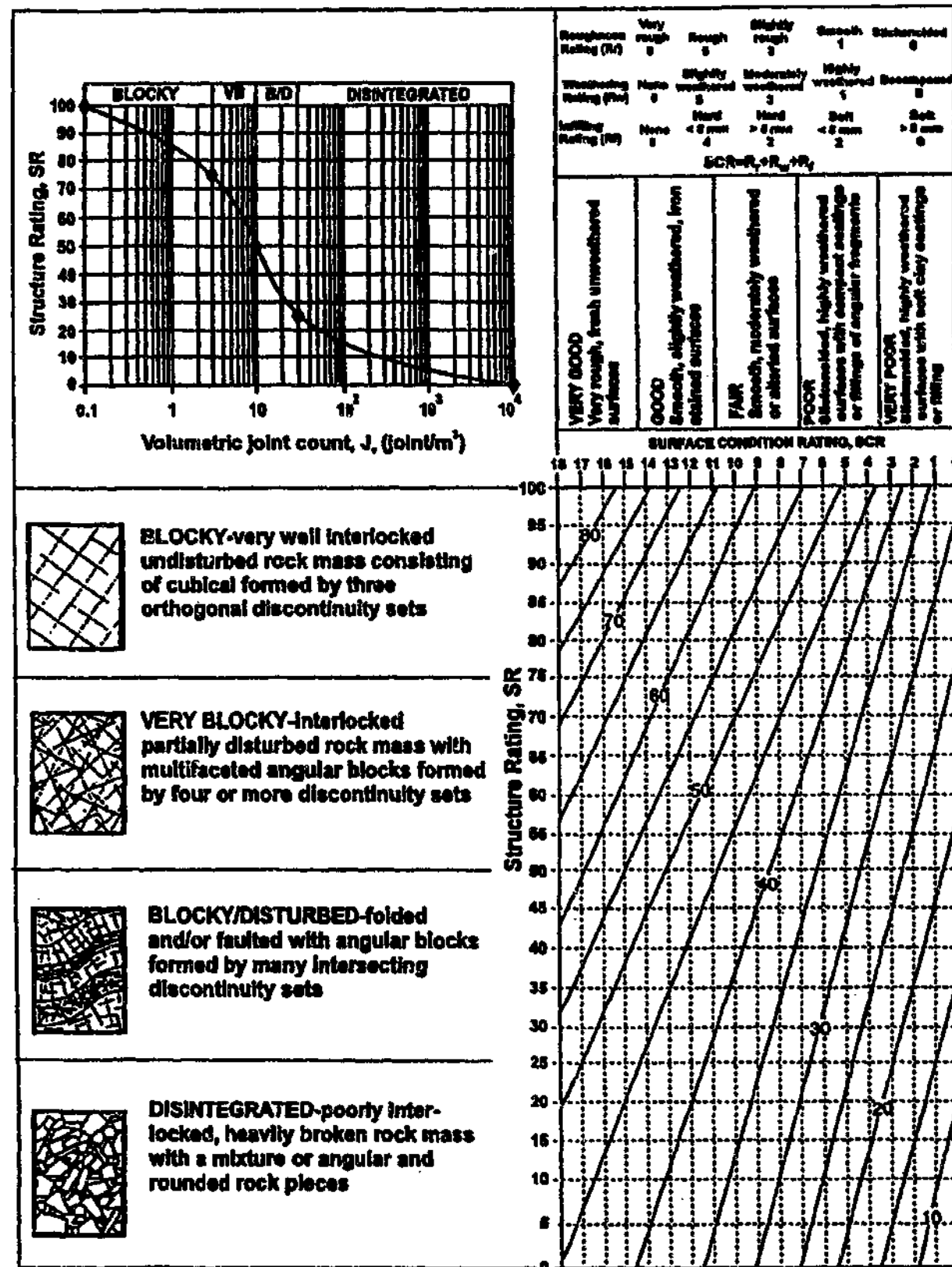


Figure 2-8: Modified GSI chart to consider structure and joint surface ratings (after Sonmez and Ulusay, 1999).

The ranges of GSI typical for various heterogeneous rock masses were discussed in Marinis and Hoek (2000). They found the most common range of GSI values for bedded and fractured siltstone, (hence possibly for Melbourne Mudstone), is between 20 and 45, as shown in Figure 2-9.

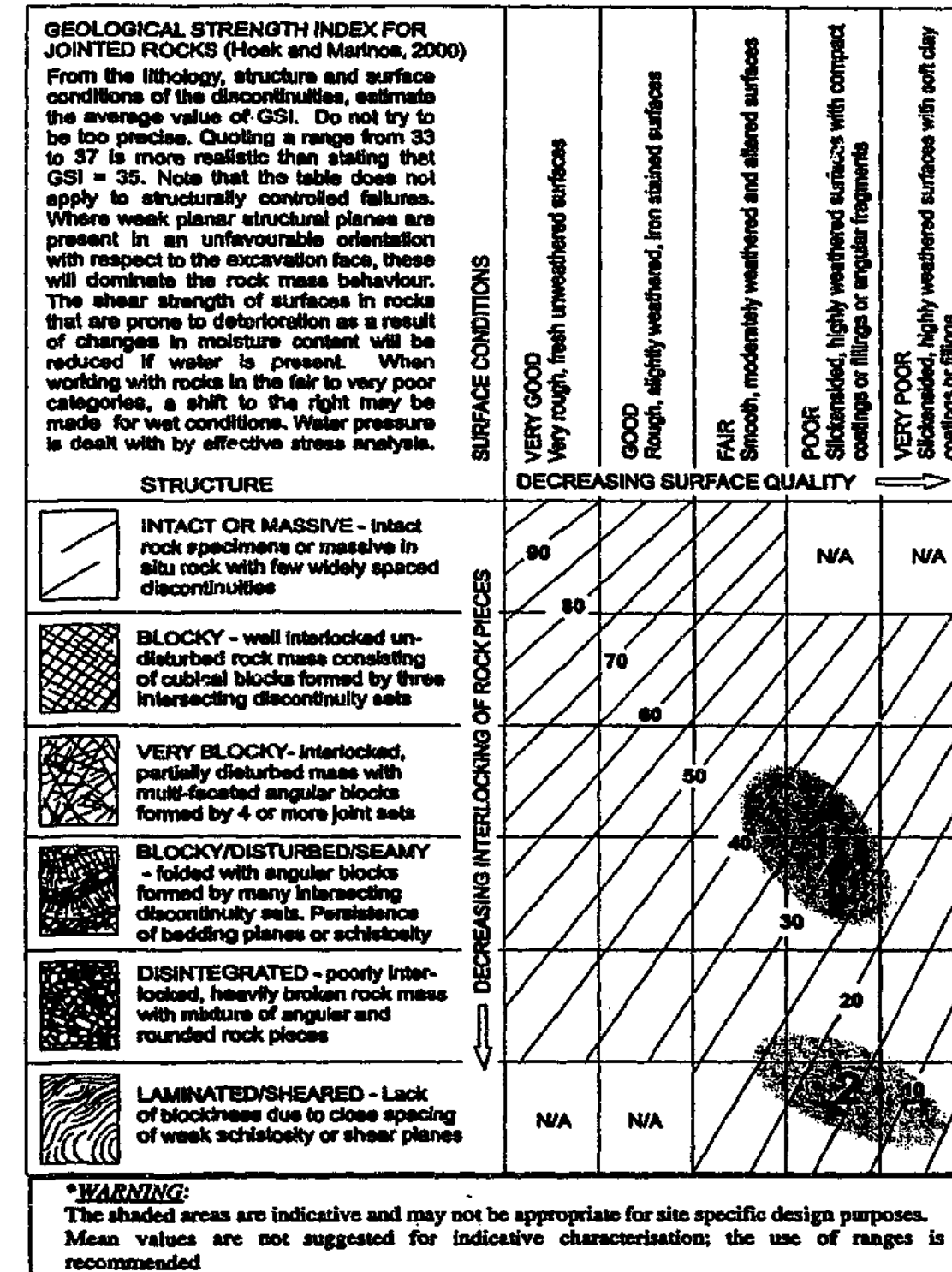


Figure 2-9: Typical GSI values for siltstones (after Marinis and Hoek, 2000).

The application of the charts shown in Figure 2-6, Figure 2-8 and Figure 2-9 can be illustrated by the following example. Consider a rock mass comprising bedded, fractured and weathered siltstone, typical of near surface Melbourne Mudstone. Assume the rock mass contains two to three joint sets that are smooth and moderately weathered, and are spaced at about 30 mm to 70 mm. The classification of such a rock mass, using Figure 2-6 may be judged to be blocky and fair, suggesting GSI values between 45 and 65. The influence of scale is not considered.

Using the modified chart in Figure 2-8, the range of GSI values judged appropriate for the rock mass described above would be between 37 and 42. The reduction in GSI values from those suggested in Figure 2-6 results from considering the joint spacing within the rock mass.

This agrees well with the range calculated by Sonmez and Ulusay (1999), but is significantly lower than the estimation from the chart in Figure 2-6. This is because siltstone in the field can rarely be described as blocky and rarely are the joints free of alteration and infill.

Therefore, the GSI criterion in its various forms provides a simple and relatively concise system for estimating rock mass strength from visual assessment.

2.3.2.4 Rock Mass Index (RMi)

The Rock Mass index (RMi) was developed by Palmstrom (1996) in an attempt to characterise the strength of jointed rock masses and is based on the principal that the strength of a rock mass is reduced by jointing. The RMi does not consider the effect of joint inclination or the anisotropic behaviour of rock masses. RMi is expressed as:

$$RMi = \sigma_c \cdot JP \quad \text{Equation 2-13}$$

where:

- σ_c is the UCS of the intact rock measured on 50 mm samples, and
- JP is the jointing parameter.

The methodology of the RMi is shown in Figure 2-10.

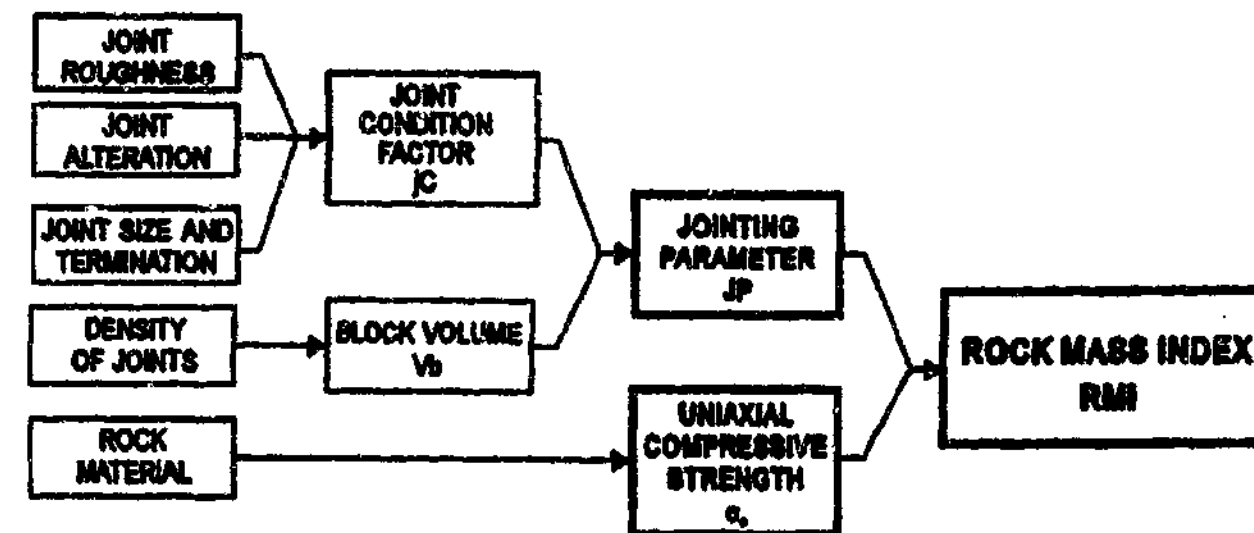


Figure 2-10: Rock mass parameters required for RMi.

The jointing parameter is a strength reduction factor representing the block size and the condition of the joint faces (assessed from their roughness and alteration) and the properties of the joints, (joint density, size and persistence).

It should be noted that rock masses might not exhibit anisotropic behaviour. As discussed earlier, the scale of the rock mass will influence the degree of anisotropy. However, failure to acknowledge the possibility of anisotropic behaviour may result in an inaccurate assessment of rock mass strength.

2.4 Laboratory studies

2.4.1 Introduction

The scientific literature contains many examples of laboratory studies that have investigated the behaviour of jointed rock masses. Some of these have been used to identify failure mechanisms occurring in the rock mass, while others have investigated the changes in the behaviour of samples as a result of introducing joints into intact rock samples.

A review of the literature has identified two commonly adopted laboratory techniques for testing rock masses. These are triaxial testing and unconfined compressive strength (UCS) testing. A

brief review of some of the many studies involving triaxial and UCS testing is presented in Section 2.4.2.

The use of direct shear testing has not been widely applied to the testing of rock masses. Examples of studies that have adopted this approach are described in Section 2.4.3.

One of the main challenges associated with testing rock masses is obtaining representative samples. Some studies have tested rock masses *in-situ* (e.g. Chappell, 1984; Miyaike et al., 1993), while others have used samples recovered during field investigations in laboratory tests (e.g. Natau et al., 1995). The recovery of rock mass samples from the field for laboratory testing is usually difficult and it is often not possible to obtain enough similar samples to allow parametric studies to be conducted.

Other investigations (e.g. Ladanyi and Archambault, 1970; Einstein and Hirschfeld, 1973; Meyers, 1994; Kulatilake et al., 1997; Singh, 1997) have tested rock masses made from synthetic materials. The fabrication of jointed rock mass samples from synthetic materials provides a means via which such parametric studies can be carried out more readily and without the inherent variability present in naturally occurring samples. Ideally, the synthetic material adopted for testing should have similar intact engineering properties as the *in-situ* material it aims to model. The use of synthetic rock also has the advantage that joint sets of known and relatively constant characteristics, such as inclination, roughness, etc, can be accurately cut into the intact blocks.

2.4.2 Triaxial and UCS testing

Most of the studies of rock mass behaviour have utilised triaxial testing and unconfined compressive strength (UCS) testing techniques (e.g. Einstein and Hirschfeld, 1973; Ryncarz and Nawrot, 1976; Meyers, 1994).

One attraction of conducting triaxial or UCS tests is that they are relatively inexpensive to perform and the equipment is readily available. Suggested test methods for intact rock are set out in Brown (1981).

The application of triaxial testing techniques to intact rock samples often requires a higher confining pressure than testing of soil because of the need to simulate a much deeper environment.

The test equipment also needs to be stronger and stiffer than that used to test soils, as the rock strength and stiffness is, in general, much higher than that of soils. This has led to the development of the Hoek cell, a high strength triaxial cell capable of applying very high pressures, but which has no control or measurement over drainage and porewater pressure. The dimensions of intact samples that have been tested in Hoek cells have ranged from core of 12 mm diameter by 25 mm long (McLamore and Gray, 1967) to core of 150 mm diameter and 300 mm long (Jaeger, 1970).

High-pressure triaxial devices that allow control of drainage and porewater pressures have also been developed and used to test intact and fractured rock samples (e.g. Chiu, 1981; Wardlaw, 1992).

The logical progression has been to use Hoek cells that can accommodate larger samples to test jointed rock masses. For example, Meyers (1994) constructed a Hoek cell capable of testing samples 150 mm in diameter and 300 mm long. The Hoek cell has allowed researchers to investigate the effects of confining pressure on the strength and deformation of the rock mass using a relatively simple and expedient test. However, observation of the sample during the test is not usually possible.

An early study of the mechanical behaviour of rock masses using triaxial testing was described by McLamore and Gray (1967). They attempted to define the compressive strength of shales and slates for different inclinations of the bedding plane, called the plane of anisotropy. They found that the strength envelope obtained from their testing was similar to that calculated from the single plane of weakness theory proposed by Jaeger (1960) (see section 2.2). They also found that failure usually occurred in one of three ways, namely:

- Shear faulting, both along and across the bedding or cleavage planes. This mechanism occurred at relatively low confining pressures.
- "Plastic" flow or slip along the bedding plane. This mechanism occurred at relatively high confining pressures.
- Failure due to the formation of kink bands, which consisted of rotation of the bedding planes. Again, this was observed at relatively high confining pressures.

This study also indicated that the number of joint sets had an impact on rock mass strength, with rock masses with no joints (intact rock) being stronger than rock masses with one joint set, which in turn were stronger than rock masses with two joint sets.

Jaeger (1970) conducted triaxial tests on core samples of jointed Panguna andesite. He found that the strength of the jointed rock mass was lower than that of the intact rock, but greater than that of the joints. Movement occurred on a number of planes, although as strain increased, one of these planes became dominant. He also observed that the failure surface was not planar.

Einstein et al. (1970) investigated the influence of jointing on rock mass behaviour and failure by conducting triaxial tests on synthetic rock mass samples. The samples had dimensions of 2" by 4" by 8" (50 mm by 100 mm by 200 mm) and were made from a material comprising Hydrocal B11 gypsum, water and celite. They found that the strength of the samples was lowest when the sample contained two orthogonal joint sets. Samples containing one joint set perpendicular to the major principal stress were stronger, while those containing one joint set parallel to the major principal stress were even stronger. However, none of the jointed rock masses were as strong as the intact rock. They found that the strength and deformability of a jointed rock mass was dependent upon:

- confining stress, where at high values, the failure mode changed from sliding along a favourably inclined joint to shear through the intact material
- joint properties
- material properties of the intact rock
- joint inclination, where samples with vertical joints were stronger than those with horizontal joints and
- joint spacing, where samples with more closely spaced joints had lower strength

Since the 1970's, laboratory studies have investigated rock mass behaviour from a number of perspectives. Some studies have used laboratory testing to develop or improve rock mass strength criteria (e.g. Hoek and Brown, 1980b; Desai and Salami, 1987; Kulatilake et al., 1997), while others have used laboratory testing to refine rock mass classification systems (e.g. Meyers, 1994). Some studies have investigated the effect of joint inclination on strength of rock masses containing one joint set (e.g. Bagheripour and Mostyn, 1996; Tien et al., 1999), while others have used triaxial testing to determine the mechanical properties of rocks for specific projects (e.g. Miyaike et al.,

1993). The effect of multiple joint sets on rock mass strength has been investigated by Singh (1997) and others. There have been studies that have involved the testing of rock masses under true triaxial conditions (e.g. Chang and Haimson, 2000). These studies have either confirmed or refined existing knowledge.

Laboratory testing has also been used to identify modes of failure. Ladanyi and Archambault (1972) constructed jointed rock mass samples from prisms with a square cross-section. The rock masses were assembled by placing the prisms in a brickwork type pattern, where the primary joint set was the through-going joints and the cross joint set was that between the primary joints. These samples were then subjected to various lateral stresses and loaded to failure. Photographs of the typical failures observed in these tests are presented in Figure 2-11.

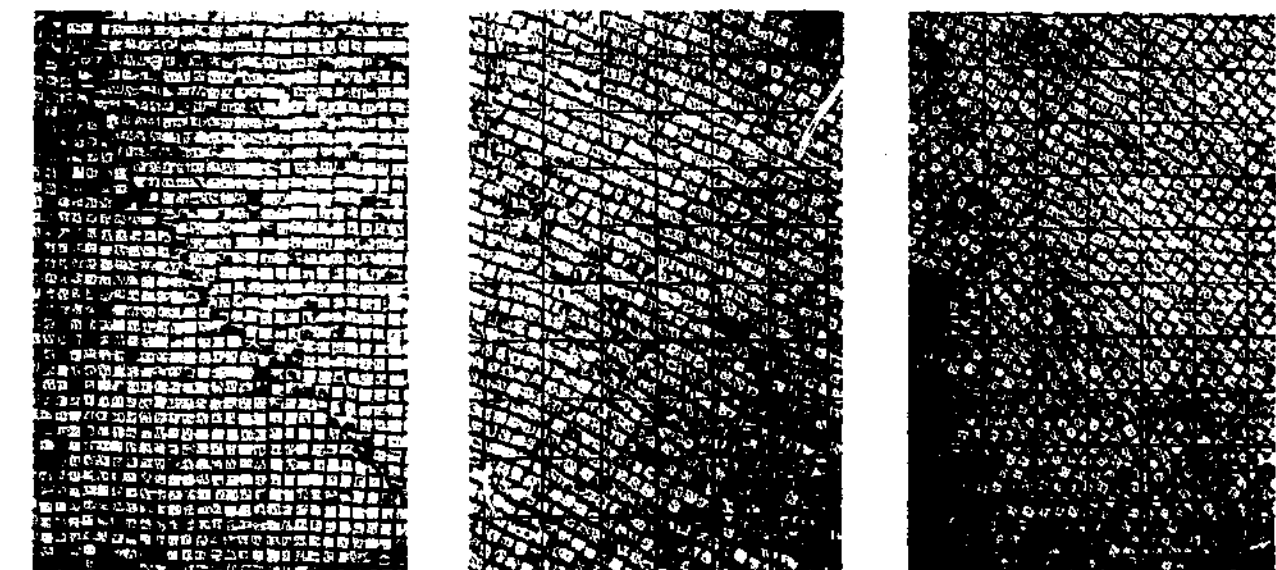


Figure 2-11: Three failure types, from left to right, shear plane, shear zone and kink band failure (after Ladanyi and Archambault, 1970).

Three failure types, dependent on the inclination of the joints formed by the prisms, were observed, namely:

- Shear plane failure, where the development of a failure plane through the prisms and along the joints was observed. This failure occurred where the joints dipped at an angle sub-parallel to the applied principal stresses.

- Shear zone failure, where localised crushing of some of the prisms was observed. This failure occurred where the angle between the direction of the principal applied stress and the primary joints was typically less than 45° .
- Kink band failure, where rotation of the prisms was observed. This failure occurred where the angle between the direction of the principal applied stress and the primary joints was typically greater than 45° .

This testing confirmed that the inclination of the joints had a significant influence on rock mass behaviour and the mechanisms by which the rock mass failed. The results of these tests also showed that the strength of the rock mass was lower than that of the intact rock, even when the dip of the joints was favourable (i.e. parallel to the major and minor principal stresses).

Singh (1997) tested rock mass samples in uniaxial compression. He found that the strength and deformation of the samples were influenced by the inclination of the joints, i.e. the sample properties were anisotropic. He identified four modes of failure for jointed rock mass samples subjected to uniaxial compression, namely splitting, shearing, rotation and sliding.

Kulatilake et al. (1997) also identified three failure modes in their testing, namely tensile failure through the intact material, combined shear and tensile failure through the joints and a mixed failure mode through the intact material and the joints. They observed that the failure mode that occurred was dependent on the inclination of the joints.

The studies described above have provided information on rock mass behaviour under conditions provided by the test arrangements. This has improved our understanding of the impact of joints on overall rock mass behaviour, including details of the failure mechanisms that can occur. However, these test methods may not provide boundary conditions and stress paths that replicate field conditions and hence direct application of the results of this testing to field conditions may be inappropriate and/or inaccurate. These concerns are discussed in Section 3.2. Nevertheless, these tests clearly indicate the possible reduction in strength and stiffness resulting from the introduction of joints to intact rock samples.

2.4.3 Direct shear testing

One of the earliest published papers on direct shear testing of rock mass samples was presented by Lajtai (1969b). In this study, direct shear tests on synthetic rock samples were carried out under constant normal load conditions. The samples were 3" (75 mm) cubes made from either plaster or kaolin-plaster. Both intact samples and samples containing the joint configurations shown in Figure 2-12 were tested.

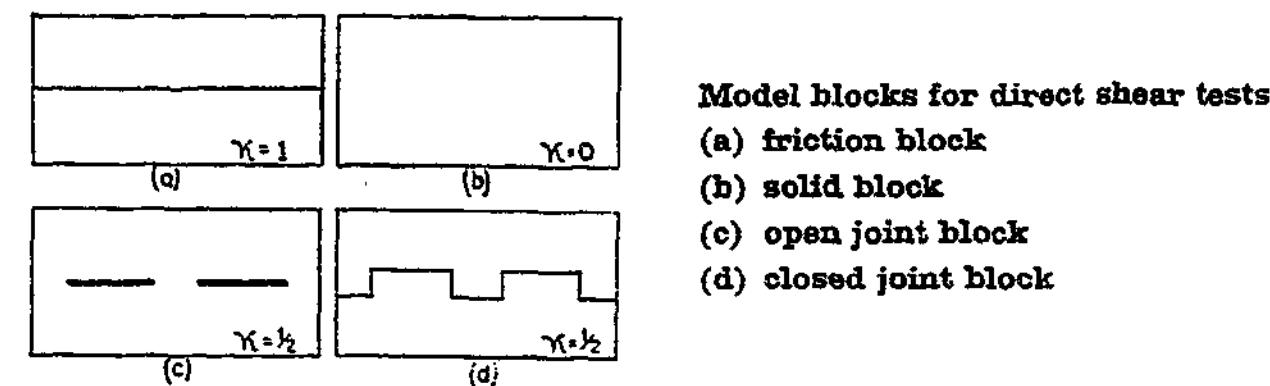


Figure 2-12: Rock mass configurations (after Lajtai, 1969b).

These joint configurations could not be considered to be representative of real joints. However, this study provided some valuable insights into the impact of joint roughness and persistence on sample strength.

Lajtai found that the direct shear strength of the intact rock was controlled by:

- the tensile strength, T_s
- the cohesion, S_0
- the angle of internal friction, ϕ_i
- the residual (ultimate) friction angle, ϕ_u and
- the normal stress acting on the shear plane, σ_n

The testing identified three failure mechanisms, namely:

- failure by tension in accordance with:

$$\tau_a = [T_s(T_s - \sigma_a)]^{0.5} \quad \text{Equation 2-14}$$

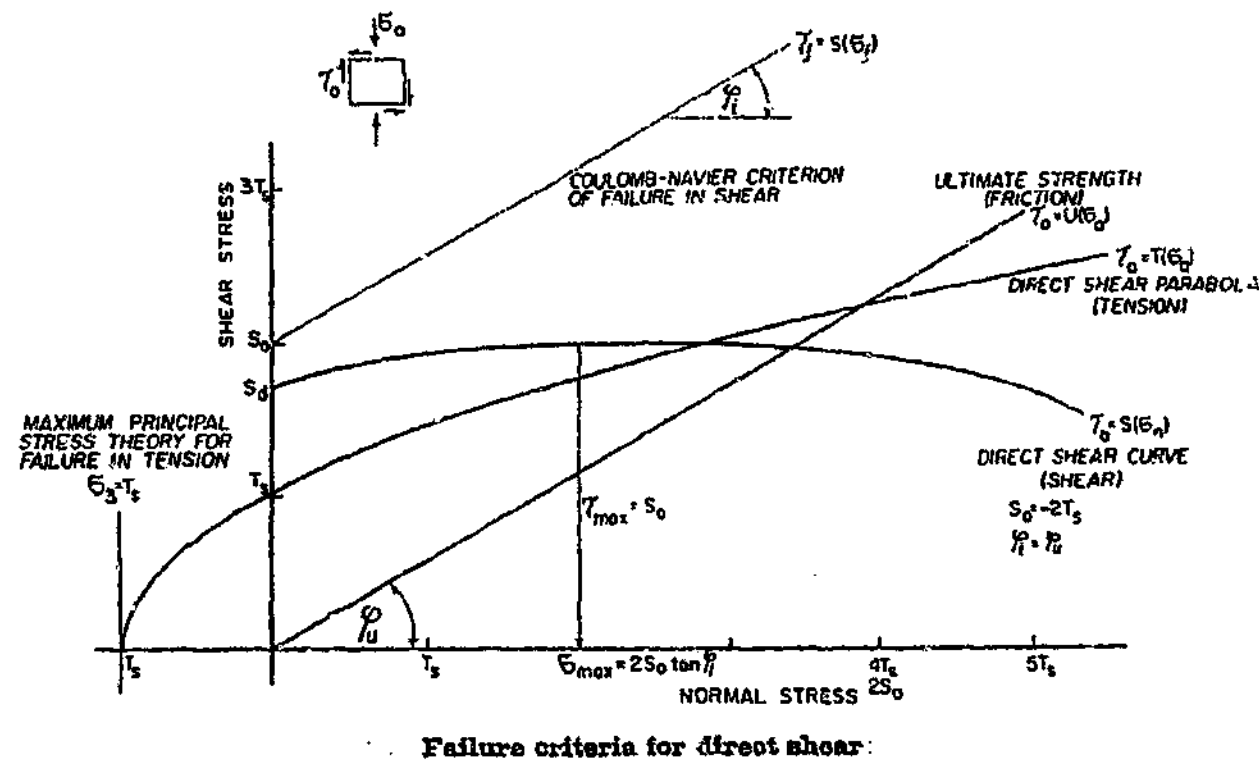
- failure by shear in accordance with:

$$\tau_a = \frac{1}{2} \left(\frac{2S_o + \sigma_a \tan \phi_i}{1 + \tan^2 \phi_i} - \sigma_a^2 \right)^{\frac{1}{2}} \quad \text{Equation 2-15}$$

- failure at ultimate strength in accordance with:

$$\tau_a = \sigma_a \tan \phi_u \quad \text{Equation 2-16}$$

The envelopes defined by these mechanisms are shown in Figure 2-13.



Failure criteria for direct shear:

Figure 2-13: Failure curves (after Lajtai, 1969b).

The strength of the samples containing joints was found to be affected by:

- the degree of separation of the joints, κ , where $\kappa=1$ for smooth flat joint planes and zero for intact rock
- a mobilisation factor, C , with assumed values between 0 and 1, which indicates that the intact rock cohesion and joint friction may not be mobilised simultaneously

- the angle of joint friction, ϕ_p

The failure conditions for the rock mass samples containing joints was thus:

$$\tau_a = C\kappa\sigma_a \tan \phi_p + (1-\kappa)[T_s(T_s - \sigma_a)]^{0.5} \quad \text{Equation 2-17}$$

for tensile failure,

$$\tau_a = C\kappa\sigma_a \tan \phi_p + \frac{1-\kappa}{2} \left(\frac{(2S_o + \sigma_a \tan \phi_i)^2}{1 + \tan^2 \phi_i} - \sigma_a^2 \right)^{\frac{1}{2}} \quad \text{Equation 2-18}$$

for shear failure, and

$$\tau_a = \sigma_a \tan \phi_u \quad \text{Equation 2-19}$$

for ultimate failure.

Patton (1966) carried out a number of shear tests on synthetic rock masses containing a single regular saw tooth joint. He developed the following equation for the shear strength of the joint:

$$\tau = \sigma \tan(\phi_u + i) \quad \text{Equation 2-20}$$

where:

- τ and σ are the shear and normal stress
- ϕ_u is the friction angle along the saw tooth and
- i is the angle of inclination of the saw teeth

The value of $(\phi_u + i)$ is theoretically limited to less than 90° . This criterion can be applied to the case of a rock mass containing one inclined joint set, and provides insight into how the fundamental behaviour of a rock mass subjected to shear is affected by the joint inclination.

Ladanyi and Archambault (1970) sought to develop a more generalised model of shear behaviour for interlocking rock surfaces. They carried out a number of direct shear tests to investigate the

sliding and shear behaviour of the blocks making up the rock surfaces. They found that brittle cracking of the blocks preceded the eventual shear failure. They noted that:

"What really appears to happen, is that the original rock blocks are first fissured and even crushed in smaller fragments by a compression mechanism, and subsequent shear occurs then across this already partially damaged rock mass."

Ladanyi and Archambault developed their joint strength model from this direct shear testing.

Direct shear tests to measure the mass strength of Carpathian flysch were conducted in the field by Thiel and Zabuski (1996). The shear tests were carried out under constant normal load (CNL) conditions using jacks. The Carpathian flysch tested was a sedimentary rock comprising interbedded sandstones and clay shales with beds dipping at 25° to 40°. The shear plane in the tests was horizontal and the plan area of the test sample was 1.0 m by 1.0 m. The rock mass was intersected by two joint sets sub-normal to the bedding planes. They found that failure occurred predominantly by sliding along the shale layers.

Afridi et al. (2001) carried out a number of laboratory direct shear tests on intact Salem Limestone samples (some with a visible plane of weakness) and on concrete-rock interfaces. The shear tests were conducted under CNL conditions, with the applied normal stress on the sample varying from 4 MPa to 14 MPa. They observed that the shear displacement required to reach peak strength increased with increased normal stress. The shear displacement at the peak strength increased from about 1 mm for 0.7 MPa normal stress, to about 3 mm for a normal stress of 5.5 MPa.

Failure occurred by the development of an inclined shear plane. The angle of inclination of the shear plane to the horizontal reduced with increased normal stress. There was evidence that shear stress concentration occurred at the leading edge of the shear plane and tensile failure occurred at the trailing edge of the shear plane. This suggests that the development of the failure plane was progressive and that stresses along the shear plane were not uniform. Rotation of the sample was also observed. This rotation is a result of the eccentric application of the shear forces and would have influenced the test results. This rotation may also not have been representative of field conditions.

The testing of rock masses using direct shear has not been adopted as widely as other methods. This may be due to a number of reasons, including:

- the uneven stress concentrations within the sample and the resulting progressive failure
- rotation of the shear boxes due to the eccentricity of the applied forces
- relative difficulty in obtaining representative samples and
- suitable testing equipment is not readily available

Nevertheless, the direct shear test offers an alternate method of testing which, as discussed in Chapter 3, has several advantages not provided by other test methods, such as triaxial and UCS testing.

2.5 Numerical modelling studies

As discussed earlier in this chapter, there have been a number of earlier studies into the behaviour of rock masses that have developed rock mass strength criteria from the back analysis of case studies or from fitting curves to field or laboratory test results. Laboratory and field testing of rock mass samples can have a number of drawbacks, including:

- they are often expensive and time consuming
- representative samples may be difficult to obtain
- the application of realistic *in-situ* conditions to the sample may not be possible and
- the size of the sample may result in scale effects

There has been an increasing trend towards assessing rock mass behaviour using numerical modelling techniques. The use of these techniques has been made more popular by improvements in computer speed and increasing software sophistication. The use of numerical techniques can overcome the constraints of scale, cost and time. The difficulty in obtaining good quality experimental results, particularly data highlighting the interactions and failure mechanisms occurring within the rock mass, however, means that validation of the numerical models is often not possible.

Numerical techniques have been used to model large-scale projects in jointed rock. This modelling usually proceeds by establishing the geometry of the structure and applying estimated strength parameters to the rock mass. These parameters may then be adjusted so that output from the numerical model agrees with the observed behaviour of the structure as construction proceeds. This observational approach may require reassessment of parameters a number of times before a satisfactory result is obtained. In some instances, the parameters may bear little resemblance to the *in-situ* rock parameters because of the inability of the numerical model to capture the behaviour of the material. Nevertheless, future performance of the structure is often assessed using these inaccurate parameters and models. The potential for errors using this type of approach is high.

2.5.1 Numerical methods

A jointed rock mass can be considered to be a discontinuum comprising rock blocks separated fully or partially by discontinuities, e.g. joints, bedding planes. Therefore, numerical methods used to analyse the behaviour of rock masses must be able to deal with the behaviour of the components of the rock mass and the interaction between them.

Several types of numerical methods have been used to model rock masses. An important feature of the method adopted for analysis is that it should be able to replicate mechanisms occurring in the rock mass and allow for the correct simulation of rock mass failure. Two approaches commonly used to model rock mass behaviour are continuum methods and discontinuum methods. These methods have been described by Sjöberg (1999), amongst others, and are outlined below.

2.5.1.1 Continuum methods

The continuum approach typically adopts plasticity theory to model material failure. The model geometry is defined and divided into zones. The model is then loaded until material failure occurs within the zones. Once a zone has failed, it cannot carry further load, so additional load is transferred to adjacent zones. Failure is often indicated by the development of a contiguous line of actively yielding zones within the model. This line of yielded zones simulates the development of a shear band. The mesh (zone) size used in the model can affect the width and inclination of the shear band. However, because the displacement field remains continuous, the actual failure surface does not develop in the model.

There are certain circumstances where continuum methods, adopting suitable rock mass parameter values, may provide reasonable predictions of rock mass behaviour. These are where the rock is essentially intact, or when joint spacing is very small compared to the size of the project, or where it is judged anisotropic behaviour can be ignored. However, for many projects, the joint spacing is such that the influence of the joints is significant and anisotropic behaviour is likely. Therefore, unless the rock mass is intact rock or completely fractured rock (e.g. gravel or rockfill), it may not be appropriate to model the rock mass as a continuum that displays isotropic behaviour and ignores the presence of joints.

One limitation of most continuum methods is that they consider only translational degrees of freedom, that is, rotation in the rock mass is ignored. This limitation is partially overcome by the Cosserat method, where new independent degrees of rotational freedom are introduced by a "Cosserat rotation" or "micro rotation" tensor. Grosso et al. (1999) found the Cosserat method modelled the stiffness and flexural beam behaviour of rock strata better than the classical continuum methods. Dai et al. (1996) used the Cosserat method to model excavation of an underground roadway and found that there was good agreement between the model and practical rock mechanics problems. However, the yield functions were selected by trial and error and in general, need to be selected with care. Although the Cosserat method appears to offer potential for modelling rock masses, it is not widely used by industry and may still suffer from problems associated with capturing the anisotropy introduced by joints and other planes of weakness.

Continuum methods can also satisfactorily model rock masses that contain a small number of discontinuities using joint or interface elements. However, these simple models often have problems with convergence and more complex models may be difficult to define geometrically. Commercially available software packages (such as FLAC, (Itasca, 1993) and PHASE2, (Rocscience, 1998)) allow an interface within the rock mass to be defined, either as the model geometry is established or by using the "ubiquitous joint" option. This allows the anisotropy of bedded rock masses such as slates, shales and mudstones, to be more accurately modelled.

2.5.1.2 Discontinuum methods

Rock masses containing multiple intersecting joint sets become very difficult to model using continuum methods. In such circumstances, discontinuum methods, such as the discrete element method, may provide a better approach.

The discontinuum method models the rock mass as an assemblage of intact rock pieces separated by explicitly defined discontinuities. This allows the interaction between the pieces and the discontinuities to be modelled, and allows modelling of the simultaneous failure of the intact rock and the discontinuities. The approach allows rotation of the intact rock pieces and displacement along the discontinuities, so the features of the failure mechanism are readily identified. A major limitation of current, commercially available discontinuum approaches is their inability to model crack initiation and propagation through intact blocks. This means that once the intact material within the model starts to fail, movement along the fracture is not allowed. However, discontinuum methods may be used to predict pre-peak behaviour, peak strength and to identify possible failure mechanisms.

The discrete element program UDEC has been used to model many rock mass problems (e.g. Dutton and Meek, 1992; Hsiung et al., 1994; Power et al., 1994; Sanderson and Zhang, 1997; Chen and Zhao, 1998; Asche and Quigley, 1999; Varley et al., 1999; Yang and Lee, 1999; Calderon, 2000; Harkness et al., 2000; Johnson et al., 2000; Yankey et al., 2000).

2.5.1.3 Reviews of numerical methods

Several reviews have been carried out on the ability of numerical methods to model rock masses. One such review was carried out by Senseny and Pucik (1999), who reviewed the development and validation of numerical codes that modelled the rock mass as a "stack of bricks". They carried out a "very precise" laboratory experiment that investigated the influence of joints on the deformation of an opening in a rock mass comprising concrete blocks where the geometry and properties of the concrete and joints were known. The data obtained from these tests allowed the validation of the computational models for the mechanics of structural deformation and failure in the jointed rock. The codes reviewed included both finite element methods (EXCALIBUR, FLEX and PRONTO) and discrete element methods (DIBS, UDEC). The authors developed the models by using the codes to assess rock mass behaviour over the following steps:

- Benchmark tests to verify the mathematical algorithms used by each of the codes
- Parametric studies to investigate the importance of selected variables on tunnel closure
- Tests on the constitutive models
- Precision tests, both dynamic and static, for tunnels in intact rock

- Model predictions for intact rock

The benchmark tests found that EXCALIBUR, FLEX and UDEC all calculated similar responses. Examination of the other codes revealed that approximations made in the algorithms were unacceptable. The validation of the models comprised two steps. The first step was to conduct a jointed rock precision test to provide data by which the model outputs could be validated. The second step involved using EXCALIBUR, FLEX and UDEC to model the jointed rock precision test.

The precision test investigated the shape of a tunnel liner under load, the deformations around a tunnel under load and the stresses within the rock mass. The deformation pattern modelled by each code was found to be similar to that observed in the tests.

The UDEC model was found to be the only model to replicate the stresses in the rock mass accurately, but did not correctly replicate the fracturing in the rock evident in the experiment. The fracturing of the rock mass was best replicated by FLEX.

The authors concluded that these codes could model rock mass behaviour and produce credible results. However, the models need to be developed with care, applied with caution and the results critically assessed. They also posed the important question of what is an acceptable level of accuracy.

A review of the numerical methods used in rock mechanics was also published by Jing and Hudson (2002). This paper reviews the methodology of the different numerical techniques and the applications for which they have been used. The authors discussed the most commonly used numerical techniques for rock mechanics applications and their advantages and shortcomings. They did not, however, make recommendations as to which methods should be utilised (or, more importantly, which methods should not).

The authors found that the commonly used continuum methods included the finite difference method (FDM), the finite element method (FEM) and the boundary element method (BEM).

The FDM was found to use computer memory and storage efficiently and allowed a more straightforward simulation of complex constitutive material behaviour. However, this technique

was also found to be inflexible in dealing with fractures, complex boundary conditions and heterogeneous materials. The explicit representation of fractures in the FDM was not easy because continuity of the functions between the neighbouring grid points was required. As a result, the FDM was generally unsuitable for modelling practical rock mechanics problems.

The FEM is widely used in science and engineering. It was one of the earliest methods that provided enough flexibility to treat the issues of material heterogeneity, non-linear deformability, complex boundary conditions, gravity and *in-situ* stresses. However, the problems associated with modelling fracture initiation and growth was found to be a major limitation of the application of FEM to rock mechanics problems.

The BEM seeks a “weak solution” at a global scale, as opposed to the FDM and FEM. That is, this method looks at the overall behaviour of the rock mass as opposed to behaviour within the rock mass. Fracture growth can be simulated in one of two ways. The first way is to divide the problem domain into multiple sub-domains with fractures along their interfaces and a pre-assumed fracture path. The alternative is the dual boundary element method (DBEM), which uses displacement and traction boundary equations at opposite surfaces of fracture elements. This makes the BEM suitable for solving problems of fracturing in homogeneous and linearly elastic domains. However, the BEM is not as efficient as the FEM in dealing with material heterogeneity or in simulating non-linear material behaviour.

Jing and Hudson (2002) concluded that the most commonly used discrete methods were the discrete element method (DEM) and the discontinuous deformation analysis (DDA) method.

The attraction of the DEM in rock mechanics is that it explicitly models the fractures in a rock mass. The key advantage of the DEM is that it allows the contact patterns within the components making up the problem domain to change with the deformation process, whereas with continuum based methods, these contact patterns remain fixed.

The DDA method is an implicit form of the DEM and has two advantages over the explicit DEM. These are that it has relatively larger time steps and that it uses closed form integrations for the stiffness matrices of the elements.

Hybrid models have combined continuum/discrete methods to model rock engineering problems, the most popular being hybrids of BEM/FEM, DEM/FEM and DEM/BEM. The authors found these hybrid models had many advantages over the singular models, but care was required to ensure continuity or compatibility conditions were met.

The application of numerical modelling techniques to rock mechanics problems is becoming more common. However, the applicability of the technique adopted needs to capture the behaviour of the rock mass. Discontinuum methods can model the deformation and rotation of the intact rock pieces and the sliding along the joints that may occur in a rock mass. For this reason, UDEC, a discontinuum method program was adopted to model the laboratory tests carried out for this study (see Chapter 8).

2.5.1.4 Numerical modelling of direct shear tests

To the author's knowledge, the literature contains only a few examples where direct shear tests on jointed rock masses have been modelled using discrete element methods. One such study was carried out by Thiel and Zabuski (1996), who modelled *in-situ* direct shear tests (see Section 2.4.3) using UDEC. Their tests on a bedded, sedimentary rock mass were at a scale where the jointing resulted in anisotropic behaviour. For comparison, the direct shear tests were also modelled using a continuum method, FLAC in this case. The results of the numerical simulations showed that:

- For the given geometry, slip along the bedding planes was observed and considered to be an important part of the failure process in the simulations. Failure zones then developed, firstly on the loaded side of the sample, then on the unloaded side followed by failure through the middle of the sample. Therefore it appeared that failure was progressive, with slip along the discontinuities, followed by shear through the rock.
- For the given geometry, dilation appeared dependent on the applied normal stress. Simulations where normal stress was low exhibited significant dilation, whereas the observed dilation in simulations with high normal stresses was not so significant.
- Separation within the sample along a joint set was observed. The separation can be observed in Figure 2-14. The displacement vectors also suggested that there was rotation within the model sample. The separation was evident in simulations where applied normal stresses were low. Separation was not observed in simulations with higher applied normal

stresses, probably because the relatively low modulus of elasticity of the flysch allowed more deformation under these higher stresses.

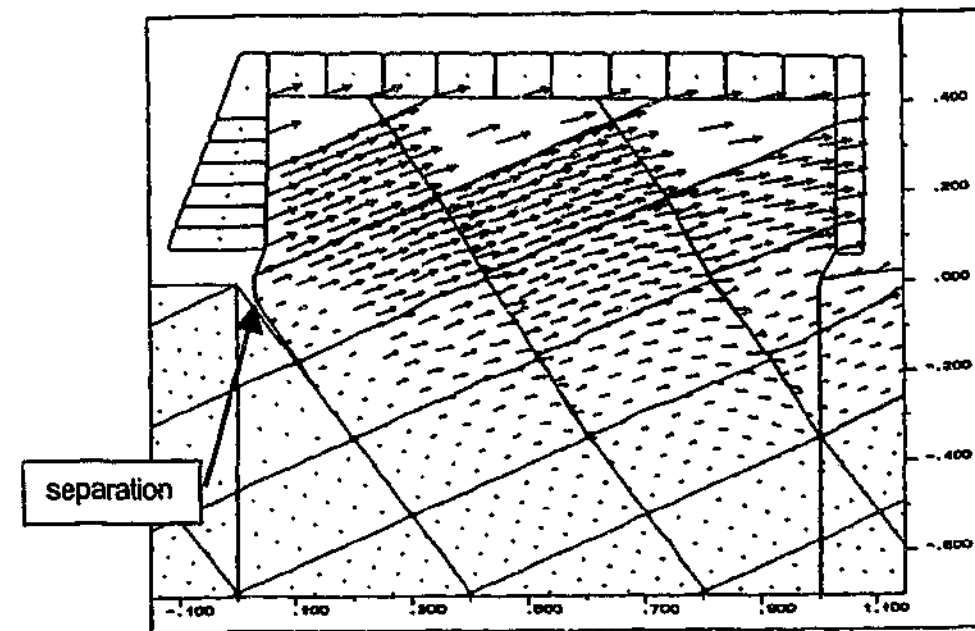


Figure 2-14: UDEC output showing separation along a joint set (after Thiel and Zabuski, 1996).

- The stress distribution within the blocks making up the model was far from homogeneous, but was dependent on the geometry of the model and direction of shear displacement, (see Figure 2-15). Stresses tended to concentrate within some of the blocks, while the remainder of the blocks remained relatively free of stress.

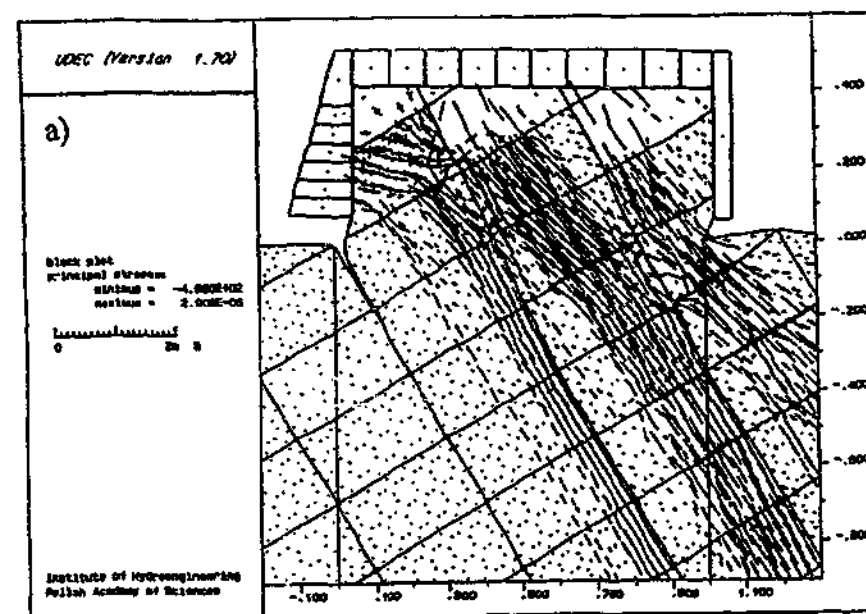


Figure 2-15: UDEC output showing stress distribution in a jointed rock mass subject to direct shear (after Thiel and Zabuski, 1996).

- The most accurate simulations of the *in-situ* test results were obtained when the model explicitly considered the bedding planes rather than treating the rock mass as an equivalent medium.
- It was found that FLAC did not simulate the test results as accurately.

This study by Thiel and Zabuski (1996) demonstrates that, with care, numerical models can be used to satisfactorily model failure mechanisms within anisotropic rock masses.

2.6 Summary

On the basis of the information available in the literature, the development of analytical criteria defining jointed rock mass behaviour has not proceeded at the same pace as that of empirical criteria. This is probably due to the complex interactions between the intact rock and the discontinuities and is further complicated by the effects of scale. Although these empirical criteria have been applied successfully on many projects, they provide little, if any, information on the interactions and failure mechanisms occurring within the rock mass. Furthermore, the degree of conservatism in the design is usually unknown and difficult to assess or confirm.

Laboratory testing studies have mostly concentrated on quantifying the effects of one or two joint sets on the strength and modulus of intact rock. Experimental studies on rock mass behaviour have mostly used triaxial and uniaxial compressive strength techniques, with limited use of biaxial and true triaxial techniques. Some testing has examined modes of failure within rock mass samples subjected to uniaxial compressive stress conditions. However, these tests may not be representative of *in-situ* conditions. The application of direct shear techniques to assess rock mass behaviour has been limited.

The use of numerical techniques has shown potential for modelling the behaviour of rock masses, particularly when complemented with laboratory or field testing, or with field observations. However, in many instances this is not the case and the assessment of performance is based purely on estimated properties and numerical model output. In such cases, there is significant potential for inaccurate assessment of behaviour to be made because of inappropriate models and/or properties.

It would therefore be useful to carry out a laboratory-testing program to obtain high quality data on the behaviour of rock masses. Such studies could concentrate on identifying and modelling the

basic interactions and failure mechanisms that occur within rock masses. This data could then be used to validate numerical models of the rock masses and assess if a particular numerical technique is suitable. This may eventually lead to greater accuracy and confidence in our assessment of rock mass strength, with potential significant benefits to both civil infrastructure and mining projects.

3 DIRECT SHEAR TESTING

3.1 Introduction

In this chapter, the laboratory techniques appropriate for assessing the behaviour of jointed rock masses are discussed.

As presented in Chapter 2, the commonly used laboratory techniques have been triaxial and UCS tests. These techniques have probably been adopted because the tests are relatively straightforward and inexpensive to perform, the test equipment is widely available and/or the samples can be obtained relatively easily.

Triaxial testing has been widely used to examine rock mass strength and much has been learned from these studies. However, this technique involves a number of simplifications that may result in an inaccurate assessment of behaviour.

One major simplification is that the shear surface through the rock mass is often coincident with the weakest joint. This may not give a true indication of the rock mass strength *in-situ*, where failure may be constrained to occur on a shear plane defined by the geometry of the loading and may involve both joints and intact rock.

Another issue is that the stiffness restraint provided by the surrounding rock cannot be simulated in a triaxial test. As a result, a false impression of the *in-situ* strength and failure mechanism may be obtained.

This chapter assesses the use of direct shear tests to measure rock mass behaviour, considers the conditions under which direct shear tests should be carried out and describes the development of the equipment used to carry out the direct shear tests in this study.

3.2 Field conditions

The load conditions applied to a rock mass sample during triaxial testing may not be representative of actual field conditions. This can be illustrated by the following example. Consider a laterally loaded pile embedded in a jointed rock mass as shown in Figure 3-1.

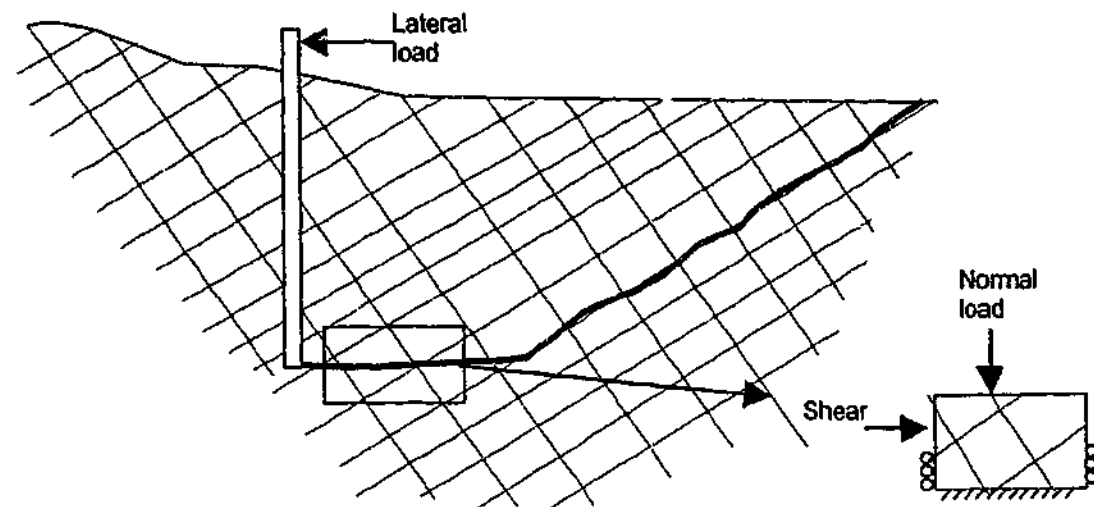


Figure 3-1: Laterally loaded pile in a jointed rock mass.

The application of lateral load on the pile can lead to failure and/or rotation of the pile and/or failure of the rock mass. If the pile rotates, the rotation will be resisted by the rock mass both in front of and behind the wall. The failure surface associated with toe resistance can be reasonably assumed to commence somewhere close to the toe of the pile and to exit the rock mass at some point at the surface. An assumed failure surface through the rock mass is shown in Figure 3-1.

The stress conditions acting on the failure surface in the vicinity of the toe are similar to those applied in a direct shear test, as indicated in Figure 3-1. Near the toe of the wall, the failure surface may involve shearing along joints and through intact rock pieces. The presence of non-persistent joints may also result in shear through intact rock. Dilation of the rock mass as it shears will be resisted directly by the overlying rock mass and indirectly by arching of the surrounding rock mass. Closer to the ground surface, the failure surface has been assumed to coincide with a joint. Direct shear testing of the joint would provide an appropriate estimate of resistance for this situation.

A triaxial test of a rock mass sample taken anywhere on the failure surface would be expected to fail along one or more joint surfaces. However, as illustrated in Figure 3-1, this may not be the case *in-situ*. The direct shear test, on the other hand, can provide a closer simulation of the stress

path followed by the rock mass at any point on the failure surface. In particular, the inclination of the failure plane relative to the joint pattern can be controlled by the direct shear apparatus and the restraint provided by the surrounding ground can be modelled by the shear box and the application of the constant normal stiffness condition (see Section 3.4).

Direct shear testing can be used to apply different sets of loading conditions to the sample. Variations of the initial normal stress acting on the rock mass, representing differing sample depths, can be easily applied in a direct shear test. The sample can also be tested under constant normal stiffness or constant normal load conditions. The fixed location of the shear plane through the sample can be used to examine the effects of varying joint inclination on sample response, thus providing information on anisotropic behaviour. Furthermore, a shear box can be constructed that allows the mechanisms occurring within the rock mass during the direct shear test to be observed. Therefore, direct shear testing can be an appropriate technique for assessing the behaviour of rock masses. It is for these reasons that the direct shear test has been adopted in this study to investigate rock mass behaviour.

3.3 Previous studies using direct shear tests

Direct shear tests have been used extensively to investigate the shear strength of rock - concrete interfaces and rock joints (e.g. Patton, 1966; Ladanyi and Archambault, 1970; Barton, 1973; Barton and Choubey, 1977; Lam, 1983; Benjelloun et al., 1990; Skinas et al., 1990; Jing et al., 1992; Seidel, 1993; Indraratna et al., 1998; Yang and Chiang, 2000; Pearce, 2001; Fardin et al., 2001; Grasselli and Egger, 2003).

Some investigations have used direct shear tests to investigate the behaviour of intact rock or rock masses containing one joint set. Lajtai (1969a) discussed the use of direct shear tests for testing intact rock samples containing a single plane of weakness. Some of the objections to the use of direct shear testing raised at that time were:

- Failure was forced along the shear plane rather than along a preferred (hence weaker) alignment. While this may be undesirable when testing isotropic samples, it is important when testing anisotropic samples (such as jointed rock masses), as the strength along any preconceived shear plane can be measured.

- One of the principal stresses under direct shear loading was tensile. This state of stress cannot be reproduced in the triaxial test. However, tensile failure of geological materials is common, so the use of direct shear tests may be reasonable.
- The eccentric application of the shear force can lead to bending of the sample or rotation of the shear box, leading to a non-uniform distribution of normal stress on the failure plane. This often results in progressive failure, which may start at points where normal stress is low. However, the shear apparatus can be modified so the amount of shear box rotation is reduced.
- The knife-edge type application of shear load can generate stress concentrations that also lead to progressive failure. This progressive failure may occur more often in reality than instantaneous failure. This would suggest a better representation of field conditions.
- Stress control to the same degree as in the triaxial test is not possible.

However, the use of direct shear testing should not be dismissed for the reasons listed above. The heterogeneous nature of rock masses and the uneven distribution of stresses within *in-situ* rock masses may well be greater than any experimental error arising from the use of direct shear techniques. The progressive nature of failure and the uneven distribution of stresses in rock masses under shear were highlighted in the study by Thiel and Zabuski (1996), whose work has been discussed earlier.

Lajtai (1969a) found that direct shear testing also has some advantages, including:

- The direct shear test allows the measurement of ultimate (residual) shear strength as it allows shear deformation to continue beyond the first stages of fracturing and strength loss. This is not possible in UCS tests and is difficult to measure accurately with triaxial tests.
- The influence of other planes of weakness on rock mass strength is substantially reduced in the direct shear test because of the rigidity of the shear box. Failure is enforced along the shear plane rather than along another discontinuity.

Afridi et al. (2001) carried out a number of shear tests on intact rock core samples. They stated that:

"...even intact rock is subjected to loading conditions similar to those present in the direct shear machine. Hence, use of other methods in which the loading geometry is entirely different from the field conditions would be futile."

Therefore, it is possible to conclude that there is no single laboratory technique best suited for assessing the behaviour of rock masses. The commonly used triaxial and UCS tests are simple and relatively inexpensive to carry out, but may not simulate field conditions accurately. Direct shear tests may better simulate field conditions for some problems, but obtaining suitable samples can be difficult and the tests expensive to conduct. The choice of test will largely depend on the availability of suitable testing equipment and samples and the engineering problem being addressed.

3.4 CNS and CNL conditions

A rock mass undergoing shear will usually dilate due to the rock blocks rotating or sliding on joints. Depending on the circumstances, this dilation may or may not be resisted by the surrounding rock mass. If there is no resistance to dilation, testing under constant normal load (CNL) conditions would be appropriate. This condition may apply to shallow failure of rock slopes. In many cases, however, the dilating rock compresses the adjacent rock mass, which can be considered to behave as a spring. As the amount of dilation increases, so does the normal stress. In this case, testing under constant normal stiffness (CNS) conditions may be more appropriate. Under such conditions and assuming the adjacent rock mass is elastic, the change in normal stress can be estimated from Hooke's Law, so that:

$$\Delta\sigma = k\Delta y \quad \text{Equation 3-1}$$

where

- k is the stiffness of the adjacent rock mass, and
- Δy is the dilation.

The CNL and CNS conditions are illustrated in Figure 3-2.

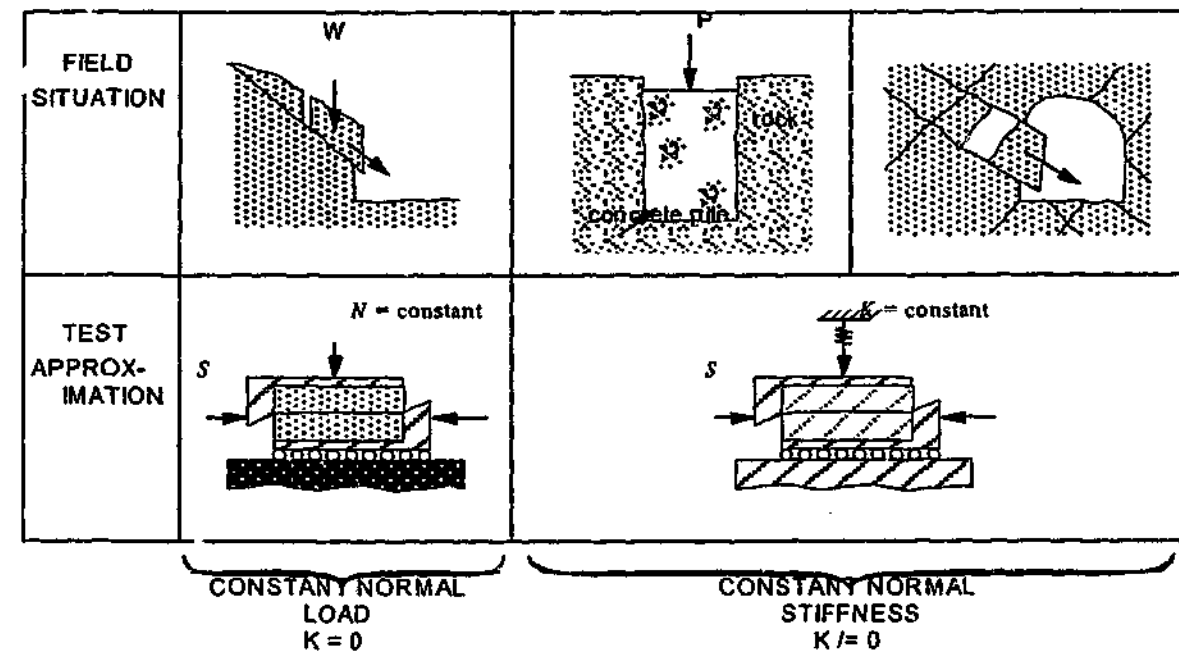


Figure 3-2: Description of CNL and CNS conditions.

The normal stress acting at any time on the failure plane can be described by:

$$\sigma_n = \sigma_{n0} + k\Delta y \quad \text{Equation 3-2}$$

The value of k depends on the Young's modulus, E , and Poisson's ratio, ν , of the rock mass, and the geometry of the problem being considered. For example, for the relatively simple case of a rough concrete pile socketed in rock, Johnston et al. (1987) found that the normal stiffness can be approximated by:

$$k = \frac{\Delta\sigma_n}{\Delta r} = \frac{E}{(1+\nu)r} \quad \text{Equation 3-3}$$

where

- $\Delta\sigma_n$ is the change in normal stress due to dilation, Δr of the socket, and
- r is the radius of the socket.

The estimation of k for other cases, however, is not as straightforward.

Skinas et al. (1990) suggested the following approximation of maximum stiffness, K_{max} from:

$$K_{max} = \frac{E.L}{2c(1-\nu^2)} \quad \text{Equation 3-4}$$

where:

- E =Young's modulus of rock mass,
- L =length of rock mass,
- ν =Poisson's ratio, and
- c =constant.

Skinas et al. (1990) does not provide any guidance on the estimation of c . In their paper, they provide a worked example in which $c=1.2$ for a synthetic rock made from a sand-barytes-cement mixture, although it is not clear what parameters c is related to or how to estimate it.

Equation 3-2 indicates that CNS conditions may be appropriate even in cases involving very shallow failure where normal stresses on the failure plane are initially very low. Under such circumstances, if dilation of the failing rock mass is restricted by the surrounding rock, a relatively large increase in normal stress may be generated and, as a consequence, result in an increase in strength.

It is for this reason that, in this study, direct shear testing under CNS conditions has been used to investigate the strength of near surface rock masses.

3.5 Monash University direct shear apparatus

Direct shear testing involves the displacement of one half of a sample relative to the other half. There are several direct shear apparatus capable of testing relatively large-scale samples. One such apparatus is located at the Imperial College of Science and Technology in London. This shear apparatus is capable of accommodating samples that are 12" by 16" (300 mm by 400 mm) and has a capacity of 1000 kN in both the shear and normal directions (Hoek and Bray, 1981).

A shear apparatus capable of shearing rock mass samples under CNS or CNL conditions has been developed at Monash University and has been used in this study. This shear apparatus is described in a number of dissertations and journal papers (e.g. Pearce, 2001; Haberfield et al., 1994; Seidel, 1993). A photograph of the Monash University shear apparatus is shown in Figure 3-3.



Figure 3-3: Monash University direct shear apparatus

The shear apparatus uses hydraulic actuators to apply normal and shear loads. Load cells attached to the ram of the actuators have a capacity of up to ± 250 kN for static conditions, and an accuracy of 0.2%, or 0.5 kN. For tests with very low initial normal stresses, (≤ 100 kPa), the load cell on the vertical actuator was replaced with a ± 50 kN load cell, which has an accuracy of 0.2% or 0.04 kN. The actuators are hydraulically powered and servo-controlled using an Instron 8800 dual digital controller. Shear loads can be applied by either load control or displacement control and under cyclic or monotonic loading conditions. CNS conditions are applied by placing the vertical actuator in load control and simulating a spring of stiffness k via a feedback system.

The shear load for the testing described in this study was applied using monotonic single ramp waveforms by placing the horizontal actuator under displacement control. Displacements were

measured using two internal and three external linear variable displacement transducers (LVDT's). The internal LVDT's were mounted within the actuators and measure actuator displacement. Two external LVDT's were used to measure vertical displacement (dilation). Each was mounted on the upper half of the shear box and measured the distance to a reference plate mounted on the lower half of the shear box. An external LVDT was used to measure shear displacement. This LVDT is fixed to the frame of the shear apparatus using a magnetic base and the tip placed against the end of the shear box.

The vertical piston applying the normal stress to the sample used roller bearings to restrain rotation of the top and bottom halves of the shear box and to minimise friction losses.

Loads and displacements in the shear and normal directions were displayed on a computer screen in real time using digitally controlled software. A program written using HP-Vee (Helfel, 1988) provides shear displacement, dilation, shear load and normal load outputs. The shear and normal stresses were calculated and displayed by the program in real time. These stresses were calculated by dividing the shear and normal loads by the corrected area of the shear plane.

3.6 Shear boxes

The shear boxes comprise upper and lower halves separated by a gap. The shear box halves need to be stiff enough to constrain the sample from rotating or translating within the box and to force the failure surface to develop in the gap between the two halves of the box.

Two shear boxes were used during this study, henceforth referred to as Type "A" and Type "B" shear boxes. The Type "A" shear box has been used in previous studies of rock joint behaviour. The larger Type "B" shear box was specifically built for this project.

3.6.1 Type "A" shear box

The Type "A" shear box comprises two halves made from steel plate and can accommodate a sample 600 mm long by 200 mm high and 160 mm deep. A photograph of the Type "A" shear box is shown in Figure 3-4.

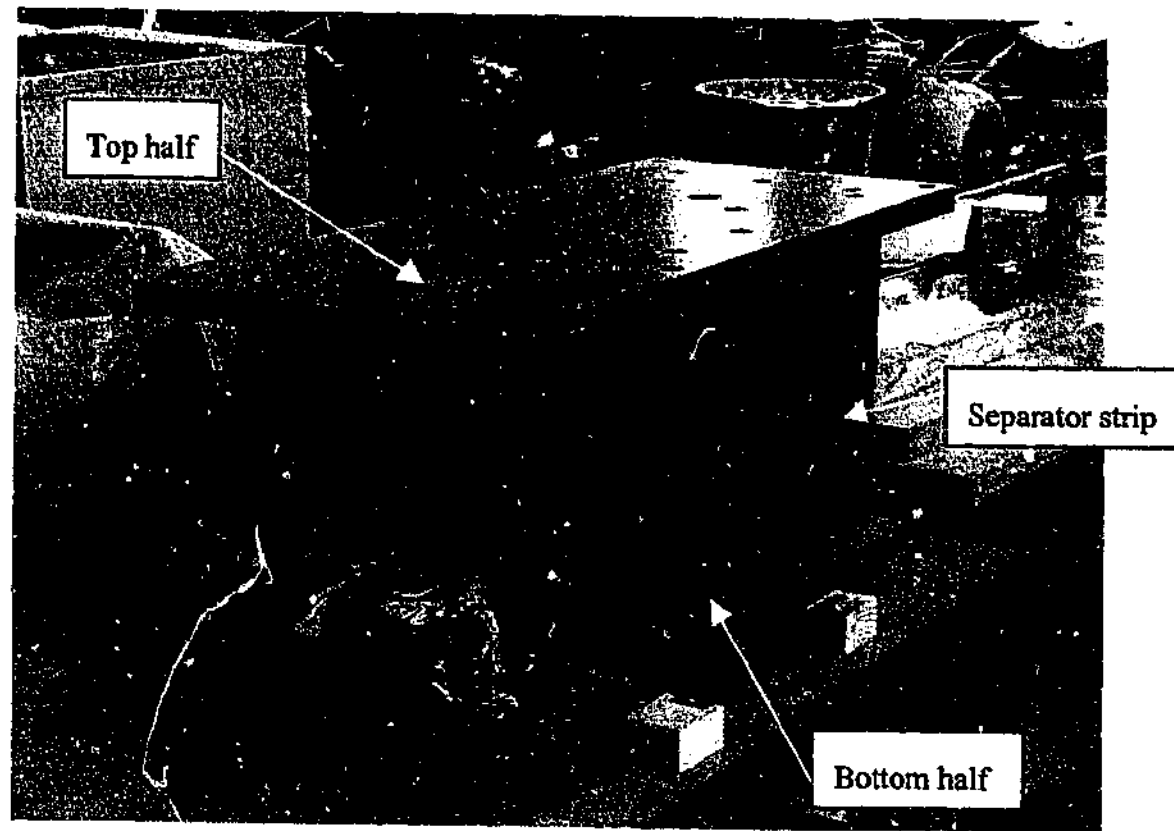


Figure 3-4: Type "A" shear box.

The two halves of the Type "A" shear box are separated with a 25 mm high separator strip.

3.6.2 Type "B" shear Box

The Type "B" shear box was designed for testing samples 400 mm long by 280 mm high by 275 mm deep, and to allow viewing of the mechanisms and failure processes occurring within the sample during testing. It is constructed from steel plate on three sides, with the front of the shear box made from perspex braced by a steel frame. The two halves of the Type "B" shear box are separated by a 10 mm high separator strip. The ends of the shear box are buttressed to reduce deflections of the box.

A photograph of the Type "B" shear box is shown in Figure 3-5. The normal load from the shear rig is transferred to a steel plate on top of the sample by adjustable studs. There are steel plates at the sides and back of the box mounted on threaded bars. Each of the side steel plates is mounted on two 20 mm diameter threaded bars, while each of the back plates is mounted on four 16 mm diameter threaded bars. Rotating these bars adjusts the position of the steel plates to bring them into contact with the sample. Once in contact with the sample, the high stiffness of the threaded bars holds the sample effectively in place without the need for plaster or grout, as used in previous

studies (e.g. Seidel, 1993). A photograph showing detail of how the sample is held in the shear box is shown in Figure 3-6.

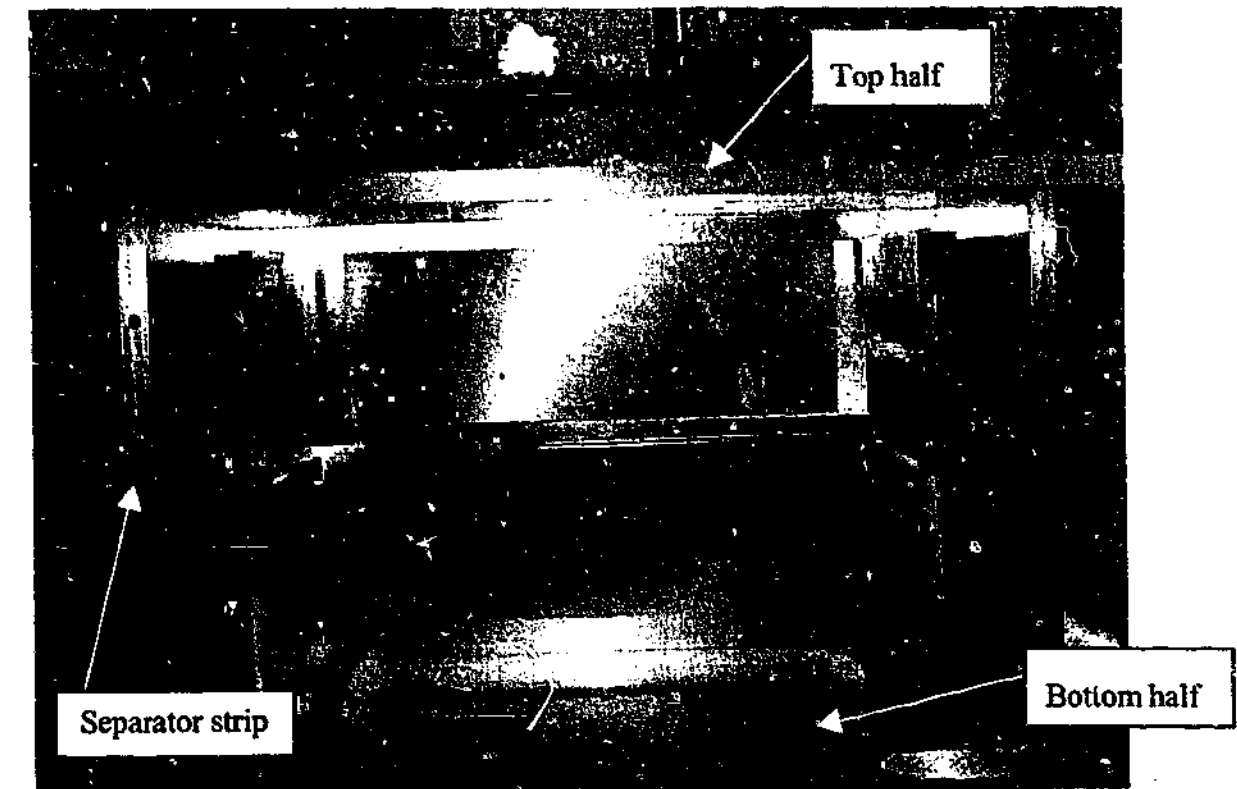


Figure 3-5: Type "B" shear box (with perspex front removed).

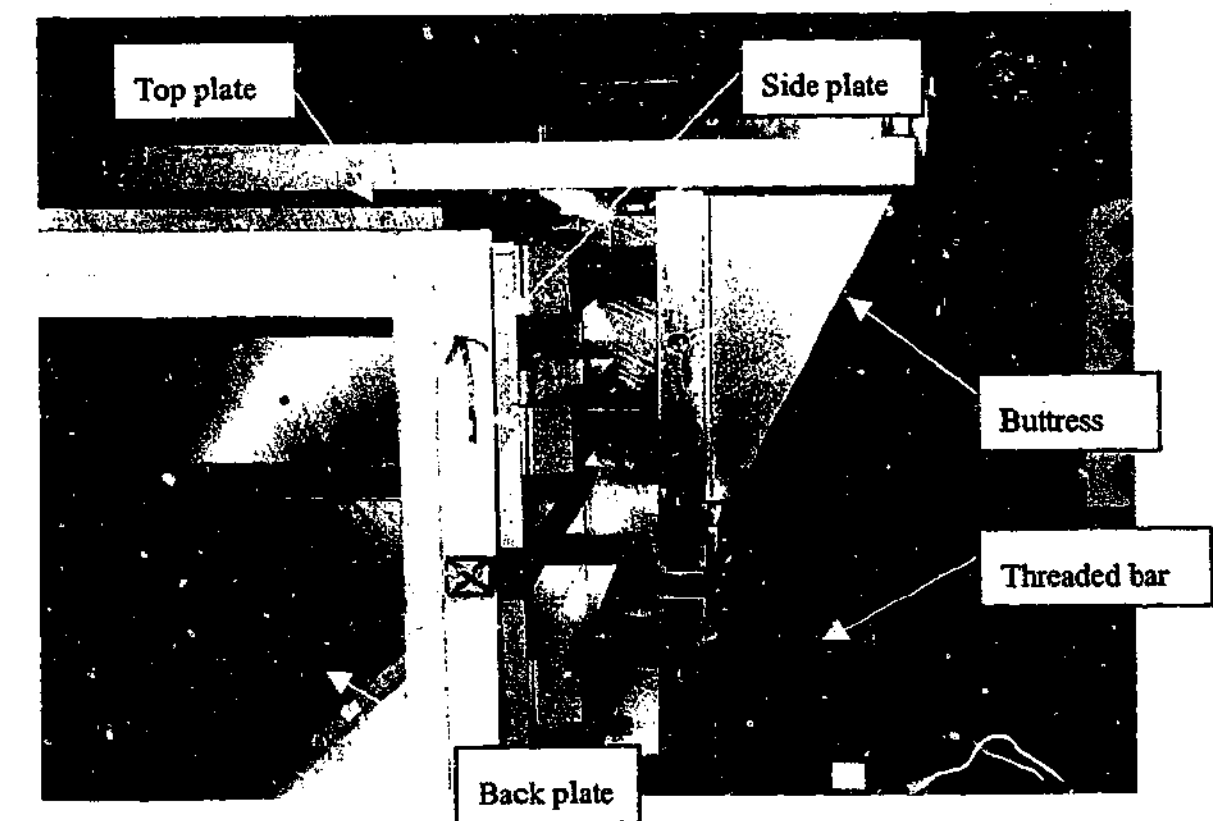


Figure 3-6: Detail of side and top plate arrangement.

The side plates can also be used to apply a horizontal confining pressure. The relationship between horizontal load resulting from torque applied to the threaded bars supporting the side plates was assessed and is shown in Figure 3-7. On average, 5 Nm torque on each of the threaded bars results in an average horizontal stress of 100 kPa being applied to the sample.

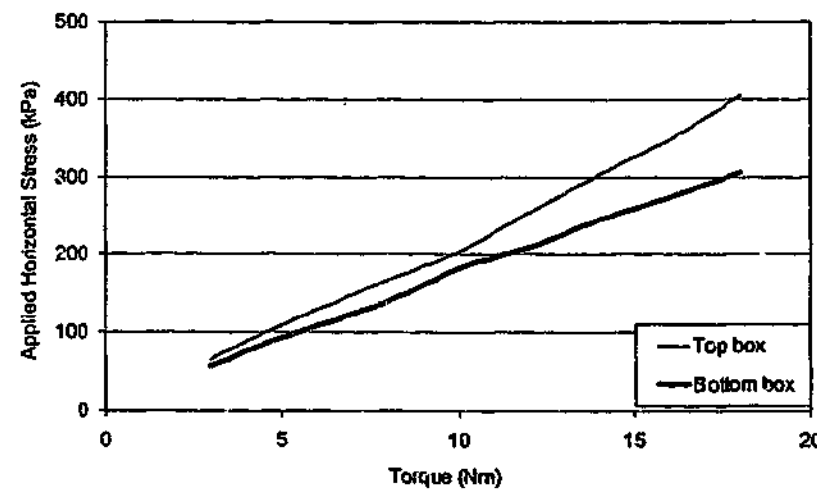


Figure 3-7: Relationship between torque applied to threaded bar and stress applied to sample.

The sample is held in the shear box by steel plates at the sides, top, bottom and back, while the front was constrained by 20 mm thick perspex. The perspex front is braced using steel (as shown in Figure 3-8) to minimise any outwards deflection resulting from dilation of the sample during shearing. The front bracing was installed after observing relatively high outwards movements of about 7 mm to 8 mm during the first two shear tests (B1 and B6). After installing the front bracing, the maximum outward movement was reduced to between about 1 mm and 3 mm.

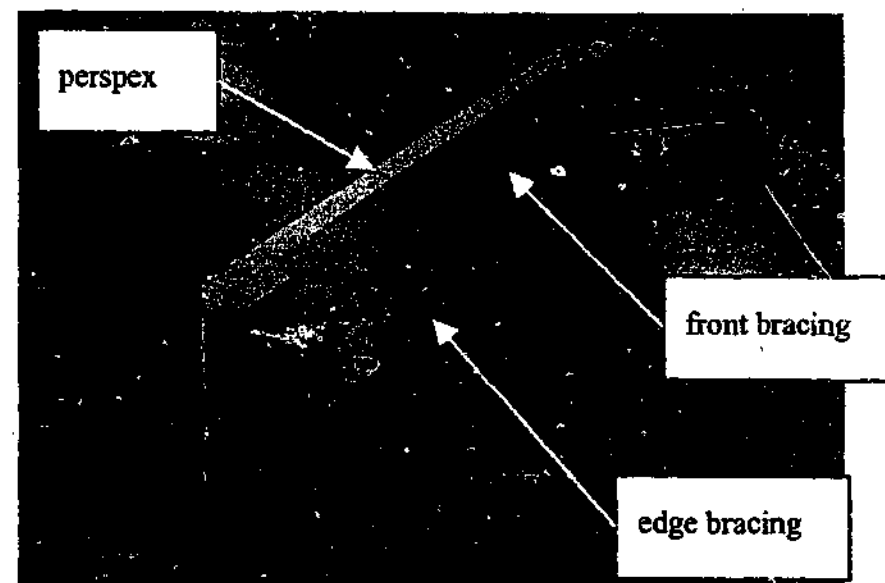


Figure 3-8: Braced perspex front of shear box.

3.7 Summary

There is no single testing technique that can accurately replicate all the conditions applied to a rock mass in the field. The commonly used techniques of triaxial and UCS testing have been used by many researchers to investigate particular aspects of rock mass behaviour. Quite often, these techniques have been adopted because the equipment and procedures are readily available and the samples are relatively easy to obtain.

This study uses direct shear tests to investigate rock mass behaviour. The use of direct shear tests on rock masses appears to have been adopted in only a few studies reported in the literature. However, direct shear testing is an alternative technique that, under many circumstances, may provide a better representation of the conditions that a rock mass is subjected to in the field. This method better simulates a number of situations commonly encountered in civil projects in which the failure surface is largely defined by the geometry of the structural unit (e.g. pile) applying the load to the rock mass. Boundary conditions that also affect the sample response, such as the application of CNL or CNS conditions, can be easily applied.

The equipment used in this study has been described. The existing Type "A" shear box is long and narrow and was designed to test rock joints. It was not particularly suited for testing rock masses. Therefore another shear box was specifically designed and fabricated for this project. The features of this larger Type "B" shear box have been described. These features include the ability to apply initial horizontal stresses to the sample and a transparent front that allows observation of the mechanisms occurring within the sample during shearing.

4 LABORATORY TESTING PROGRAM

4.1 Program objectives

As discussed in Section 2.4.2, Einstein et al. (1970) concluded that rock mass behaviour (strength and deformability) was influenced by the:

- confining stresses (i.e. boundary conditions) applied to the rock mass,
- material properties (in particular the unconfined compressive strength (UCS) of the intact rock),
- joint spacing,
- joint inclination with respect to the applied loads, and
- joint properties (e.g. joint roughness, cohesion).

It is anticipated that the number of joint sets, the stiffness of the joints and the stiffness applied to the rock mass could also affect rock mass strength.

The laboratory testing program conducted in this study aimed to provide a preliminary assessment of the influence of variations in the first four parameters listed above on rock mass strength and failure mechanisms as observed during CNS direct shear testing. In addition, the effect of introducing a third joint set was also investigated. The influence of joint properties was not investigated due to the difficulty of producing joints with different roughness and strength.

4.2 Test configuration

The rock masses were fabricated by cutting joint sets into an intact block of synthetic rock. The joint inclination was measured with respect to the shear plane. The sample was then sheared by laterally displacing the lower half of the shear box while allowing the upper half of the sample to dilate vertically against a known stiffness. A schematic diagram of a sample in the shear box is shown in Figure 4-1.

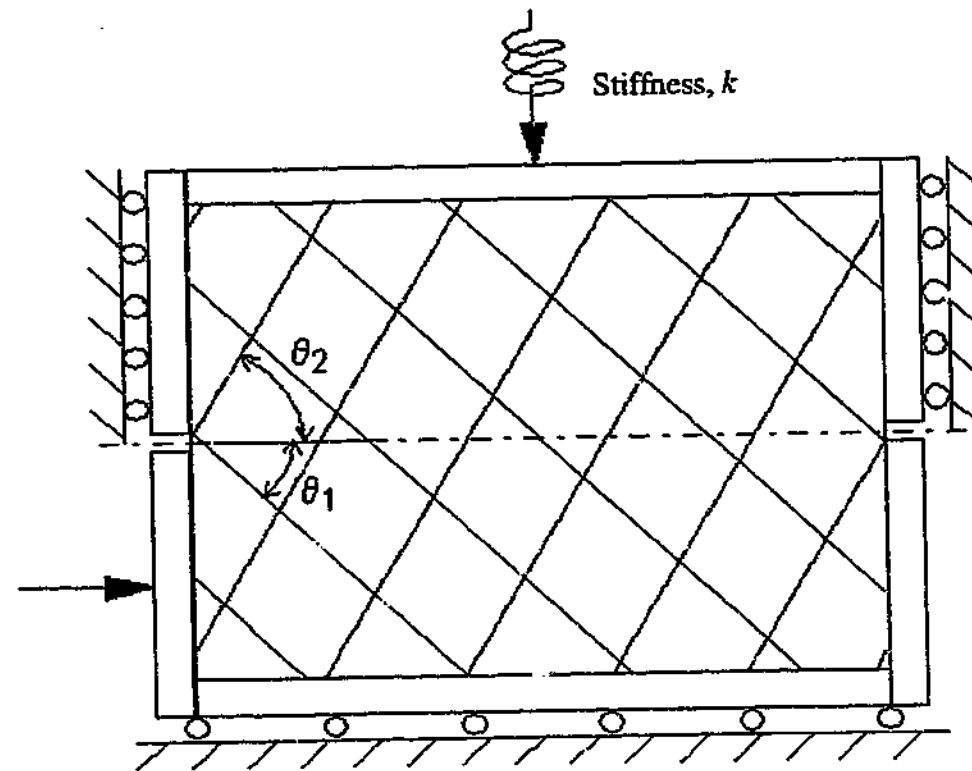


Figure 4-1: Shear test and jointing configuration.

The sign convention adopted for joint inclination assumes that joints inclined clockwise downwards from the horizontal, taken to be θ_1 , are negative, and those inclined clockwise upwards from the horizontal, θ_2 , are positive. In some cases, a third joint set, θ_3 , was cut into the sample. The joint spacing of the θ_1 joint set was the same as that of the θ_2 joint set (and the θ_3 joint set where applicable). The profile of the sample shown in Figure 4-1 was consistent with depth, i.e. the sample approximated the two-dimensional condition.

An initial (vertical) normal stress was applied to the sample at the beginning of each test. Once the test had commenced, the normal stress increased or decreased according to the amount of dilation measured and the specified normal stiffness, k . Given this study examines rock mass behaviour from a civil engineering perspective, relatively low values of initial normal stress were adopted.

As discussed in Section 3.4, the estimation of an appropriate value of stiffness, k , is difficult. The equation suggested by Skinas et al. (1990), repeated in equation 4-1, may provide a suitable estimation of K_{max} .

$$K_{max} = \frac{E.L}{2c(1-\nu^2)}$$

Equation 4-1

Assuming a rock mass modulus, $E=150$ MPa, sample length, $L=0.4$ m, Poisson's ratio, $\nu=0.25$ and the constant, $c=1.2$, the maximum stiffness, $K_{max}=25$ kN/mm. The value of c used is the same as that used in Skinas et al. (1990), as Skinas et al. (1990) do not provide any directions on how c is obtained. Based on a sample plan area of 0.4 m by 0.28 m, the value of $K_{max}=225$ kPa/mm can be estimated. A value of $k=200$ kPa/mm was therefore adopted. This value appears reasonable for near surface rock masses and is less than that adopted by Pearce (2001), who used $k=400$ kPa/mm to 800 kPa/mm for her tests on joints in Johnstone.

4.3 Jointed rock mass tests

4.3.1 Type "A" tests

The Type "A" tests were carried out while construction of the Type "B" shear box was being completed. The default Type "A" sample typically had an intact rock strength of about 5 MPa and contained two joint sets (θ_1 , θ_2), inclined at $(-45^\circ, +15^\circ)$ and spaced at 70 mm. The default boundary conditions in the Type "A" tests were an initial normal stress of 100 kPa and a constant normal stiffness of 200 kPa/mm. To examine the effects of varying the parameters listed in Section 4.1, Type "A" samples were manufactured and tested to assess:

- The influence of initial normal stress. One sample was subjected to an initial normal stress of 200 kPa and another to 400 kPa.
- The influence of intact rock strength. An attempt was made to produce significantly weaker blocks. However, these blocks were found to have intact rock strengths of about 4 MPa. It was therefore not possible to make any firm conclusions regarding intact rock strength on rock mass behaviour from the results of the Type "A" tests.
- The influence of joint spacing. Two samples with joint sets spaced at 50 mm were manufactured.
- The influence of a third joint set. Three samples contained a third joint set inclined at $+75^\circ$ were manufactured.

The same value of normal stiffness was used for all Type "A" tests. The influence of varying the joint inclination was not investigated in the Type "A" tests.

A summary of the Type "A" test results is presented in Appendix A. Detailed results of the Type "A" tests are presented in Appendix B, where they are presented in graphical form with plots of:

- shear stress, τ , versus normal stress, σ_n ,
- shear stress, τ , versus shear displacement, dx
- normal stress, σ_n , versus shear displacement, dx , and
- dilation, dy , versus shear displacement, dx .

The shear and normal stresses were calculated by dividing the applied load acting by the corrected cross-sectional area of the sample, i.e. the width of the sample multiplied by the length of the sample minus displacement. The shear and normal stresses are therefore average stresses acting on the shear plane.

4.3.2 Type "B" tests

The default Type "B" sample typically comprised an intact rock strength of about 3 MPa and contained two joint sets inclined at $(-45^\circ, +15^\circ)$ and spaced at 70 mm. The default boundary conditions comprised an initial normal stress of 100 kPa, an (estimated) initial horizontal stress of about 100 kPa and a constant normal stiffness of 200 kPa/mm. The effect of variations in the parameters listed in Section 4.1 on rock mass strength in direct shear were examined using the Type "B" samples. Variations in parameters included:

- Testing of two samples with an initial normal stress of either 50 kPa or 300 kPa. This allowed the influence of initial normal stress on sample behaviour to be assessed.
- Testing of four samples made from material with an intact rock strength of about 2 MPa. This allowed the influence of intact rock strength on sample behaviour to be assessed.
- Testing of six samples constructed with a joint spacing of about 32 mm. This allowed the influence of joint spacing on sample behaviour to be assessed.

- Testing of 11 samples containing two joint sets with different inclinations. This allowed the effect of joint inclination on sample behaviour to be assessed.
- Testing of five samples constructed with variations in inclination within each joint set of $\pm 5^\circ$. This allowed the influence of minor variations in joint inclination on sample behaviour to be assessed.
- Testing of seven samples that contained a third joint set. This allowed the influence of the introduction of a third joint set on sample behaviour to be assessed.

The same default horizontal stress and constant normal stiffness was applied to all the Type "B" samples.

A summary of the Type "B" test results is presented in Appendix A. Detailed results of the Type "B" tests are also presented in graphical form in Appendix B. A visual record of rock mass behaviour at various stages of each Type "B" shear test has been compiled in Appendices B and C. The visual records of the Type "A" tests were not available as the shear box used in these tests did not allow direct observation of the sample during testing.

4.4 Summary of laboratory testing

The laboratory program was divided into stages so the effects of varying one of the parameters could be observed. The rock mass samples were prepared so that, as far as practical, only one of the parameters was varied from the default condition. The parameters examined in each stage of the testing program are summarised in Table 4-1. A full description of the laboratory testing program is included in Appendix A.

Table 4-1: Summary of laboratory testing program.

Parameter varied	Type "A" tests	Type "B" tests
joint inclination (2 sets)	A3	B1, B2, B3, B4, B5, B6, B7, B7A, B26, B27, B28, B29, B30
joint inclination (3 sets)	A4	B8, B9
joint inclination $\pm 5^\circ$ (2 sets)	-	B10, B10A, B11, B12, B31
joint inclination $\pm 5^\circ$ (3 sets)	-	B13
intact rock strength, UCS	A1, A2	B18, B19, B19A, B20, B21
joint spacing	A5, A6	B14, B15, B16, B17
initial normal stress, σ_{ni}	A7, A8	B22, B23, B24, B25

5 SAMPLE PREPARATION

5.1 Introduction

There have been a number of studies (see Chapter 2) that have used laboratory tests to examine the behaviour of jointed rock mass samples. These tests allowed the sample behaviour to be measured under controlled conditions. Ideally, in such studies the properties of the intact rock and joints that make up the sample should be known and similar to those occurring in the field. Previous studies into rock mass behaviour include those that have tested samples that have been either recovered from the field (e.g. Jaeger, 1960; McLamore and Gray, 1967), or that have been fabricated using a synthetic soft rock material (e.g. Meyers, 1994; Singh, 1997).

Rock mass samples of a scale suitable for testing in the laboratory are often difficult (and expensive) to retrieve from the field in a relatively undisturbed state. Disturbance can occur during retrieval, transportation and preparation of the sample. Field samples are also likely to contain significant variations in parameters such as intact rock strength, joint spacing, joint inclination, joint infill and joint strength. These variations can mask the influence of each of these parameters on rock mass behaviour, making meaningful parametric studies using field samples very difficult. In addition, it may not be possible to quantify some of the properties of the rock mass and analysis of the tests thus relies on estimated rather than measured values. For this project, it was essential that rock and joint properties were known, repeatable and controllable. Hence the choice was made to use synthetic rather than natural rock.

Rock mass samples that have been fabricated in the laboratory allow for tighter control of the rock mass parameters, particularly joint inclination, joint spacing and intact rock strength. The selection of an appropriate material to model the intact rock is therefore important. This material will need to have similar properties to the rock encountered in the field. It is also desirable for the intact material to be relatively homogeneous, isotropic and to have reproducible engineering properties. Moreover, the samples need to be of a scale that will allow the interactions between the intact rock and the joints to develop and be observed.

This study investigates the behaviour of jointed, soft rock masses, representing in particular the sedimentary rock that underlies much of the Melbourne metropolitan area. This rock, commonly

referred to as Melbourne Mudstone, consists of interbedded siltstones, claystones and sandstones of Silurian and Lower Devonian age. According to Johnston (1992), the uniaxial compressive strength of the weathered Melbourne Mudstone generally varies between about 0.5 MPa to 20 MPa, depending on the degree of weathering. Recent experience with tunnelling in the Melbourne area indicates that the uniaxial compressive strength of fresh Melbourne Mudstone can be as high as 80 MPa. Johnston and Choi (1986) have shown that saturated water content is an excellent indicator of the properties of Melbourne Mudstone.

5.2 Sample material

The use of natural Melbourne Mudstones in the test program was not considered feasible due to the difficulties with sourcing and obtaining a relatively large number of samples. Therefore, rock mass samples similar to the soft Melbourne Mudstone were manufactured from a synthetic soft rock called Johnstone (Johnston and Choi, 1986). This material was developed by simulating the processes that form sedimentary rock. Johnstone is produced by combining crushed siltstone with cement, water and set accelerant and then consolidating the mixture under load. The properties of this rock, as with the naturally occurring Melbourne Mudstone, can be correlated with its saturated moisture content (or porosity or void ratio). Further details regarding the development of Johnstone can be found in Johnston and Choi (1986).

There are a number of advantages in using Johnstone for this study. These include Johnstone:

- is relatively homogeneous and isotropic,
- has reproducible engineering properties which are similar to the natural Melbourne Mudstone and show a similar correlation with saturated water content (or void ratio), and
- is manufactured with a stress history. The stress history of a soft rock is important, particularly where failure is likely to occur through the intact rock.

Typical properties of the Johnstone used in this study are presented in Table 5-1. The properties of Melbourne Mudstone obtained from characterisation tests conducted by Chiu (1981) are also presented in Table 5-1 for comparison.

Table 5-1: Typical engineering properties of Johnstone used in this study and of natural Melbourne Mudstone.

Material	UCS (MPa)	E_{50} (MPa)	σ_t (kPa)	c (kPa)	ϕ	ν
Johnstone ($w \approx 14\%$)	3.5 (2.5-5.6)	400 (185-540)	600	300	35°	0.22
Johnstone ($w \approx 20\%$)	1.8 (0.8-2.5)	275 (140-400)	-	-	-	-
Melbourne Mudstone ($w=10\%$)	1.8-3.0	200-800	110-700	940	40.4°	0.25
Melbourne Mudstone ($w=14\%$)	1.5-2.9	200-400	70-300	520	33.6°	0.32

Table 5-1 shows that the Johnstone with $w \approx 14\%$ has similar properties to the Melbourne Mudstone with $w=10\%$ although the UCS of the Johnstone is slightly higher than that of the Melbourne Mudstone. The Johnstone with $w \approx 20\%$ has similar properties to the Melbourne Mudstone with $w=14\%$.

5.3 Johnstone manufacture

The manufacture of Johnstone is modelled on the natural process that leads to the formation of Melbourne Mudstone, albeit at a greatly accelerated rate. The Johnstone was manufactured in two block sizes. Blocks made for testing in the existing Type "A" shear box have been denoted Type "A" blocks. Similarly, blocks for testing in the Type "B" shear box have been denoted Type "B" blocks. The methodology and equipment used in the manufacture of the Johnstone blocks are described below.

5.3.1 Johnstone ingredients

The Johnstone blocks were made using the ingredients listed in Table 5-2.

Table 5-2: Recipes for Johnstone block manufacture.

Ingredient	Type "A" block	Type "B" block
Crushed siltstone powder	28.8 kg	70.0 kg
Ordinary cement (type GP)	0.72 kg	1.75 kg
Water	3.456 kg	8.4 kg
Set accelerant (10% CaCl ₂)	0.37 kg	0.9 kg

The siltstone powder was produced by crushing siltstone boulders and cobbles recovered from a local quarry in Scoresby, Victoria. These were broken down to gravel size before being passed through a mill to produce a fine powder. The powder was then stored in 200 L drums until required. The particle size distributions of natural mudstone and the powder used in this study are presented in Figure 5-1

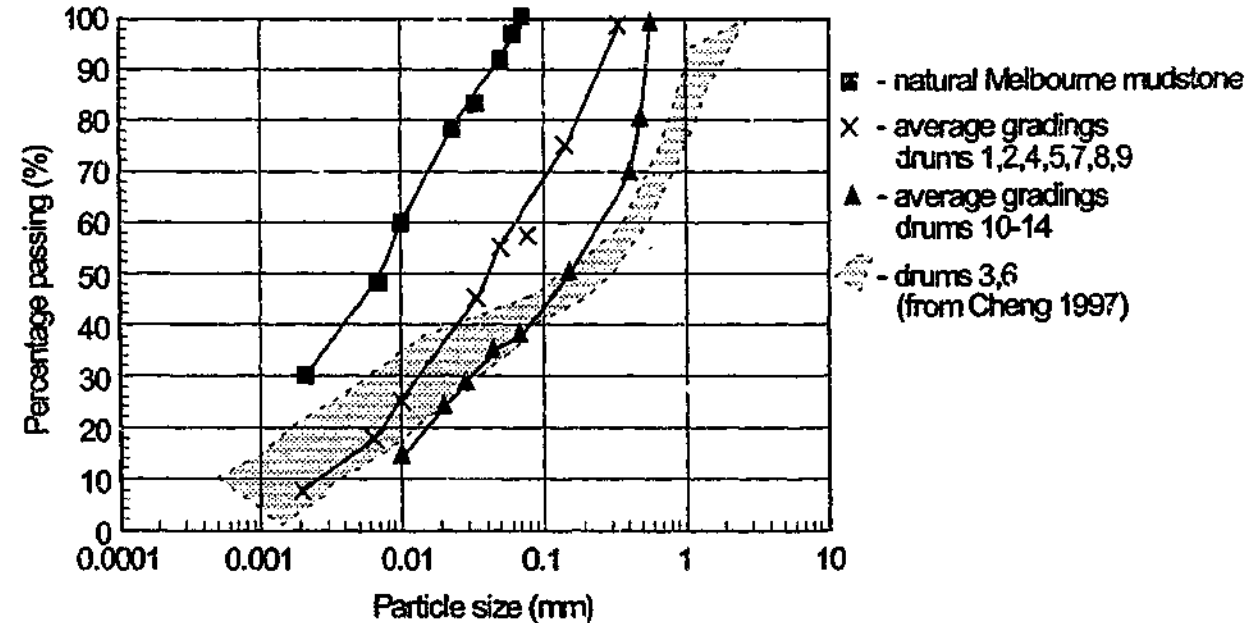


Figure 5-1: Grading curves of siltstone powder used in Johnstone manufacture.

The Type "A" blocks and some of the early Type "B" blocks were made from the siltstone powder left over from the work of Cheng (1997). Once the supply of this powder was exhausted, more powder was produced by passing crushed siltstone through a mill. This new powder was also

passed through a sieve to produce a finer powder. The remainder of the Type "B" blocks were produced using this powder.

5.3.2 Johnstone batching process

The batching process consisted of mixing the siltstone powder and cement for about 30 seconds in a 70 litre pan mixer. A solution of tap water and set accelerant was then gradually added to the dry mixture over a 30 second period. The blended ingredients were mixed for a further 90 seconds, after which the Johnstone could be seen to be forming small balls. The mixture was then removed from the mixer.

5.3.3 Johnstone block production

The Johnstone blocks were formed by placing the mixed ingredients into a mould and subjecting the mixture to a vertical consolidating pressure. The mixture was placed in the mould in layers about 30 mm thick. Each layer was tamped and the upper surface scarified before the next layer was placed.

Two moulds were used to produce the Johnstone blocks. The first blocks produced, denoted as Type "A" blocks, were 560 mm long by 165 mm high by 150 mm wide with a mass of about 33 kg. However, the majority of the Johnstone blocks were Type "B" blocks, which were 420 mm long by 280 mm high by 270 mm wide with a mass of about 81 kg.

The schematic arrangement of the Type "B" mould is shown in Figure 5-2. The arrangement for the Type "A" mould was similar to the Type "B" mould. The porous plates provide drainage pathways for water as the Johnstone consolidates.

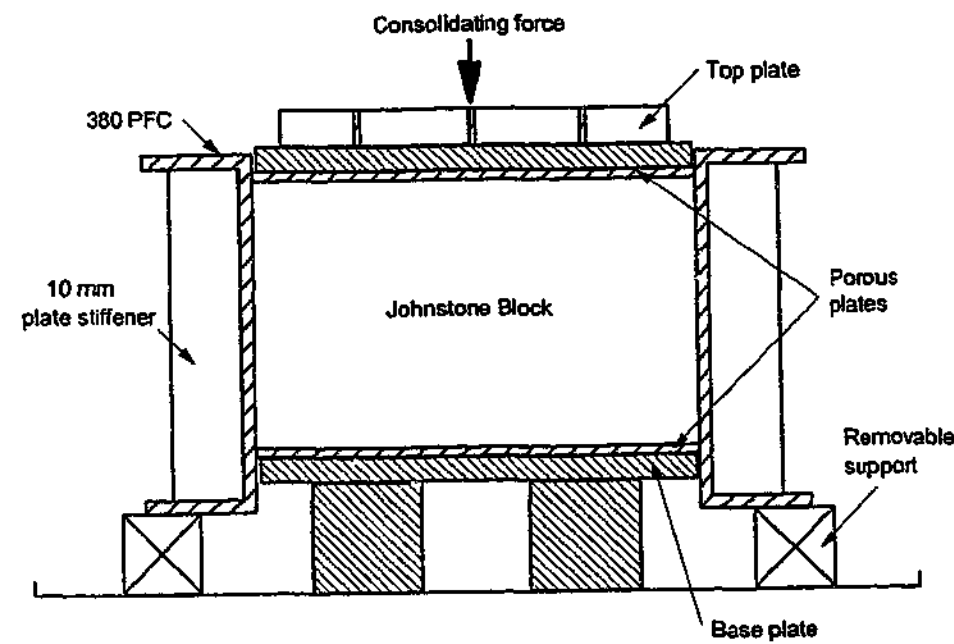


Figure 5-2: Arrangement of the Type "B" mould.

A photograph of the Type "B" mould prior to placement of the Johnstone mixture is shown in Figure 5-3.

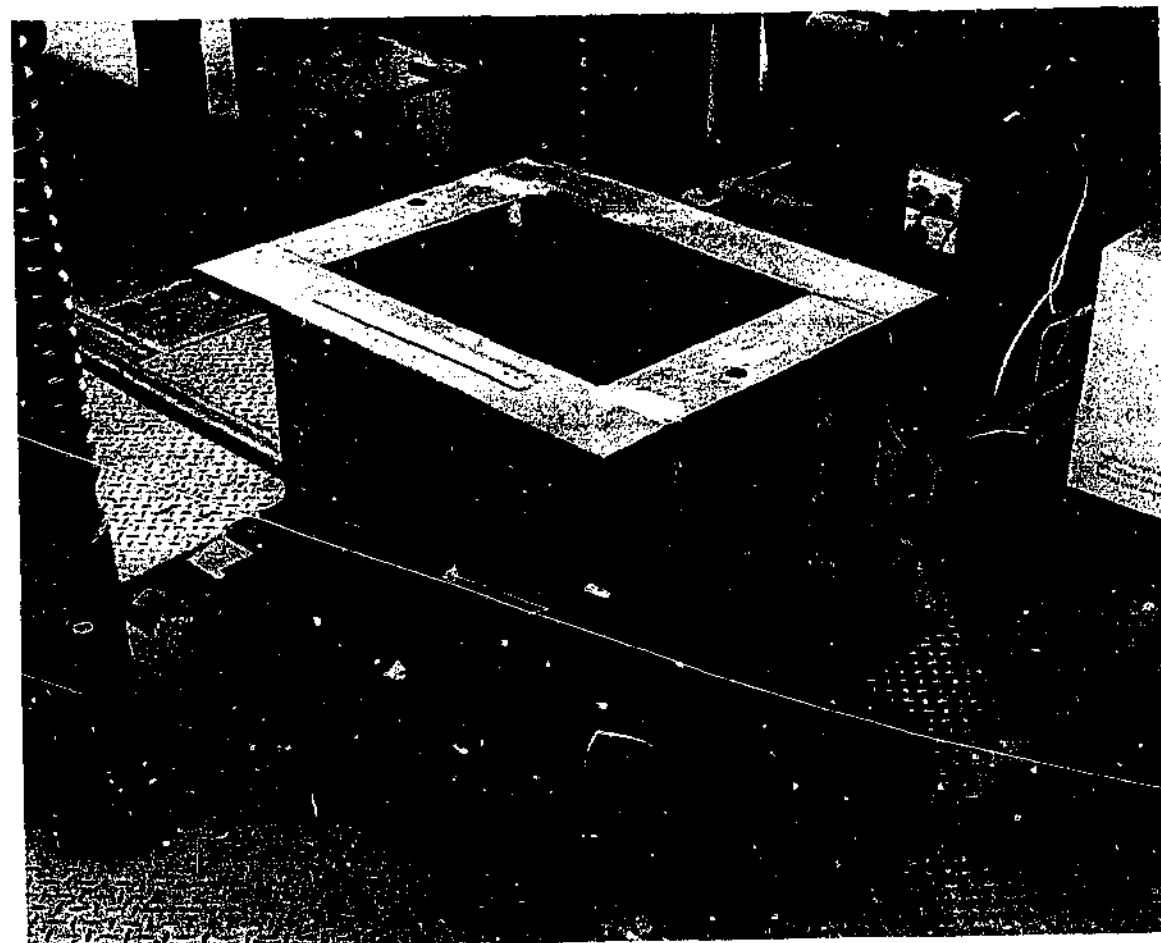


Figure 5-3: Type "B" mould arrangement prior to placement of Johnstone mixture.

Once the Johnstone mixture had been placed in the mould, a stiffened steel top plate was placed on the porous plate and the mould placed in a hydraulic press. The supports for the mould were removed and an axial pressure applied to the mixture via the top and base plates. Figure 5-4 shows the Type "B" mould ready for placement in the hydraulic press.

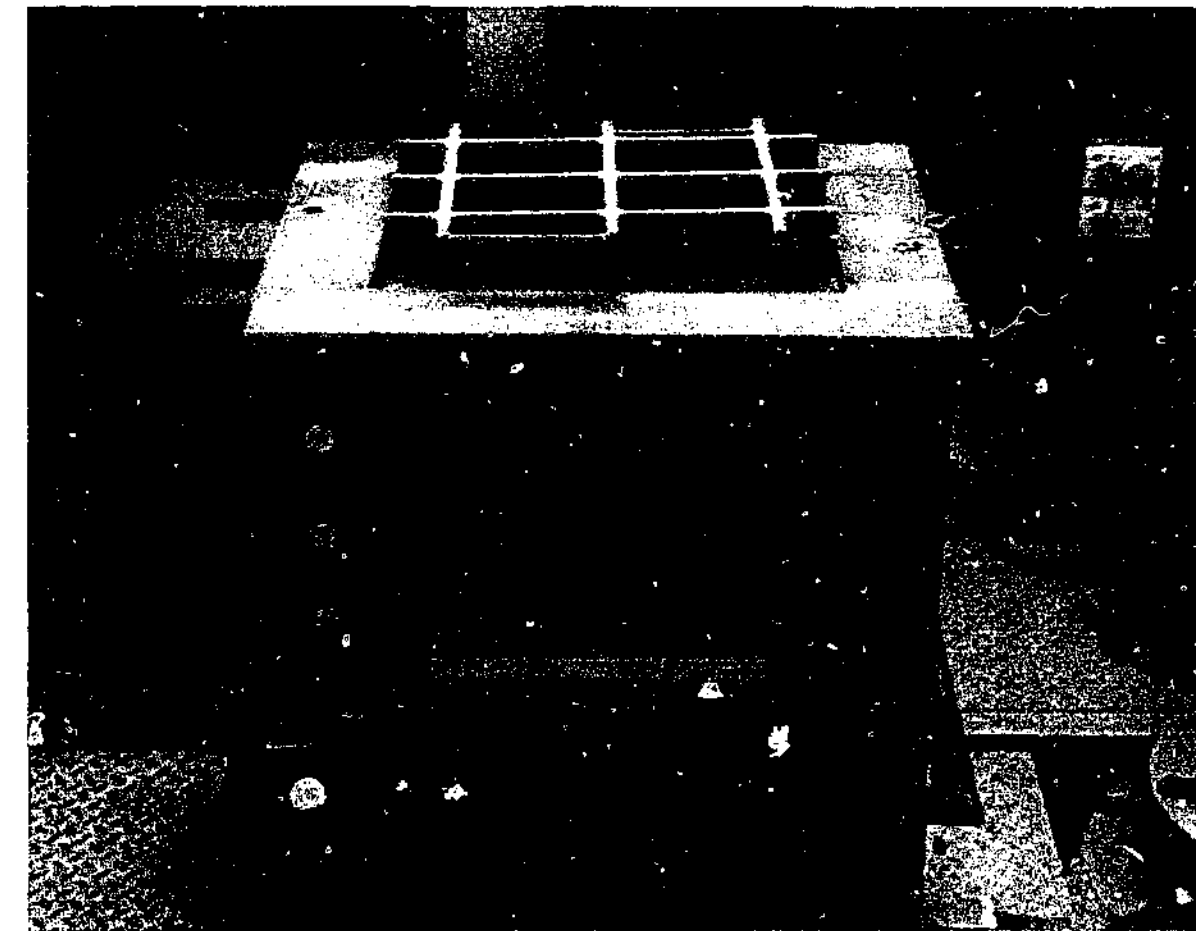


Figure 5-4: Type "B" mould containing Johnstone mixture ready for placement in hydraulic press (note stiffened top plate arrangement).

The mixture was left under load to consolidate. A typical pressure of 3 MPa was applied for a minimum of four and a half hours, by which time vertical displacement of the sample had effectively ceased. The Johnstone block was then removed from the mould by placing the mould on a frame, placing a plunger on the top plate and using the hydraulic press to extrude the sample. The plunger arrangement is shown in Figure 5-5.

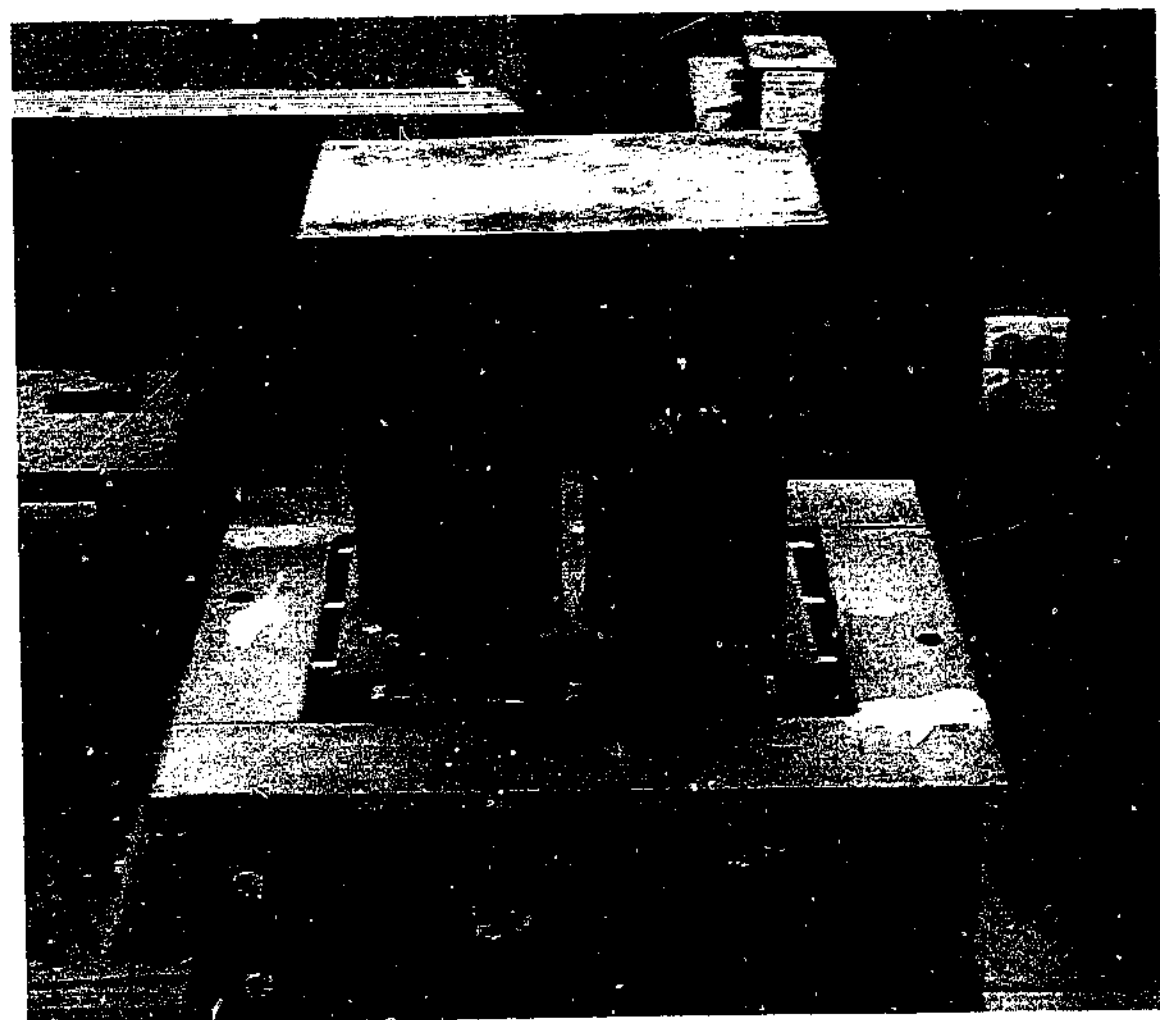


Figure 5-5: Plunger placed on top plate.

The extruded sample was placed in a high humidity room for at least 28 days to cure. Further details on the procedures for batching, mixing, placing and consolidating the Johnstone can be found in Johnston and Choi (1986).

Each block of Johnstone took one day to produce. The ingredients were measured out the day before, so that batching could commence at the start of the day. The batching process took about 15 minutes, placement of the Johnstone mixture in the mould took about 45 minutes and application of the consolidating load another 30 minutes. The consolidating load was maintained for about 6 hours, during which time the ingredients for the next block were prepared. Removal of the consolidating load, extrusion of the sample and transfer of the Johnstone block to the high humidity room took about an hour. The process of making the Johnstone blocks was physically demanding.

5.4 Johnstone properties

The Johnstone blocks were tested to assess their engineering properties. These tests were generally carried out on samples recovered from the rock mass after shear testing. Properties measured included saturated moisture content, unconfined compressive strength, secant modulus, tensile strength, intact friction angle, intact cohesion and joint friction angle. Details of these properties follow.

5.4.1 Saturated moisture content

The saturated moisture content of the Johnstone used in each shear and UCS test was measured. A piece of the Johnstone was recovered from each sample and vacuum saturated under water for at least 24 hours in a desiccator before being tested. Moisture contents were measured to assist in developing a study specific correlation between saturated moisture content and the strength and secant modulus of the Johnstone, and to provide an indication of the consistency between the Johnstone blocks.

5.4.2 UCS and modulus testing

Unconfined compressive strength tests were carried out on core samples recovered, where possible, from each rock mass sample after shear testing. Cores were chosen from areas of the sample that appeared to be relatively lightly loaded and to have suffered no observable damage during the shear testing. The core samples were obtained using a 54 mm diameter core barrel. The ends of the core were prepared using a diamond saw. The UCS and secant modulus values were measured in tests that were carried out in general accordance with the ISRM procedure "Suggested Methods for Determining the Uniaxial Compressive Strength and Deformability of Rock Materials" (Brown, 1981).

However, some of these cores did not comply with this standard in that they did not achieve a length to diameter ratio of between 2:1 and 3:1. This was due to breakage during coring or during core sample preparation. Several tests were on triangular prisms with each side about 65 mm in length (from samples B24 and B25) rather than on core samples. This was because suitable cores could not be obtained from these samples. These prisms were tested to give indicative strength values only.

The variation of UCS and secant modulus with saturated moisture content for the Johnstone produced for this project is shown in Figure 5-6 and Figure 5-7 respectively.

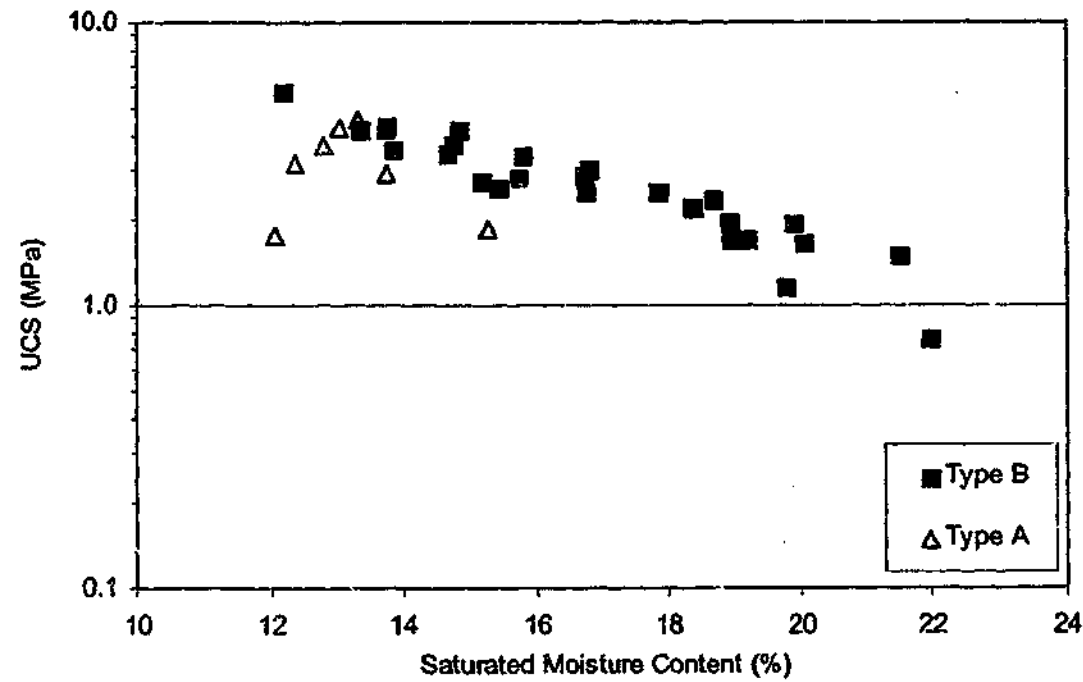


Figure 5-6: Correlation between saturated moisture content and UCS for Type "B" blocks.

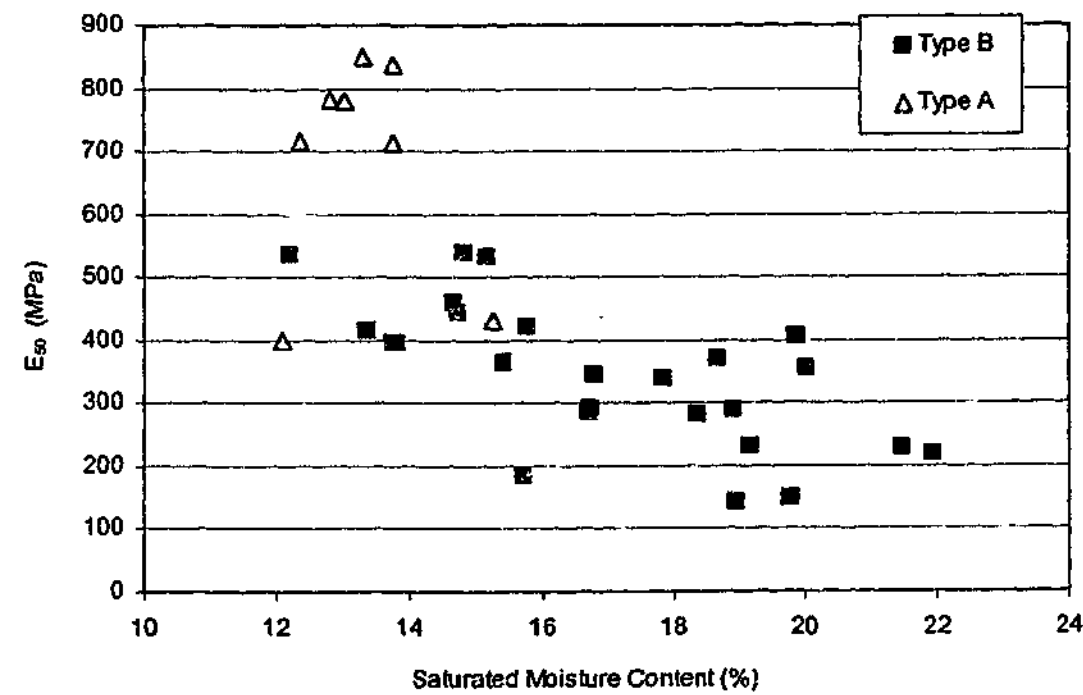


Figure 5-7: Correlation between saturated moisture content and secant modulus.

There appears to be a good correlation between the saturated moisture content and the UCS of the Type "B" Johnstone blocks manufactured in this study. The UCS values for the Type "A" blocks appear to be generally less than for the Type "B" blocks for the same moisture content. This is thought to be due to the quality of the cement used to make the Type "A" blocks. It is possible that the cement used in the Type "A" blocks had deteriorated before use. Therefore, all the Type "B" blocks were manufactured using fresh cement.

The correlation between saturated moisture content and secant modulus shows more scatter.

The correlation between the saturated moisture content, m/c , and the UCS and modulus of the Type "B" Johnstone blocks can be approximated by:

$$UCS = -0.4m/c + 9.5 \quad \text{Equation 5-1}$$

$$E = -29m/c + 840 \quad \text{Equation 5-2}$$

Figure 5-8 and Figure 5-9 compare the UCS and secant modulus values obtained from the Type "B" samples during this study with earlier studies.

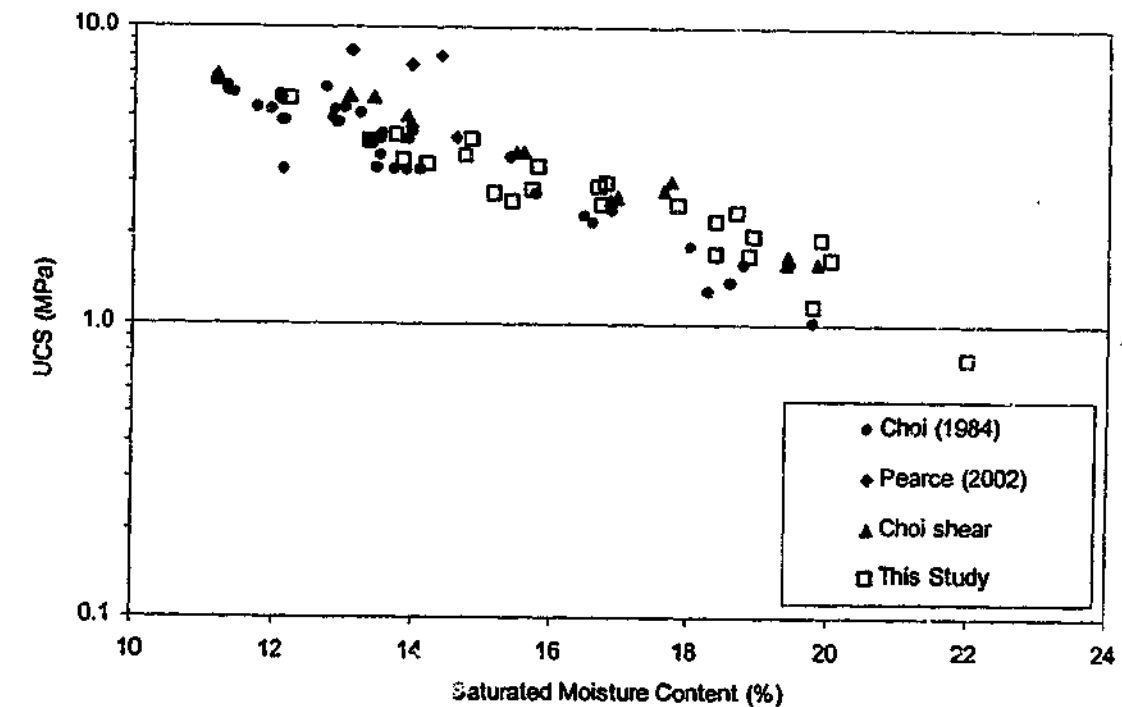


Figure 5-8: Comparison of UCS test results with earlier studies.

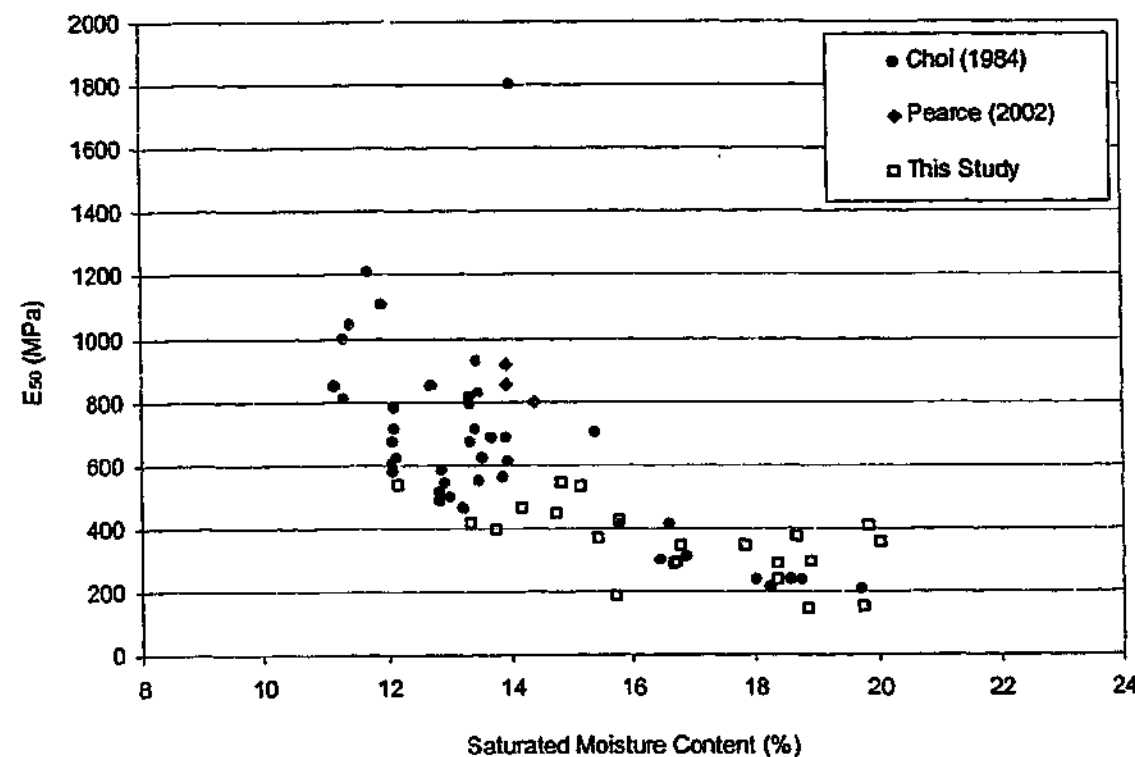


Figure 5-9: Comparison of secant modulus test results with earlier studies.

Figure 5-8 and Figure 5-9 indicate that the UCS and secant modulus values obtained in this study are similar to those of earlier studies.

5.4.3 Brazilian testing

The tensile strength of the Johnstone was assessed from Brazilian tests. Two cores (from Tests B5 and B18) were prepared and tested in accordance with ISRM procedure "Suggested Method for Determining Indirect Tensile Strength by the Brazilian Test" (Brown, 1981). It was found that the tensile strength of the Johnstone produced in this project was similar to that of earlier studies. The ratio of compressive to tensile strength was found to be about 5, which is close to a ratio of 7 suggested by Johnston (1985) for soft argillaceous rocks.

5.4.4 Rock triaxial testing

Consolidated, drained (CD) triaxial tests were carried out to assess the effective friction angle and cohesion of the intact Johnstone. These tests were carried out on core samples recovered from tests B4 (UCS=3.0 MPa) and B10 (UCS=3.5 MPa). A backpressure of 0.9 MPa was used in all tests. The cell pressure was varied for each test so that effective confining pressures of 0.5 MPa, 2.4 MPa

and 3.0 MPa were applied. Samples were saturated in the cell to obtain a minimum B value of 0.95. The samples were then consolidated to their nominated effective confining stress and sheared at a rate of 0.004 mm/sec.

The stress paths obtained from the CD triaxial tests are plotted in p-q space in Figure 5-10 and Figure 5-11. The UCS value has also been included. A linear trendline has been generated through the peak values to allow estimation Mohr-Coulomb strength parameters.

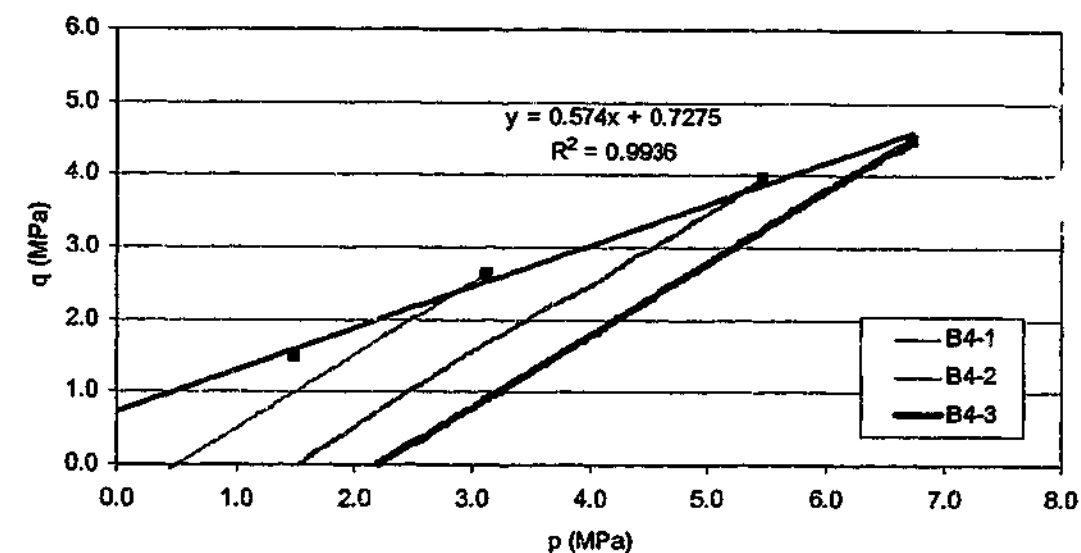


Figure 5-10: Stress paths and peak envelope for Test B4 samples.

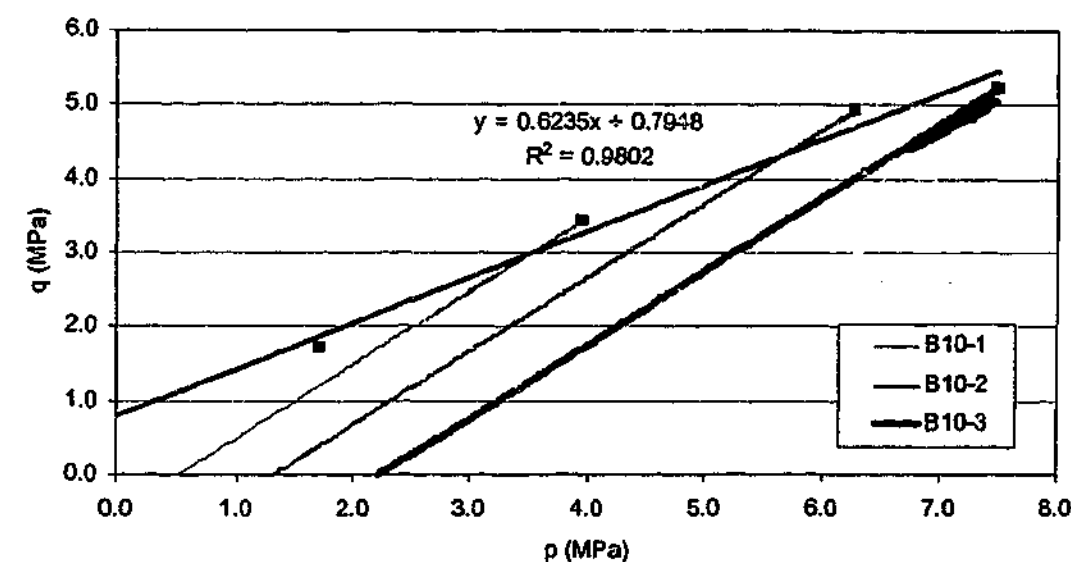


Figure 5-11: Stress paths and peak envelope for Test B10 samples.

The effective Mohr-Coulomb strength parameters for the Johnstone used in Test B4 ($\phi'=35^\circ$, $c'=1040$ kPa) and Test B10 ($\phi'=39^\circ$, $c'=980$ kPa) were assessed from the envelopes of the p-q curves. These values have been plotted against earlier results from Kodikara (1989) and are shown in Figure 5-12 and Figure 5-13.

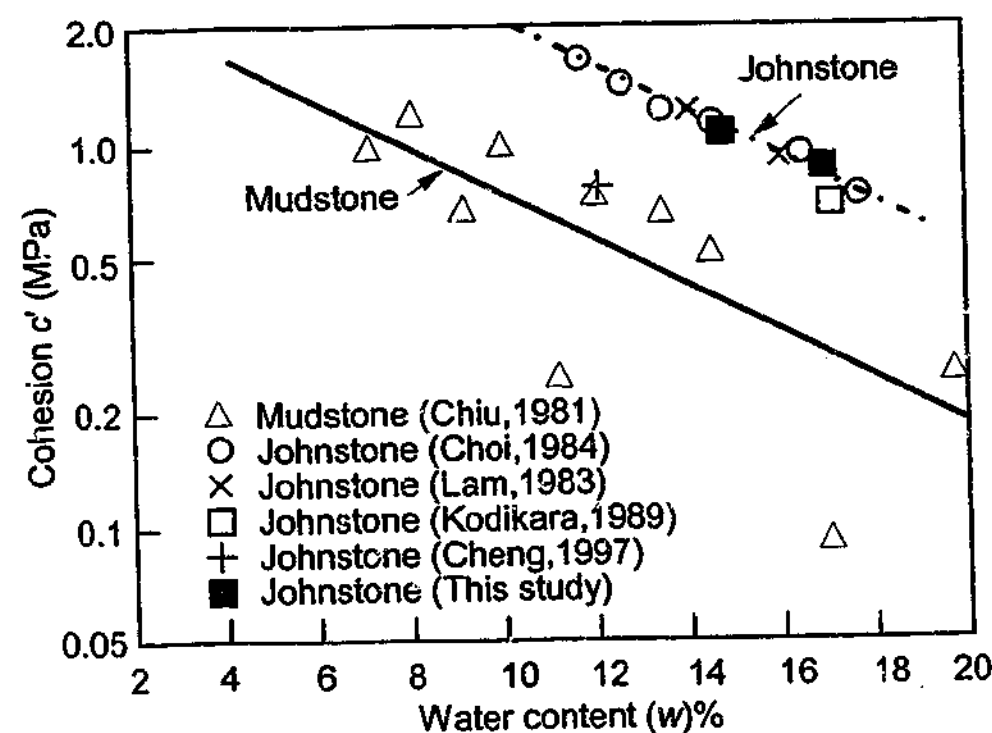


Figure 5-12: Variation of cohesion with saturated moisture content.

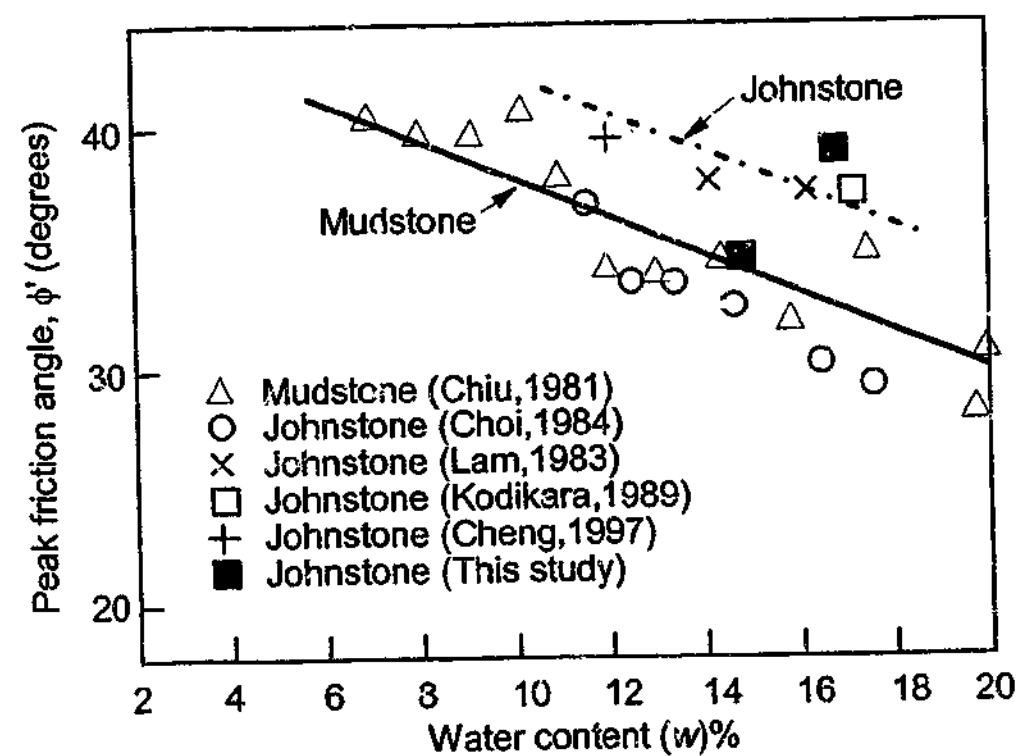


Figure 5-13: Variation of friction angle with saturated moisture content.

5.4.5 Rock joint properties

Joints were cut into the intact Johnstone blocks using a (circular) diamond saw (see Section 5.5.1). This produced a smooth, unaltered, planar joint. A photograph of a typical joint surface is shown in Figure 5-14.

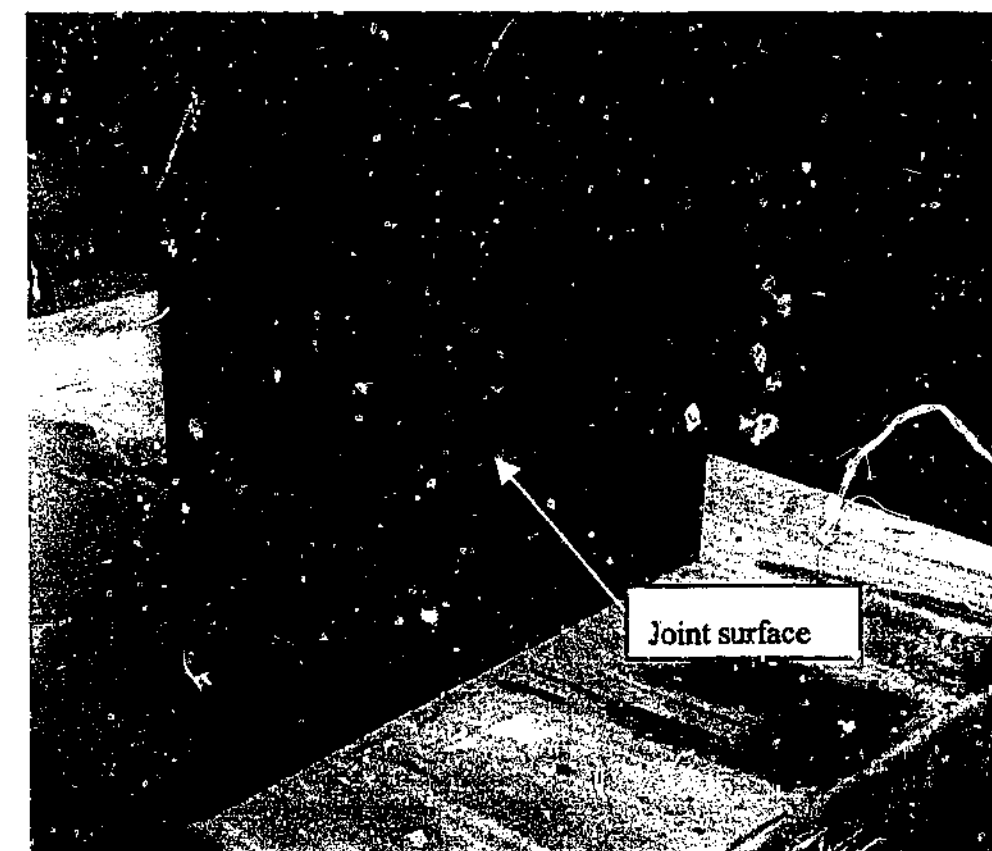


Figure 5-14: Typical joint surface produced by cutting process.

The friction angle of a typical joint was obtained by testing a rock block containing a single horizontal joint in direct shear. The joint friction angle, ϕ_j , measured from this test (see test Joint in Appendix B) was 29° . Another test (Test B28) was carried out on a rock mass containing vertical and horizontal joints. The joint friction angle measured in this test was 28° . A joint friction angle of 28° has been adopted for this study.

5.5 Jointed rock mass sample fabrication

5.5.1 Cutting apparatus

Joints were cut into the intact blocks using circular saws fitted with diamond blades. The Type "A" blocks were cut using a common brick-cutting saw. The Type "B" blocks were cut using a block saw that was specifically designed and built for this project.

5.5.1.1 Brick saw

A brick-cutting saw, similar to those used on construction sites to cut bricks and tiles, was used to cut joints into the Type "A" blocks. The brick saw used in this study has a blade diameter of 410 mm, a blade thickness of 3 mm and spins at 2850 rpm (blade tip velocity ≈ 61 m/s). The blade is cooled by water, which also washes away the cuttings.

5.5.1.2 Block saw

A custom-built block saw, shown in Figure 5-15, was used to cut the joints into the Type "B" blocks. The block saw has a blade diameter of 800 mm, a blade thickness of 4.5 mm and spins at 950 rpm (blade tip velocity ≈ 40 m/s). Water was used to cool the blade and wash away cuttings from the blade and sample.

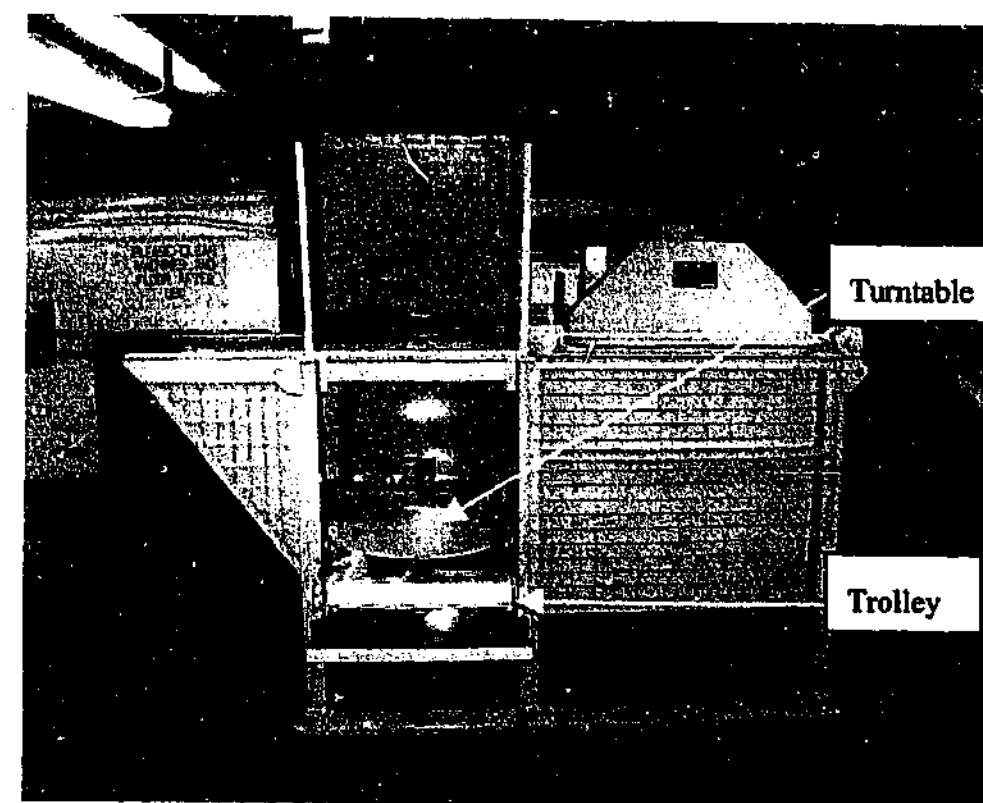


Figure 5-15: Block saw, showing turntable and trolley arrangement.

5.5.2 Cutting procedure-Type "A" blocks

Prior to cutting the joints, the desired jointing pattern was inscribed onto the surface of the block. The Type "A" blocks were cut by placing the block on the tray of the brick saw and aligning the scribed joint with the blade. The tray and block were then pushed towards and past the blade to cut the joint.

5.5.3 Cutting procedure-Type "B" blocks

Prior to cutting the joints, the desired jointing pattern was inscribed onto the block surface, an example of which is shown in Figure 5-16.



Figure 5-16: Jointing pattern scribed on block surface.

The block saw was designed to allow Johnstone blocks up to 300 mm deep to be cut. The Johnstone block is placed on a specially designed pallet that allows the block to be transported and fastened to the turntable, as shown in Figure 5-17.

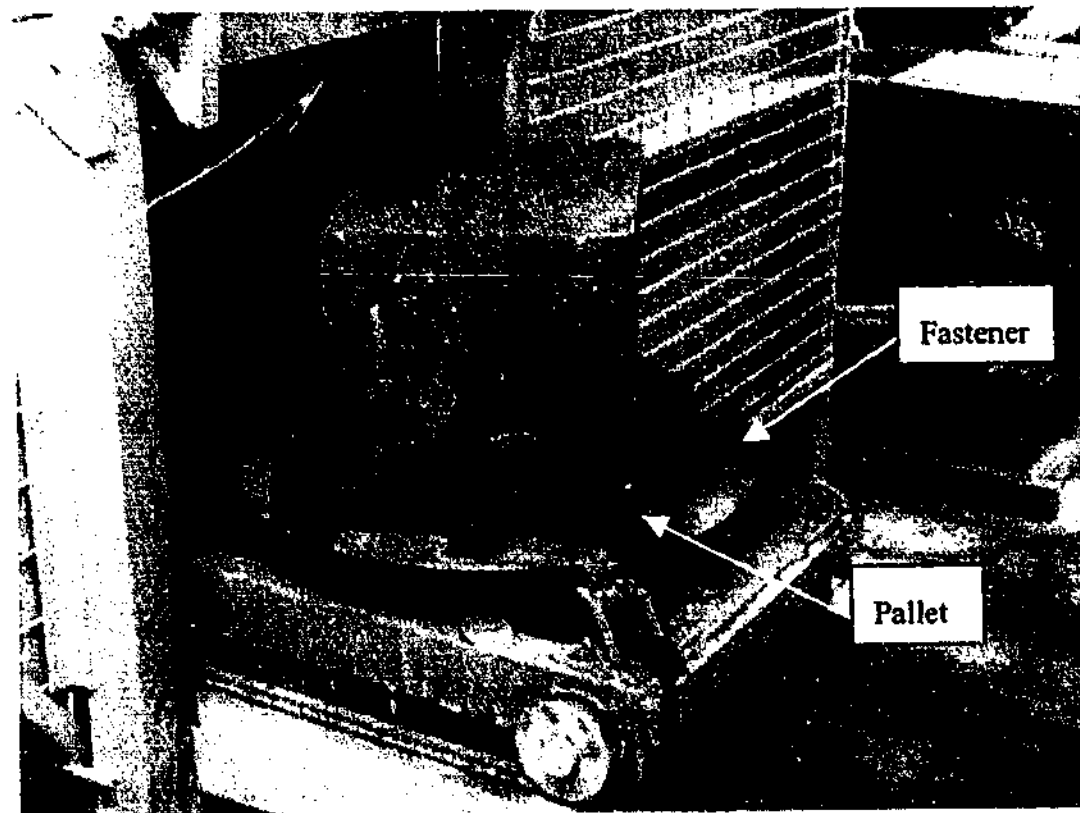


Figure 5-17: Block on pallet fastened to turntable.

The block is placed on a turntable that can be rotated so the inscribed joint is aligned with the blade, as shown in Figure 5-18, and locked in position. It is estimated from measurements taken of the finished samples that the joint inclinations cut into the samples produced for this study were accurate to within $\pm 0.5^\circ$.

The turntable is located on a trolley as shown in Figure 5-15 and Figure 5-17. The trolley moves at right angles to the blade and allows joint spacing to be controlled to within ± 2 mm. Once the joint is aligned with the blade, the trolley is locked in position and the blade pulled through the block.

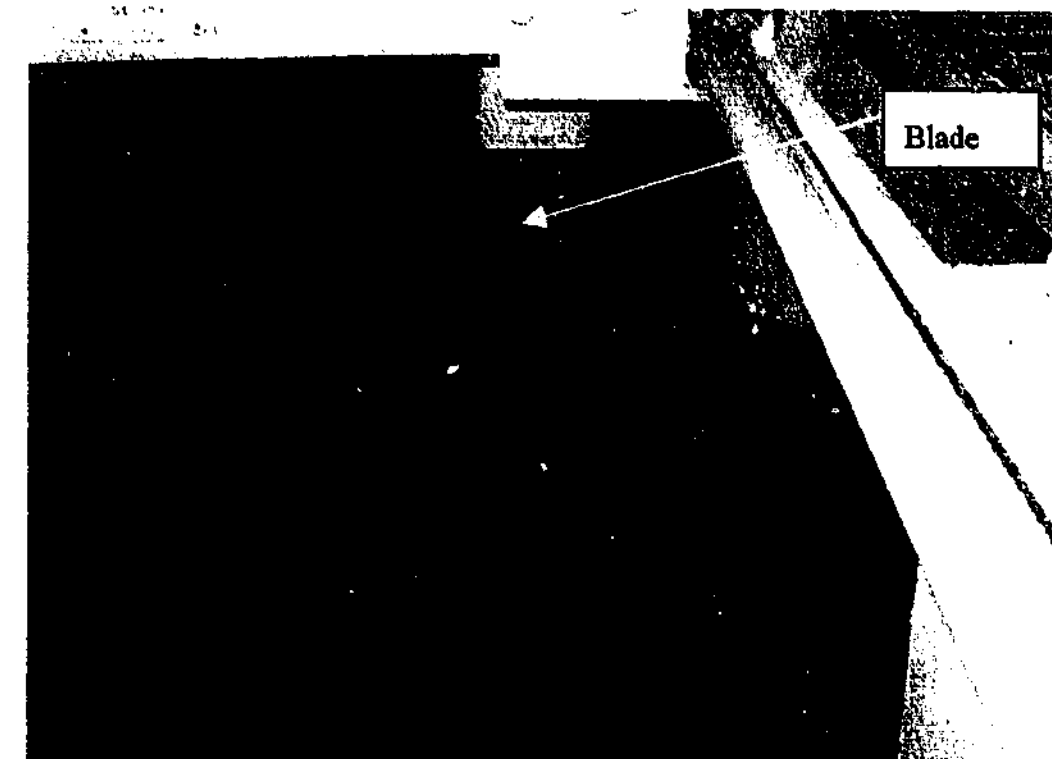


Figure 5-18: Detail showing positioning of block and scribed joint with respect to blade.

For this study, the first joint set was cut by moving the trolley one joint spacing after each cut. This resulted in parallel joints and the removal of about 5 mm of Johnstone with each cut, as shown in Figure 5-19.



Figure 5-19: Block after first joint set has been cut.

After all the joints in the first joint set had been cut, the blocks were pushed together to close the gaps and the inscribed lines of the uncut joints aligned. Plywood falsework was placed around the sample and the gaps between the Johnstone and the falsework filled with packing material (plasterboard) as shown in Figure 5-20. The packing material reduced movement of the Johnstone as the blade passed through the sample and also prevented pieces at the edge of the block from falling off the turntable and breaking during the cutting process.

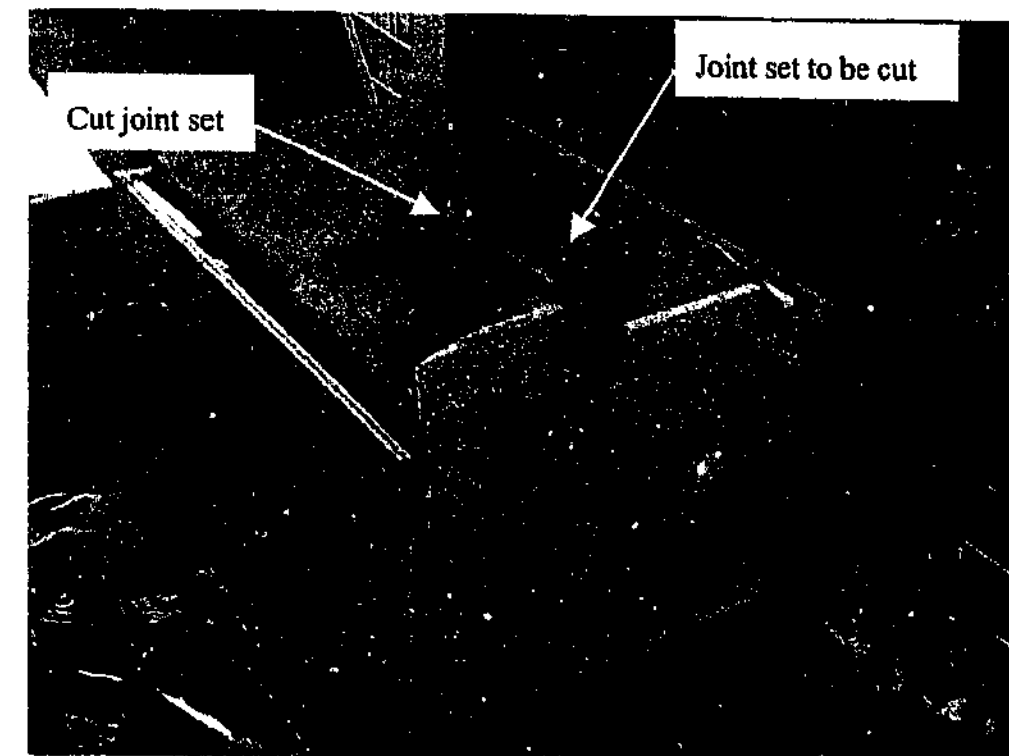


Figure 5-20: Sample with realigned joints surrounded by falsework.

The second joint set was then aligned with the blade and cut by pulling the blade along each of the inscribed lines. This produced a sample with two nominally parallel, equally spaced joint sets, as shown in Figure 5-21.

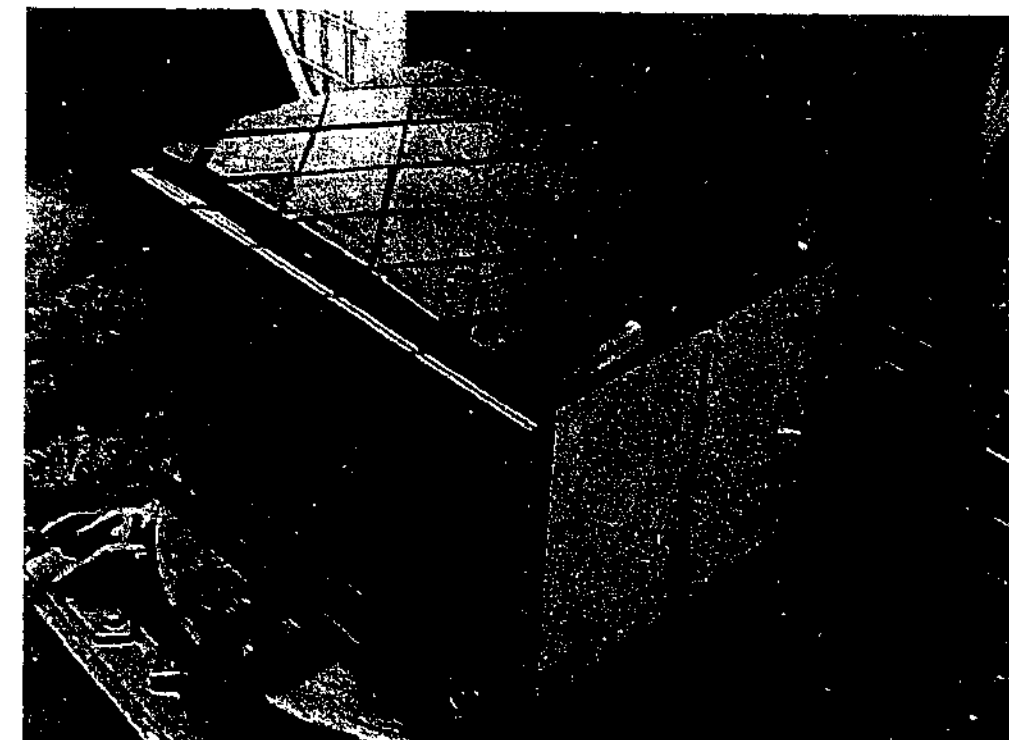


Figure 5-21: Sample after second joint set had been cut.

For samples containing three joint sets, the process of closing the gaps produced by the cuts, realigning the uncut joint set, fitting the falsework and packing material and cutting the joints was repeated.

The time taken to inscribe and cut the joint sets into each block was about 45 minutes for blocks with two joint sets and about an hour for blocks with three joint sets.

5.5.4 Rock mass sample assembly

The cutting process produced a number of small prisms of intact rock. The jointed rock mass was produced by assembling these prisms so that the joints were aligned.

The pieces of the Type "A" sample were reassembled on a flat surface so that the joints were as aligned and as planar as practical. The sample was then wrapped in plastic food wrap, placed in a plywood form and encapsulated in plaster.

The pieces of the Type "B" rock mass were placed in a form made from steel plate that had been ground flat. The form had removable sides to facilitate assembly of the rock mass. Figure 5-22 shows the steel form with one side removed.



Figure 5-22: Steel form used to encapsulate Type "B" samples in plaster.

Prior to assembly of the rock mass, the sides of the steel form were removed and the base covered with plastic food wrap. Reference lines were drawn on the plastic wrap to aid alignment of the joints. Each piece of intact rock was then removed from the cut block, cleaned of any cuttings and smear and placed in the same relative position on the steel base. A partially assembled rock mass, with joints that appear to be aligned, clean, smooth and planar is shown in Figure 5-23.

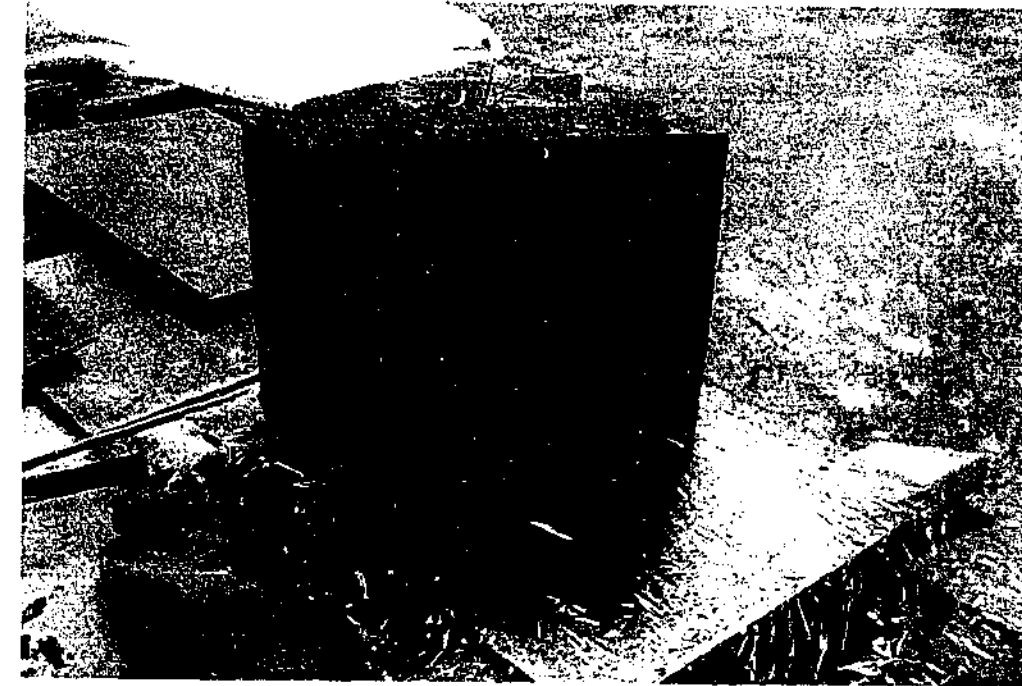


Figure 5-23: Partially assembled rock mass on steel base.



Figure 5-24: Reassembled rock mass.

The reassembly process was continued until the rock mass had been completed, as shown in Figure 5-24. The reassembled rock mass shown has some joints that do not appear to be tight and is missing some of the small outer pieces. The joint aperture was partially reduced by wrapping the reassembled rock mass in plastic food wrap. The plastic food wrap also prevented the ingress of plaster into the joints and prevented the plaster from drawing water out of the Johnstone.

The cutting process removed about 5 mm of rock material with each cut. This meant that when the sample was reassembled, the outer surface of the rock mass was often uneven. Some of the smaller pieces at the edge of the sample were also lost. This meant the contact between the rock mass sample and the shear box would not be even. To overcome this problem, the steel form was placed around each sample and the volume between the form and the sample filled with plaster. The form also comprised 18 mm plywood strips on either side of the shear plane to form a void in the plaster. Figure 5-25 shows a reassembled sample wrapped in plastic food wrap surrounded by the steel form prior to plaster being placed in the void between the sample and the steel form. The plywood strips used to form a void at each end of the shear plane can also be seen. The encapsulating plaster allowed the sample to be handled, transported, placed in the shear box and tested without loss of joint alignment. This also meant the outer profile of the sample was consistent, reducing shear box preparation time.

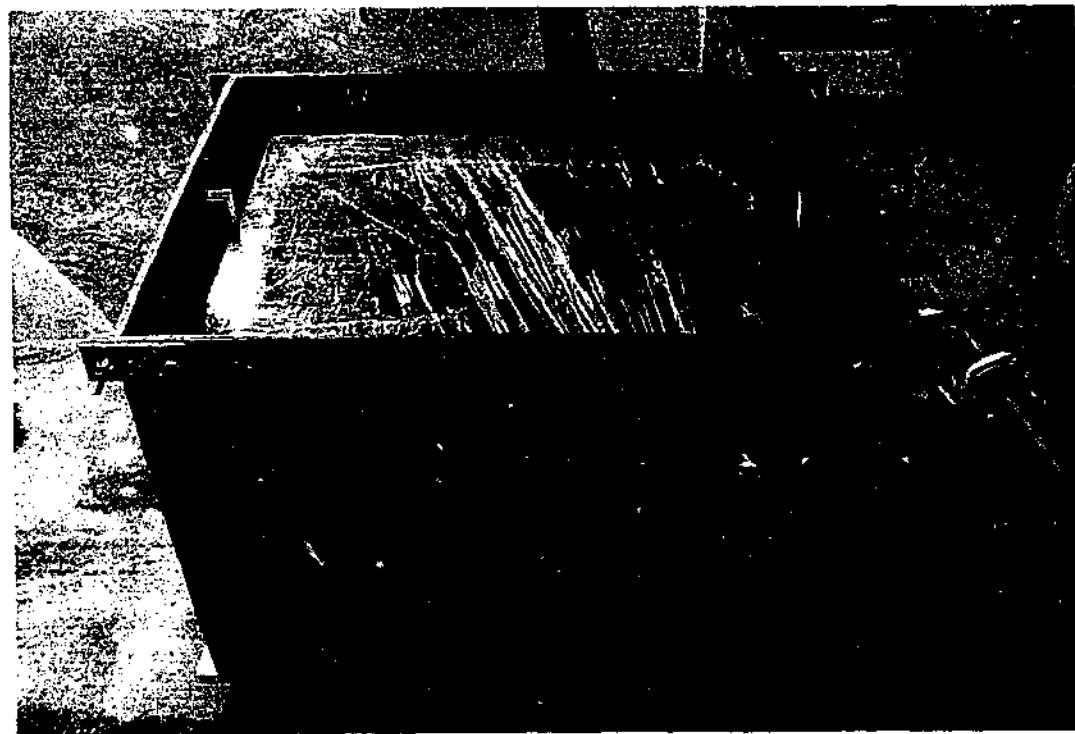


Figure 5-25: Reassembled sample in steel form.

Once the encapsulating plaster had cured, the sides of the steel form and the plywood strips at either end of the shear plane were removed. The sample was then rotated forward onto a pallet. A typical jointed rock mass sample ready for installation into the shear box is shown in Figure 5-26. The joints in this finished rock mass now appear to be reasonably tight and the void formed at one end of the shear plane can be clearly seen.

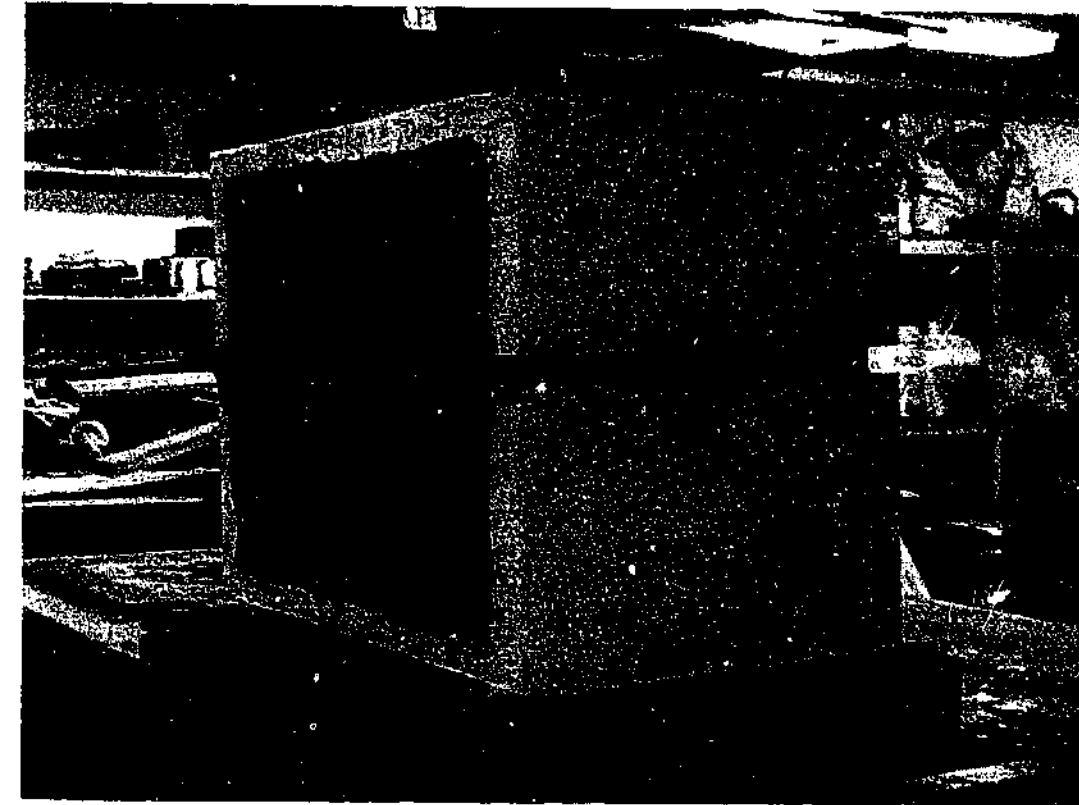


Figure 5-26: Reassembled sample encapsulated in plaster.

Each sample took about 30 minutes to reassemble and wrap in plastic. Mixing and pouring the plaster took about another 20 minutes. The plaster was left to cure for about two hours before the steel form was removed. The plaster was then allowed to air cure for about 30 minutes before the rock mass sample was placed in a high humidity room until required for testing.

The quality of samples improved over the duration of the project. The joints in the early samples were not as well aligned or as tight as in later samples, but still appeared to be reasonably planar. The samples with three joint sets were considerably more difficult to fabricate. However, the joints in these samples also appeared to be reasonably planar, as shown in Figure 5-27.

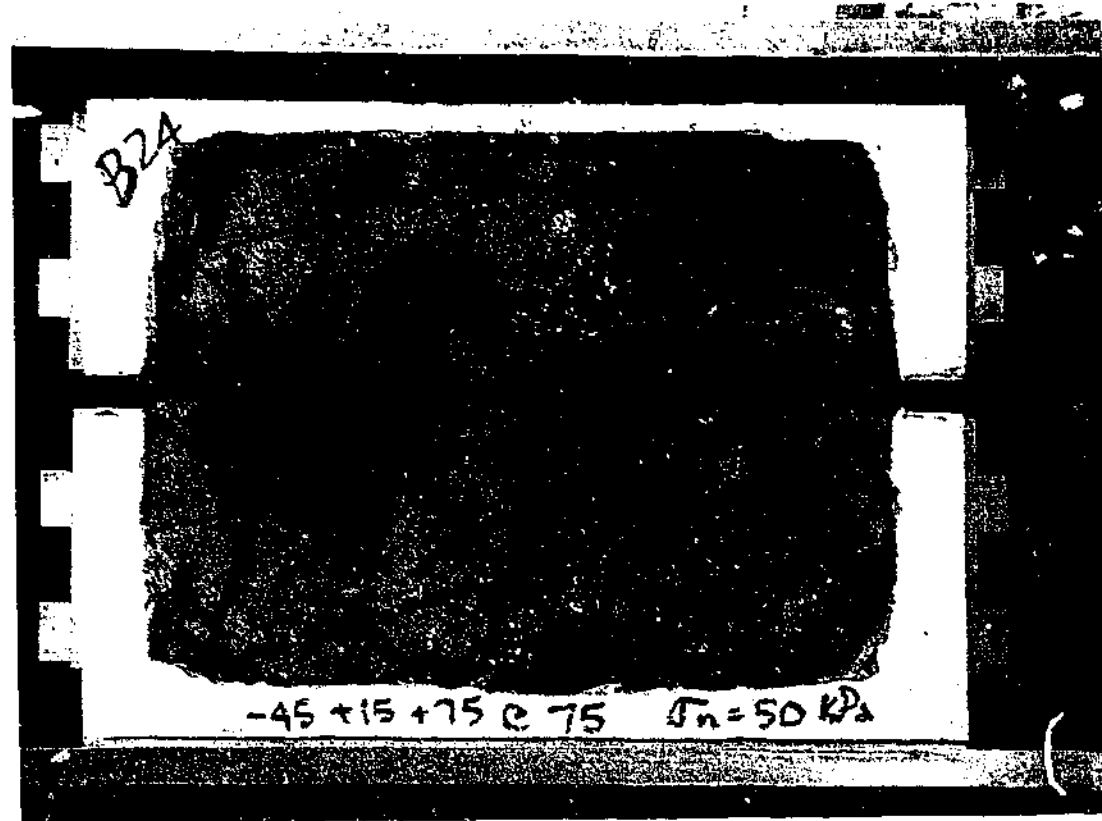


Figure 5-27: Sample containing three joint sets (from Test B24).

5.5.5 Shear test procedure-preparation

5.5.5.1 Type "A" shear tests

On the day prior to testing, the Type "A" sample was taken from the high humidity room and placed in the lower half of the Type "A" shear box. The sample was then cast into the lower half of the shear box using plaster. A void was formed along the shear plane using 25 mm thick rubber strips. The top half of the shear box was then placed over the sample and fixed to the bottom half of the shear box using the separator strips. The top plate was removed so that the top half of the shear box could be filled with plaster. The top plate was then immediately reinstated and the sample bolted into the CNS shear apparatus and left overnight for the plaster to cure.

On the morning of the test, the rubber strips and exposed food wrap were removed and the external LVDT's and reference plates fitted. Further details of testing using the Type "A" shear box can be found in Pearce (2001).

5.5.5.2 Type "B" shear tests

The Type "B" samples were placed in the shear box immediately before testing. The sample was taken from the high humidity room and placed between the side plates of the Type "B" shear box. The top plate was then placed on the sample, as shown in Figure 5-28.

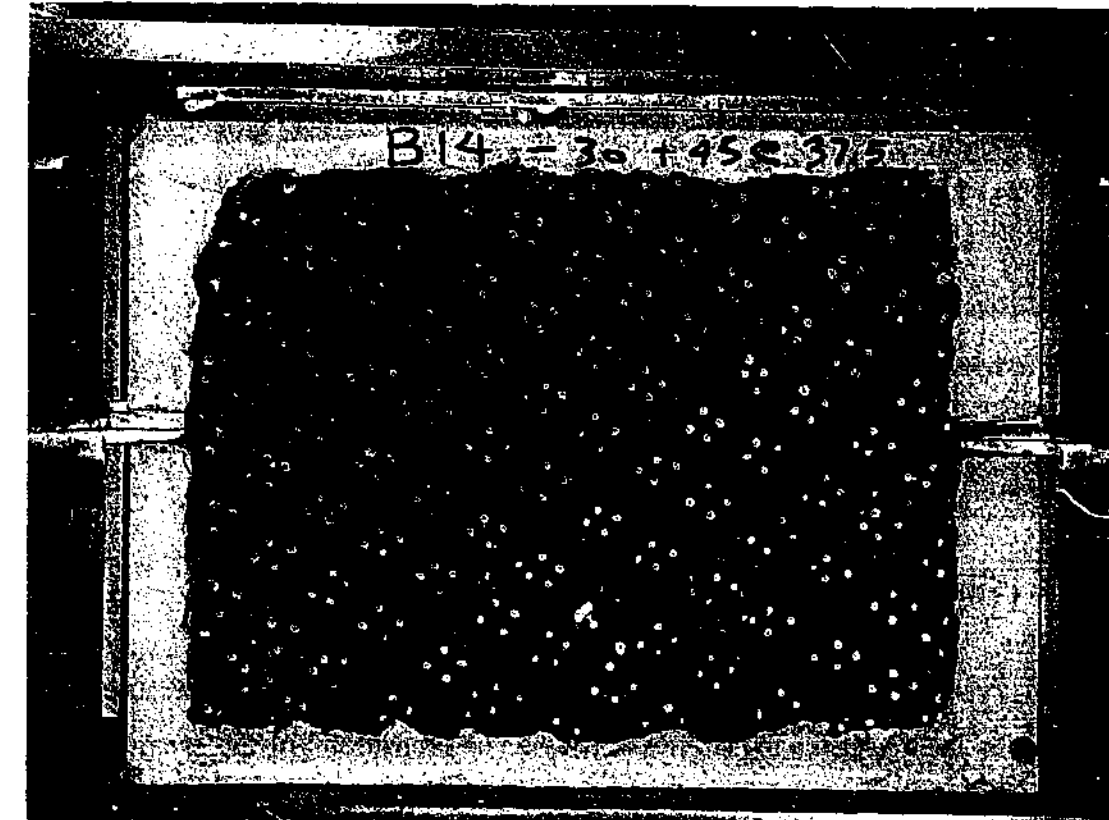


Figure 5-28: Rock mass sample encapsulated in plaster, showing voids at each end of shear plane and uneven outer surface and loss of smaller pieces at edge of Johnstone (from Test B14).

The lower perspex front was used to push the sample into the shear box as it was bolted into position. The rear plates were brought forward until they made contact with the sample. The top plate was then aligned with the four studs in the top of the shear box, and the studs then brought into contact with the top plate. The upper perspex front was then bolted into place. The side plates were brought into contact with the sample by rotating the threaded bars. A torque was applied to the threaded bars so that an inferred horizontal stress of 100 kPa was applied to the ends of the sample. The shear box was then bolted into the CNS shear apparatus. The separator strips joining the upper and lower halves of the shear box were removed and the external LVDT's and reference plates were then fitted to the shear box. Figure 5-29 shows the shear box containing a sample after placement in the shear apparatus.

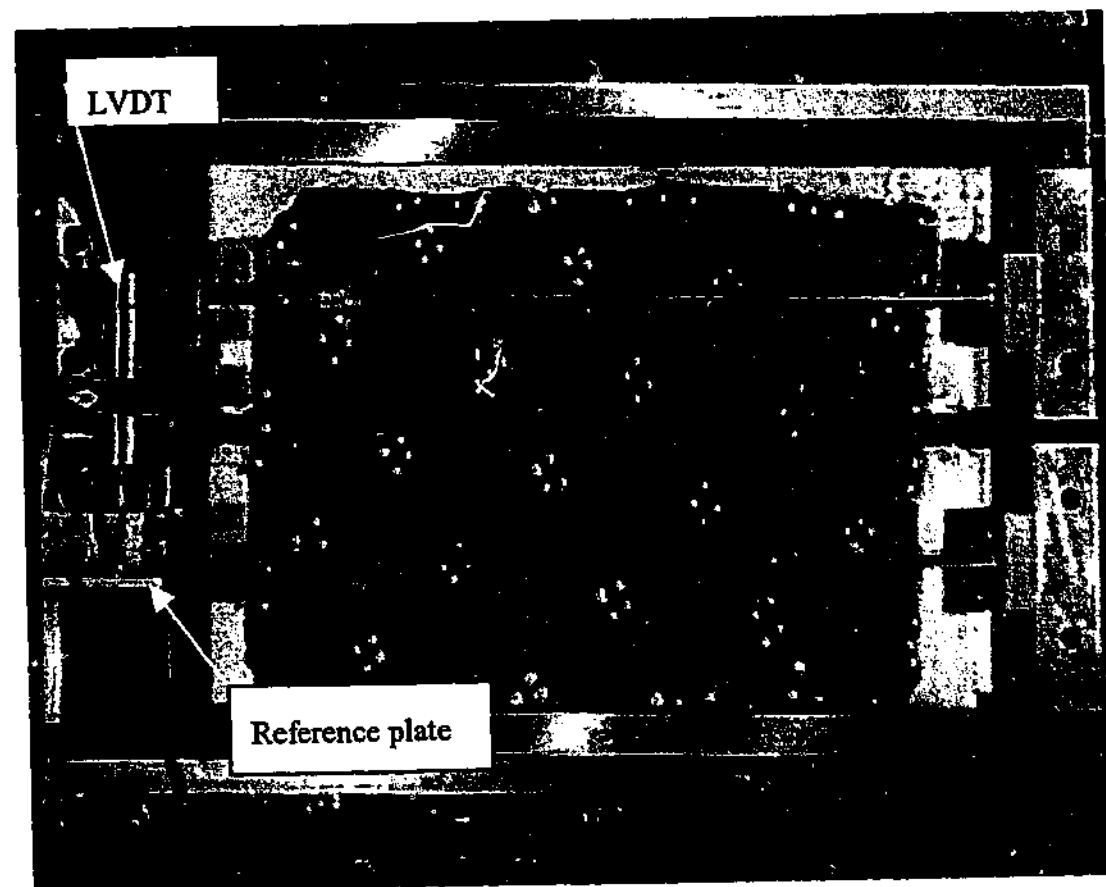


Figure 5-29: Shear box with sample placed in shear apparatus (from Test B3).

The Type "B" samples could be placed in the shear box and tested on the same day because there was no need to wait for the encapsulating plaster to cure. The preparation of the sample in the shear box and the placement of the shear box in the shear apparatus took about an hour.

5.5.6 Shear test procedure-execution

The shear test comprised the following stages:

- Application of initial normal stress. The initial normal stress was applied as a monotonic linear ramp to the target stress (typically 100 kPa). The duration of the ramp was 300 seconds.
- Application of consolidating stress. After the initial normal stress had been reached, it was maintained for a further 300 seconds to allow excess porewater pressures to dissipate.
- Application of shear displacement. The lower half of the sample was displaced at a rate of 0.5 mm/min. The upper half of the shear box was allowed to dilate under CNS conditions. The lower half of the shear box was displaced typically between 30 mm and

60 mm, which allowed measurement of the pre-peak behaviour and some of the post-peak behaviour.

5.5.7 Shear test-tidy up

After each shear test, the shear box was removed from the shear apparatus and the sample removed from the shear box and inspected to assess the extent of damage to the rock. Pieces of the intact rock were recovered for saturated moisture content testing. Where possible, core samples were taken from the intact rock for UCS, triaxial or Brazilian testing. The remainder of the sample was discarded. The shear boxes were then cleaned and prepared for the next test.

5.6 Summary

The manufacture of the modelling material (Johnstone) used in this study has been briefly described in this chapter. The engineering properties of the Johnstone were assessed and found to be similar to those used in earlier studies and of the natural parent Melbourne Mudstone.

The equipment used to manufacture and cut joints into the Johnstone was also described. Most of the equipment was designed and built specifically for this project.

The processes involved in the fabrication of the sample have also been discussed. It has been demonstrated that joint patterns can be cut to relatively tight tolerances.

The preparation of the samples in the shear boxes, the placement of the shear boxes in the shear apparatus and the test procedures have also been outlined.

The time taken for each of these processes has been presented. Typically, each Johnstone block took about a day to manufacture, each sample took about half a day to prepare and the placement and testing of each sample took about half a day.

6 RESULTS OF DIRECT SHEAR TESTS

6.1 Introduction

This chapter describes the laboratory direct shear tests on jointed rock mass samples carried out for this project. These shear tests were conducted under relatively tightly controlled and consistent conditions that attempted to simulate the *in-situ* conditions typically experienced by near surface rock masses. The samples were carefully manufactured to enable the influence of intact rock strength (UCS), joint inclination, joint spacing, number of joint sets, initial normal stress and sample geometry on rock mass behaviour to be examined.

Measurements of average shear stress, normal stress, dilation and shear displacement applied to the sample were made during each test. The UCS, secant modulus and saturated moisture content of the intact material, and joint and machine compliance were measured subsequent to direct shear testing. The behaviour of the Type "B" samples was also recorded using time-lapse photography.

The behaviour of the samples during the consolidation and shear stages of the test is examined. Video footage of the tests was used to help identify the pre-peak and failure mechanisms within the samples as shear displacement occurred. Two dominant pre-peak mechanisms and three failure mechanisms were identified. These are described in this chapter and analysed in Chapter 7. The observed influence of each of the parameters listed above on sample behaviour is also discussed.

6.2 Consolidation phase

6.2.1 Introduction

This study examines the behaviour of rock mass samples subjected to direct shear under low normal stresses. Most of the rock mass samples were consolidated to an initial normal stress of 100 kPa prior to testing, which represents about four metres of overburden (assuming a deep water table).

To investigate the effect of initial normal stress on sample behaviour, two Type "B" samples were consolidated at 50 kPa and another two at 300 kPa. One Type "A" sample was consolidated at 200 kPa and another at 400 kPa.

6.2.2 Application of initial normal stress

The normal stress was applied as a monotonic linear ramp to the target initial normal stress, and then maintained to consolidate the sample by allowing time for excess porewater pressures within the rock mass to dissipate. A typical example of the variation of normal stress with time during the consolidation phase, (from Test B2), is shown in Figure 6-1.

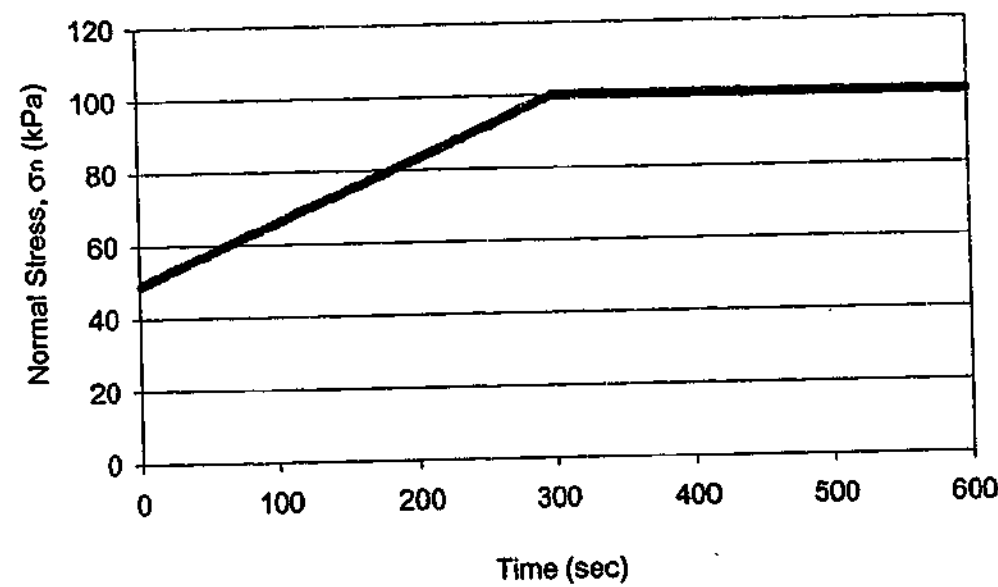


Figure 6-1: Graph showing applied normal stress with time (Test B2).

6.2.3 Vertical displacement resulting from normal stress

The variation of vertical displacement of the top of the shear box during consolidation was measured. It has been assumed this movement reflects deformation occurring within the sample. A typical test result showing displacement versus normal stress, (from Test B2), is shown in Figure 6-2.

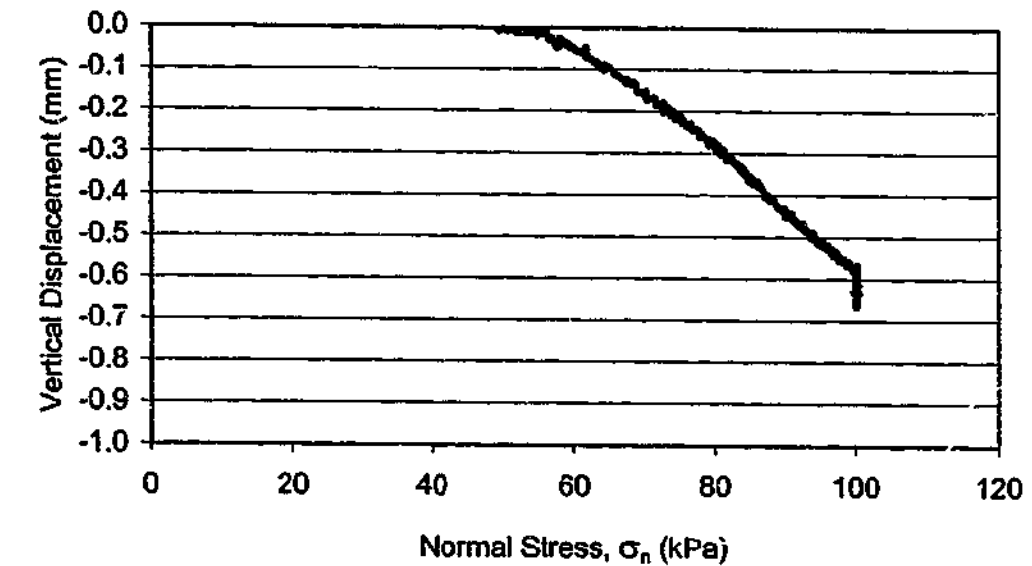


Figure 6-2: Graph showing vertical displacement of the top of the shear box with applied normal stress (Test B2).

In assessing the behaviour shown in Figure 6-2, it should be noted that the self-weight of the plunger arrangement and the top half of the shear box provided an initial normal stress of about 50 kPa. The vertical displacement due to this normal stress occurred before the LVDT's could be attached to the shear box and could not be measured. Figure 6-2 shows that above about 55 kPa, there is a near linear relationship between vertical displacement and normal stress.

Typically, after the target initial normal stress was attained, a small amount of ongoing displacement was measured over a period of five minutes. This is shown in Figure 6-2 by the vertical line at 100 kPa normal stress. This ongoing displacement is attributed to the dissipation of excess porewater pressures within the rock mass and perhaps some minor creep effects.

6.2.4 Vertical displacement with time

The vertical displacement of the top of the shear box with time is illustrated in Figure 6-3. Over the first 300 seconds, the measured displacement increases with increasing normal stress, suggesting the sample is behaving in an essentially elastic manner. The normal stress was then maintained for another 300 seconds. The vertical displacement continued, albeit at a much reduced and declining rate.

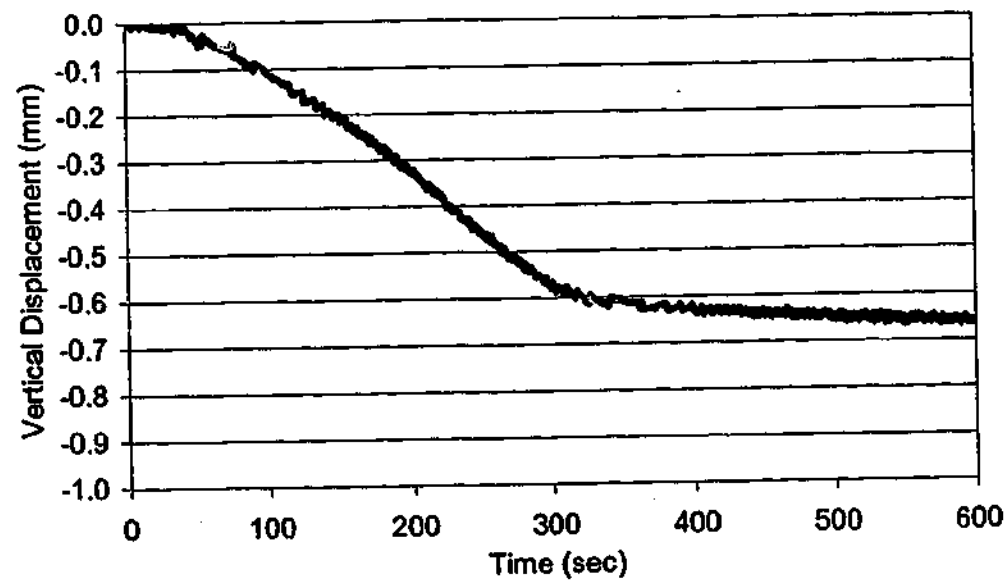


Figure 6-3: Graph showing vertical displacement of top of the shear box with time (Test B2).

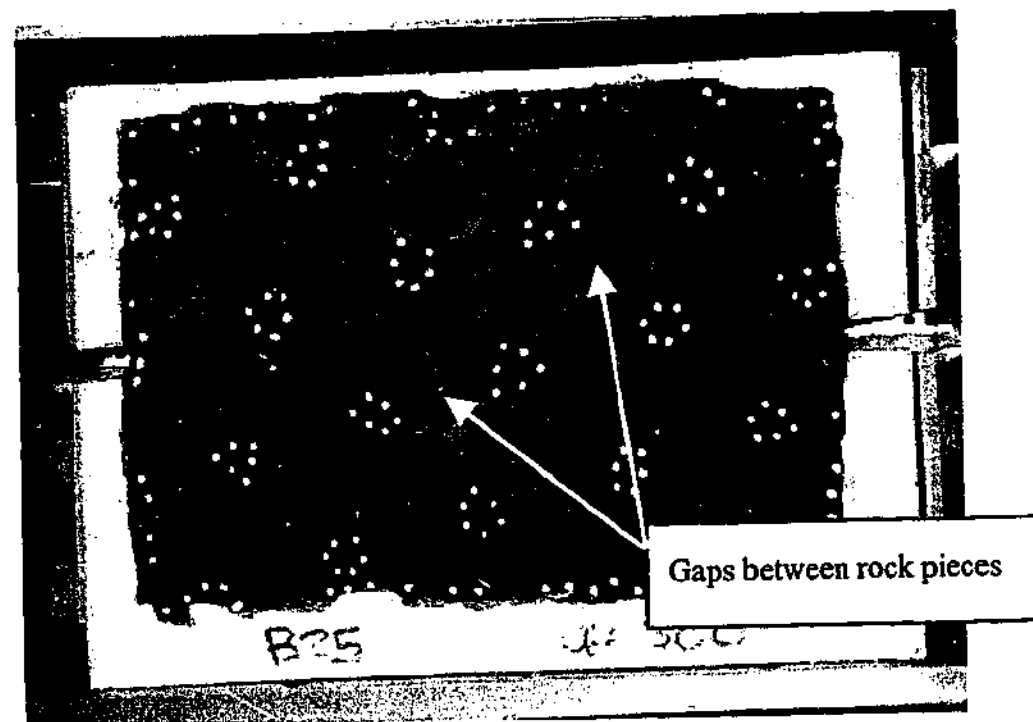


Figure 6-4: Sample B25 prior to application of initial normal stress.

The application of the initial normal stress resulted in some joint closure, as shown in Figure 6-4 and Figure 6-5, taken from Test B25. Figure 6-4 shows the sample after it has been placed in the shear box, but has not been subjected to any applied stresses. There are several gaps between the rock pieces, despite efforts during the fabrication process to ensure all the joints were tight.

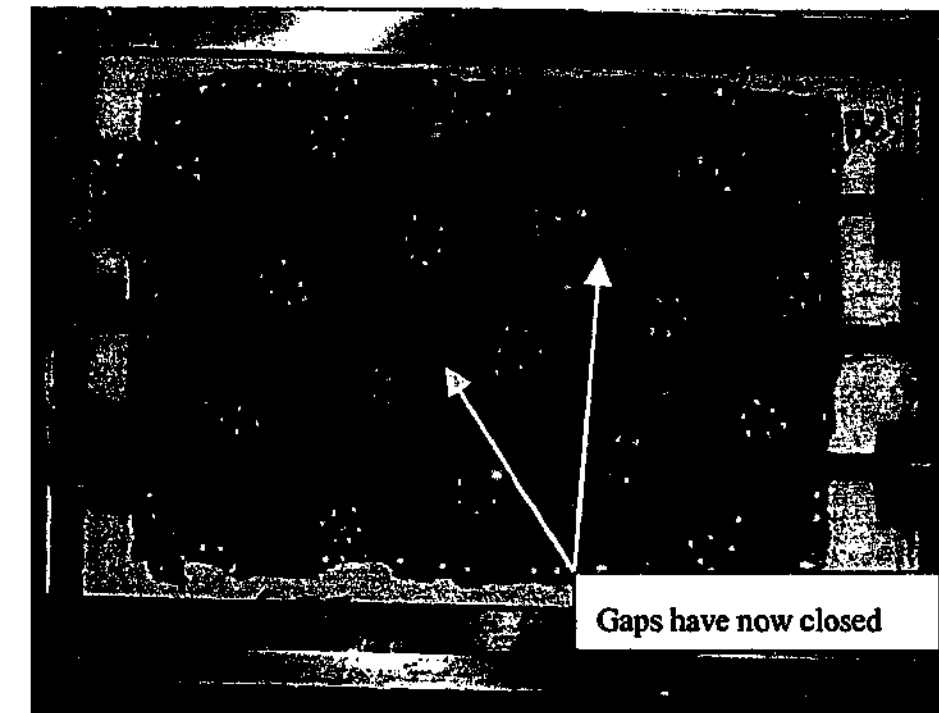


Figure 6-5: Sample B25 after application of initial normal stress.

The same sample is shown in Figure 6-5 after an initial normal stress of 300 kPa has been applied. Some closure of the gaps is evident.

The vertical displacement measured during the consolidation of this sample therefore included a contribution from joint closure as well as from elastic effects.

Two consolidation tests were carried out on intact concrete blocks to assess the impact of the preparation procedure on the repeatability of the behaviour exhibited between tests. Displacements of about 1.0 mm at 600 kPa normal stress were recorded for each test. This repeatability provided confidence that the preparation procedure was reasonably consistent between tests.

Pearce (2001) assessed that the deformation of the shear apparatus resulting from the application of a stress of 1 MPa was about 0.1 mm. For the normal stress of 600 kPa applied in these tests, a displacement of about 0.06 mm would be expected.

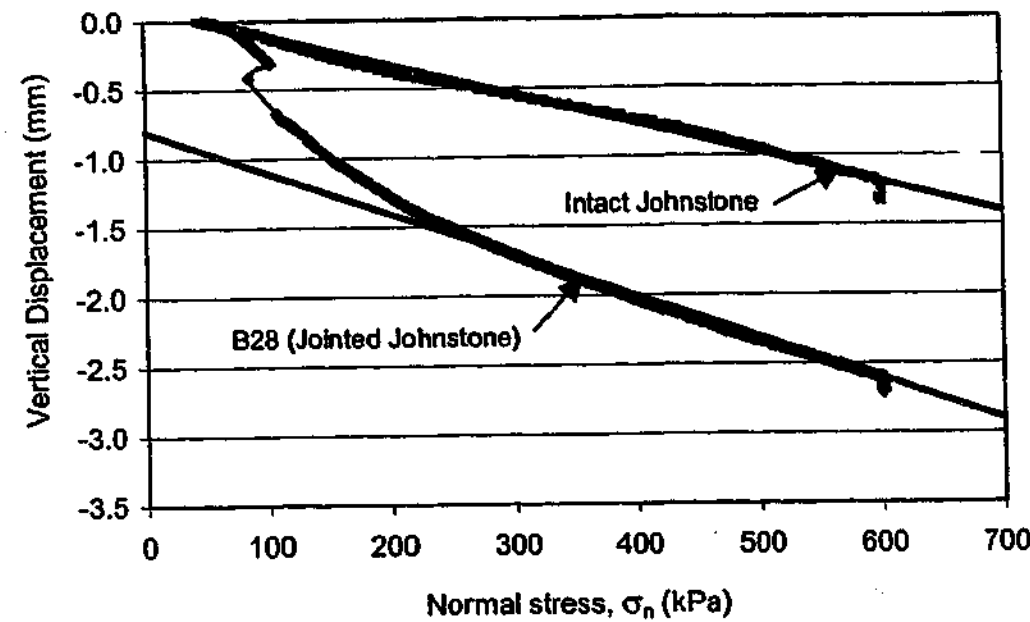


Figure 6-6: Effect of jointing on vertical displacement.

The presence of jointing in the sample increases the measured vertical displacement, as shown in Figure 6-6. This figure compares the vertical deformation of an intact block of Johnstone with that of the same block after horizontal and vertical joint sets spaced at 70 mm had been cut into the sample, as shown in Figure 6-7.

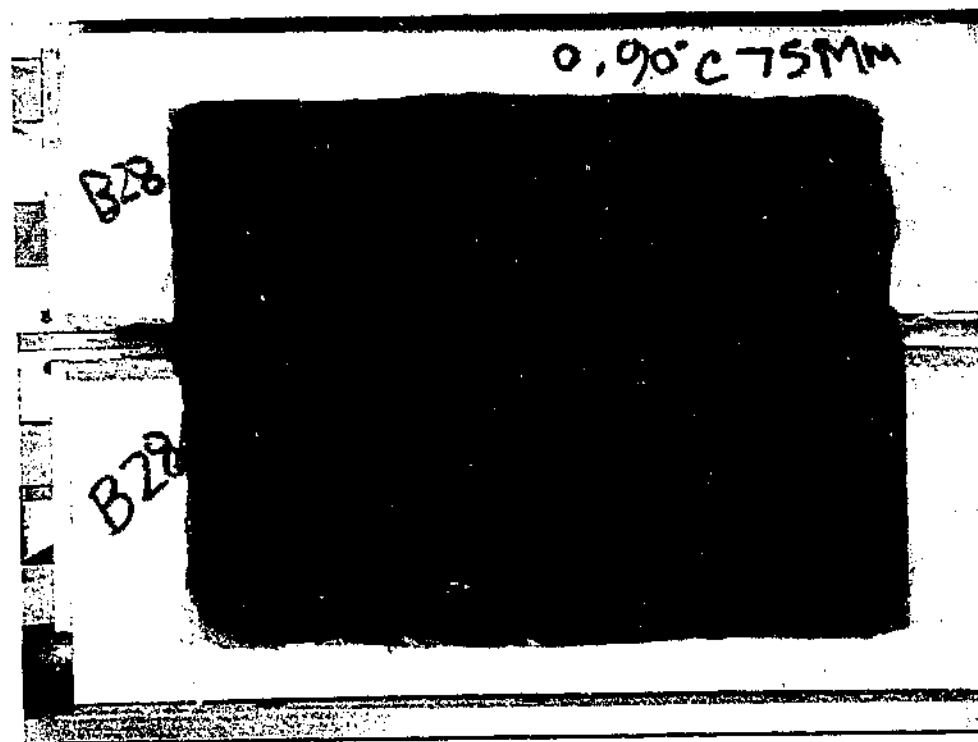


Figure 6-7: Sample B28, used to measure effect of jointing on rock mass modulus.

The trend lines shown in Figure 6-6 were used to assess the compressive Young's moduli of the samples. Values of about 130 MPa for the intact Johnstone block and about 88 MPa for the jointed rock mass were obtained. Assuming that the compliance of the sample/shear box interface remained constant, this would indicate that (as expected), the modulus of a rock mass decreases with the introduction of joints into the rock mass.

The tests on intact and jointed samples were used to calculate joint normal stiffness. It was assumed that the change in measured vertical displacement between the intact and jointed sample was the result of the introduction of the joints.

The normal stiffness of the joint was calculated by treating the rock mass as a series of elastic springs connected in series. The intact rock was represented by springs with a stiffness calculated using one-dimensional Hooke's law and Young's modulus obtained from the UCS tests. The joints were represented by springs of an unknown stiffness. The displacements of all springs in series were summed and set equal to the total displacement of the sample (after allowing for the compliance of the sample/shear box interface). The joint normal stiffness of the joints cut into the sample using the block saw was calculated using this model to be about 1000 kPa/mm.

6.3 Shear behaviour

The behaviour of the rock mass during the shear tests was recorded by measuring and plotting the following outputs:

- shear stress, τ , versus normal stress, σ_n ,
- shear stress, τ , versus, shear displacement, dx ,
- normal stress, σ_n , versus shear displacement, dx , and
- dilation, dy , versus shear displacement, dx .

Examples of these graphs, taken from Test B19A, are presented in Figure 6-8.

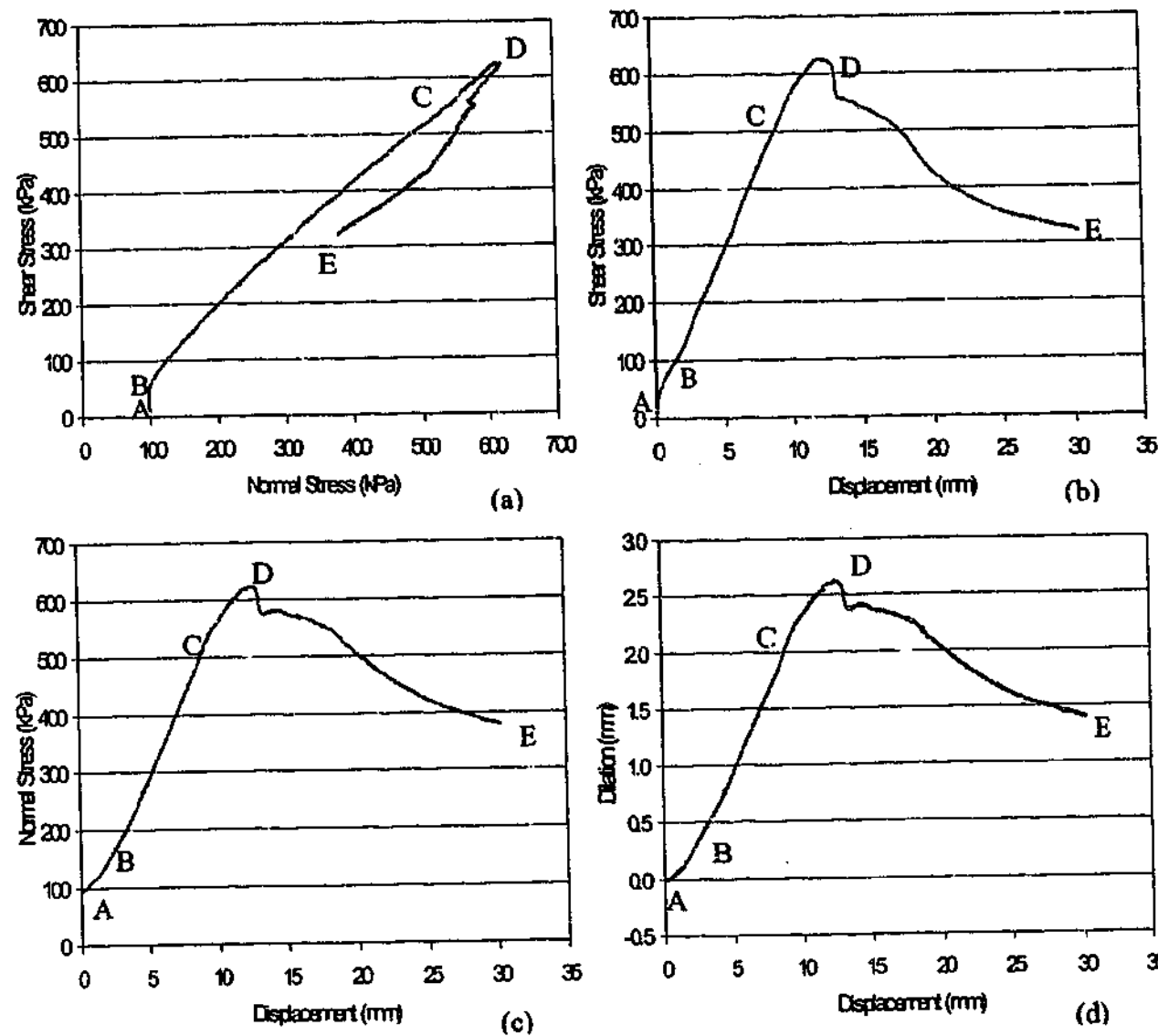


Figure 6-8: Graphs of test output (Test B19A).

Each of these graphs exhibits an essentially linear relationship between the outputs up to failure. Once peak values of shear stress, normal stress and dilation have been reached, these fall and continue to decrease with further shear displacement.

To assist with the analysis of the shear tests, the graphs of the measured outputs were divided into four phases as shown in Figure 6-8, namely initial (A-B), pre-peak (B-C), failure (C-D) and post-peak (D-E).

The video footage of the tests was used to identify the mechanisms within the sample during the pre-peak and failure stages of the tests.

6.3.1 Initial phase (A-B)

6.3.1.1 Shear stress versus normal stress

A nominal horizontal confining stress of 100 kPa was applied to the samples prior to placing the shear box into the shear apparatus. The sample was then consolidated under an initial (vertical) normal stress of typically 100 kPa.

It can be observed in Figure 6-8(a) that during this phase, the shear stress initially increases, accompanied by a slight reduction in normal stress. As the shear stress increases further (as a result of increasing displacement), normal stress starts to increase due to the sample starting to dilate against the normal stiffness.

6.3.1.2 Shear stress versus shear displacement

Figure 6-8(b) indicates that shear stress increases on commencement of shear displacement. After shear displacement has reached about 2 mm, the rate at which the shear stress increases becomes greater. This suggests that there may have been some initial compliance within the sample, such as joint closure. However, as the change in the rate at which the shear stress increases is small, it is inferred that this compliance is minimal.

6.3.1.3 Dilation versus shear displacement

Figure 6-8(d) shows a lag in the measured dilation with the commencement of shear displacement. This implies that the sample moves horizontally a short distance before any upward movement of the top of the shear box is recorded. The dilation of the sample is resisted by the normal stress applied to the sample. Figure 6-9 shows the dilation-displacement behaviour of similar samples subjected to different initial normal stresses.

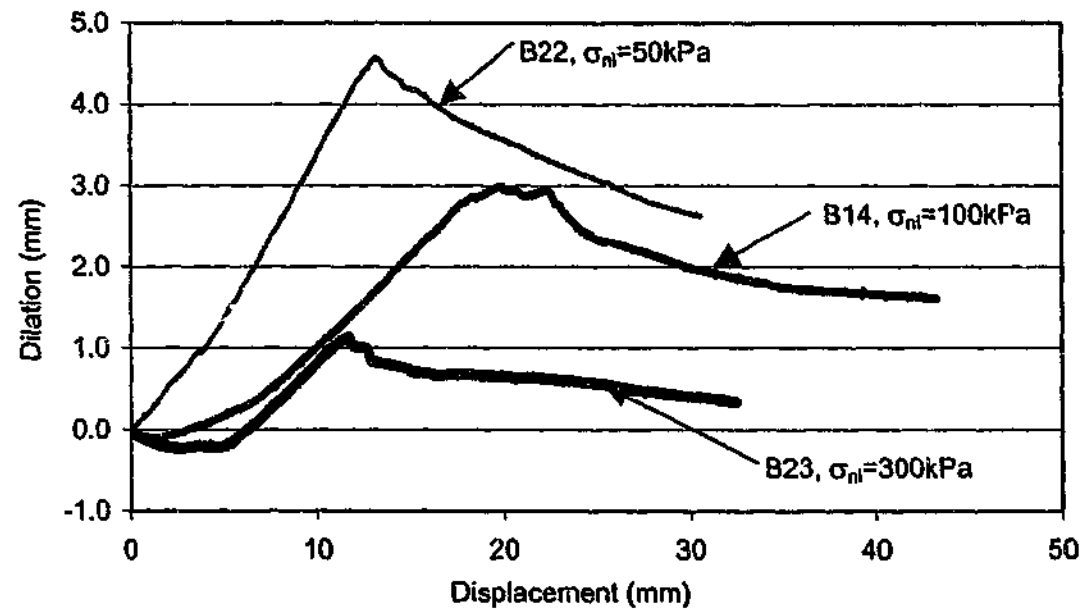


Figure 6-9: Effect of initial normal stress on initial dilation.

It can be seen from Figure 6-9 that the initial normal stress has a significant effect on the amount of initial dilation and the displacement before the samples begin to dilate. It can be observed that higher values of initial normal stress can cause “negative dilation”, which may be a result of elastic compression of the sample resulting from stress redistribution within the sample.

Negative dilation was not measured in the shear tests carried out on the intact Johnstone sample (Test B32A) and the intact concrete sample (Test B33C). This suggests (as described below) it is the presence of jointing, hence reduced contact area after a small amount of displacement, which results in negative dilation. Where negative dilation was observed, it occurred at the commencement of displacement. The typical average shear displacement recorded before the measured dilation became positive was:

- zero for intact rock,
- about 2 mm for rock masses containing two joint sets with $\sigma_{ni} = 100$ kPa,
- about 7 mm for rock masses containing two joint sets with $\sigma_{ni} = 200$ kPa,
- about 4.5 mm for rock masses containing three joint sets with $\sigma_{ni} = 100$ kPa, and
- about 15 mm for rock masses containing three joint sets with $\sigma_{ni} = 200$ kPa.

Negative dilation may be explained by considering a simplified rock mass containing two intersecting joint sets, as shown in Figure 6-10.

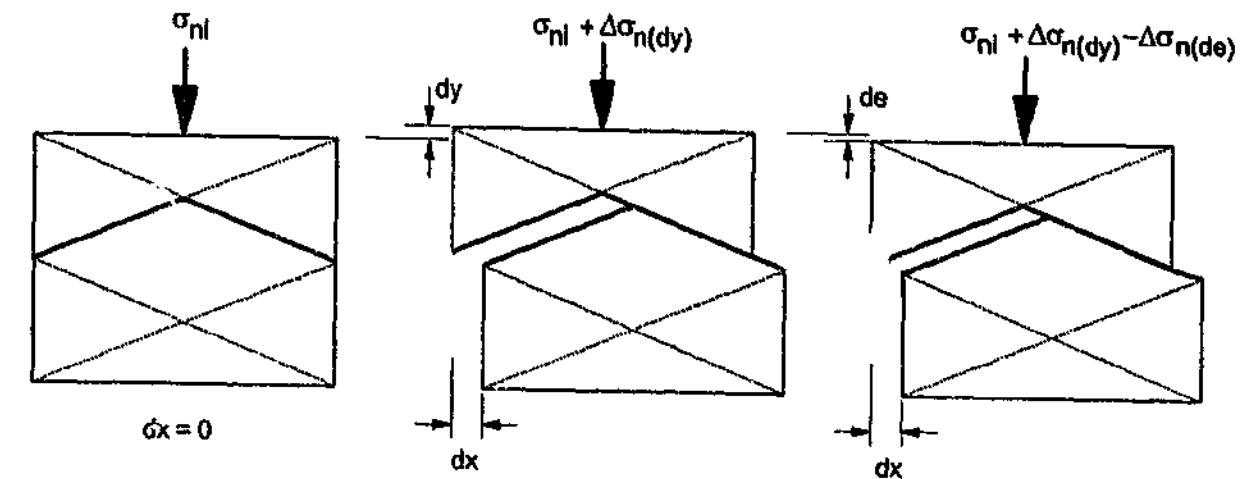


Figure 6-10: Dilation and elastic deformation resulting from CNS conditions.

Initially, the sample is loaded so that the normal load acts over the entire plan area of the sample, resulting in an average initial normal stress, σ_{ni} . After a small increment of shear displacement, dx , the contact area is reduced so that only the leading face is in contact. The normal stress is calculated over the corrected area of the sample (rather than the contact area), so the applied load is now acting on a smaller area and results in elastic deformation.

After further shear displacement, dilation, dy occurs. Under CNS conditions, this will increase the normal stress by the amount $\Delta\sigma_{n(dy)}$, which is related to the stiffness and the dilation. The normal stress acting on the leading face is now $\sigma_{ni} + \Delta\sigma_{n(dy)}$. However, this increased normal stress results in further elastic deformation, de . Under CNS conditions, the reduction in normal stress due to elastic deformation, $\Delta\sigma_{n(de)}$, will reduce the normal stress to:

$$\sigma_{ni} + \Delta\sigma_{n(dy)} - \Delta\sigma_{n(de)} \quad \text{Equation 6-1}$$

The CNS condition, therefore, not only works against dilation of the sample, but also works to overcome the negative dilation. As the top of the sample deflects downwards, the applied normal stress is reduced. This also reduces elastic effects, so that after a small amount of shear displacement, these elastic effects have been overcome. When the sample is subjected to higher initial normal stresses, the elastic deformations are larger and require greater shear displacement to be overcome. The largest values of negative dilation were measured in:

- Test A8, subjected to $\sigma_{ni} = 400$ kPa, negative dilation of 0.45 mm was measured.
- Test B23, subjected to $\sigma_{ni} = 300$ kPa, negative dilation of 0.23 mm was measured.
- Test B25, subjected to $\sigma_{ni} = 300$ kPa, negative dilation of 0.35 mm was measured.

6.3.1.4 Normal stress versus shear displacement

The behaviour shown in the normal stress-shear displacement graphs (e.g. Figure 6-8c) is similar to the behaviour shown in the dilation-shear displacement graphs (e.g. Figure 6-8d). This is because, under CNS conditions, the normal stress is directly related to dilation by the normal stiffness.

6.3.2 Pre-peak phase (B-C)

6.3.2.1 Shear stress versus normal stress

The pre-peak behaviour of the shear stress-normal stress (τ - σ) graphs was found to be essentially linear. The slope of the line between points B and D was estimated for each test and has been designated by the symbol ϕ_{pp} .

From testing of rock joints, it is well established that the shear resistance of a block containing a single joint with friction angle, ϕ_j , inclined at an angle i , can be estimated from:

$$\tau = \sigma \tan(\phi_j + i) \quad \text{Equation 6-2}$$

The shear tests carried out in this study were set up so that if sliding were to occur, it would be along the joint set inclined at $i = \theta_1$. If the joint friction angle is ϕ_j , the resultant τ - σ graph for sliding along this joint should have a slope of $\phi_{pp} = (\theta_1 + \phi_j)$.

In cases of sliding on joints, this angle is often referred to as the “apparent friction angle” of the joint. This term has been adopted in this study to define the slope of the linear, pre-peak phase of each test, irrespective of whether the pre-peak mechanism is sliding or something else (e.g. rotation).

When a value of apparent friction angle, $\phi_{pp} = (\theta_1 + \phi_j)$ was obtained, it was observed (from video footage) that sliding was occurring. However, for lower values of apparent friction angle, other mechanisms were observed occurring in the rock mass.

The measured values of ϕ_{pp} and θ_1 for each test have been plotted in Figure 6-11. A line representing $(\phi_j + \theta_1)$, where $\phi_j = 28^\circ$ has also been plotted.

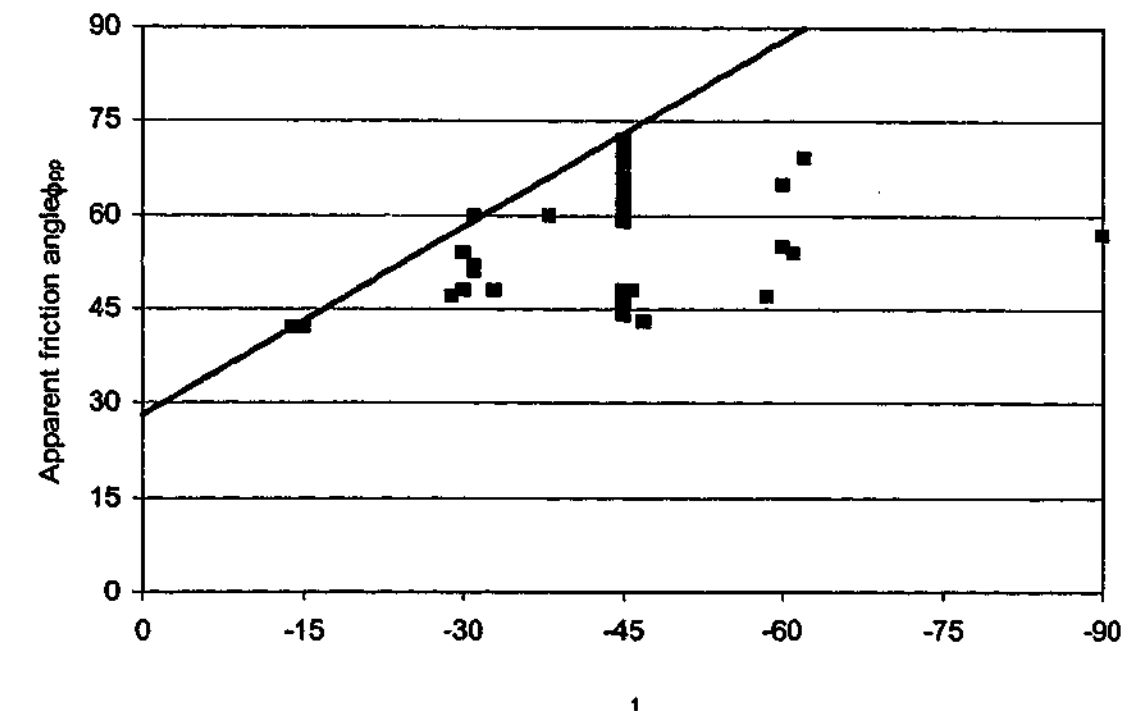


Figure 6-11: Measured apparent friction angles, ϕ_{pp} for values of θ_1 .

It can be observed in Figure 6-11 that only a few tests appear to have an apparent friction angle that suggests that sliding along the θ_1 joint set is occurring. As expected, sliding appears to occur in the two tests where θ_1 is 15° . Sliding along the θ_1 joint set is inferred in only one or two tests where θ_1 is 30° or 45° . The majority of the tests did not exhibit behaviour associated with sliding along the θ_1 joint set. This was confirmed by the video footage. The τ - σ graph for Test B1 is shown in Figure 6-12.

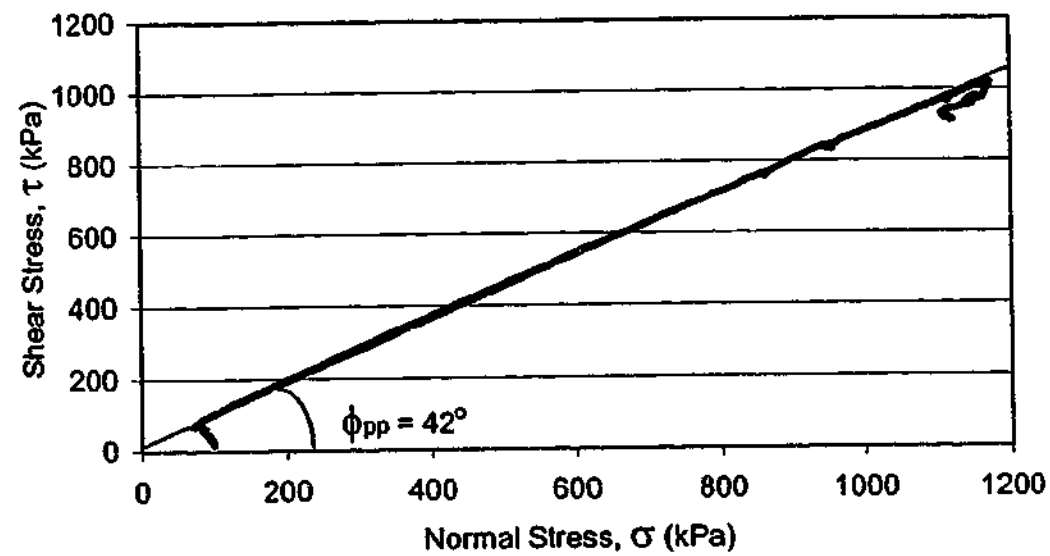


Figure 6-12: τ - σ graph for Test B1.

For Test B1, $\theta_1=15^\circ$, $\phi_j=28^\circ$ and the measured value of $\phi_{pp}=42^\circ$. Sliding along the θ_1 joint set for this test would be expected (from equation 6-2) to produce an apparent friction angle, $\phi_{pp}=43^\circ$, which is very close to the 42° measured during the test. The video footage of this test confirmed that sliding along the θ_1 joint set occurred, as shown in Figure 6-13. The relative displacement along the central θ_1 joint can be clearly seen, whereas no significant displacement can be observed along any other joint.

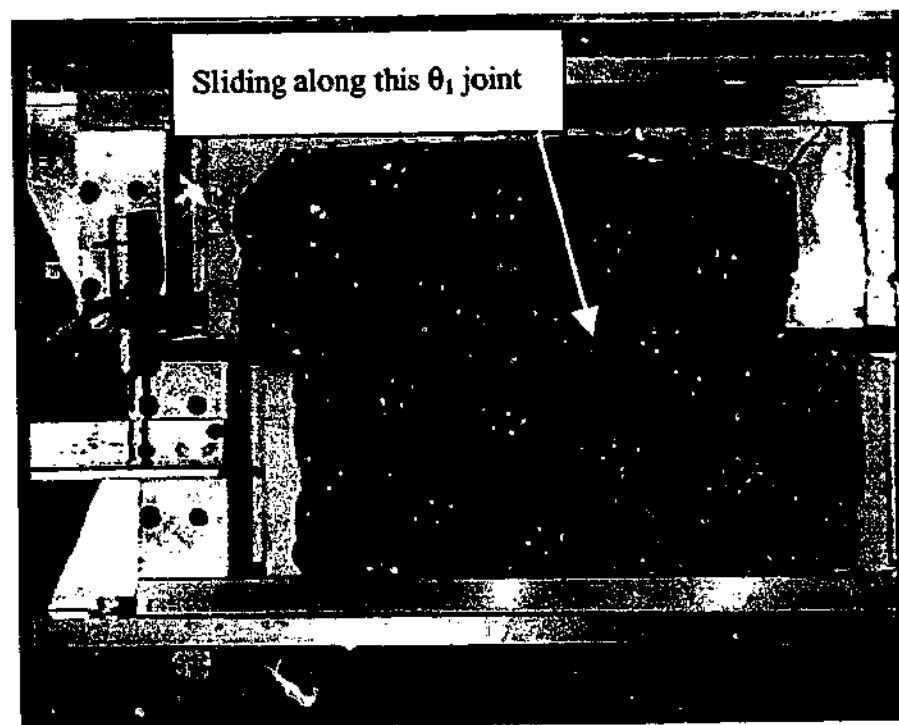


Figure 6-13: Evidence of sliding along the θ_1 joint set (Test B1).

The value of ϕ_{pp} measured in many of the shear tests, as shown in Figure 6-11, indicates a mechanism other than sliding along the θ_1 joint set has occurred. These tests were typically those where $\theta_1 = 30^\circ$.

Thiel and Zabuski (1996) carried out a number of *in-situ* direct shear tests on jointed rock masses. They described how, rather than sliding along a joint, separation occurred across one of the joints in the rock mass as it was sheared (see Section 2.5.1.4). Similar separation across a joint was observed in the video footage taken of the shear tests in this study where sliding was not observed.

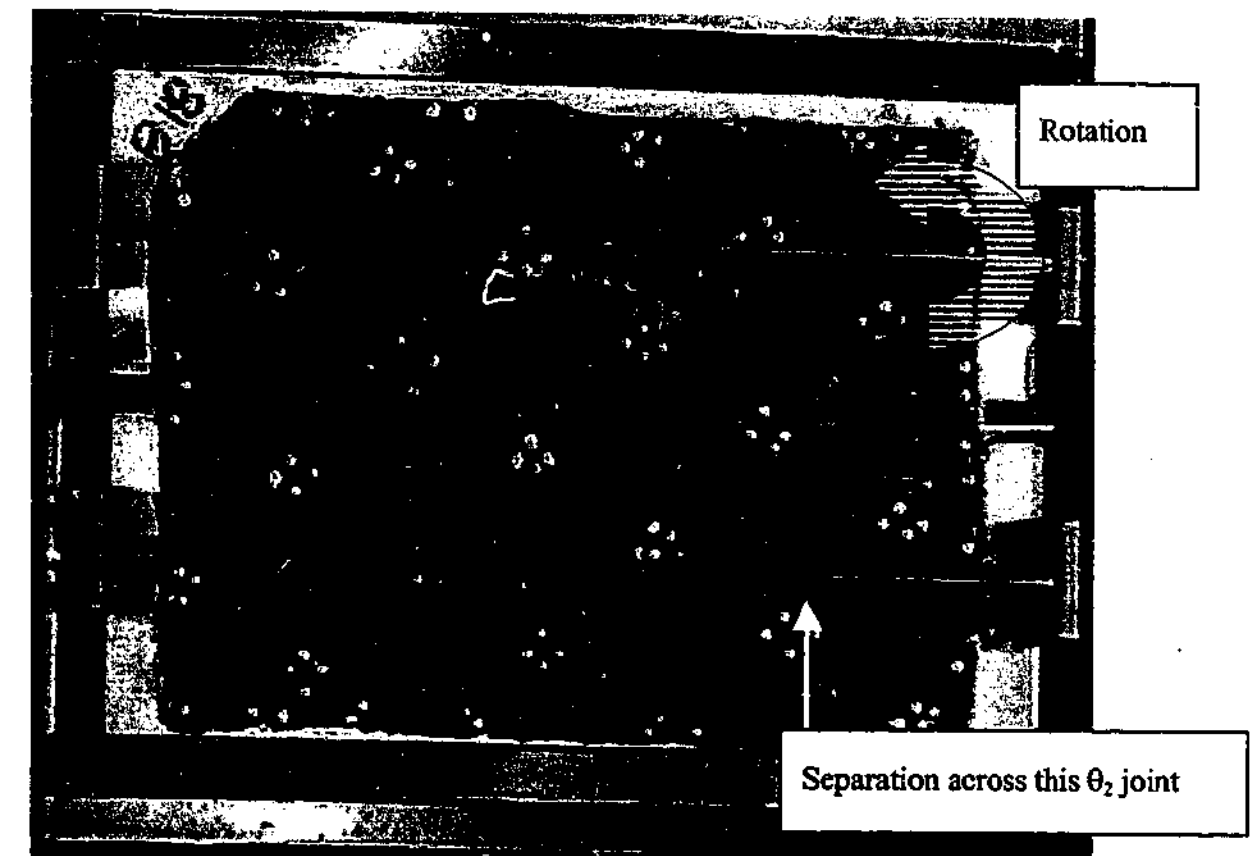
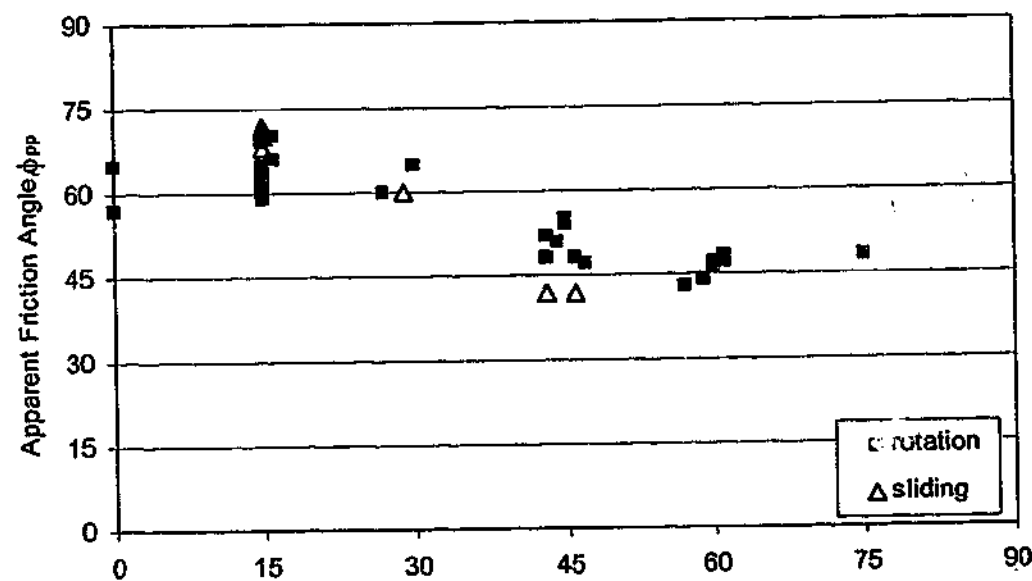


Figure 6-14: Separation along the θ_2 joint set (bottom right) in Test B18.

An example of this separation is shown in Figure 6-14. The horizontal movement of the bottom half of the sample, coupled with the vertical movement of the top half of the sample, causes an apparent rotation of the block, with the opening of the θ_2 joints closest to the ends of the shear plane. This can be seen in the bottom right hand joint in Figure 6-14. Separation also occurred across the top left-hand joint, but was less evident due to the rock pieces above that joint dropping and resting on the joint.

It is important to emphasise that rotation of the shear box was prevented due to the relatively high stiffness of the testing apparatus. Therefore, the observed apparent rotation is the result of displacement and/or rotation of the rock pieces within the sample rather than the result of shear box rotation.

The values of apparent friction angle are plotted against θ_2 in Figure 6-15 in which different symbols have been used to differentiate between observed sliding and rotation.



2

Figure 6-15: Variation of apparent friction angle, ϕ_{pp} , with θ_2 .

Figure 6-15 indicates that there appears to be a strong relationship between ϕ_{pp} and θ_2 in the tests where rotation occurs (but not with θ_1 —see Figure 6-11). Therefore, it would appear that the apparent friction angle of the rock mass was influenced by joint inclination for both sliding and rotation mechanisms. That is, if θ_1 was low enough to allow sliding to occur, the measured apparent friction angle is $(\theta_1 + \phi_j)$. If rotation occurred, the value of the apparent friction angle appears to be dependent on θ_2 .

The τ - σ curves of Test B6 and B9 are shown in Figure 6-16. The value of θ_2 in these tests was 15° . The linear, pre-peak portions of the τ - σ responses have been extrapolated back to zero normal stress. Figure 6-16 indicates an apparent negative cohesion. This apparent negative

cohesion was not observed in the τ - σ response of samples with other jointing configurations. This suggests the samples where $\theta_2=15^\circ$ may have behaved differently to the other samples.

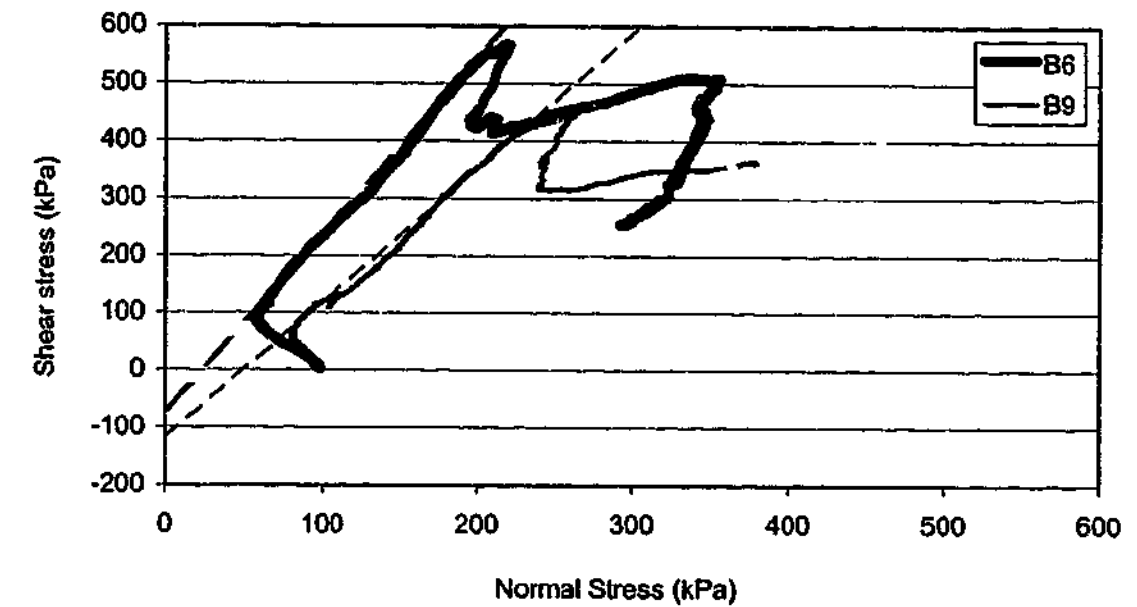


Figure 6-16: Inferred negative cohesion extrapolated from τ - σ plots of Tests B6 and B9.

The conditions that govern whether pre-peak sliding or rotation occurs are discussed further in Chapter 7.

6.3.2.2 Shear stress versus shear displacement

After a small amount of shear displacement, the gradient of the shear stress-shear displacement response was generally constant and linear. For the test shown in Figure 6-8(b), the gradient decreased slightly as the failure stress was approached. This slight decrease was observed in most of the tests.

While this study does not consider deformation of rock masses, the relative slopes of the shear stress-shear displacement curves may be of interest and can be used to estimate the shear stiffness of the samples. The simplified typical pre-peak shear stress-shear displacement responses of the samples are presented in Figure 6-17. These curves have been obtained by drawing a line between the origin and the average of the measured values of peak shear stress and displacement at failure. The average response of the samples that exhibited sliding

behaviour are shown, together with the average responses of the samples that exhibited rotational behaviour, grouped by the value of θ_2 .

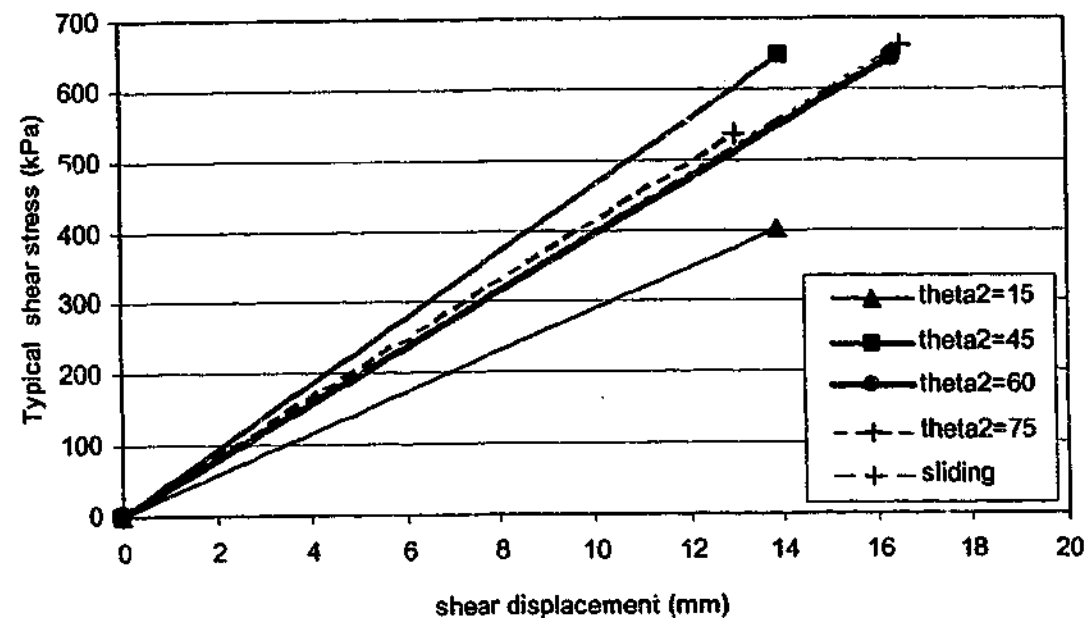


Figure 6-17: Simplified pre-peak shear stress-shear displacement behaviour of samples.

It can be observed in Figure 6-17 that, in general, the rock masses tested exhibited similar shear stiffness. The average shear displacement at which peak shear stress occurred was about 14 mm. The average peak shear stress was reasonably consistent for both sliding and rotational behaviour, except for the tests where θ_2 was 15°, where a significantly lower average peak shear stress was observed.

6.3.2.3 Dilation versus shear displacement

Once the sample began to dilate (after the initial contraction), the rate of increase in dilation with respect to displacement was relatively uniform until just prior to failure, when the dilation rate reduced. Dilation increases the normal stress acting on the sample under CNS conditions until the combination of stresses in the sample are such that failure occurs.

The gradient of the dilation-shear displacement response has been interpreted as a dilation angle, ψ . Graphs showing the influence of θ_1 and θ_2 on the dilation angle are shown in Figure 6-18 and Figure 6-19.

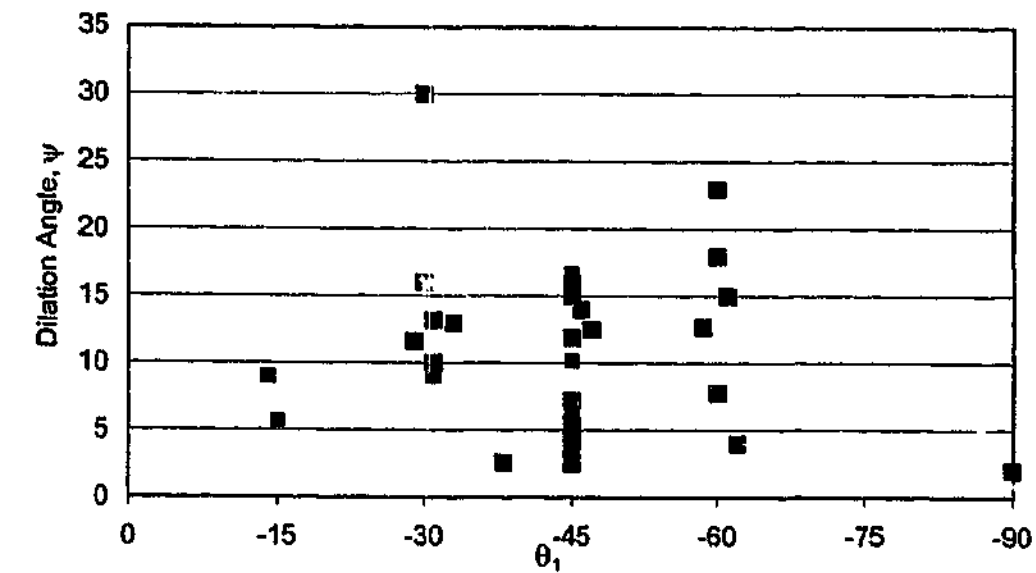


Figure 6-18: Influence of θ_1 on dilation angle, ψ .

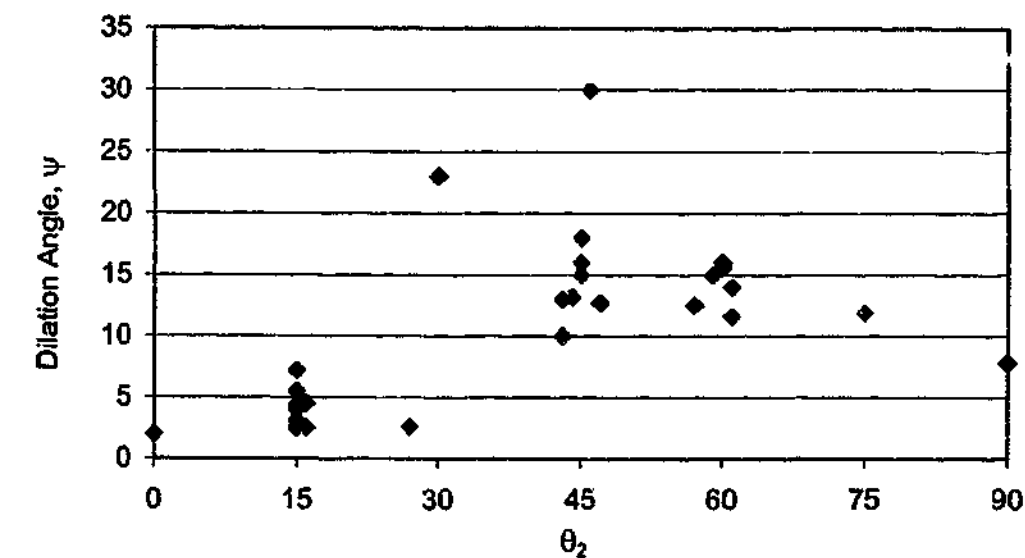


Figure 6-19: Influence of θ_2 on dilation angle, ψ .

It would appear that the dilation angle correlates better with θ_2 than with θ_1 . There appears to be a trend with relatively larger dilation angles for values of $\theta_2=45^\circ$, 60° and 75° . In most cases, lower dilation angles were observed for values of $\theta_2=15^\circ$, 30° and 90° .

The effects of initial normal stress on dilation can be seen in Figure 6-9. It would appear that higher initial normal stresses result in smaller dilation angles.

6.3.2.4 Normal stress versus shear displacement

Due to the imposed CNS conditions, the normal stress versus shear displacement behaviour will essentially mirror that of the dilation versus shear displacement behaviour.

6.3.3 Peak phase (C-D)

6.3.3.1 Shear stress versus normal stress

Failure was indicated on the τ - σ graphs by the sudden reduction in both shear stress and normal stress and indicated that the peak shear strength of the sample had been reached.

6.3.3.2 Shear stress versus shear displacement

Figure 6-8(b) shows that just prior to failure, a slight decrease in the rate of shear stress could be observed. Failure of the sample, signified by the loss of shear strength, occurred abruptly.

6.3.3.3 Dilation versus shear displacement

The measured dilation reached a localised peak and then dropped at failure. As can be observed in Figure 6-8(d), dilation rate decreased over several millimetres of shear displacement immediately prior to failure. It was observed that peak shear stress occurred at peak dilation. The variation of the normal stress was similar to that of dilation.

6.3.4 Post-peak phase (D-E)

6.3.4.1 Shear stress versus normal stress

The post-peak behaviour of the samples generally displayed continuing reduction of both shear stress and normal stress, as shown in Figure 6-8(a) and Figure 6-12. However, the τ - σ responses for most of the samples where the θ_2 joint set was inclined at 15° , such as those

shown in Figure 6-20, show a smaller drop from peak shear and normal stress, followed by a gradual increase in both shear and normal stresses.

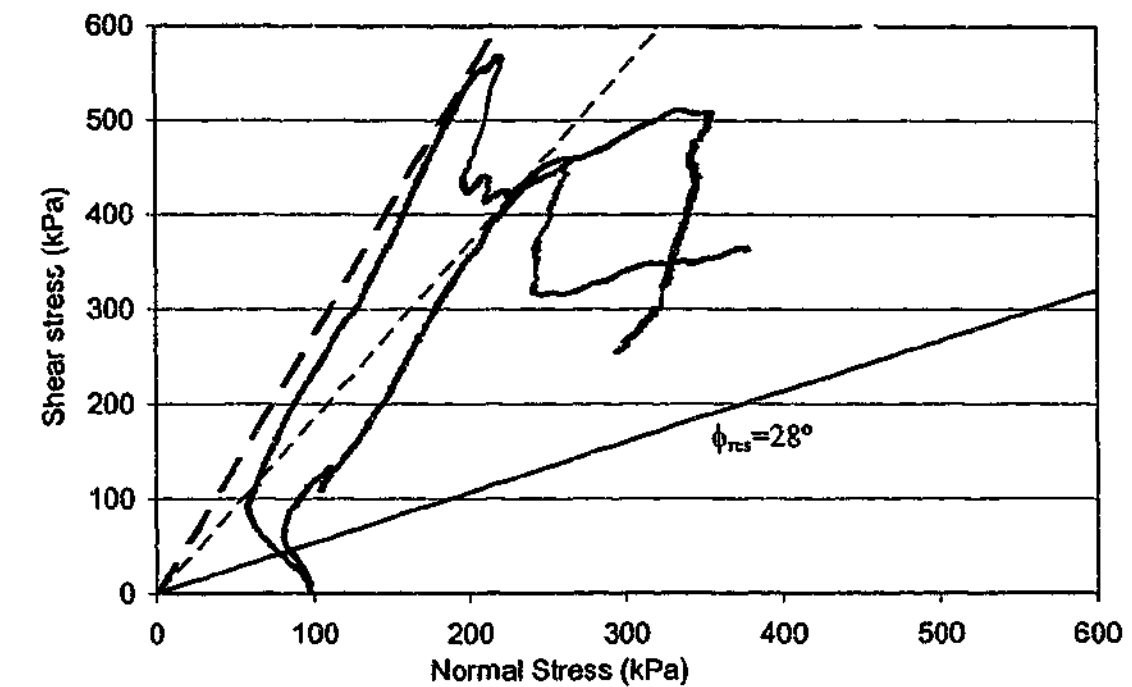


Figure 6-20: τ - σ responses from Tests B6 and B9.

This more gradual increase in shear and normal stress may be the result of sliding along the failure surface. It would be expected that if shear displacement continued to very large values, a residual friction angle of $\phi_{res}=28^\circ$ would be reached.

6.3.4.2 Shear stress versus shear displacement

In all tests, shear stress was observed to drop sharply after failure occurred. After this drop, the shear stress decreased more gradually as shear displacement continued. In some tests, however, the shear stress was maintained or even increased slightly after the initial drop from peak stress, as shown in Figure 6-21. These tests were mostly those where $\theta_2=15^\circ$. It appears that after the peak shear stress was reached, the shear stress dropped, then increased as sliding along the failure surface occurred, until further fracture of the intact rock occurred.

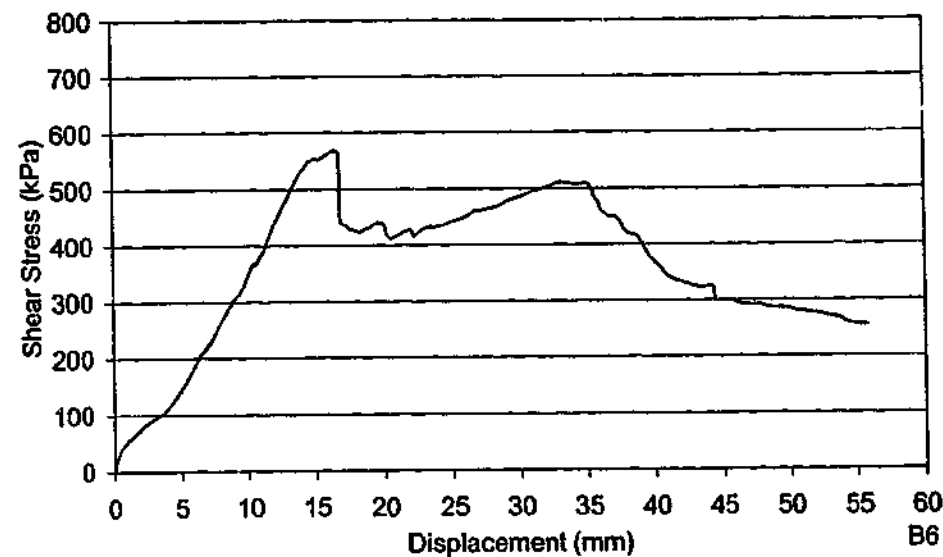


Figure 6-21: Post-peak behaviour of sample B6 ($\theta_2=15^\circ$).

6.3.4.3 Dilation versus shear displacement

Once peak dilation had been reached, the measured dilation (hence normal stress) was observed to behave in one of two ways:

- Typically, dilation reduced with further displacement.
- For tests on samples with $\theta_2=15^\circ$, dilation either increased or was maintained with further shear displacement, as shown in Figure 6-22. This behaviour was similar to that of the post-peak shear stress with displacement described in Section 6.3.4.2.

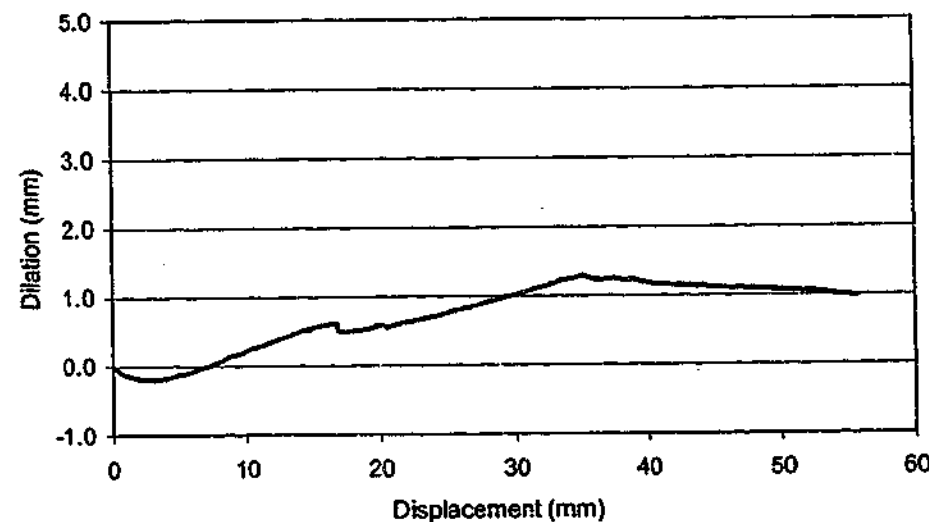


Figure 6-22: Dilation measured during Test B6.

As shown in Figure 6-22, sample B6 ($\theta_1=45^\circ$, $\theta_2=15^\circ$) failed at a shear displacement of about 17 mm. A drop in dilation occurred at this displacement. However, as shear displacement continued, dilation began to increase again, exceeding that which was measured at failure. This relatively ductile behaviour, together with the lower dilation angles, suggests that samples with $\theta_2 = 15^\circ$ may behave differently after failure than samples with higher values of θ_2 .

6.3.5 Progressive failure

It can be observed in Figure 6-8(d) that the rate of dilation declines as peak strength is approached. This "rounding" of the graph just prior to peak dilation was possibly due to the progressive failure of the sample observed during the direct shear tests.

The failure process resulting from shearing a jointed rock mass was described by Ladanyi and Archambault (1970):

"...in each test in which eventually a failure of the rods occurred, the ultimate shear failure was preceded by cracking of the blocks in a typical brittle manner. It is concluded therefrom that the assumption of a simple shear failure occurring across an intact rock material may be oversimplified. What really appears to happen, is that the original rock blocks are first fissured and even crushed in smaller fragments by a compression mechanism, and subsequent shear occurs then across this already partially damaged rock mass."

This is the process of progressive failure. This may result from the uneven stress distribution within the samples common in direct shear tests, as suggested by a number of researchers (e.g. Lajtai, 1969a; Dounias and Potts, 1993; Thiel and Zabuski, 1996).

The majority of shear tests carried out during this study also exhibited progressive failure behaviour. The process of progressive failure, using the results from Test B19A presented in Figure 6-8(a) to (d), is described below.

As shear displacement commenced, separation within the rock mass can be observed. Figure 6-23 shows the separation within the rock mass at a displacement of 6 mm. Up to this displacement, the pieces within the sample remained intact and the gradients of the shear stress-displacement and dilation-displacement responses are relatively constant.

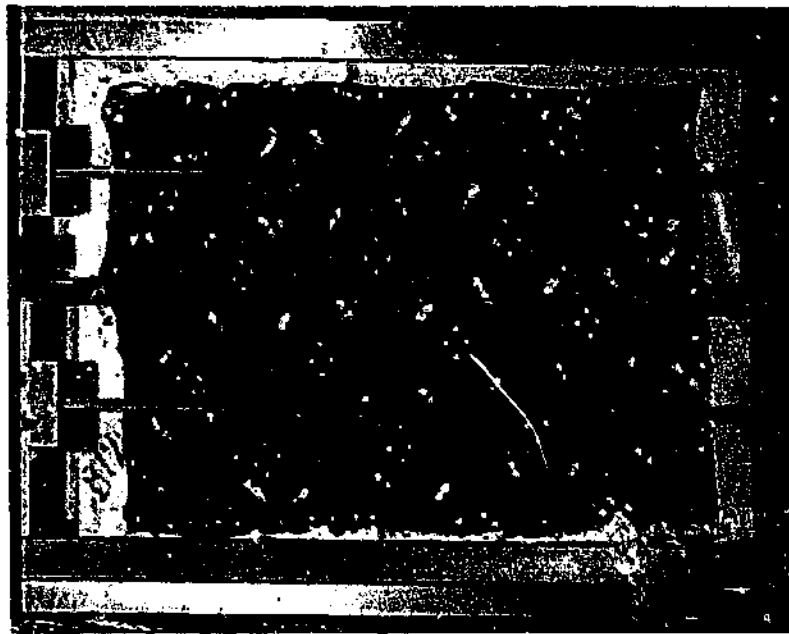


Figure 6-23: Separation in Test B19A at displacement=6 mm.

Shear displacement continued until crack initiation due to tensile failure occurred near the ends of the shear plane, as shown in Figure 6-24. This cracking commenced at a shear displacement of about 8 mm.

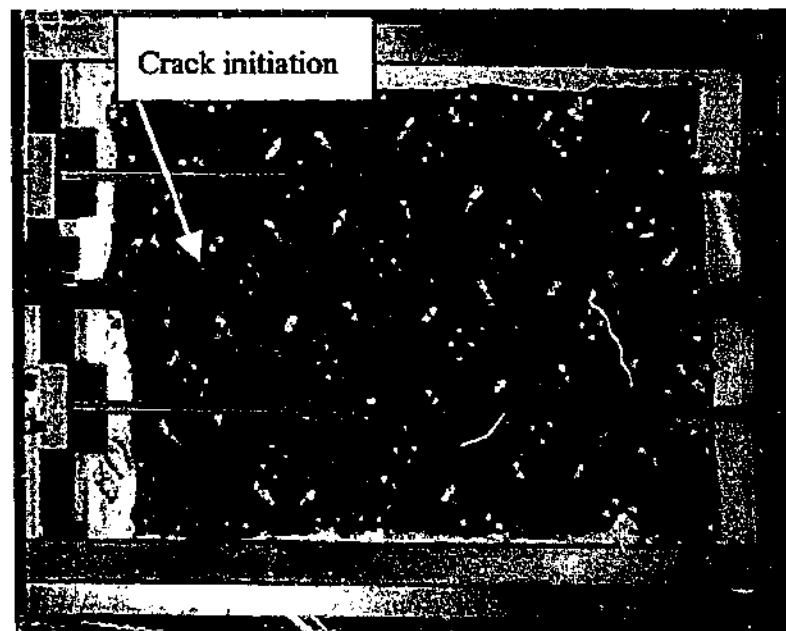


Figure 6-24: Crack initiation and further rotation in Test B19A at shear displacement=8 mm.

At this displacement, Figure 6-8(b) and (d) show that the shear stress and dilation rates began to decrease. At this point, the amount of normal stress developed as a result of sample dilation had reached a level where tensile failure of the intact pieces within the rock mass began. This

corresponds to the fissuring and crushing of the blocks by the compression mechanism described by Ladanyi and Archambault (1970).

As shear displacement increased, crack initiation and propagation continued. Figure 6-25 shows the sample at a shear displacement of 13 mm. Further tensile cracking can be observed, as well as the initial development of a shear plane. At this point, peak shear stress and dilation were reached.

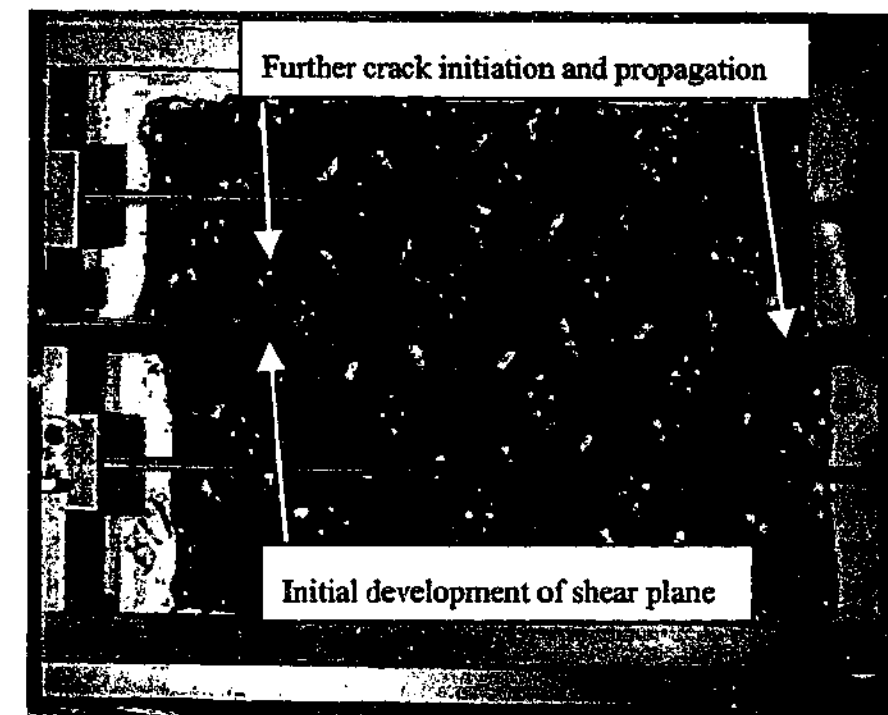


Figure 6-25: Further crack initiation and propagation and initial development of shear plane at displacement=13 mm.

After further shear displacement, crack propagation and the initiation of new cracks appeared to cease. However, the shear plane continued to develop, as shown in Figure 6-26. This suggests that the compression mechanism causing the tensile cracking was no longer acting on the sample and that the rock mass was now failing by shear through the partially damaged rock mass.

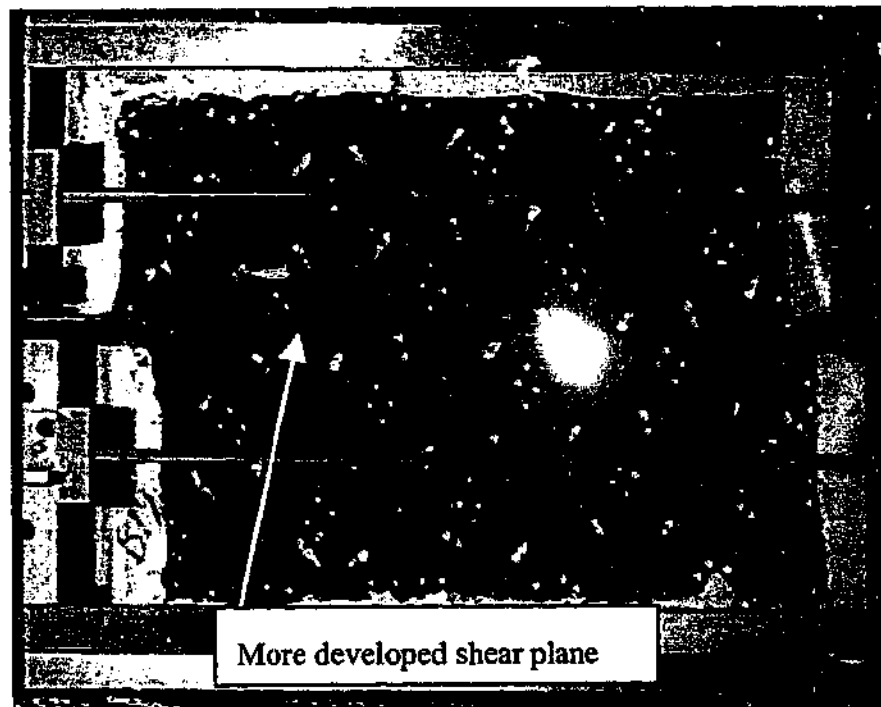


Figure 6-26: Continuing development of shear plane at shear displacement=27 mm.

The dilation response presented in Figure 6-8(d) showed a gradual decrease in dilation with continuing displacement after peak dilation. This suggests that rotation of the sample had ceased and the effective separation of the sample into two halves allowed the top half of the sample to move downwards under the applied normal stress.

6.3.6 Summary of rock mass behaviour

The typical behaviour of the rock mass samples at each stage of the shear test has been examined, using both the measured outputs and the video footage. Compliance effects have been shown to be minimal. Negative dilation was observed in most shear tests and has been explained as being due to elastic effects and to the application of CNS conditions.

Each sample was observed to behave in one of two ways with increasing shear displacement.

1. Sliding along the θ_1 joint set was suggested in some tests by the measured outputs and confirmed by the video footage.
2. Alternatively, in samples where sliding was not observed, separation across the θ_2 joint sets was observed and appeared to result from the rotation of a number of blocks within

the sample. The pre-peak behaviour of the samples exhibiting rotational behaviour also seemed to be influenced by the value of θ_2 .

The progressive failure of the sample during shearing has been explained using the video footage and measured outputs from Test B19A. This observed failure process agrees with that described by Ladanyi and Archambault (1970).

6.4 Observation of pre-peak and failure mechanisms

6.4.1 Introduction

The video footage of the Type "B" shear tests allowed observation of the mechanisms occurring within the rock mass prior to and at failure. Two pre-peak mechanisms were identified from this footage, namely sliding along the θ_1 joint set or an apparent rotation about the θ_2 joint set. These were introduced in the previous section and are considered more fully below.

6.4.2 Sliding followed by asperity shear

As discussed in Section 4.2, the shear test was configured so that if sliding were to occur, it would occur along the θ_1 joint set. Sliding along the θ_1 joint set was observed when the value of θ_1 was generally less than about 30° .

Consider the idealised, two-dimensional rock mass in Figure 6-27. The jointing pattern forms what is essentially a very rough rock joint, with "joint asperities" formed by the intact pieces of rock.

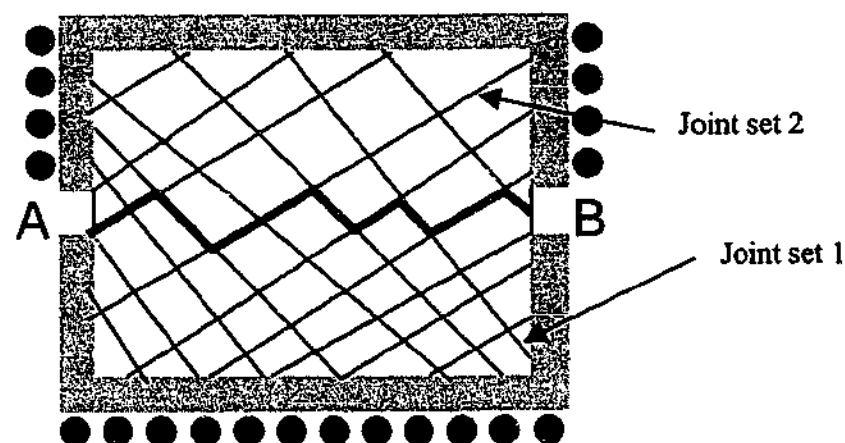
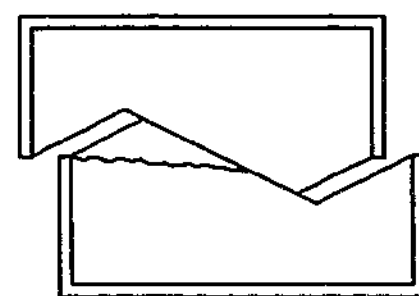


Figure 6-27: Very rough rock joint formed by jointing configuration.

The mechanical behaviour of very rough rock joints, consisting of sliding on, then shearing through an asperity, has been modelled by a number of researchers, including Haberfield and Johnston (1994), Kodikara and Johnston (1994), Seidel and Haberfield (1995) and Yang and Chiang (2000).

If the inclination of the joint sets allows, sliding along a joint set will continue until shearing through the asperities begins. As displacement continues, a failure surface will eventually form between points A and B.

A simplified diagram of sliding along a joint set and shear through a single asperity is shown in Figure 6-28.



Sliding/Asperity Shear

Figure 6-28: Simplified diagram of sliding followed by asperity shear.

Figure 6-29, for example, shows the very rough rock joint formed in Test B4. There is evidence of sliding along the θ_1 joint set and shear through the asperities.

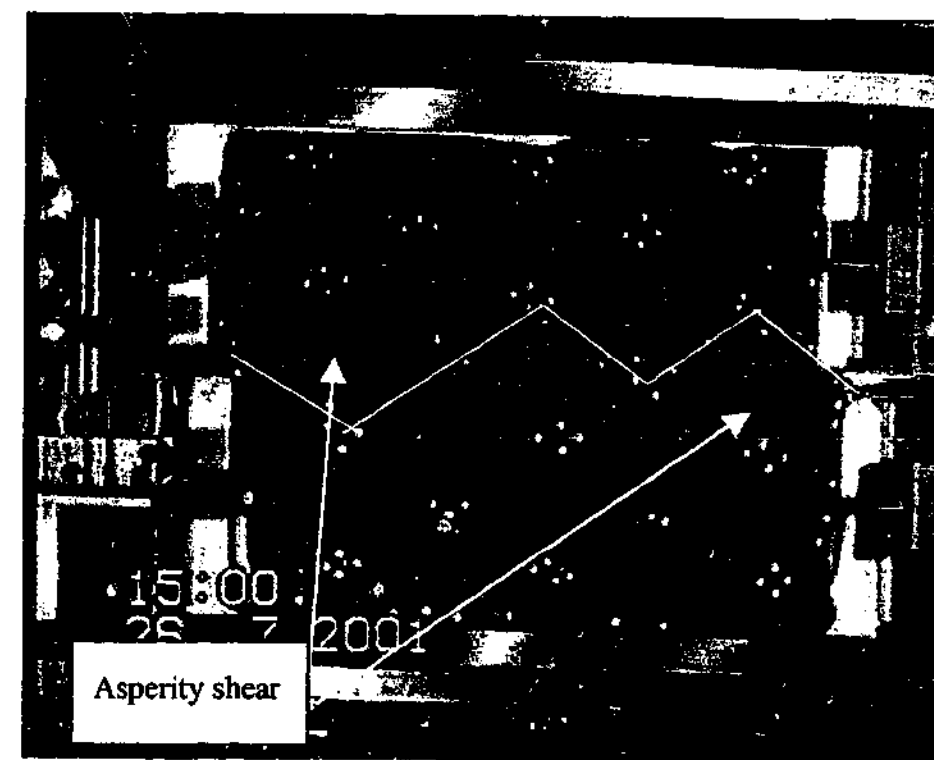


Figure 6-29: Formation of very rough rock joint with sliding and asperity shear (Test B4).

6.4.3 Rotation followed by shear

For the tests where no sliding was observed, separation within the sample at each end of the shear plane was observed. This separation resulted from applying a shear displacement to the bottom half of the sample and gave the appearance that part of the rock mass was rotating. Also, because no sliding along the θ_1 joint set was observed, it would appear that the θ_1 joint set, from a mechanistic perspective, could be ignored.

Two types of failure mechanisms were identified where rotation was the pre-peak behaviour. These were strut shear and block shear, so named because of the shape of the portion of the rock mass that appeared to rotate.

6.4.3.1 Strut shear

This failure mechanism occurred by shear through a strut connecting the ends of the shear box, shown schematically in Figure 6-30.

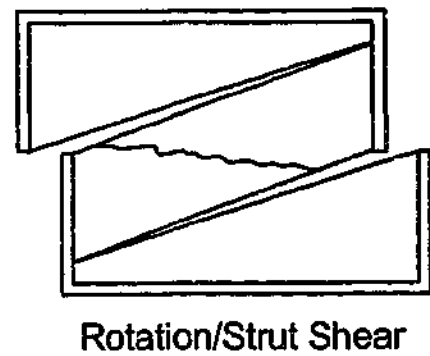


Figure 6-30: Simplified diagram of rotation followed by strut shear.

This failure mechanism was observed when θ_2 was less than the angle of the diagonal of the sample, θ_d . The length of the shear plane is controlled by the width of the strut (i.e. the spacing of the θ_2 joint set). Figure 6-31 shows an example of the strut rotation and failure observed in Test B9.

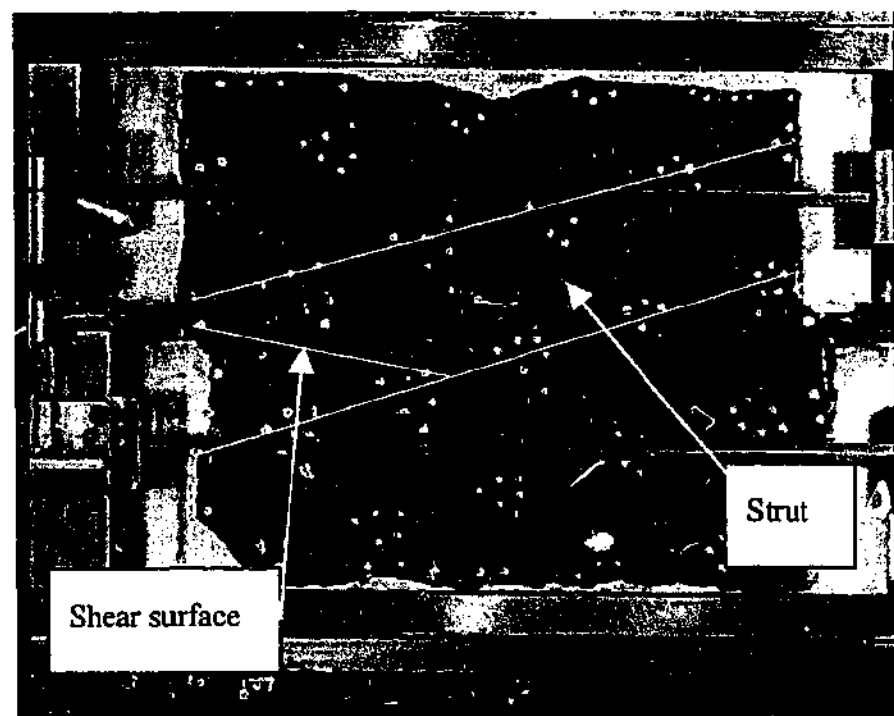


Figure 6-31: Shape of strut and length of shear surface (Test B9).

6.4.3.2 Block shear

This failure mechanism occurred by failure through a block bounded by the top and bottom of the shear box and the θ_2 joints nearest the ends of the shear plane, as shown schematically in Figure 6-32.

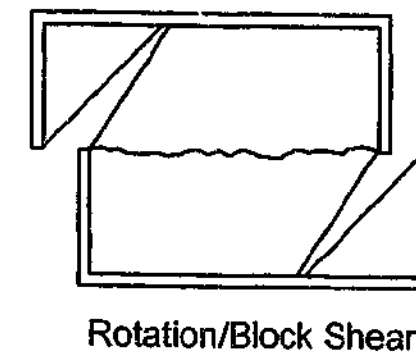


Figure 6-32: Simplified diagram of rotation followed by block shear.

This failure was observed when θ_2 was greater than the angle of the diagonal of the sample, θ_d . The length of the shear surface was typically the length of the rock mass. An example of the block rotation and failure observed in Test B14 is shown in Figure 6-33.

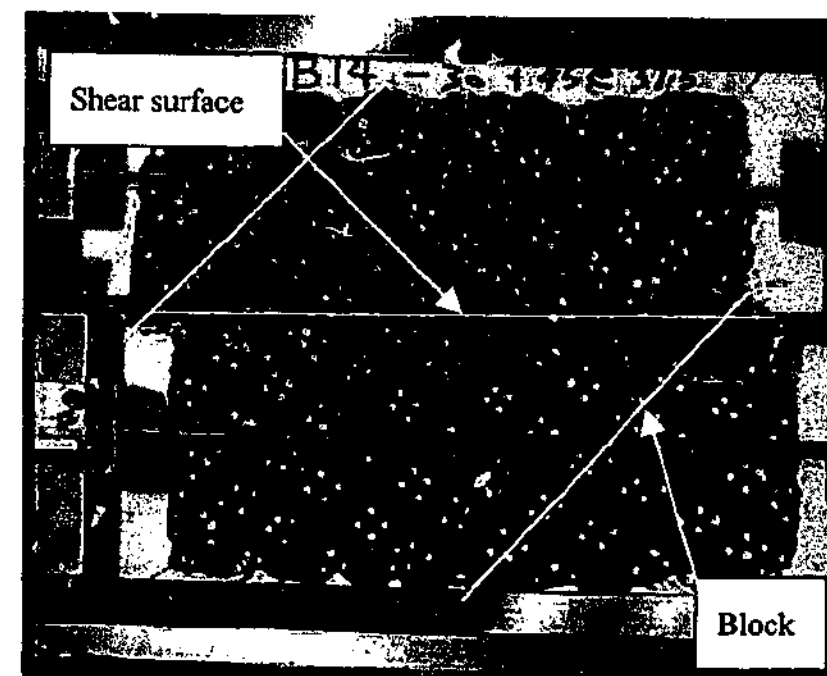


Figure 6-33: Shape of block and length of shear surface (Test B14).

Theoretical models of the pre-peak and failure mechanisms are developed in Chapter 7.

6.5 Influence of parameters on sample behaviour

The shear behaviour of the rock mass samples tested in this study was found to be dependent on joint inclination, joint spacing, number of joint sets, intact rock strength and initial normal stress. This concurs with studies by others documented in the literature (refer to Section 2.4.2). The stiffness applied to the sample may also influence sample behaviour, but was not considered in this study. The sample behaviour was also observed to be anisotropic, so the effect of rotating the joint set inclinations with respect to the shear plane inclination is also a factor that affects shear strength.

The influence of the above parameters was assessed relative to the behaviour observed in tests on samples comprising the following default parameters:

- Two joint sets (inclined at either $-30^\circ, 45^\circ; -45^\circ, 15^\circ; -45^\circ, 60^\circ; -60^\circ, 45^\circ$),
- Joint spacing=70 mm,
- Intact rock strength=3 MPa, and
- Initial normal stress, $\sigma_n=100$ kPa.

The laboratory testing program was divided into stages so that the influence of each of the above parameters could be examined. During the tests, the shear stress, normal stress, shear displacement and dilation were measured.

The normalised pre-peak stress paths for all the Type "B" tests plotted in Figure 6-34 provide an overall indication of sample behaviour. It will be demonstrated in Section 6.5.2 that normalising the shear and normal stresses with the uniaxial compressive strength (UCS) of the intact rock effectively removes the influence of intact rock strength on sample behaviour. The normalised shear and normal stresses have been denoted $\bar{\tau}$ versus $\bar{\sigma}$ respectively, while the normalised peak shear and normal stresses have been denoted $\bar{\tau}_p$ and $\bar{\sigma}_p$ respectively. Figure 6-34 shows a relatively wide variation in behaviour that reflects the impact of the above parameters on the normalised shear strengths of the samples.

The strength envelopes for a single horizontal joint coincident with the shear plane (represented by the dotted line) and of an intact rock sample (represented by the chain line) are also included in Figure 6-34. As would be expected, results for the samples tested in this study fall between these two lines.

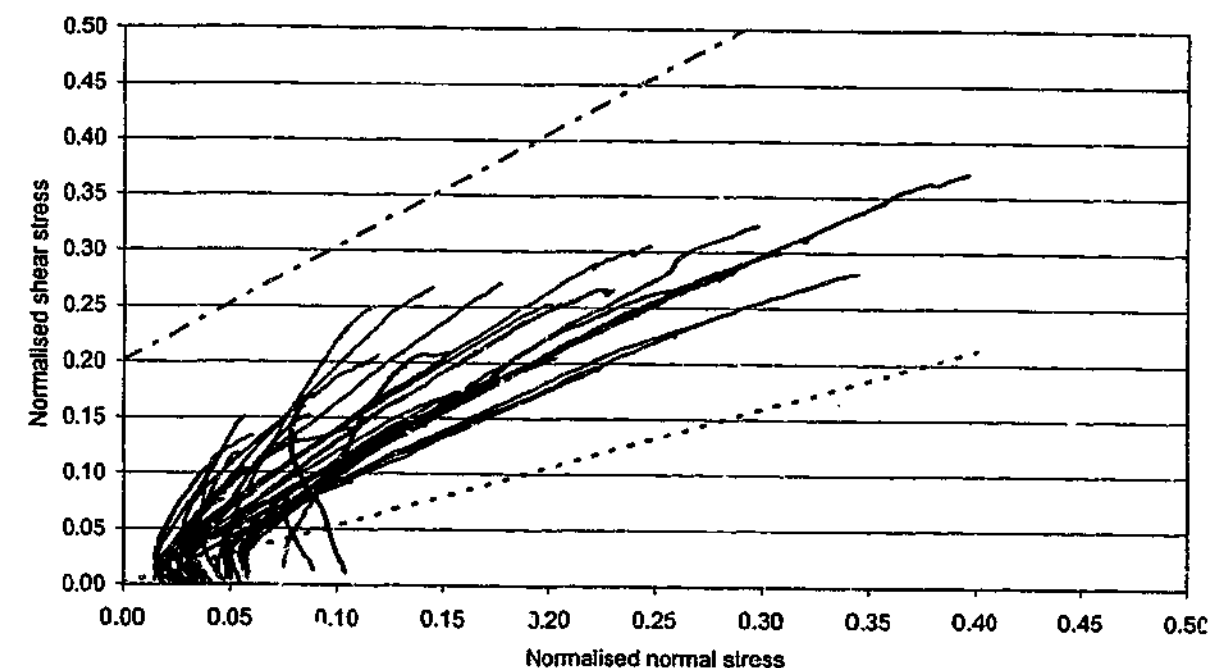


Figure 6-34: Pre-peak $\bar{\tau}$ - $\bar{\sigma}$ behaviour of the Type "B" samples.

Figure 6-35 shows the normalised shear, $\bar{\tau}_p$ and normal, $\bar{\sigma}_p$, stresses at peak. It can be observed from this figure that there appears to a reasonable correlation between $\bar{\tau}_p$ and $\bar{\sigma}_p$. The trend line shown in Figure 6-35 is a power function starting at the origin (as it has been assumed the samples have no tensile strength). While some scatter about this trend line is evident, the scatter is relatively small considering the range in joint inclinations and spacings tested. The equation of this global trendline is:

$$\bar{\tau}_p = 0.54\bar{\sigma}_p^{0.52} \quad \text{Equation 6-3}$$

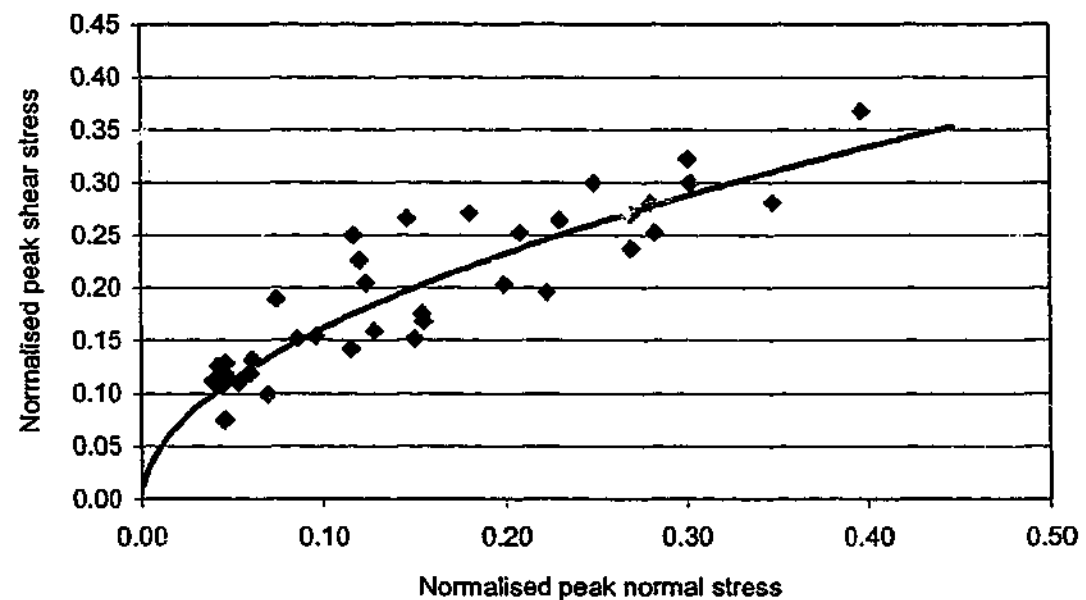


Figure 6-35: Variation of normalised peak shear stress versus normalised peak normal stress for the Type "B" tests.

The test results of normalised peak shear stress versus shear displacement at failure are presented in Figure 6-36, normalised peak normal stress versus shear displacement at failure in Figure 6-37 and dilation versus shear displacement at failure in Figure 6-38. There does not appear to be any clear correlation of normalised peak shear strength, normalised peak normal stress and dilation at failure with shear displacement.

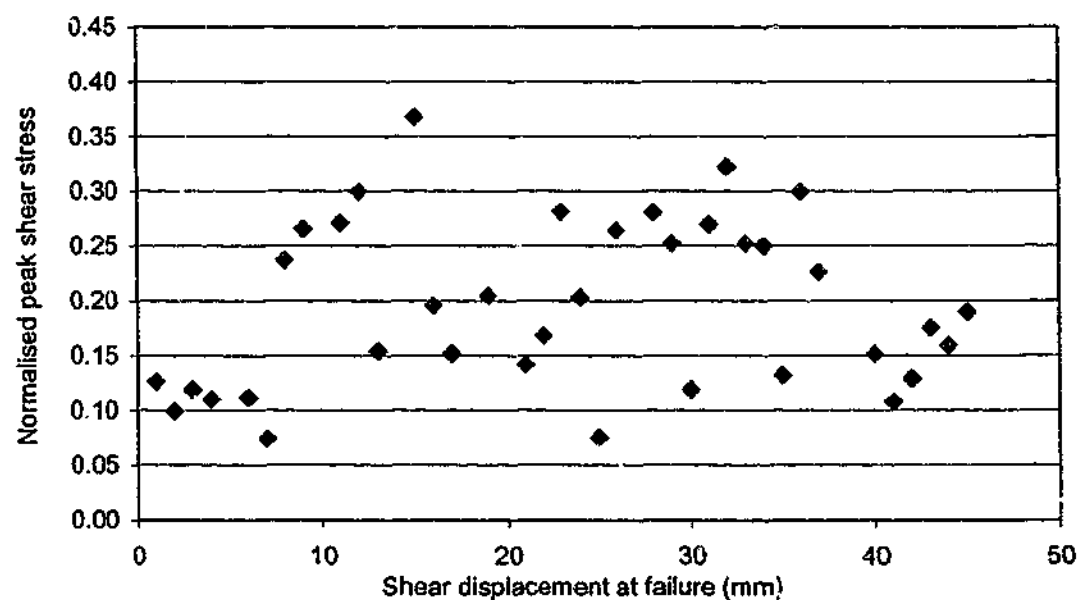


Figure 6-36: Variation of normalised peak shear stress versus shear displacement at failure for the Type "B" tests.

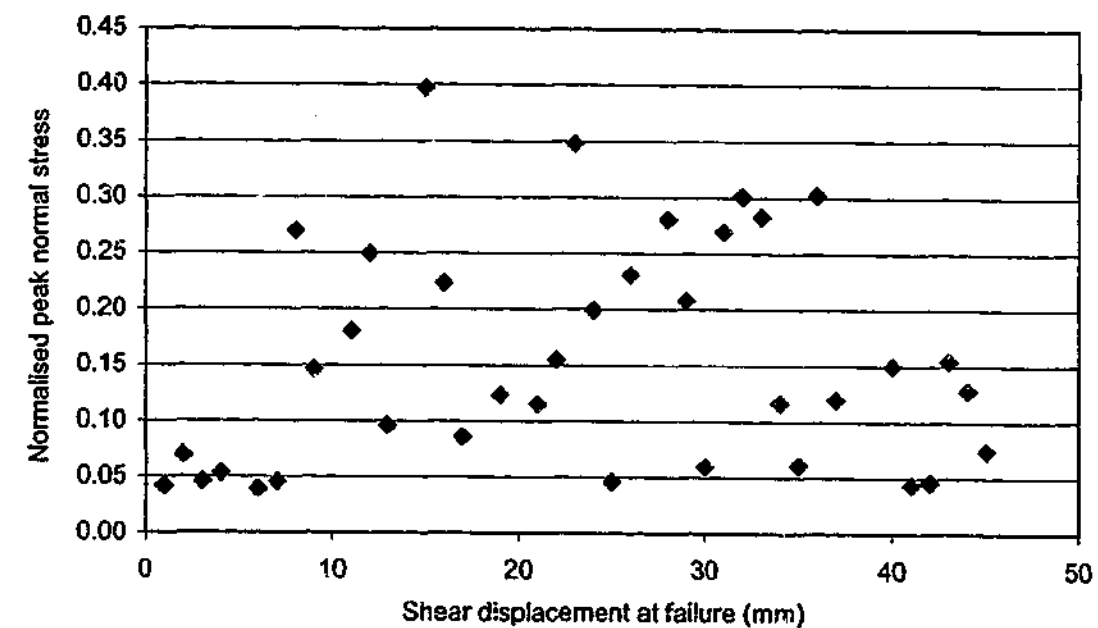


Figure 6-37: Variation of normalised peak normal stress versus shear displacement at failure for the Type "B" tests.

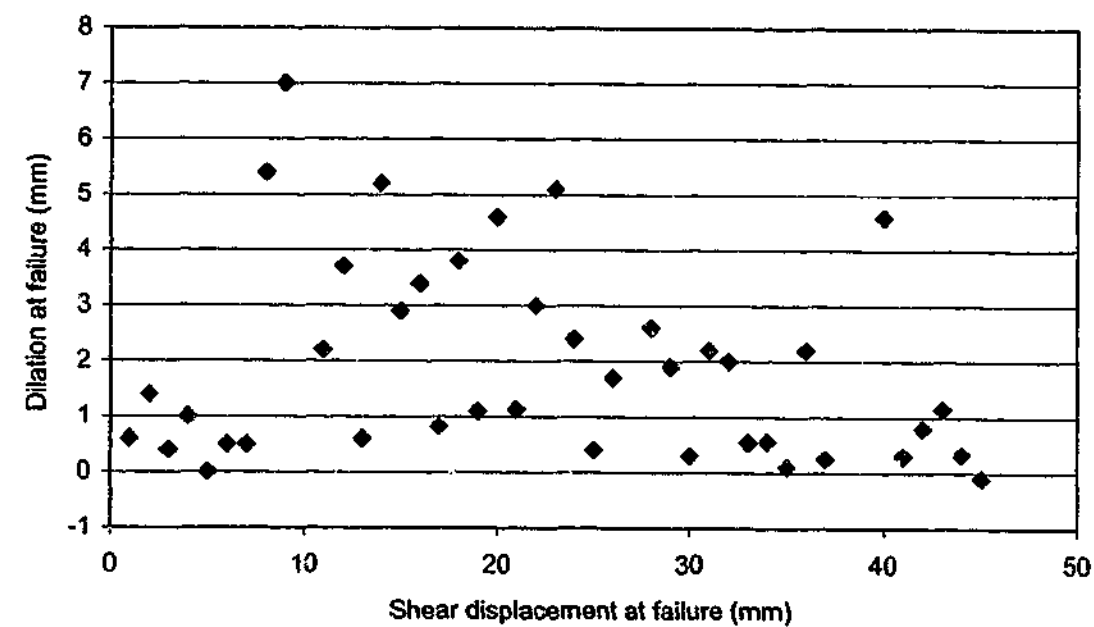


Figure 6-38: Variation of dilation at failure versus shear displacement at failure for the Type "B" tests.

6.5.1 Joint inclination

Eleven Type "B" tests were carried out to study the influence of joint inclination on sample strength. The samples were manufactured from Johnstone blocks of similar intact strength. The joint sets for each test were cut at different inclinations to the shear plane while maintaining a

constant spacing between joints. The same boundary conditions (initial normal stress and normal stiffness) were applied in each test. This allowed the influence of joint inclination on the pre-peak and failure mechanisms and peak shear stress to be assessed. The influence of joint inclination on Type "A" samples was not investigated.

The joint sets were varied, with the θ_1 joint set inclined at -15° , -30° , -45° , -60° or -75° and the θ_2 joint set inclined at 15° , 30° , 45° , 60° or 75° . The combination of joint inclinations produced an included angle between the joint sets that varied between 60° and 120° . In four tests, a third joint set was also cut into the rock. These test results are discussed in Section 6.5.4. Graphs showing normalised peak shear stress versus normalised peak normal stress, normalised peak shear stress versus displacement at failure and dilation versus displacement at failure are presented in Figure 6-39 to Figure 6-41.

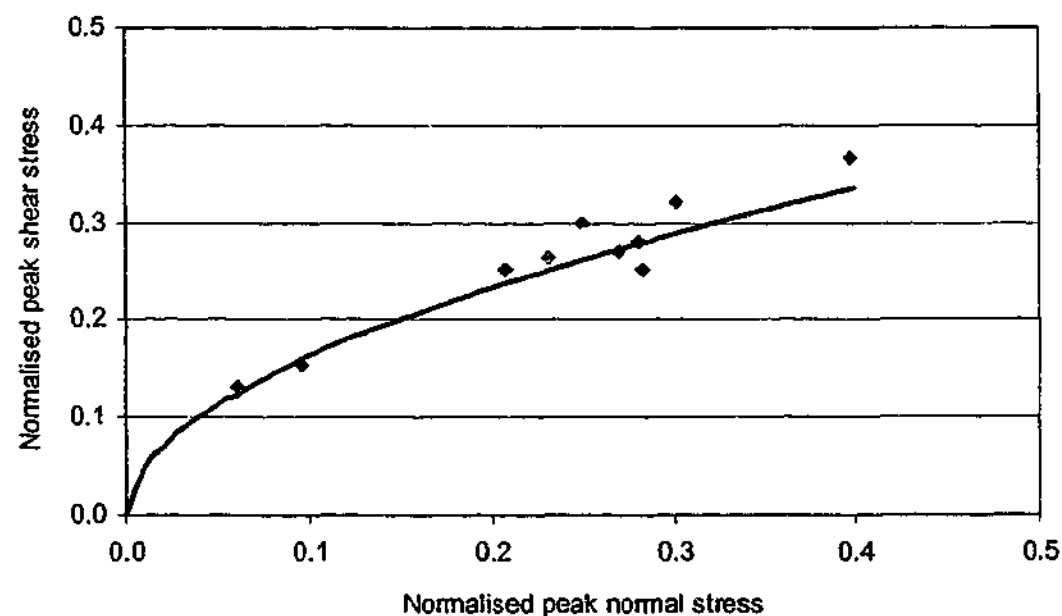


Figure 6-39: $\bar{\tau}_p$ versus $\bar{\sigma}_p$ response for samples containing two joint sets.

Figure 6-39 indicates that there appears to be a reasonable correlation between normalised peak shear and normal stresses. The global trend line has also been plotted in Figure 6-39.

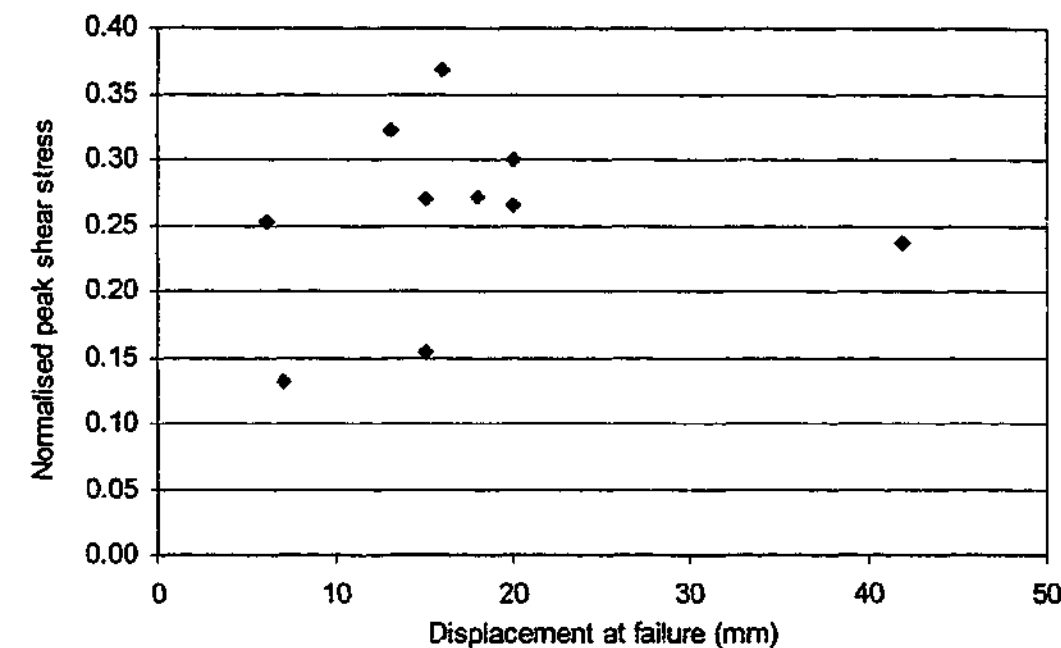


Figure 6-40: $\bar{\tau}_p$ versus displacement at failure plot for rock masses containing two joint sets.

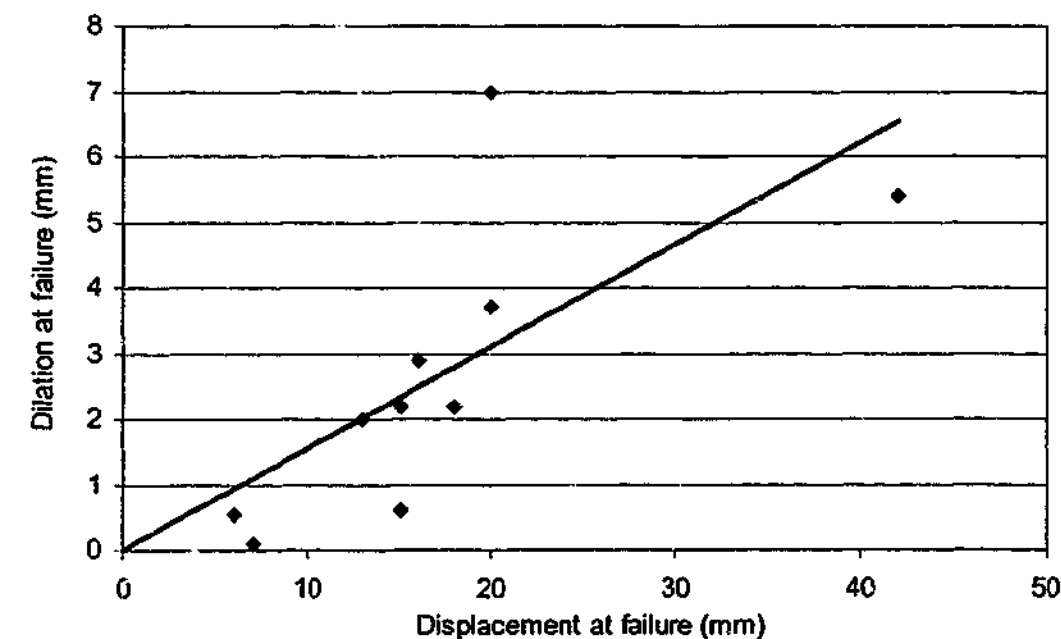


Figure 6-41: Dilation at failure versus displacement at failure plot for rock masses containing two joint sets.

The correlation between normalised peak shear stress and shear displacement at failure shown in Figure 6-40 is poor, while a reasonable relationship between dilation and displacement at failure can be observed in Figure 6-41. The average dilation angle is about 9° .

The influence of joint inclination on the observed pre-peak behaviour and failure mechanism is summarised in Table 6-1.

Table 6-1: Effect of joint inclination on pre-peak and failure mechanism.

θ_1	θ_2	Pre-peak / failure mechanism
-15°	45°	Sliding / asperity shear
-30°	30°	Sliding / asperity shear
-30°	45°	Rotation / block shear
-45°	15°	Rotation / strut shear
>-45°	>30°	Rotation / block shear

For tests in which $\theta_1 = -15^\circ$, sliding was observed along the θ_1 joint set irrespective of the inclination of the other (θ_2) joint set. Failure occurred by asperity shear.

For tests in which $\theta_1 = -30^\circ$ and $\theta_2 = 30^\circ$, sliding followed by asperity shear was observed. When $\theta_2 = 45^\circ$, rotation followed by block shear was observed.

For the tests in which $\theta_1 = -45^\circ$, rotation followed by either strut or block shear was observed, depending on the value of θ_2 .

The anisotropy introduced by joint inclination can be examined further by comparing test results with the same included angle between θ_1 and θ_2 , A , but with varying inclination of θ_1 with respect to the shear plane (see Figure 6-42).

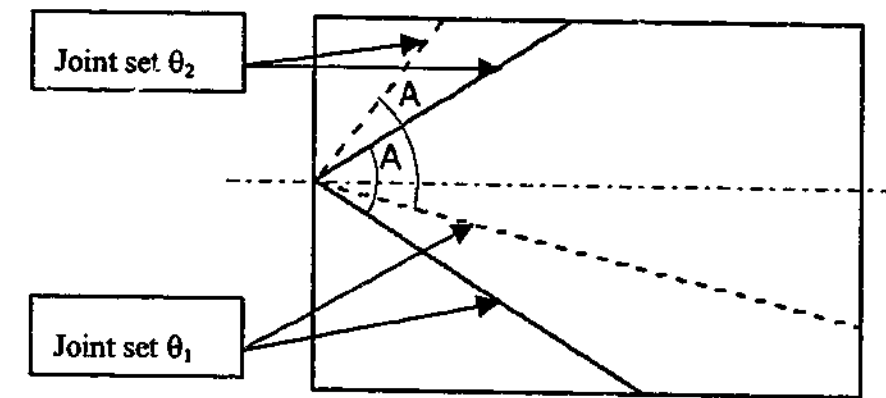


Figure 6-42: Rotation of joint sets while maintaining a constant included angle, A .

Figure 6-43 shows the variation in normalised peak shear strength with joint inclination with respect to the shear plane for samples with the same included angle between the joint sets. The global trend line has also been plotted.

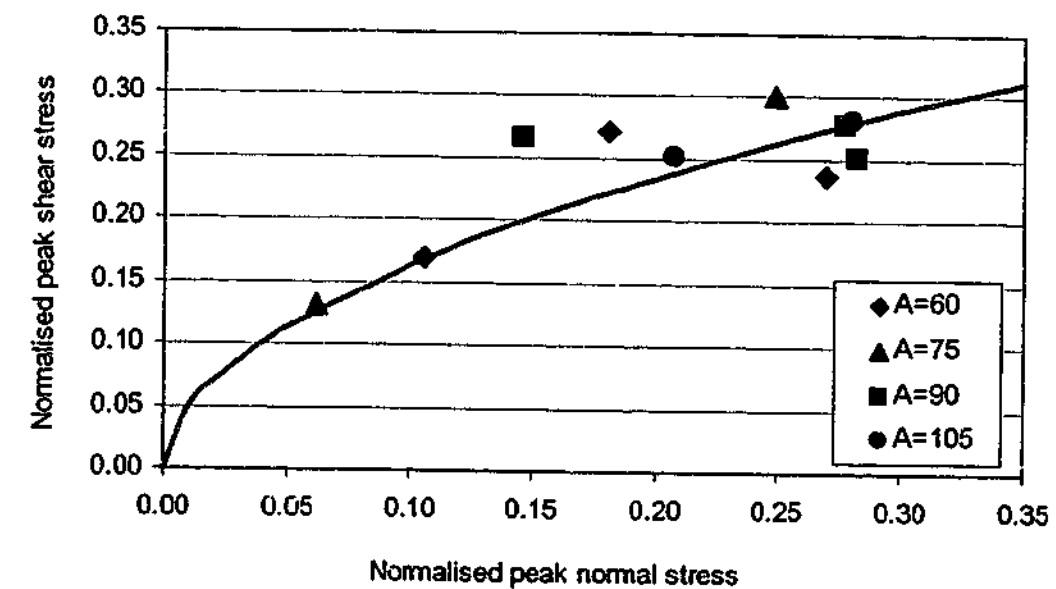


Figure 6-43: Effect of included angle on $\bar{\tau}_p$ versus $\bar{\sigma}_p$.

Figure 6-43 indicates the rotation of the joint sets can produce a significant change in normalised peak strengths. For example, the values of $\bar{\tau}_p$ for rock masses with an included angle of 60° between the joint sets range from about 0.15 to about 0.27, depending on θ_1 . This indicates the failure mechanism may have changed, resulting in significantly different peak strengths. The normalised stress paths to failure for the tests with an included angle of 60° are plotted in Figure 6-44. The (extrapolated) stress path for a horizontal joint has also been

included, as the sample will have the strength of a joint if the joints are rotated a further 15° in either direction, because then either θ_1 or θ_2 will be coincident with the shear plane.

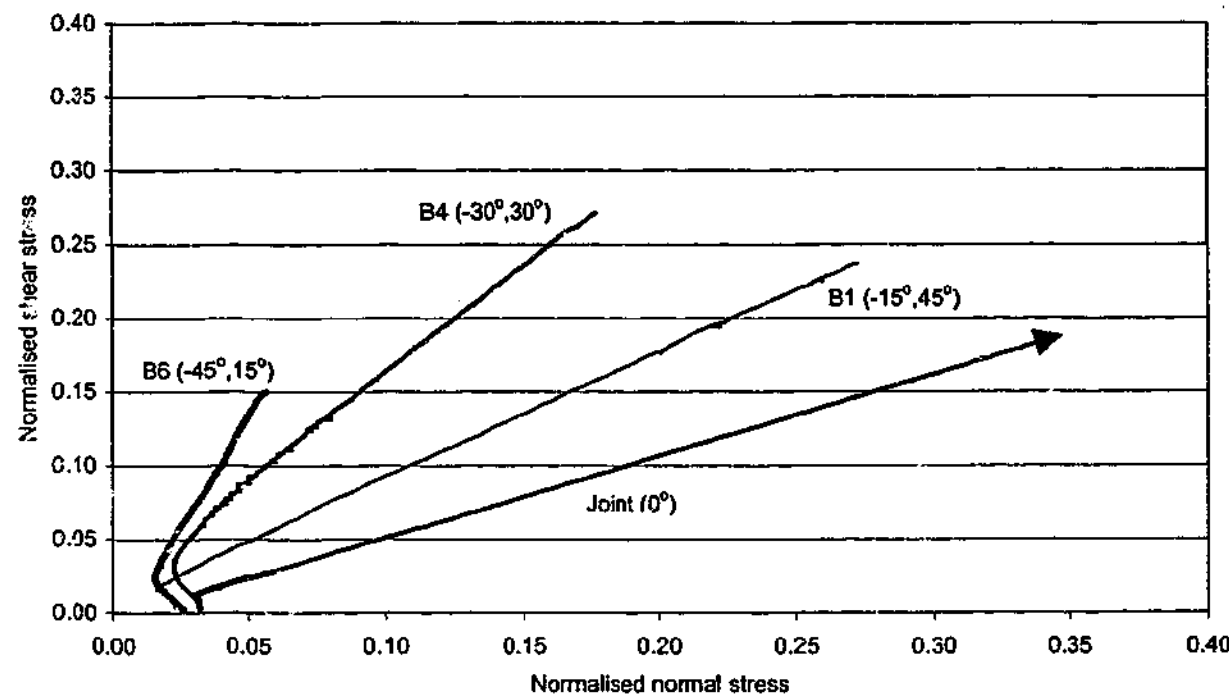


Figure 6-44: Stress paths of samples with included angle=60°.

The pre-peak and failure mechanisms of samples B1 and B4 listed in Table 6-1 were sliding followed by asperity shear, while for sample B6, rotation was followed by strut shear. Figure 6-44 shows how the change in joint inclination has reduced the peak stresses and altered the stress paths. As θ_1 increases (becomes more negative or steeper), the peak normalised shear stress increases to a maximum measured value of 0.27 at $\theta_1 = -30^\circ$, then reduces to 0.15 for $\theta_1 = -45^\circ$. Similar observations were made when the included angle was 75°. When the included angle was either 90° or 105°, the peak normalised shear stress was reasonably consistent for the joint inclinations tested.

Figure 6-45 shows the plots of $\bar{\tau}_p$ against θ_1 and θ_2 so that the influence of each on sample strength can be observed.

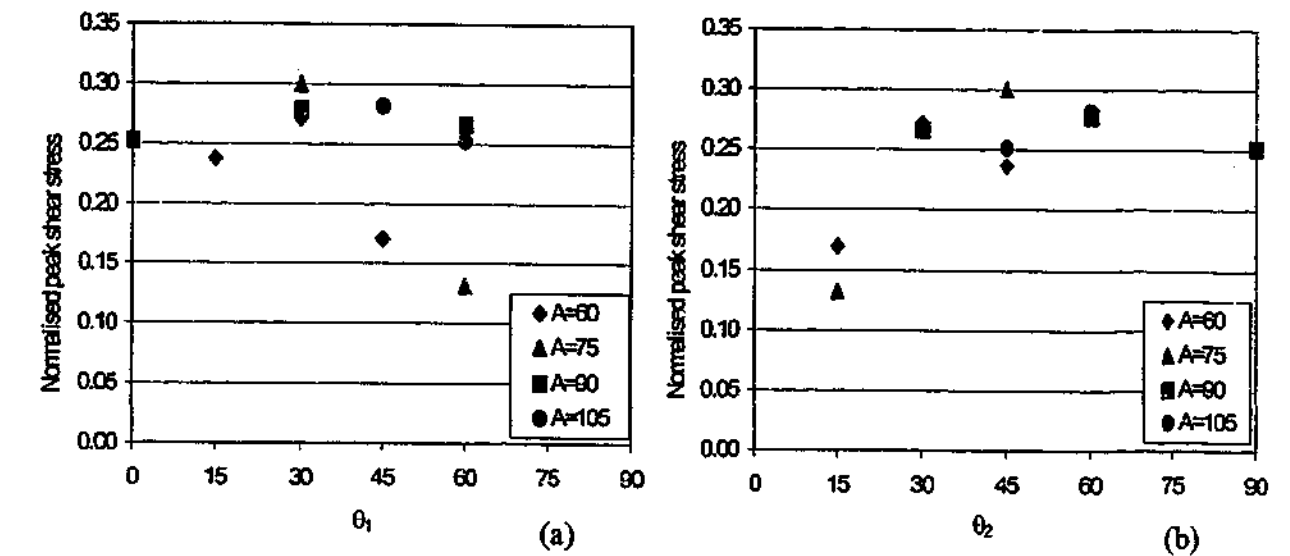


Figure 6-45: Normalised peak shear strength versus inclination of the θ_1 and θ_2 joint sets.

Figure 6-45 would appear to indicate that the inclination of the θ_1 joint set has little effect on $\bar{\tau}_p$, except in two tests, for which $\theta_2 = 15^\circ$ and lower values of $\bar{\tau}_p$ were obtained. This is more clearly shown in Figure 6-45(b). The failure mechanism in these tests was strut shear. The remaining points were from tests where the failure mechanisms were either asperity shear or block shear.

The effect of θ_2 on the behaviour of the Type “B” samples with two joint sets is shown in Figure 6-46. Tests with the same value of θ_2 have been plotted using the same symbol. There appears to be an increase in normalised peak shear stress as θ_2 increases.

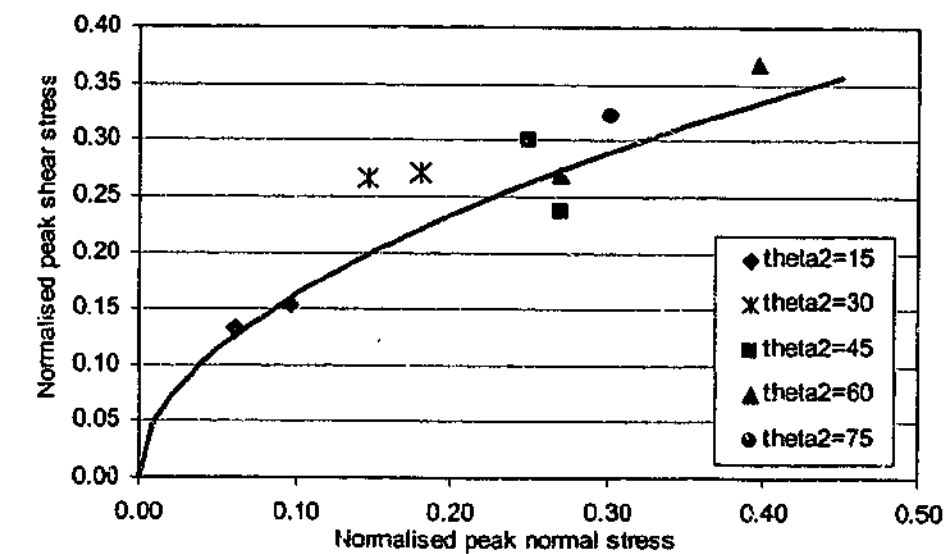


Figure 6-46: Effect of θ_2 on the normalised peak stresses for Type “B” samples with two joint sets.

Figure 6-47 shows the variation between $\bar{\tau}_p$ and the displacement at failure. It can be observed that the displacement at failure generally fall between about 5 mm and 20 mm, although there is one data point (Test B1) where the displacement is about 42 mm. Video footage of Test B1 indicates that sliding along the θ_1 joint set occurred. As sliding occurred, there was an increase in normal stress due to dilation of the sample and the application of the CNS condition. However, the relatively shallow angle meant that a large shear displacement was required to build up stresses within the sample to the point where failure occurred.

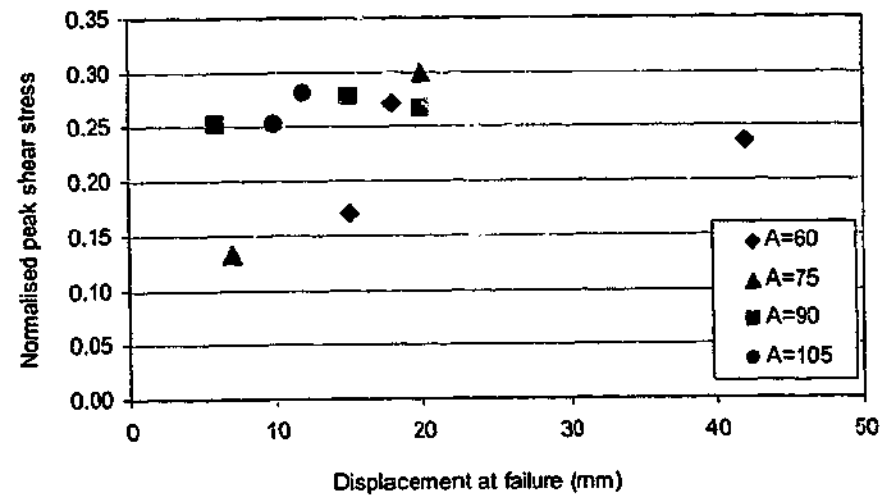


Figure 6-47: Effect of included angle on $\bar{\tau}_p$ versus displacement at failure.

The influence of θ_1 and θ_2 on shear displacement at failure is shown in Figure 6-48. There does not appear to be any clear correlation between the shear displacement at failure and the values of θ_1 and θ_2 .

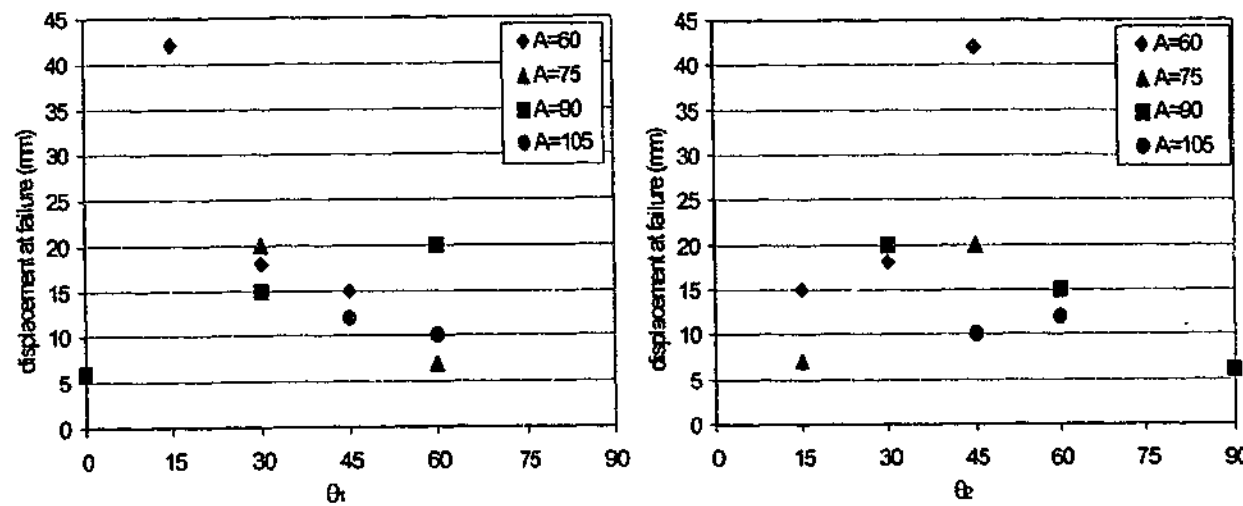


Figure 6-48: Shear displacement at failure versus inclination of the θ_1 and θ_2 joint sets.

Figure 6-49 shows the dilation at failure plotted against the included angle.

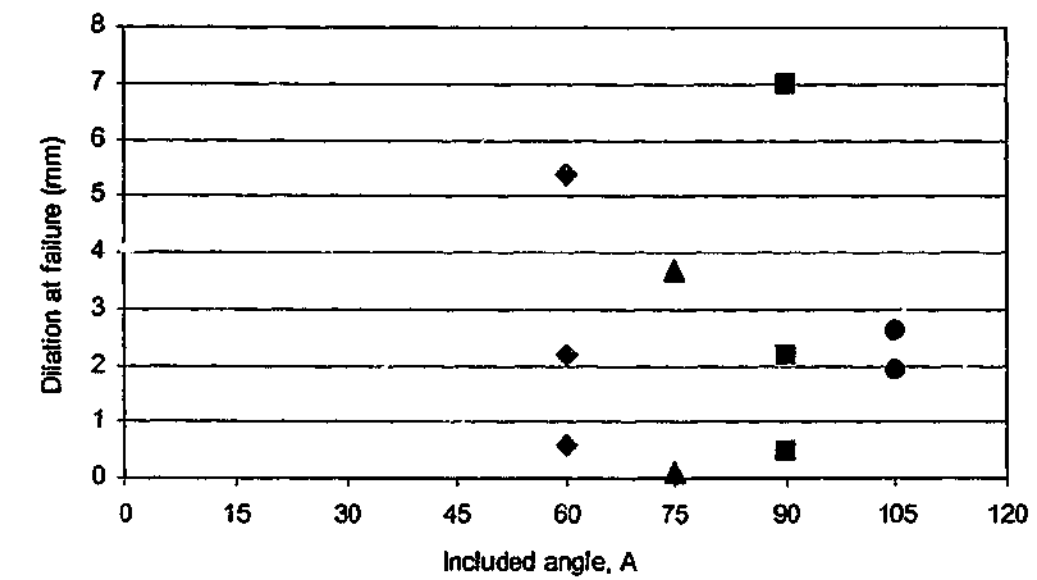


Figure 6-49: Dilation at failure versus included angle.

Figure 6-49 shows varying the inclination of θ_1 while maintaining the included angle can result in significant changes in the measured dilation at failure. Figure 6-50 shows the variation of dilation at failure with θ_1 and θ_2 . There does not appear to be any clear correlation with θ_1 , but dilation appears to be significantly larger for values of $30^\circ \leq \theta_2 \leq 60^\circ$. This may be due to the rotation of the sample and is analysed further in Chapter 7.

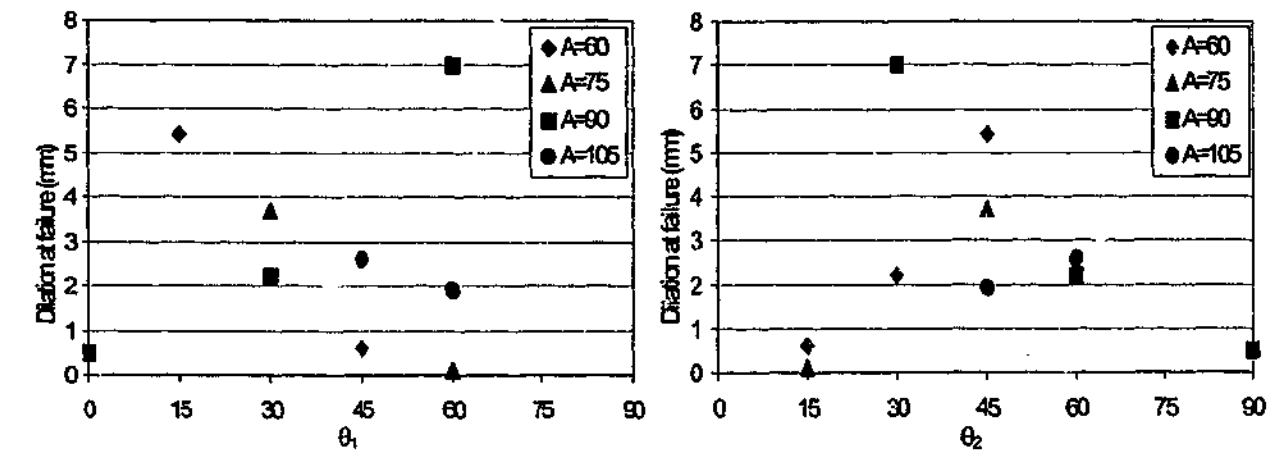


Figure 6-50: Dilation at failure versus inclination of the θ_1 and θ_2 joint sets.

It should be noted that the behaviour of the normalised peak normal stress would reflect the dilation behaviour due to the application of the CNS condition.

The effects of rotating the included angle on the normalised peak shear stress and the observed failure mechanisms have been summarised in Table 6-2.

Table 6-2: Effect of joint inclination on Type “B” rock mass behaviour and peak strength.

Included Angle	Test	θ_1, θ_2	$\bar{\tau}_p$	Pre-peak / failure mechanism
60°	B1	-15°, 45°	0.237	Sliding / asperity shear
	B4	-30°, 30°	0.271	Sliding / asperity shear
	B6	-45°, 15°	0.154	Rotation / strut shear
75°	B5	-30°, 45°	0.300	Rotation / block shear
	B30	-60°, 15°	0.132	Rotation / strut shear
90°	B26	-30°, 60°	0.270	Rotation / block shear
	B2	-60°, 30°	0.266	Rotation / block shear
	B28	-90°, 0°	0.252	Rotation / block shear
105°	B19A	-45°, 60°	0.281	Rotation / block shear
	B20	-60°, 45°	0.252	Rotation / block shear

Table 6-2 indicates the failure mechanisms vary with the joint inclination of the joint sets with respect to the shear plane. Where a change of failure mechanism was observed, e.g. on samples containing included angles of 60° and 75°, the impact on normalised peak shear strength was significant, i.e. the peak strength differed by a factor of about two. For the tests that failed by the same mechanisms, $\bar{\tau}_p$ remained reasonably consistent.

6.5.2 Intact rock strength

6.5.2.1 Type “B” tests

The influence of intact rock mass strength of the Type “B” samples was assessed in four tests, where the same joint configurations were cut into Johnstone blocks with lower intact strength

(UCS). The stress plots up to failure for the tests on samples made from Johnstone of differing strengths are presented in Figure 6-51. The thicker lines represent the samples made from the stronger Johnstone.

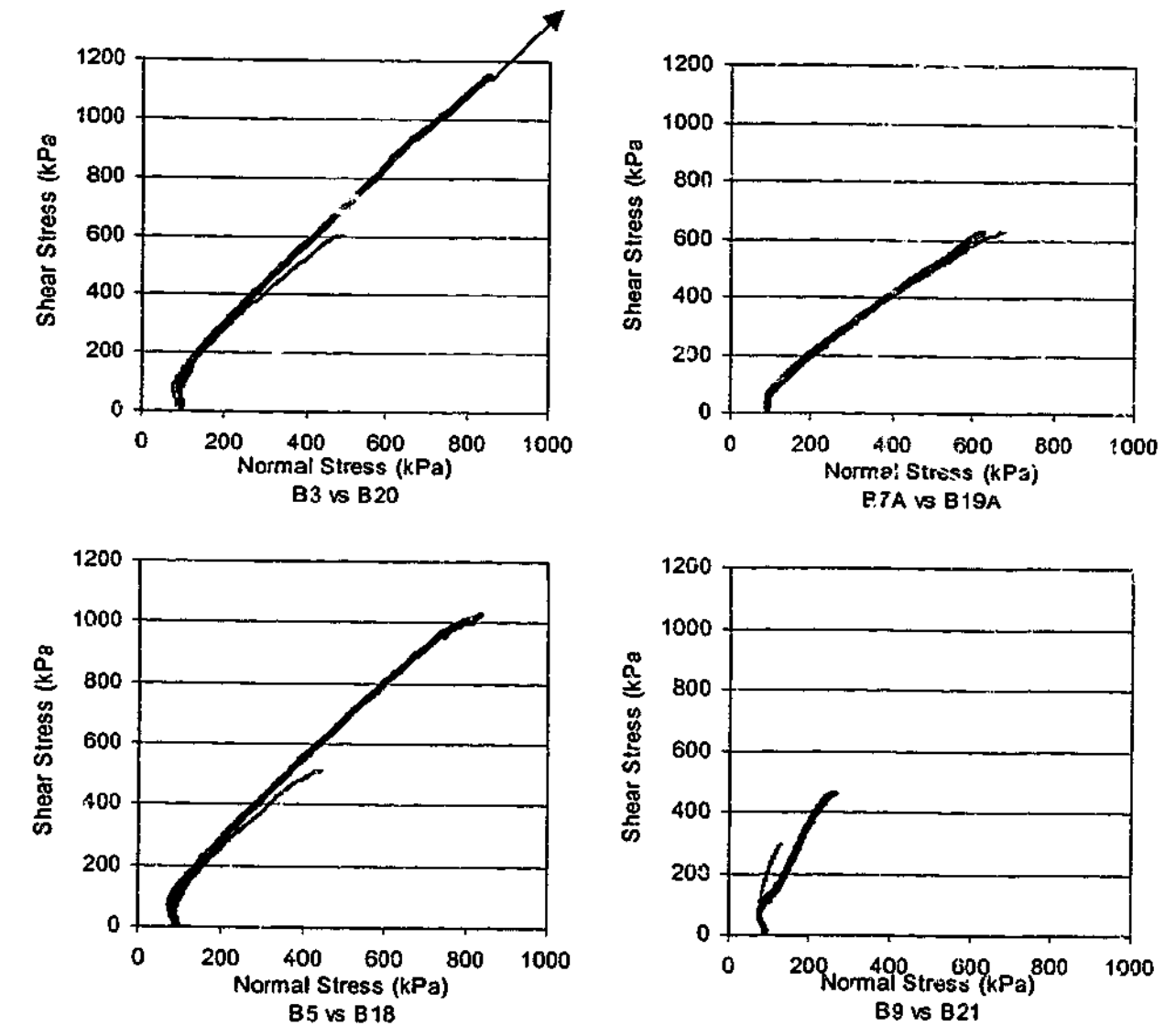


Figure 6-51: Comparison of pre-peak stress plots of tests on samples with differing intact rock strength.

Figure 6-51 shows that the stress path plots have similar form, but the samples made from stronger Johnstone reached higher peak stresses, as would be expected. As shown in Figure 6-52, normalising the stresses with respect to the UCS of the intact rock reduces the influence of intact rock strength. The normalised $\bar{\tau}_p$, $\bar{\sigma}_p$ space is used henceforth as a method of essentially removing the impact of variations in intact rock strength from the test results.

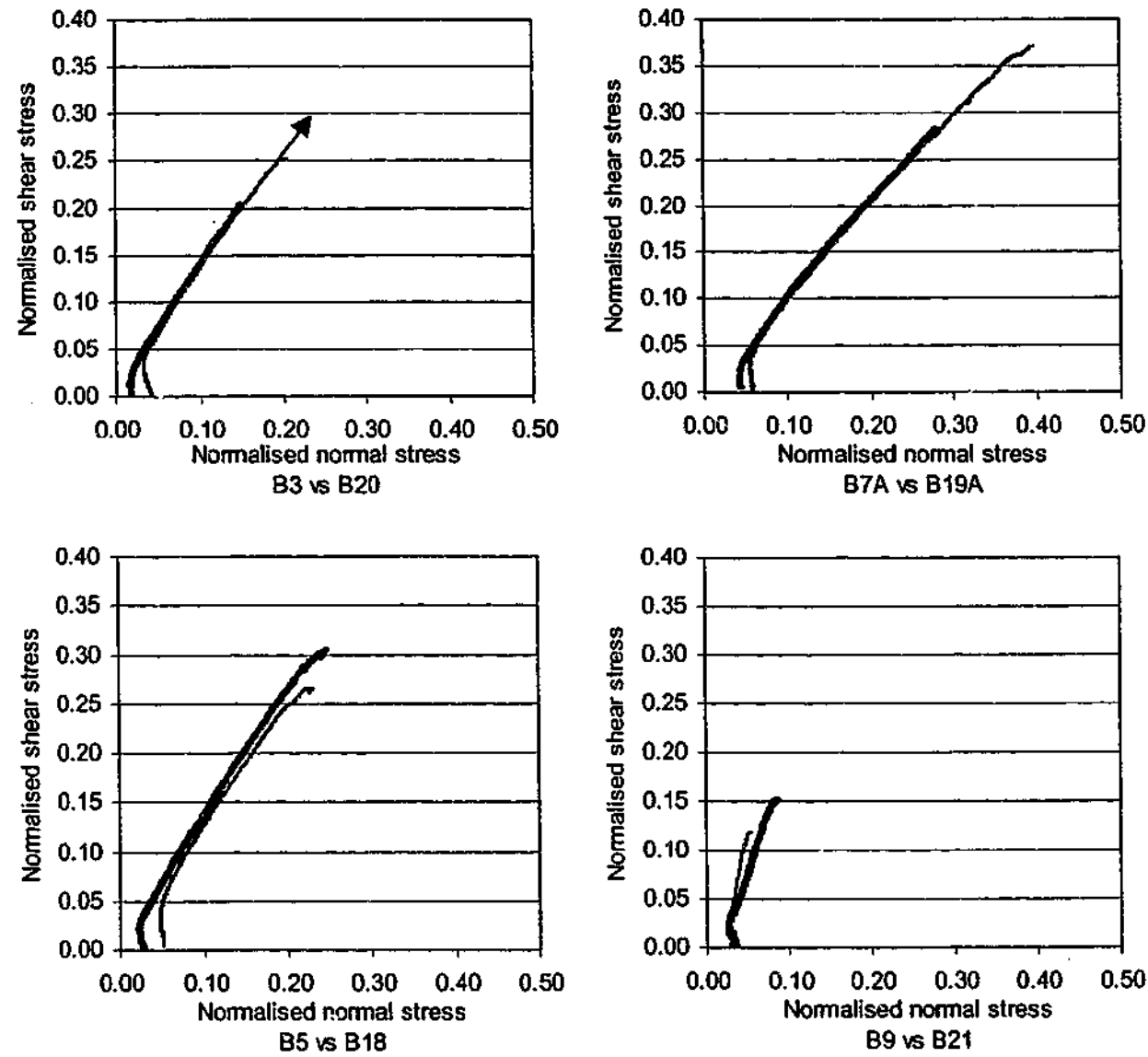


Figure 6-52: Comparison of normalised pre-peak stress plots of tests on Type "B" samples with differing intact rock strength.

Figure 6-53 shows the displacement at which peak shear stress was reached for the samples where the influence of intact rock strength was investigated. While discussion of the deformation of the sample is not within the scope of this study, this graph may still be of interest as it can be used to compare deformations at failure.

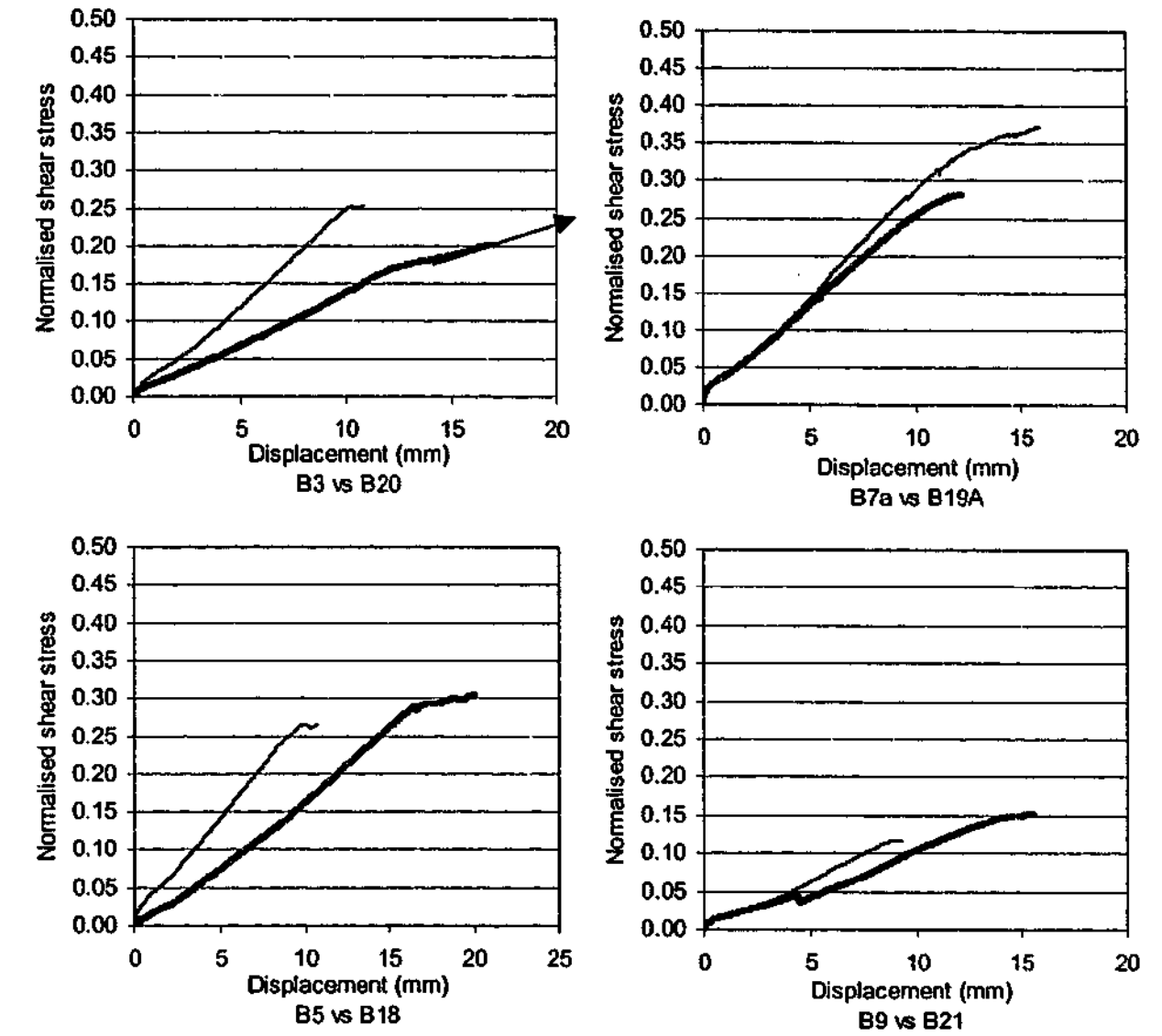


Figure 6-53: Comparison of normalised shear stress versus displacement graphs for Type "B" samples with differing intact rock strength.

Figure 6-53 shows that the samples made from stronger Johnstone have a less stiff response in normalised space and a greater shear displacement to reach peak strength. This may be because greater displacement (leading to dilation) is required for the stresses to increase to the point at which failure occurs. This is confirmed by comparing the dilation versus displacement curves, as shown in Figure 6-54.

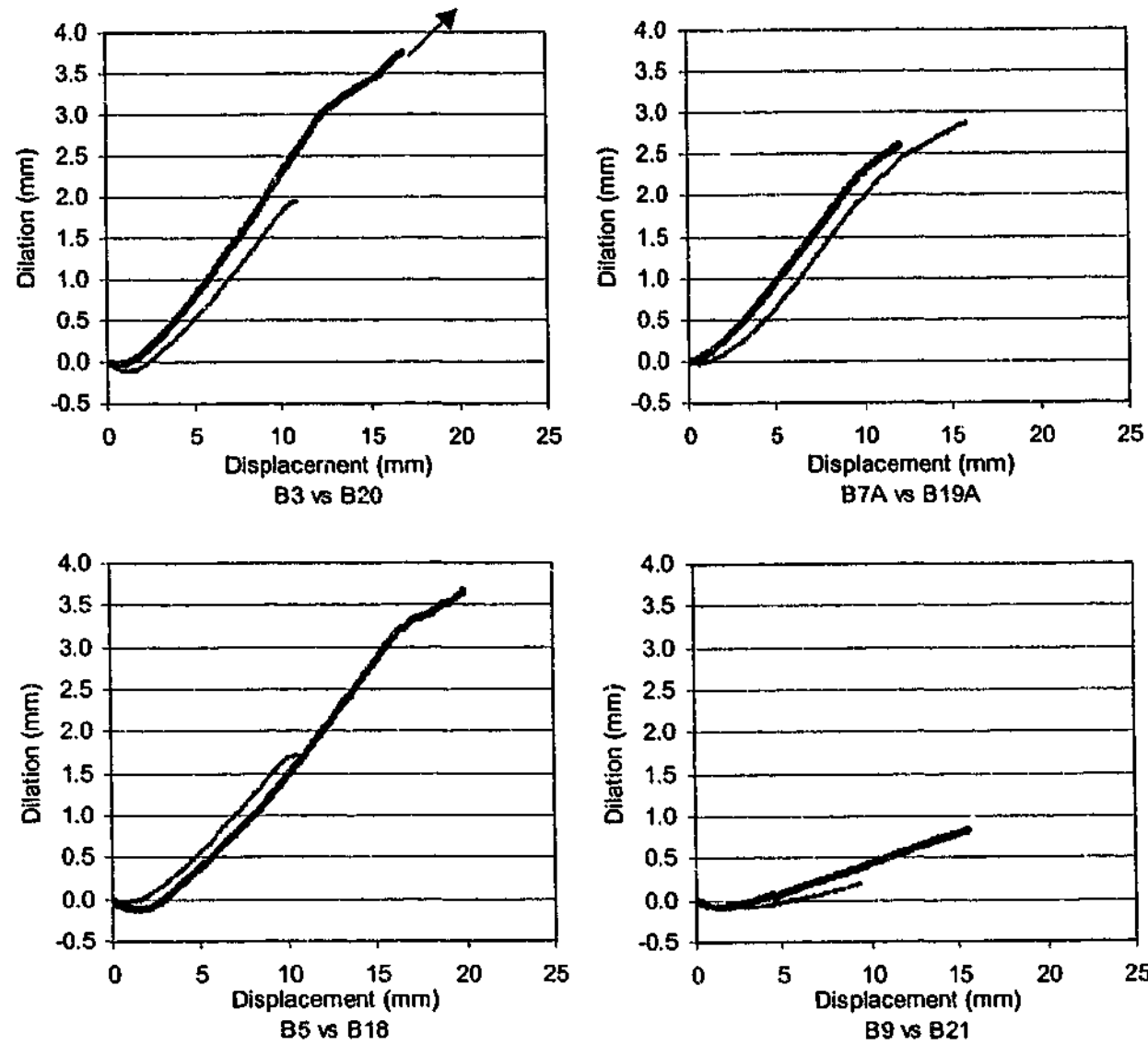


Figure 6-54: Comparison of dilation versus displacement graphs for Type “B” samples with differing intact rock strengths.

It can be observed in Figure 6-54 that the stronger samples in three of the tests failed at a greater dilation. This suggests that rock masses with higher intact rock strength may deform more than similar rock masses with lower intact rock strength before failure occurs (for the test conditions assumed in this study).

The normalised peak shear strengths and failure mechanisms recorded from the tests where UCS was varied are summarised in Table 6-3.

Table 6-3: Effect of UCS on behaviour of Type “B” samples.

Test ($\theta_1, \theta_2, \theta_3^1$)	UCS (MPa)	$\frac{UCS_{weak}}{UCS_{strong}}$	τ_p (kPa)	$\left(\frac{\tau_{p(weak)}}{\tau_{p(strong)}}\right)$	Pre-peak / Failure mechanism
B5 (-30°, 45°)	3.37		1010		
B18	1.93	0.57	510	0.50	Rotation / block shear
B3 (-60°, 45°)	5.66		>1160		
B20	2.38	0.42	600	<0.51	Rotation / block shear
B19A (-45°, 60°)	2.21		620		
B7A	1.70	0.77	625	1.01	Rotation / block shear
B9 (-45°, 15°, 75°)	3.03		460		
B21	2.52	0.83	300	0.65	Rotation / strut shear
Average		0.72		0.72	

Table 6-3 lists the UCS of the intact Johnstone blocks used in the tests and the peak shear stresses of the samples. The table also includes the ratios of intact strengths and peak shear stresses. On average, there appears to be a good correlation between the reduction of intact rock strengths and the reduction in peak shear strength of the samples. Variation of the intact rock strength was not observed to affect the pre-peak or failure mechanism.

6.5.2.2 Type “A” tests

The effect of varying the intact rock strength on the behaviour of the Type “A” samples is listed in Table 6-4.

¹ θ_3 as applicable

Table 6-4: Effect of UCS on behaviour of Type "A" samples.

Test ($\theta_1, \theta_2, \theta_3$)	UCS (MPa)	$\frac{UCS_{weak}}{UCS_{strong}}$	τ_p (kPa)	$\left(\frac{\tau_{p(weak)}}{\tau_{p(strong)}}\right)$	ϕ_{pp}	Inferred ² pre-peak / failure mechanism
A1 (-45°, 15°)	4.68		590		72°	Sliding / asperity or Rotation / strut shear
A3	3.28	0.70	390	0.66	70°	
A4 (-45°, 15°, 75°)	5.45		600		65°	Rotation / block shear
A2	5.04	0.92	500	0.83	63°	
Average		0.81		0.74		

Table 6-4 lists the UCS of the intact Johnstone blocks and compares the ratio of intact rock strength with the ratio of peak shear strength of the samples. On average, there appears to be a good correlation between the ratio of intact strength and the ratio of peak shear strength of the Type "A" samples, in that a reduction of intact rock strength resulted, on average, in a similar reduction in rock mass strength. Variation of the intact rock strength did not appear to affect the inferred pre-peak or failure mechanisms.

6.5.3 Sub-Parallel Jointing

Five tests were carried out to examine the influence of small variations ($\pm 5^\circ$) in joint inclination within the same joint set on sample strength. Four of these tests were on samples comprising two joint sets, while one other was on a sample containing three joint sets. The sensitivity of the failure mechanisms to these small variations in joint inclination was also investigated. Two of the samples tested, B10 and B12, did not fail. A comparison of the normalised stress plots of the tests with sub-parallel jointing is presented in Figure 6-55, with the thicker line representing

² The failure mechanisms for the Type "A" samples were inferred from the apparent friction angle, ϕ_{pp} , obtained from the τ - σ curves.

the sample with sub-parallel joints. The comparison between Test B4 and Test B10 has not been included.

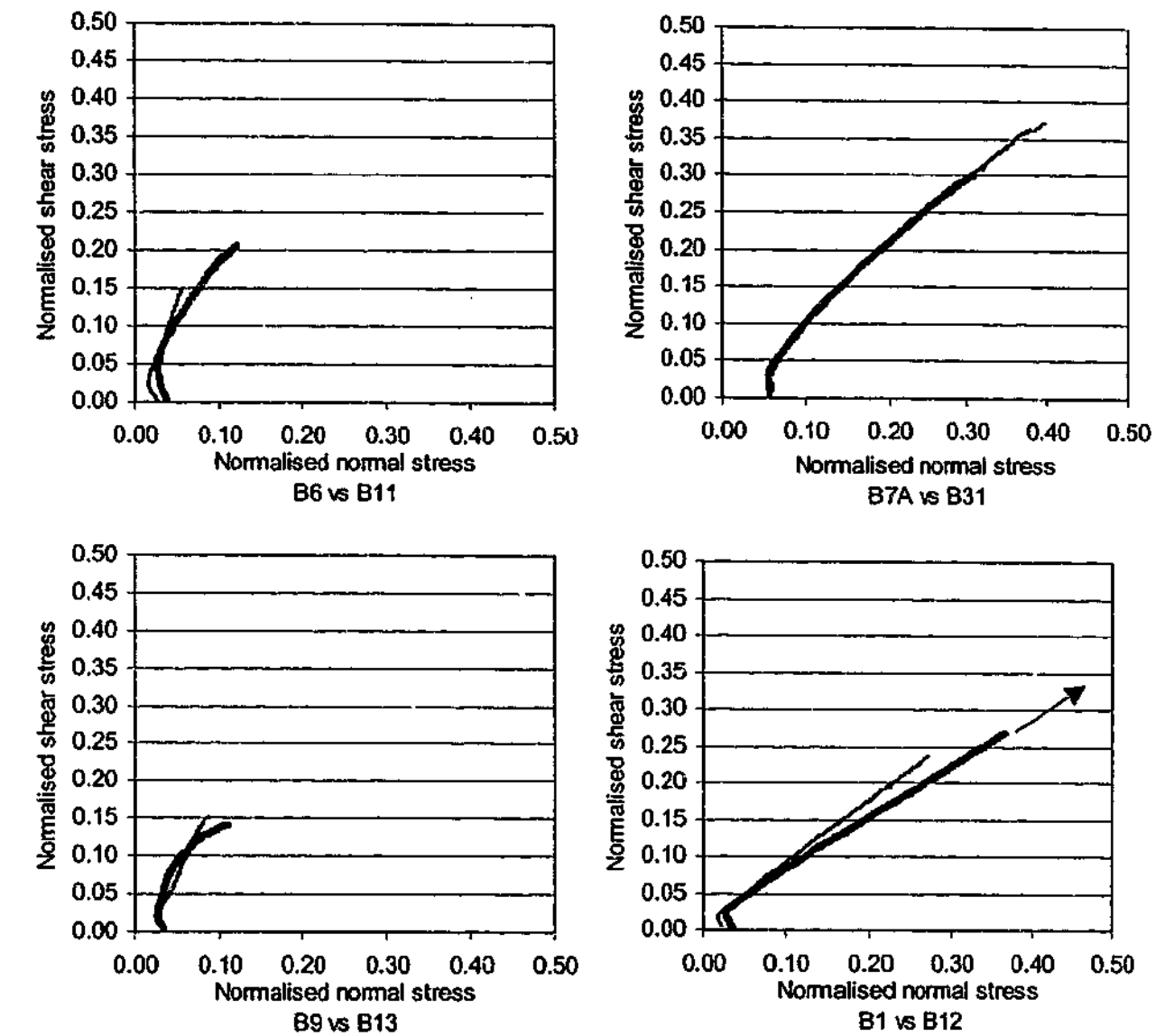


Figure 6-55: Comparison of the normalised stress plots of the Type "B" samples with sub-parallel jointing.

The normalised stress paths plotted in Figure 6-55 show that small variations in the joint inclination, in general, do not appear to significantly affect the behaviour of the sample. The comparison of Tests B1 and B12 shows the difference between sliding along a joint inclined at 15° and 12°. Tests B7A and B31 failed by block shear, while Tests B9 and B13 failed by strut shear. However, Test B6 failed by strut shear while Test B11 failed by asperity shear. It is difficult to distinguish the change in failure mechanism from the graph.

A comparison of the normalised shear stress, $\bar{\tau}$ and dilation with displacement are presented in Figure 6-56 and Figure 6-57 respectively.

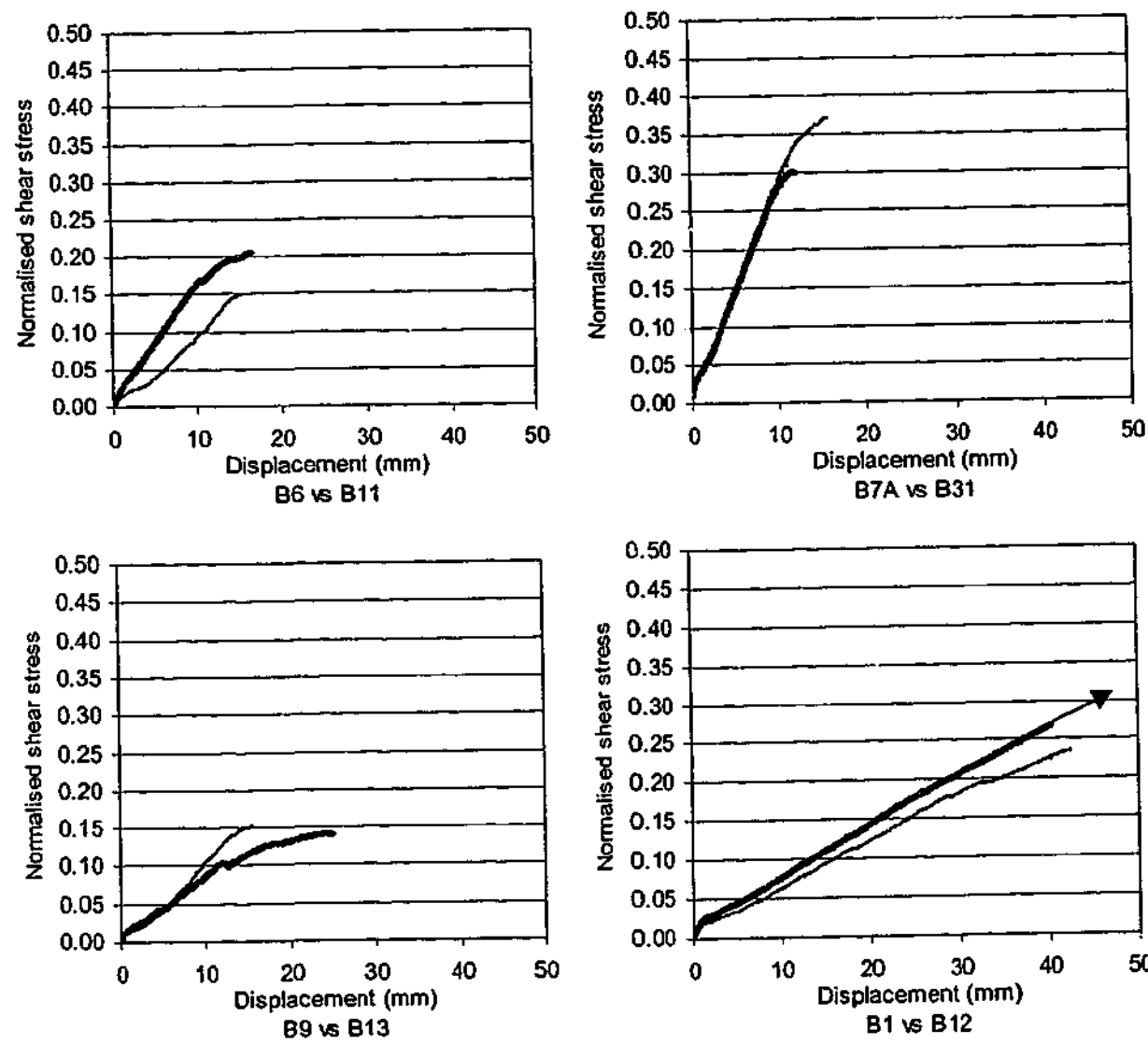


Figure 6-56: Comparison of $\bar{\tau}$ versus displacement for Type "B" samples with sub-parallel joints.

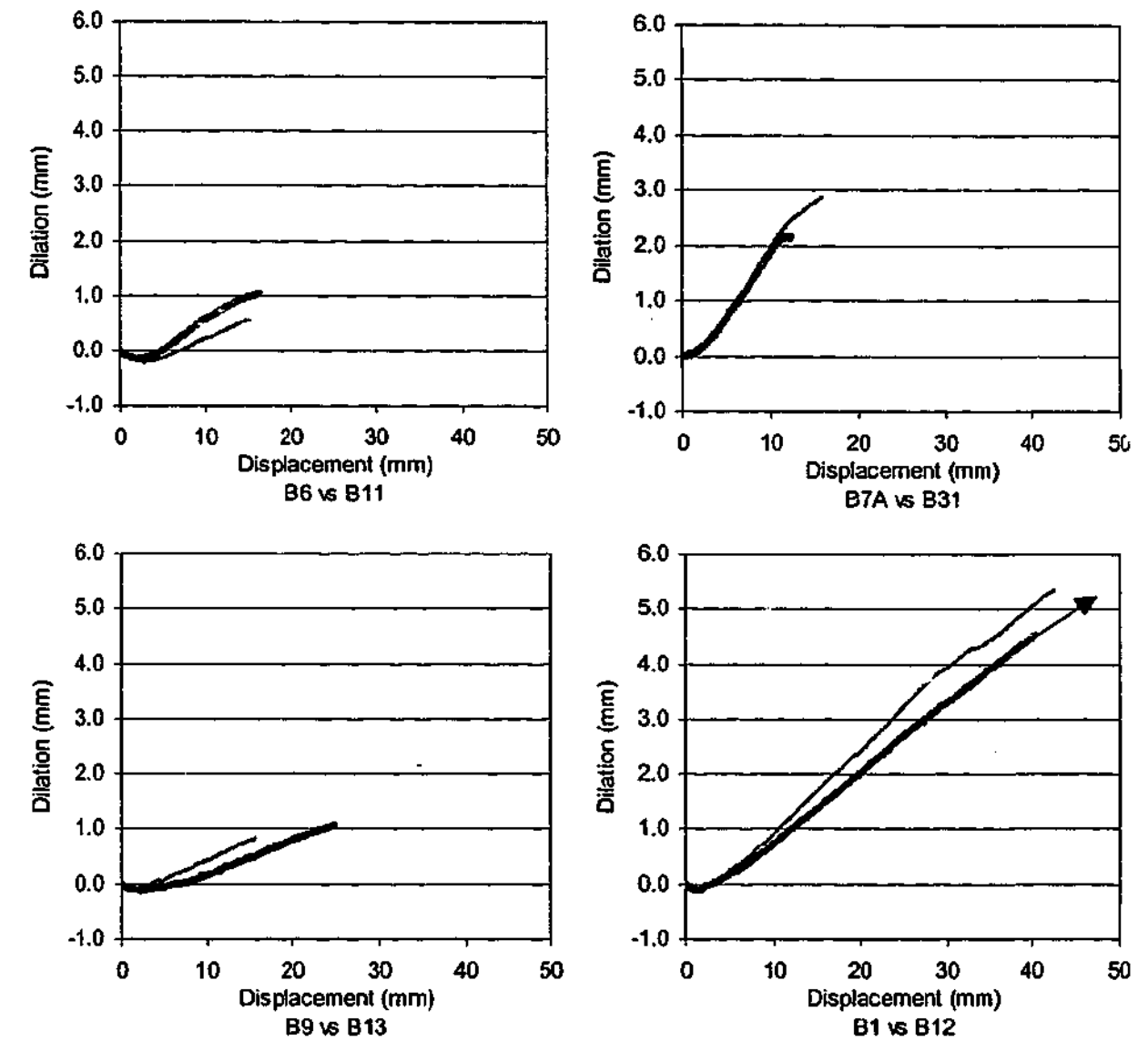


Figure 6-57: Comparison of dilation versus displacement for Type "B" samples with sub-parallel joints.

It can be seen from Figure 6-56 and Figure 6-57 that the small variations in joint inclination did not produce significant changes in $\bar{\tau}$ and dilation versus displacement. However, there appears to be a more significant difference in the normalised shear stress versus displacement plot for Tests B6 and B11. The reasons for this are discussed later in this section.

The influence of small variations in joint inclination on sample behaviour is summarised in Table 6-5.

Table 6-5: Effect of small variations in joint inclination on Type "B" sample behaviour.

Test	Joint Inclination	$\bar{\tau}_p$	Pre-peak / failure mechanisms
B1	-15°, 45°	0.237	Sliding / asperity shear
B12	-13°, 43° ±5°	>0.271	Sliding / no failure occurred
B4	-30°, 30°	0.271	Sliding / asperity shear
B10	-30°, 30° ±5°	>0.253	Sliding / no failure
B7A	-45°, 60°	0.368	Rotation / block shear
B31	-45°, 60° ±5°	0.299	Rotation / block shear
B6	-45°, 15°	0.154	Rotation / strut shear
B11	-40°, 15° ±5°	0.205	Sliding / asperity shear
B9	-45°, 15°, 75°	0.152	Rotation / strut shear
B13	-45°, 15°, 75° ±5°	0.142	Rotation / strut shear

For the jointing configurations tested, there was no change in failure mechanism as a result of small variations in joint inclination, except for Tests B6 and B11. Test B6 failed by strut shear. However, Test B11 failed by sliding along a joint inclined at -35°. This result shows the sensitivity of failure mechanism to joint inclination. The angles of θ_1 in sample B11 were inadvertently cut at -40°±5°. It can be seen, however, that the peak strengths were different as a result of the change in mechanism.

In general, samples that failed by the same failure mechanism yielded similar values of normalised peak shear stress. The normalised peak strengths from tests where strut shear was observed were very similar to each other (B6=0.154, B9=0.152 and B13=0.142). The normalised peak strengths from tests where block shear was observed were also similar (B7A=0.368 and B31=0.299). The value of θ_2 appears to dictate whether strut or block shear occurs. It was observed that Tests B7A and B31, which failed by block shear, had higher peak shear strengths than Tests B6, B9 and B13, which failed by strut shear.

For the tests where sliding along θ_1 was observed, samples with sub-parallel joints did not fail. Sliding was observed in Test B12 along a joint inclined at $\theta_1=-12^\circ$ as compared with Test B1, where sliding was observed along a joint inclined at $\theta_1=-15^\circ$. The sliding in Test B10 was observed along a joint inclined at $\theta_1=-25^\circ$, compared to Test B4, where sliding was observed along a joint inclined at $\theta_1=-30^\circ$. The lower dilation and resultant normal stresses did not generate sufficient stress conditions in the samples to produce shear failure through the shallow asperities formed by the intersecting joints.

6.5.4 Number of joint sets

6.5.4.1 Type "B" tests

Two tests were carried out to investigate the effects of introducing a third joint set to the rock mass (B1 vs. B8, B6 vs. B9). The third joint set was inclined at 75° to the shear plane and produced intact rock pieces in the shape of equilateral triangular prisms. The effect of introducing a third joint set on the peak strengths of the Type "B" samples is shown in Figure 6-58. The thicker line represents the samples containing three joint sets.

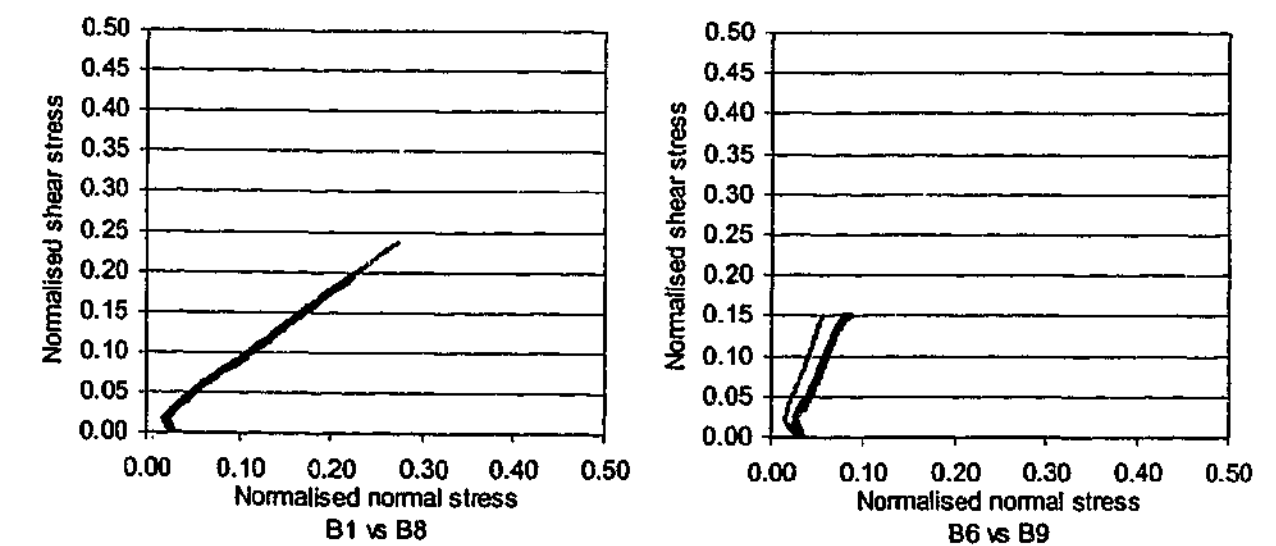


Figure 6-58: Effect of third joint set on normalised peak stresses for Type "B" tests.

It can be seen from Figure 6-58 that, for the jointing configurations tested, the third joint set did not significantly affect the stress paths up to failure.

The normalised shear stress and dilation versus shear displacement plots for the samples with two and three joint sets are presented in Figure 6-59 and Figure 6-60 respectively.

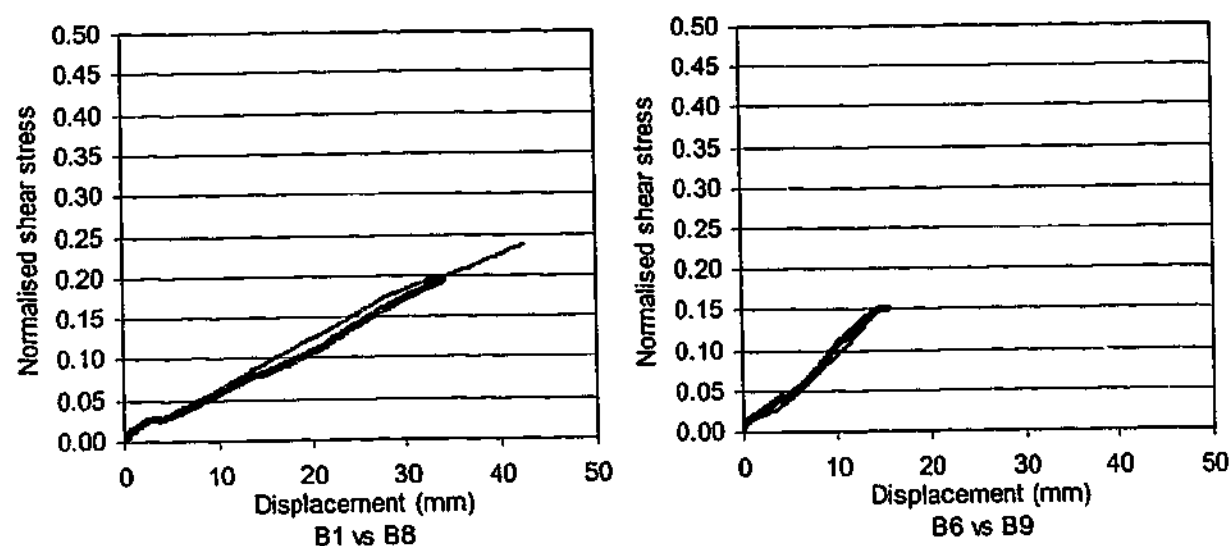


Figure 6-59: Effect of third joint set on $\bar{\tau}$ versus displacement for Type "B" tests.

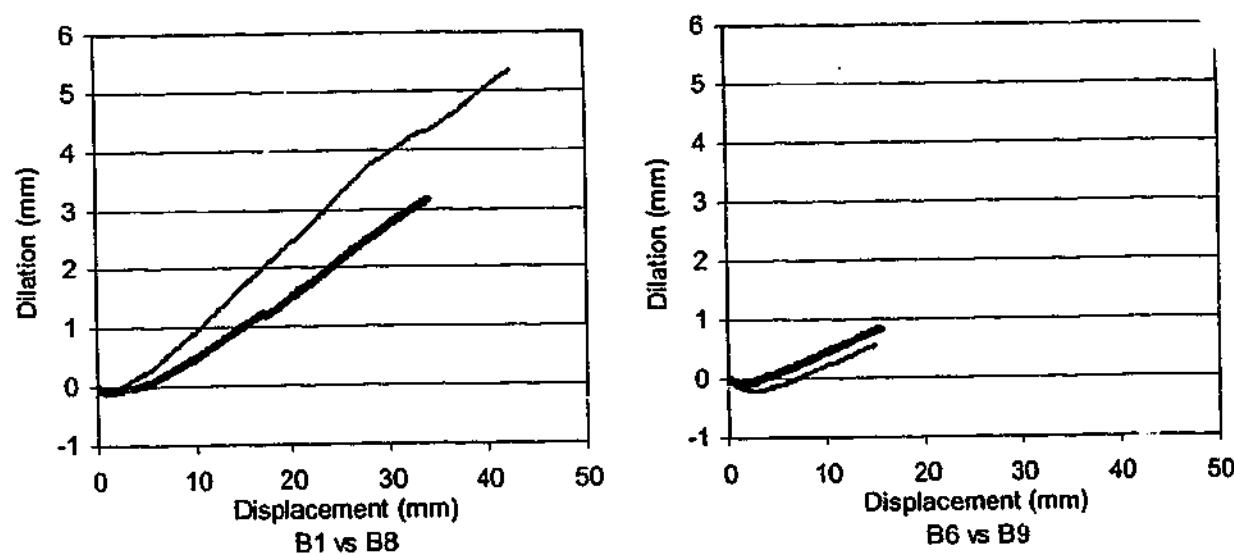


Figure 6-60: Effect of third joint set on dilation versus displacement for Type "B" tests.

Figure 6-59 and Figure 6-60 suggest that the introduction of a third joint set results in minor reductions of both normalised peak shear and normal strengths, as well as displacement at failure. However, these test results are inconclusive and further work is required to confirm this trend.

The effect of the number of joint sets on the pre-peak and failure mechanisms and normalised peak shear stresses of the Type "B" samples is summarised in Table 6-6. The measured peak shear stresses of the samples containing three joint sets were slightly lower than those containing two joint sets. This suggests that the third joint set in these tests was inclined such that it had almost no effect on the strength of the rock mass. However, it may be possible to introduce a third joint set inclined in such a way that it will alter the failure mechanism. For example, if the third joint set introduced to sample B6 was inclined at a favourable (shallow) angle to the shear plane, the failure mechanism would change from strut shear to sliding, resulting in an increase in peak shear stress and greater displacement and dilation at failure. However, it was not practically possible to fabricate samples using the block saw that contained three joint sets with planar joints that were not made up of equilateral triangles.

Table 6-6: Effect of number of joint sets on the behaviour of Type "B" samples.

Test ($\theta_1, \theta_2, \theta_3$)	$\bar{\tau}_p$	Pre-peak / Failure Mechanism
B1 (-15°, 45°)	0.237	Sliding / asperity shear
B8 (-15°, 45°, -75°)	0.196	Sliding / asperity shear
B6 (-45°, 15°)	0.152	Rotation / strut shear
B9 (-45°, 15°, 75°)	0.152	Rotation / strut shear

6.5.4.2 Type "A" tests

The results of the Type "A" tests on samples where a third joint set was introduced are summarised in Table 6-7, together with a comparison of the normalised peak shear stresses, inferred friction angle, ϕ_{pp} , and inferred failure mechanisms obtained from the Type "A" tests.

Table 6-7: Effect of number of joint sets on the behaviour of Type “A” samples.

Test ($\theta_1, \theta_2, \theta_3$)	$\bar{\tau}_p$	ϕ_{pp}	Inferred Pre-peak / Failure Mechanism
A1 (-45°, 15°)	0.126	72°	Sliding / asperity or rotation / strut shear
A4 (-45°, 15°, 75°)	0.110	65°	Rotation / block shear
A3 (-45°, 15°)	0.119	70°	Sliding / asperity or rotation / strut shear
A2 (-45°, 15°, 75°)	0.099	63°	Rotation / block shear
A5* (-45°, 15°)	0.112	71°	Sliding / asperity or rotation / strut shear
A6* (-45°, 15°, 75°)	0.074	59°	Rotation / block shear

*Tests A5 and A6 contained more closely spaced joints.

Table 6-7 indicates that the introduction of a third joint set appeared to slightly decrease the normalised peak strength of the Type “A” samples, an outcome similar to the Type “B” tests. The change in ϕ_{pp} suggests the pre-peak mechanism has changed. In the Type “A” tests, the average apparent friction angle for the samples with two joint sets is about 71°. When the third joint set was introduced, this average reduced to about 63°. The pre-peak behaviour of the samples containing two joint sets was inferred to be either sliding or strut rotation, whereas neither of these mechanisms were inferred in the samples containing three joint sets.

6.5.5 Joint spacing

6.5.5.1 Type “B” tests

Four samples were manufactured with more closely spaced joints. For the samples containing two joint sets (Tests B5 and B14; B7A and B15; B20 and B16), the spacing of each joint set was reduced from a nominal spacing of 70 mm to about 30 mm to 35 mm. These tests failed by rotation and block shear. For the samples with three joint sets (Tests B9 and B17), the spacing

was reduced from about 65 mm to about 30 to 35 mm. These samples failed by rotation and strut shear.

The effect of joint spacing on the normalised stress paths of the Type “B” samples is shown in Figure 6-61. The thicker lines represent samples with closer joint spacing.

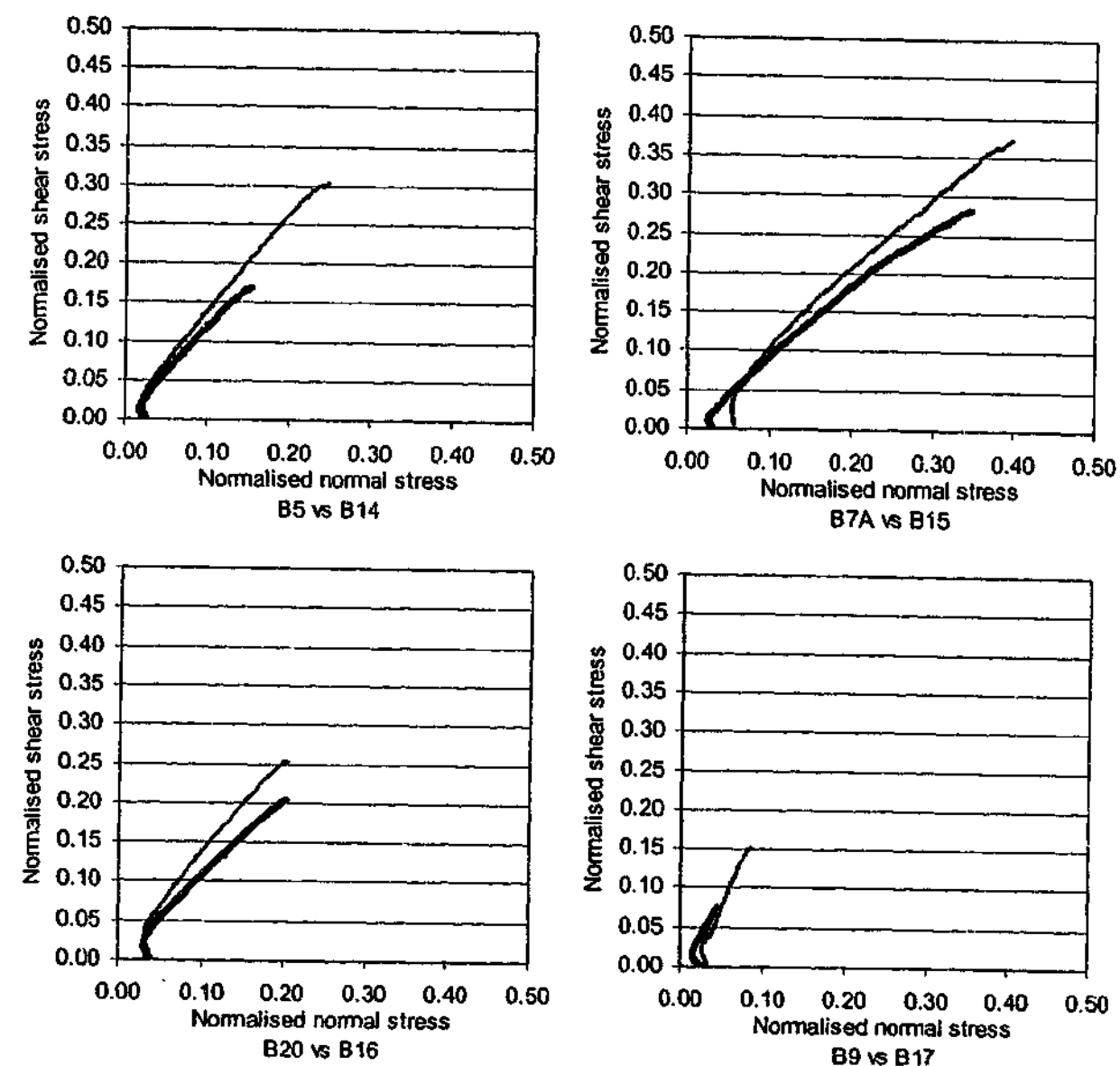


Figure 6-61: Effect of joint spacing on the normalised peak stresses of the Type “B” samples.

Figure 6-61 indicates that the decrease in joint spacing has only a minor impact on the stress path but results in lower peak stresses in the samples tested. The apparent friction angle in the samples where $\theta_2=45^\circ$ (Tests B5, B14, B20, B16) changed from about 54° to about 48° as the spacing was decreased, which suggests the pre-peak mechanisms may have changed.

When the failure mechanism is block shear, failure occurs by shearing through the intact material along most of the shear plane. Therefore, the joint spacing has less influence, other than perhaps to slightly reduce the length of shear plane through the intact material. The effect of joint spacing on samples that failed by strut shear is more pronounced. The cross-sectional area influenced the shear stress that could be resisted by the strut. Therefore, halving the area would be expected to result in a similar reduction in shear strength. This is confirmed by the average results from Tests B9 and B17.

The normalised shear stress and dilation versus shear displacement graphs for samples with different joint spacing are presented in Figure 6-62 and Figure 6-63.

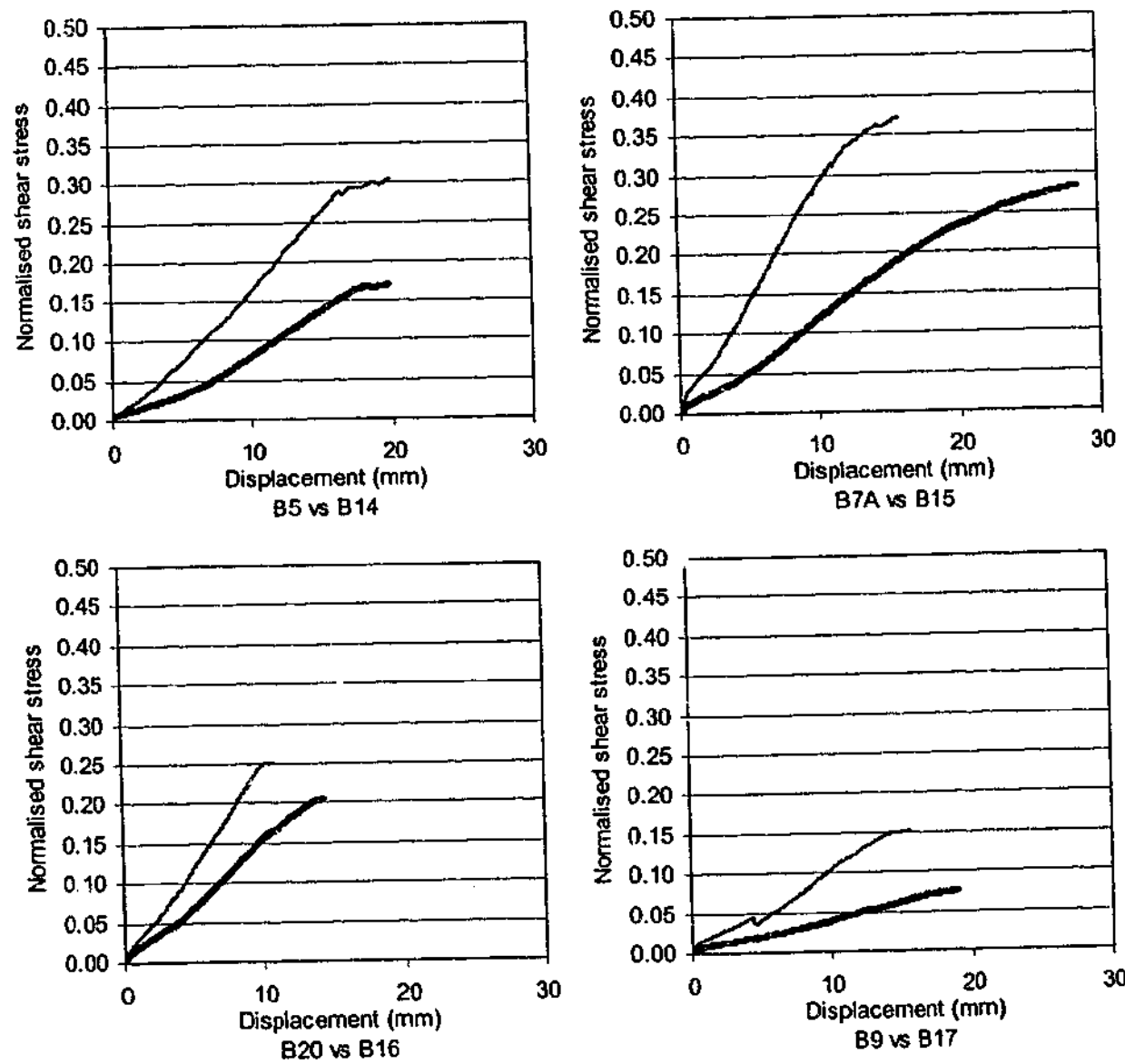


Figure 6-62: Effect of joint spacing on $\bar{\tau}$ and displacement at failure for Type "B" tests.

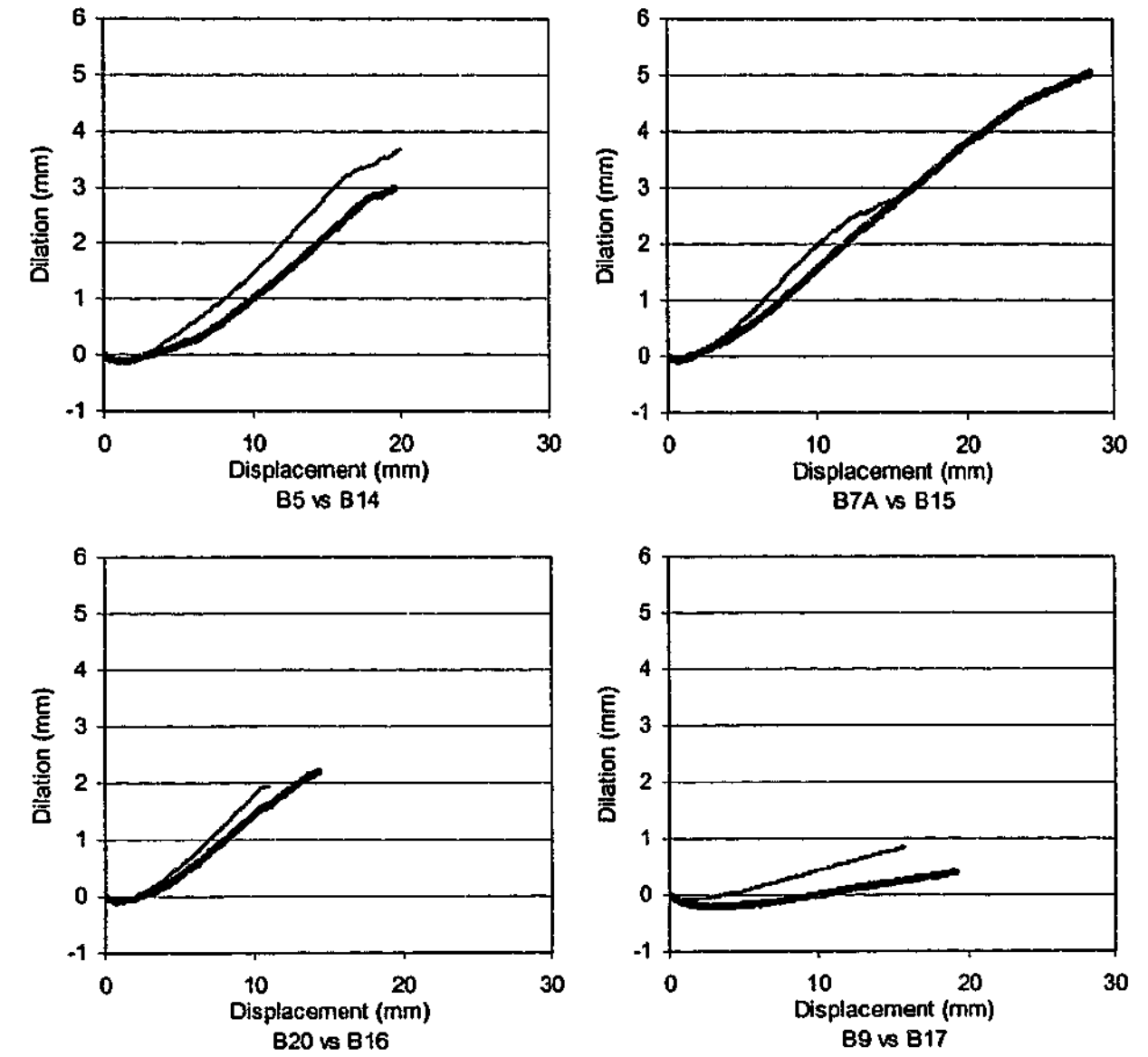


Figure 6-63: Effect of joint spacing on dilation and displacement at failure for Type "B" tests.

Figure 6-62 and Figure 6-63 show that closer joint spacing produces lower peak stresses at a higher value of shear displacement. The greater shear displacement at failure is likely to be due to the higher number of joints in the sample and the resultant cumulative effects of compression of the joints. The measured dilation at failure did not appear to vary much.

The effect of joint spacing on normalised peak shear strengths and failure mechanisms is summarised in Table 6-8.

Table 6-8: Effect of joint spacing on behaviour of Type “B” samples.

Test ($\theta_1, \theta_2, \theta_3$)	Spacing (mm)	ϕ_{pp}	$\bar{\tau}_p$	$\frac{\bar{\tau}_{p(close)}}{\bar{\tau}_{p(wide)}}$	Pre-peak/failure mechanism
B5 (-30°, 45°)	70	54°	0.300		Rotation / block shear
B14	30-35	51°	0.168	0.60	
B20 (-60°, 45°)	70	54°	0.252		Rotation / block shear
B16	30-35	47°	0.203	0.81	
B7A (-45°, 60°)	70	47°	0.368		Rotation / block shear
B15	30-35	43°	0.281	0.76	
B9 (-45°, 15°, 75°)	65	61°	0.152		Rotation / strut shear
B17	30-35	60°	0.075	0.55	

6.5.5.2 Type “A” tests

The typical joint spacing in the Type “A” tests (A1 and A2) was 70 mm. This spacing was reduced to 45 mm for two tests (A5 and A6). The effect of joint spacing on the normalised peak shear stresses and inferred failure mechanisms of the Type “A” samples is summarised in Table 6-9.

Table 6-9: Effect of joint spacing on peak shear strength of Type “A” samples.

Test ($\theta_1, \theta_2, \theta_3$)	Spacing (mm)	ϕ_{pp}	$\bar{\tau}_p$	$\frac{\bar{\tau}_{p(close)}}{\bar{\tau}_{p(wide)}}$	Inferred pre-peak / failure mechanism
A1 (-45°, 15°)	75	72°	0.126		Sliding / asperity shear or Rotation / strut shear
A5	50	71°	0.112	0.89	
A2 (-45°, 15°, 75°)	75	63°	0.099		Rotation / block shear
A6	50	59°	0.074	0.75	

It can be observed from Table 6-9 that the magnitude of the reduction in peak shear strength was not similar to that of the reduction of spacing. The measured apparent friction angle suggests the failure mechanism may have been either sliding and asperity shear or strut shear for Type “A” samples containing two joint sets, and block shear for samples with three joint sets, as discussed in Section 6.5.2.2.

6.5.6 Initial normal stress

6.5.6.1 Type “B” tests

The effect of variations in initial normal stress, σ_{ni} , on sample behaviour was also investigated. Most samples tested in this study were subjected to $\sigma_{ni}=100$ kPa. Two tests were carried out on samples subjected to an initial normal stress of 50 kPa and another two at 300 kPa. The τ - σ responses up to failure recorded from these tests are presented in Figure 6-64. The tests subjected to $\sigma_{ni}=50$ kPa are represented by the thinnest line, those with $\sigma_{ni}=100$ kPa are represented by the medium thickness line and those with $\sigma_{ni}=300$ kPa are represented by the thickest line. The stress paths for Tests B22 and B14 were almost identical and appear as a single line.

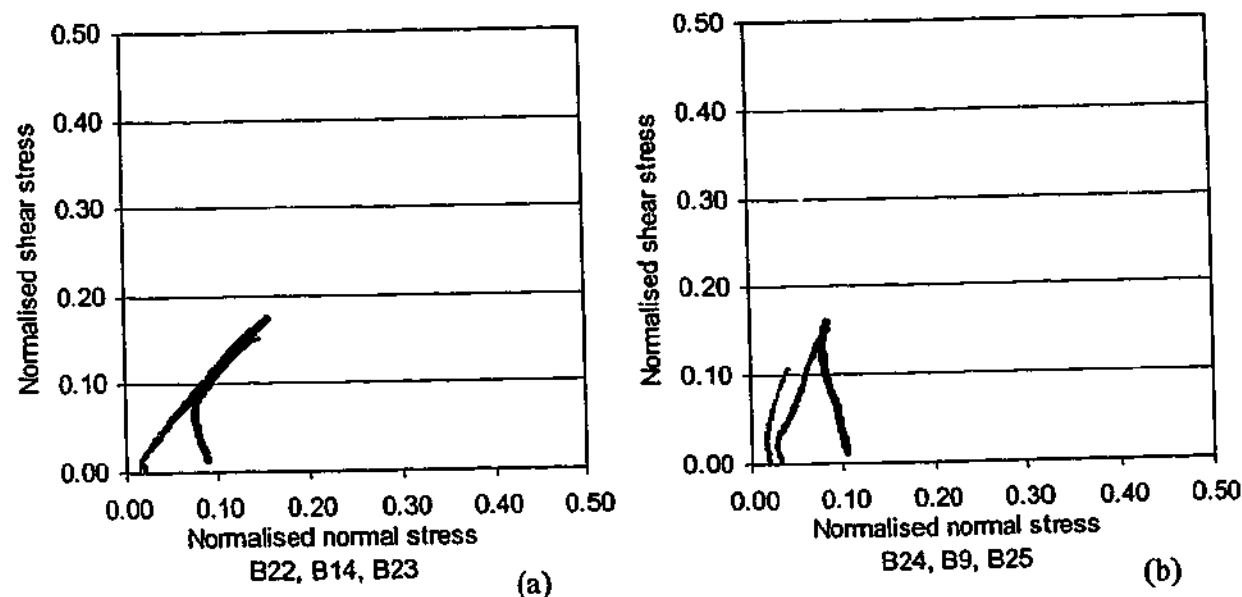


Figure 6-64: Effect of initial normal stress on normalised τ - σ response.

Block rotation was observed in the samples with two joint sets (B22, B14, B23), while strut rotation was observed in the samples containing three joint sets (B24, B9, B25). The difference in the pre-peak behaviour between the block and strut rotation is clearly shown in the stress plots presented in Figure 6-64(a) and (b).

The normalised shear stress of the samples with two joint sets (Figure 6-64(a)) appeared to increase until a line representing the apparent friction angle was reached, after which the shear strength increased at this angle until the sample failed. These tests failed at a similar value of normalised peak shear stress.

The normalised shear stress of the samples with three joint sets (Figure 6-64(b)) appeared to increase until a line representing the strength envelope was reached, at which the sample failed. For these tests, a similar value of $\bar{\tau}_p$ was reached for the samples subjected to $\sigma_{ni}=100$ kPa and 200 kPa, whereas the sample subjected to $\sigma_{ni}=50$ kPa failed at a lower stress.

The pre-peak plots of $\bar{\tau}$ versus shear displacement and dilation versus shear displacement for Type "B" samples subjected to different initial normal stresses are presented in Figure 6-65 and Figure 6-66 respectively.

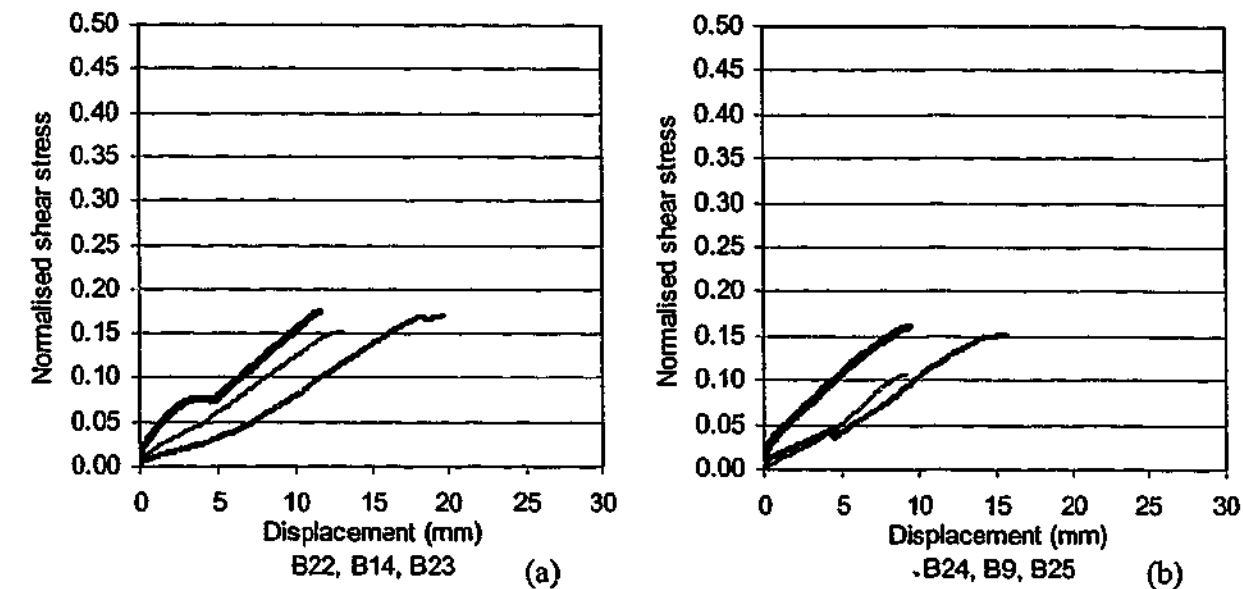


Figure 6-65: Effect of σ_{ni} on pre-peak $\bar{\tau}$ versus displacement behaviour of Type "B" samples.

Figure 6-65 indicates the samples subjected to the default normal stress of 100 kPa appear to fail at a greater displacement. However, nearly all the samples fail at about the same normalised shear stress.

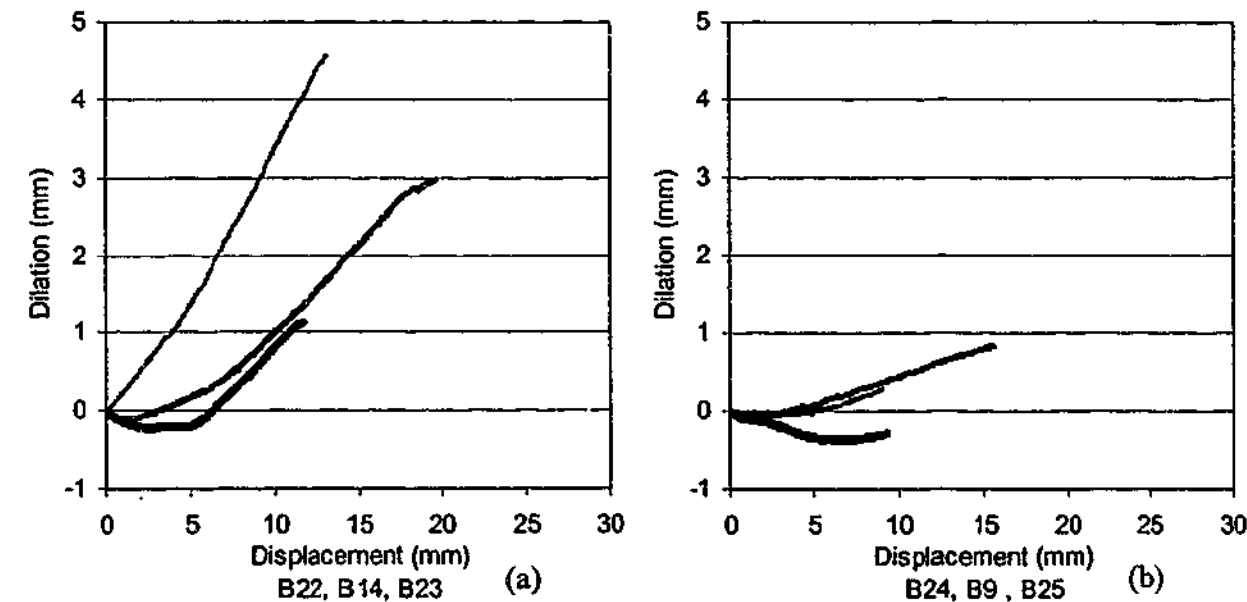


Figure 6-66: Effect of σ_{ni} on pre-peak dilation versus displacement behaviour of Type "B" samples.

Figure 6-66 indicates that, in general, that dilation at failure decreases as initial normal stress increases.

The effect of initial normal stress on normalised peak shear strengths and observed pre-peak and failure mechanisms is summarised in Table 6-10.

Table 6-10: Effect of initial normal stress on Type “B” sample behaviour.

Test ($\theta_1, \theta_2, \theta_3$)	σ_{ni} (kPa)	$\bar{\sigma}_{ni}$	$\bar{\tau}_p$	Pre-peak / Failure mechanism
B22 (-30°, 45°)	50	0.015	0.151	Rotation / block shear
B14	100	0.022	0.168	Rotation / block shear
B23	300	0.089	0.175	Rotation / block shear
B24 (-45°, 15°, 75°)	50	0.020	0.108	Rotation / strut shear
B9	100	0.033	0.152	Rotation / strut shear
B25	300	0.104	0.159	Rotation / strut shear

There appears to be a slight increase in normalised peak strength as initial normal stress increases. The values of $\bar{\tau}_p$ were also similar for all the tests except B24.

6.5.6.2 Type “A” tests

The effects of varying the initial normal stress applied to Type “A” samples were also investigated. Two shear tests were carried out where the initial normal stress was increased from 100 kPa to either 200 kPa or 400 kPa. The normalised peak shear strengths obtained from these tests are summarised in Table 6-11.

Table 6-11: Effect of initial normal stress on Type “A” sample strength.

Test (θ_1, θ_2)	σ_{ni} (kPa)	$\bar{\sigma}_{ni}$	$\bar{\tau}_p$
A1 (-45°, 15°)	100	0.021	0.126
A7	200	0.038	0.129
A8	400	0.096	0.189

The effect of initial normal stress on Type “A” sample strength is inconclusive. The initial normal stress appears to have had little impact on the normalised peak strengths for Tests A1 and A7, but has produced a significant increase in both $\bar{\sigma}_{ni}$ and $\bar{\tau}_p$ for Test A8. It is possible that the normalised peak shear stress measured from Test A7 or Test A8 may be experimental outliers. There is general agreement between the increases in applied and normalised initial normal stresses. However, this agreement is not reflected in the values of peak normalised shear stress.

6.5.7 Rock mass geometry

An indication of the effect of the overall geometry of the rock mass sample on sample behaviour can be assessed by comparing the results of tests of Type “A” and Type “B” samples. The Type “A” samples were typically 450 mm long by 165 mm high by 150 mm deep. The Type “B” samples were typically 390 mm long by 280 mm high by 275 mm deep. Comparisons of the results of the Type “A” and Type “B” samples with two joint sets (Test A3 versus Test B6) and three joint sets (Test A2 versus B9) have been made. The normalised stress plots to failure are plotted in Figure 6-67, in which the Type “A” results are represented by the thicker lines.

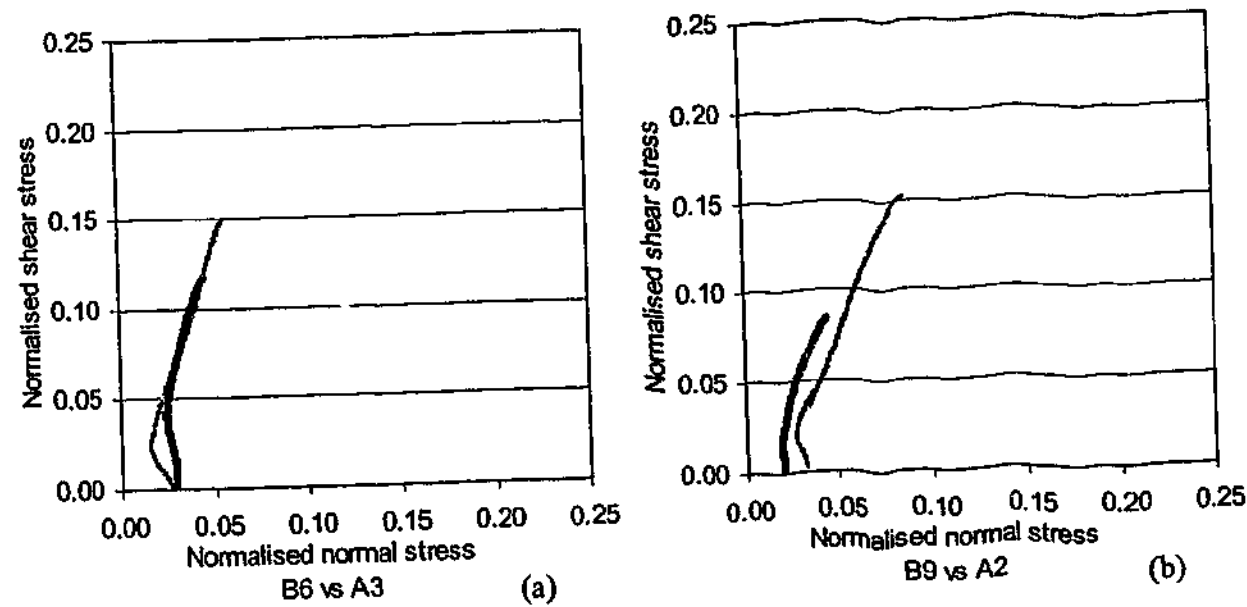


Figure 6-67: Effect of geometry on normalised stress behaviour.

It appears that both the Type “A” and “B” samples exhibited similar pre-peak behaviour, i.e. the geometry appears to have had little influence on the behaviour of the sample for the joint configurations tested. However, the Type “B” samples failed at higher normalised stresses.

The effect of sample geometry on the behaviour of $\bar{\tau}$ and dilation versus shear displacement is presented in Figure 6-68 and Figure 6-69.

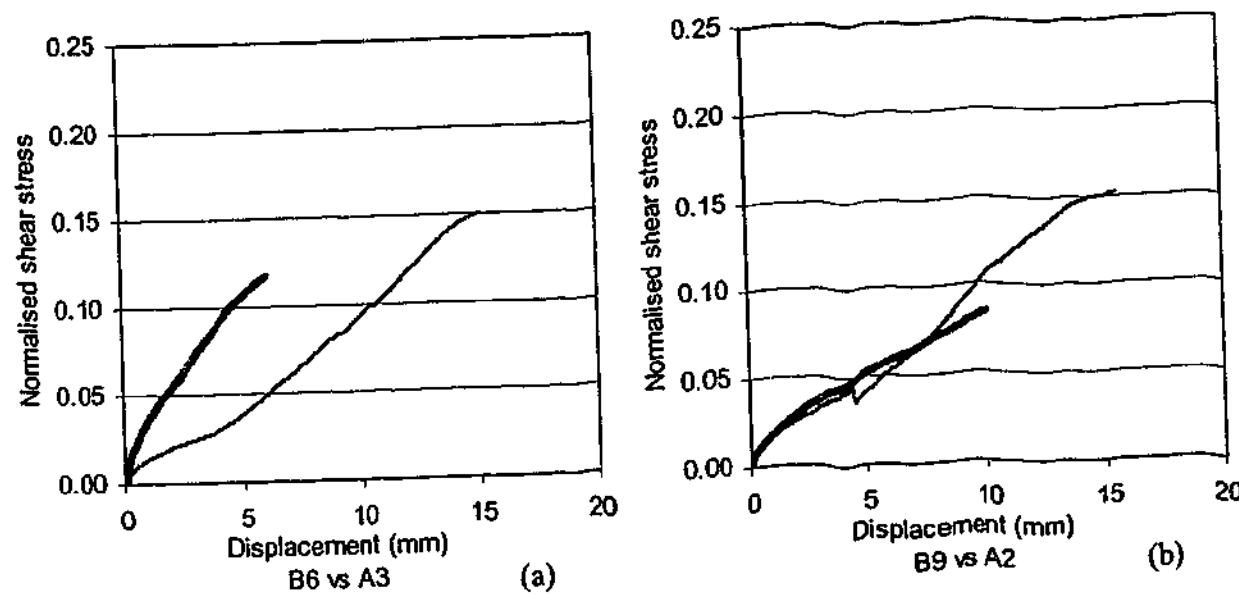


Figure 6-68: Effect of geometry on normalised shear stress versus displacement behaviour.

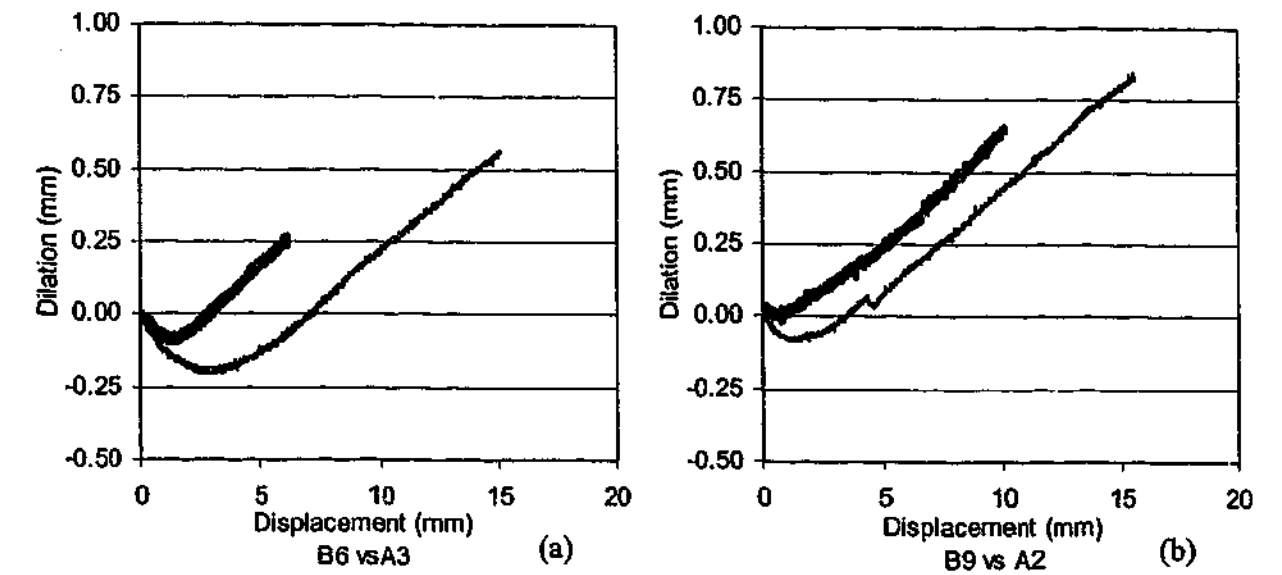


Figure 6-69: Effect of geometry on dilation versus displacement behaviour.

These figures indicate that the samples exhibit generally similar behaviour, with the Type “B” samples appearing to fail at higher stresses and after greater displacement. The Type “A” test show less negative dilation, which may be due to fewer joints and decreased depth of the sample.

The effect of rock mass geometry on normalised peak shear strengths and failure mechanisms is summarised in Table 6-12.

Table 6-12: Effect of geometry on rock mass behaviour.

Test ($\theta_1, \theta_2, \theta_3$)	ϕ_{pp}	$\bar{\tau}_p$	Pre-peak / failure mechanism
B6 (-45°, 15°)	70°	0.154	Rotation / strut shear
A3	70°	0.119	Sliding / asperity shear or Rotation / strut shear (inferred)
B9 (-45°, 15°, 75°)	61°	0.152	Rotation / strut shear
A2	63°	0.099	Rotation / block shear (inferred)

It would appear that the samples with two joint sets produced similar apparent friction angles, as did those with three joint sets. This suggests that similar pre-peak mechanisms occurred and

this is confirmed by the comparison of the stress paths. The values of $\bar{\tau}_p$ measured in the Type "B" tests were about 30% greater than those recorded in the Type "A" tests. This variation may be the result of normalising the Type "A" results with incorrect values of UCS, as discussed in Section 5.4.2

The effect of geometry of the sample on the failure mechanism is illustrated in Figure 6-70 and considered below.

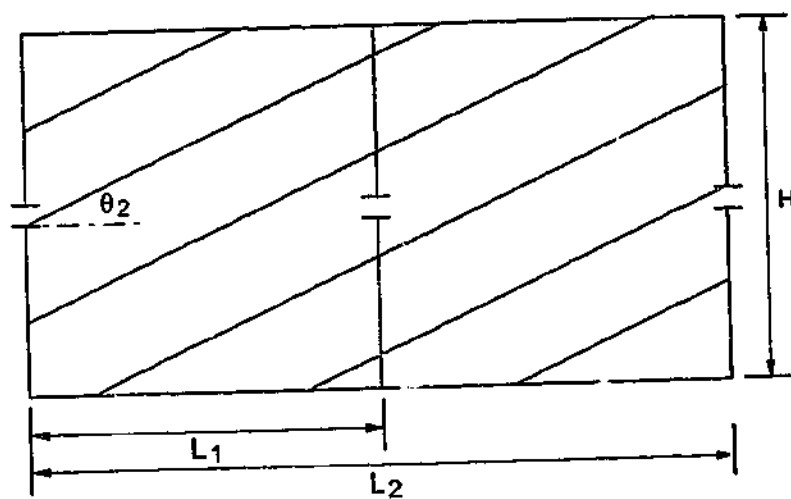


Figure 6-70: Effect of rock mass geometry on failure mechanism.

Failure by strut shear was observed when a strut was formed between the ends of the shear box. If the geometry of the sample were changed so the ends of the same "strut" were now between the top and bottom of the shear box, then block shear would then become the failure mechanism. For a sample with height H and length L_1 , (see Figure 6-70), strut shear would be the anticipated failure mechanism. If the sample length increases to L_2 , block shear would be the anticipated failure mechanism. The change in failure mechanism would also be expected to affect the peak shear strength of the sample. The geometry of a sample with L_1 shown in Figure 6-70 represents a Type "B" sample, while the geometry of a sample with L_2 represents a Type "A" sample.

It should be noted that sliding and asperity shear were not observed in the tests summarised in Table 6-12. From other test results, however, sliding was observed for values of $\theta_1=15^\circ$, irrespective of the inclination of the other joint set(s). It is anticipated that if sliding were the pre-peak behaviour, changing in the rock mass geometry would not affect the pre-peak mechanism.

Therefore, there is the possibility that where rotational behaviour occurs, the failure mechanism (hence peak strength) could be affected by sample geometry.

6.5.8 Summary of the effects of rock mass parameters on rock mass behaviour

The influence of several parameters on the behaviour of the samples tested for this project have been investigated and described. Variations in these parameters were observed to affect the behaviour of the samples in direct shear as follows:

- Changes in the joint inclination affected pre-peak and failure mechanisms, stress paths and stresses at which failure occurred. The inclination of the joint sets relative to the shear plane was (as expected) found to produce anisotropic behaviour.
- Reduction of the strength of the intact rock in the sample was found to cause a corresponding loss of sample shear strength. However, the pre-peak and failure mechanisms did not appear to change, resulting in similar stress paths between these tests irrespective of the intact rock strength. Normalising the stresses measured in each test by dividing them by the UCS of the intact rock was found to reduce the scatter in test results produced by variations in intact rock strength.
- Variation of joint inclinations up to $\pm 5^\circ$ did not significantly affect the pre-peak behaviour or the stresses at peak. Larger variations of joint inclination have the potential to change the pre-peak and failure mechanisms.
- Increasing the number of joint sets from two to three did not affect the pre-peak behaviour, but slightly reduced the peak stresses for the jointing configurations tested. It is likely that a third joint set could be introduced that would change the stress paths and peak stresses, an example of which is the introduction of a shallow joint that would change the mechanism from rotation to sliding.
- Decreasing the joint spacing produced a reduction in peak stresses. This was particularly evident in samples that failed by strut shear. There also appeared to be a change of the pre-peak mechanism in the samples where $\theta_2=45^\circ$ and joint spacing was reduced.

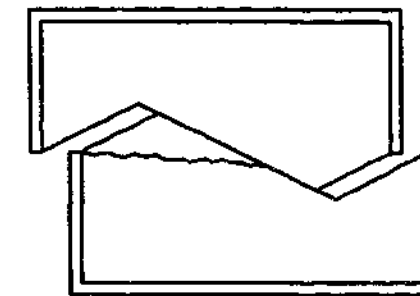
- Increasing the initial normal stress affected the stress paths by increasing the amount of negative dilation. The stress paths appeared to reach and follow a strength envelope defined by the apparent friction angle. The changes in initial normal stress were not observed to change the failure mechanisms.
- The overall geometry of the samples tested in this study was not observed to influence the stress paths to failure, but did produce different values of normalised peak shear stress.

7 ANALYSIS OF DIRECT SHEAR TESTS

7.1 Introduction

The pre-peak and failure mechanisms observed in the samples during shear testing were described in Chapter 6 and are presented again in Figure 7-1, Figure 7-2, and Figure 7-3. These were:

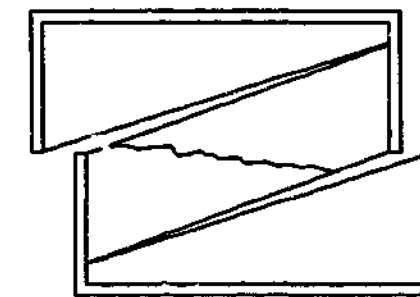
- sliding along the θ_1 joint set, followed by shear through one or several of the intact pieces of the rock mass along the shear plane,



Sliding/Asperity Shear

Figure 7-1: Sliding along an asperity followed by shear through the intact material.

- rotation of a strut formed by the intact pieces making up the rock mass between the ends of the shear box, followed by shearing through that strut, and



Rotation/Strut Shear

Figure 7-2: Rotation of a strut followed by shear through the strut.

- rotation of a block formed by the intact pieces making up the rock mass between the top and bottom of the shear box and the ends of the shear plane, followed by shearing through that block.

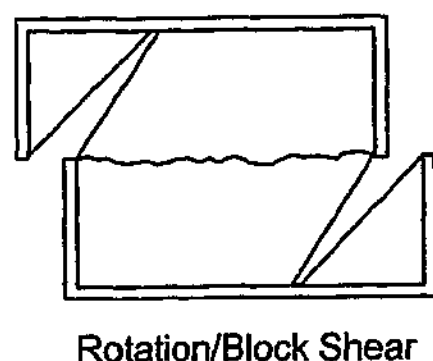


Figure 7-3: Rotation of a block followed by shear through the block.

The pre-peak and failure mechanisms appeared to be dependent on joint inclination and rock mass geometry. In this chapter, simple kinematic models are developed to simulate the mechanisms by which the samples failed. A comparison is also made between the test results and the GSI model.

7.2 Analysis of pre-peak and failure mechanisms

7.2.1 Failure by sliding / asperity shear

Sliding along what could be considered a very rough rock joint in the rock mass was observed in tests where both θ_1 and θ_2 were low (typically less than 30°). This mechanism consisted of sliding along the θ_1 joint set and separation across the θ_2 joint set, until the stress conditions resulted in shear through an asperity formed by the intact rock pieces. Sliding was inferred when the apparent friction angle, ϕ_{pp} , was similar to the sum of $(\theta_1 + \phi_j)$ and confirmed by video footage of the test.

This process is very similar to sliding along regular triangular joint profiles as observed by Lam and Johnston (1989), or sliding along irregular triangular profiles as observed by Kodikara and Johnston (1994), Yang and Chiang (2000) and Seidel and Haberfield (2002).

The majority of samples tested during this study comprised two joint sets, with joints within each joint set parallel and regularly spaced. This produced a semi-regular joint profile, as shown by the thick line in Figure 7-4. This joint profile can be considered as a very rough rock joint with an irregular profile.

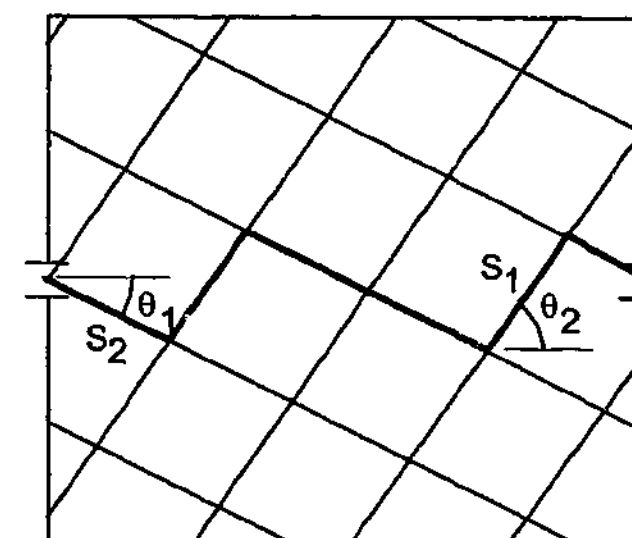


Figure 7-4: Very rough rock joint formed by jointing pattern.

Studies on the behaviour of very rough rock joints with irregular profiles have been carried out by Kodikara and Johnston (1994), Yang and Chiang (2000), Indraratna et al. (1998) amongst others. These very rough rock joints comprised a number of triangular asperities. When these joints were sheared, sliding occurred along the steepest asperity, and continued until the strength of that asperity was reached and the asperity failed. The shear stress was then transferred to the next steepest asperity. The apparent friction angle, ϕ_{pp} , measured from the τ - σ graphs as sliding continued along the asperity was found to be similar to the sum of the asperity angle and the friction angle of the joint, that is $(\theta_1 + \phi_j)$.

The very rough rock joint shown in Figure 7-4 comprises asperities made up of intact pieces that vary slightly in size due to construction tolerances. Joint inclinations may also vary by small amounts, but for the purposes of this discussion, this is of secondary importance. Therefore, it is likely that one piece will be slightly larger than the others and become the dominant asperity. The shear strength of this asperity can be calculated and compared with the shear strength obtained from sliding along the face of the asperity. When the shear stress required to continue sliding exceeds the shear strength of the asperity, failure by shearing through the asperity will result. Depending on block size, once this dominant asperity fails, load will be transferred on to the next most dominant asperity, and so on until an entire shear plane is formed.

7.2.1.1 Shear strength for sliding

The shear force for sliding along a surface with a friction angle of ϕ_j that is inclined at an angle of θ_1 (e.g. an asperity) can be calculated from:

$$S = N \tan(\theta_1 + \phi_j) \tag{Equation 7-1}$$

Each increment of shear displacement produces an increment of dilation. Under CNS conditions, the normal force, N , will increase due to this dilation. This means that each increment of shear displacement will result in dilation and an increase in N against the CNS conditions. As a result, the shear force to maintain sliding will increase with shear displacement until this asperity fails.

7.2.1.2 Shear strength for asperity shear

As sliding along the asperity leads to more dilation and an increase in normal stress, the stresses within the asperity will increase until the shear strength of the asperity is exceeded and failure by shearing through the asperity occurs. The shear strength of an asperity has been calculated previously by Ladanyi and Archambault (1970) and Lam and Johnston (1989). Consider the asperity and the hypothetical shear surface shown in Figure 7-5.

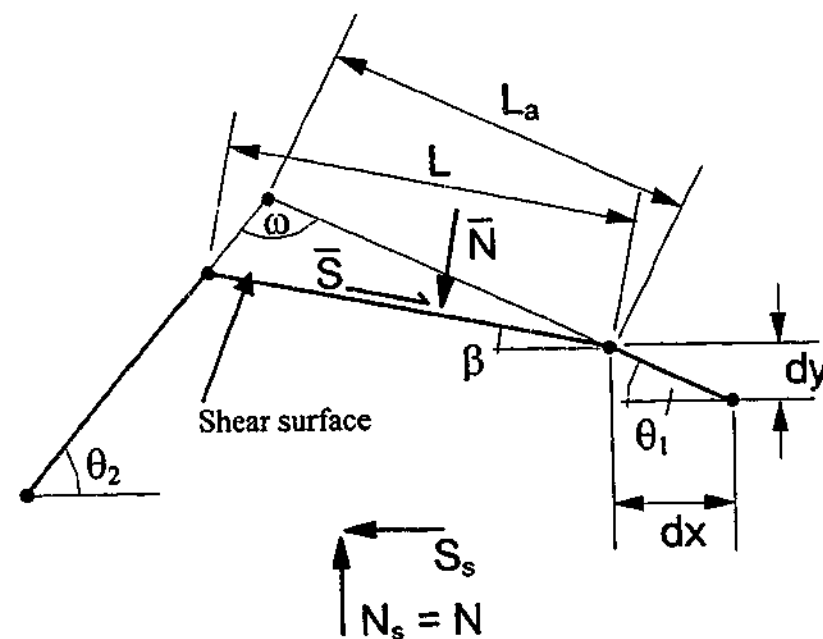


Figure 7-5: Diagrammatic representation of shear through an asperity.

An asperity has been defined by the θ_1 and θ_2 joints and contains an included angle, ω . For a small increment of shear displacement, dx , sliding along the θ_1 joint surface will occur. This produces dilation, dy , and increases the normal stress acting on the asperity. The contact length of the asperity becomes L_a .

The external (horizontal) shear force, S_s , required to cause shear through an asperity can be calculated from the equation:

$$S_s = N \tan \phi_i + cL \tag{Equation 7-2}$$

where:

- N is the external (vertical) normal force,
- ϕ_i is the friction angle of the intact rock,
- c is the cohesion of the intact rock, and
- L is the length of the shear surface.

However, the inclination of the shear surface may not necessarily be horizontal, but may be inclined at some angle, β , which can be positive or negative. Therefore, the shear and normal forces acting along the shear surface, together with the length of that shear surface need to be calculated.

Resolving the forces in Figure 7-5 produces the relationship:

$$S_s = N \tan(\phi_i + \beta) + \frac{cL}{\cos \beta(1 - \tan \phi_i \tan \beta)} \tag{Equation 7-3}$$

The length, L , of the shear surface can be calculated using the sine law, so that:

$$L = \frac{L_a \sin \omega}{\sin(\beta + \theta_2)} \tag{Equation 7-4}$$

Substituting equation 7-4 into equation 7-3 produces equation 7.5, which can be used to calculate the shear load required to cause failure along a plane inclined at β to the horizontal by:

$$S_s = N \tan(\phi_i + \beta) + \frac{cL_a \sin \omega}{\sin(\beta + \theta_2) \cos \beta (1 - \tan \phi_i \tan \beta)} \quad \text{Equation 7-5}$$

There will be a value of β that will yield the minimum load required to cause shearing through the asperity. This angle can be calculated using trial and error methods programmed into a spreadsheet.

The asperity geometry and material parameters were input into the spreadsheet. Thus, for each increment of dx , the corresponding value of L_a , dy and normal force could be calculated. The normal force was used to calculate the shear force required to cause sliding along the asperity using equation 7-1.

The normal force resulting from each increment of displacement is used to calculate the shear force required to shear through the asperity. Equation 7-5 was used to calculate S_s for various values of β . The minimum shear load required to cause shear through the asperity was calculated and compared to the shear load required to continue sliding along the asperity. Therefore, as displacement increased, the shear load required to continue sliding increased until shear failure through the asperity along a surface inclined at β occurred. The failure envelope is therefore the lesser of the sliding and asperity shear force. The shear and normal stresses at failure are then obtained by dividing the shear and normal forces by the area of the failure surface. Such an envelope, based on Test B4, is shown in Figure 7-6.

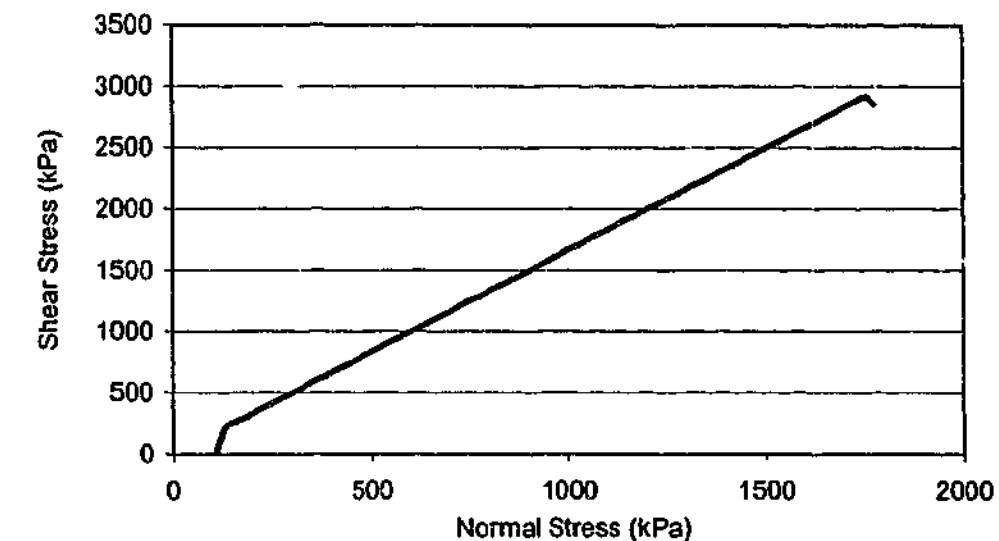


Figure 7-6: τ - σ response for asperity failure calculated by spreadsheet (based on test B4).

For the example shown in Figure 7-6, the shear stress at failure is about 2,900 kPa at a normal stress of about 1,800 kPa. This represents the stresses acting on the single asperity. To allow a comparison with the laboratory test results to be made, the peak stresses were calculated over the plan area of the sample, corrected for shear displacement.

The shear stress versus normal stress and shear stress versus shear displacement graphs from the tests and calculated by the model are compared in Figure 7-7. The model output is represented by the thickest line. It can be observed that the peak shear strengths are similar, although the normal stress (from dilation) and shear displacement from the test are greater than those predicted by the model.

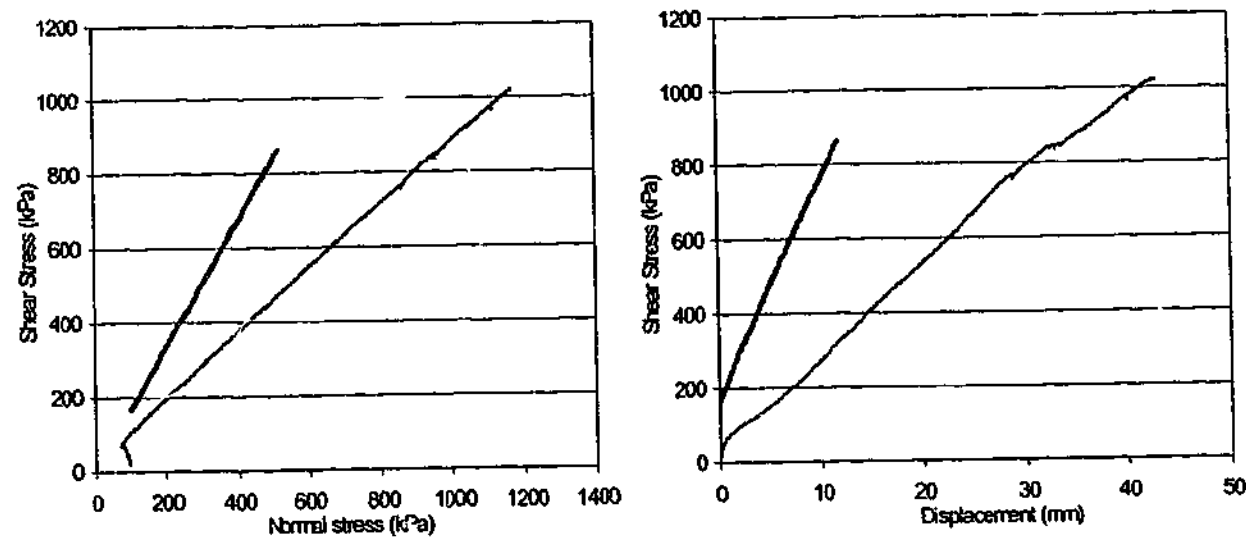


Figure 7-7: Comparison of shear stress, normal stress and displacement obtained from spreadsheet and test results (Test B1).

Table 7-1 compares the values measured during the tests where asperity shear was observed with those calculated using the spreadsheet. The peak stresses have been normalised by dividing them by the UCS of the intact rock making up the sample.

Table 7-1: Comparison of observed outputs and calculated values for tests failing by asperity shear.

Test	$\bar{\tau}_p$		$\bar{\sigma}_p$		dx (mm)		dy (mm)	
	observed	calculated	observed	calculated	observed	calculated	observed	calculated
B1	0.24	0.29	0.27	0.18	42	13	5.4	2.2
B4	0.27	0.29	0.18	0.18	18	13	2.2	2.2
B8	0.20	0.17	0.17	0.17	34	35	3.4	2.0

It can be seen in Table 7-1 that the calculated normalised peak shear stress, $\bar{\tau}_p$, is close to that observed in the tests. The calculated normalised peak normal stress, $\bar{\sigma}_p$, and shear displacement at failure, dx, were also close to that observed in Tests B4 and B8, but not as close in Test B1. The calculated dilation of the sample at failure, dy, was generally less than that observed in the tests. This simple model does not consider elastic effects and compression of the joints within the sample due to the applied shear or normal forces. Such comparisons will allow the shedding of load from the dominant asperity as discussed by Haberfield and Johnston (1994). As a result,

shear displacement is under-predicted. However, for rock masses where sliding followed by asperity shear was observed, the calculated shear stresses at peak were close to those measured in the laboratory.

In the analysis presented above, the shear failure surface has been assumed to be planar. Seidel, 1993) modelled asperity shear as a slope stability problem, adapting the solution for weightless c-φ soil proposed by Sokolovsky (1960). The shear failure surface obtained from the Sokolovsky solution comprised two planes connected by a log-spiral curve. As the asperity angle became steeper, the failure surface was found to become flatter.

Seidel calculated the asperity failure stress using the Sokolovsky solutions for asperity angles between 0° and 22.5°, adopting c=760 kPa and φ_i=36°. The Sokolovsky solution was extrapolated for an asperity angle of 27.5°, as the Sokolovsky solution is not suited to asperity angles greater than 22.5°. A spreadsheet was used to calculate asperity failure stress for asperity angles between 22.5° and 60°. The failure stresses for the two different failure surfaces are plotted against asperity angle in Figure 7-8.

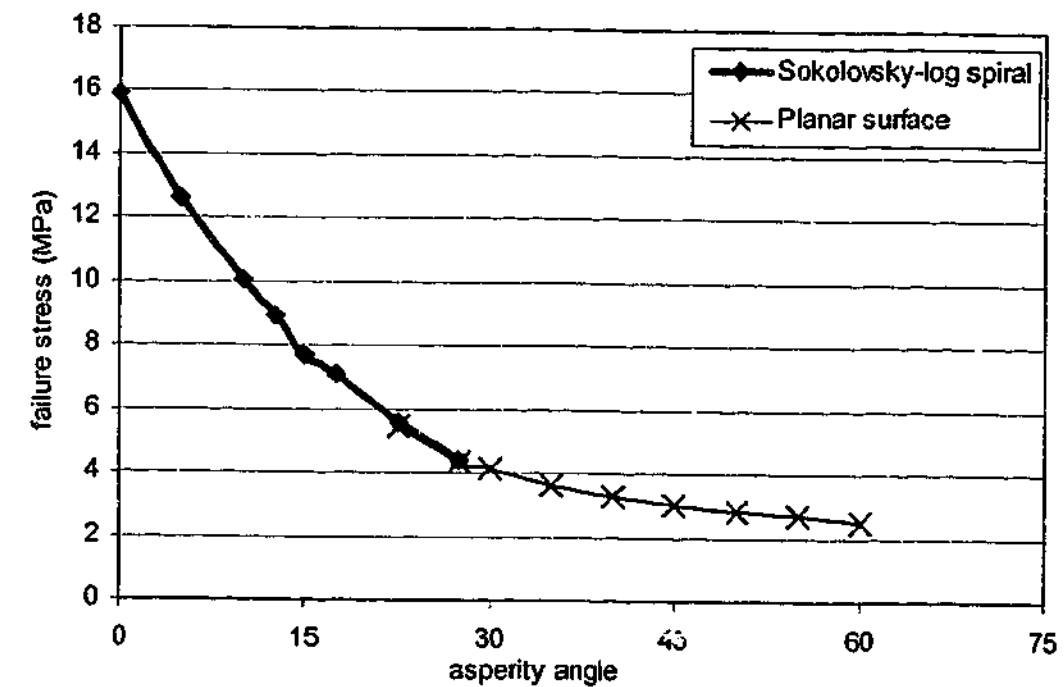


Figure 7-8: Comparison of failure stress obtained from Sokolovsky and planar failure surfaces.

There appears to be very good agreement between the Sokolovsky solution and that calculated by the spreadsheet for asperity angles between 20° and 30°. In particular, the simple solution

for a planar shear surface through the asperity appears to be logical extension to the Sokolovsky solution for asperity angles greater than 22° . This infers that for these asperity angles, the shear failure surface can be treated as planar. As the asperity angles in the rock masses tested in this study are typically greater than 15° , the planar surface model is considered to be satisfactory.

The angle of the joint set that will allow sliding to occur is limited to $(\theta_1 + \phi_j) = 90^\circ$, at which the shear load required to initiate shear failure by sliding in theory becomes infinite. Even as the value of $(\theta_1 + \phi_j)$ approaches 90° , considerable shear load is required to cause sliding along the joint set. Depending on the size and intact rock strength of the asperity, this shear load may cause failure through the asperity before sliding can occur. This produces a different pre-peak mechanism in these rock masses.

7.2.2 Rotational behaviour

In the tests where sliding along the θ_1 joint set was not observed, part of the sample appeared to rotate as shear displacement increased. The rotating part of the sample appeared to be defined by the inclination of the θ_2 joint set and the joint spacing, which comprised principally the sample between the bottom left and top right ends of the shear box, as shown in Figure 7-2 and Figure 7-3.

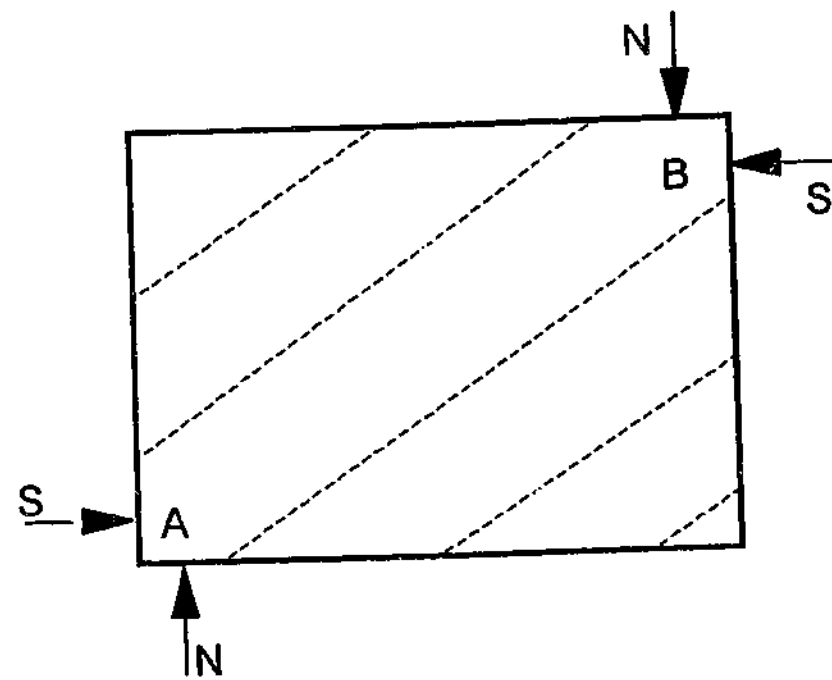


Figure 7-9: Forces acting on a block subjected to direct shear.

The rotation within the sample is a result of the eccentric forces applied to the sample by the direct shear test. Consider the forces acting on a block, as shown in Figure 7-9. The applied loads will produce a moment on the block. If joints are introduced to this rock mass, such as those shown dotted in Figure 7-9, separation across those joints will occur with displacement of the shear box. This results in a strut forming between the corners of the sample. This strut resists the shear load in axial compression, as shown in Figure 7-10. There will be little or no load carried by the remainder of the rock mass.

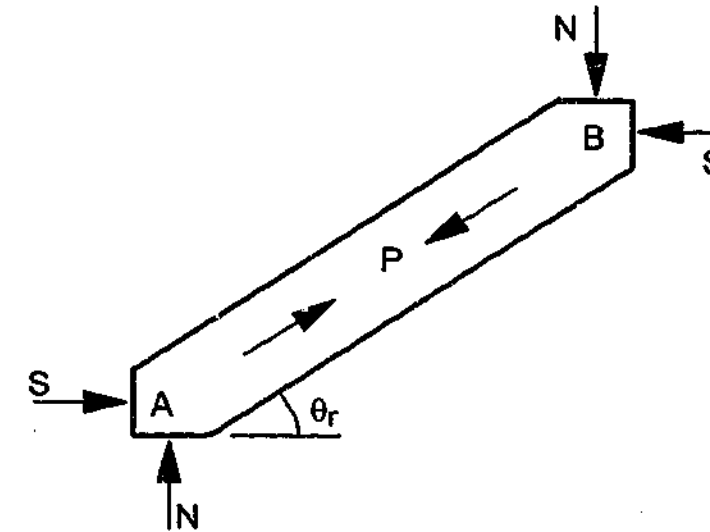


Figure 7-10: Forces acting on a strut inclined at θ_r .

To achieve moment equilibrium in a strut inclined at θ_r :

$$N \cos \theta_r = S \sin \theta_r \quad \text{Equation 7-6}$$

This can be rearranged to give:

$$S = N \cot \theta_r \quad \text{Equation 7-7}$$

But:

$$\cot \theta_r = \tan(90^\circ - \theta_r) \quad \text{Equation 7-8}$$

so:

$$S = N \tan(90^\circ - \theta_r) \quad \text{Equation 7-9}$$

Dividing both sides of the equation by area to obtain stresses, and substituting $\theta_r = \theta_2$, the shear strength can be written as:

$$\tau = \sigma \tan(90^\circ - \theta_2) \quad \text{Equation 7-10}$$

Therefore, if rotation were occurring about the θ_2 joint set, the value of the apparent friction angle, ϕ_{pp} , obtained from the τ - σ curve, would be defined by $(90^\circ - \theta_2)$. The values of ϕ_{pp} measured from the Type "B" tests have been plotted against $(90^\circ - \theta_2)$ in Figure 7-11.

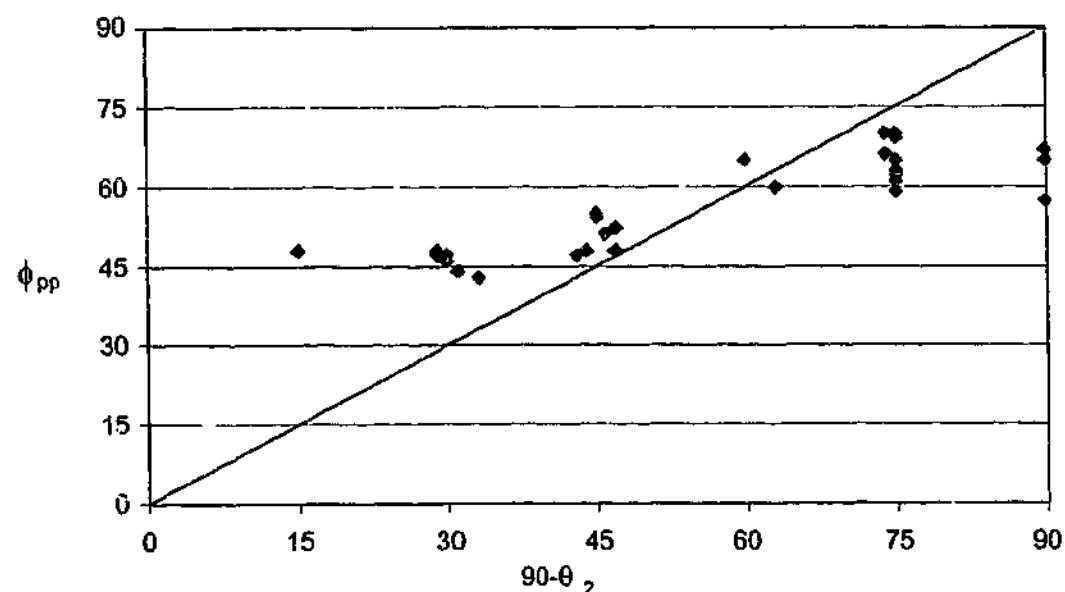


Figure 7-11: Relationship between apparent friction angle, ϕ_{pp} , and θ_2 .

Figure 7-11 shows that rotation about the θ_2 joint set appears to occur for values of $(90^\circ - \theta_2) = 60^\circ$, or when $\theta_2 = 30^\circ$. For other values of θ_2 , the value of ϕ_{pp} is consistent, but does not appear to rotate around about θ_2 , but some other angle, θ_r , which can be calculated from $\theta_r = (90^\circ - \phi_{pp})$. A comparison of the observed and calculated values of ϕ_{pp} for the Type "B" rock masses is presented in Table 7-2.

Table 7-2: Predicted and observed values of ϕ_{pp}

No of Joint Sets (θ_2)	Estimated ϕ_{pp} from $(90^\circ - \theta_2)$	Average test ϕ_{pp}	Test θ_r (inferred)
Nil (Intact)	-	67°	23°
One ($\theta_1 = 60^\circ$)	-	65°	25°
Two ($\theta_2 = 15^\circ$)	75°	70°	20°
Two ($\theta_2 = 30^\circ$)	60°	65°	25°
Two ($\theta_2 = 45^\circ$) (s = 70 mm)	45°	54°	36°
Two ($\theta_2 = 45^\circ$) (s = 32 mm)	45°	48°	42°
Two ($\theta_2 = 60^\circ$)	30°	46°	44°
Two ($\theta_2 = 75^\circ$)	15°	48°	42°
Two ($\theta_2 = 0^\circ$ or 90°)	-	57°	33°
Three ($\theta_2 = 15^\circ$ or 75°)	75° or 15°	63°	27°

Table 7-2 provides greater detail of the jointing than that shown in Figure 7-11. Table 7-2 shows there is a reasonable correlation (within 5°) between calculated and average observed values of ϕ_{pp} for the tests when $\theta_2 = 15^\circ$ and 30° , and when $\theta_2 = 45^\circ$ and joint spacing was 32 mm. This suggests one of two things:

- that rotation occurs about the θ_2 joint set, or put differently, the shear and normal forces are acting on the ends of a strut inclined at θ_2 , or
- that the strut behaves similarly to an intact block.

For the remaining tests, the correlation between predicted and average observed values of ϕ_{pp} was poor, which suggests that the shear and normal forces were not acting at the ends of a strut inclined at θ_2 .

It would appear that the inferred rotation angle is not always the same as the angle of the θ_2 joint sets. What can be observed is that there are three typical values of θ_r . The average values of θ_r and the values of θ_2 to which they applied were:

- $\theta_r=23^\circ$ (20° to 27°). Tests on intact blocks, rock masses with one joint set inclined at $\theta_1=60^\circ$, rock masses with one joint set inclined at $\theta_2=15^\circ$ and rock masses with three joint sets.
- $\theta_r=36^\circ$. Tests on rock masses with two joint sets with $\theta_2=45^\circ$ and spacing=70 mm.
- $\theta_r=43^\circ$ (42° to 44°). Tests on rock masses with two joint sets with $\theta_2=75^\circ$ and 60° , and 45° with spacing=32 mm.

If the position of the shear and normal forces can be reasonably determined, then the value of θ_r can be obtained. Take the simplest case of the pre-peak behaviour of an intact sample, as shown in Figure 7-9.

The visual footage showed the intact blocks appeared to rotate slightly within the shear box as shear displacement increased (see Test B32 in Appendix C). It would be reasonable to assume that the moments applied by the shear and normal forces produced this rotation. The intact block may be considered as a horizontal strut subjected to eccentric forces. If the block rotates even a few degrees, the vertical forces, N , will act at the ends of the block, at points A and B (see Figure 7-9). Determining the location of the horizontal shear force, S , is more problematic.

Some shear tests in this study were carried out on intact Johnstone and concrete blocks. A diagram of the test arrangement is presented in Figure 7-12. The shear box used in the Type "B" tests applied the shear force through a steel plate mounted on two threaded bars. For the purposes of this discussion, it has been assumed this produces a relatively uniformly distributed load (UDL) on the ends of the sample. The UDL can be approximated by a point load acting midway between the threaded bars. The location of these loads can be used to derive θ_r , which in turn can be used to predict the value of ϕ_{pp} .

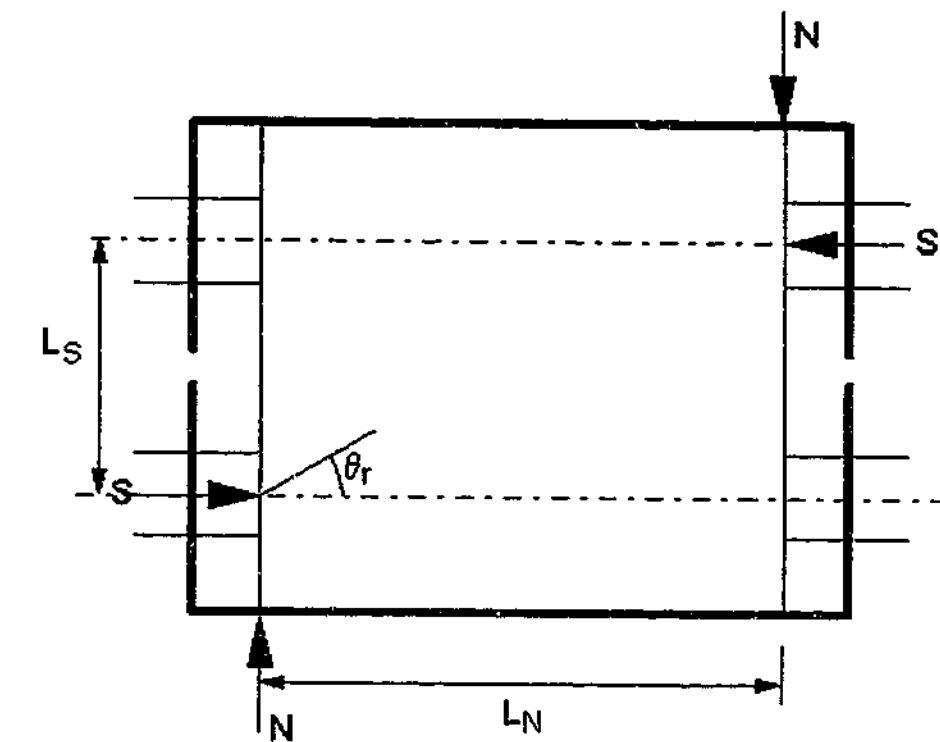


Figure 7-12: Assumed location of forces applied by the Type "B" shear box.

The effective lever arm of the shear load can be taken as the distance between the midpoints of the threaded bars, L_S . This distance is about 182 mm. The length of the sample was typically about 390 mm, which was the distance of the lever arm of the normal load, L_N . This gives an effective θ_r of 25° , or $\phi_{pp} = (90^\circ - 25^\circ) = 65^\circ$. From Table 7-2 the average value of ϕ_{pp} for the intact blocks was 67° .

This value of ϕ_{pp} was also typical for rock masses with one steep θ_1 joint set, for rock masses with θ_2 less than 30° and for rock masses containing three joint sets. As mentioned earlier, if sliding was not observed, the θ_1 joint set can be ignored from a mechanistic viewpoint. This effectively makes the sample "intact", so it should behave as a block. The rock masses with three joint sets also appear to behave as an intact block, but whether this occurs because the pieces within the block "lock up" or because a strut forms along either the 15° or 75° joint set will be discussed later. It may be worth noting that although the samples behave as an intact block mechanistically, the presence of jointing reduces the strength of the rock mass below that of the intact rock.

Consider now the series of struts that are formed when θ_2 is greater than the angle of the diagonal across the sample, θ_d . Typically $\theta_d=36^\circ$ for Type "B" samples. These struts form a

block, as shown in Figure 7-3. The tests where shear through a block occurred produced remarkably consistent values of ϕ_{pp} (see Figure 7-11). This suggests for θ_2 greater than θ_d , the shape of the rotating sample and the location of the forces acting on the sample remain effectively the same. However, the precise location of the application of the resultant forces is unclear.

One method of assessing the location of the forces acting on the blocks is the strut analogy. If the strut analogy is adopted, the shear forces should act at the ends of the struts that make up the block. Consider a sample constrained in the shear box as shown in Figure 7-13.

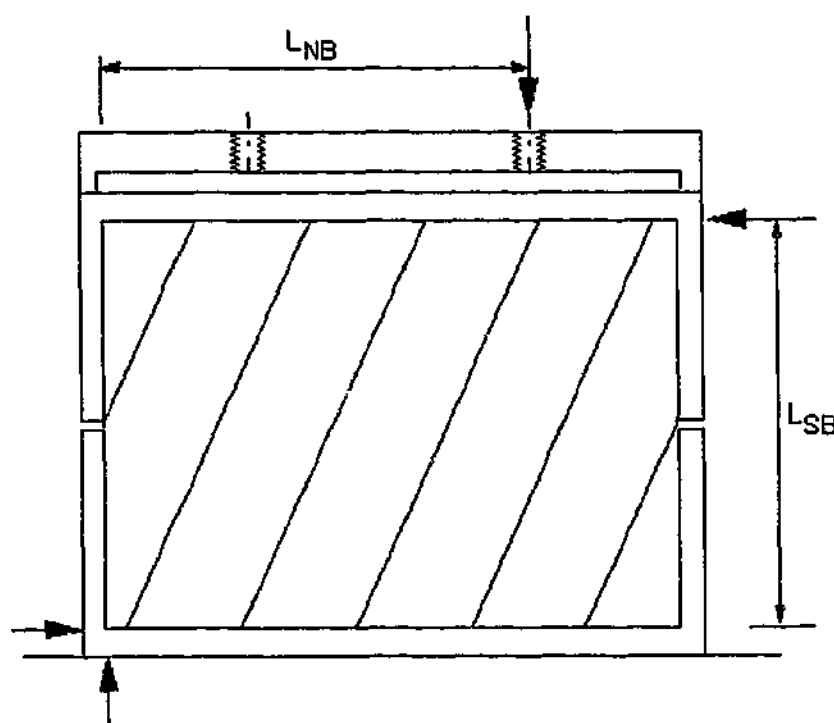


Figure 7-13: Location of forces for block shear.

The locations of the normal forces have now changed from those acting on the intact blocks. The upward normal force still acts at the left hand end of the shear plane. However, the downward normal force can be treated as acting through the right hand stud, in much the same way as the shear forces were thought to act midway between the threaded bars for intact rock masses. This means the shear and normal forces are applied at the same location for all tests where block shear occurs, hence similar values of ϕ_{pp} .

The predicted values of ϕ_{pp} for tests that rotate as a block were calculated using a value of $L_{NB}=294$ mm and a sample height, $L_{SB}=280$ mm, resulting in a calculated value of $\phi_{pp}=46^\circ$. The

calculated values of ϕ_{pp} for block shear have been compared in Table 7-3 to the values of ϕ_{pp} measured in the laboratory tests where block shear was observed.

Table 7-3: Calculated and predicted values of ϕ_{pp} for block rotation.

Test (θ_2)	Predicted ϕ_{pp}	Actual ϕ_{pp}
B26 (61°)	46°	47°
B31 (60°)	46°	46°
B7 (61°)	46°	48°
B7A (60°)	46°	47°
B15 (57°)	46°	43°
B19 (60°)	46°	44°
B19A (60°)	46°	46°
B27 (75°)	46°	48°
B14 (44°)	46°	51°
B16 (47°)	46°	47°
B22 (46°)	46°	48°
B23 (43°)	46°	48°

There appears to be relatively good agreement between the calculated and measured values of ϕ_{pp} for tests where block shear occurs. However, there may be other combinations of the locations at which the forces are applied that produce similar values of ϕ_{pp} .

7.2.2.1 Pre-peak behaviour of rock masses containing three joint sets

Two of the rock mass samples with three joint sets included one joint set inclined at $\theta_2=15^\circ$. The pre-peak behaviour of these samples and the samples containing two joint sets with $\theta_2=15^\circ$

was similar, in that low dilation and similar values of ϕ_{pp} were measured (see Section 6.5.4.1). This suggests that shearing through the strut inclined at $\theta_2=15^\circ$ was the failure mechanism for Type "B" samples tested containing three joint sets. This was observed by viewing the video footage of Tests B9 and B21 and confirmed by the measured results. Figure 7-14 shows the strut and failure surface formed in Test B21.

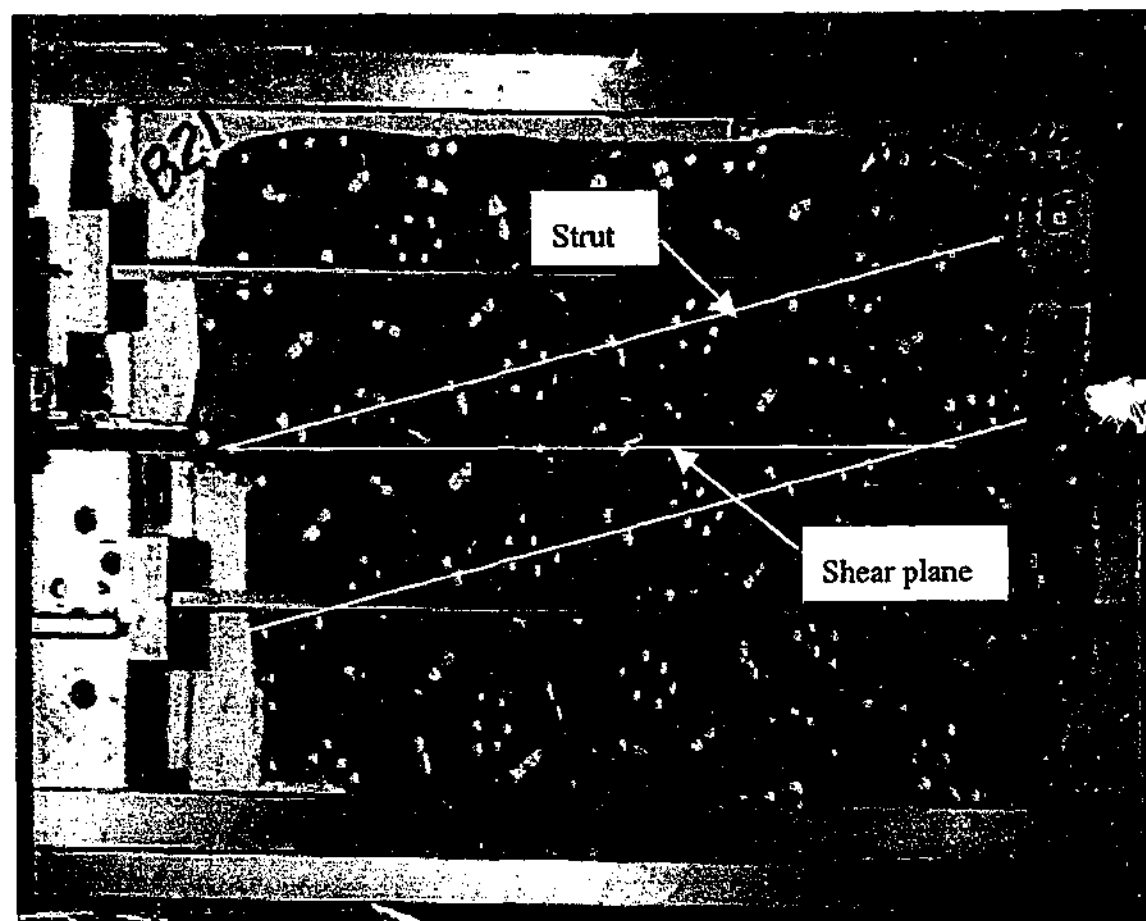


Figure 7-14: Shear plane through strut formed in sample B21.

It can be observed that the failure surface through the strut between the bottom left and top right ends of the shear box is coincident with the shear plane and that the length of this failure surface is less than the length of the sample.

7.2.2.2 Dilation

Consider again the strut shown in Figure 7-10. The amount of dilation varies significantly with the value of the angle of inclination of the strut, θ_r . The action of the shear and normal loads will produce an axial compressive force, P , in the strut, which can be calculated from:

$$P = S \cos \theta_r + N \sin \theta_r \quad \text{Equation 7-11}$$

The shear force required to overcome the initial normal load is:

$$S = \frac{N}{\tan \theta_r} \quad \text{Equation 7-12}$$

For small values of θ_r , including the case of intact blocks, the magnitude of S required to produce a vertical component large enough to overcome the initial normal stress and allow dilation to occur will be large. It is likely that failure of the strut in compression will occur either before rotation begins or shortly afterwards.

However, as θ_r becomes larger, less shear force is required to produce a vertical component in the strut to overcome the initial normal load. This results in relatively larger dilations. Under CNS conditions, increasing dilation will lead to higher normal loads on the sample, so that more shear force is required to achieve the same shear displacement. This will lead to greater forces acting in the strut, which will lead to elastic deformation due to the compression of the strut. The force in the strut will increase with shear displacement until failure occurs.

7.2.2.3 Pre-peak behaviour for samples with $\theta_2=45^\circ$.

Rotational behaviour was observed prior to failure in the samples where $\theta_2=45^\circ$, although consistently different values of ϕ_{pp} were observed in samples with more closely spaced joints (32 mm nominal) and those with more widely spaced joints (70 mm nominal).

When the joint spacing was 32 mm, the measured value of $\phi_{pp}=48^\circ$, was similar to that of the other tests in which the sample rotated as a block. A similar value of ϕ_{pp} is also obtained if rotation about $(90^\circ-\theta_2)$ is assumed. When the joint spacing was increased to 70 mm, $\phi_{pp}=54^\circ$. The reason for this change is unclear. However, the consistency of the results suggests that the location of the shear and normal forces have changed. The change in the values of ϕ_{pp} is discussed below.

7.2.2.3.1. Pre-peak behaviour for samples with $\theta_2=45^\circ$ and closely spaced joints.

The apparent friction angle, ϕ_{pp} , predicted for strut rotation where $\theta_2=45^\circ$ is 45° . The value of ϕ_{pp} predicted for block rotation is 48° . Using the measured outputs to assess pre-peak behaviour did not clearly indicate which mechanism occurred. Video footage was required to confirm the pre-peak behaviour of these samples.

Consider the rock mass sample from Test B16 shown in Figure 7-15.

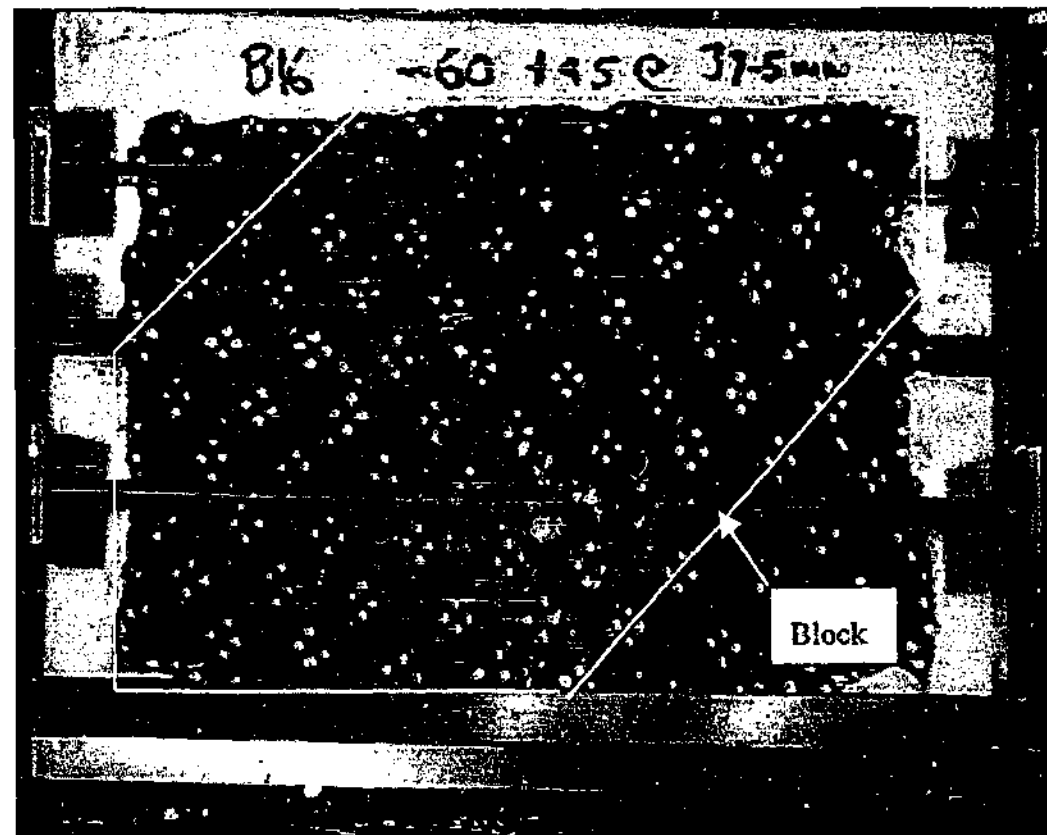


Figure 7-15: Block formed in rock mass with $\theta_2=45^\circ$ and spacing=32 mm (Test B16).

Figure 7-15 shows that the block is made up of struts with at least one end terminating at either the top or bottom of the shear box. The same occurs in the samples where θ_2 is greater than 45° . Therefore, it would appear that the apparent friction angle of 48° for the samples with closely spaced joints occurs as a result of rotation about the same θ_2 angle for samples failing by block shear rather than rotating about θ_2 . This behaviour was confirmed by the video footage (see Appendix C).

7.2.2.3.2. Pre-peak behaviour for samples with $\theta_2=45^\circ$ and widely spaced joints.

These samples should produce a value of apparent friction angle, $\phi_{pp}=45^\circ$ for strut rotation and 48° for block rotation. However, the measured value of $\phi_{pp}=54^\circ$.

Figure 7-16 shows a rock mass with the same joint inclinations as the sample in Figure 7-15, but with more widely spaced joints.

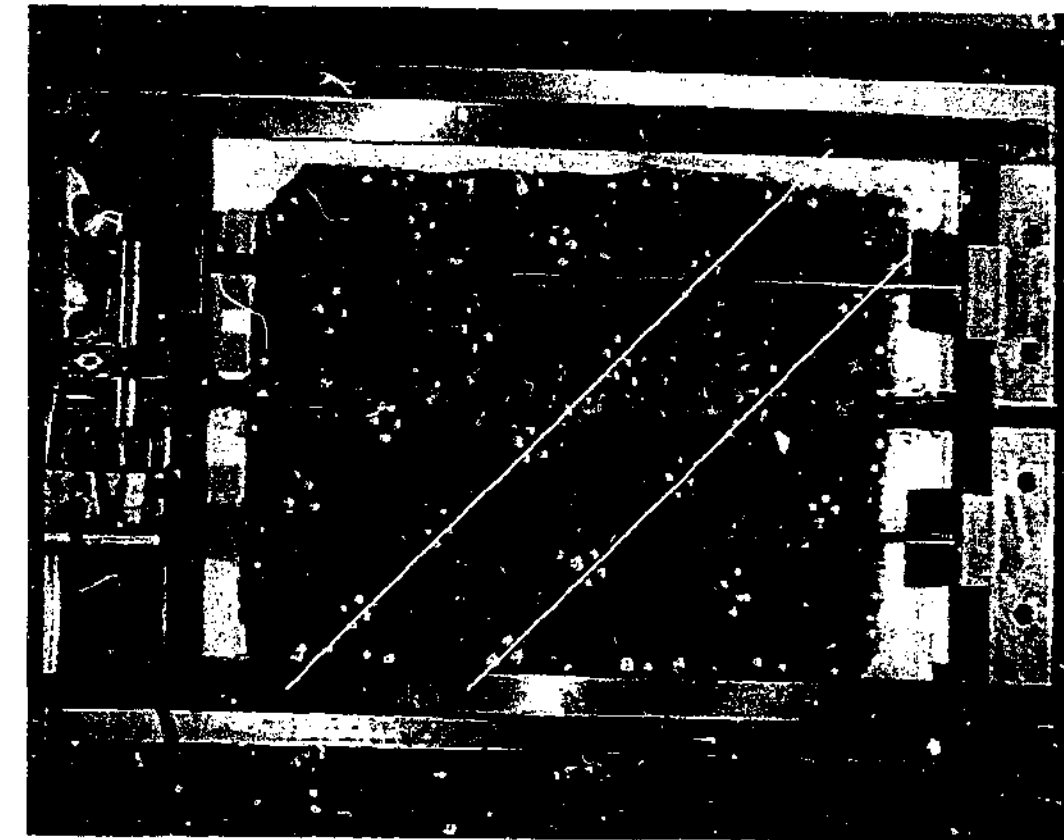


Figure 7-16: Diagonal of a rock mass with $\theta_2=45^\circ$ and spacing=70 mm (Test B20).

It can be observed in Figure 7-16 that a strut connects the corners of the sample i.e. forms a diagonal across the sample. This may represent a special case where rotation of the diagonal of the sample occurs, rather than rotation of the block.

Using the strut analogy again, assume the shear forces act at the ends of the struts. The angle of the diagonal, $\theta_d=36^\circ$, so the value of $\phi_{pp}=(90^\circ-\theta_d)=54^\circ$. The calculated value of $\phi_{pp}=54^\circ$ for samples with spacing=70 mm is very close to the average value of ϕ_{pp} measured in the tests. This suggests for this case, the forces acting on the sample are effectively located at the corners of the sample.

7.2.2.4 Pre-peak behaviour—sliding or rotation?

The pre-peak behaviour of the rock mass will be governed by the mechanism that requires the least value of shear force, S , to generate shear displacement, and this will depend on the joint inclination.

The value of S required for sliding along the θ_1 joint set can be estimated from:

$$S = N \tan(\theta_1 + \phi_j) \quad \text{Equation 7-13}$$

The value of S required for strut rotation can be estimated from:

$$S = N \tan(90^\circ - \theta_2) \quad \text{Equation 7-14}$$

The value of S required for block rotation can be estimated from:

$$S = N \tan(90^\circ - \theta_r) \quad \text{Equation 7-15}$$

where θ_r for the Type "B" tests was about 42° . For the special case where a strut formed the diagonal of the sample, θ_r was found to be about 36° .

Therefore, the minimum value of S obtained from equations 7-13, 7-14 and 7-15 can be used to determine the pre-peak behaviour of the rock mass. For example, consider the rock masses with joint sets inclined at -30° , 30° (Test B4, shown in Figure 7-17) and -30° , 45° (Test B5, shown in Figure 7-18). The apparent friction angle for sliding in both tests is $(\theta_1 + \phi_j) = (30^\circ + 28^\circ) = 58^\circ$. The apparent angle for strut rotation in Test B4 is $(90^\circ - \theta_2) = (90^\circ - 30^\circ) = 60^\circ$, while the apparent friction angle for block rotation about the diagonal in Test B5 is $(90^\circ - \theta_r) = (90^\circ - 36^\circ) = 54^\circ$. Therefore, the sample in Test B4 should fail by sliding, while the sample in Test B5 should fail by rotation. This was confirmed by the video footage.

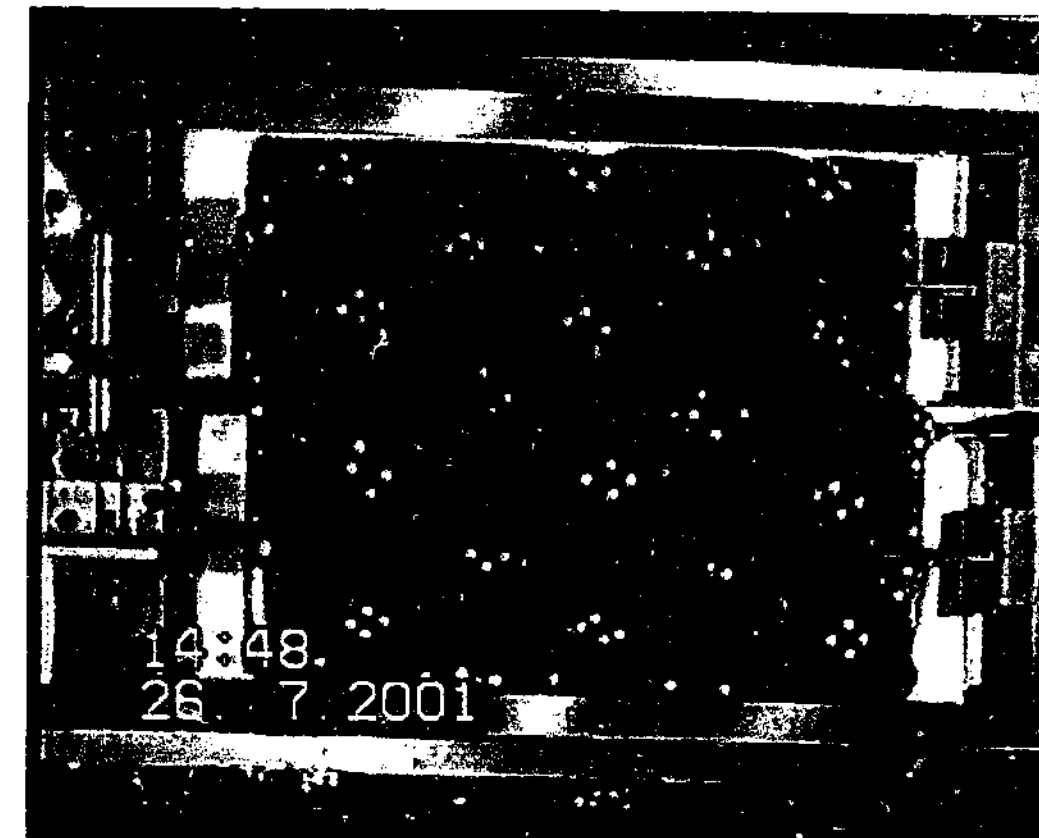


Figure 7-17: Sliding behaviour exhibited by sample B4.

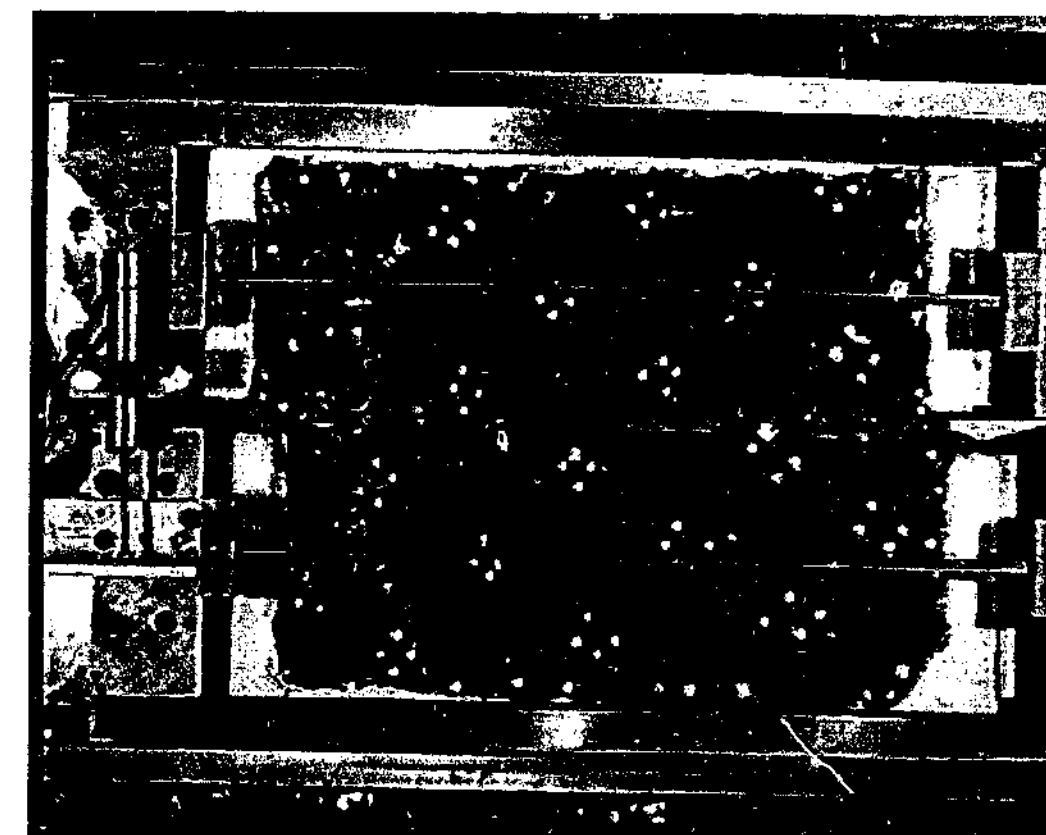


Figure 7-18: Rotational behaviour exhibited by sample B5.

For the tests where $\theta_1=45^\circ$, the apparent friction angle for sliding is estimated to be 73° . The strut rotation behaviour exhibited in Test B6, when $\theta_2=15^\circ$ leads to an apparent friction angle of $(90^\circ-15^\circ)=75^\circ$. These values of apparent friction angle are very similar, and from the interpretation of the graphical output, either behaviour can be expected. Video footage, however, confirmed strut rotation was the pre-peak behaviour.

For the tests where $\theta_1=60^\circ$, the apparent friction angle for sliding is estimated to be 88° . The propensity for sliding within a rock mass containing one joint set such that $\theta_1=60^\circ$ was examined in Test B29. The shear force required to cause sliding was greater than the strength of the intact material, so the sample failed in shear prior to any sliding occurring on the θ_1 joint set.

7.2.3 Shear failure through a strut or block.

The shear stress required to generate a shear plane through the intact blocks within the sample depends on the area of the sample coincident with the shear plane. If a strut, as shown in Figure 7-2, resists the shear load, this area is less than that of the sample. Where a block, as shown in Figure 7-3, resists the shear load, the area is the same as the sample.

The shear box fixes the location of the shear plane. This means the average value of β in equation 7-5 becomes zero, although local variations along the shear plane can occur. The length of the shear surface of a strut, L remains constant, and can be calculated from the joint spacing, s , by:

$$L = \frac{s}{\sin \theta_2} \quad \text{Equation 7-16}$$

The shear force required to cause failure along a horizontal surface in the strut can be estimated as:

$$S_s = N \tan(\phi_i) + \frac{cs}{\sin \theta_2} \quad \text{Equation 7-17}$$

The shear force required to cause rotation of the strut has been given by equation 7-9, namely:

$$S = N \tan(90^\circ - \theta_r) \quad \text{Equation 7-18}$$

It can be assumed θ_r has either the intact block value of $\theta_r=25^\circ$ or that $\theta_r=\theta_2$.

Consider the end of the rotating strut shown in Figure 7-19

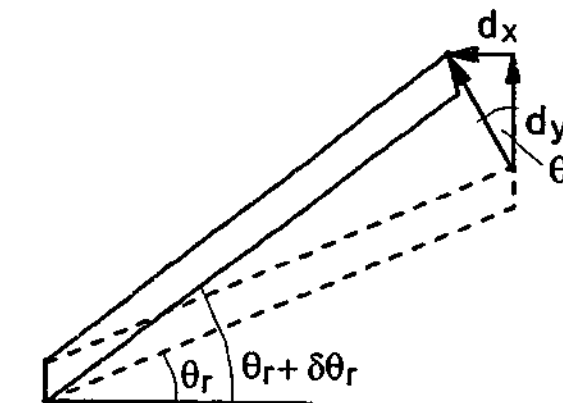


Figure 7-19: Increments of dilation and displacement as a result of rotation.

A small amount of rotation, $\delta\theta_r$, will result in dilation and a relative shear displacement. The dilation and shear displacement resulting from this rotation can be estimated from the equation:

$$\frac{dx}{dy} = \tan \theta_r \quad \text{Equation 7-19}$$

Inverting this equation gives:

$$\frac{dy}{dx} = \cot \theta_r = \tan(90 - \theta_r) \quad \text{Equation 7-20}$$

which in turn gives:

$$dy = dx \tan(90 - \theta_r) \quad \text{Equation 7-21}$$

The normal load acting on the strut will increase as a result of this dilation in accordance with the stiffness.

This means that when the value of θ_1 is low, small amounts of shear displacement will produce large dilations. This in turn will increase the normal stress acting on the end of the strut, which increases the axial load within the strut. However, the vertical component of the load acting in the strut may not be large enough to overcome the initial normal load, so shearing through the strut occurs before rotation of the strut is observed, as shown in Figure 7-14.

For larger values of θ_2 , a block that has the same area as the sample resists the shear load. The location of the moments acting on the block remains the same. This means that the peak shear forces should be approximately the same for these samples.

Where shear occurs through a strut, the reduced area of shear plane will require less shear force to cause failure than that observed through a block. This relatively lower failure load can also be used to confirm the failure mechanism.

The shear stresses required to rotate a strut or block, based on the rotation angle, θ_1 , and the dilation resulting from shear displacement given in equation 7-21 have been programmed into a spreadsheet. These stresses are compared to those required to initiate shear through the shear plane, given by equation 7-17. The peak shear stress has been calculated and normalised by dividing by the UCS of the intact material. The normalised peak shear stresses, $\bar{\tau}$, obtained from the spreadsheet and the laboratory tests are summarised in Table 7-4.

Table 7-4: Comparison of calculated and measured normalised peak shear stress.

θ_2	Calculated		Measured			
	peak τ (kPa)	$\bar{\tau}$	Test	peak τ kPa)	UCS (MPa)	Average $\bar{\tau}$
15°	425	0.142	B6	570	3.70	0.146
			B30	260	1.97	
30°	885	0.294	B2	1100	4.14	0.266
45°	1105	0.368	B5	1010	3.37	0.276
			B20	600	2.38	
45° (close spacing)	1105	0.368	B14	760	4.52	0.155
60°	1550	0.517	B26	550	2.04	0.319
			B7A	625	1.70	
75°	1550	0.517	B27	535	1.66	0.322

The peak shear stress values calculated by the spreadsheet have been normalised by dividing by an assumed UCS of 3.0 MPa. The values listed in Table 7-4 are plotted in Figure 7-20.

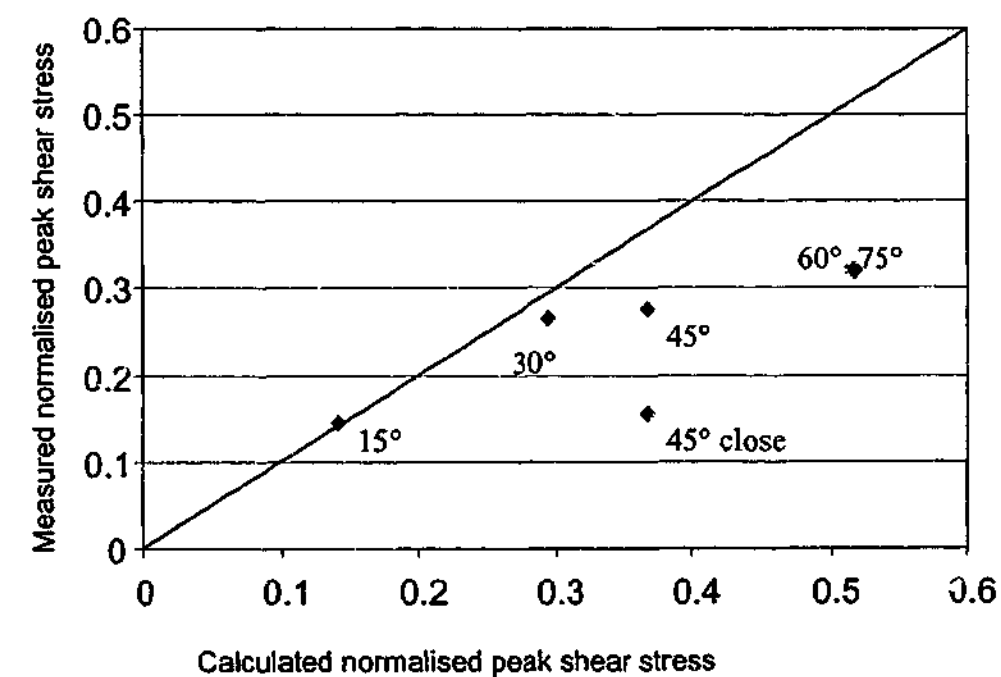


Figure 7-20: Comparison of calculated and measured $\bar{\tau}_p$ for strut and block rotation.

It can be seen that there is good agreement between the calculated values of normalised peak shear stress and those measured during the shear tests for values of θ_2 up to 30° , i.e. those less than θ_a , or those samples that fail by strut shear. The agreement between the samples that fail by block shear is poor.

The peak shear stresses have been calculated for the same boundary conditions for the samples where θ_2 was 45° and where θ_2 was equal or greater than 60° . Given the constant length of shear plane and the same rotational behaviour, the same values of peak shear stress are calculated. These calculated values are higher than those measured in the tests. This may be a result of tensile failure in some of the pieces making up the laboratory sample. This was observed to reduce the length of the failure surface (in these tests) to about two thirds of the sample length. The damage observed in the samples due to progressive failure may have therefore reduced the length of the shear surface, hence the shear strength of the sample.

7.3 Comparison with Hoek-Brown GSI criterion

The samples tested in this study have been judged to represent rock masses classified using the Hoek-Brown GSI chart shown in Figure 2-6 and Figure 7-21 as Blocky/Fair. The strength envelope for a typical rock mass with this classification has been generated using the equations in section 2.3.2.3 and the values suggested in Figure 7-21 and transposed to the τ - σ plane. This envelope is compared to the peak strengths measured in the laboratory tests, as shown in Figure 7-22.

GENERALISED HOEK-BROWN CRITERION		SURFACE CONDITION	VERY GOOD Very rough, unweathered surfaces	GOOD Rough, slightly weathered, iron stained surfaces	FAIR Smooth, moderately weathered or altered surfaces	POOR Slitkenided, highly weathered surfaces with compact coatings or fillings containing angular rock fragments	VERY POOR Slitkenided, highly weathered surfaces with soft clay coatings or fillings
STRUCTURE							
	BLOCKY -very well interlocked undisturbed rock mass consisting of cubical blocks formed by three orthogonal discontinuity sets	m_b/m_s 0.60 s 0.190 a 0.5 E_r 75,000 ν 0.2 GSI 85	0.60 0.190 0.5 75,000 0.2 85	0.40 0.062 0.5 40,000 0.25 75	0.26 0.015 0.5 20,000 0.25 62	0.10 0.003 0.5 9,000 0.25 48	0.08 0.0004 0.5 3,000 0.25 34
	VERY BLOCKY-interlocked, partially disturbed rock mass with multifaceted angular blocks formed by four or more discontinuity sets	m_b/m_s 0.40 s 0.062 a 0.5 E_r 40,000 ν 0.2 GSI 75	0.40 0.062 0.5 40,000 0.2 75	0.29 0.021 0.5 24,000 0.25 65	0.16 0.003 0.5 9,000 0.25 48	0.11 0.001 0.5 5,000 0.25 38	0.07 0 0.53 2,500 0.3 25
	BLOCKY/SEAMY-folded and faulted with many intersecting discontinuities forming angular blocks	m_b/m_s 0.24 s 0.012 a 0.5 E_r 18,000 ν 0.25 GSI 60	0.24 0.012 0.5 18,000 0.25 60	0.17 0.004 0.5 10,000 0.25 50	0.12 0.001 0.5 6,000 0.25 40	0.08 0 0.5 3,000 0.3 30	0.06 0 0.55 2,000 0.3 20
	CRUSHED-poorly interlocked, heavily broken rock mass with a mixture of angular and rounded blocks	m_b/m_s 0.17 s 0.004 a 0.5 E_r 10,000 ν 0.25 GSI 50	0.17 0.004 0.5 10,000 0.25 50	0.12 0.001 0.5 6,000 0.25 40	0.08 0 0.5 3,000 0.3 30	0.06 0 0.55 2,000 0.3 20	0.04 0 0.60 1,000 0.3 10

Figure 7-21: Suggested Hoek-Brown GSI parameter values based on classification (from Hoek et al., 1995).

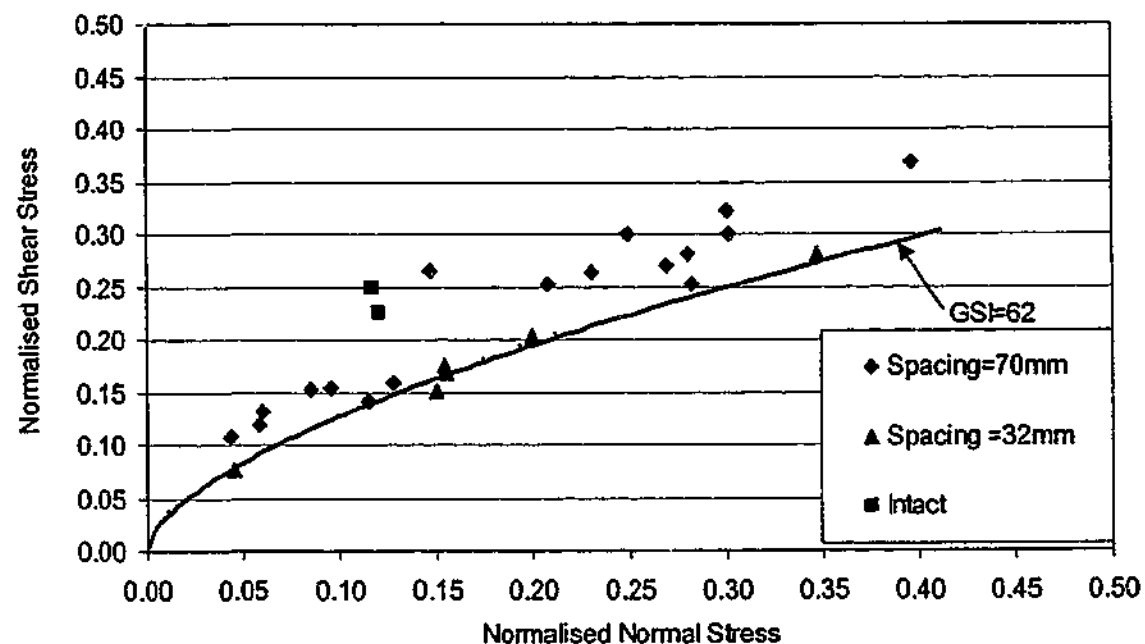


Figure 7-22: Comparison of laboratory test results with Hoek-Brown strength envelope for blocky/fair rock masses.

Figure 7-22 shows that the Hoek-Brown envelope provides a good lower bound to the strength of the Type "B" samples, particularly for those samples where joint spacing was relatively close. This concurs with the comments in Hoek (1983) on this criterion providing a lower bound estimate of rock mass strength (refer to Section 2.3.2.1). The value of the spacing variable used to generate this envelope was the default value of 0.015 suggested in Figure 7-21. For more widely spaced joints, the GSI value remains the same, but the value of the spacing variable should increase. If the value of the spacing variable was increased to 0.189, which is close to the maximum value listed in the GSI chart, an envelope that better fits the samples with more widely spaced joints is generated, as shown in Figure 7-23.

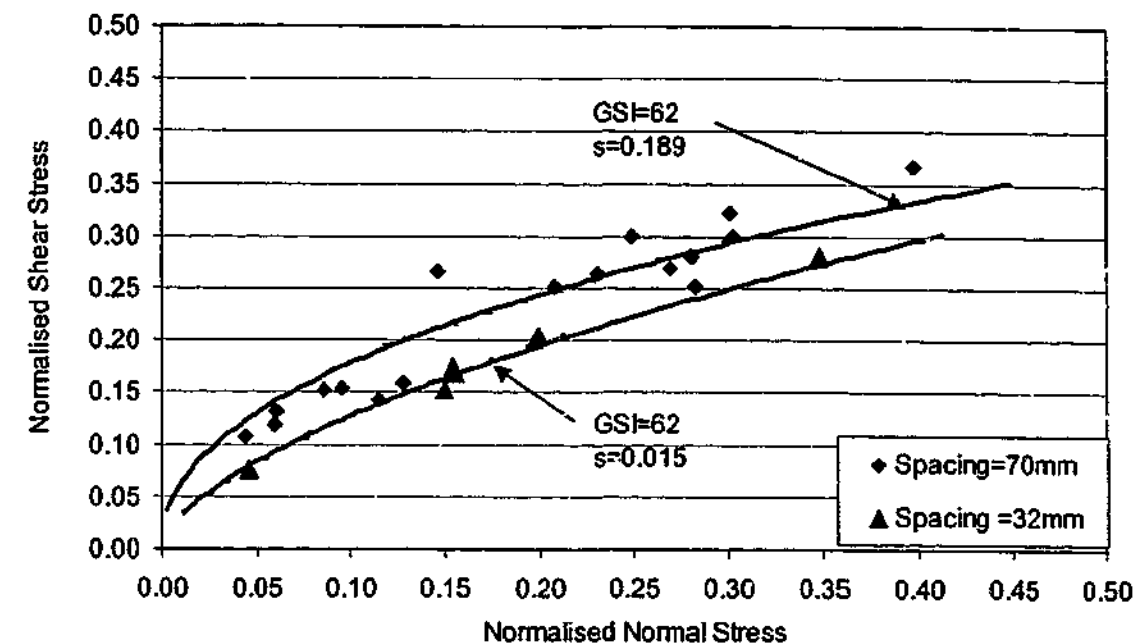


Figure 7-23: GSI strength envelopes generated using differing values of spacing variable.

Figure 7-23 shows that the GSI envelopes more closely match the test results when the spacing variable is adjusted. However, the selection of the spacing variable was arbitrary and needs to become more rigorous. Nevertheless, the potential of the GSI system is highlighted by this comparison.

The good fit of the Hoek-Brown GSI envelope to the test results was unexpected, especially considering the relatively wide variations in joint inclinations and spacing within the samples tested in this study.

7.4 Failure in Type "A" tests

The Type "A" samples were produced with either two or three joint sets. All the Type "A" samples were constructed with two joint sets inclined at -45° and 15° , while some samples were constructed with a third joint set inclined at 75° , as shown in Figure 7-24.

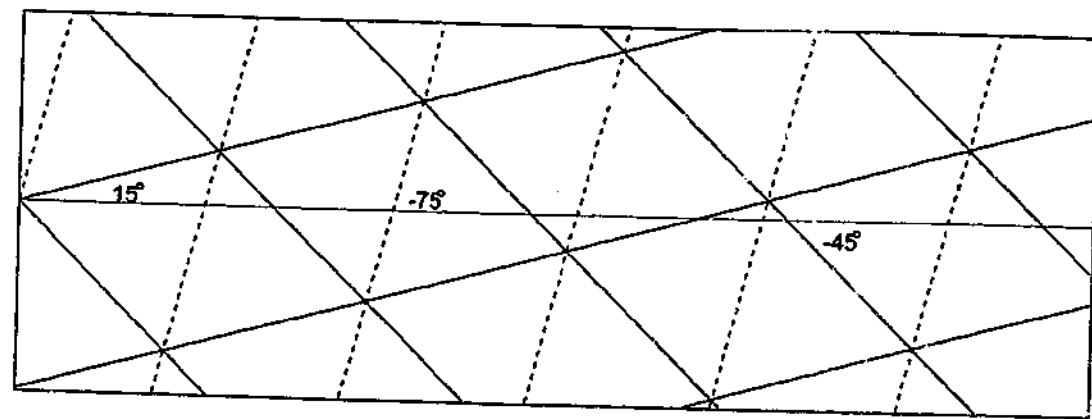


Figure 7-24: Typical joint configurations of the Type "A" samples.

The Type "A" shear box did not allow viewing of the sample, other than for the 25 mm gap between the shear box halves. This meant that direct observation and filming of the Type "A" sample behaviour could not be carried out. The pre-peak behaviour of the Type "A" samples was inferred from the measured apparent pre-peak friction angle, ϕ_{pp} . The measured ϕ_{pp} , together with the apparent friction angles for sliding and strut shear are presented in Table 7-5.

Table 7-5: Summary of measured and predicted values of ϕ_{pp} for Type "A" tests.

Joint Sets ($\theta_1, \theta_2, \theta_3$)	Test ϕ_{pp} (average)	Sliding $\phi_{pp}=(\theta_1+\phi_l)$	Strut rotation $\phi_{pp}=(90^\circ-\theta_2)$	Rotation angle $\theta_r=(90^\circ-\phi_{pp})$
Two (-45°, 15°)	71° (68° to 72°)	73°	75°	19°
Three (-45°, 15°, 75°)	62° (59° to 65°)	73°	75° or 15°	28°

The average apparent friction angle of the Type "A" samples with two joint sets was 71°. The average apparent friction angle of the Type "A" samples with three joint sets was 62°. The equation for sliding will produce a value of $\phi_{pp}=(45^\circ+28^\circ)=73^\circ$, while rotation about $\theta_2=15^\circ$ will produce $\phi_{pp}=75^\circ$. This infers that the pre-peak mechanism for Type "A" samples with two joint sets is either sliding or strut rotation (due to the similarity between the two values).

Block rotation results in a value of ϕ_{pp} defined by $(90^\circ-\theta_r)$. Applying the shear and normal forces at the ends of the shear plane (typically 450 mm long) and the top and bottom of the sample (typically 200 mm) results in $\theta_r=24^\circ$. Therefore, block rotation yields $(90^\circ-24^\circ)=66^\circ$. It

appears the Type "A" samples with three joint sets fail by block rotation, so the introduction of a third joint set appears to have resulted in a different failure mechanism.

7.5 Summary

The results of the test program provided evidence of three mechanisms by which samples can fail when subjected to CNS direct shear. The observed failure mechanisms and the conditions under which they occurred were:

- Sliding along a joint set inclined at θ_1 to the shear plane, with failure occurring by shearing through a macro-asperity formed by the joint sets. This mechanism occurred when the θ_1 and θ_2 joint sets were inclined within about 30° of the shear plane. This mechanism did not produce the lowest peak shear strengths.
- Rotation of a strut within the sample, with failure occurring by shearing through the strut. This mechanism occurred when θ_1 was inclined such that sliding could not occur and θ_2 is inclined such that a strut was formed with ends located between the lower left and the upper right ends of the shear box. This mechanism resulted in relatively low peak shear strengths. A special case of strut rotation was observed when a strut formed the diagonal of the sample.
- Rotation of a block comprising most of the rock mass, with failure occurring by shearing along the full length of the shear plane. This mechanism occurred when θ_1 was inclined such that sliding could not occur and θ_2 was inclined such that the ends of the struts were between the top and bottom of the shear box. This mechanism resulted in relatively high peak shear strengths.

These mechanisms were modelled using simple mechanics and equations programmed into spreadsheets. The estimation of rock mass strengths for sliding and shearing through an asperity were modelled satisfactorily, as were the assessments of strut shear. The modelling of block shear over-estimated rock mass shear strength. This may be because the model did not consider the damage to the sample arising from progressive failure.

The results of the peak stresses measured in this study compare well with the GSI criterion proposed by Hoek. The GSI criterion for blocky/fair rock masses appeared to agree with the

lower bound of the measured rock mass strengths. If the largest value of spacing variable was assumed, a near upper bound strength envelope was obtained. The GSI criterion may produce both upper and lower bound estimates of rock mass strength by varying the spacing variable. More precise definition of the spacing variable, however, will require further work.

8 UDEC MODELLING OF DIRECT SHEAR TESTS

8.1 Introduction

The modelling of jointed rock masses using numerical techniques has become increasingly popular in recent years, probably because of the availability of sophisticated numerical software packages and high speed computers. At the same time, cost and practicality considerations have made laboratory and field testing less attractive.

As discussed in Chapter 2, a number of numerical modelling techniques have been used to model rock masses. An important feature of the technique used is that it should replicate the mechanisms occurring in the rock mass as it is loaded and allow for the realistic representation of rock mass failure. Two approaches commonly used to model rock mass behaviour are continuum methods and discontinuum methods (see Section 2.5.1).

In this project, the behaviour of the rock blocks within the sample had a large impact on the measured performance of the sample. Therefore a program using the discontinuum approach, UDEC, (Itasca, 2000) was adopted to model the direct shear tests. The UDEC modelling of the laboratory tests was carried out primarily to assess the ability of UDEC to replicate the mechanisms and failure processes observed during the laboratory tests. The UDEC model was also used to calculate the shear and normal displacements and stresses so that CNS conditions could be applied and a comparison with the laboratory results could be made.

8.2 Development of the UDEC model

The UDEC code reaches a solution by applying boundary conditions to a model and calculating the resulting displacements and stresses until equilibrium is reached or a specified number of cycles (or steps) have been performed.

The UDEC model was developed in the following stages:

- establishment of the model geometry

- assignment of material and joint models and properties
- application of boundary conditions
- development of FISH routines to calculate displacements and stresses
- development of a FISH routine to calculate and apply the normal stress increases due to dilation as a result of the constant normal stiffness and
- presentation of results

The flow chart for the UDEC model is presented in Figure 8-1.

The development and modelling of these stages, except for the FISH routines, was relatively straightforward. The development of the FISH routines to calculate displacements, stresses and to apply the CNS conditions was more complex. The development of each of the stages is described in the following sections.

8.2.1 Model geometry

The geometry of the numerical model was based on the geometry of the shear box and fabricated rock mass sample. The samples used in the laboratory tests were typically about 390 mm long by 280 mm high and 270 mm deep. A void of 18 mm was formed at either end of the shear plane. A comparison of the sample and the sample defined in UDEC is shown in Figure 8-2.

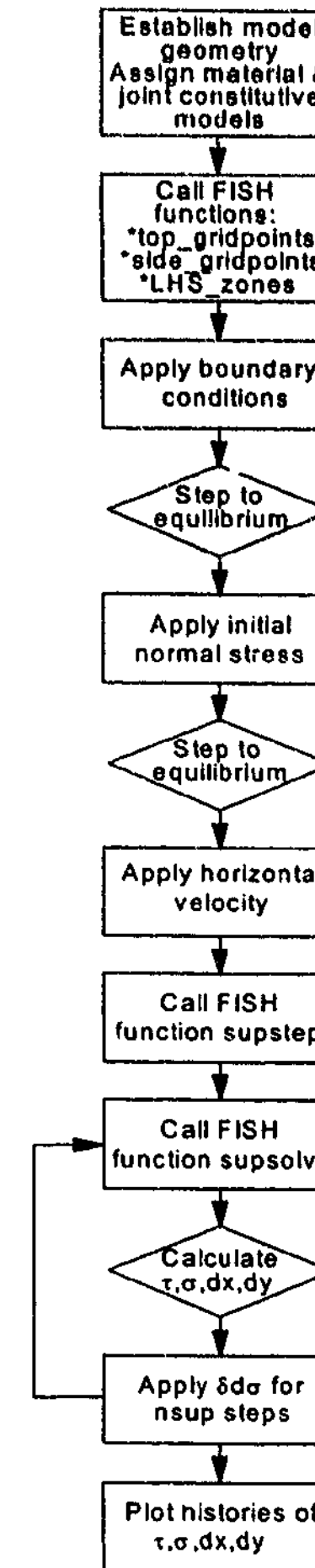


Figure 8-1: Flow chart of UDEC model.

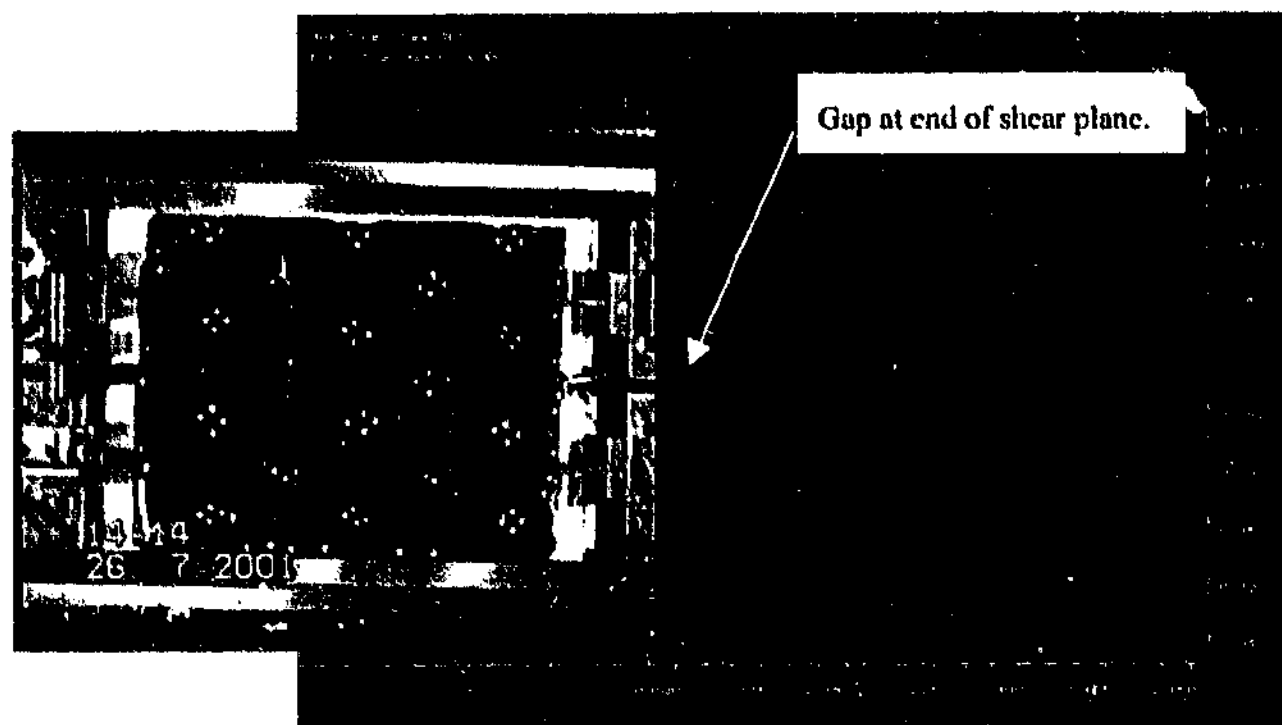


Figure 8-2: Comparison between model and test sample geometry (Test B4).

The UDEC model has been developed for a rock mass 400 mm long by 300 mm high, with a void of 10 mm at either end of the shear plane, as shown in Figure 8-2. UDEC is a two dimensional program that treats the model as being in plane strain, with an out-of-plane thickness of 1 unit.

In the UDEC model, the confinement provided by the shear box was modelled by an outer steel layer 20 mm thick. Two 10 mm gaps on the shear plane at either end of the shear box were established to separate the top and bottom halves of the shear box. The encapsulating plaster was not modelled separately, but was included as part of the rock mass. The top and side plates of the shear box were not explicitly modelled, but can be considered to be part of the shear box.

The rock mass is confined within the shear box. Each of the joint sets in the numerical model originates at the left hand end of the shear plane. This reflects the positioning of the joints cut into the laboratory sample. The joints have been inclined at the same angle as measured in the laboratory test, with a variability of $\pm 0.5^\circ$. The joint spacing has been set to that recorded in the test, but with a variability of ± 2 mm. This reflects the accuracy with which joints could be cut into the test samples.

8.2.2 Material and joint constitutive models and properties

The values for the various intact rock and joint parameters were obtained from standard laboratory tests carried out as part of the testing program described in Chapter 4. Table 8-1 lists the parameter values adopted in the numerical models.

Table 8-1: Material properties used in the UDEC model.

PROPERTY	STEEL	JOHNSTONE (REGULAR) (12%<m/c<17%)	JOHNSTONE (SOFT) (18%<m/c<20%)
Tests		B1-B7, B8-B17, B22-B25	B7A, B18-B21, B26-B31
Density	7 800 kg/m ³	2200 kg/m ³	2200 kg/m ³
E_{50}	210 000 MPa	400 MPa	275 MPa
ν	0.3	0.25	0.25
ϕ_i		37°	37°
Cohesion		1.0 MPa	0.6 MPa
Dilation angle		9°	9°
Tensile strength		0.70 MPa	0.35 MPa
Bulk Modulus	175 000 MPa	265 MPa	185 MPa
Shear Modulus	80 000 MPa	160 MPa	110 MPa

The bulk modulus, K , and shear modulus, G , values are used by UDEC. These were calculated from secant modulus (E_{50}) and Poisson's ratio (ν) by:

$$G = \frac{E_{50}}{2(1+\nu)} \tag{Equation 8-1}$$

$$K = \frac{E_{50}}{3(1-2\nu)} \tag{Equation 8-2}$$

The numerical model contains two material types and three joint types. The constitutive models for each are described below.

The shear box is made from steel and was modelled to behave as an isotropic, elastic material. Typical values for the density and Poisson's ratio of the steel were used. The modulus of the steel was doubled in the numerical model to simulate the buttressing of the sides of the shear box and so reduce any deflections in the steel box.

The intact Johnstone was modelled as a Mohr-Coulomb material. The material properties used in the UDEC model are presented in Table 8-1, and have been obtained from the testing described in Chapter 5. The density of the Johnstone was measured from samples used in the rock triaxial testing program. The secant modulus was assessed from the UCS test output. A Poisson's ratio value of 0.25 was chosen, based on laboratory work carried out on Johnstone by Kodikara (1989). The friction angle and cohesion of the Johnstone were obtained from rock triaxial tests and from Choi (1984). The tensile strength was obtained from Brazilian tests.

The three joint types are the rock-rock joints, the steel-steel joints and the interface between the steel and the rock. The joint properties adopted for the UDEC model are presented in Table 8-2.

Table 8-2: Joint properties used in the UDEC models.

PROPERTY	STEEL-STEEL	ROCK JOINTS	ROCK-STEEL
Joint normal stiffness	1 000 000 MPa/m	1 000 MPa/m	1 000 MPa/m
Joint shear stiffness	100 000 MPa/m	100 MPa/m	100 MPa/m
Joint friction angle	28°	27°	28°
Joint cohesion	10 MPa	0 MPa	0 MPa
Joint dilation angle	0°	0°	0°
Joint tensile strength	10 000 MPa	0 MPa	0 MPa

The properties of the rock-rock joints were either obtained during the laboratory testing program or estimated from the compliance test results. The joint friction angle and joint normal stiffness were obtained from laboratory tests. A joint shear stiffness of 10% of the joint normal stiffness was

adopted. This is in general agreement with Kulhawy and Goodman (1980), who found that joint normal stiffness of sedimentary rocks was about two to 10 times the joint shear stiffness. The joint cohesion and tensile strength were known to be zero as there was no joint infill or any significant bonding between the joint surfaces. The steel-rock joints have been given the same properties as the rock-rock joints. The steel-steel joints were given properties so that movement or separation along these joints was precluded.

8.2.3 Boundary conditions

The boundary conditions applied to the numerical model were:

- An initial horizontal stress, $\sigma_{hi}=100$ kPa. In the numerical model, this stress was applied using the "in-situ stress" command. This modelled the inferred initial horizontal stress of 100 kPa that was applied to the sample by the side plates of the shear box prior to each laboratory shear test.
- A typical initial normal (vertical) stress, $\sigma_{ni}=100$ kPa, although some of the tests were carried out with $\sigma_{ni}=50, 200, 300$ or 600 kPa. These were applied using the "boundary stress" command and modelled the consolidation load that was applied to the sample at the start of each laboratory shear test.
- An initial out of plane stress of 300 kPa was applied to the model using the "in-situ szz" command. Plane strain conditions were approximated in the laboratory tests. This caused the out of plane stresses to increase as out of plane movement was suppressed. The out of plane movement of the laboratory sample was restricted by steel plates at the rear and braced 20 mm thick perspex at the front of the sample.
- An applied constant normal stiffness, $k=200$ kPa/mm. This value of normal stiffness was applied in the laboratory shear tests. The normal stiffness in the UDEC model was applied by a FISH function that increases the normal stress on the sample by the increment of:

$$\Delta\sigma_n = k\Delta y$$

Equation 8-3

8.2.3.1 Initial horizontal stress, σ_{hi}

Once the initial horizontal stresses were defined, the UDEC model applied the stress to the sample using either a “solve” or “step” command.

The “solve” command allows the program to carry out enough iterations so that the default out-of-balance force does not exceed 100. The out of balance force is the sum of the forces accumulated at each of the grid points in the deformable blocks in the model. At equilibrium or steady plastic flow, the forces on one side of a grid point nearly balance the opposing force. For the UDEC models of the shear test, equilibrium was assumed when the sum of the out-of-balance forces dropped below 200.

In some cases, it took a large number of cycles to reach equilibrium. In order to expedite computations, a limit was placed on the number of iterations the program could carry out. This is achieved by using the “step” command, followed by the desired maximum number of steps. For this initial stage of the model, the maximum number of steps was set at 10 000. None of the UDEC models based on the laboratory shear tests required 10 000 steps to reduce the out-of-balance force limit to 200 after applying the initial horizontal stress. This occurred because the “in-situ stress” command distributes the nominated stress evenly within the material specified, in this case, through the Johnstone.

8.2.3.2 Initial normal stress, σ_{ni}

Once the horizontal stress had been applied in the UDEC model, the initial normal stress was applied and the model again allowed to step towards equilibrium. This took longer to achieve because of the uneven vertical stress distribution through the model and the nature of the application of stresses by UDEC.

The initial normal stress was applied to the top of the shear box, as occurred in the laboratory test. However, as UDEC applies the stress instantaneously, the model loads, deforms, rebounds and deforms again. Damping within the model attenuates the amplitude of this process with time until the out-of-balance force measured in the sample reaches a point considered to be equilibrium. This external application of stress requires more steps to reach a more evenly distributed stress within the model and low out-of-balance forces. UDEC can plot the history of the out-of-balance forces.

The history plot showing the unbalanced force for Test B4 during application of the initial normal stress is shown in Figure 8-3.

Job Title : Test B4
From File : testb4.sav

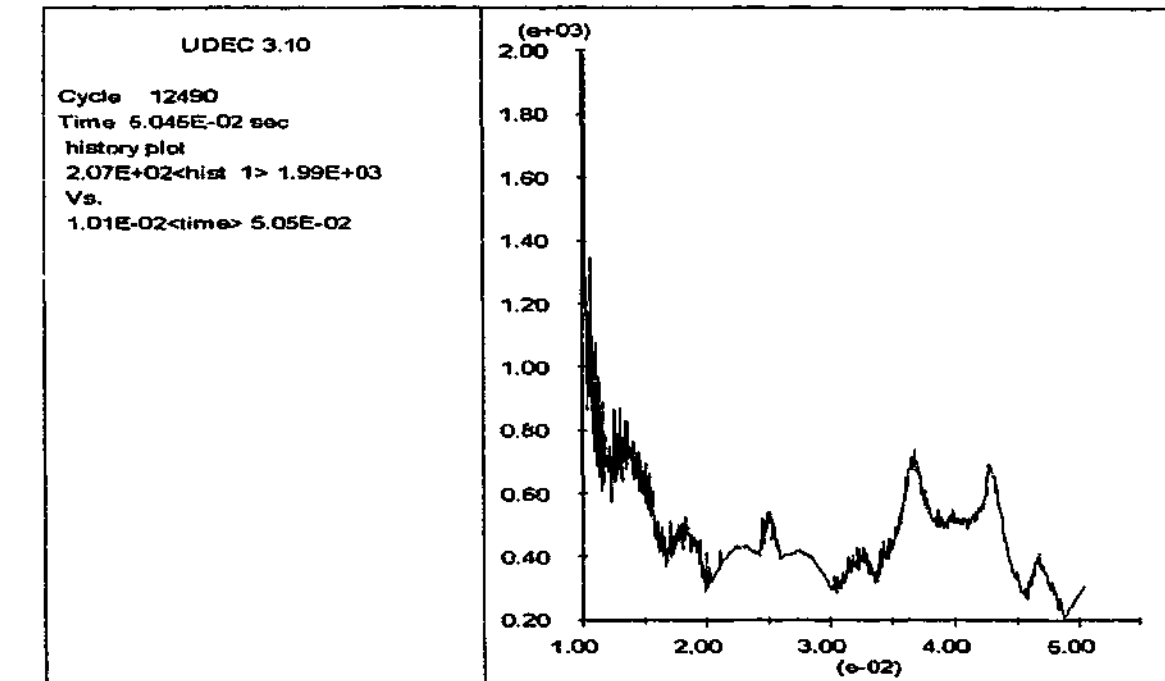


Figure 8-3: Out-of-balance history plot for Test B4.

Figure 8-3 indicates that the magnitude of the unbalanced force attenuated quickly before converging towards a value of about 200. This behaviour was observed in all tests and suggested convergence was occurring. For this stage of the model, equilibrium was considered to be when the sum of the out of balance forces had reached 200 or the model had run for 10 000 steps. The limit of 10 000 steps was reached in all tests, although the history plots of the unbalanced forces for the tests indicated that the out-of-balance forces were close to the 200 limit.

The effect of not achieving equilibrium at this stage on the UDEC results was checked in two cases, illustrated in Figure 8-4 and Figure 8-5. The UDEC outputs for the tests where equilibrium was defined as an out-of-balance force of 100 is represented by the thicker line, while the thinner line represents the UDEC outputs where equilibrium was defined as an out-of-balance force of 200 or 10 000 steps.

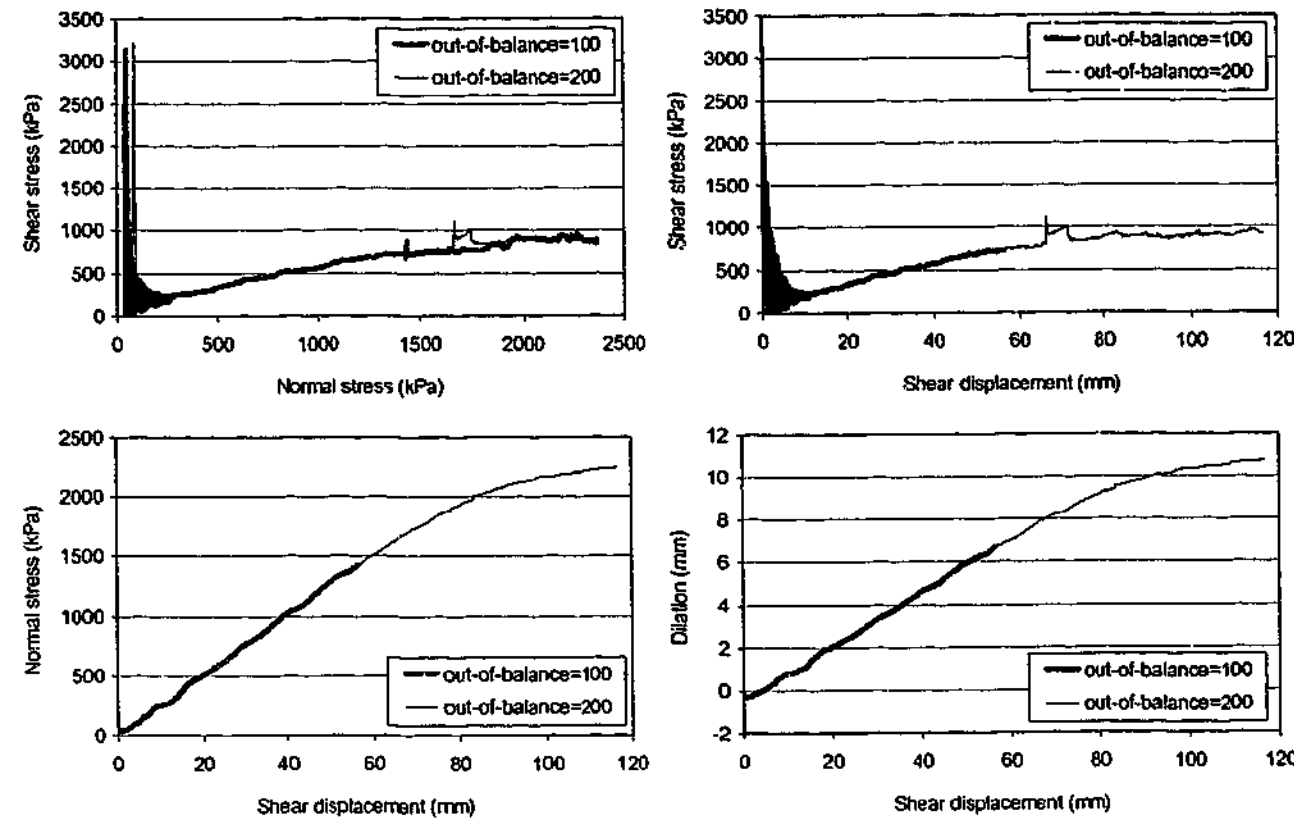


Figure 8-4: Comparison of UDEC outputs for different out-of-balance limits (from Test B7A).

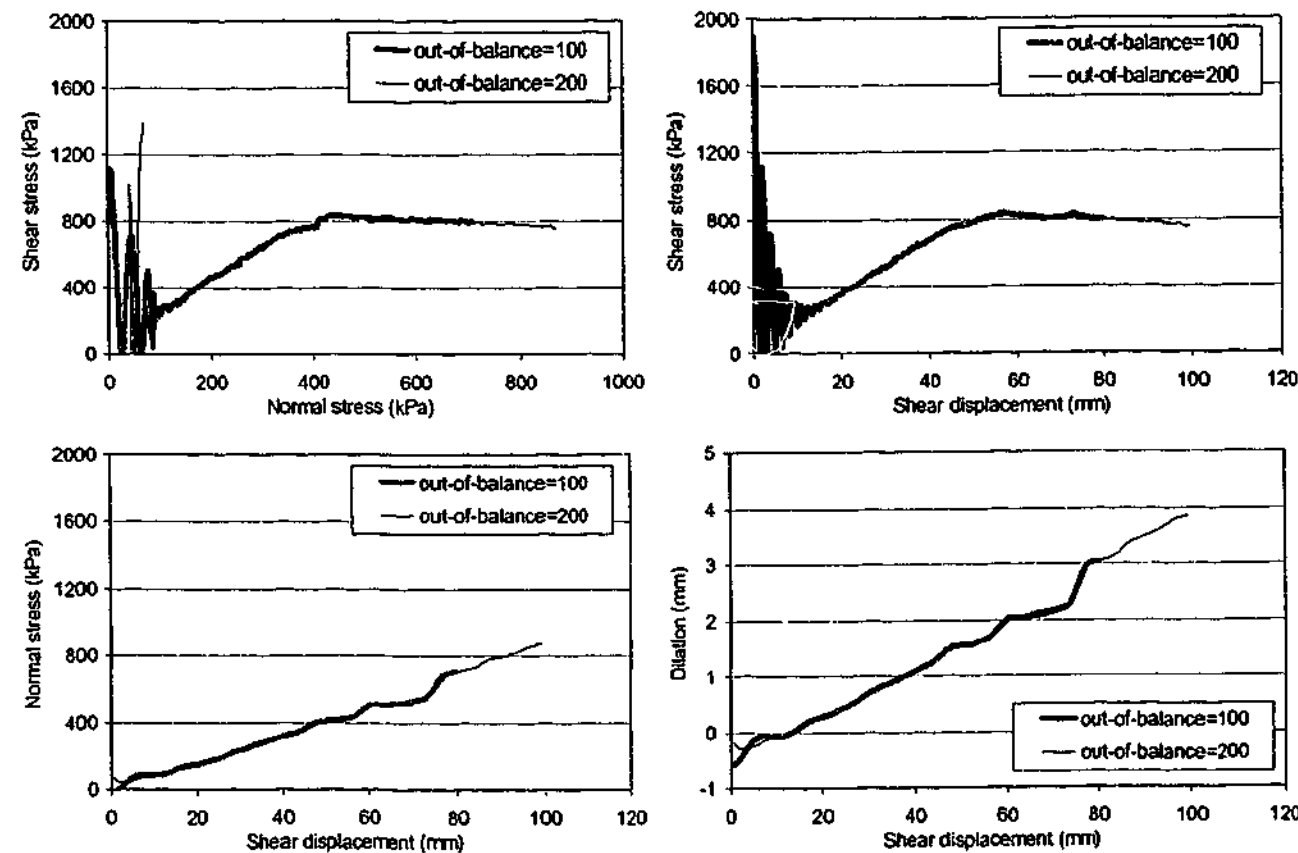


Figure 8-5: Comparison of UDEC outputs for different out-of-balance limits (from Test B6).

The results represented by the thicker line have been truncated so the thinner can be observed. It appears that both outputs are almost identical and implies setting a limit of 10 000 on the number of cycles to shorten the run time of the model did not cause a significant loss of accuracy in the UDEC model calculations.

The oscillations in the shear stress calculated by the UDEC model were the result of the instantaneous application of horizontal velocity to the sample. These oscillations quickly attenuated with damping and became more stable.

8.2.3.3 Horizontal velocity, v_{xel}

Following the application of the initial stresses, a horizontal (x-direction) velocity was applied to the sides of the bottom half of the shear box. The x-direction velocity for deformable blocks was applied using the “boundary v_{xel} ” command. The selection of velocity is a function of the total displacement required and the timestep generated by the software. The timestep, Δt , was derived from:

$$\Delta t = 2 \min\left(\frac{m}{k}\right)^{\frac{1}{2}} \tag{Equation 8-4}$$

where:

- m is the mass of the smallest block in the system, and
- k is the maximum contact stiffness.

This timestep was calculated in computer time, not in real time. The shear velocity was chosen so that the shear displacement obtained from:

$$\Delta x = v \Delta t \tag{Equation 8-5}$$

was similar to the shear displacement observed during laboratory testing. An x-velocity of 0.1 was applied to the model and produced total shear displacements of up to 100 mm.

8.2.4 FISH routines

In the numerical model, FISH functions were written to:

- establish the arrays of gridpoints at which the x- and y-displacements were to be calculated
- calculate average horizontal (x-direction) displacements
- calculate average vertical (y-direction) displacements
- calculate x-direction stresses from which the shear stresses could be derived
- apply constant normal stiffness conditions and
- control the execution of the model

As the philosophy behind the development of the UDEC model was to replicate the laboratory test as closely as possible, the calculation of displacements and stresses was done in much the same way as they were measured during the laboratory tests. The laboratory measurements were made using external LVDT's and load cells connected to the shear box.

For the UDEC model, displacements in both the x- and y-directions were calculated for the shear box rather than for any point in the rock mass. The forces in the y-direction were calculated from the initial normal stress, the amount of dilation and the normal stiffness. The forces in the horizontal direction were calculated by establishing a load cell in the lower left end of the shear box.

The model was executed by a FISH routine that, in turn, stepped through the program, calculated displacements and stresses and applied the increments of normal stress resulting from the normal stiffness. The FISH routines are described below.

8.2.4.1 FISH routines to set up gridpoint arrays

The UDEC model was divided into deformable, triangular zones by the "gen edge" command. Each zone in the model had a centroid. The corners of the zones were the gridpoints. Each of the

gridpoints and zones were given a number by UDEC. It was possible to define a range containing the gridpoints or zones of interest and store the numbers by which UDEC identified them in an array. That way, the stresses or displacements acting on them could be used in calculations. However, as UDEC stepped to equilibrium, the gridpoints and zones could move. This meant that the gridpoint and zone numbers of interest had to be identified and stored in an array before any stepping occurred.

The shear stresses were calculated by turning the inner half of the lower left end of the shear box into a load cell. The FISH routine "LHS_zones" selected the zones whose centroid was located in the inner half of the left hand end of the bottom shear box into zones and stored their identifying number in an array. Figure 8-6 shows how the gridpoints and zones of interest were identified.

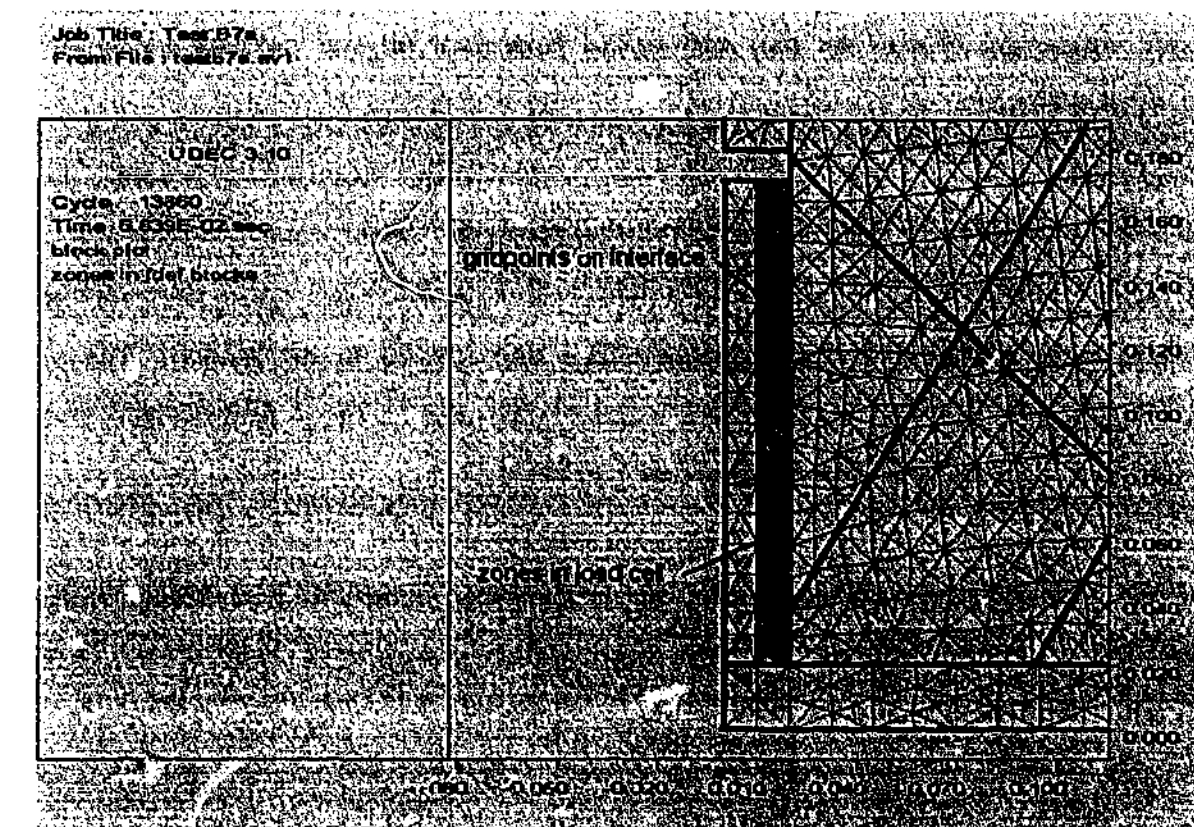


Figure 8-6: Diagram showing zones in load cell and gridpoints on interface.

FISH routines were used to establish three arrays in the code, "top_gridpoints", "side_gridpoints" and "LHS_zones". At each step, UDEC calculated, amongst other things, the displacements at each gridpoint and loads in each zone within the model. Therefore, by identifying the gridpoints and zones of interest within the model, the x and y displacements and shear load could be calculated.

A FISH routine was set up to calculate x-displacements at the left end of the lower shear box. The FISH routine "side_gridpoints" selected the grid points on the interface between the rock and the inside of the steel plate of the lower left hand side of the shear box and stored their identifying numbers in an array.

The y-displacements of the top steel plate of the shear box were recorded. The FISH routine "top_gridpoints" selected the gridpoints that were located on the interface between the bottom face of the top steel plate of the shear box and the rock mass and stored their identifying numbers in an array.

The establishment of these arrays meant the program could track the gridpoint or zone numbers and use the displacements and stresses calculated at these points to derive x-displacement, dilation and shear stress, irrespective of how far they had moved from their original position during the execution of the model.

8.2.4.2 FISH routines to measure displacements and stresses

FISH routines were written to calculate displacements and stresses in the model. The y-displacement was calculated by a FISH routine called "top_disp". The x-displacement was calculated by "side_disp" and the shear stress by "side_stress".

The "top_disp" and "side_disp" routines summed the displacement at each of the gridpoints in the "top_gridpoints" and "side_gridpoints" arrays respectively. An average displacement was calculated by dividing the sum of the displacements of the gridpoints in each array by the number of gridpoints in that array.

The x-direction stress acting in the load cell was calculated by dividing the sum of the x-direction stresses by the number of zones in the load cell. However, the shear stress obtained during laboratory testing was calculated by dividing the measured shear load by the area of the shear plane. In the UDEC model, the shear stress measured in the load cell was converted to a shear load by multiplying the average shear stress by the height of the load cell. The shear stress was then calculated by dividing the shear force by the length of the shear plane. The length of the shear plane was not corrected for shear displacement.

8.2.4.3 FISH routines to apply CNS conditions

The application of CNS conditions required tracking the dilation during shear displacement. The FISH routine "top_array" not only calculated the dilation of the top of the shear box, but also calculated the incremental normal stress to be applied to the sample. The initial normal stress and normal stiffness were specified at the beginning of the routine. As the top of the shear box dilated, the normal stress acting on the sample was calculated by multiplying the calculated dilation by the normal stiffness.

A plot of the relationship between normal stress and dilation for Test B4 is presented in Figure 8-7. It can be seen that a linear relationship exists and the gradient of the output, which represents stiffness, is 200 kPa/mm.

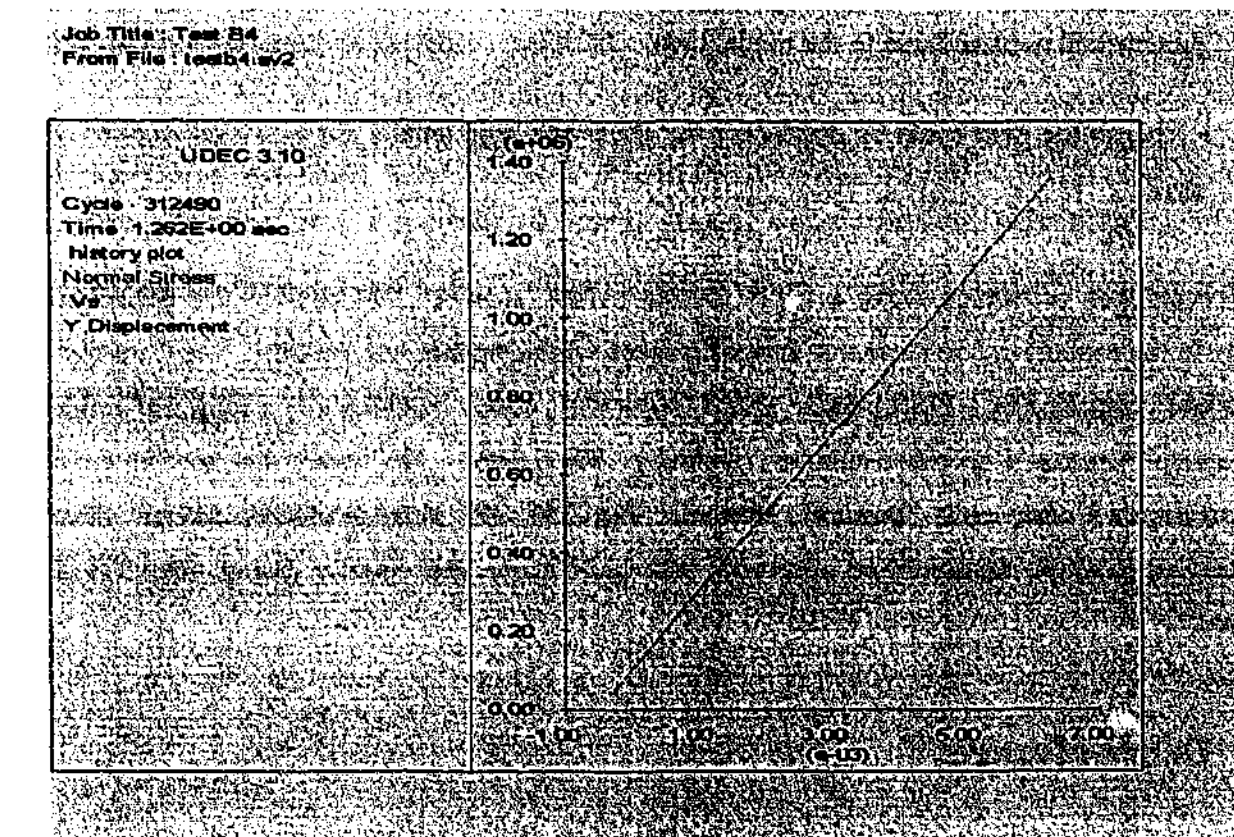


Figure 8-7: Relationship between normal stress and dilation (Test B4).

The change in normal stress resulting from this dilation was not applied to the model automatically. UDEC applies any boundary stress as an incremental stress, not as a total stress. Therefore, the incremental normal stress due to changes in dilation needed to be added to the existing boundary stresses already being applied by the UDEC model.

8.2.4.4 FISH routines controlling the program

The laboratory shear tests were carried out under horizontal displacement control. The UDEC model was designed to do the same. However, any changes in normal stress arising from the constant normal stiffness condition needed to be applied as the horizontal displacement occurred.

The program was therefore controlled by a FISH routine that:

- displaced the lower half of shear box horizontally by an increment dependent on the x-velocity, the timestep and the specified number of steps
- called the FISH routine that calculated x- and y-displacements
- called the FISH routine that calculated incremental normal stress and added the incremental normal stress to the model then
- began the next cycle by displacing the shear box horizontally the specified number of steps

This process was performed using a FISH routine called "supstep" that applied the horizontal velocity to the model for 250 steps and then calculated displacements and stresses. The "supstep" routine was controlled by a FISH routine called "supsolve", which was basically a loop that called the "supstep" function a specified number, (typically 1000), times. This meant that normal stress was incremented after each "supstep" routine. The 250 000 steps produced enough shear displacement to allow failure to be observed, both graphically and visually (using the MOVIE function).

8.2.5 Output of results

The following graphical outputs were obtained from the numerical model:

- shear stress versus normal stress
- shear stress versus shear displacement
- normal stress versus shear displacement and

- dilation versus shear displacement

UDEC has the capacity to track the history of any gridpoint, zone or defined function in the model. The parameters above, being defined FISH routines were recorded as histories. A movie showing plots of displacements and plastic failures every 5000 steps was also made. This meant any failure mechanisms could be visually identified and compared with the laboratory footage. The UDEC MOVIE outputs have been included on a CD in Appendix C. The graphs listed above are shown at the end of the movie for each test.

8.3 Comparison of test and UDEC outputs

Each of the laboratory shear tests was modelled using UDEC. The primary reason for developing the UDEC model was to assess the ability of UDEC to replicate the displacement and failure mechanisms observed in the laboratory tests.

The UDEC model for each test was executed and the peak stresses and x- and y- displacements at failure estimated from the generated output graphs. These outputs were grouped by failure mechanism and/or θ_2 angle. A visual comparison of the mechanisms modelled by UDEC and observed in the laboratory tests was made. A comparison of the ratio of the average UDEC calculations to the laboratory test result was also made and is presented in Table 8-3. The 95% confidence interval, CI, (average \pm one standard deviation) is also presented.

Both the laboratory sample and the UDEC model appeared to exhibit similar pre-peak behaviour. However, post-peak behaviour was poorly modelled by UDEC, as it does not allow slip to occur between zones that have failed and has not been written to handle large strain deformations within the blocks.

Table 8-3: Average ratio of UDEC calculations to laboratory results based on mechanism and θ_2 angle.

mechanism	tests	same visually	Average ratio of UDEC/Test result at failure				
			dx	dy	τ	σ	ϕ_{pp}
Sliding	4	Y	2.6	1.6	0.9	1.4	0.9
Strut ($\theta_2=15^\circ$)	8	Y	3.9	2.4	1.2	1.5	0.8
Block ($\theta_2=30^\circ$)	1	Y	2.9	1.1	1.0	1.4	0.8
Block ($\theta_2=45^\circ$)	7	Y	3.2	1.4	0.8	1.5	0.6
Block ($\theta_2=60^\circ$)	5	Y	2.8	1.7	0.8	1.5	0.6
Block ($\theta_2=75^\circ$)	1	Y	6.0	2.8	1.1	2.2	0.6
Overall	26		3.3	1.8	1.0	1.5	0.7
Std Deviation			1.3	1.1	0.4	0.6	0.2
95% CI			2.0–4.6	0.7–2.9	0.6–1.4	0.9–2.1	0.5–0.9

A comparison of the peak stresses and displacements calculated by the UDEC model and those measured during the laboratory tests indicates that the UDEC model:

- Significantly over-estimated the shear displacement at failure.
- Estimated the peak shear stress reasonably closely.
- Over-estimated the dilation and normal stress at failure.

Comparisons between the laboratory and numerical modelling outputs need to be made with care. The differences between the outputs can occur for a number of reasons.

The main reason is that numerical models assume and apply completely homogeneous properties to the materials in the sample, which in reality, are rarely completely homogeneous. The laboratory sample will always contain flaws and non-homogeneous zones that will affect its behaviour. The

strength of the joints in a laboratory sample will also vary slightly, as will the inclination and spacing of the joint sets. Some variation can be applied to the geometry of the joint sets in UDEC, but the numerical model will only be a simplified version of the real thing. Even the treatment of the intact rock material using Mohr-Coulomb parameters is an approximation of the actual behaviour.

Another reason is the inability of the numerical model to simulate the failure processes in the intact rock (such as crack initiation and propagation, as discussed earlier). The maintenance of the spatial relationships within the blocks means that even though failure in the zones has occurred, no slip between those zones can occur. This means that displacements may be over estimated by UDEC.

While the limitations discussed above may be true, the usefulness of the numerical modelling should not be understated. The numerical model can be used to confirm the mechanisms within and the overall behaviour of the laboratory sample. They can also be used to examine the effects of changes in sample properties or behaviour once they have been calibrated against observed behaviour. This is probably the greatest asset of numerical modelling.

If the model can be described as a good representation of the laboratory test, it may then be used with guarded confidence as a predictive tool. The model can then replace the need for intensive laboratory testing, or can be used to model parameters that cannot be practically incorporated into a sample.

It is therefore necessary to define what a successful attempt at modelling rock mass behaviour is. For this study, getting UDEC to replicate the pre-peak behaviour and failure mechanisms observed in the laboratory was judged to be confirmation that the use of UDEC was appropriate, given the complexity of the system being modelled and the variability of the laboratory samples.

8.3.1 Pre-Peak and failure behaviour

Video footage of the laboratory tests identified three mechanisms occurring within the samples prior to failure, namely sliding/asperity shear, rotation/strut shear and rotation/block shear. The MOVIE feature in UDEC was used to capture screen plots of failure in the rock masses as shearing occurred. The video footage and the UDEC movies were compared to see if they showed the same

pre-peak behaviour and failure mechanisms. The three mechanisms were observed in both the UDEC and laboratory outputs for each test, as discussed below.

8.3.1.1 Sliding / asperity shear

The video footage of the tests where sliding followed by asperity shear was the failure mechanism showed that sliding occurred along the θ_1 joint set until failure by asperity shear occurred. A comparison between the test footage and the UDEC movie of a test where sliding was observed, Test B1, is shown in Figure 8-8. Both images show that sliding has occurred along the θ_1 joint set closest to the shear plane.

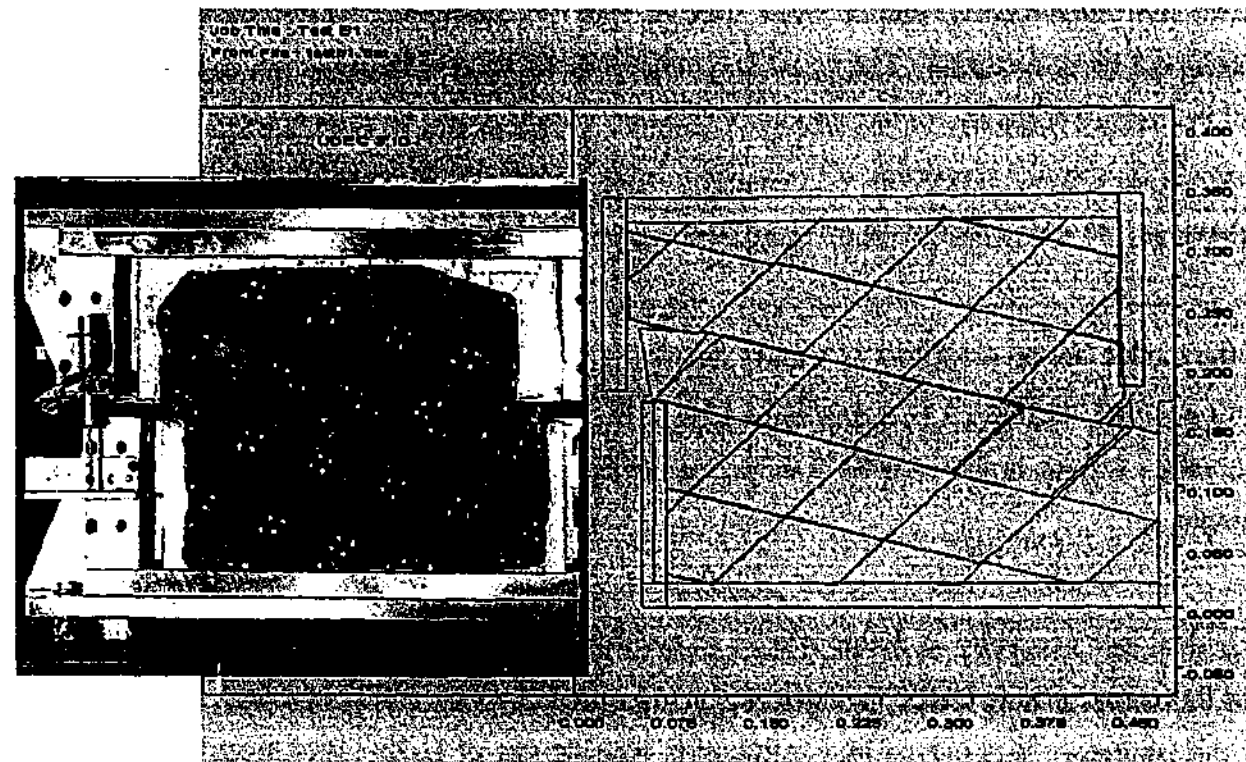


Figure 8-8: Pre-peak behaviour of sample and UDEC model (Test B1).

As the shear displacement increased, shearing through the blocks at the ends of the shear plane began, followed by the development of a shear plane. The UDEC movie exhibits a similar failure process, although the shear band is wider than that observed in the laboratory test.

The calculated UDEC output has been compared to the test results in Figure 8-9. The thicker lines represent the laboratory test results.

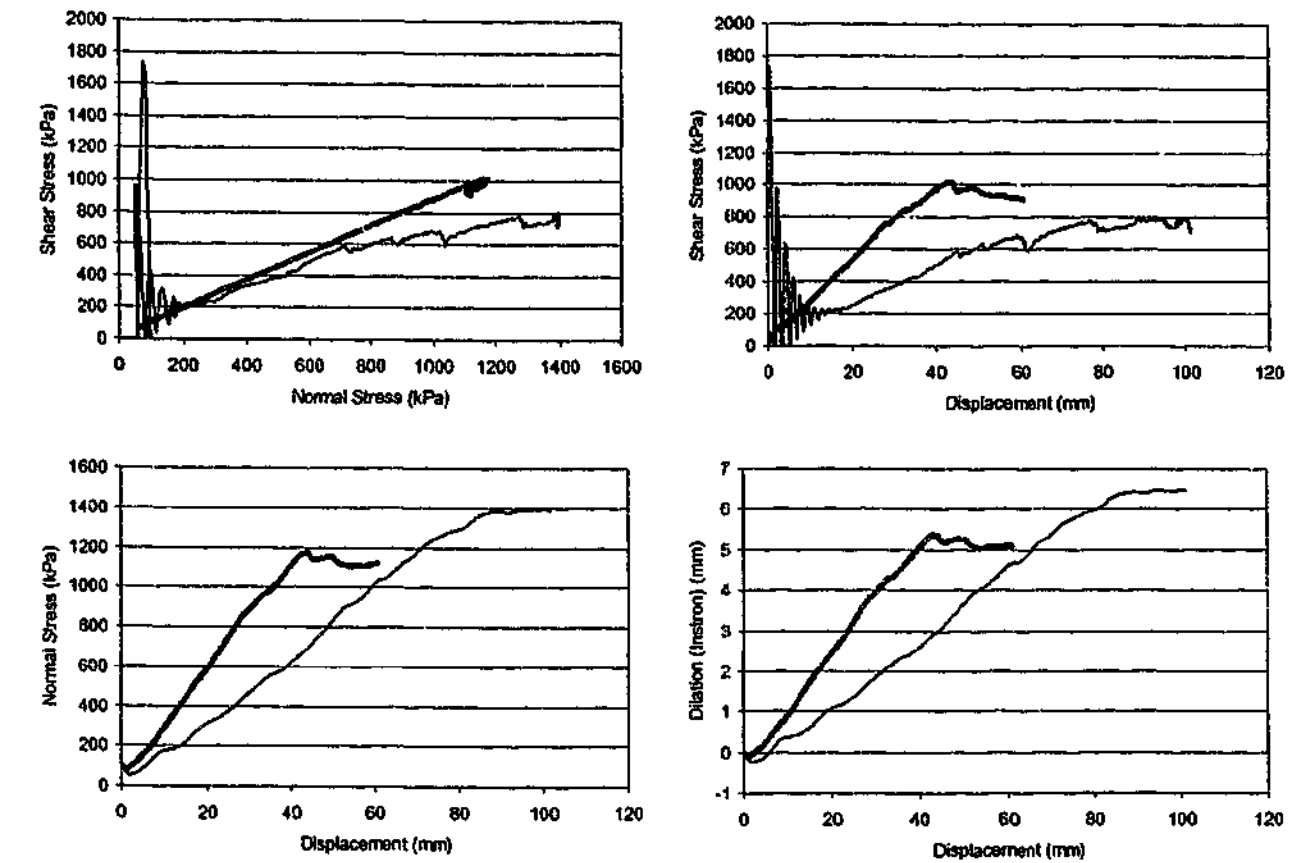


Figure 8-9: Comparison of test results and UDEC output for sliding/asperity shear mechanism (Test B1)

Figure 8-9 shows that at the commencement of shear, the shear stress calculated by the UDEC model oscillates as the out-of-balance forces head towards equilibrium. This is the result of the instantaneous application of velocity to the sample. Once this oscillation has stabilised, there is a reasonable similarity between the τ - σ responses of the test results and the UDEC model.

The selection of the stresses at which the UDEC model has failed may not be obvious. In Figure 8-9, failure of the “UDEC sample” appears to begin when shear stress is about 600 kPa and displacement is about 45 mm. The graphs of normal stress and dilation do not show any obvious signs that failure has begun. The shear stress increases to about 800 kPa at a displacement of about 75 mm after which there is no further increase in shear stress. It is at this point that global failure is judged to have occurred. The calculated dilation at failure was about 6 mm.

The gradual increase in shear stress after 600 kPa may be due to the progressive failure being simulated by the UDEC model. The UDEC movie output for this test (see Appendix C) shows a number of zones yielding during this period. The UDEC MOVIE output when displacement is

about 45 mm is shown in Figure 8-10, where failure within some of the intact blocks can be observed.

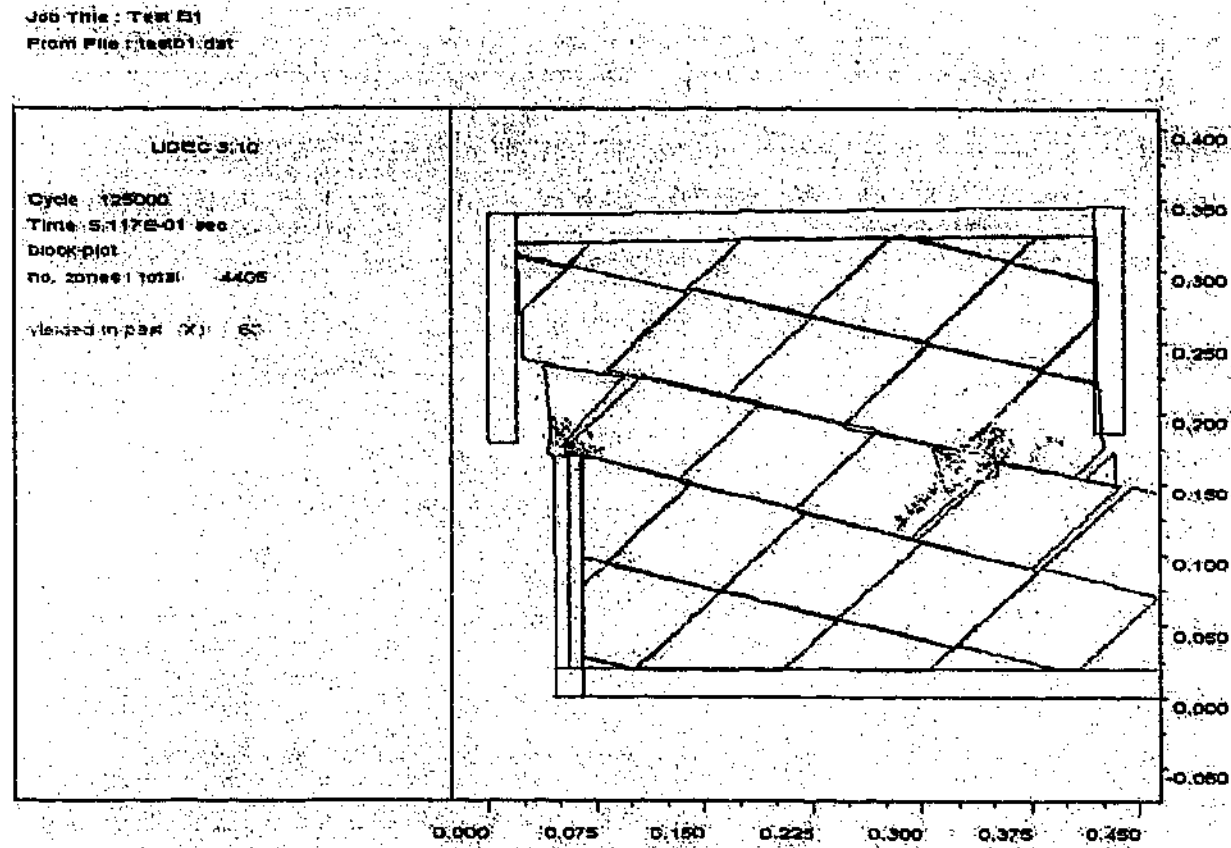


Figure 8-10: UDEC output when shear displacement is about 45 mm (Test B1).

Failure of the sample was assumed by the development of a contiguous failure band adjacent to the shear plane. Figure 8-11 shows the UDEC output when the displacement is about 75 mm, where failure through the sample and the elastic deformation of the intact rock pieces can be observed.

Job Title: Test B1
From File: TestB1.dat

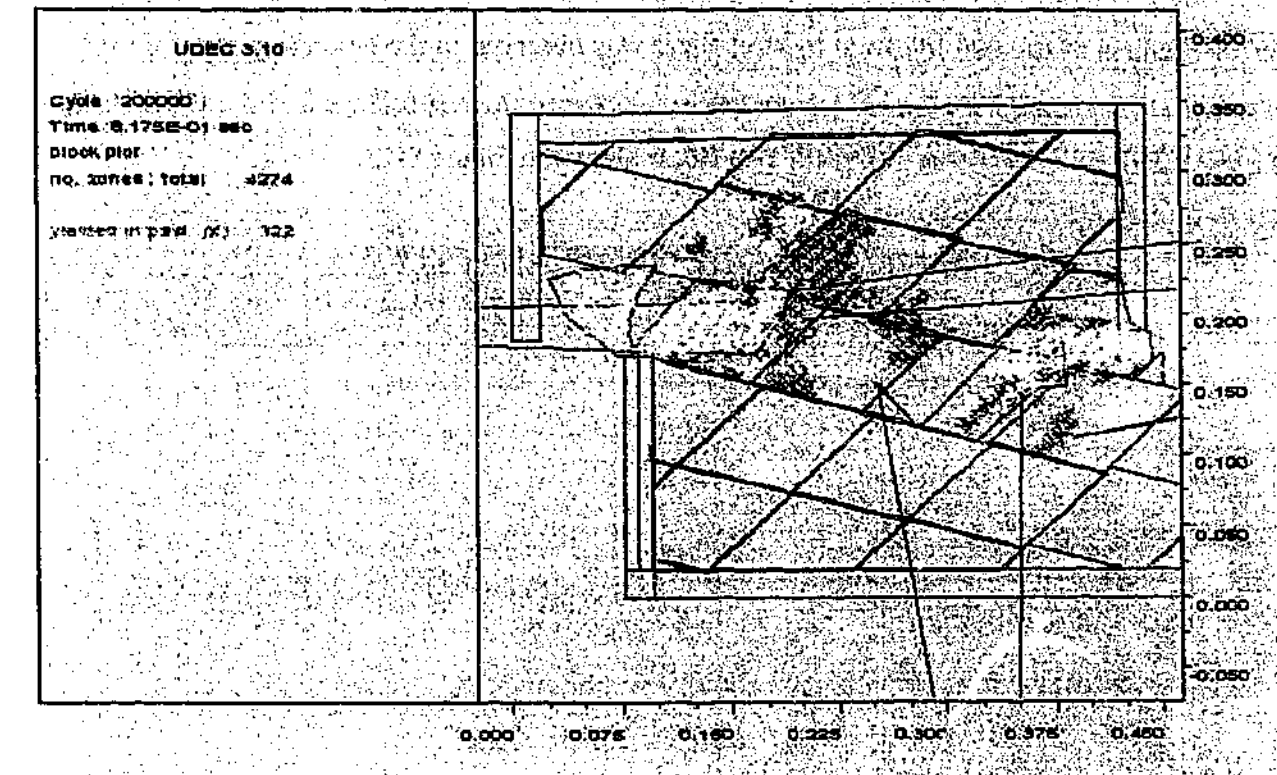


Figure 8-11: UDEC output when shear displacement is about 75 mm (Test B1).

The peak shear stress calculated by UDEC of about 800 kPa is less than the 1000 kPa measured in the test. The displacement at failure, judged to be about 75 mm is significantly greater than the 42 mm measured in the test.

From, Table 8-3, the UDEC model for sliding, on average, predicts peak shear strength within 10%, while the shear displacement is nearly two and a half times that observed in the tests. The dilation and normal stress at failure are over predicted by 60% and 40% respectively. The angle of the τ - σ plot, ϕ_{pp} , prior to reaching peak is slightly under predicted as a result of the higher normal stress, but is still within 10%. Therefore, the UDEC model of samples that failed by sliding replicated the mechanism and the peak shear stress, but did not accurately replicate the peak normal stress and the displacement and dilation at failure measured in the laboratory tests.

8.3.1.2 Rotation / strut shear

The mechanism of rotation followed by strut shear was observed in the laboratory tests of samples with 2 or 3 joint sets where $\theta_2=15^\circ$. A comparison between the test footage and the UDEC movie of a test where strut shear was observed, Test B6, is shown in Figure 8-12.

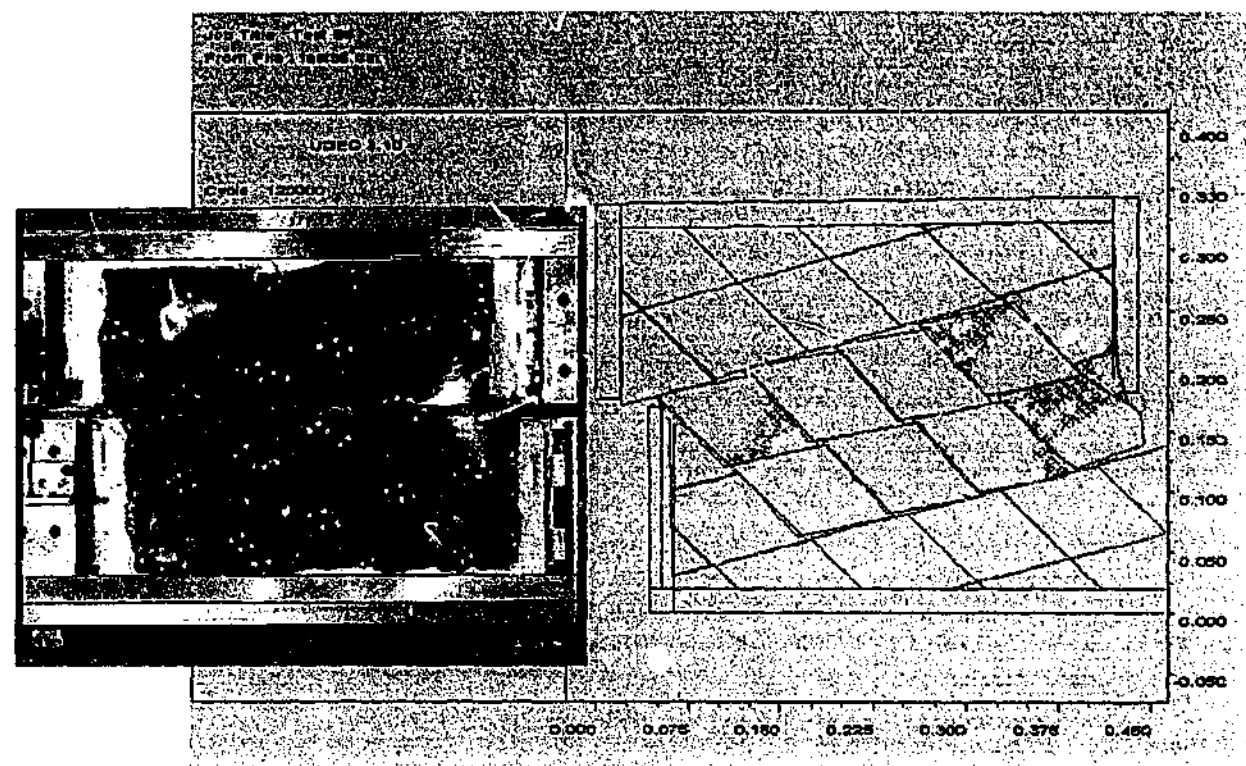


Figure 8-12: Pre-peak behaviour of sample and UDEC model (Test B6).

For the tests of the samples with two joint sets and where $\theta_2=15^\circ$, (Tests B6 and E30), the UDEC movie shows no sliding on the θ_1 joint set and the majority of the failure occurring in the strut between the lower left and top right ends of the shear box, as shown in Figure 8-12. This indicates that the strut is resisting most of the shear load. The tests on samples containing three joint sets also indicate that most of the load is resisted by this strut action.

The calculated UDEC outputs have been compared to the measured laboratory test results in Figure 8-13. The thicker lines represent the laboratory test results.

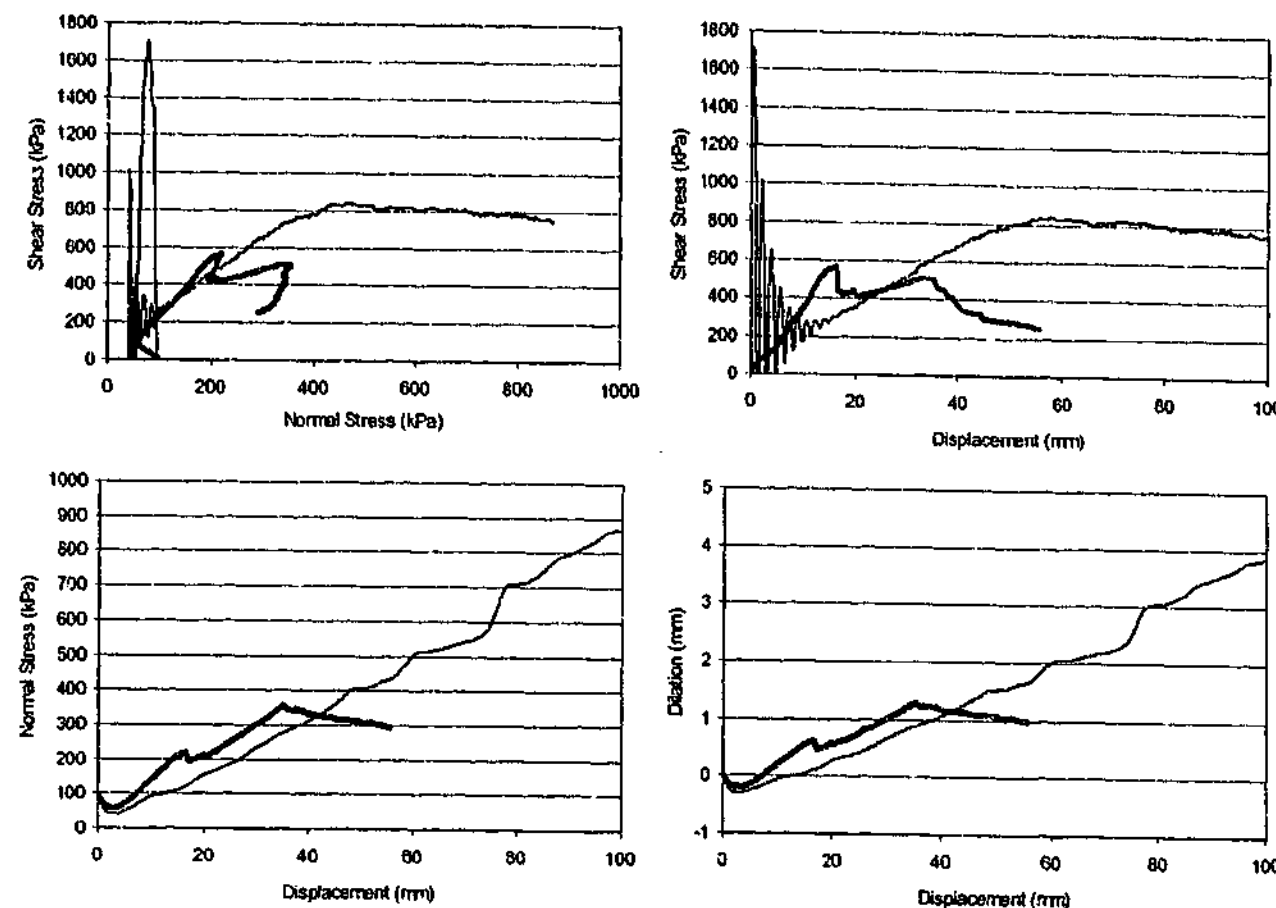


Figure 8-13: Comparison of test results and UDEC output for rotation/strut shear mechanism (Test B6).

Figure 8-13 shows that for the rotation/strut shear mechanism, UDEC appears to over estimate the peak stresses, displacement and dilation. The UDEC model appears to fail at a shear stress of about 810 kPa at a displacement of about 55 mm and a dilation of about 1.7 mm. The test results showed peak shear stress to be about 590 kPa at a displacement of about 15 mm, and a dilation of 0.6 mm. This dilation is lower than the dilation at failure of sample modelled in Test B1, which was about 6 mm. This reflects the relative dilational behaviour of the two mechanisms.

It is of interest that the dilation at failure calculated by the UDEC model is nearly three times that observed in the test. However, the difference between the two results is less than 1 mm (over a sample height of 300 mm).

From Table 8-3, the UDEC model for strut shear, on average, over estimates peak shear strength by 20%, while the calculated shear displacement at failure is up to four times that actually observed. The average dilation at failure is over estimated by a factor of 2.4, while normal stress at failure is over estimated by 50%. The average angle of ϕ_{pp} prior to reaching peak is slightly under estimated

as a result of the higher normal stress, but is still within 20%. Therefore, the UDEC model of samples that failed by strut shear replicated the mechanism and the peak shear stress, but did not otherwise produce similar numbers to those measured in the laboratory tests.

8.3.1.3 Rotation / block shear

Rotation followed by block shear was the failure mechanism observed in the remainder of the laboratory tests. Block shear involves the rotation of a block defined by θ_2 and the ends of the shear plane. A comparison between the test footage and the UDEC movie of a test where block shear was observed, Test B7A, is shown in Figure 8-14.

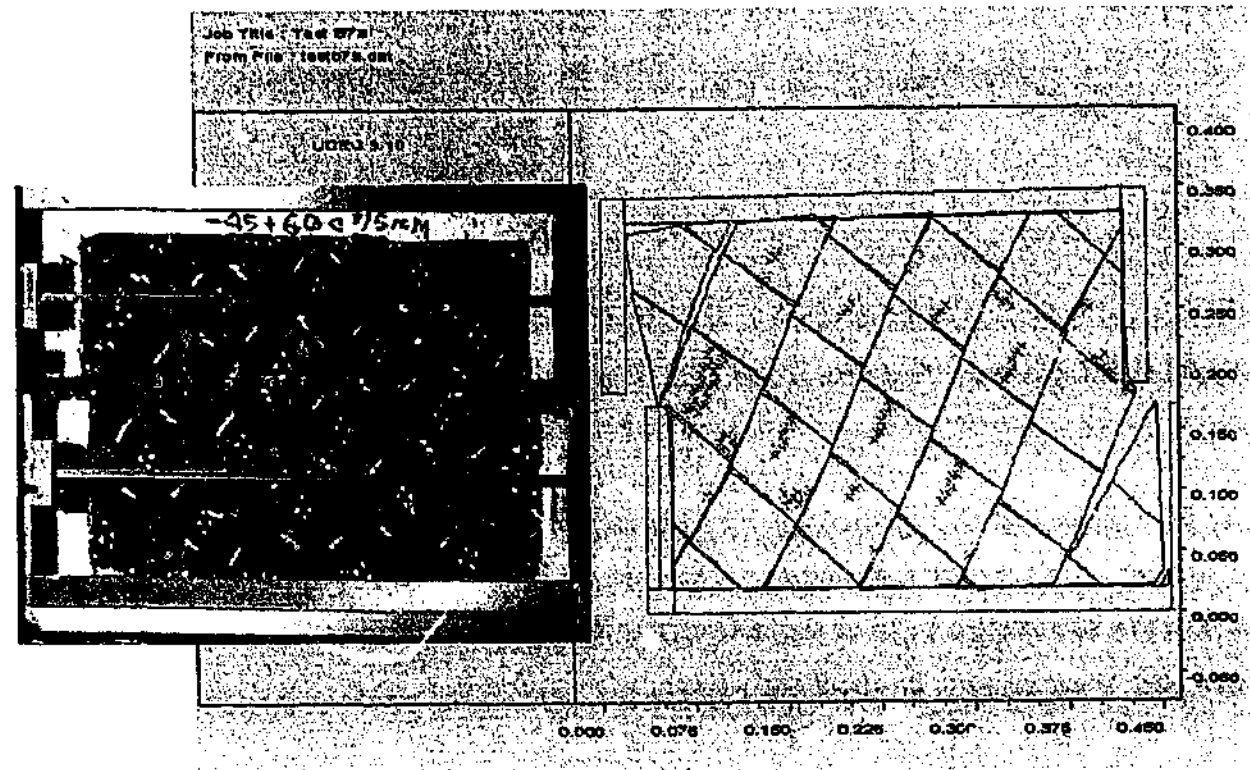


Figure 8-14: Pre-peak behaviour of sample and UDEC model (Test B7A).

It can be seen in both cases that the block rotates initially, so that the increase in normal stress causes the outer blocks to fail in tension. This is followed by the formation of a shear plane. Rotation of the block is evident and failure can be observed in the outer struts forming the block.

The calculated UDEC outputs have been compared to the measured laboratory test results in Figure 8-15. The thicker lines represent the laboratory test results.

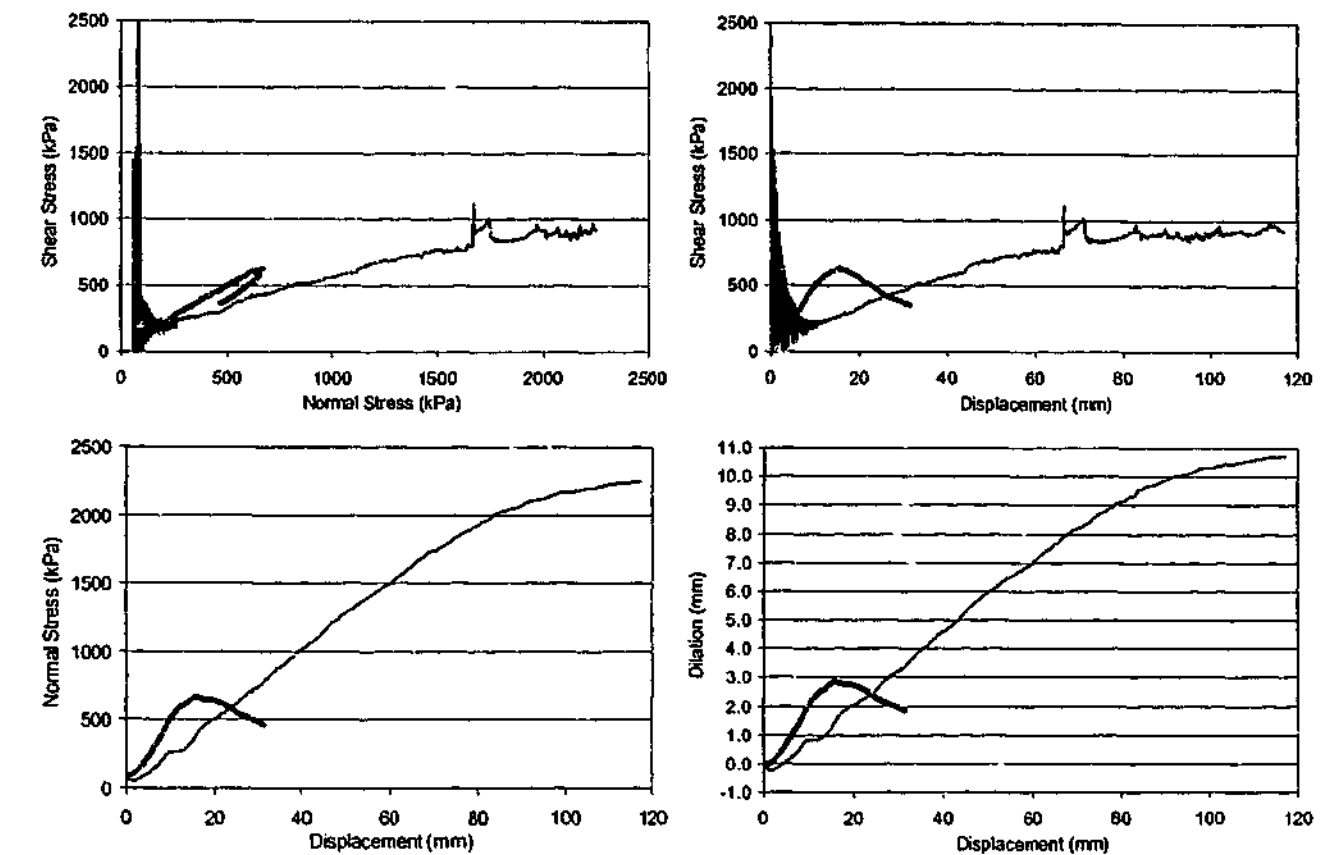


Figure 8-15: Comparison of test results and UDEC output for rotation/block shear mechanism (Test B7A)

Figure 8-15 shows that for Test B7A, where rotation/block shear was observed, UDEC estimates a peak shear stress of about 750 kPa at a displacement of 65 mm. This compares with a peak shear stress of about 630 kPa at a displacement of 16 mm measured in the laboratory test.

From Table 8-3, the UDEC model for block shear in rock masses where θ_2 varies between 30° and 60° estimates, on average, peak shear strengths of $\pm 20\%$ of those observed in the laboratory tests. The shear displacement at failure is typically between 3 and 4 times that actually observed, while the average dilation and normal stress at failure are over estimated by between 10% and 70%. The average ϕ_{pp} angle prior to reaching peak is under estimated by about 20 to 40% as a result of the lower shear stress and higher normal stress.

The UDEC model of Test B27 (where $\theta_2=75^\circ$) calculated the peak shear strength within 10%, but over estimated shear displacement, dilation and normal stress at failure by a significant amount.

These results suggest that, on average, the UDEC model replicated the pre-peak mechanisms and estimated the average peak shear stresses to typically within $\pm 40\%$, but did not produce similar values of peak normal stress and shear displacement and dilation at failure to those measured in the laboratory tests.

8.4 Overall predictions

The UDEC model has been used to calculate the behaviour of jointed rock masses undergoing direct shear. The peak shear stress and dilation behaviour of the rock masses are of most interest. Graphs comparing the UDEC output of normalised peak shear strength and dilation at failure with the laboratory results are shown in Figure 8-16 and Figure 8-17.

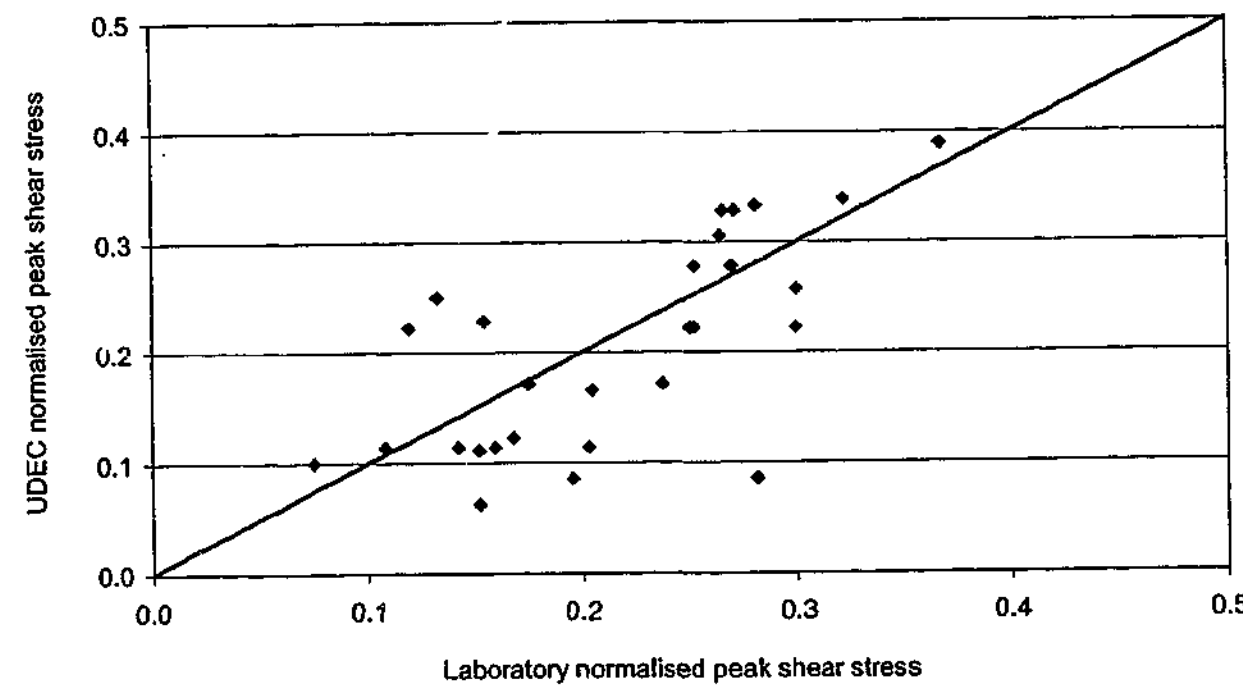


Figure 8-16: Comparison of UDEC prediction of normalised peak shear strength with test results.

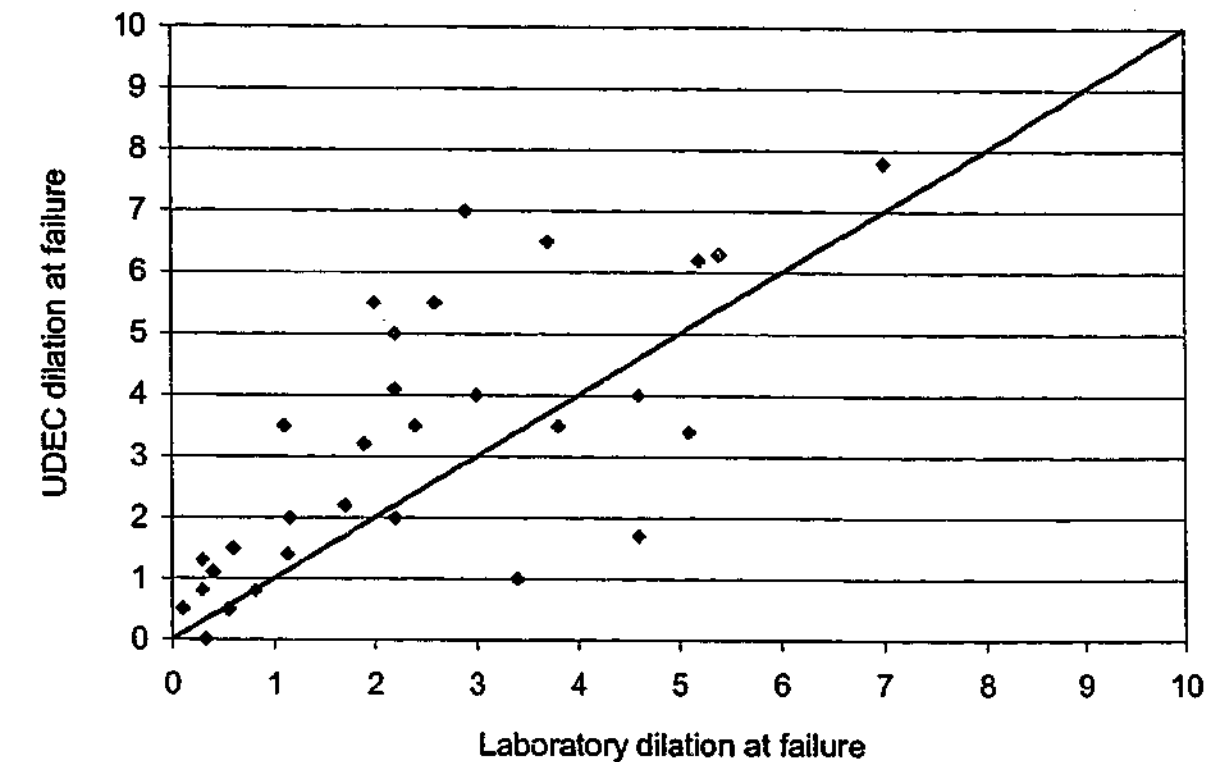


Figure 8-17: Comparison of UDEC prediction of dilation at failure with test results.

It can be seen that the normalised shear strength at failure estimated using UDEC correlates reasonably well with the observed laboratory test results, although there are some outliers. The dilations calculated using UDEC are typically higher than those observed in the laboratory tests.

8.5 Parametric study using UDEC model

The outputs calculated by the UDEC model have been compared to the test results and appear to provide a reasonable simulation of rock mass behaviour. In the following sections, the UDEC model is used to assess rock mass behaviour for a greater range of joint spacings.

8.5.1 Effect of joint spacing

The laboratory testing program included tests on rock masses that were similar in their properties except for joint spacing. Two of these tests, B14 (typical spacing 32 mm) and B5 (typical spacing 70 mm) have been modelled using UDEC. Further tests have been run using the UDEC model, with joint spacings of 25 mm, 50 mm and 90 mm. The peak stresses calculated by these models have been normalised by an assumed UCS=3.0 MPa. The normalised peak stresses and

displacements at failure estimated using UDEC have been compared, where possible, with those measured in the laboratory shear tests in Table 8-4.

Table 8-4: Comparison of laboratory and UDEC normalised peak stresses and displacements.

Test	spacing	LAB				UDEC			
		dx	dy	$\bar{\tau}$	$\bar{\sigma}$	dx	dy	$\bar{\tau}$	$\bar{\sigma}$
B5-25	25 mm	-	-	-	-	45	2.5	0.10	0.20
B14	32 mm	19	3.0	0.17	0.16	53	3.8	0.16	0.29
B5-50	50 mm	-	-	-	-	58	5.5	0.21	0.40
B5	70 mm	20	3.7	0.30	0.24	73	7.7	0.34	0.55
B5-90	90 mm	-	-	-	-	54	6.8	0.34	0.49

The laboratory tests indicated that as the spacing increased, so too did the normalised peak shear stress. They also show the increase in normalised peak shear stress to be about the same proportion as the increase in spacing. The calculated UDEC output also shows a trend that as joint spacing increases, the normalised peak shear strength also increases.

Comparisons of the UDEC outputs for the samples with different joint spacings are presented in Figure 8-18 and Figure 8-19.

The movies generated by UDEC for the tests where spacing was varied are presented on the CD in Appendix C, in the UDEC Spacing Output directory.

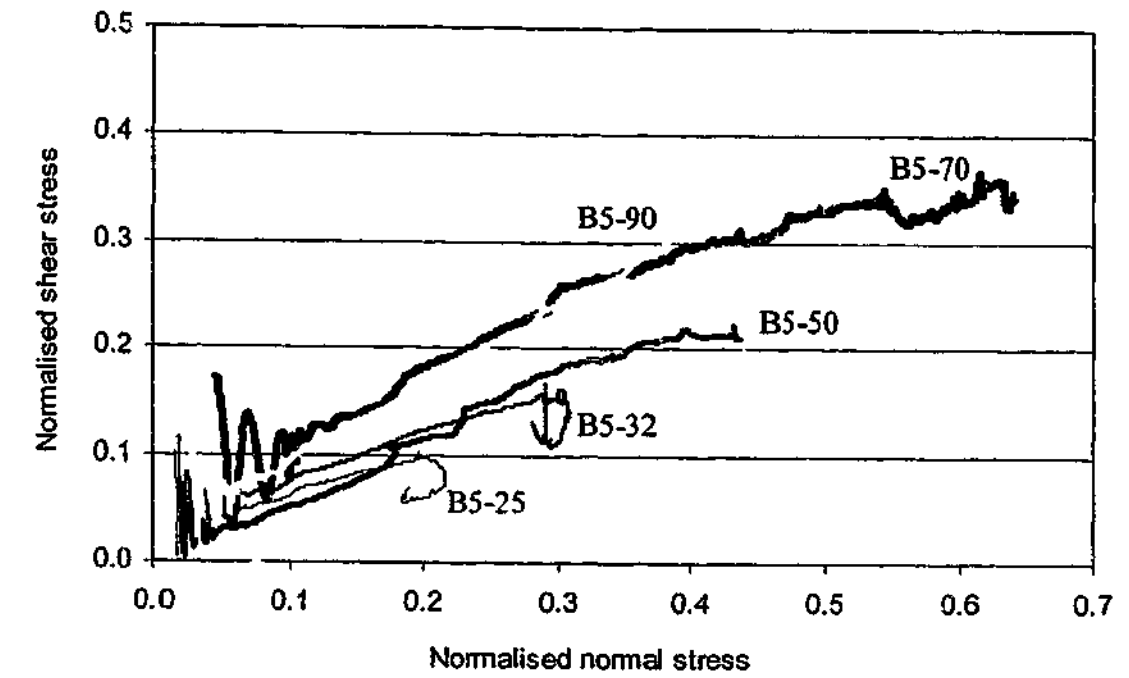


Figure 8-18: τ - σ response calculated by UDEC for samples with different joint spacing.

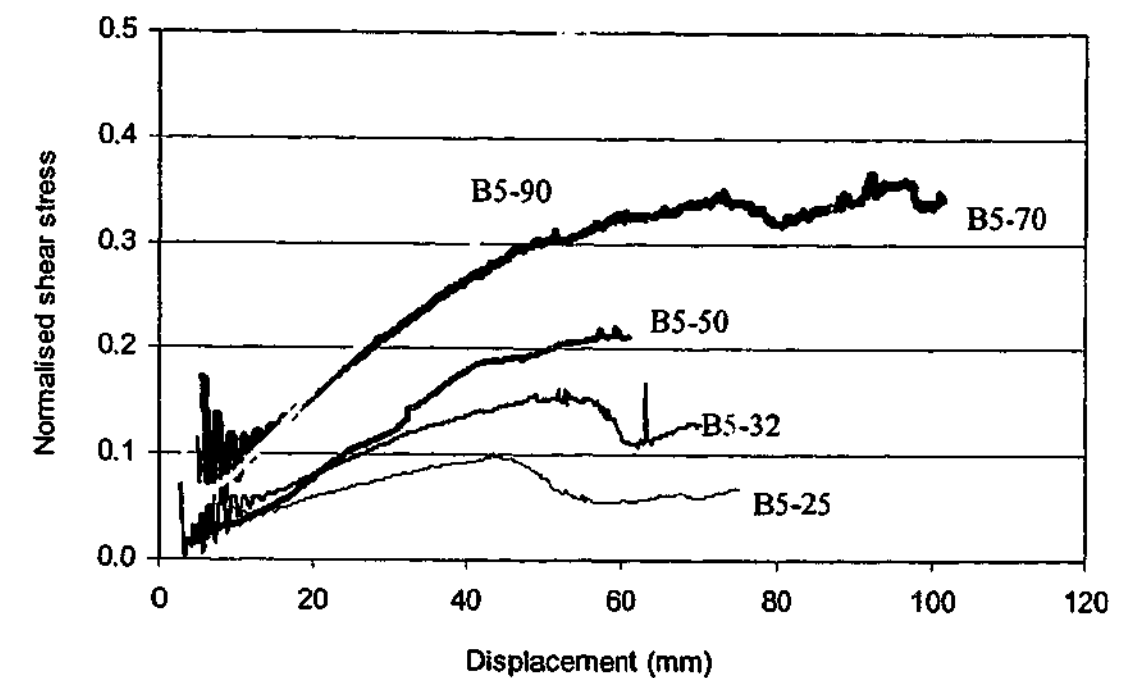


Figure 8-19: Normalised shear stress versus shear displacement response calculated by UDEC for samples with different joint spacing.

Figure 8-18 and Figure 8-19 show that the normalised shear stress increases as joint spacing increases. However, the responses for the samples with joint spacings of 70 mm and 90 mm are similar. This suggests that, for the size of the Type “B” samples, the influence of joint spacing may become similar once joint spacing exceeds about 70 mm.

8.6 Extrapolation of UDEC model to hard rock masses

The UDEC model was also used to model direct shear tests of hard rock masses by adopting intact rock and rock joint properties that may be appropriate for fresh granite. The steel shear box has also been strengthened to reduce deformation of the shear box. This simulation was run to assess whether the pre-peak and failure mechanisms observed in soft rock masses could also occur within hard rock masses. This simulation may also provide an indication of the peak stresses and displacements resulting when hard rock masses of a similar scale are subjected to direct shear.

The intact rock parameters used in the UDEC models of hard rock masses are presented in Table 8-5 and the joint parameters adopted are presented in Table 8-6.

Table 8-5: Material properties used in the UDEC models of hard rock masses.

PROPERTY	STEEL	GRANITE
Density	7 800 kg/m ³	2 500 kg/m ³
E_{sec}	210 000 MPa	60 000 MPa
ν	0.3	0.25
Bulk modulus	330 000 MPa	44 000 MPa
Shear modulus	155 000 MPa	30 000 MPa
Friction angle	-	50°
Cohesion	-	36 MPa
Dilation angle	-	2°
Tensile strength	-	12 MPa

Table 8-6: Joint properties used in the UDEC models of hard rock masses.

PROPERTY	STEEL-STEEL	ROCK-ROCK	ROCK-STEEL
Joint normal stiffness	950 000 MPa/m	1000 MPa/m	1000 MPa/m
Joint shear stiffness	95 000 MPa/m	100 MPa/m	100 MPa/m
Joint friction angle	35°	35°	35°
Joint cohesion	10 MPa	0 MPa	0 MPa
Joint dilation angle	0°	0°	0°
Joint tensile strength	10 000 MPa	0 MPa	0 MPa

The UDEC model for the hard jointed rock mass was run for 500 000 steps and at a greater horizontal velocity of 0.5.

Comparisons of the laboratory test result and the UDEC response for soft and hard rock masses that fail by sliding/asperity shear (from Test B4) are presented in Figure 8-20 to Figure 8-22.

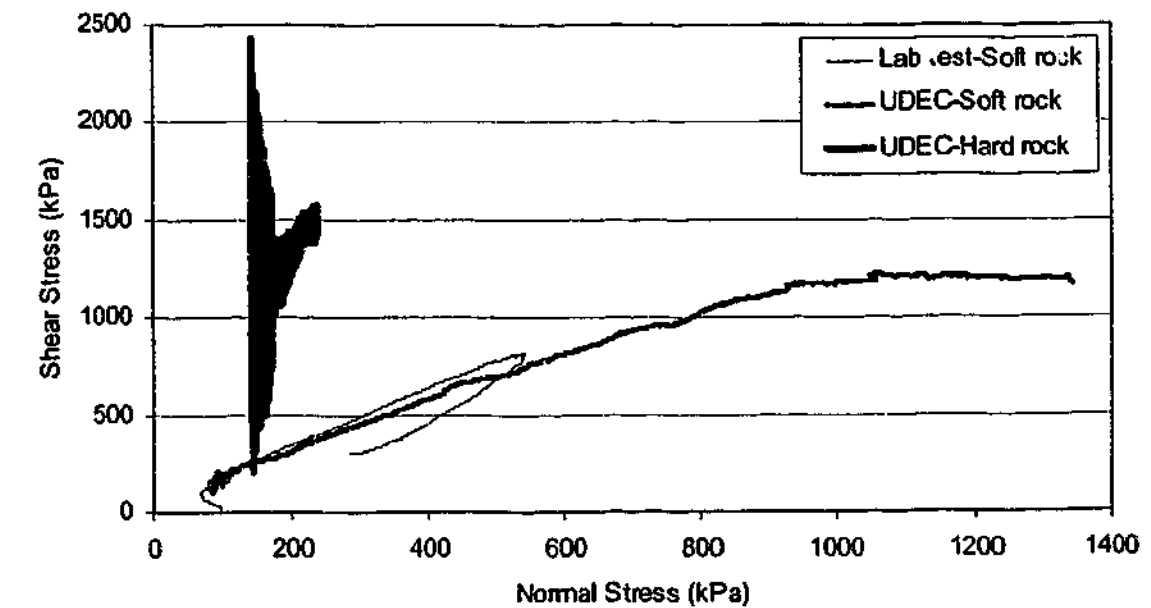


Figure 8-20: Comparison of τ - σ response of hard and soft rock masses.

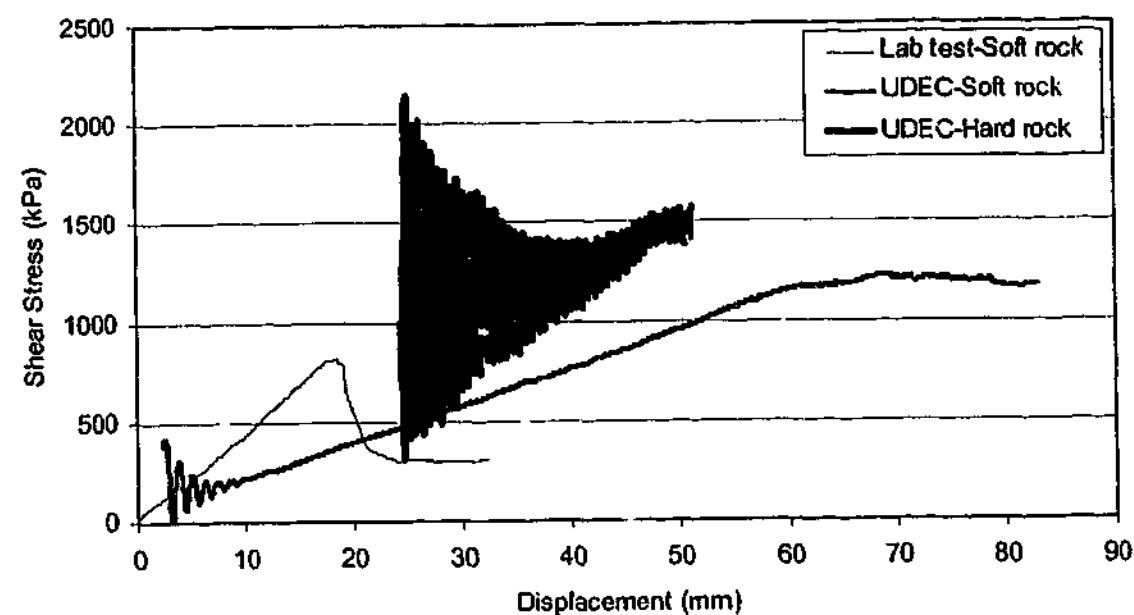


Figure 8-21: Comparison of shear stress versus shear displacement response of hard and soft rock masses.

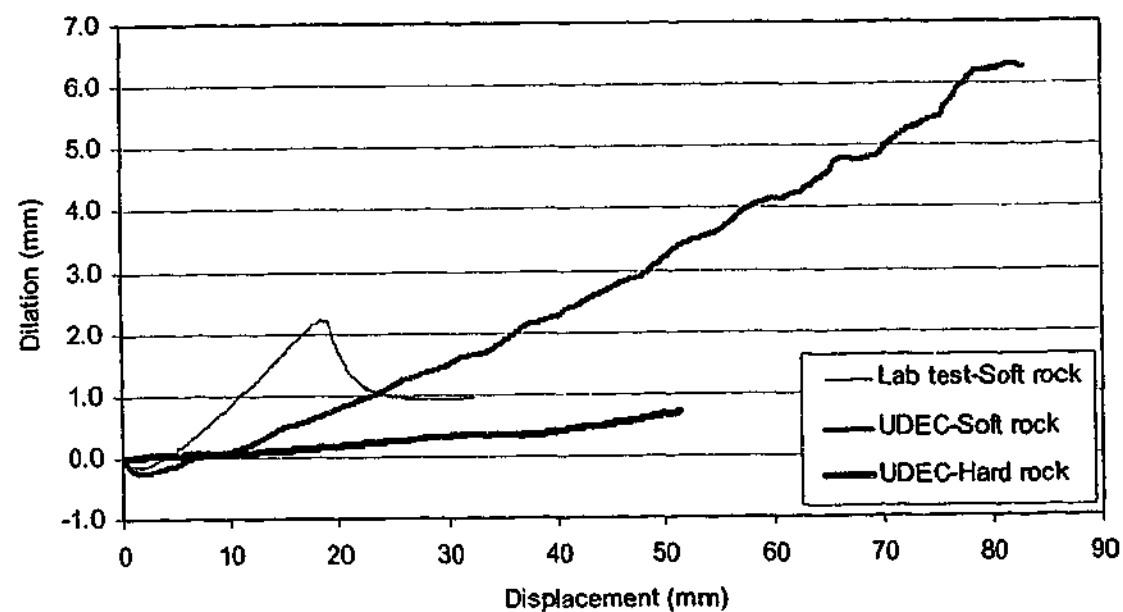


Figure 8-22: Comparison of dilation versus shear displacement response of hard and soft rock masses.

The shear stress of the hard rock mass calculated by UDEC oscillates significantly more than that calculated for the soft rock. This may be a function of the instantaneous nature of external velocity application and the damping characteristics of the hard rock. The peak shear stress of the hard rock mass calculated by the UDEC model is higher than that of the softer rock masses, about double that

measured in the laboratory test and not much higher than that calculated by UDEC for the soft rock mass.

Table 8-7 provides a comparison of the output of the UDEC models for hard and soft jointed rock masses with the results measured from the laboratory testing.

Table 8-7: Comparison of UDEC predictions for soft and hard rock masses.

Pre-peak/failure type	Slidir.g/ asperity shear	Rotation/ strut shear	Rotation/ block shear
Test	B4	B6	B7
Hard rock pre-peak/failure type same as soft rock	Y	Y	Y
Failure τ -hard rock (kPa)	1500	1290	1550
Failure τ -soft rock (kPa)	1200	730	695
Failure τ -laboratory (kPa)	810	570	625
Failure d_y -hard rock (mm)	0.6	0.7	7.6
Failure d_y -soft rock (mm)	4.1	1.2	5.7
Failure d_y -laboratory (mm)	2.2	0.6	2.9
Failure σ -hard rock (kPa)	210	260	1620
Failure σ -soft rock (kPa)	900	350	1160
Failure σ -laboratory (kPa)	540	355	675
Failure d_x -hard rock (mm)	48	71	134
Failure d_x -soft rock (mm)	62	44	48
Failure d_x -laboratory (mm)	18	15	16

Table 8-7 shows that the UDEC model of the hard rock mass calculated greater shear stress at failure. While this was expected, the increase in shear stress at failure was only about two to threefold, despite the significantly higher intact strength of the hard rock.

The larger amount of shear displacement in the hard rock mass prior to failure was unexpected. A stronger (hence stiffer) material would not be expected to deform as much as a weaker material, certainly at the loads calculated in the model. The amount of shear displacement may therefore be affected by the amount of overlap occurring in the model, which would exaggerate the calculated displacement. Consider the output taken from the UDEC MOVIE for Test granblock (based on TestB7) shown in Figure 8-23.

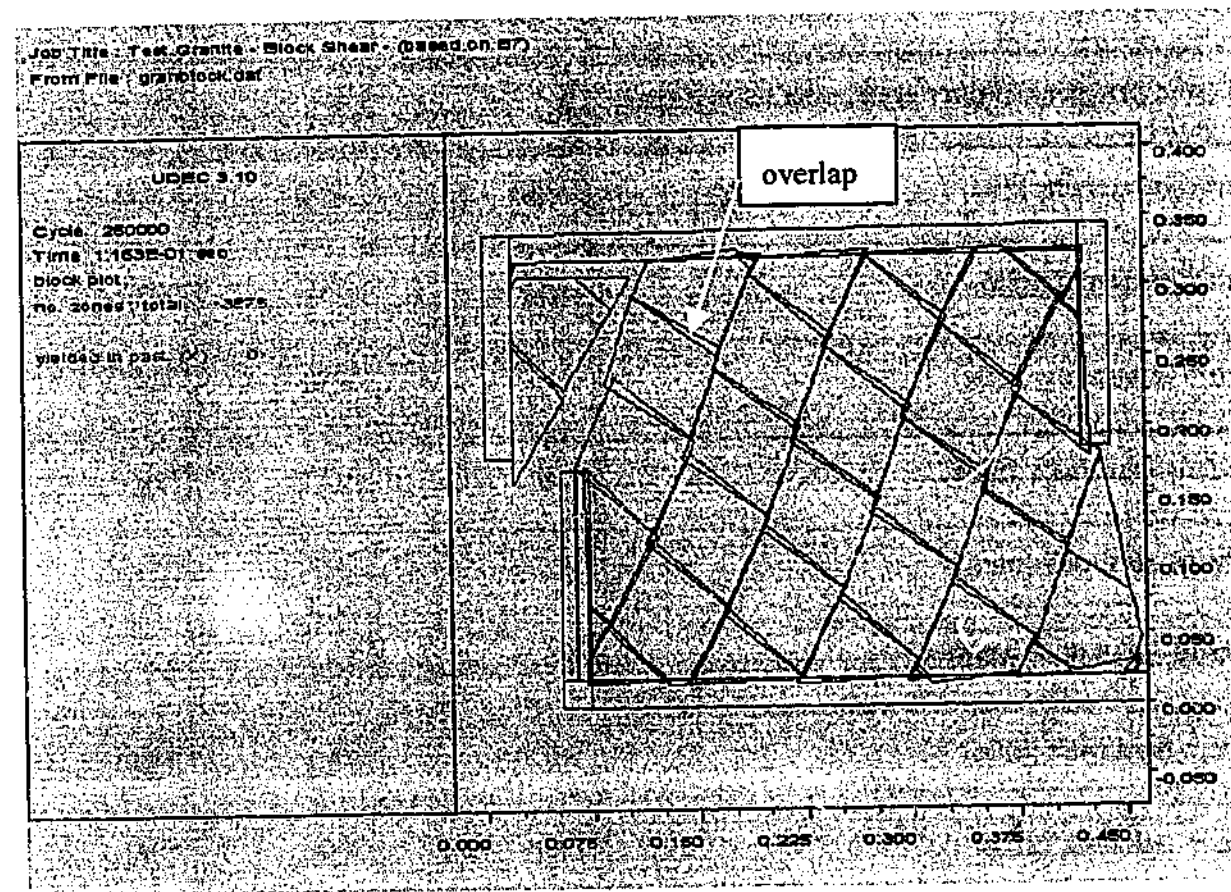


Figure 8-23: Pre-peak behaviour of hard rock mass in UDEC model of Test B7.

Figure 8-23 shows the overlap of the blocks in the hard rock mass. This overlap may increase the amount of shear displacement and decrease the amount of dilation at failure. If the UDEC model was not allowed to overlap to this extent, then the model did not converge to a solution.

The reduced dilation calculated by the hard rock UDEC model may also be the result of the higher modulus and lower value of Poisson's ratio. This reduces the amount of elastic deformation, so

that as the sample is loaded in the horizontal direction, there will be less deformation in the vertical direction than was calculated for the soft rock.

The UDEC movies for the hard rock masses are on the CD in Appendix C, in the UDEC Hard Rock Output directory. The outputs from the UDEC modelling indicate that similar failure mechanisms occur in both the soft and hard rock masses. The UDEC model also confirms that a laboratory direct shear testing program on hard, jointed rock masses of similar scale will require a shear apparatus capable of applying significantly higher loads to a very strong shear box, and may, as such, not be practically feasible.

8.7 Summary

The distinct element code, UDEC, has been used to model the laboratory tests. This modelling was carried out primarily to assess if the UDEC model could replicate the pre-peak behaviour and failure mechanisms observed in laboratory samples subjected to direct shear under CNS conditions. The ability of UDEC to calculate and track the stresses and displacements occurring during the tests was also investigated.

It was found that the UDEC models were capable of replicating the mechanisms observed in the laboratory tests reasonably well. Visually, the pre-peak behaviour of both the laboratory tests and the numerical models was similar for each of the failure mechanisms. Overall, UDEC estimates of peak shear and normal stresses were reasonably close to the measured laboratory values. However, shear displacement and dilation were significantly higher than the measured laboratory values.

The UDEC model has been used to assess the effect of joint spacing on sample behaviour. Overall, the model showed that as joint spacing increased, peak shear strength also increased. The observed pre-peak behaviour within the rock mass was similar, irrespective of the joint spacing.

Rock masses comprising intact rock of much higher strengths have also been modelled, so the effect of high intact rock strength on failure mechanisms and peak stresses and displacements could be observed. It was found that the failure mechanisms were similar, but the magnitudes of the peak shear strength were lower and the shear displacements at peak were higher than anticipated.

As a result of these comparisons, it is the author's opinion that the use of UDEC to model the behaviour of rock masses can be undertaken with a greater degree of confidence. The main reason for this opinion is the demonstrated ability of UDEC to correctly capture the mechanisms occurring within the sample. This suggests that there is a significant potential for better estimates of rock mass strength to be obtained using UDEC, even for very complex problems.

9 SUMMARY AND CONCLUSIONS

This study has investigated the use of direct shear tests to assess the behaviour of rock masses. The results of direct shear tests on samples manufactured from Johnstone have been measured and analysed. A visual recording of the behaviour of the sample has also been made.

9.1 Development of equipment and techniques

A synthetic sedimentary rock called Johnstone was used for the laboratory testing. The rock mass samples were fabricated by cutting joints into the Johnstone blocks, reassembling the pieces and encapsulating them in plaster. These samples were tested using direct shear under constant normal stiffness conditions using the existing direct shear apparatus at Monash University. A shear box was specifically constructed for this testing program. The shear box, referred to as the Type "B" shear box, has a braced perspex front that allows samples to be viewed during shear testing. This allowed a visual record of each Type "B" shear test to be made.

Methods and equipment for making rock mass samples suitable for testing in the direct shear apparatus were also developed.

9.2 Observation and modelling of rock mass behaviour

The video footage obtained from the shear tests, together with the measured behaviour, showed that the rock mass behaved in one of three ways when subjected to direct shear. These were:

- sliding along a shallow joint set, followed by shear failure through an asperity formed by the joints,
- rotation of a strut formed between the ends of the shear box, followed by shear failure through the strut, and
- rotation of a block comprising most of the sample, followed by shear through the block.

The conditions under which each mechanism occurred have been discussed. Simple mechanistic models were developed to simulate the above mechanisms and allow the assessment of the peak shear strength of the sample. The values calculated using these models for samples exhibiting sliding/asperity shear and rotation/strut shear behaviour were found to be reasonably close to those measured in the laboratory tests. The calculated values for rotation/block shear were found to be higher than those measured in the laboratory.

The GSI envelope calculated using parameters judged to be suitable for the rock mass samples compared well with the strength envelope formed by the normalised peak stresses measured during the testing.

9.3 Effects of varying sample parameters

The effect of varying the sample parameters on sample strength was investigated during this study. It was observed that:

- Variations of joint inclination could result in different pre-peak and failure mechanisms and affect peak strength of the sample.
- Variation of intact rock strength and spacing affected the peak strength of the sample, but not the pre-peak and failure mechanisms. The peak strength of the sample was reduced when either intact rock strength or joint spacing were reduced.
- Variations of initial normal stress, geometry, small variations in joint inclination and the introduction of a third joint set did not appear to have a significant effect on pre-peak and failure mechanisms or on peak strength for the samples tested.
- The effect on rock mass behaviour resulting from the different sample geometries tested was inconclusive.

9.4 UDEC modelling

Each of the Type "B" shear tests were modelled using UDEC to assess the ability of UDEC to replicate the behaviour of the sample as it underwent shear. The UDEC model was able to apply CNS conditions and calculate stresses and displacements. A visual record of the UDEC sample

behaviour was made using the MOVIE function. It was found that the movie generated by the UDEC model appeared to exhibit similar behaviour to that recorded in the laboratory tests. The average peak shear stresses calculated using the UDEC models and those measured in the laboratory tests were also found to be similar, while the calculated average peak normal stresses were found to be reasonably similar to those measured in the laboratory. However, the UDEC calculations of dilation and shear displacement at failure were not particularly close.

9.5 Limitations and further research

This study represents a preliminary investigation into the shear strength of jointed rock masses. Some of the directions further research could take are listed below.

9.5.1 Rock mass geometry

The pre-peak behaviour and failure mechanisms may have been influenced by the sample geometry. The geometry of the sample was related to the geometry of the Johnstone block and the available space within the shear apparatus. The Type "B" blocks were developed specifically for this project. Testing samples of different geometry may provide different mechanisms and rock mass strengths.

9.5.2 Joint inclination and spacing

The inclination of the joint sets in rock masses with three joint sets was restricted by the loss of rock material during the cutting process. If the joint pattern did not form equilateral triangles, then one of the joint sets would not be planar, leading to possible interlocking of the intact pieces in the rock mass and inconsistent joint properties. If a means of introducing multiple joint sets that produces aligned joints can be developed, the investigation of samples with three or four joint sets could be undertaken.

The joint spacing was limited by the need to form intact rock pieces that could be handled without breaking easily. A closer joint spacing also means that the sample will be smaller due to the loss of material with each cut. While using a stronger material will assist handling of the small rock pieces, it will adversely affect the cutting process and may produce a stronger rock mass, which in turn would require a stronger shear box and stiffer testing apparatus. An alternative method of

cutting joints into the intact block may be required to investigate the effects of joint inclination and spacing more fully. The effects of varying the spacing of each joint set could also be investigated, together with the effects of significant variations of joint spacing within each joint set.

It would also be of interest to introduce joint sets that strike at different orientations to those carried out in this study, i.e. producing a three-dimensional jointing pattern. However, suitable cutting and assembly would need to be developed.

9.5.3 Joint properties

The joints cut into the rock masses tested in this study were smooth, planar and persistent with zero cohesion. This was adopted to remove the influence of the joint properties on sample strength and to produce joints with similar behaviour, and also out of practical necessity. If a means of producing joints that are rough can be developed, the influence of these joints on sample behaviour might be assessed.

The effect of joint cohesion on rock mass behaviour could be investigated by coating the joints in the rock mass with a suitable bonding agent. The influence of non-persistent joints on rock mass behaviour could be assessed if non-persistent joints could be formed using a suitable adhesive to glue some of the rock pieces together.

9.5.4 Refinement of strength criteria

The results of this study show good agreement between the peak strengths obtained from the tests and those calculated using the Hoek-Brown GSI criterion. The laboratory tests also indicate that the joint spacing appears to influence the value of the s parameter. Additional work may further refine the influence of joint spacing and sample size on this parameter, and develop a more rigorous approach to its selection.

9.5.5 Improvement of numerical model

The numerical model of the shear tests developed using UDEC shows that UDEC appears to be able to replicate the displacement mechanisms occurring within a rock mass subjected to CNS direct shear. Despite being able to capture these mechanisms, only reasonable agreement was

obtained between calculated and measured peak strengths and poor agreement between calculated and measured shear displacements and dilations at failure. The introduction of Voronoi polygons to the model may provide a method of improving the accuracy of the models. The Voronoi mesh allows the creation of cracks between the polygons and the subsequent mechanical behaviour of the new joints.

9.5.6 Application to field studies

The models tested in this study, by necessity, were very simplified representations of rock masses that may be encountered in the field. It would be interesting to compare the mechanisms described in this study with those observed to have occurred in the field, if such observations are available.

Alternatively, tests on samples recovered from the field would also be of interest. These samples could be classified *in-situ* using GSI, then recovered and tested. The results of these tests may then be used to further develop our understanding of rock mass behaviour.

10 REFERENCES

- Afridi, A. J., Kwon, S. and Wilson, J. W. (2001). "Investigation of rock failure in a direct shear machine." Transactions of the Institution of Mining and Metallurgy, Section A: Mining Technology 110: pp 158-162.
- Amadei, B. (1988). "Strength of a regularly jointed rock mass under biaxial and axisymmetric loading conditions." International Journal of Rock Mechanics and Mining Sciences & Geomechanics Abstracts 25(1): pp 3-13.
- Asche, H. R. and Quigley, A. (1999). Tunnelling design on the Northside Storage Tunnel Project. 10th Australian tunnelling conference; The Race for Space, Melbourne, Victoria, Australia.
- Bagheripour, M. H. and Mostyn, G. (1996). "Prediction of the Strength of Jointed Rock - Theory and Practice". Eurock '96, Balkema, pp 231-238.
- Barton, N. (1973). "Review of a new shear-strength criterion for rock joints." Engineering Geology 7(4): pp 287-332.
- Barton, N. (2002). "Some new Q-value correlations to assist in site characterisation and tunnel design." International Journal of Rock Mechanics and Mining Sciences 39(2): pp 185-216.
- Barton, N. and Choubey, V. (1977). "The shear strength of rock joints in theory and practice." Rock Mechanics. Supplementum = Felsmechanik. Supplementum = Mecanique des Roches. Supplementum 10(1-2): pp 1-54.
- Barton, N., Lien, R. and Lunde, J. (1974). "Engineering Classification of Rock Masses for the Design of Tunnel Support." Rock Mechanics. Supplementum = Felsmechanik. Supplementum = Mecanique des Roches. Supplementum 6(4): pp 189-236.
- Benjelloun, Z. H., Boulon, M. and Billaux, D. (1990). "Experimental and numerical investigation on rock joints". International Symposium on Rock Joints, Loen, Norway, A. A. Balkema, Rotterdam, pp 171-178.
- Bieniawski, Z. T. (1973). "Engineering Classification of Jointed Rock Masses." The Civil Engineer in South Africa: pp 335-343.
- Bieniawski, Z. T. (1979). "The geomechanics classification in rock engineering applications". 4th Congress of the International Society for Rock Mechanics, Montreux, Switzerland, Vol. 2, pp 41-48.
- Brown, E. T. (1981). "Rock characterization testing and monitoring ISRM suggested methods." 221 pages.
- Calderon, A. R. (2000). The application of back-analysis and numerical modeling to design a large pushback in a deep open pit mine, Colorado School of Mines, Golden, CO, United States: 160.
- Chang, C. and Haimson, B. C. (2000). "Rock strength determination using a new true triaxial loading apparatus, and the inadequacy of Mohr-type failure criteria". Pacific rocks 2000: "Rock Around the Rim", 4th North American Rock Mechanics Symposium, Seattle, WA, United States, pp 1321-1327.
- Chappell, B. A. (1984). "Determination of Rock Mass Modulus". 4th Australia-New Zealand Conference on Geomechanics, Perth, Western Australia, I E Aust, pp 555-562.
- Chen, S. G. and Zhao, J. (1998). "A study of UDEC modelling for blast wave propagation in jointed rock masses." International Journal of Rock Mechanics and Mining Sciences & Geomechanics Abstracts 35(1): pp 93-99.

- Cheng, F. K. K. (1997). A laboratory study of the influence of wall smear and residual drilling fluids on rock socketed pile performance. PhD Dissertation, Dept of Civil Engineering, Monash University.
- Chiu, H. K. (1981). Geotechnical Properties and Numerical Analyses for Socketed Pile Design in Weak Rock. PhD Dissertation, Dept of Civil Engineering, Monash University.
- Choi, S. K. (1984). The bearing capacity of foundations in weak rock. PhD Dissertation, Dept of Civil Engineering, Monash University.
- Dai, C., Muehlhaus, H., Meek, J. and Fama, M. D. (1996). "Modelling of blocky rock masses using the Cosserat method". International Journal of Rock Mechanics and Mining Sciences & Geomechanics Abstracts 33(4): pp 425-432.
- Deere, D. U. (1963). "Technical description of rock cores for engineering purposes." Felsmechanik und Ingenieurgeologie 1(1): pp 16-22.
- Desai, C. S. and Salami, M. R. (1987). "Constitutive model for rocks." Journal of Geotechnical Engineering 113(5): pp 407-423.
- Dounias, G. T. and Potts, D. M. (1993). "Numerical analysis of drained direct and simple shear tests." Journal of Geotechnical Engineering 119(12): pp 1870-1891.
- Dutton, A. J. and Meek, J. L. (1992). "Distinct element modelling of longwall gate road roof support". 7th International Conference on Computer Methods and Advances in Geomechanics, Cairns, Queensland, Australia.
- Einstein, H. H. and Hirschfeld, R. C. (1973). "Model Studies on Mechanics of Jointed Rock." Journal of the Soil Mechanics and Foundations Division 99(SM3): pp 229-248.
- Einstein, H. H., Nelson, R. A., Bruhn, R. W. and Hirschfeld, R. C. (1970). "Model Studies of Jointed-Rock Behavior. Rock mechanics, theory and practice: 11th symposium on Rock mechanics, Berkeley, CA, United States, pp 83-103.
- Fairhurst, C. (1964). "On the validity of the "Brazilian" test for brittle materials." Int. J. Rock Mech. Min. Sci. 1: pp 535-546.
- Fardin, N., Stephansson, O. and Jing, L. (2001). "The scale dependence of rock joint surface roughness". International Journal of Rock Mechanics and Mining Sciences 38(5): pp 659-669.
- Fossum, A. F. (1985). "Effective elastic properties for a randomly jointed rock mass." International Journal of Rock Mechanics and Mining Sciences & Geomechanics Abstracts 22(6): pp 467-470.
- Gerrard, C. M. (1982a). "Elastic models of rock masses having one, two and three sets of joints." International Journal of Rock Mechanics and Mining Sciences 19(1): pp 15-23.
- Gerrard, C. M. (1982b). "Equivalent elastic moduli of a rock mass consisting of orthorhombic layers." International Journal of Rock Mechanics and Mining Sciences 19(1): pp 9-14.
- Grasselli, G. and Egger, P. (2003). "Constitutive law for the shear strength of rock joints based on three-dimensional surface parameters." International Journal of Rock Mechanics and Mining Sciences 40(1): pp 25-40.
- Grosso, N., Graziani, A. and Bardani, C. (1999). "Static analysis of tunnels in blocky rock masses by using a Cosserat equivalent continuum". 9th International Congress on Rock Mechanics-Applied rock mechanics: Safety and Control of the Environment, Paris, France, A. A. Balkema, pp 175-180.
- Haberfield, C. M. and Johnston, I. W. (1994). "A mechanistically-based model for rough rock joints." International Journal of Rock Mechanics and Mining Sciences & Geomechanics Abstracts 31(4): pp 279-292.

- Haberfield, C. M., Seidel, J. P. and Johnston, I. W. (1994). "Laboratory Modelling of Drilled Piers in Soft Rock". International Conference on Design and Construction of Deep Foundations, US Highway Administration, pp 1520-1534.
- Harkness, R. M., Powrie, W., Zhang, X., Brady, K. C. and O'Reilly, M. P. (2000). "Numerical Modelling of Full-Scale Tests on Drystone Masonry Retaining Walls." Geotechnique 50(2): pp 165-179.
- Helfel, R. (1988). Visual programming with HPVee. New Jersey, Prentice Hall.
- Hoek, E. (1983). "Twenty-third Rankine Lecture; Strength of Jointed Rock Masses." Geotechnique 33(3): pp 185-223.
- Hoek, E. and Bray, J. W. (1981). Rock Slope Engineering, 3rd edition, 358 pages, The Institute of Mining and Metallurgy, London.
- Hoek, E. and Brown, E. T. (1980a). "Empirical strength criterion for rock masses." Journal of the Geotechnical Engineering Division, ASCE, 106(GT9): pp 1013-1036.
- Hoek, E. and Brown, E. T. (1980b). Underground Excavations in Rock, 527 pages, The Institute of Mining and Metallurgy, London.
- Hoek, E. and Brown, E. T. (1988). "The Hoek-Brown Failure Criterion - a 1988 update". 15th Canadian Rock Mechanics Symposium: Engineering for Underground Excavations, Toronto, Canada, pp 31-38.
- Hoek, E. and Brown, E. T. (1997). "Practical estimates of rock mass strength." International Journal of Rock Mechanics and Mining Sciences & Geomechanics Abstracts 34(8): pp 1165-1186.
- Hoek, E., Kaiser, P. K. and Bawden, W. F. (1995). Support of Underground Excavations in Hard Rock. 215 pages, Rotterdam, A A Balkema.
- Hoek, E., Wood, D. and Shah, S. (1992). "A Modified Hoek-Brown Failure Criterion For Jointed Rock Masses". Eurock'92, London, Thomas Telford, pp 209-213.
- Hsiung, S. M., Ghosh, A., Chowdhury, A. H. and Ahola, M. P. (1994). "Evaluation of Rock Joint Models and Computer Code UDEC against Experimental Results". NUREG/CR (United States. Nuclear Regulatory Commission).
- Indraratna, B., Haque, A. and Aziz, N. (1998). "Laboratory modelling of shear behaviour of soft joints under constant normal stiffness conditions." Geotechnical and Geological Engineering 16(1): pp 17-44.
- Itasca (1993). FLAC users manual. Minneapolis, USA.
- Itasca (2000). Universal Distinct Element Code. Minneapolis, USA.
- Jaeger, J. C. (1960). "Shear Failure of Anisotropic Rocks." Geol. Mag. XCVII(1): pp 65-72.
- Jaeger, J. C. (1970). "Behavior of Closely Jointed Rock". Rock mechanics, theory and practice: 11th symposium on Rock mechanics, proceedings, Berkeley, CA, United States, pp 57-68.
- Jing, L. and Hudson, J. A. (2002). "Numerical Methods in Rock Mechanics." International Journal of Rock Mechanics and Mining Sciences 39(4): pp 409-427.
- Jing, L., Nordlund, E. and Stephansson, O. (1992). "An experimental study on the anisotropy and stress-dependency of the strength and deformability of rock joints." International Journal of Rock Mechanics and Mining Sciences & Geomechanics Abstracts 29(6): pp 535-542.
- Johnson, J. R., MacLaughlin, M. and Langston, R. (2000). "Discrete element analysis of failure modes in a slope at the Stillwater Mine". 35th symposium on Engineering Geology and Geotechnical Engineering, Pocatello, ID, United States.

- Johnston, I. W. (1985). "Strength of intact geomechanical materials." Journal of Geotechnical Engineering, ASCE, 111(6): pp 730-749.
- Johnston, I. W. (1992). "Silurian and Lower Devonian engineering properties. Engineering Geology of Melbourne". Proceedings of the seminar on engineering geology of Melbourne. W. A. Peck, J. L. Neilson, R. J. Olds and K. D. Seddon. Melbourne, Victoria, Australia, A. A. Balkema. 1: pp 95-108.
- Johnston, I. W. and Choi, S. K. (1986). "A synthetic soft rock for laboratory model studies." Geotechnique 36(6): pp 251-263.
- Johnston, I. W., Lam, T. S. K. and Williams, A. F. (1987). "Constant normal stiffness direct shear testing for socketed pile design in weak rock." Geotechnique 37(1): pp 83-89.
- Kodikara, J. (1989). Shear Behaviour of Rock-Concrete Joints and Side-Resistance of Piles in Weak Rock. PhD Dissertation, Dept of Civil Engineering, Monash University, 507 pages.
- Kodikara, J. K. and Johnston, I. W. (1994). "Shear behaviour of irregular triangular rock-concrete joints." International Journal of Rock Mechanics and Mining Sciences & Geomechanics Abstracts 31(4): pp 313-322.
- Kulatilake, P. H. S. W., He, W., Um, J. and Wang, H. (1997). "A physical model study of jointed rock mass strength under uniaxial compressive loading". NY Rocks '97, 36th U. S. Rock Mechanics Symposium, New York, NY, United States.
- Kulhawy, F. H. (1978). "Geomechanical model for rock foundation settlement." J. Geotech. Eng. Div. (ASCE) 104(GT2): pp 211-227.
- Kulhawy, F. H. and Goodman, R. E. (1980). "Design of Foundations on Discontinuous Rock". International conference on structural foundations on rock, Sydney, Australia.
- Ladanyi, B. and Archambault, G. (1970). "Simulation of Shear Behavior of a Jointed Rock Mass". Rock mechanics, theory and practice: 11th symposium on Rock mechanics, proceedings, Berkeley, CA, United States, pp 105-125.
- Ladanyi, B. and Archambault, G. (1972). "Evaluation de la resistance au cisaillement d'un massif rocheux fragmente; Evaluation of shear resistance of a fragmented rock mass." Engineering Geology-Geologie de l'Ingenieur, Report of the ... Session - International Geological Congress 24(13): pp 249-260.
- Lajtai, E. Z. (1969a). "Shear strength of weakness planes in rock." International Journal of Rock Mechanics and Mining Sciences 6(5): pp 499-515.
- Lajtai, E. Z. (1969b). "Strength of discontinuous rocks in direct shear." Geotechnique 19(2): pp 218-233
- Lam, T. S. K. (1983). "Shear Behaviour of Concrete-Rock Joints". PhD Dissertation, Dept of Civil Engineering, Monash University.
- Lam, T. S. K. and Johnston, I. W. (1989). "Shear behavior of regular triangular concrete/rock joints; evaluation." Journal of Geotechnical Engineering 115(5): pp 728-740.
- Li, C. (2000). "Deformation modulus of jointed rock masses in three-dimensional space". GeoEng 2000- An international conference on geotechnical and geological engineering, Melbourne, Technomic.
- Marinos, P. and Hoek, E. (2000). "GSI: A geologically friendly tool for rock mass strength estimation". GeoEng2000-An international conference on geotechnical and geological engineering, Melbourne, Technomic.
- McLamore, R. and Gray, K. (1967). "The Mechanical Behaviour of Anisotropic Sedimentary Rocks." J. Engng for Industry, Trans. Am. Soc. of Mech. Eng., Ser. B 89: pp 62-73.

- Meyers, A. G. (1994). The Determination of Rock Strength for Engineering Design. PhD Dissertation, Dept of Civil Engineering, University of Adelaide: 453 pages.
- Miyaike, Y., Mizuno, N., Momose, Y. and Nakamura, J. (1993). "Experimental and analytical studies on mechanical properties of layered soft rock mass". 2nd international workshop on Scale effects in rock masses, Lisbon, Portugal, pp 125-132.
- Natau, O., Fliege, O., Mutschler, T. and Stech, H. J. (1995). "True triaxial tests of prismatic large scale samples of jointed rock masses in laboratory". International Congress on Rock Mechanics, Chiba, Japan.
- Palmstrom, A. (1996). "Characterizing rock masses by the RMI for use in practical rock engineering; Part 1, The development of rock mass index (RMI)." Tunnelling and Underground Space Technology 11(2): pp 175-188.
- Patton, F. D. (1966). "Multiple modes of shear failure in rock". 1st Internat. Soc. Rock Mechanics Cong., Lisbon, pp 509-513.
- Pearce, H. A. (2001). "Experimental and Analytical Investigation into the Shear Behaviour of Rock Joints". PhD Dissertation, Dept of Civil Engineering, Monash University, 272 pages.
- Peres-Rodrigues, F. (1990). "Deformability of a rock mass formed by an anisotropic rock and cut by a jointing system with orthotropic symmetry; application of the theory to a real case". First international workshop on scale effects in rock masses. ed. Pinto Da Cunha. Loen, Norway: pp 239-244.
- Power, W. L., Perriam, R. P. A., Crossing, K. and Muir, M. (1994). "Deformation modelling of the Sand King region, Western Australia". 12th annual Australian geological convention-Geoscience Australia; 1994 and beyond, Perth, Western. Australia., Australia.
- Priest, S. D. (1993). "Discontinuity Analysis for Rock Engineering." Chapman and Hall, London, 473 pages.
- Ramamurthy, T. and Arora, V. K. (1993). "A Classification for Intact and Jointed Rocks". Geotechnical Engineering of Hard Soils-Soft Rocks. A. A. Balkema, Rotterdam. pp 235-242.
- Rocscience, I. (1998). Phase2. Toronto, Canada.
- Ryncarz, T. and Nawrot, W. (1976). "Model Investigations on Some Mechanical Properties of Jointed Rock Masses." Archivum Gornictwa 11(2): pp 133-153.
- Sanderson, D. J. and Zhang, X. (1997). "Modelling and prediction of localized flow in fractured rock-masses". 1997 AAPG international conference and exhibition, Vienna, Austria.
- Seidel, J. P. (1993). "The Analysis and Design of Pile Shafts in Weak Rock". PhD Dissertation, Dept of Civil Engineering, Monash University, 476 pages.
- Seidel, J. P. and Haberfield, C. M. (1995). "The application of energy principles to the determination of the sliding resistance of rock joints." Rock Mechanics and Rock Engineering 28(4): pp 211-226.
- Seidel, J. P. and Haberfield, C. M. (2002). "A theoretical model for rock joints subjected to constant normal stiffness direct shear." International Journal of Rock Mechanics and Mining Sciences - Australian rock mechanics 39(5): pp 539-553.
- Senseny, P. E. and Pucik, T. A. (1999). "Development and validation of computer models for structures in jointed rock." International Journal for Numerical and Analytical Methods in Geomechanics 23(8): pp 751-778.
- Singh, M. (1997). "Engineering Behaviour of Jointed Model Materials". PhD Dissertation, Civil Engineering Department, Indian Institute of Technology, 339 pages.

- Sjoberg, J. (1999). "Analysis of Large Scale Rock Slopes". PhD Dissertation, Division of Rock Mechanics. Luleå University of Technology, 682 pages.
- Skinas, C. A., Bandis, S. C. and Demiris, C. A. (1990). "Experimental investigations and modelling of rock joint behaviour under constant stiffness". International Symposium on Rock Joints, Loen, Norway, A. A. Balkema, Rotterdam, pp 301-308.
- Sokolovsky, V. V. (1960). Statics of Soil Media. London, Butterworth Scientific Publications.
- Sonmez, H. and Ulusay, R. (1999). "Modifications to the geological strength index (GSI) and their applicability to the stability of slopes." Int. J. Rock Mech. Min. Sci. 36: pp 743-760.
- Terzaghi, K. (1946). "Rock defects and loads on tunnel supports". Rock tunnelling with steel supports, Youngstown, Ohio, Commercial Shearing and Stamping Co. pp 15-99.
- Thiel, K. and Zabuski, L. (1996). "Failure phenomena in large-scale direct shear test". 2nd North American rock mechanics symposium; Rock mechanics tools and techniques, Montreal, PQ, Canada, pp 1977-1984.
- Tien, Y. M., Wang, C. Y., Juang, C. H. and Lee, D. H. (1999). "Mechanical behavior of artificial anisotropic rock masses". 37th U. S. rock mechanics symposium: Rock mechanics for industry, Vail, CO, United States, pp 357-363.
- Varley, P. M., Parkin, R. J. H. and Patel, R. (1999). "Design of the power caverns for Pergau hydroelectric project, Malaysia." Institution of Mining and Metallurgy, Transactions, Section A: Mining Industry 108: pp 1-7.
- Wardlaw, H. (1992). "Investigation into the effects of jointing on the strength of soft rock masses". MEngSci Thesis, Dept of Civil Engineering, Monash University.
- Wickham, G. E., Tiedemann, H. R. and Skinner, E. H. (1972). "Support determinations based on geologic predictions." North American Rapid Excavation and Tunnelling Conference, Proceedings, American Institute of Mining, Metallurgical and Petroleum Engineers, New York, 1: pp 43-64.
- Yang, Z. Y. and Chiang, D. Y. (2000). "An experimental study on the progressive shear behavior of rock joints with tooth-shaped asperities." International Journal of Rock Mechanics and Mining Sciences 37(8): pp 1247-1259.
- Yang, Z. Y. and Lee, W. S. (1999). "Modelling the failure mechanisms of rock mass models by UDEC". 9th international congress on rock mechanics, Paris, France, A. A. Balkema, pp 981-984.
- Yankey, G., Deschamps, R., McCray, M. and Bentler, D. J. (2000). "Parametric study and subsurface exploration plan for Bluestone Dam". Geo-Denver 2000 Slope stability 2000, Denver, CO, United States.
- Yoshinaka, R., Yamabe, T. and Nishimatsu, Y. C. (1986). "Joint stiffness and the deformation behaviour of discontinuous rock." International Journal of Rock Mechanics and Mining Sciences & Geomechanics Abstracts 23(1): pp 19-28.

APPENDIX A

SUMMARY OF LABORATORY PROGRAM AND TEST RESULTS

LABORATORY TESTING PROGRAM—TYPE "A" TESTS.....	A-3
LABORATORY TESTING PROGRAM—TYPE "B" TESTS.....	A-4
SUMMARY OF TYPE "A" TEST RESULTS.....	A-6
SUMMARY OF TYPE "B" TEST RESULTS.....	A-7

LABORATORY TESTING PROGRAM—TYPE “A” TESTS

TEST	TEST DATE	UCS ¹ (MPa)	$\theta_1, \theta_2, \theta_3^2$	spacing (mm)	σ_{ci} (kPa)	COMMENTS
vary UCS						
A1	25-10-2000	5	-45°, 15°	75	100	
A2	24-10-2000	5	-45°, 15°, 75°	75	100	
vary $\theta_1, \theta_2, \theta_3$						
A3	18-10-2000	4	-45°, 15°	75	100	
A4	29-8-2000	4	-45°, 15°, 75°	75	100	
Joint	19-10-2000	4	0°	-	100	Measure ϕ_j
vary spacing						
A5	31-8-2000	4	-45°, 15°	50	100	
A6	20-10-2000	4	-45°, 15°, 75°	50	100	
vary σ_{ci}						
A7	10-10-2000	4	-45°, 15°	75	200	
A8	17-10-2000	4	-45°, 15°	75	400	

¹ Nominal value.

² θ_3 as applicable.

LABORATORY TESTING PROGRAM—TYPE "B" TESTS

TEST	TEST DATE	UCS (MPa)	$\theta_1, \theta_2, \theta_3$	Spacing (mm)	σ_{nl} (kPa)	COMMENTS
Stage 1 - Vary $\theta_1, \theta_2, \theta_3$						
B1	10-5-2001	3.0	-15°,45°	70	100	
B2	24-7-2001	3.0	-60°,30°	70	100	
B3	25-7-2001	3.0	-60°,45°	70	100	
B4	26-7-2001	3.0	-30°,30°	70	100	
B5	27-7-2001	3.0	-30°,45°	70	100	
B6	15-5-2001	3.0	-45°,15°	70	100	
B7	23-8-2001	3.0	-45°,60°	70	100	
B7A	8-5-2002	3.0	-45°,60°	70	100	
B8	24-8-2001	3.0	-15°,-75°,45°	70	100	
B9	28-8-2001	3.0	-45°,15°,75°	70	100	
Stage 2 - repeat Stage 1 with $\theta_1, \theta_2, \theta_3 \pm 5^\circ$						
B10	29-8-2001	3.0	-30°,30°	70	100	
B10A	29-8-2001	3.0	-30°,30°	70	100	
B11	30-8-2001	3.0	-45°,15°	70	100	
B12	31-8-2001	3.0	-15°,45°	70	100	
B13	10-10-2001	3.0	-45°,15°,75°	70	100	
Stage 3 - vary spacing						
B14	11-10-2001	3.0	-30°,45°	37.5	100	
B15	12-10-2001	3.0	-45°,60°	37.5	100	use block B7
B16	16-10-2001	3.0	-60°,45°	37.5	100	
B17	17-10-2001	3.0	-45°,15°,75°	50	100	

TEST	TEST DATE	UCS (MPa)	$\theta_1, \theta_2, \theta_3$	spacing (mm)	σ_{nl} (kPa)	COMMENTS
Stage 4 - vary UCS						
B18	8-11-2001	1.5	-30°,45°	75	100	
B19	9-11-2001	1.5	-45°,60°	75	100	failure not reached using small load cell
B19A	14-1-2002	1.5	-45°,60°	75	100	test repeated using large load cell
B20	15-1-2002	1.5	-60°,45°	75	100	
B21	16-1-2002	1.5	-45°,15°,75°	75	100	
Stage 5 - vary σ_{nl}						
B22	7-11-2001	3.0	-30°,45°	37.5	50	
B23	18-10-2001	3.0	-30°,45°	37.5	300	
B24	8-11-2001	3.0	-45°,15°,75°	70	50	
B25	19-10-2001	3.0	-45°,15°,75°	70	300	
Supplementary tests						
B26	9-5-2002	3.0	-30°,60°	70	100	
B27	10-5-2002	3.0	-45°,75°	70	100	
B28	17-1-2002	3.0	-90°,0°	70	100	
B29	18-1-2002	3.0	-60°	70	100	assess sliding on steep joints
B30	14-5-2002	3.0	-60°,15°	70	100	
B31	16-5-2002	3.0	-45°±5°,60°±5°	70	100	
Compliance tests						
B28A	11-1-2002	3.0	-	-	600	assess joint compliance
B32	7-5-2002	3.0	-	-	600	intact Johnstone block compliance
B32A	11-1-2002	3.0	-	-	100	intact Johnstone with shear
B33A	15-1-2002	>30	-	-	600	intact concrete block #1
B33B	15-5-2002	>30	-	-	600	intact concrete block #2
B33C	15-1-2002	>30	-	-	100	intact concrete block with shear

SUMMARY OF TYPE "A" TEST RESULTS

SUMMARY OF TEST RESULTS

$\phi = 28$

TYPE "A"

TEST	test inputs					test outputs												
	Nominal/Actual Joint angles			Joint spacing mm	σ_1 kPa	UCS* MPa	Apparent friction angle ϕ_{pp}	Sliding friction angle $(\theta_1 + \phi)$	Rotation friction angle $(90 - \theta_2)$	Pre-failure deflection mm	Peak τ	Peak σ	Normalised Peak τ Peak σ		negative dilation @ failure	dilation @ failure	negative dilation displ	Dilation angle @ failure
A1	-45	15	-	75	100	4.68	72	73	75	6	590	195	0.126	0.042	-0.05	0.6	2.0	6.5
A2	-45	15	75	75	100	5.04	63	73	75	20	500	350	0.089	0.069	0.00	1.4	-	4.4
A3	-45	15	-	75	100	3.28	70	73	75	6	390	150	0.119	0.048	-0.10	0.4	3.0	5.2
A4	-45	15	75	75	100	5.45	65	73	75	11	600	290	0.110	0.053	-0.05	1.0	2.0	7.2
Joint	0	-	-	-	100	-	29	28	-	-	-	-	-	-	-	-	-	1.2
A5	-45	15	-	50	100	4.48	71	73	75	10	500	175	0.112	0.039	-0.05	0.5	4.0	5.7
A6	-45	15	75	50	100	4.17	59	73	75	15	310	190	0.074	0.048	-0.05	0.5	5.0	2.5
A7	-45	15	-	75	200	5.20	71	73	75	9	670	240	0.129	0.046	-0.10	0.8	5.0	10.2
A8	-45	15	-	75	400	4.17	68	73	75	8	790	310	0.189	0.074	-0.45	-0.1	10.0	16.7

*using Type "B" correlation

A-6

SUMMARY OF TEST RESULTS

$\phi = 28$

TYPE "B"

TEST	test inputs					test outputs												
	Nominal/Actual Joint angles			Joint spacing mm	σ_1 kPa	UCS* MPa	Apparent friction angle ϕ_{pp}	Sliding friction angle $(\theta_1 + \phi)$	Rotation friction angle $(90 - \theta_2)$	Pre-failure deflection mm	Peak τ	Peak σ	Normalised Peak τ Peak σ		negative dilation @ failure	dilation @ failure	negative dilation displ	Dilation angle @ failure
B1	-14	43	-	75	100	4.30	42	42	47	42	1020	1160	0.237	0.270	-0.10	5.4	2.0	9.0
B2	-60	30	-	75	100	4.14	65	85	60	20	1100	605	0.266	0.146	-0.20	7.0	3.0	23.0
B3	-60	45	-	75	100	5.66	55	89	45	>19	>1160	>850	-	-	-0.05	>3.8	0.0	18.0
B4	-31	29	-	75	100	2.99	60	59	61	19	810	540	0.271	0.181	-0.20	2.2	4.0	9.0
B5	-30	45	-	75	100	3.37	54	58	45	20	1010	840	0.300	0.249	-0.10	3.7	2.5	16.0
B6	-45	15	-	75	100	3.70	70	73	75	15	570	355	0.154	0.096	-0.20	0.6	7.0	5.5
B7	-46	61	-	75	100	4.15	48	74	29	>24	>1110	>1130	-	-	-0.05	5.2	-	14.0
B7A	-45	60	-	70	100	1.70	47	73	30	16	625	675	0.368	0.397	-0.05	2.9	1.5	15.6
B8	-15	46	-75	75	100	3.27	42	43	44	34	840	730	0.196	0.223	-0.10	3.4	4.0	5.7
B9	-45	15	75	75	100	3.03	61	73	75	15	460	260	0.152	0.086	-0.10	0.8	3.5	4.2
B10	-30 +/- 5	30 +/- 5	-	75	100	3.44	53	51	60	>23	>1080	>870	-	-	-0.20	3.8	2.5	11.0
B11	-45 +/- 5	15 +/- 5	-	75	100	2.59	60	61	75	16	530	320	0.205	0.124	-0.15	1.1	5.0	7.0
B12	-13 +/- 5	43 +/- 5	-	75	100	2.73	40	39	47	>40	>740	>1000	-	-	-0.15	4.6	2.5	7.0
B13	-46 +/- 5	15 +/- 5	74 +/- 5	75	100	2.82	62	61	75	25	400	325	0.142	0.115	-0.10	1.1	6.5	3.7
B14	-31	44	-	30-32	100	4.52	51	59	46	19	760	700	0.168	0.155	-0.10	3.0	3.0	13.2
B15	-47	57	-	30-35	100	3.22	43	75	33	27	905	1120	0.281	0.348	-0.10	5.1	1.5	12.5
B16	-59.5	47	-	30-35	100	2.66	47	86.5	43	14	540	530	0.203	0.199	-0.10	2.4	3.0	12.7
B17	-38	27	84	30-55	100	3.91	60	66	63	19	295	180	0.075	0.048	-0.20	0.4	10.0	2.6
B18	-31	43	-	70	100	1.93	52	59	47	10	510	445	0.264	0.231	-0.05	1.7	1.0	10.0
B19	-45	59	-	70	100	2.21	44	73	31	>9	>460	>460	-	-	-0.01	>1.9	-	15.0
B19A	-45	60	-	70	100	2.21	46	73	30	12	620	620	0.281	0.281	-0.01	2.6	-	16.0
B20	-61	45	-	70	100	2.38	54	89	45	10	600	495	0.252	0.208	-0.10	1.9	2.0	15.0
B21	-45	16	74	70	100	2.52	66	73	74	9	300	150	0.119	0.060	-0.10	0.3	5.5	2.5
B22	-30	46	-	32	50	3.40	48	56	44	13	515	510	0.151	0.150	-0.01	4.6	-	30.0
B23	-33	43	-	30-37	300	3.37	48	61	47	12	590	520	0.175	0.154	-0.23	1.2	6.0	13.0
B24	-45	16	74	70	50	2.50	70	73	74	8	270	110	0.108	0.044	-0.05	0.3	3.0	4.5
B25	-45	15	75	60-70	300	2.89	62	73	75	9	460	370	0.159	0.128	-0.35	0.3	15.0	3.1
B26	-29	61	-	70	100	2.04	47	57	29	15	550	550	0.270	0.270	-0.02	2.2	1.0	11.6
B27	-45	75	-	70	100	1.86	48	73	15	13	535	500	0.322	0.301	0.00	2.0	0.0	11.9
B28	-90	0	-	70	100	1.15	57	118	90	6	290	325	0.252	0.283	-0.01	0.6	-	2.0
B29	-60	-	-	70	100	1.80	65	88	90	6	450	210	0.250	0.117	-0.05	0.6	2.0	7.8
B30	-62	15	-	70	100	1.97	69	90	75	7	260	120	0.132	0.081	-0.13	0.1	5.5	4.0
B31	-45 +/- 5	60 +/- 5	-	70	100	1.72	46	67	27	12	515	520	0.299	0.302	0.00	2.2	0.0	14.1
B32A(JS)	-	-	-	-	100	1.15	67	-	90	3.5	260	138	0.226	0.120	0.00	0.25	0	-
B33C(Conc)	-	-	-	-	100	-	65	-	90	-	-	-	-	-	-	-	-	-

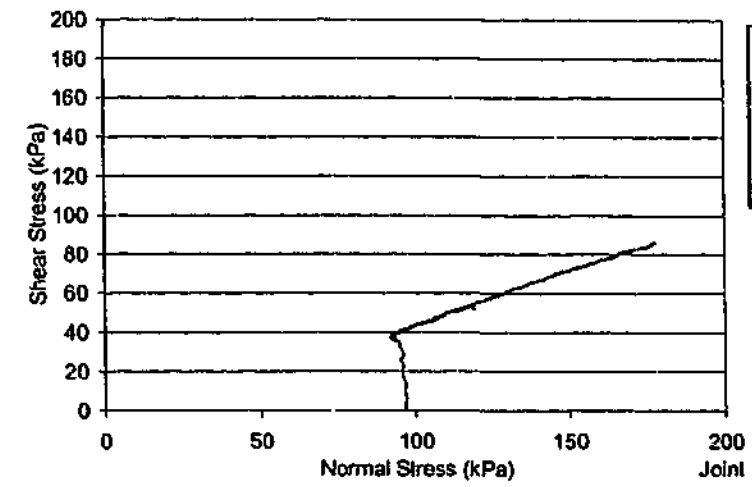
*using UCS Test results where possible

A-7

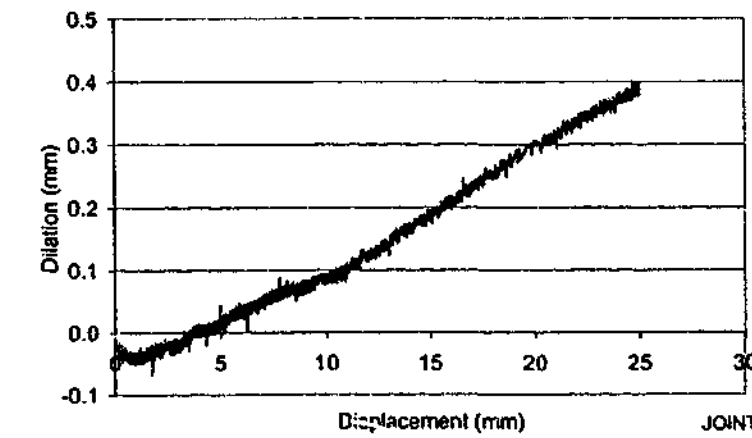
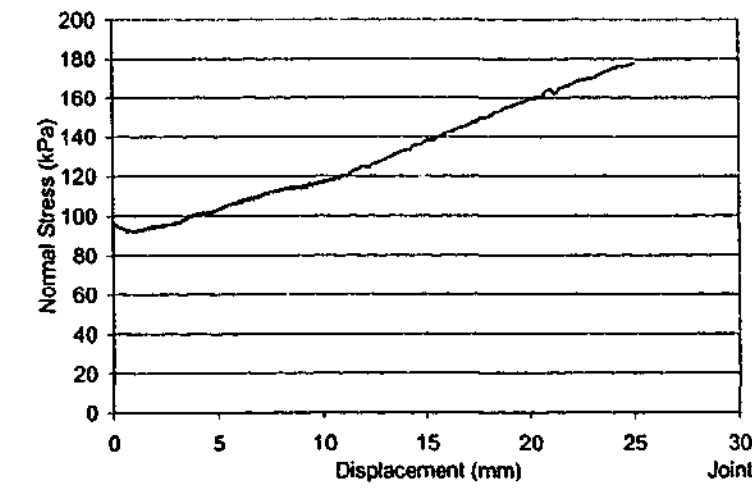
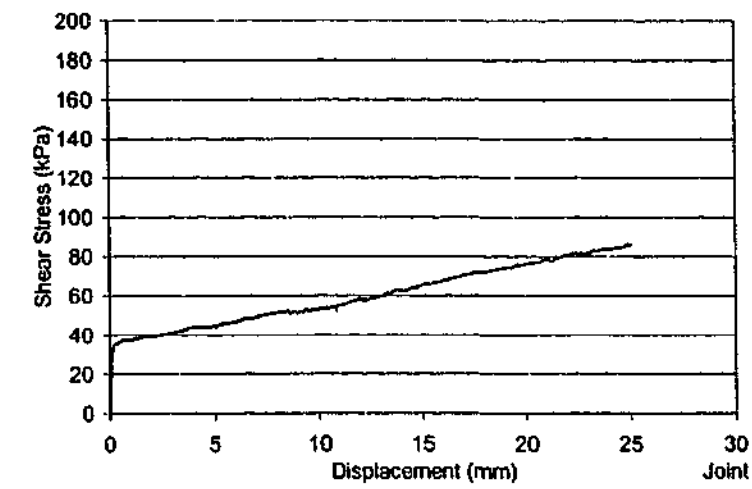
SUMMARY OF TYPE "B" TEST RESULTS

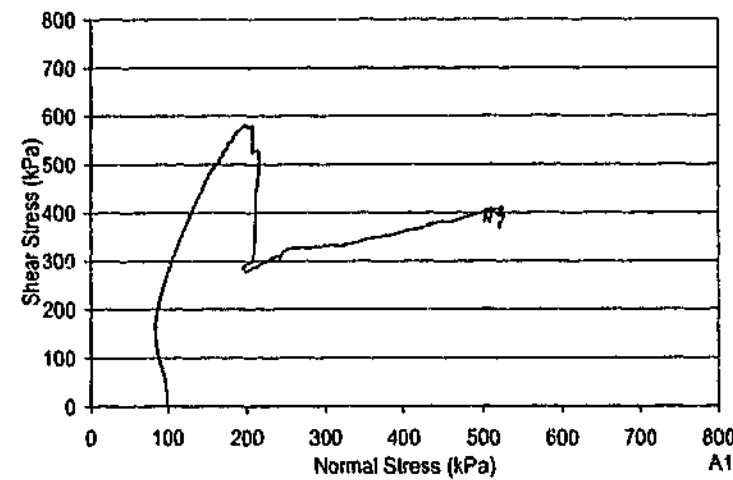
APPENDIX B

SHEAR TEST RESULTS

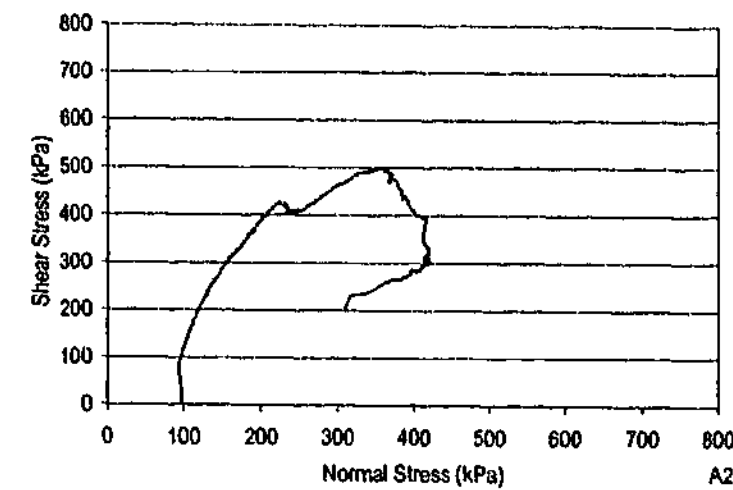
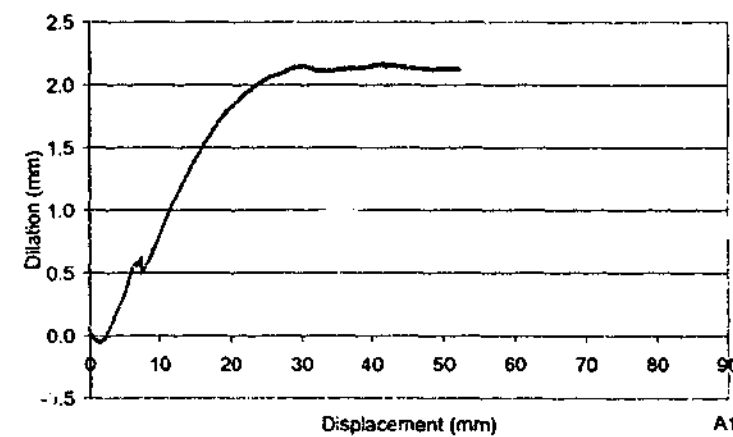
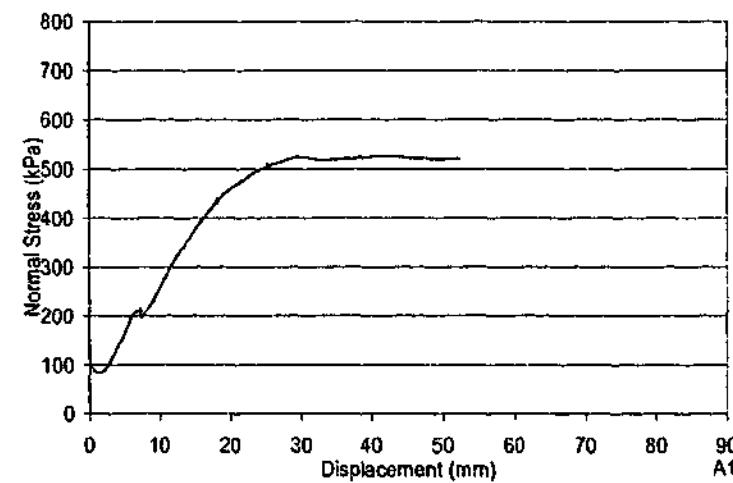
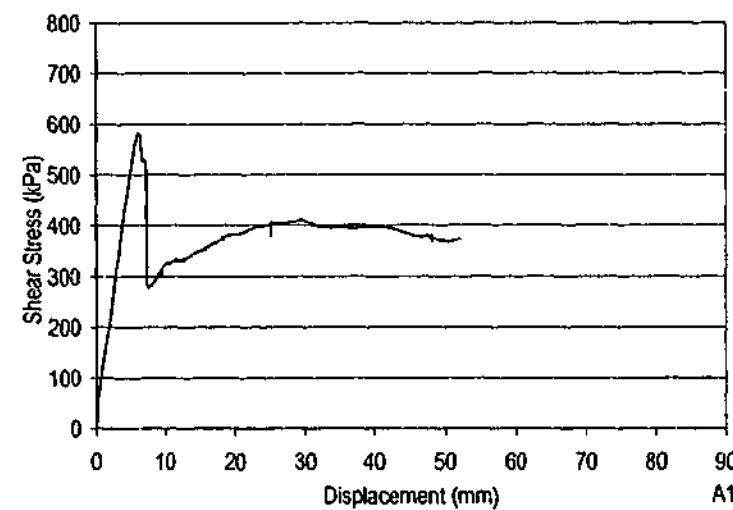


Test Details		Joint
θ_1	=	0°
σ_{ni}	=	100 kPa
k_v	=	200 kPa/mm

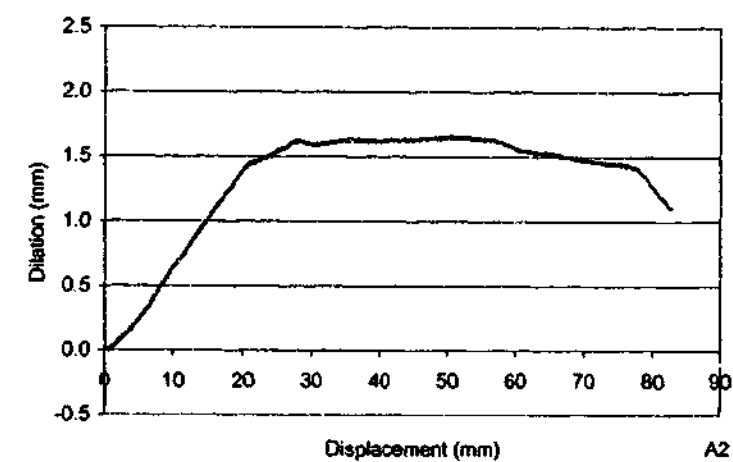
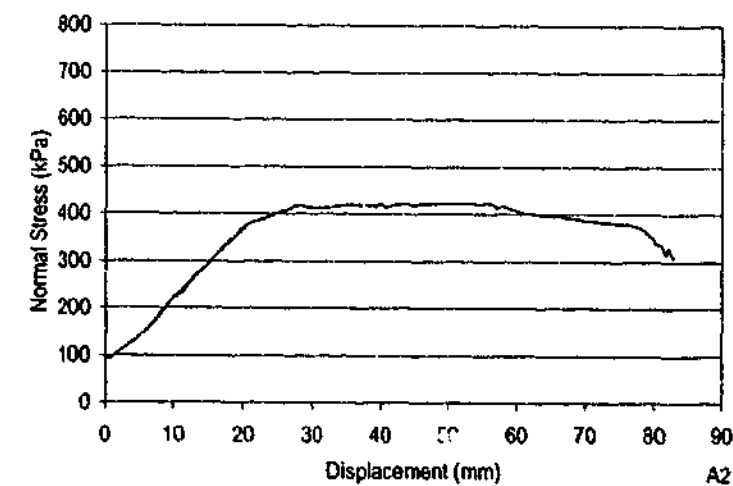
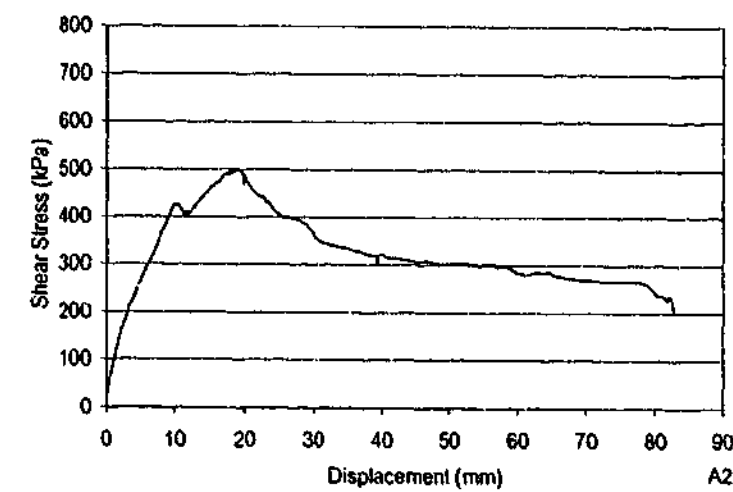


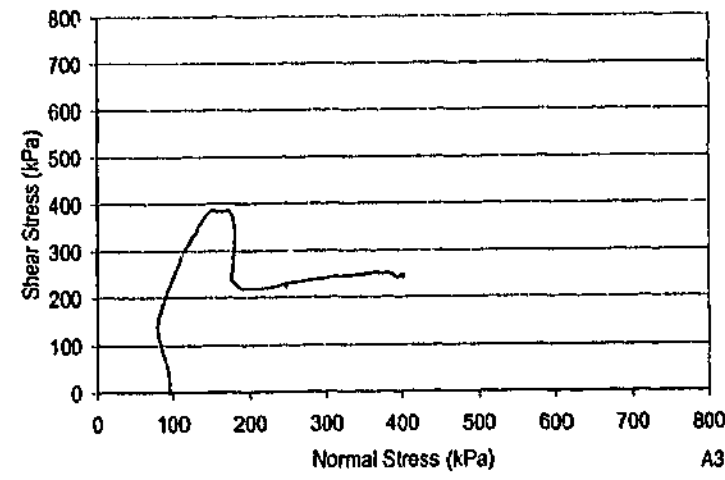


Test Details A1	
θ_1	= -45°
θ_2	= 15°
θ_3	= n/a $^\circ$
spacing	= 70 mm
σ_{ni}	= 100 kPa
k_v	= 200 kPa/mm
UCS	= 4.68 MPa

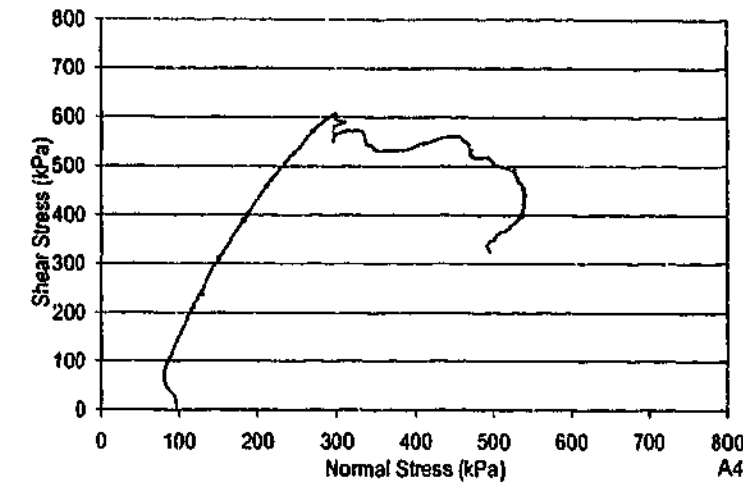
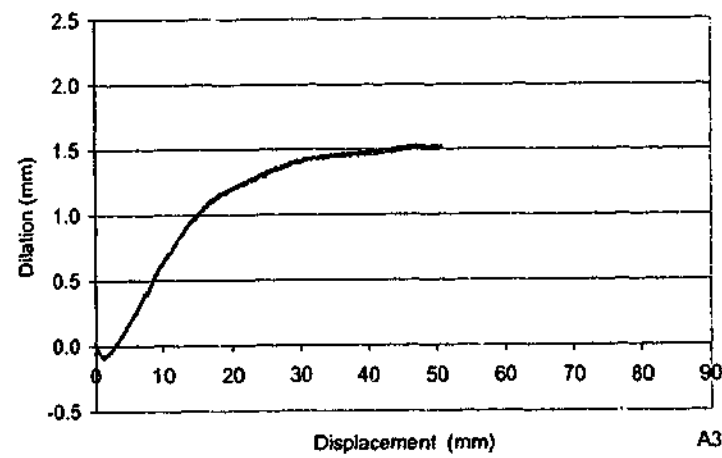
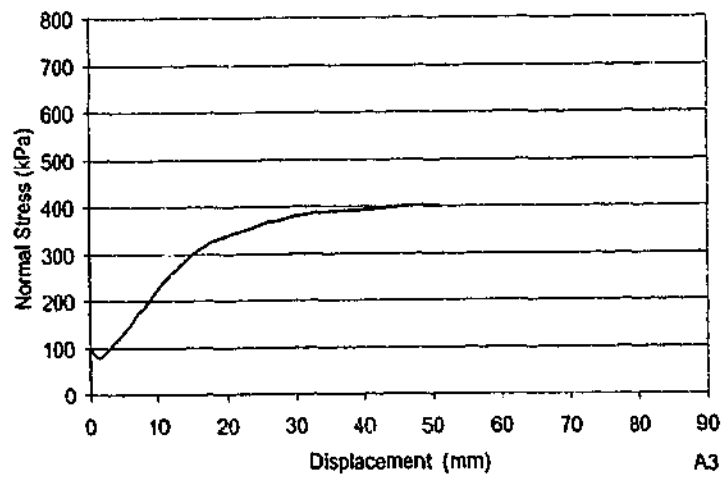
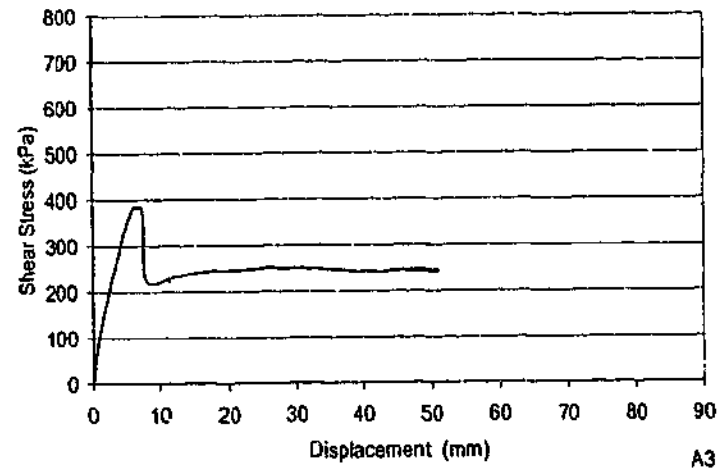


Test Details A2	
θ_1	= -45°
θ_2	= 15°
θ_3	= 75°
spacing	= 70 mm
σ_{ni}	= 100 kPa
k_v	= 200 kPa/mm
UCS	= 5.04 MPa

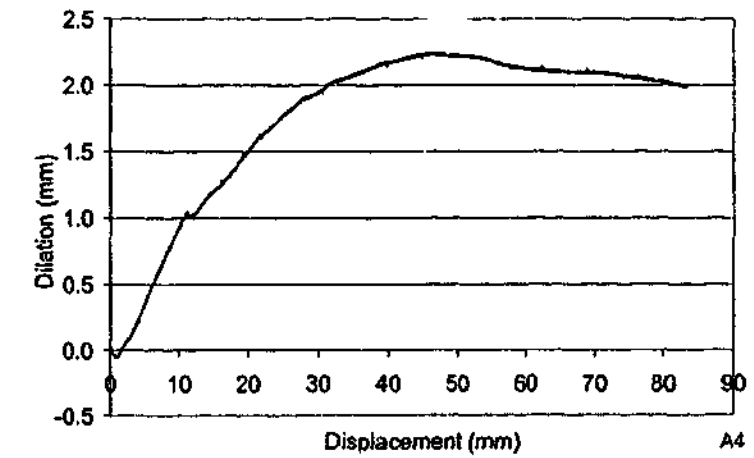
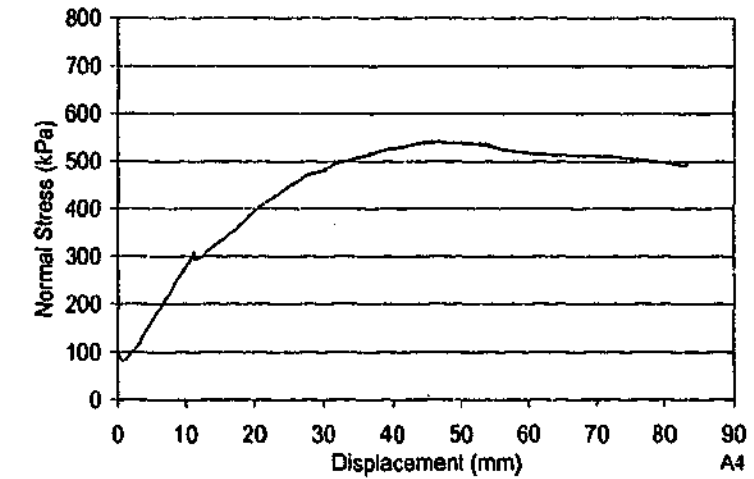
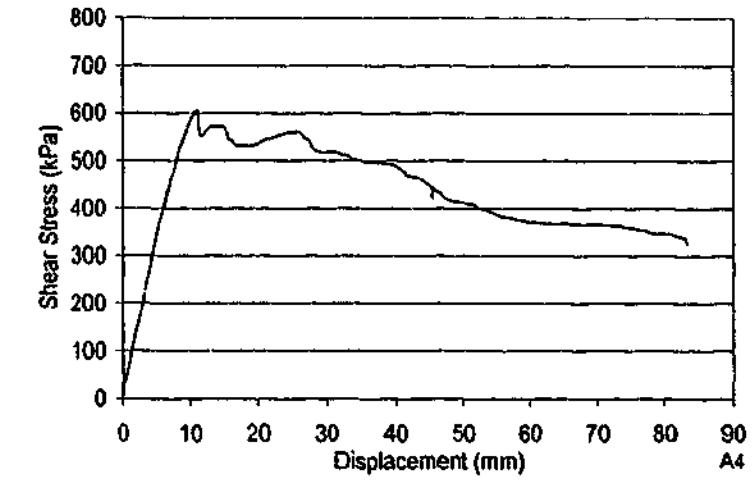


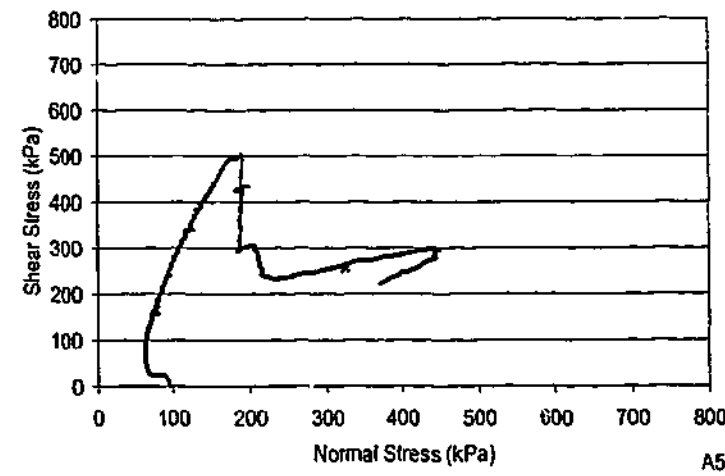


Test Details		A3
θ_1	=	-45°
θ_2	=	15°
θ_3	=	n/a $^\circ$
spacing	=	70 mm
σ_{ni}	=	100 kPa
k_v	=	200 kPa/mm
UCS	=	3.28 MPa

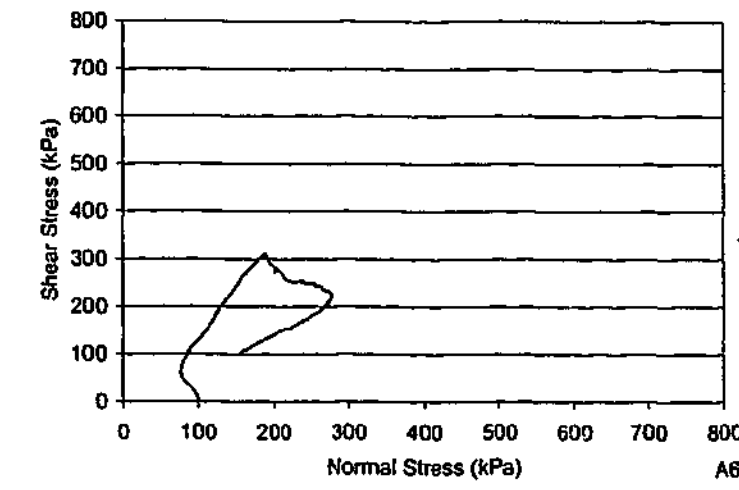
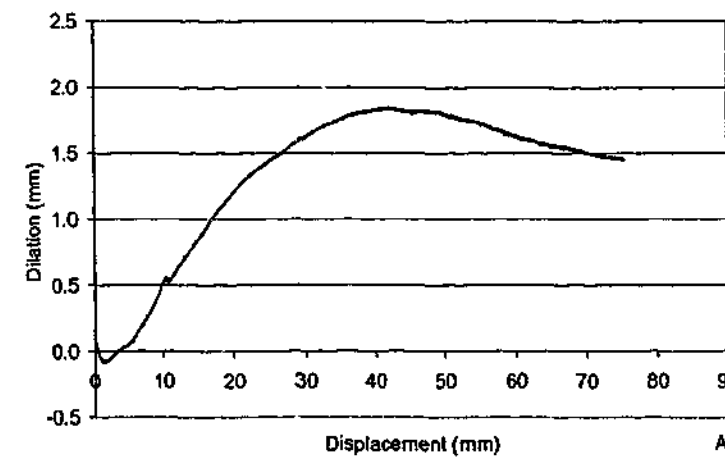
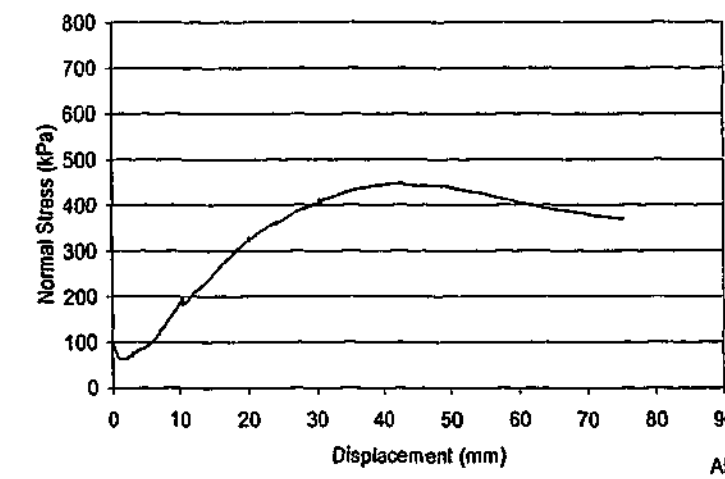
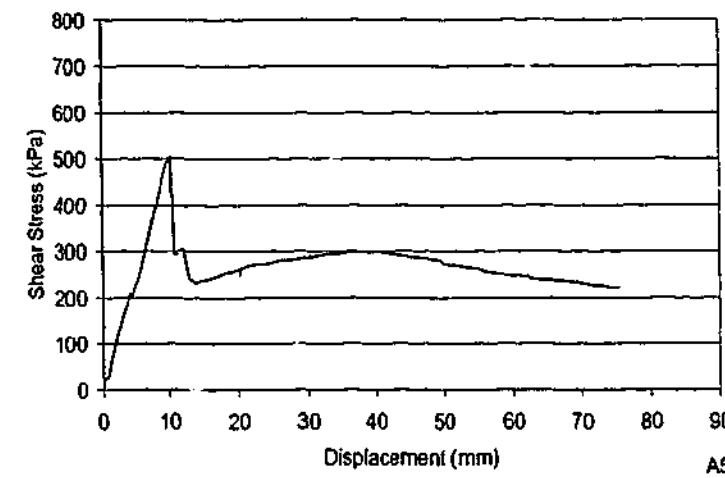


Test Details		A4
θ_1	=	-45°
θ_2	=	15°
θ_3	=	75°
spacing	=	70 mm
σ_{ni}	=	100 kPa
k_v	=	200 kPa/mm
UCS	=	5.45 MPa

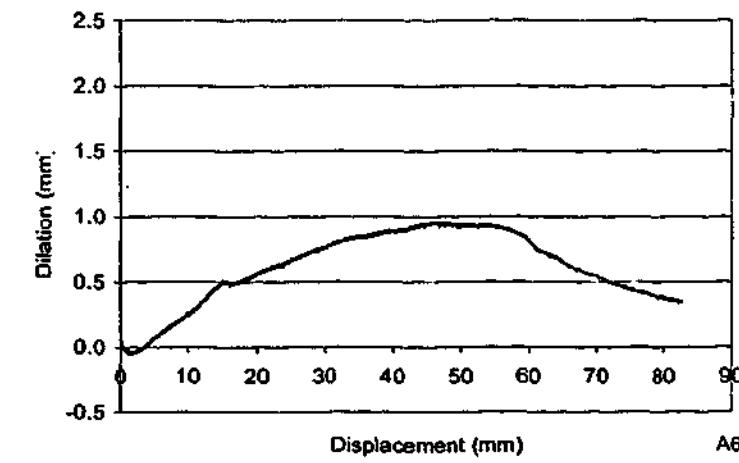
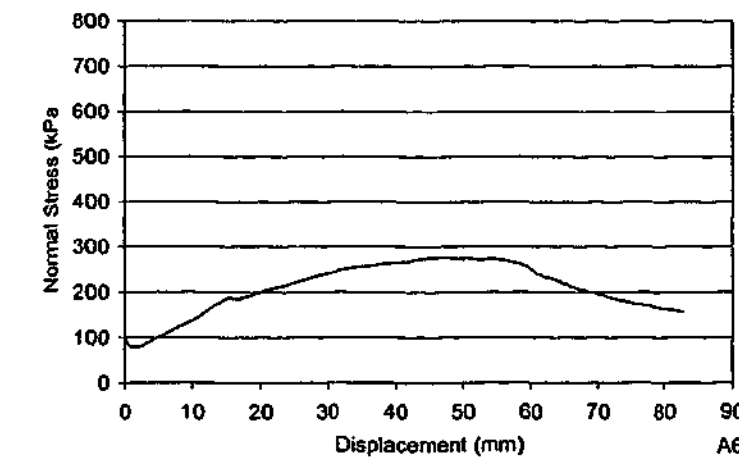
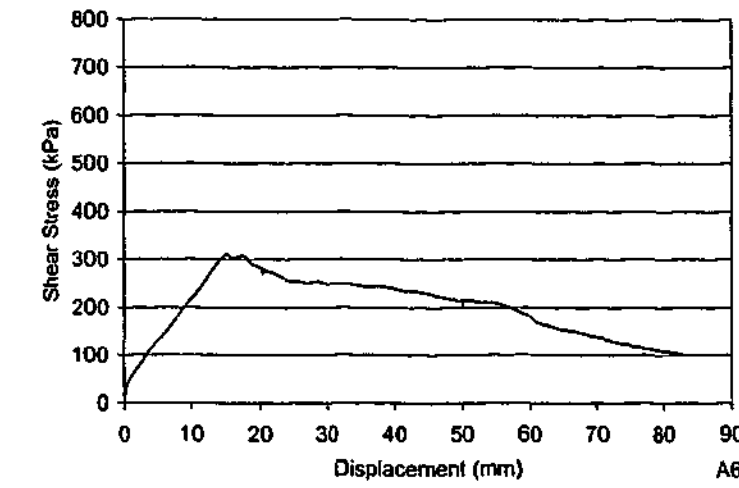


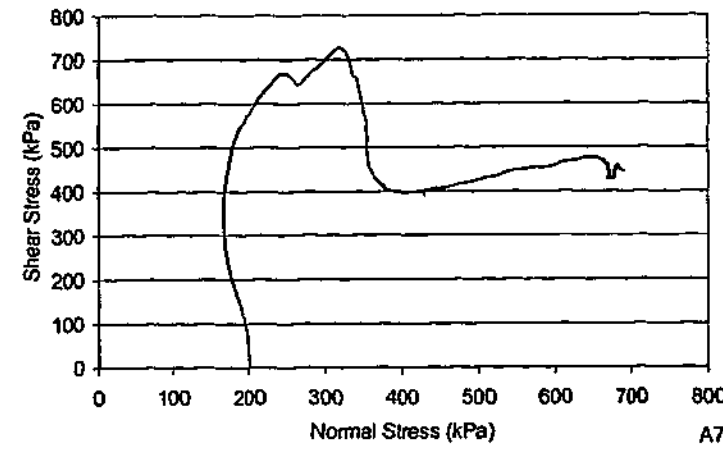


Test Details A5	
θ_1	= -45°
θ_2	= 15°
θ_3	= n/a°
spacing	= 50 mm
σ_{ni}	= 100 kPa
k_v	= 200 kPa/mm
UCS	= 4.48 MPa

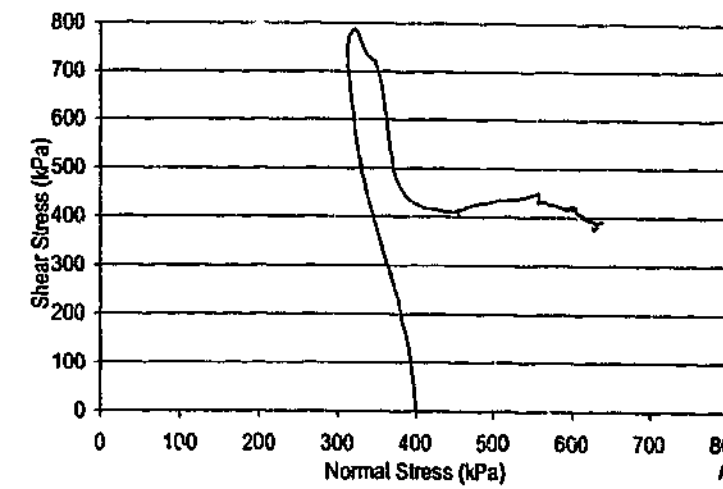
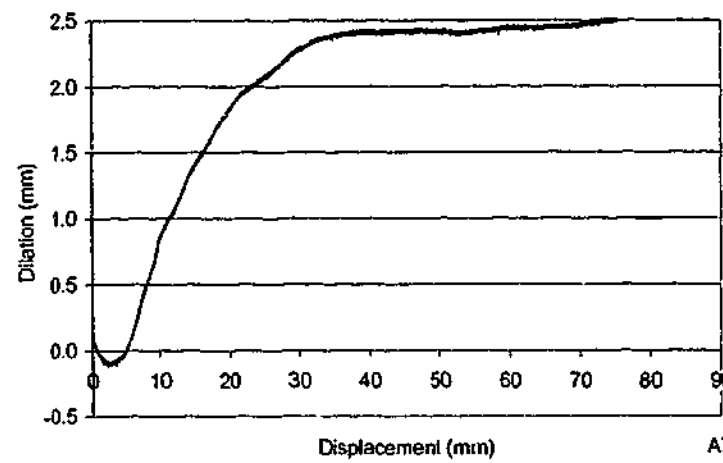
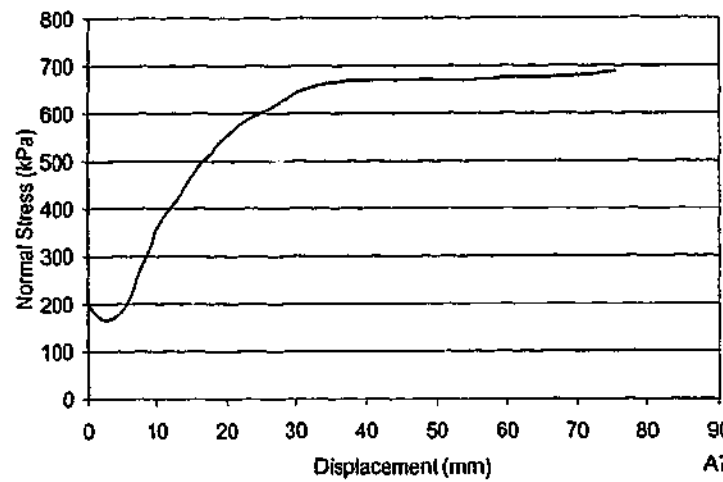
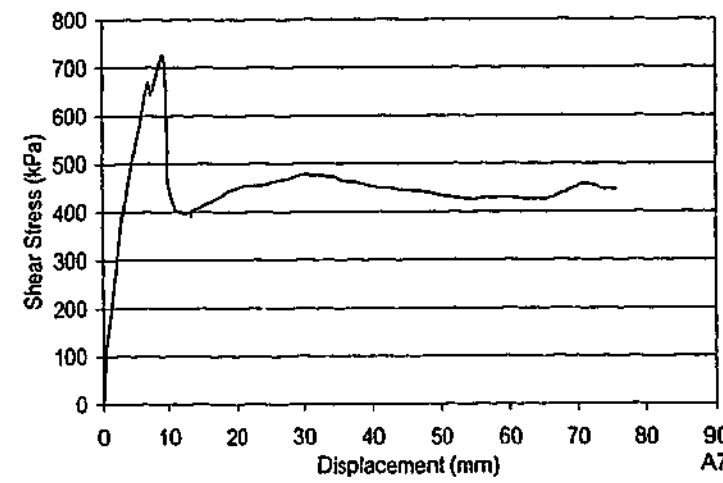


Test Details A6	
θ_1	= -45°
θ_2	= 15°
θ_3	= 75°
spacing	= 50 mm
σ_{ni}	= 100 kPa
k_v	= 200 kPa/mm
UCS	= 4.17 MPa

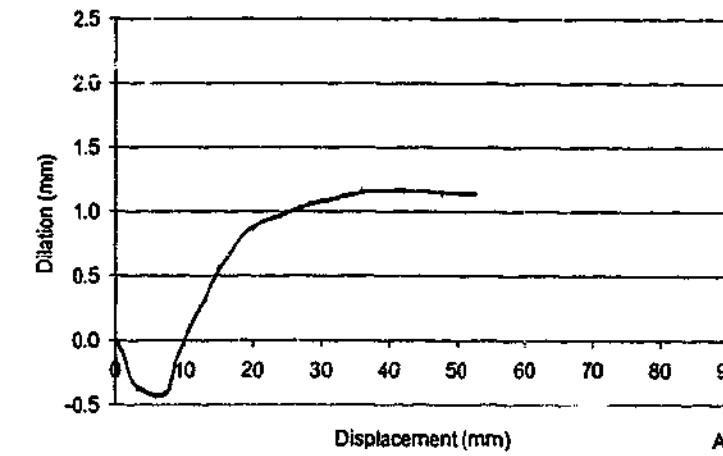
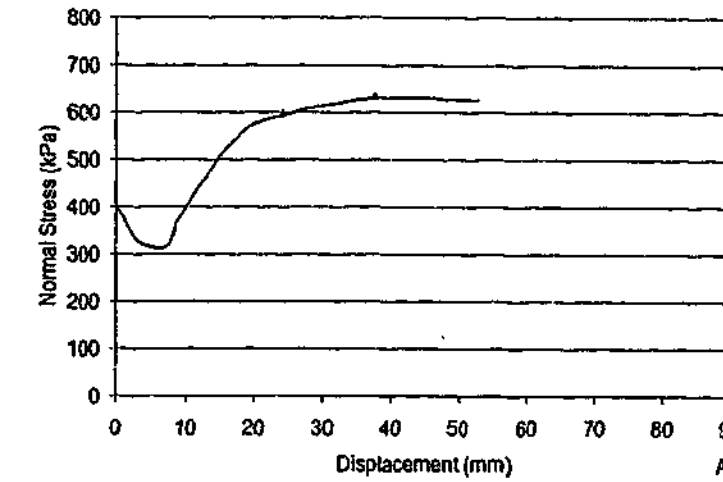
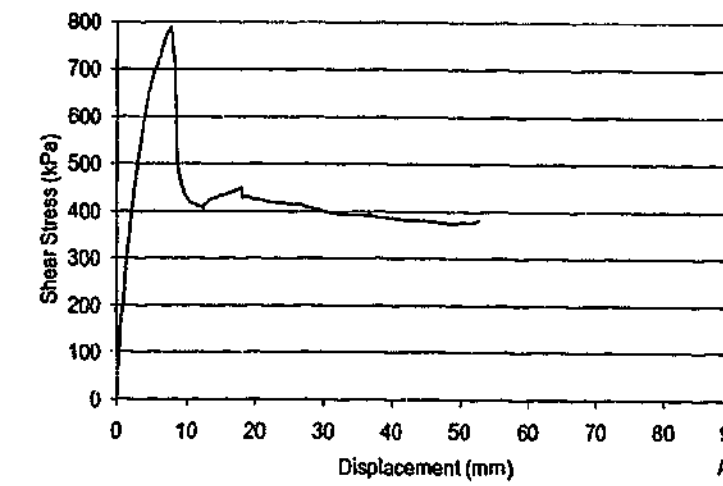


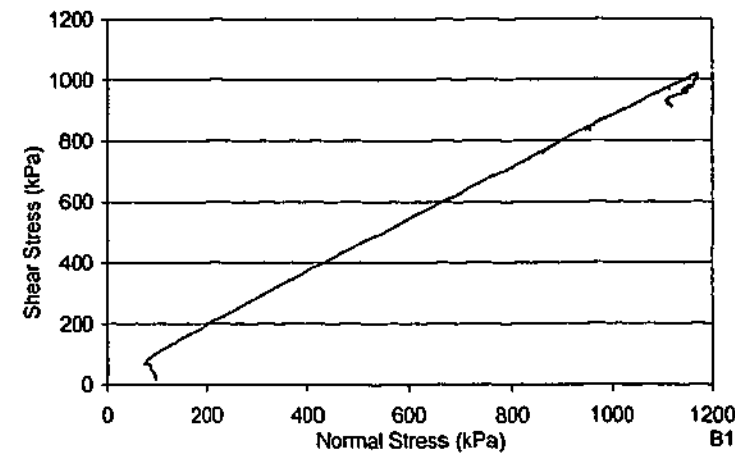


Test Details		A7
θ_1	=	-45°
θ_2	=	15°
θ_3	=	n/a $^\circ$
spacing	=	70 mm
σ_{ni}	=	200 kPa
k_v	=	200 kPa/mm
UCS	=	5.20 MPa



Test Details		A8
θ_1	=	-45°
θ_2	=	15°
θ_3	=	n/a $^\circ$
spacing	=	70 mm
σ_{ni}	=	400 kPa
k_v	=	200 kPa/mm
UCS	=	4.17 MPa





Test Details		B1
θ_1	=	-14°
θ_2	=	43°
θ_3	=	n/a $^\circ$
spacing	=	70 mm
σ_{ni}	=	100 kPa
k_v	=	200 kPa/mm
UCS	=	4.30 MPa

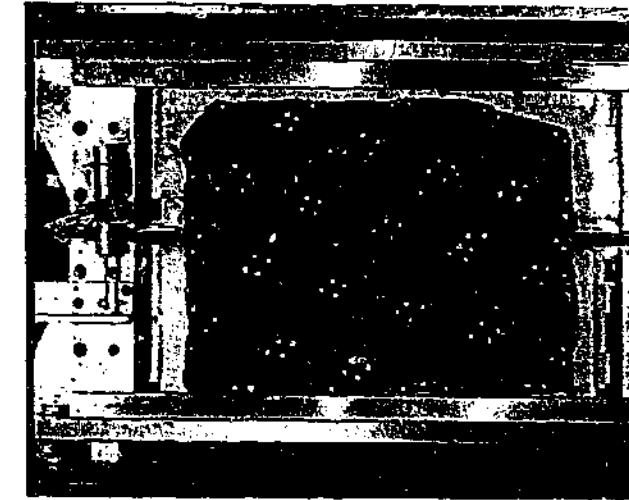
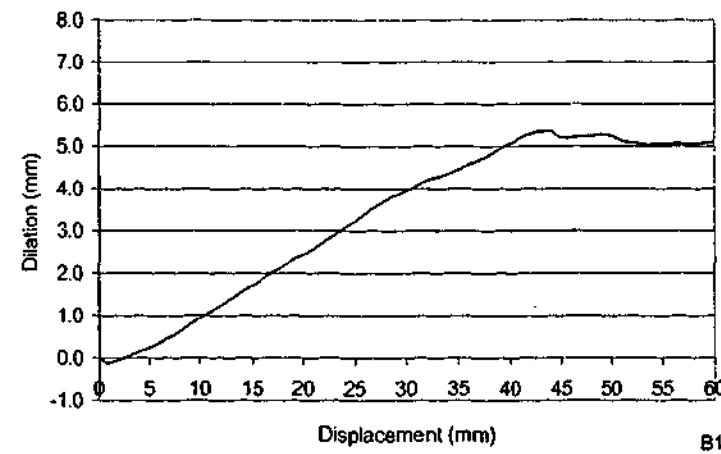
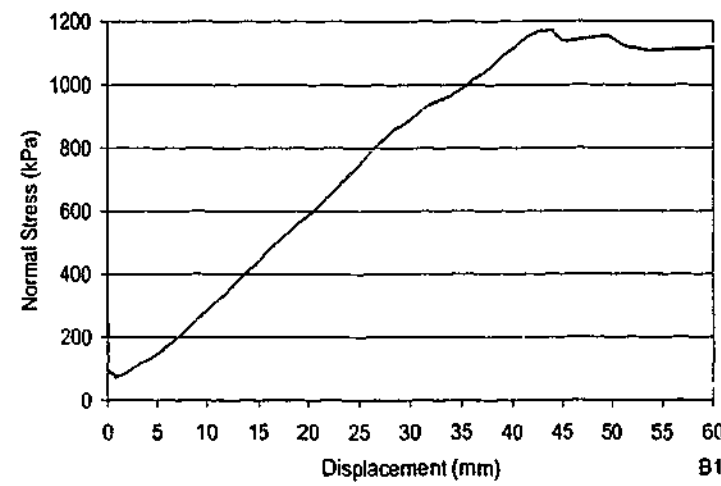
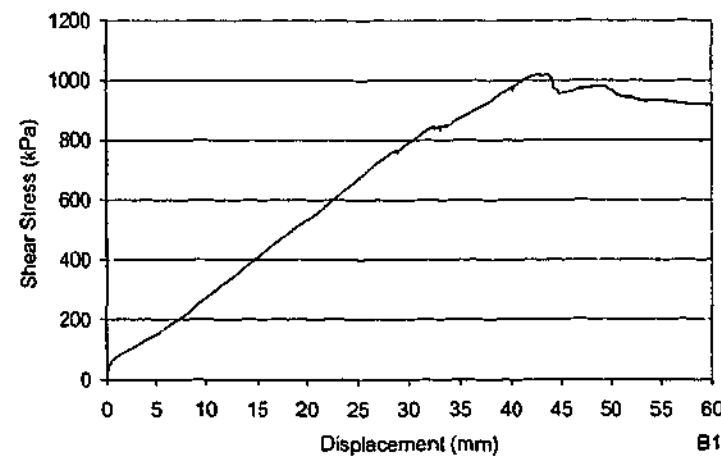


Figure B1-1 – dx=0 mm

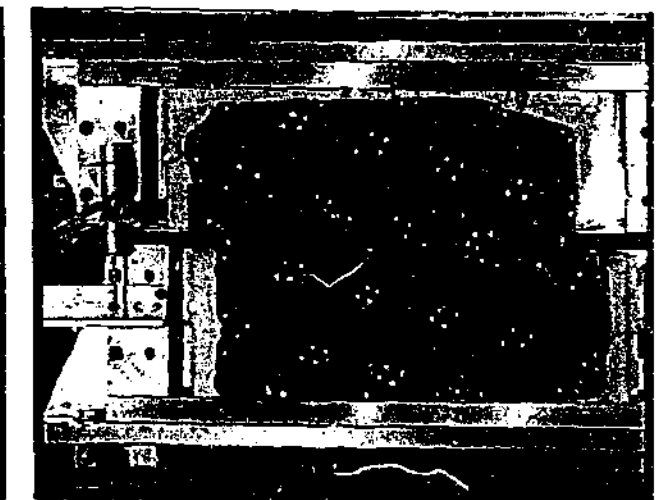


Figure B1-2 – dx=26 mm

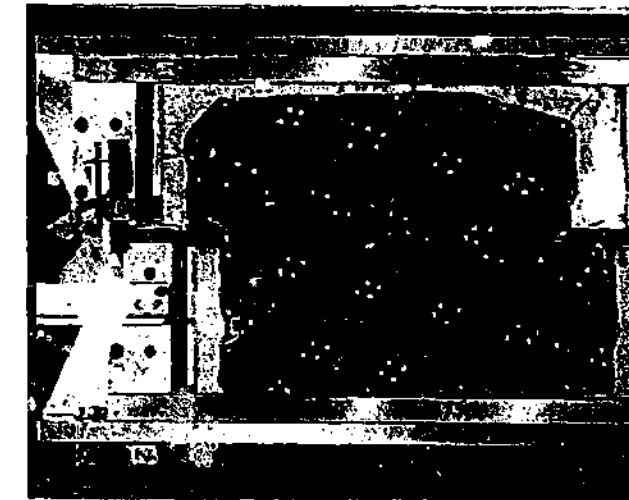


Figure B1-3 – dx=33 mm

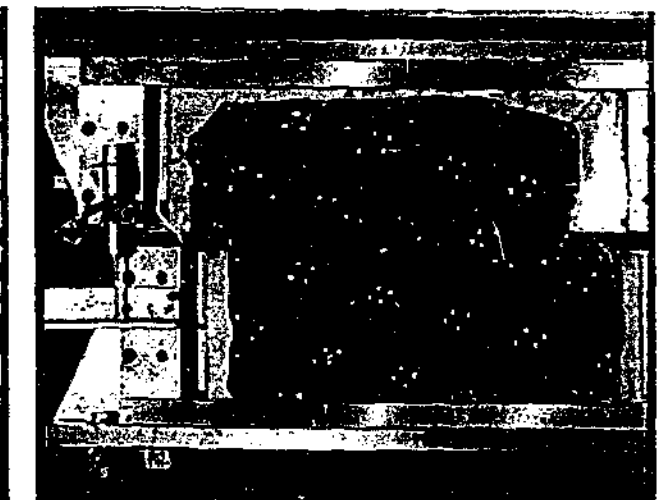


Figure B1-4 – dx=38 mm

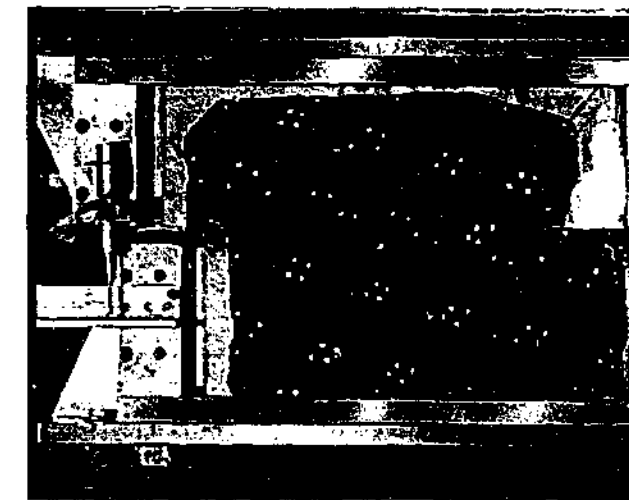


Figure B1-5 – dx=41 mm

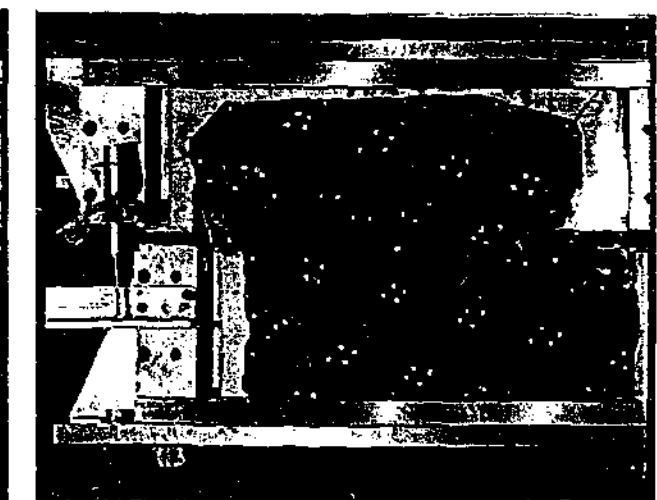
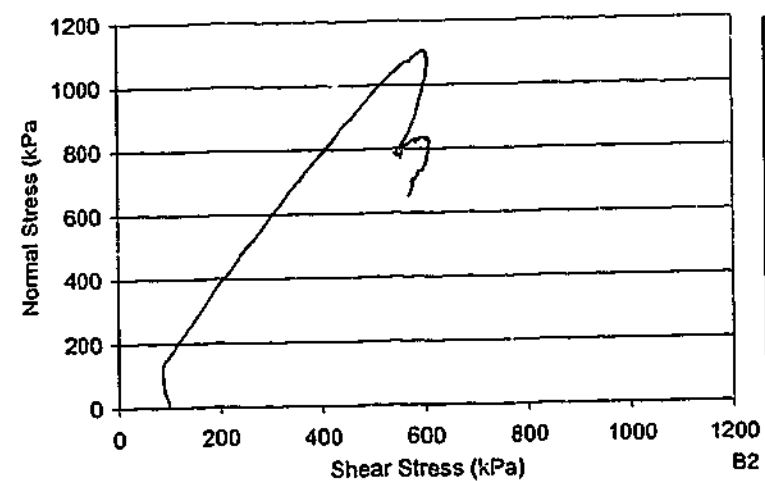


Figure B1-6 – dx=54 mm

TEST B1			
$\theta_1 = -45^\circ$	$\theta_2 = 15^\circ$	$\theta_3 = n/a$	spacing = 70 mm
$\sigma_{ni} = 100$ kPa	$k_v = 200$ kPa/mm		UCS = 4.30 MPa



Test Details		B2
θ_1	=	-60°
θ_2	=	30°
θ_3	=	n/a $^\circ$
spacing	=	70 mm
σ_{ni}	=	100 kPa
k_v	=	100 kPa/mm
UCS	=	4.14 MPa

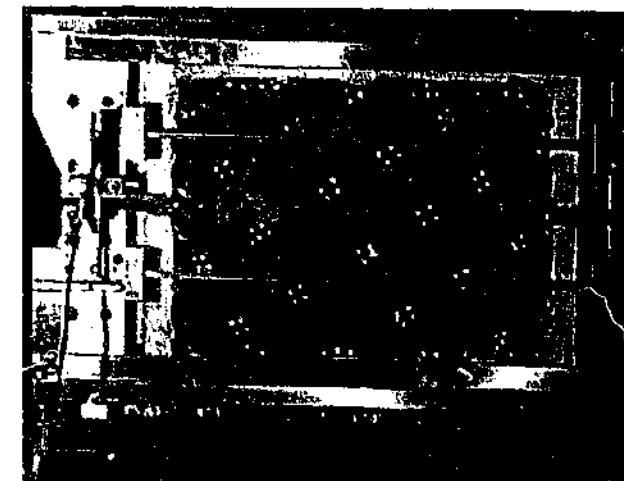
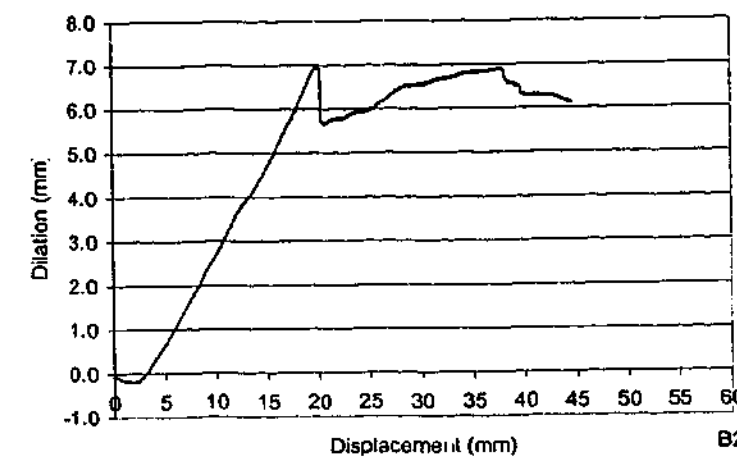
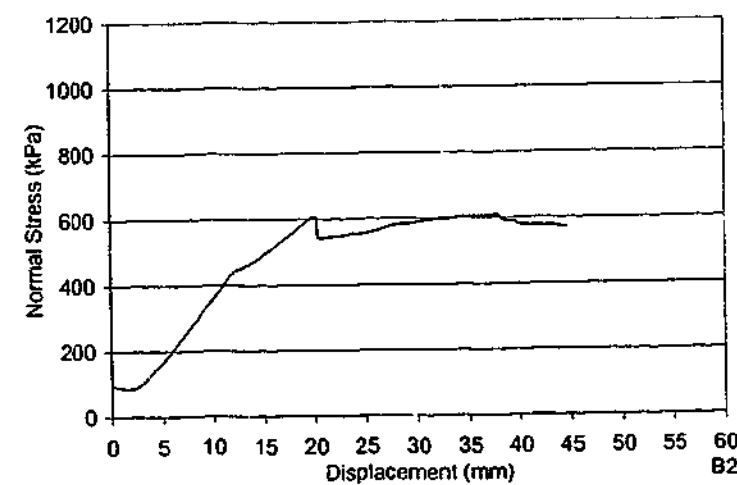
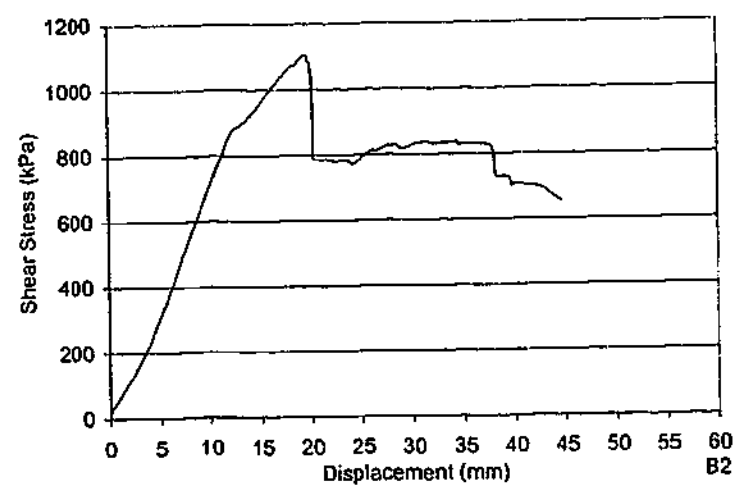


Figure B2-1 – dx = 0 mm

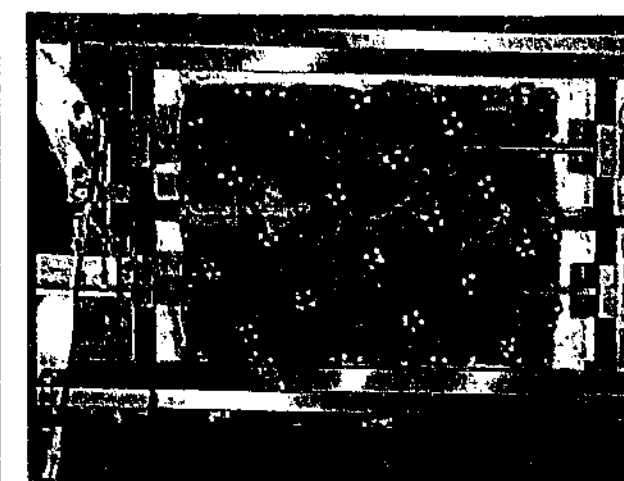


Figure B2-2 – dx = 7 mm

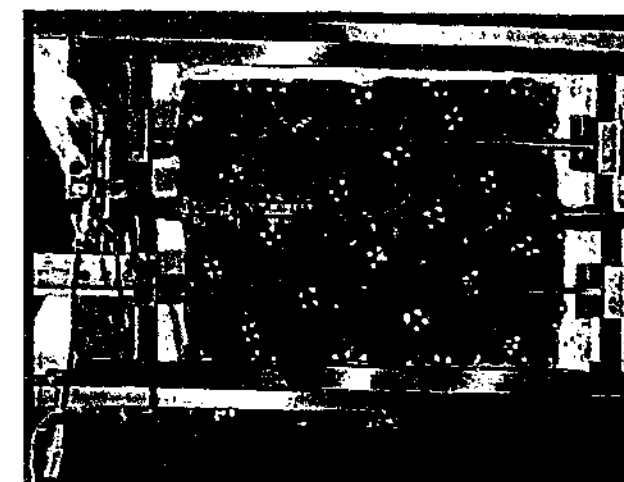


Figure B2-3 – dx = 10 mm

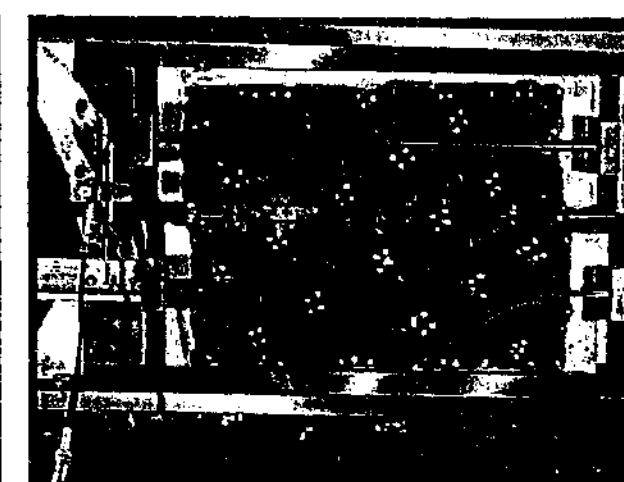


Figure B2-4 – dx = 15 mm

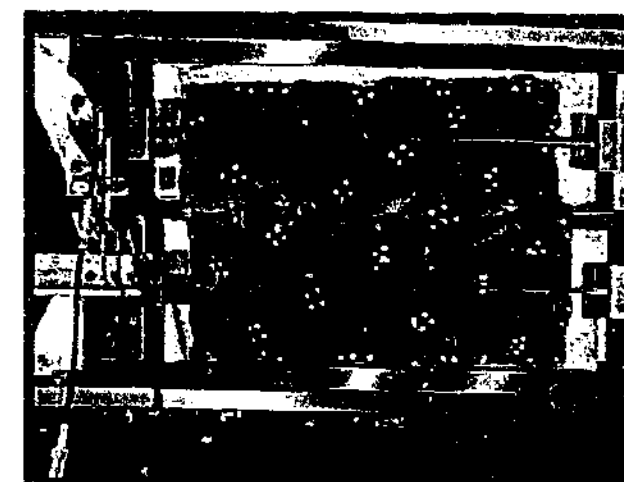


Figure B2-5 – dx = 18 mm

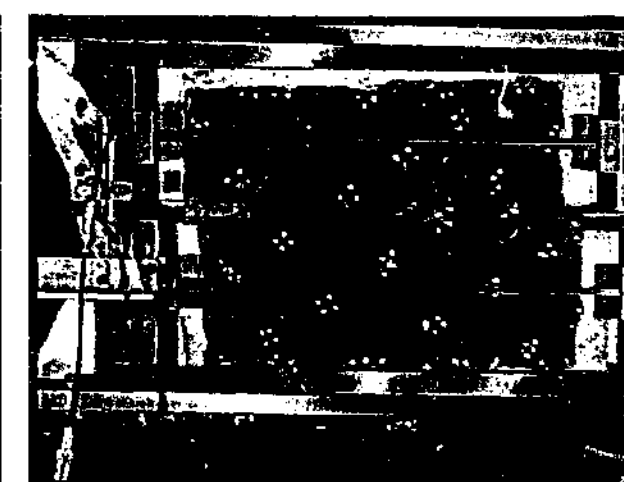
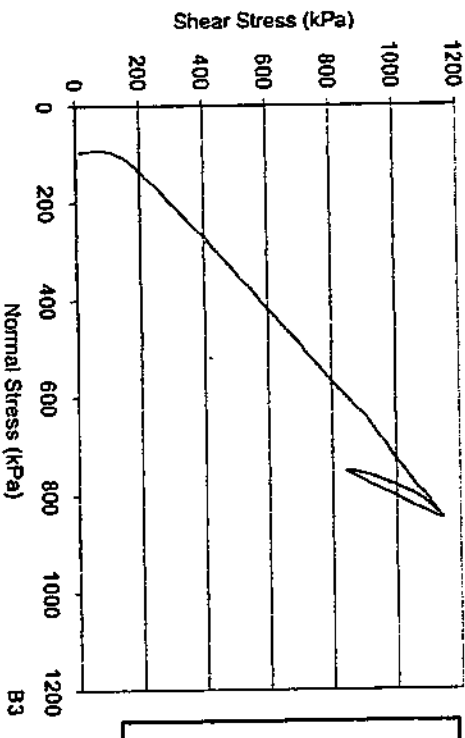
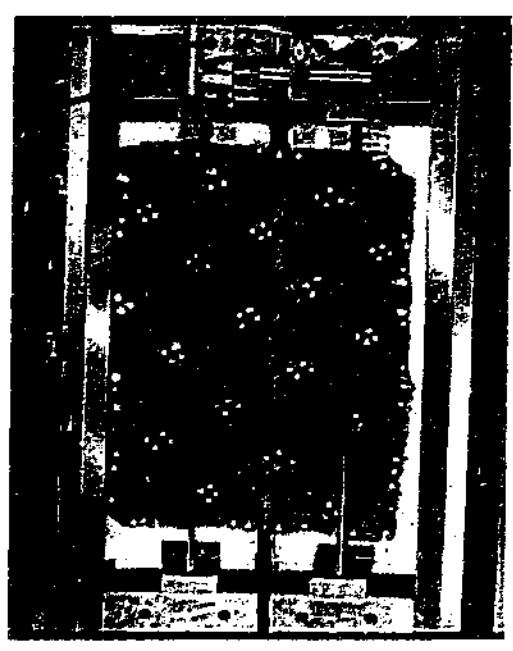
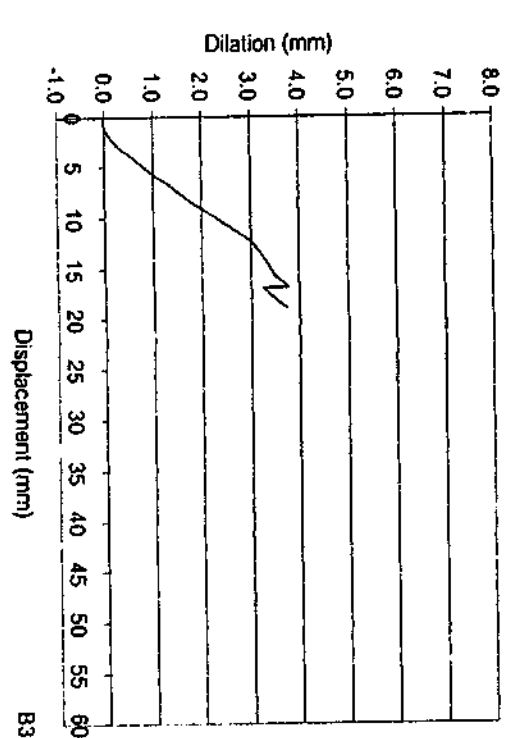
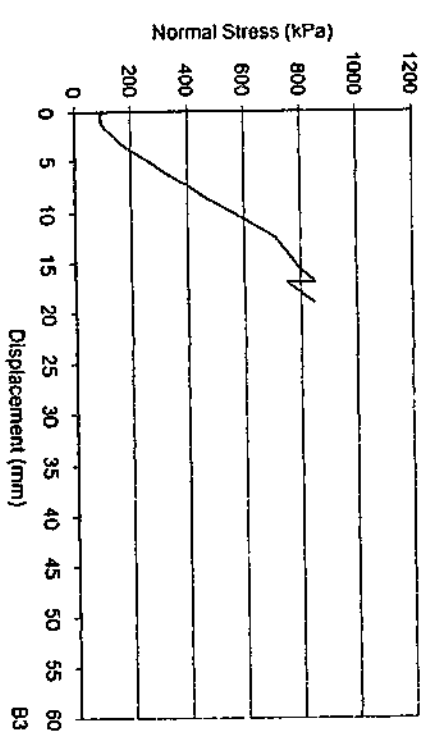
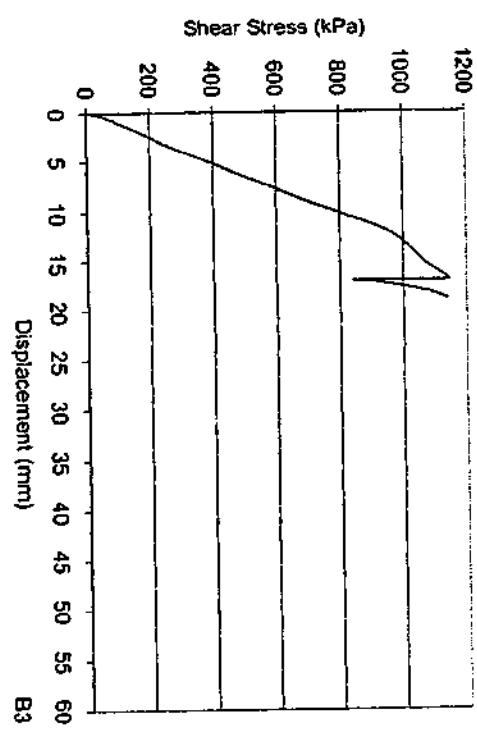


Figure B2-6 – dx = 38 mm

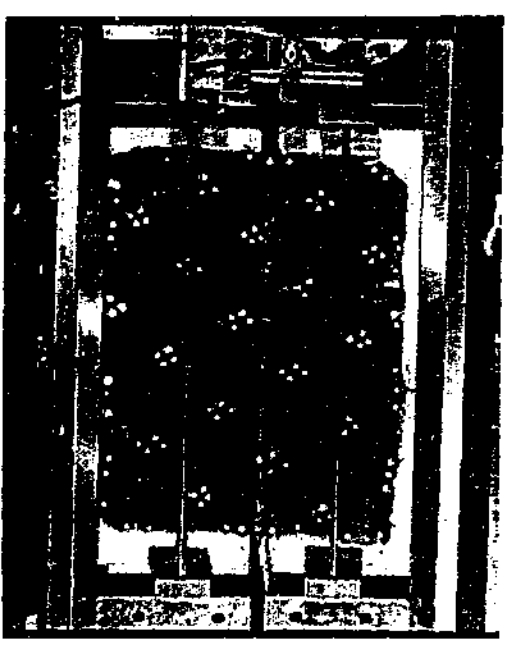
TEST B2			
$\theta_1 = -60^\circ$	$\theta_2 = 30^\circ$	$\theta_3 = n/a$	spacing = 70 mm
$\sigma_{ni} = 100$ kPa	$k_v = 100$ kPa/mm	UCS = 4.14 MPa	



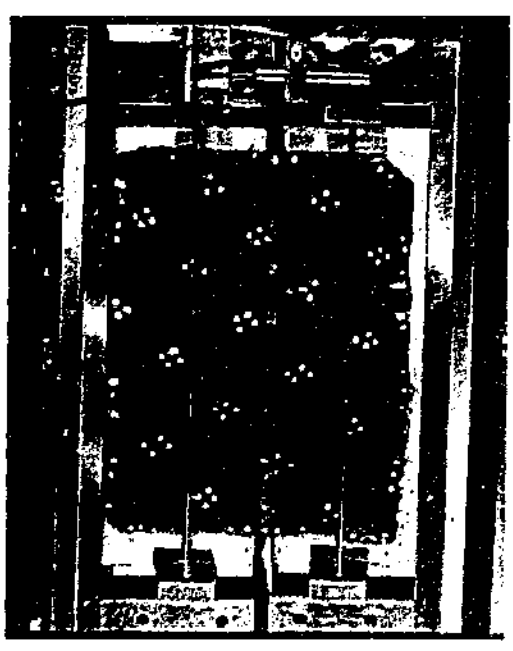
Test Details		B3
θ_1	=	-60°
θ_2	=	45°
θ_3	=	n/a°
spacing	=	70 mm
σ_m	=	100 kPa
k_v	=	200 kPa/mm
UCS	=	5.66 MPa



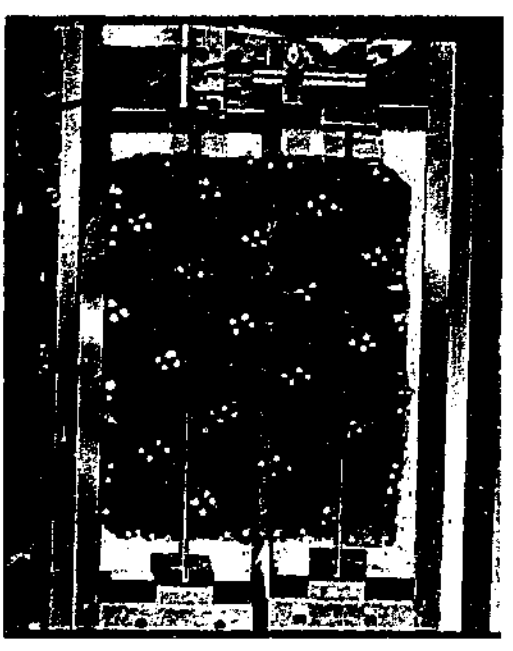
Test B3-1 - dx = 0 mm



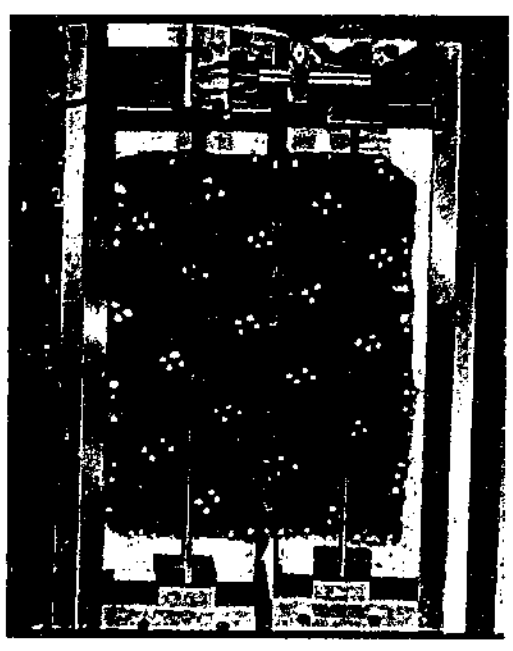
Test B3-2 - dx = 3 mm



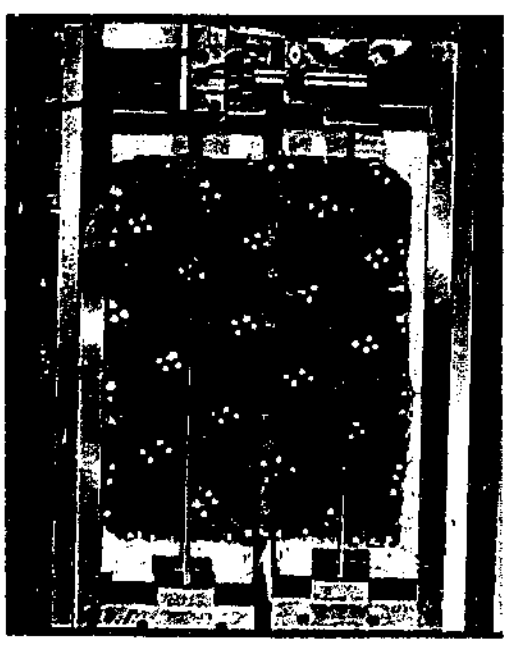
Test B3-3 - dx = 6 mm



Test B3-4 - dx = 9 mm

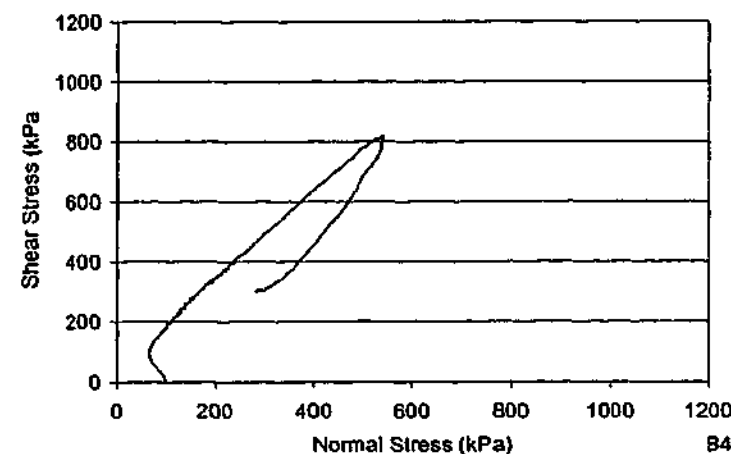


Test B3-5 - dx = 12 mm

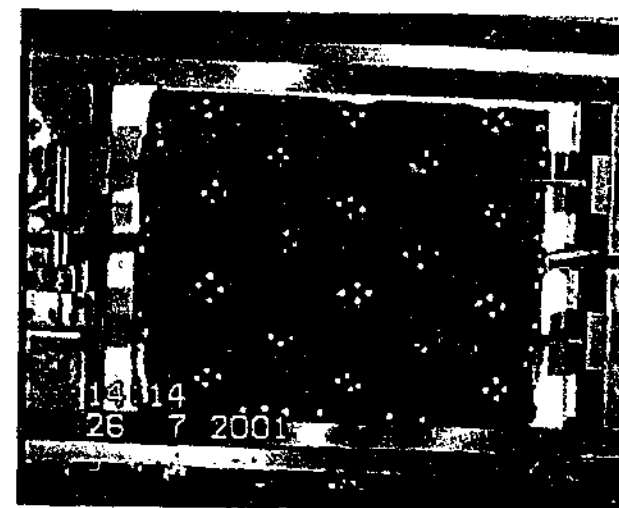
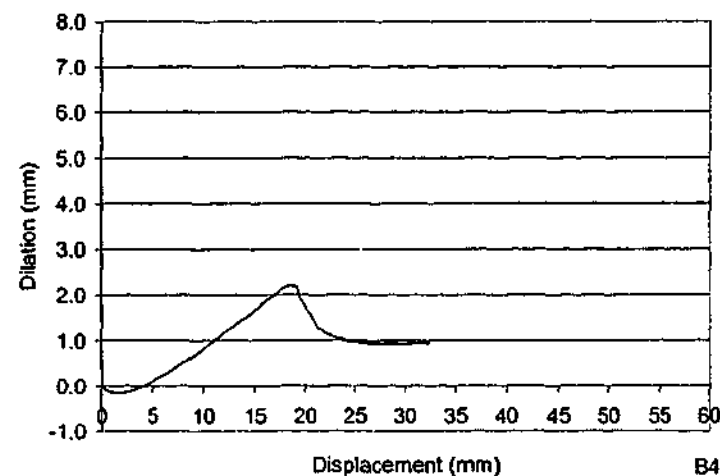
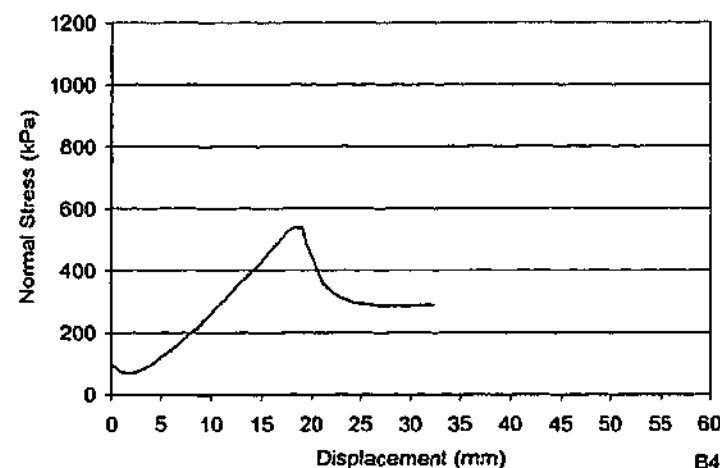
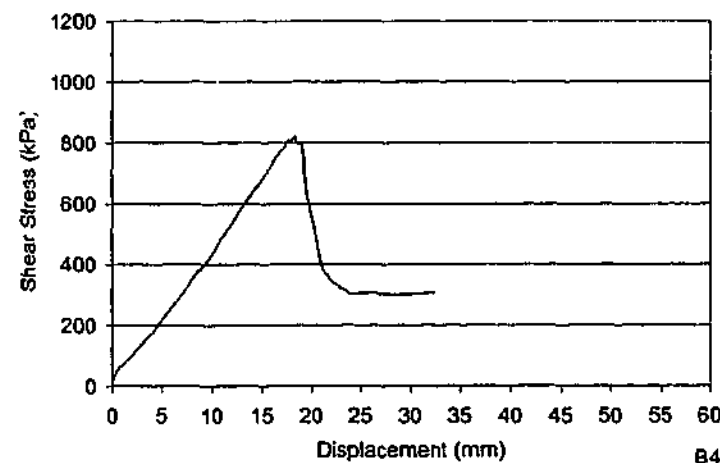


Test B3-6 - dx = 15 mm

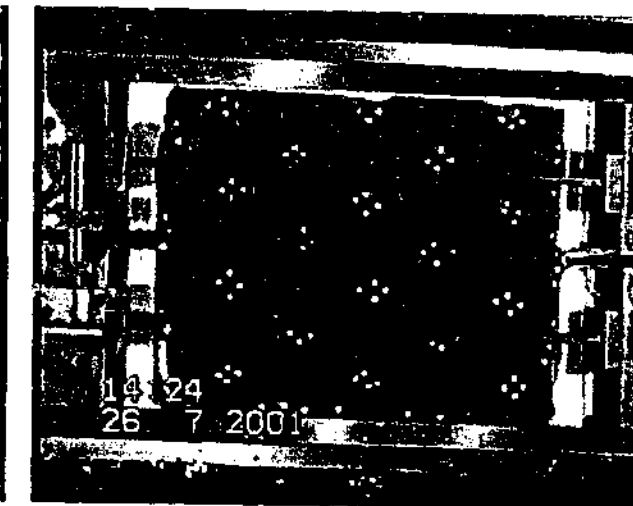
TEST B3		
$\theta_1 = -60^\circ$	$\theta_2 = 45^\circ$	$\theta_3 = n/a$
$\sigma_m = 100 \text{ kPa}$	$k_v = 200 \text{ kPa/mm}$	spacing = 70 mm
		UCS = 5.66 MPa



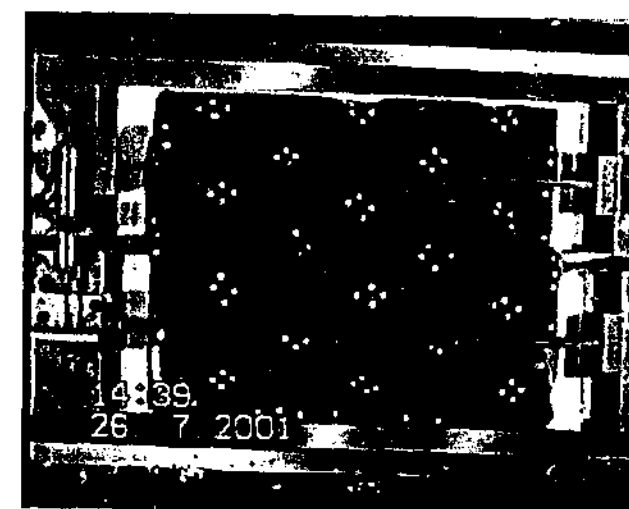
Test Details B4	
θ_1	= -31°
θ_2	= 29°
θ_3	= n/a
spacing	= 70 mm
σ_{ni}	= 100 kPa
k_v	= 200 kPa/mm
UCS	= 2.99 MPa



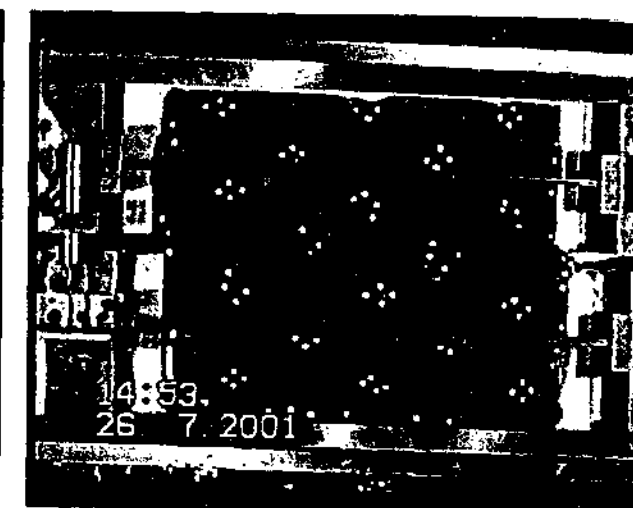
Test B4-1 – dx = 0 mm



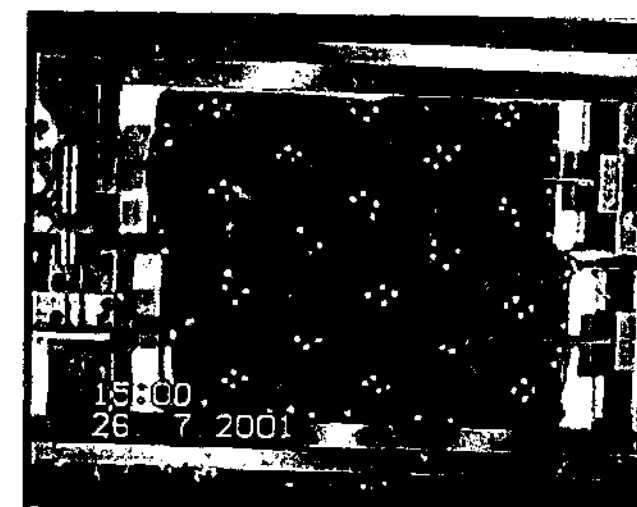
Test B4-2 – dx = 5 mm



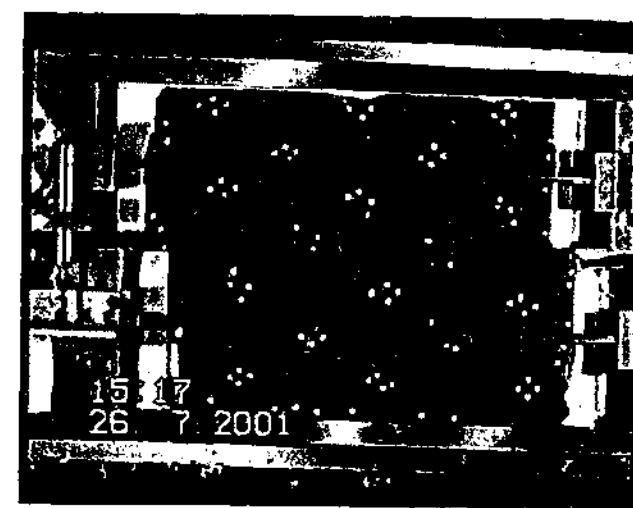
Test B4-3 – dx = 10 mm



Test B4-4 – dx = 18 mm

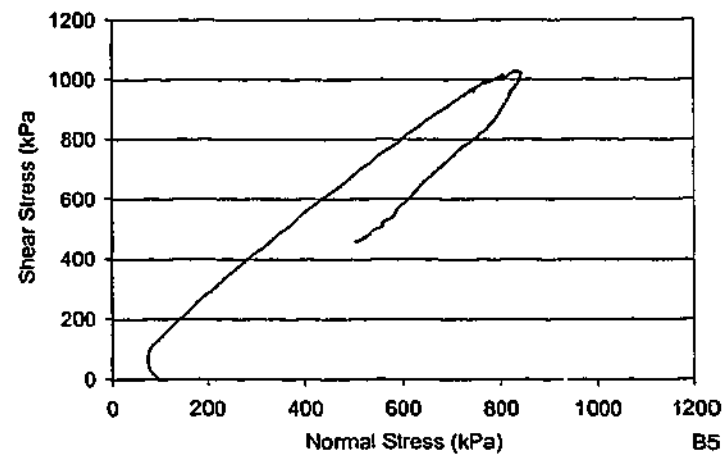


Test B4-5 – dx = 24 mm

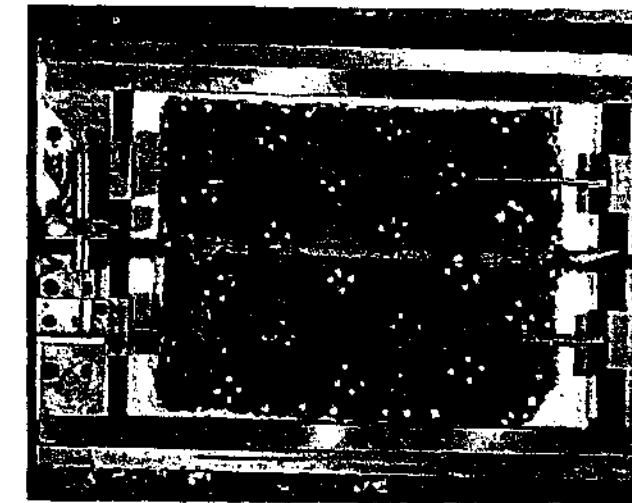
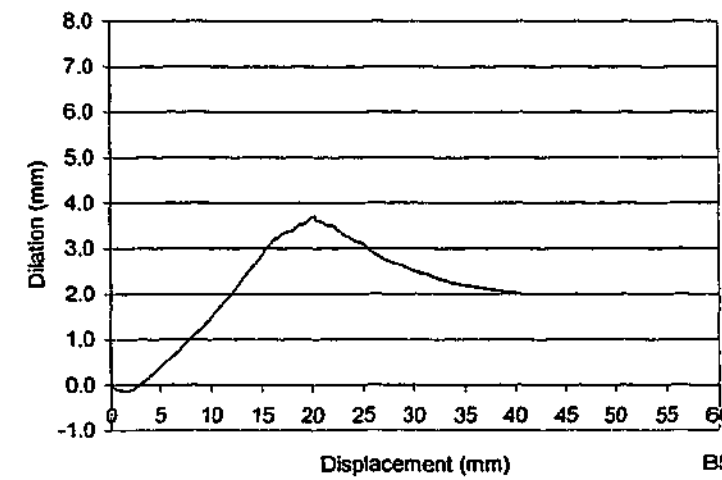
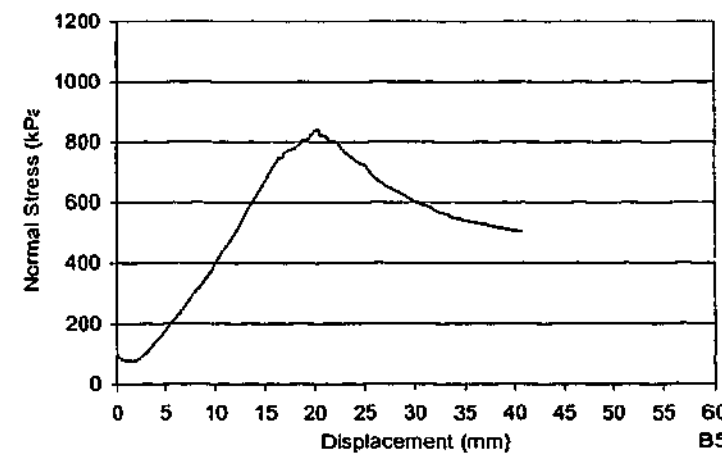
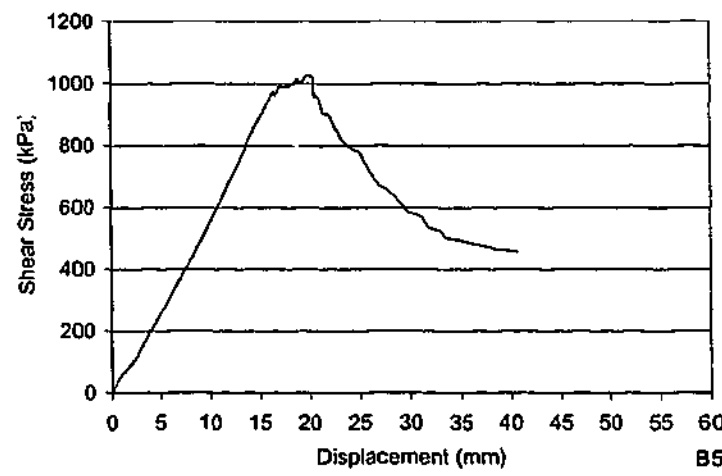


Test B4-6 dx = 32 mm

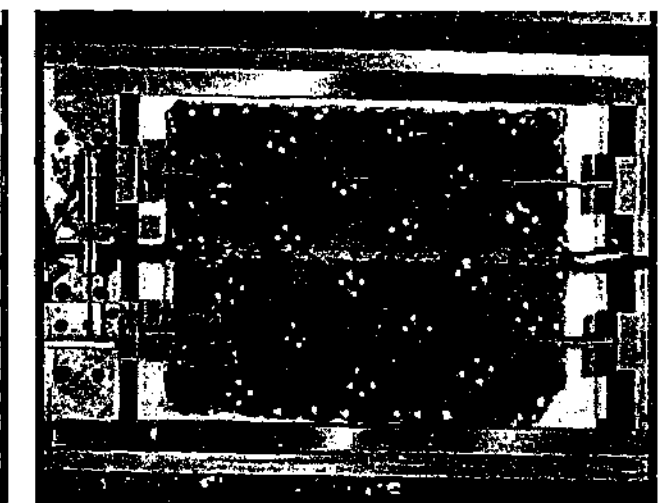
TEST B4			
$\theta_1 = -30^\circ$	$\theta_2 = 30^\circ$	$\theta_3 = n/a$	spacing = 70 mm
$\sigma_{ni} = 100$ kPa	$k_v = 200$ kPa/mm		UCS = 2.99 MPa



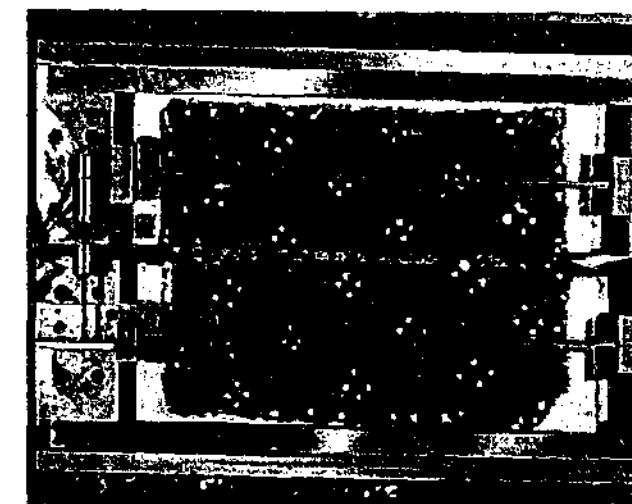
Test Details		B5
θ_1	=	-30°
θ_2	=	45°
θ_3	=	n/a $^\circ$
spacing	=	70 mm
σ_{ni}	=	100 kPa
k_v	=	200 kPa/mm
UCS	=	3.37 MPa



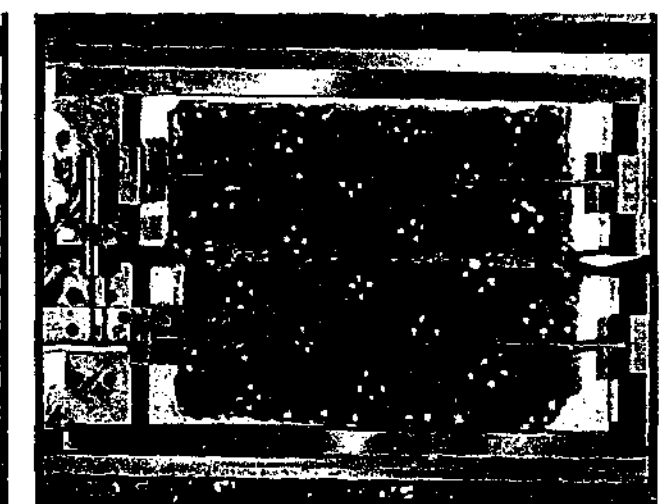
Test B5-1 – dx = 0 mm



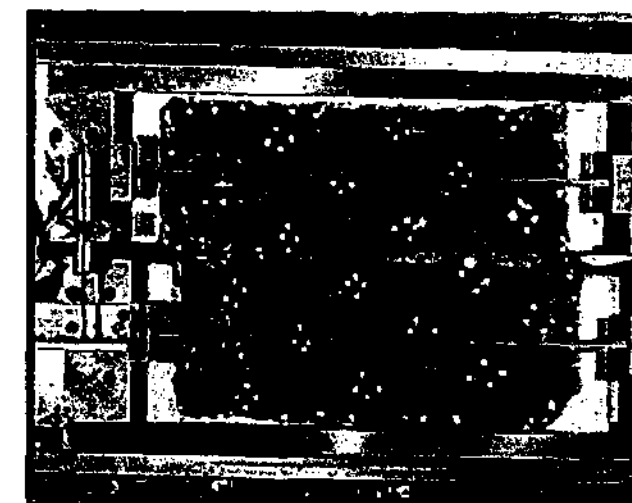
Test B5-2 – dx = 3 mm



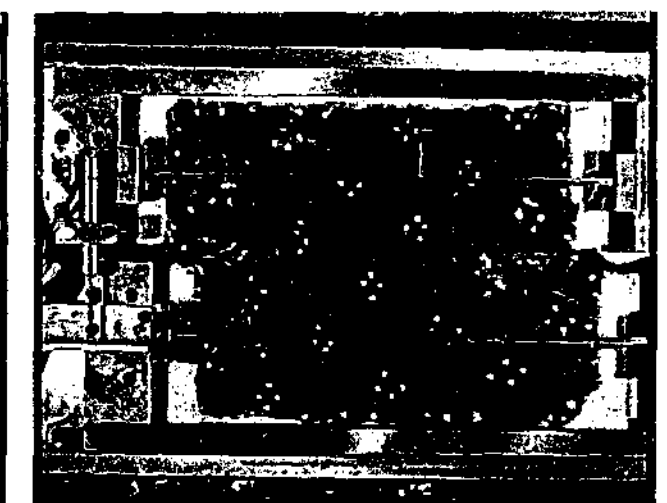
Test B5-3 – dx = 10 mm



Test B5-4 – dx = 14 mm

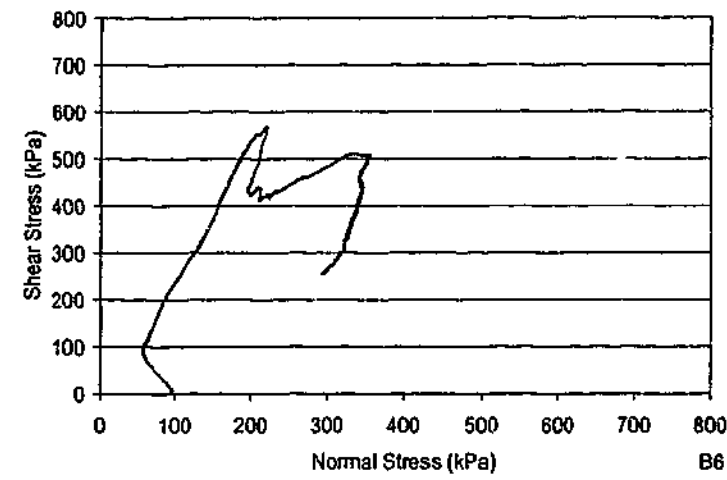


Test B5-5 – dx = 19 mm

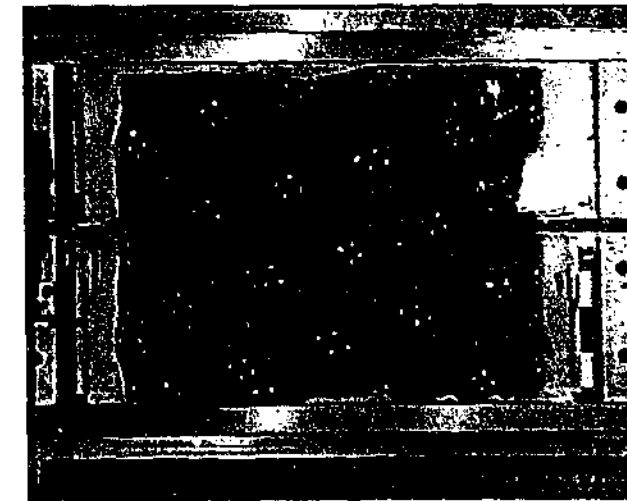
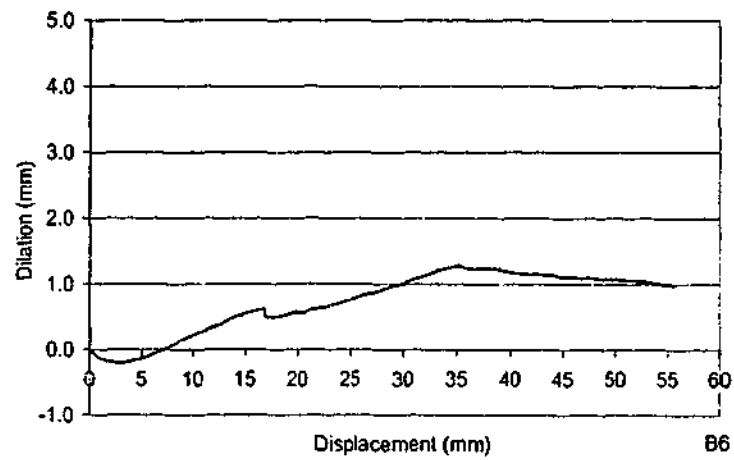
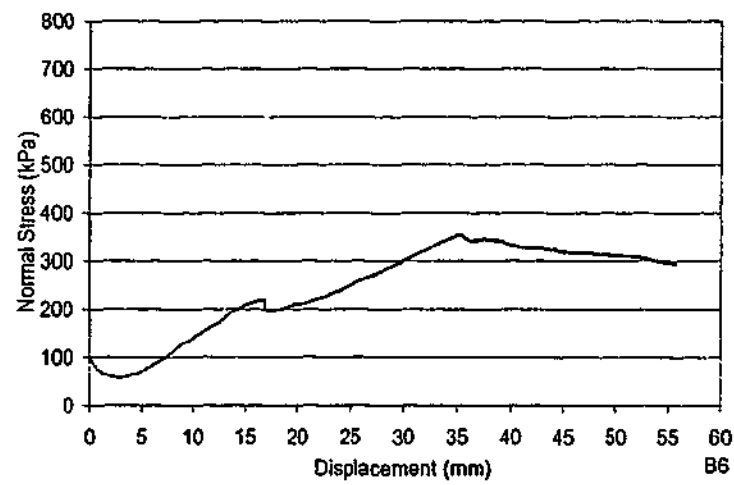
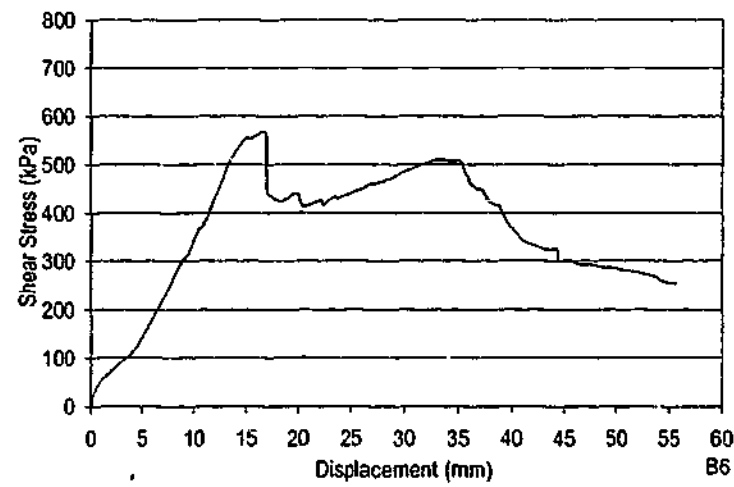


Test B5-6 – dx = 33 mm

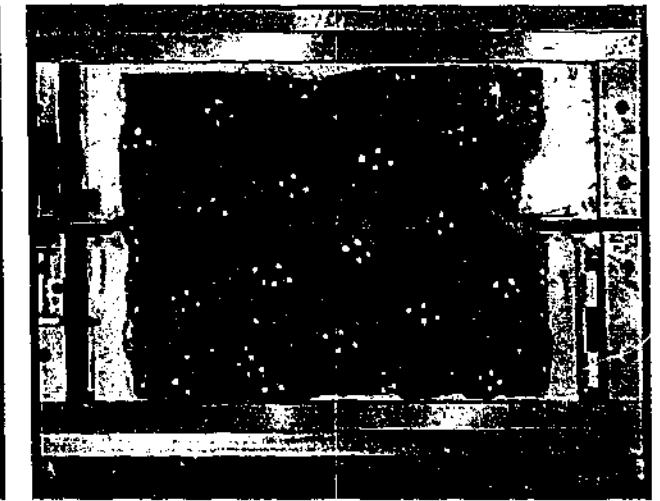
TEST B5						
$\theta_1 = -30^\circ$	$\theta_2 = 45^\circ$	$\theta_3 = n/a$	spacing = 70 mm			
$\sigma_{ni} = 100$ kPa	$k_v = 200$ kPa/mm		UCS = 3.37 MPa			



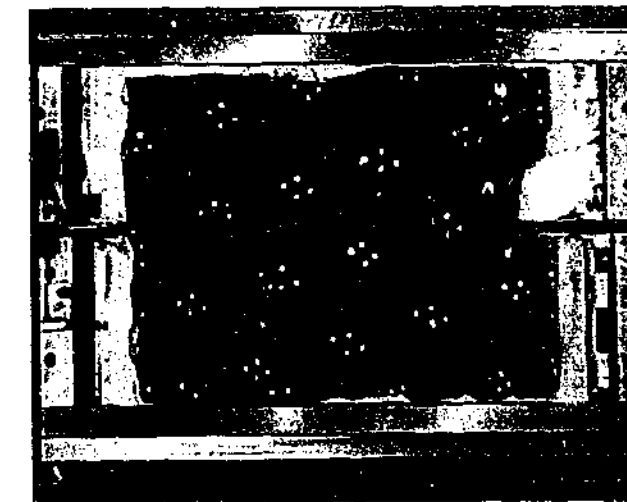
Test Details B6	
θ_1	= -45°
θ_2	= 15°
θ_3	= n/a $^\circ$
spacing	= 70 mm
σ_{ni}	= 100 kPa
k_v	= 200 kPa/mm
UCS	= 3.70 MPa



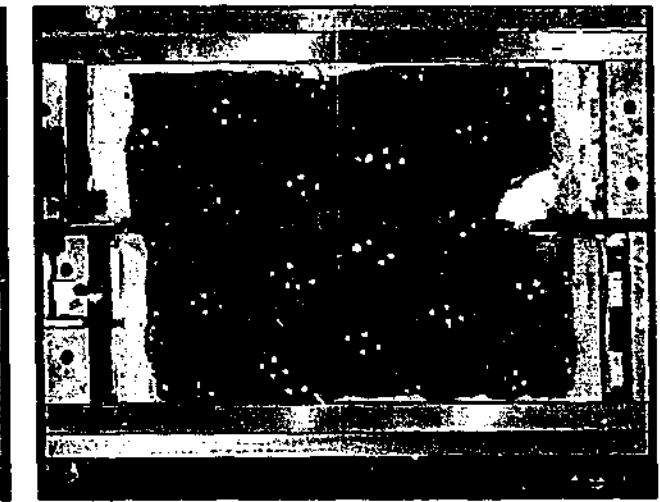
Test B6-1 – dx = 0 mm



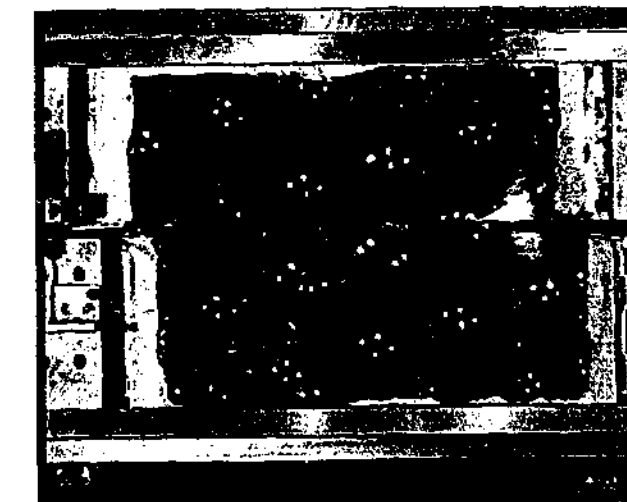
Test B6-2 – dx = 4 mm



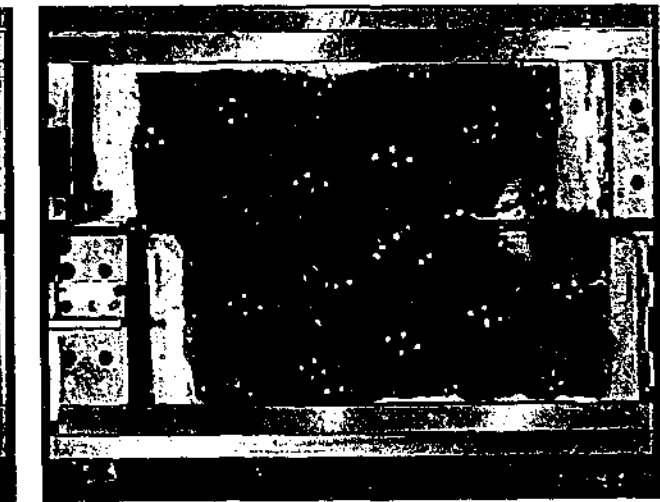
Test B6-3 – dx = 8 mm



Test B6-4 – dx = 19 mm



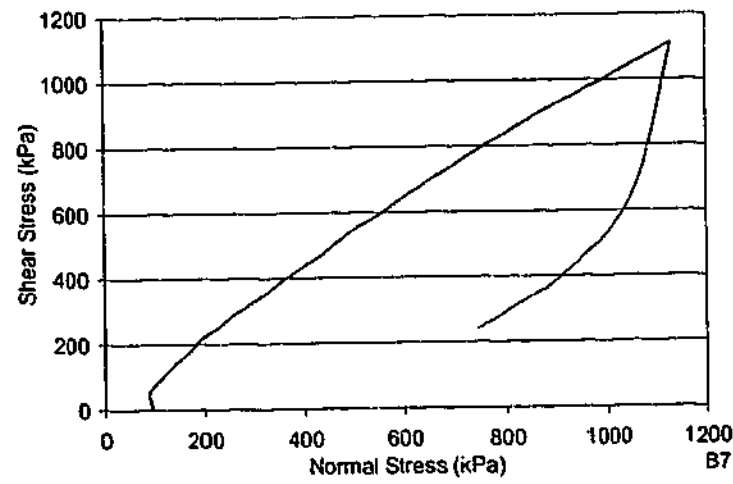
Test B6-5 – dx = 29 mm



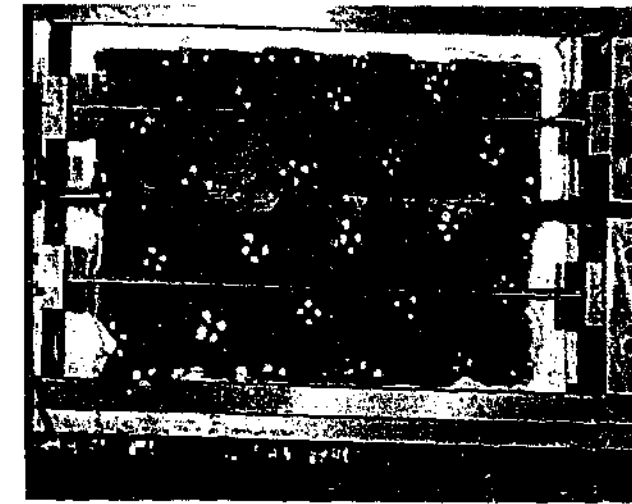
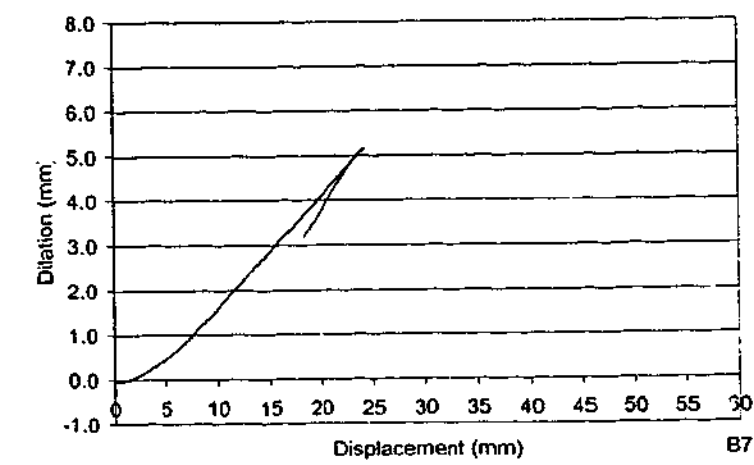
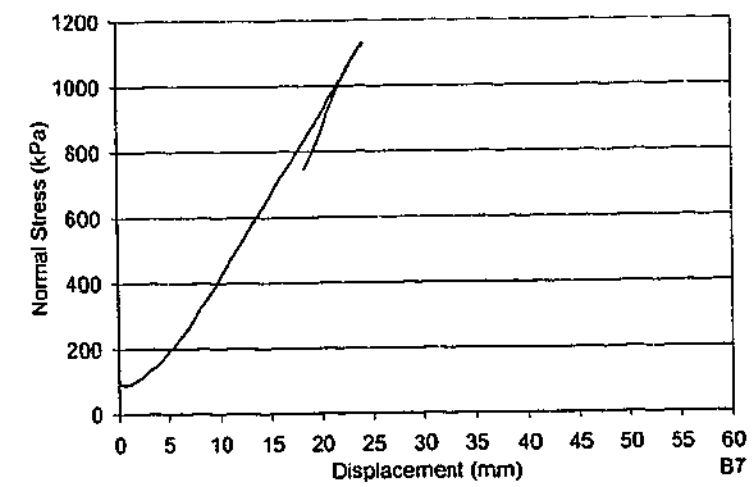
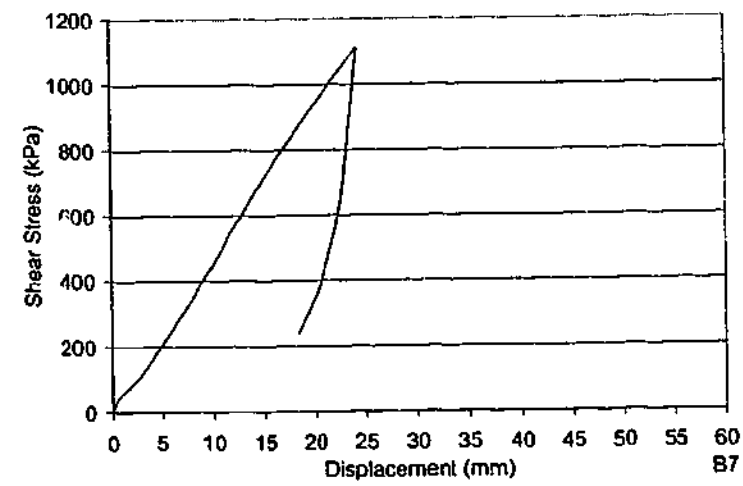
Test B6-6 – dx = 50 mm

TEST B6

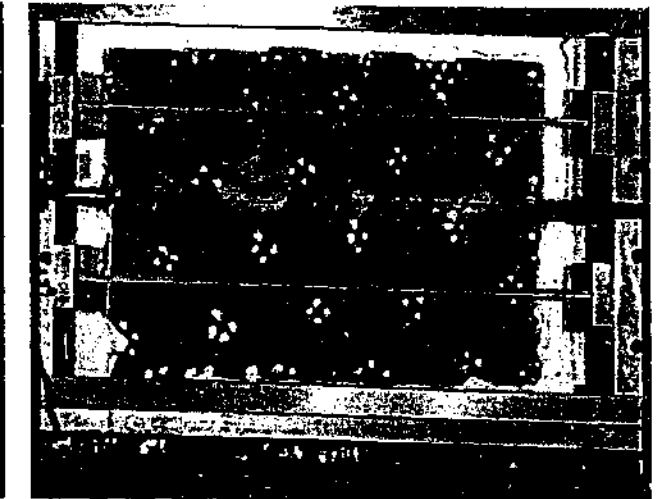
$\theta_1 = -45^\circ$ $\theta_2 = 15^\circ$ $\theta_3 = \text{n/a}$ spacing = 70 mm
 $\sigma_{ni} = 100 \text{ kPa}$ $k_v = 200 \text{ kPa/mm}$ UCS = 3.70 MPa



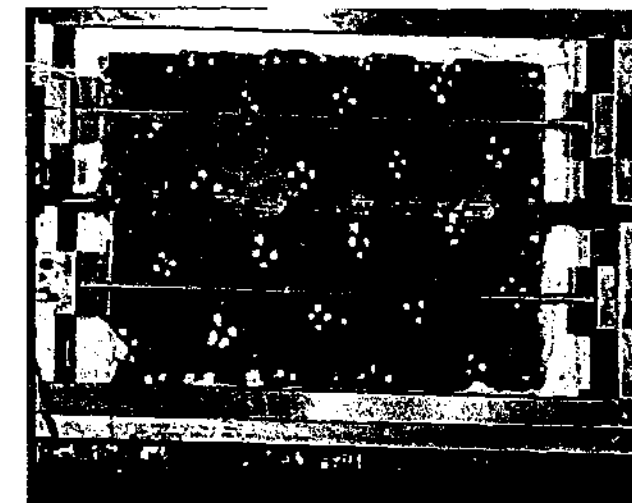
Test Details		B7
θ_1	=	-46°
θ_2	=	61°
θ_3	=	n/a
spacing	=	70 mm
σ_{ni}	=	100 kPa
k_v	=	200 kPa/mm
UCS	=	4.15 MPa



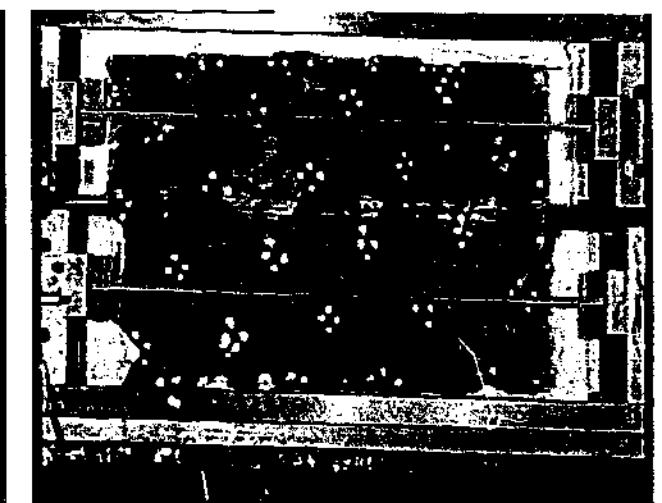
Test B7-1 – dx = 0 mm



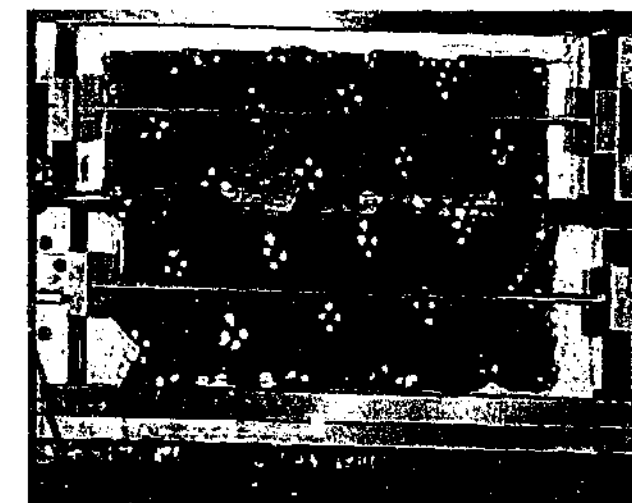
Test B7-2 – dx = 4 mm



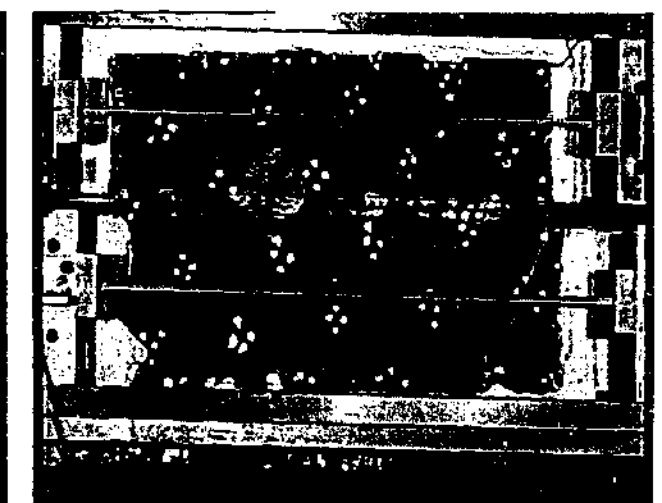
Test B7-3 – dx = 9 mm



Test B7-4 – dx = 15 mm

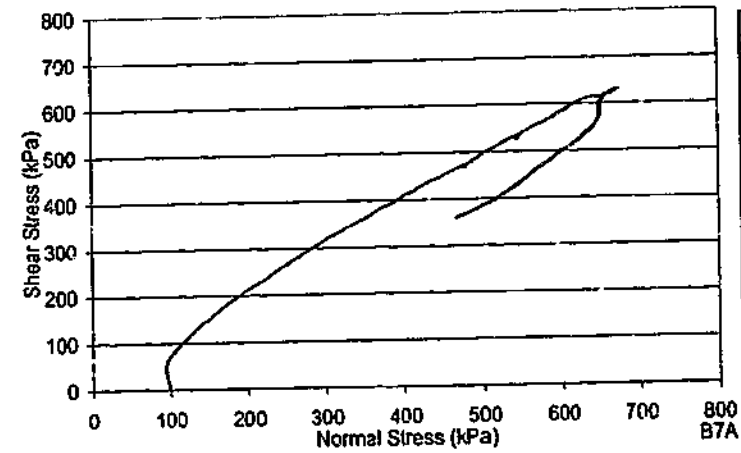


Test B7-5 – dx = 19 mm

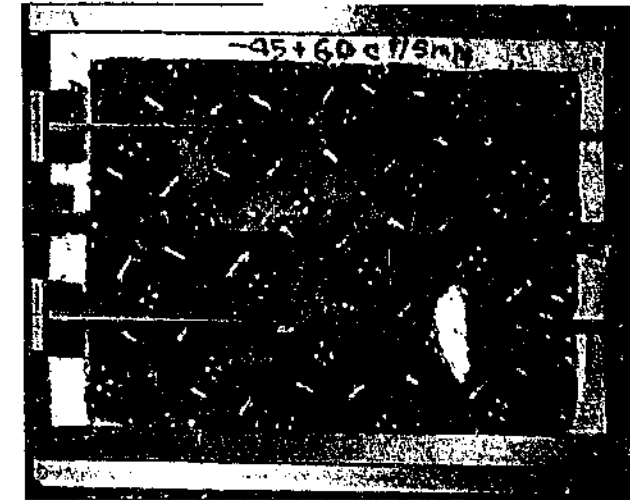
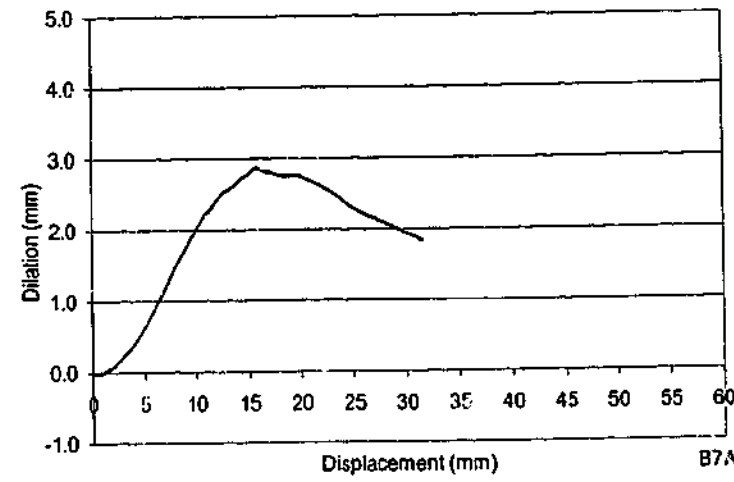
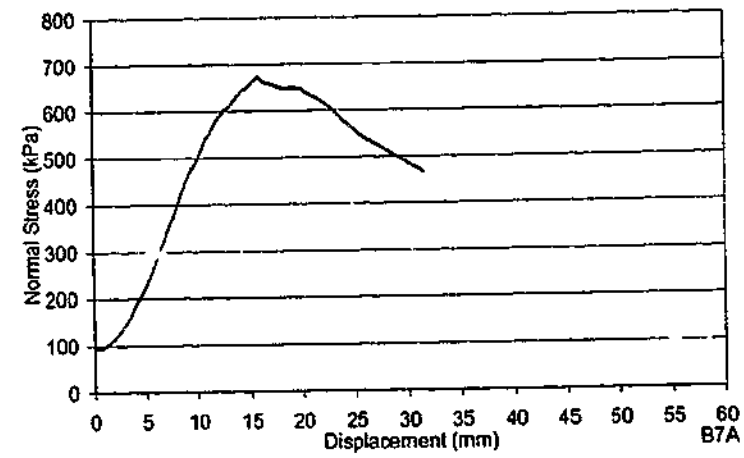
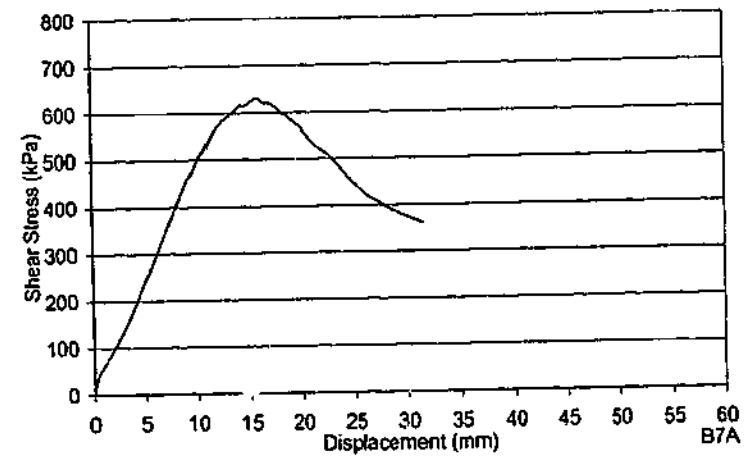


Test B7-6 – dx = 23 mm

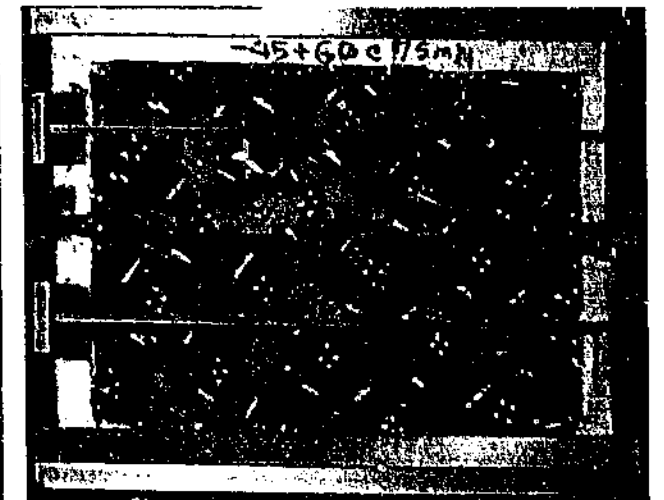
TEST B7					
$\theta_1 = -46^\circ$	$\theta_2 = 61^\circ$	$\theta_3 = n/a$	spacing = 70 mm		
$\sigma_{ni} = 100$ kPa	$k_v = 200$ kPa/mm		UCS = 4.15 MPa		



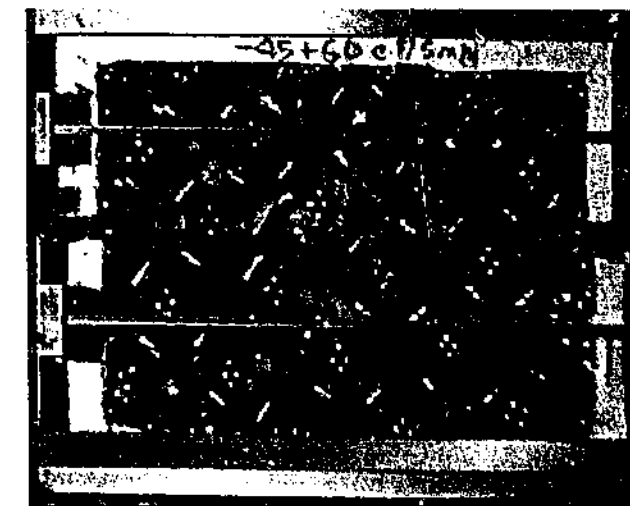
Test Details B7A	
θ_1	= -45°
θ_2	= 60°
θ_3	= n/a
spacing	= 70 mm
σ_{ni}	= 100 kPa
k_v	= 200 kPa/mm
UCS	= 1.70 MPa



Test B7A-1 – dx = 0 mm



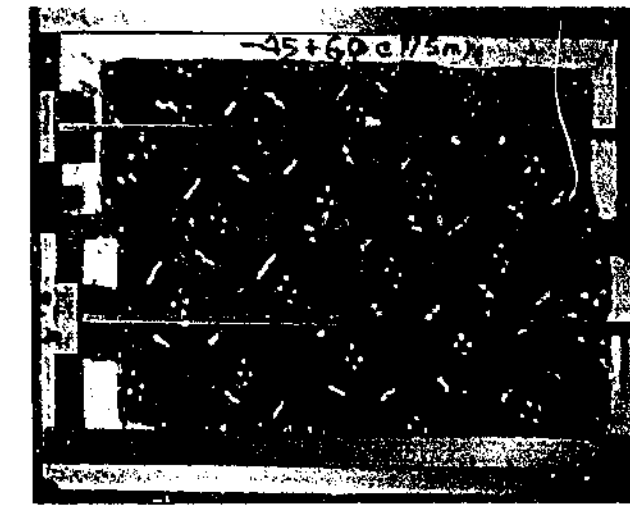
Test B7A-2 – dx = 5 mm



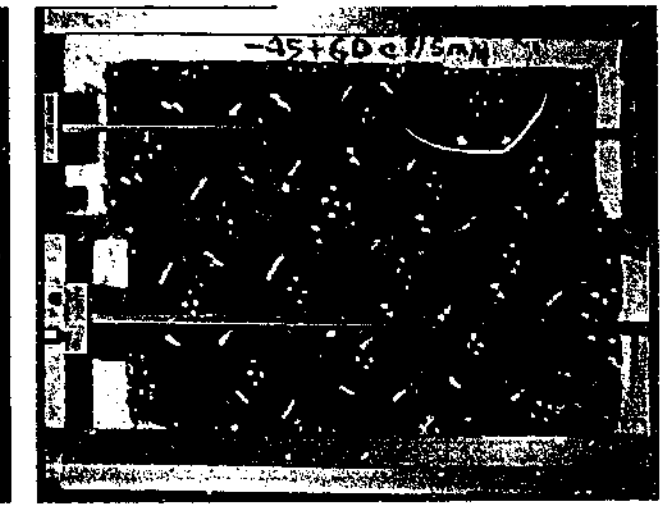
Test B7A-3 – dx = 10 mm



Test B7A-4 – dx = 15 mm

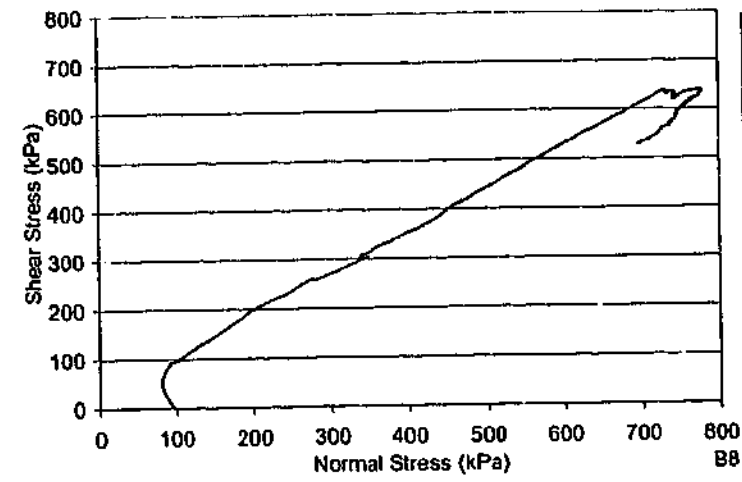


Test B7A-5 – dx = 20 mm

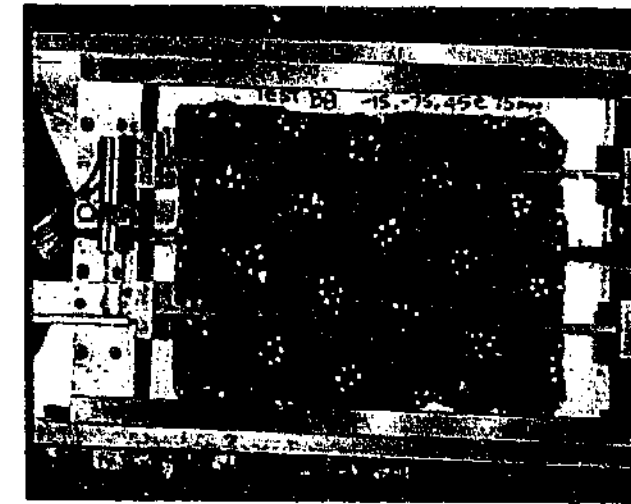
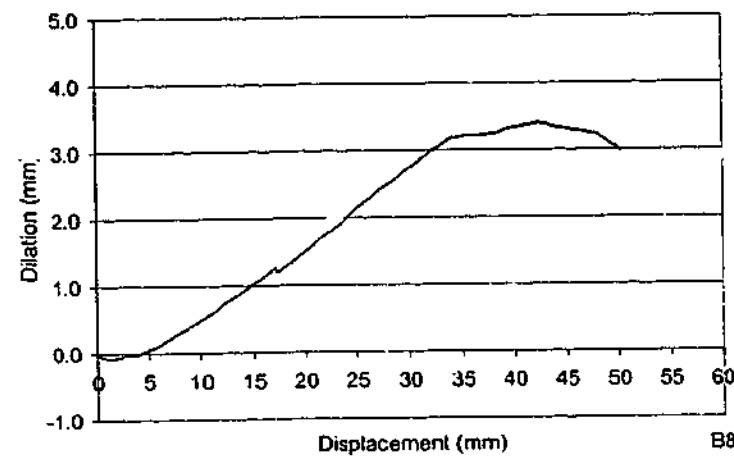
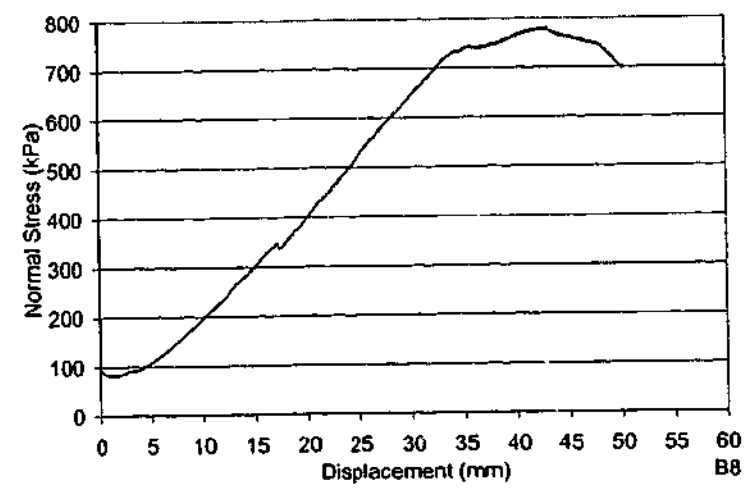
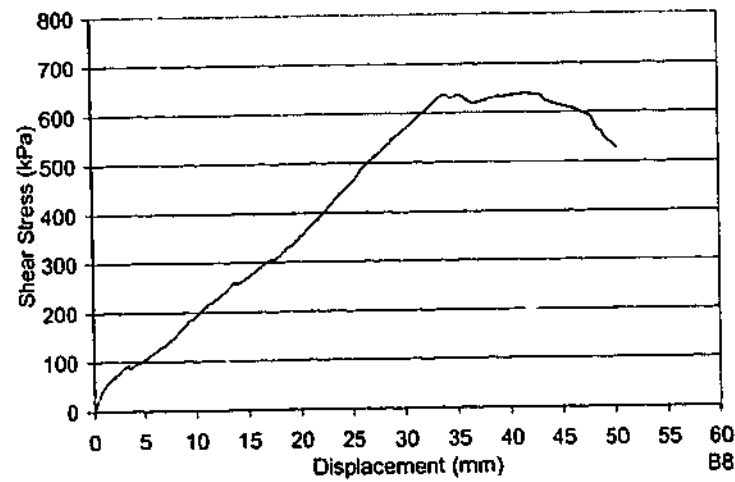


Test B7A-6 – dx = 25 mm

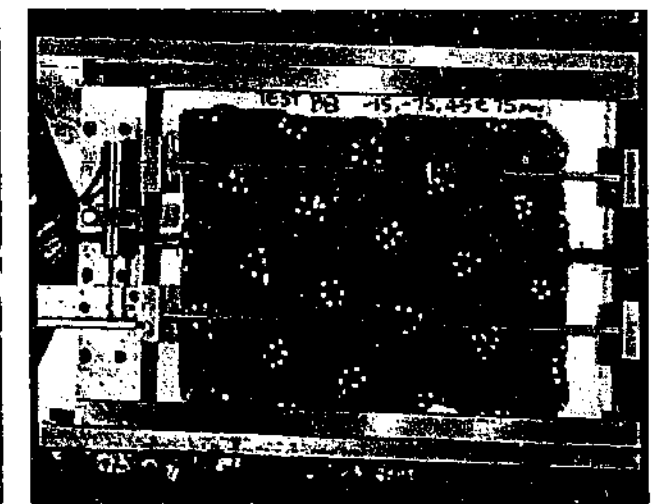
TEST B7A			
$\theta_1 = -45^\circ$	$\theta_2 = 60^\circ$	$\theta_3 = n/a$	spacing = 70 mm
$\sigma_{ni} = 100 \text{ kPa}$	$k_v = 200 \text{ kPa/mm}$		UCS = 1.70 MPa



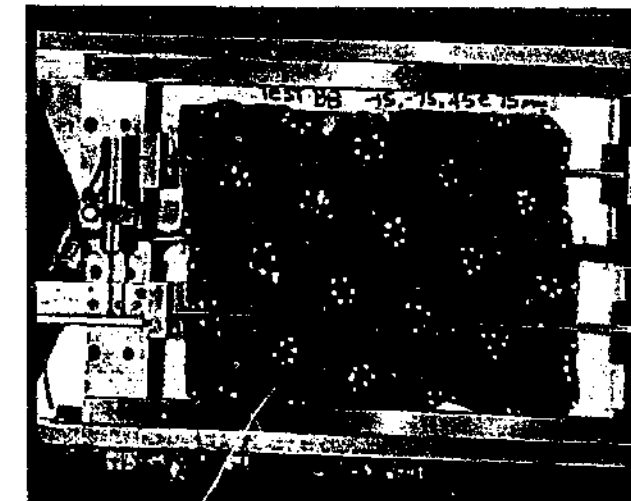
Test Details B8	
θ_1	= -15°
θ_2	= 46°
θ_3	= -75°
spacing	= 70 mm
σ_{ni}	= 100 kPa
k_v	= 200 kPa/mm
UCS	= 3.27 MPa



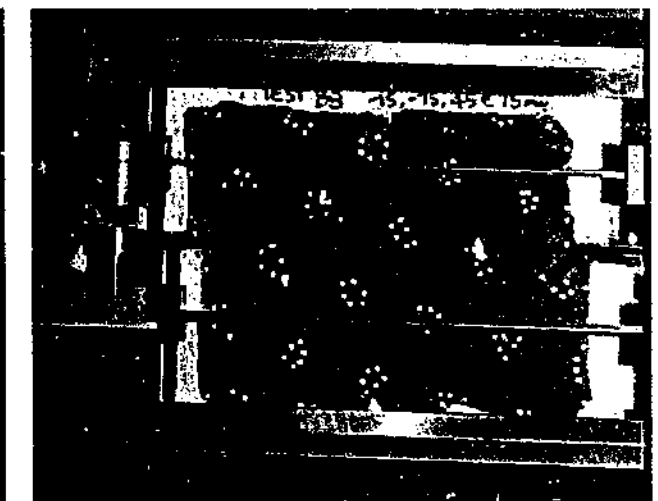
Test B8-1 – dx = 0 mm



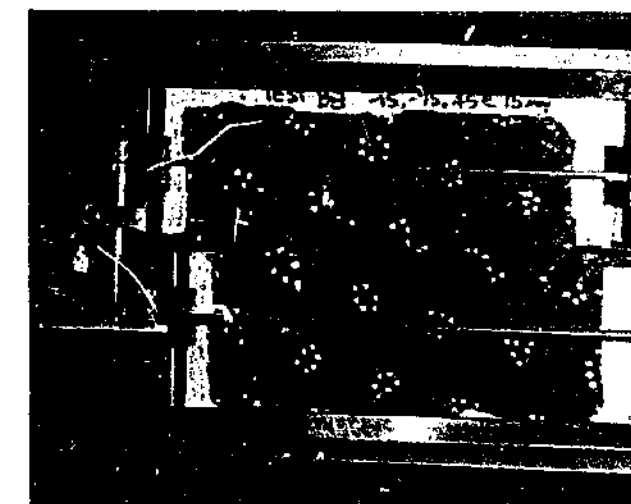
Test B8-2 – dx = 3 mm



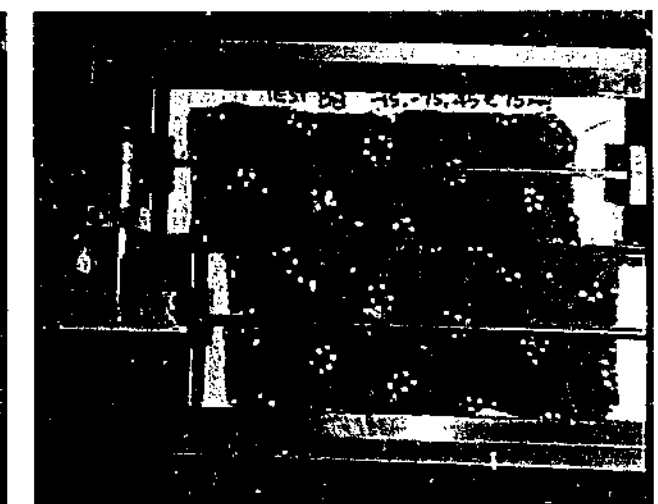
Test B8-3 – dx = 10 mm



Test B8-4 – dx = 17 mm

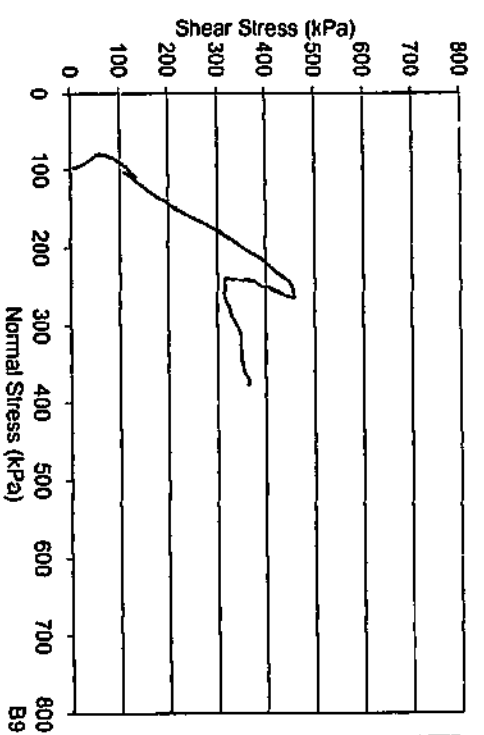


Test B8-5 – dx = 33 mm

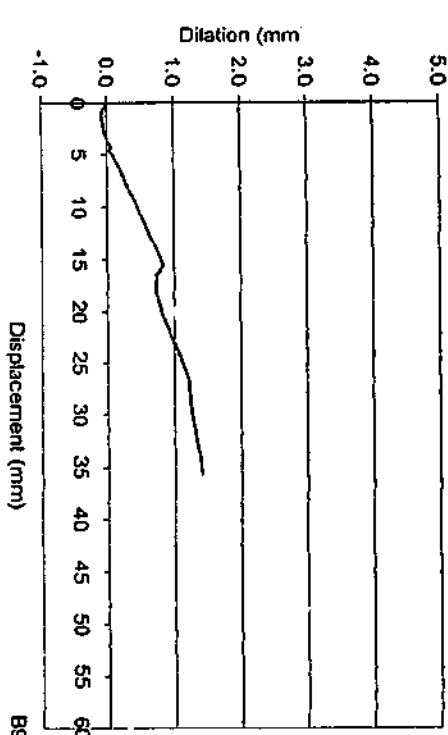
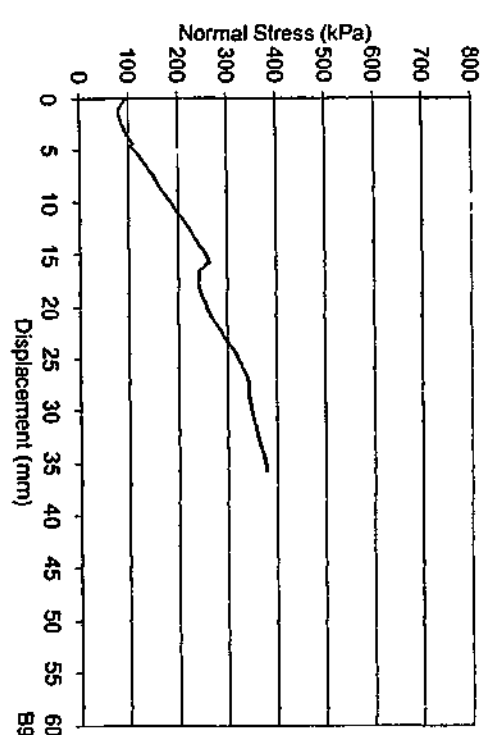
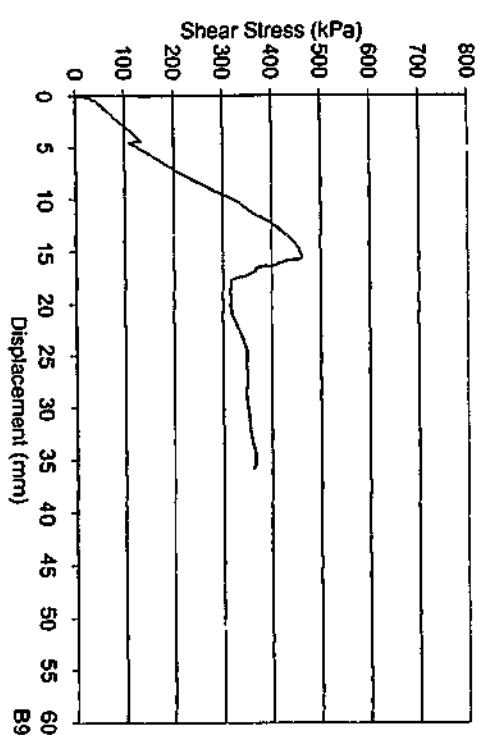


Test B8-6 – dx = 45 mm

TEST B8					
$\theta_1 = -15^\circ$	$\theta_2 = 46^\circ$	$\theta_3 = -75^\circ$	spacing = 70 mm		
$\sigma_{ni} = 100$ kPa	$k_v = 200$ kPa/mm		UCS = 3.27 MPa		



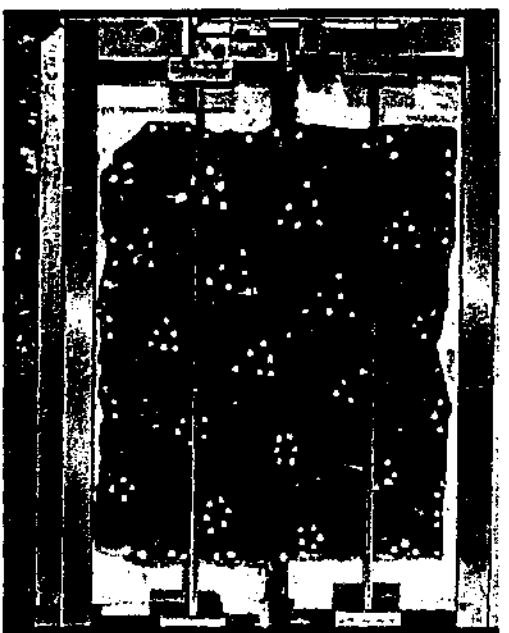
Test Details		B9
θ_1	=	-45°
θ_2	=	15°
θ_3	=	75°
spacing	=	70 mm
σ_m	=	100 kPa
k_v	=	200 kPa/mm
UCS	=	3.03 MPa



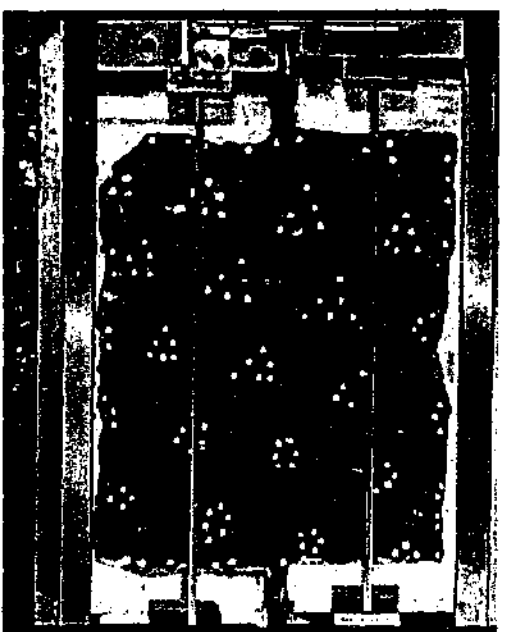
Test B9-1 - dx = 0 mm



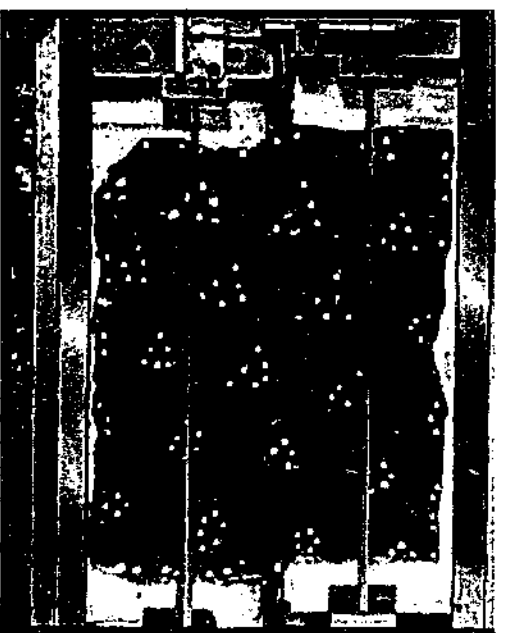
Test B9-2 - dx = 2 mm



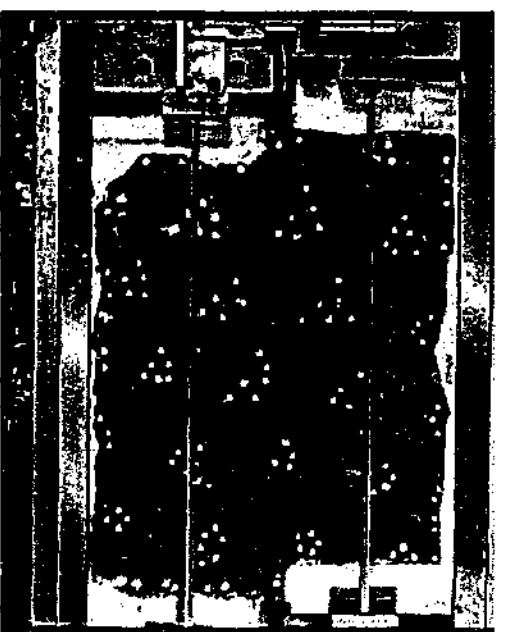
Test B9-3 - dx = 6 mm



Test B9-4 - dx = 14 mm

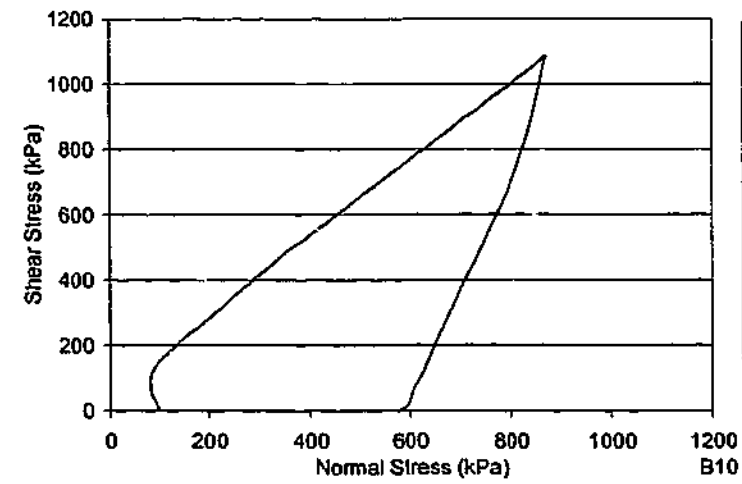


Test B9-5 - dx = 20 mm

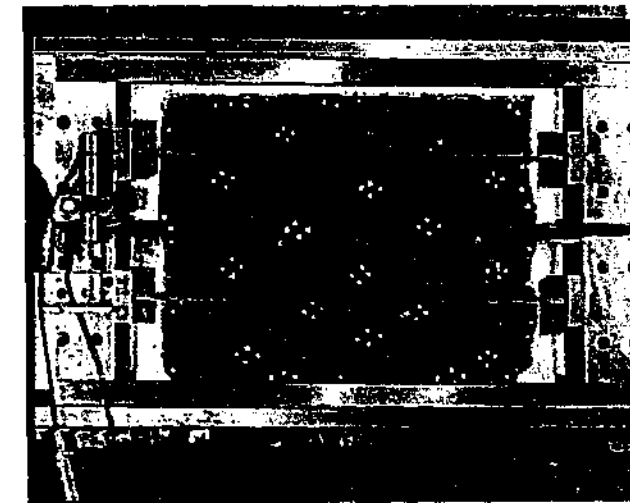
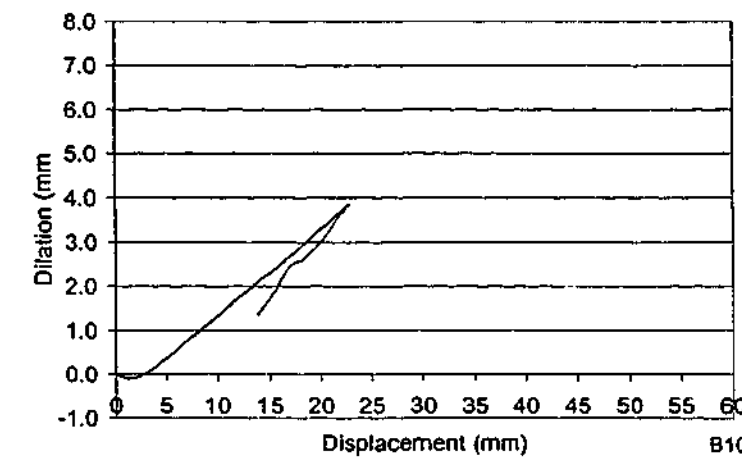
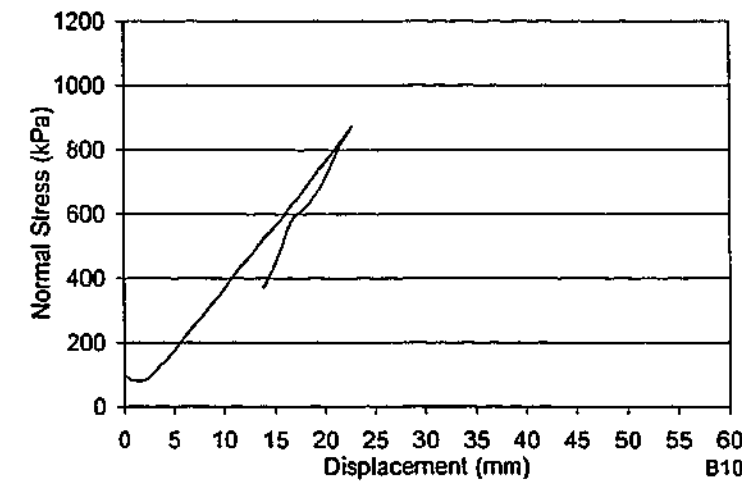
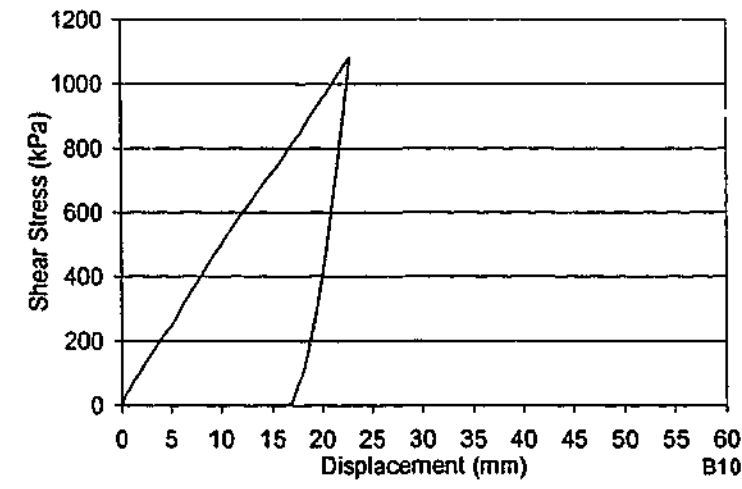


Test B9-6 - dx = 32 mm

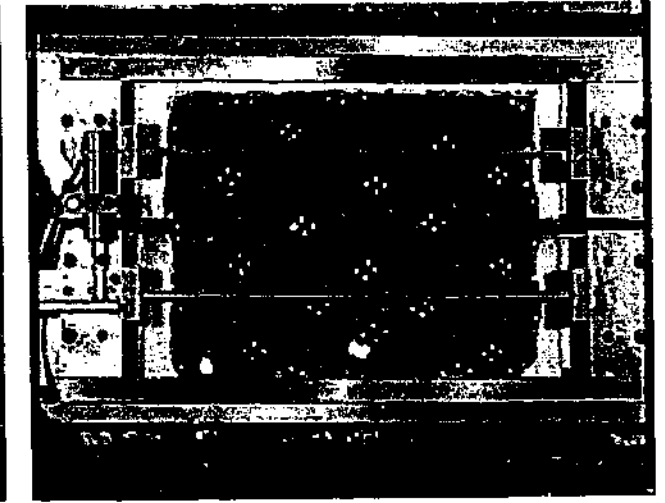
TEST B9		
$\theta_1 = -45^\circ$	$\theta_2 = 15^\circ$	$\theta_3 = 75^\circ$
$\sigma_m = 100$ kPa	$k_v = 200$ kPa/mm	spacing = 70 mm
		UCS = 3.03 MPa



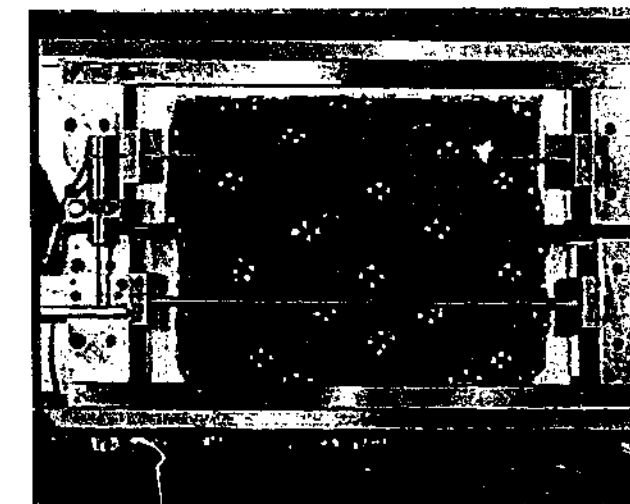
Test Details B10	
θ_1	= $-30 \pm 5^\circ$
θ_2	= $30 \pm 5^\circ$
θ_3	= n/a°
spacing	= 70 mm (nom)
σ_{ni}	= 100 kPa
k_v	= 200 kPa/mm
UCS	= 3.44 MPa



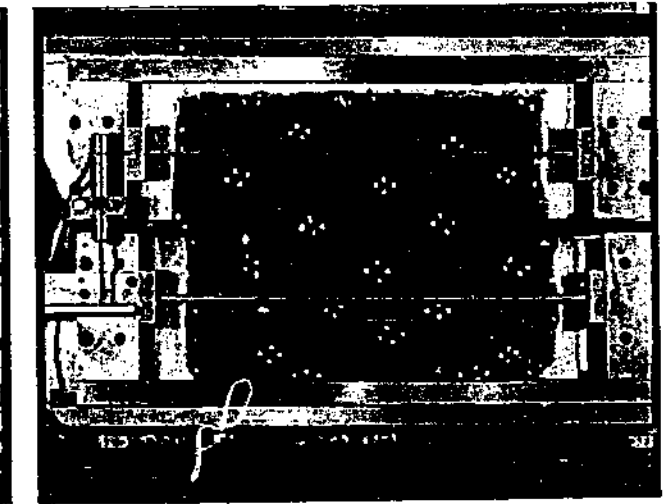
Test B10-1 – dx = 0 mm



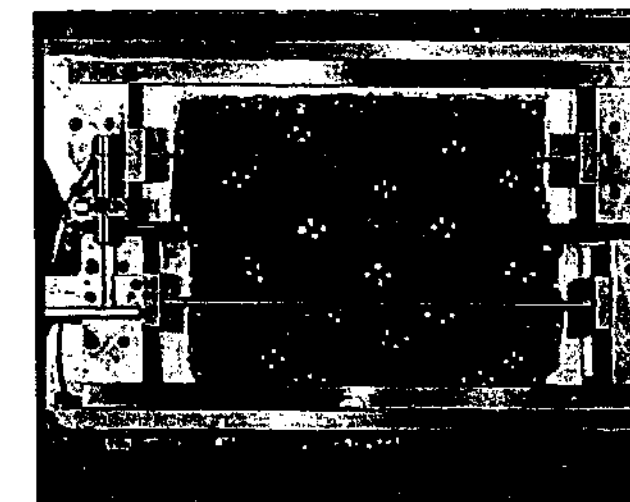
Test B10-2 – dx = 2 mm



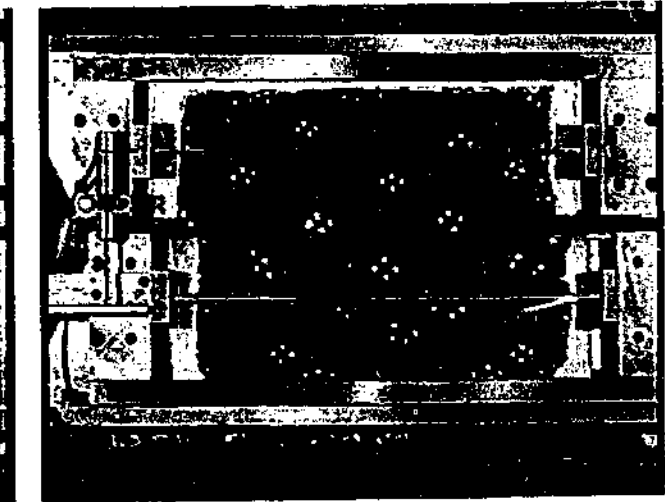
Test B10-3 – dx = 9 mm



Test B10-4 – dx = 13 mm

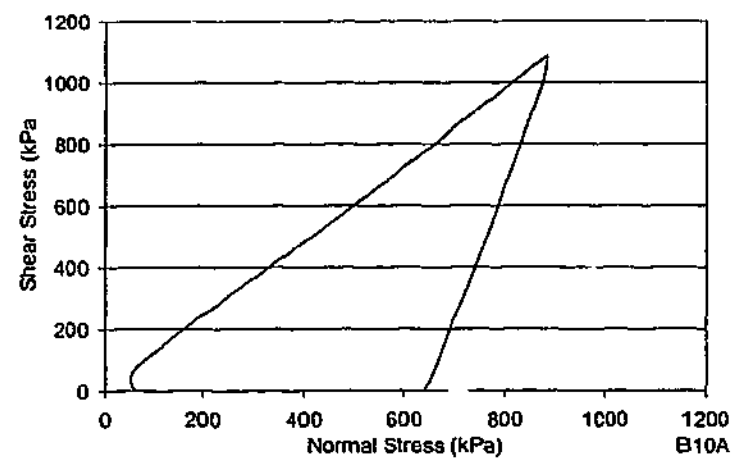


Test B10-5 – dx = 18 mm

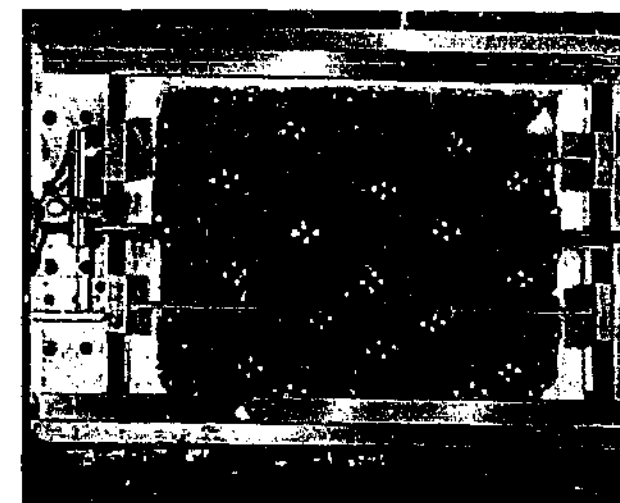
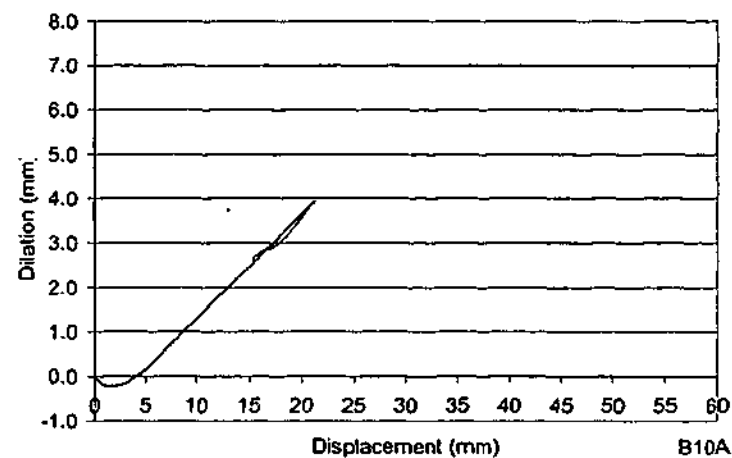
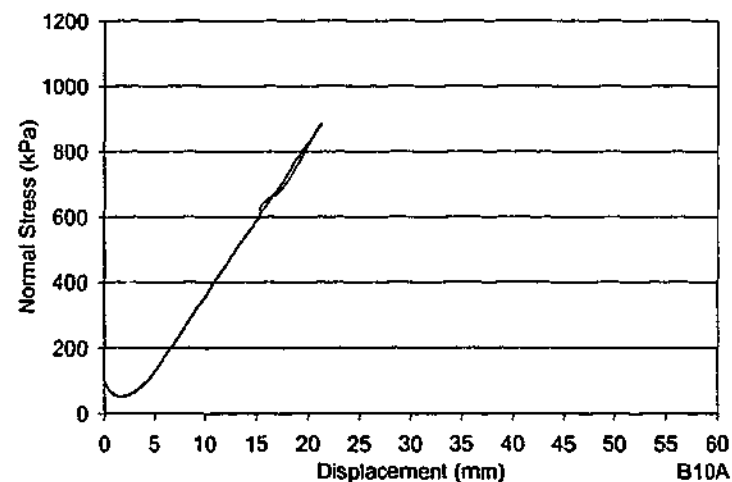
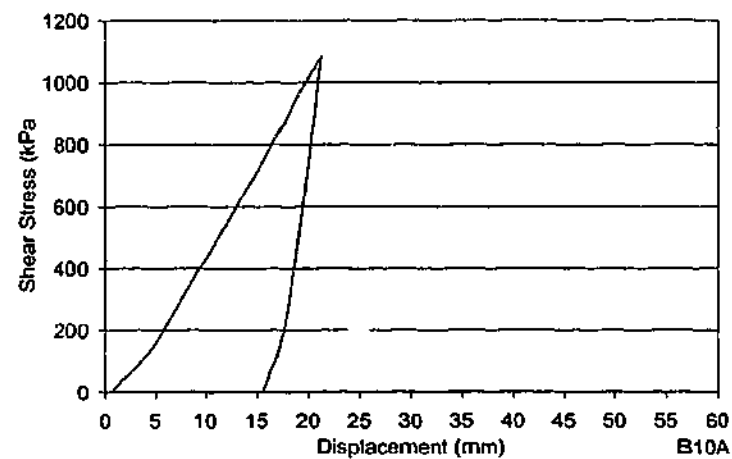


Test B10-6 – dx = 22 mm

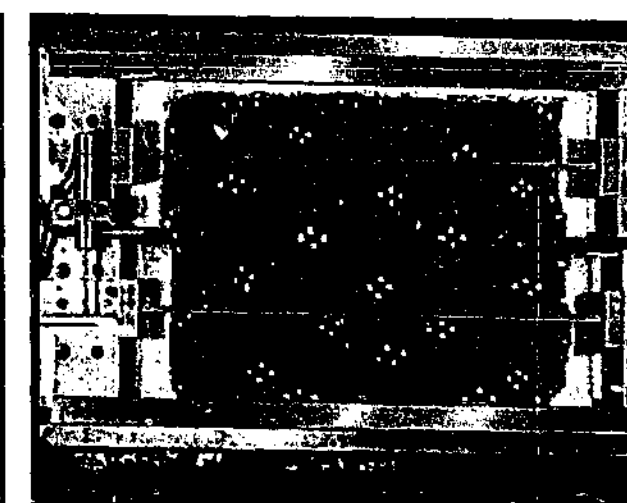
TEST B10			
$\theta_1 = -30 \pm 5^\circ$	$\theta_2 = 30 \pm 5^\circ$	$\theta_3 = n/a^\circ$	spacing = 70 mm (nom)
$\sigma_{ni} = 100$ kPa	$k_v = 200$ kPa/mm		UCS = 3.44 MPa



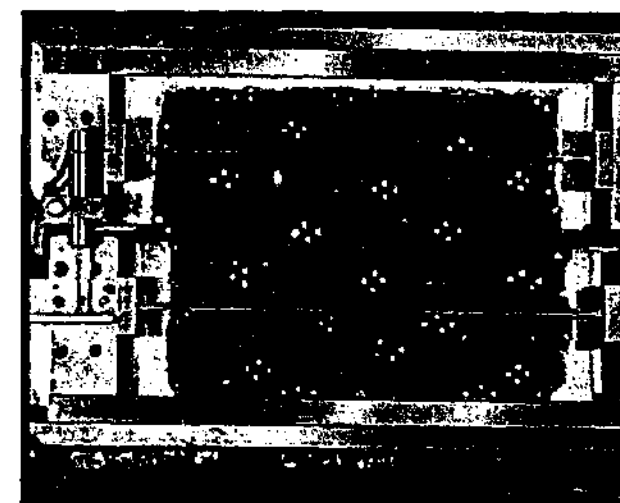
Test Details B10A	
θ_1	= $-30 \pm 5^\circ$
θ_2	= $30 \pm 5^\circ$
θ_3	= n/a°
spacing	= 70 mm (nom)
σ_{ni}	= 100 kPa
k_v	= 200 kPa/mm
UCS	= 3.44 MPa



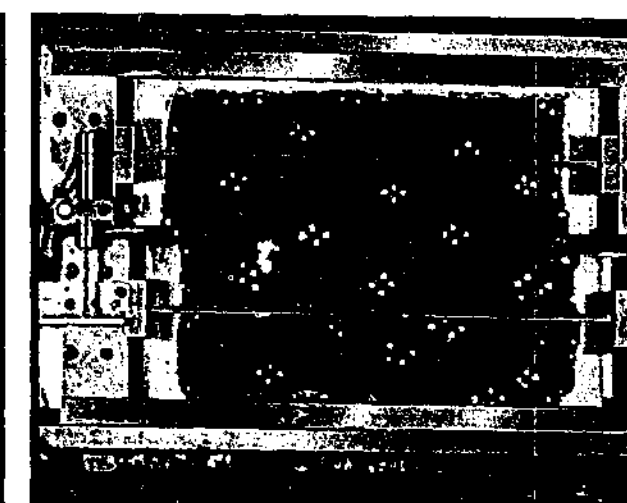
Test B10A-1 - dx = 0 mm



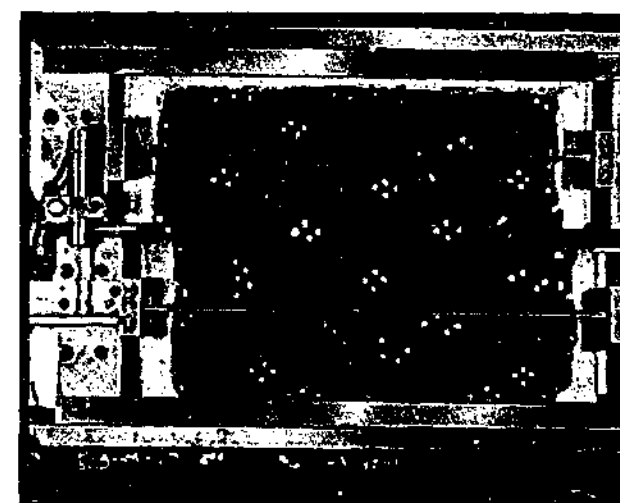
Test B10A-2 - dx = 4 mm



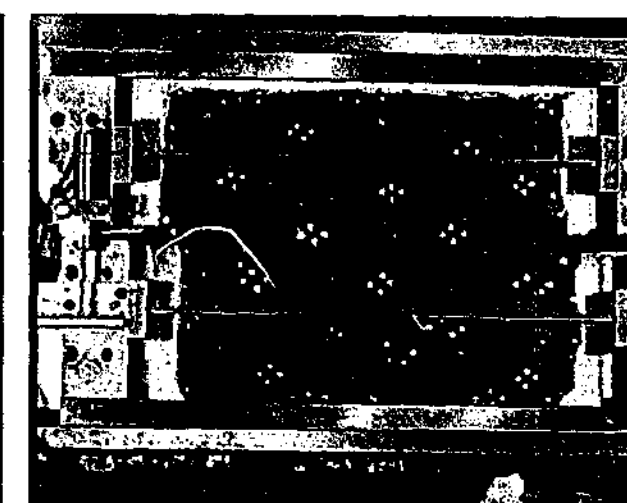
Test B10A-3 - dx = 10 mm



Test B10A-4 - dx = 13 mm

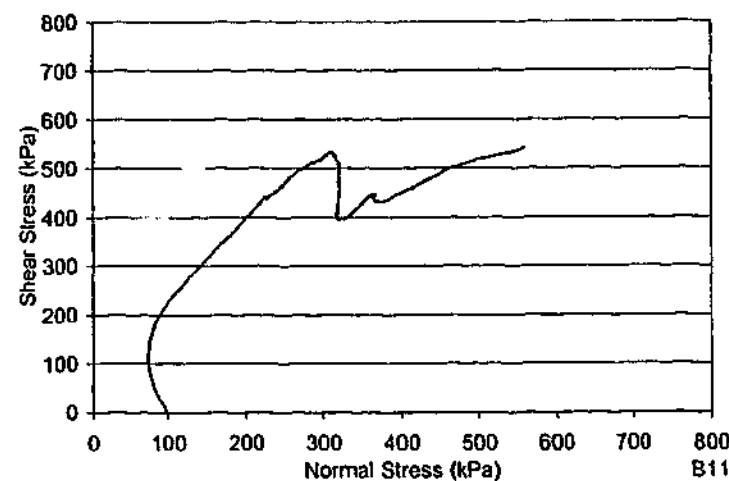


Test B10A-5 - dx = 15 mm

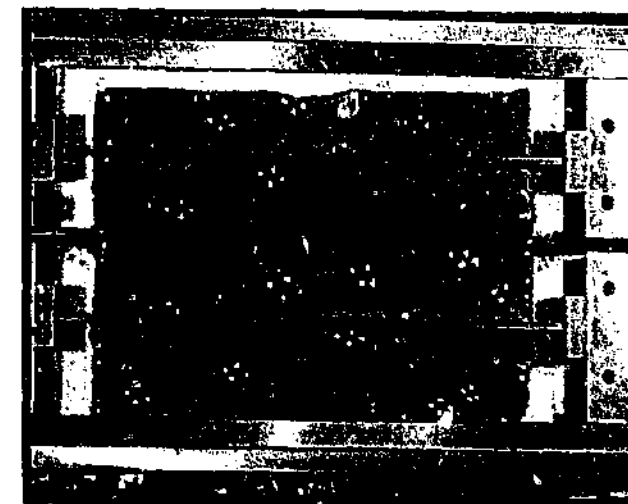
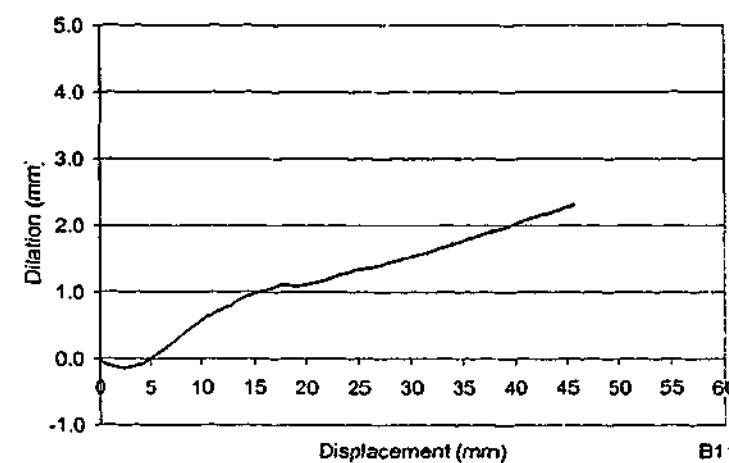
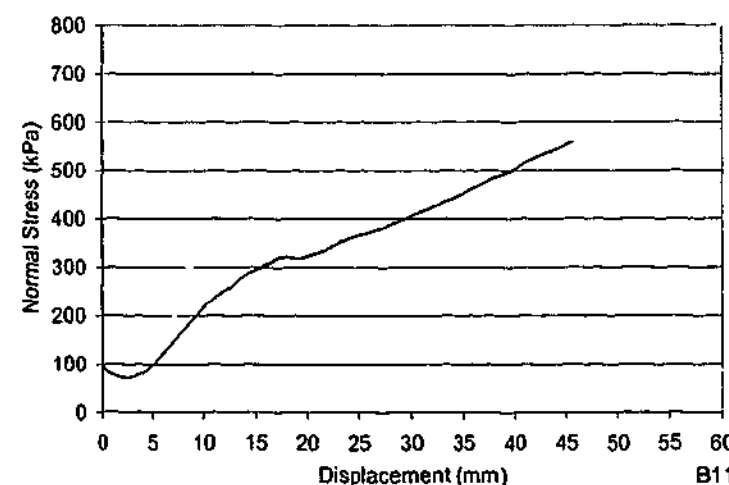
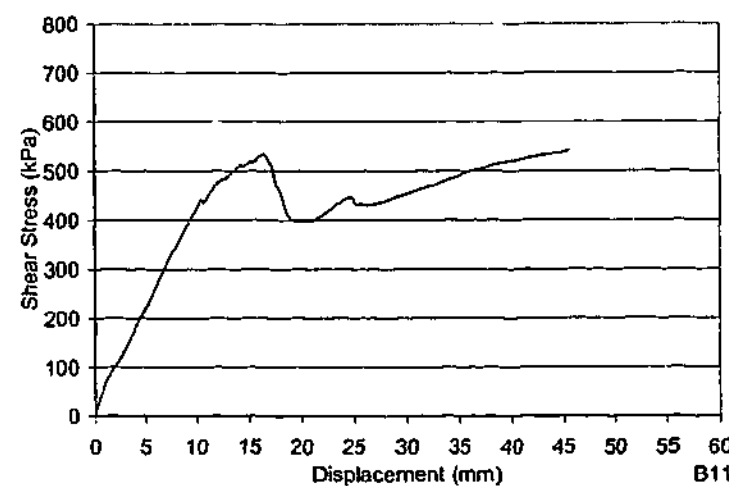


Test B10A-6 - dx = 17 mm

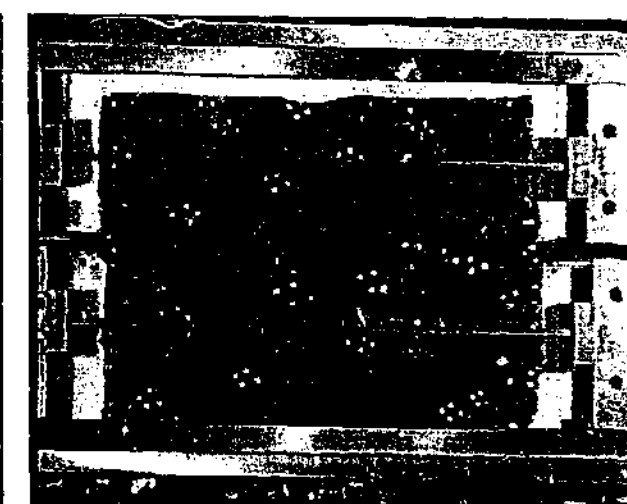
TEST B10A			
$\theta_1 = -30 \pm 5^\circ$	$\theta_2 = 30 \pm 5^\circ$	$\theta_3 = n/a^\circ$	spacing = 70 mm (nom)
$\sigma_{ni} = 100$ kPa	$k_v = 200$ kPa/mm		UCS = 3.44 MPa



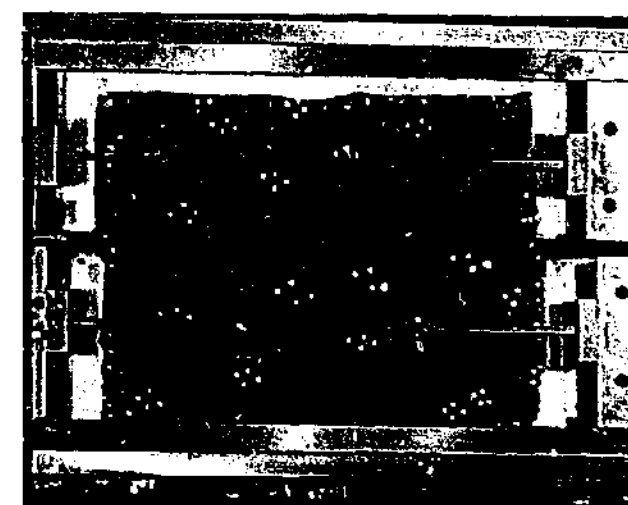
Test Details B11
 $\theta_1 = -45 \pm 5^\circ$
 $\theta_2 = 15 \pm 5^\circ$
 $\theta_3 = n/a^\circ$
 spacing = 70 mm (nom)
 $\sigma_{ni} = 100$ kPa
 $k_v = 200$ kPa/mm
 UCS = 2.59 MPa



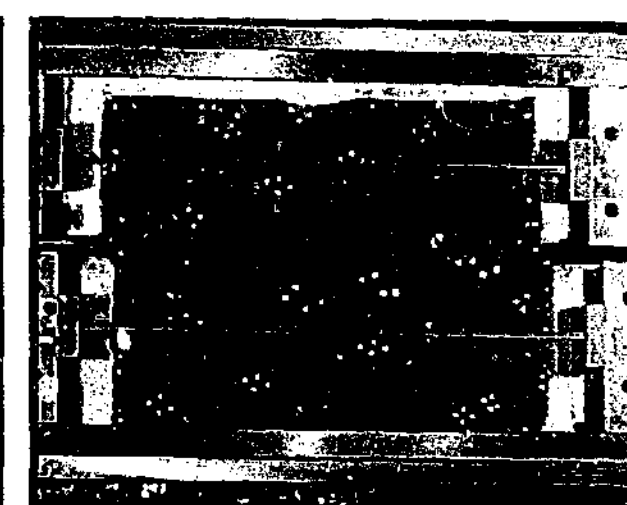
Test B11-1 – dx = 0 mm



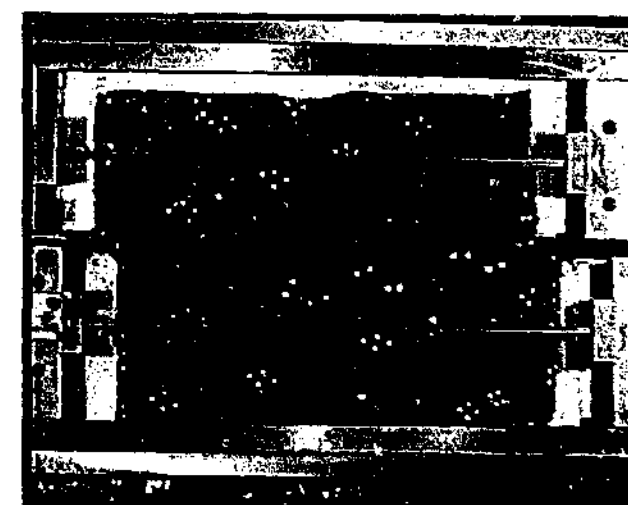
Test B11-2 – dx = 6 mm



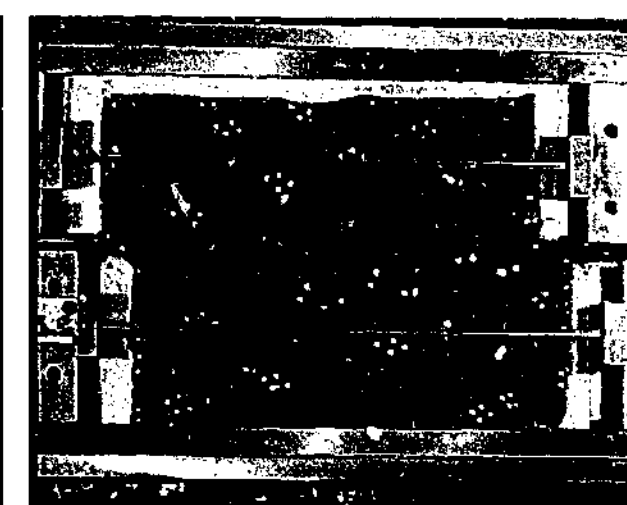
Test B11-3 – dx = 11 mm



Test B11-4 – dx = 15 mm

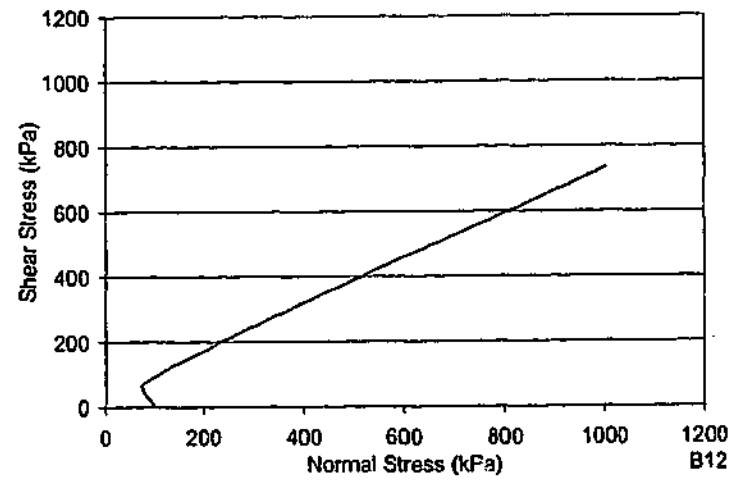


Test B11-5 – dx = 24 mm

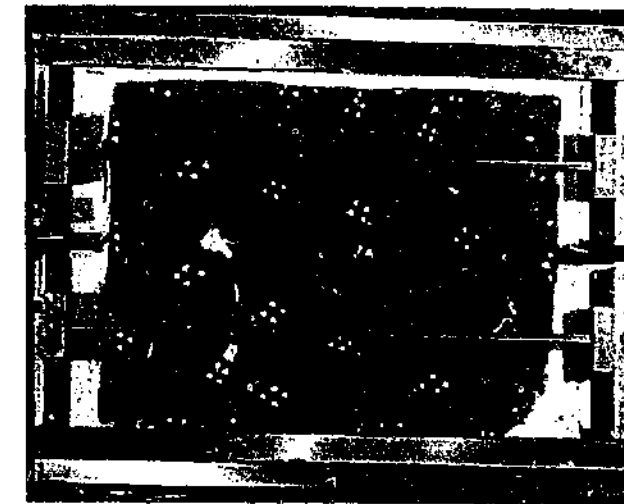
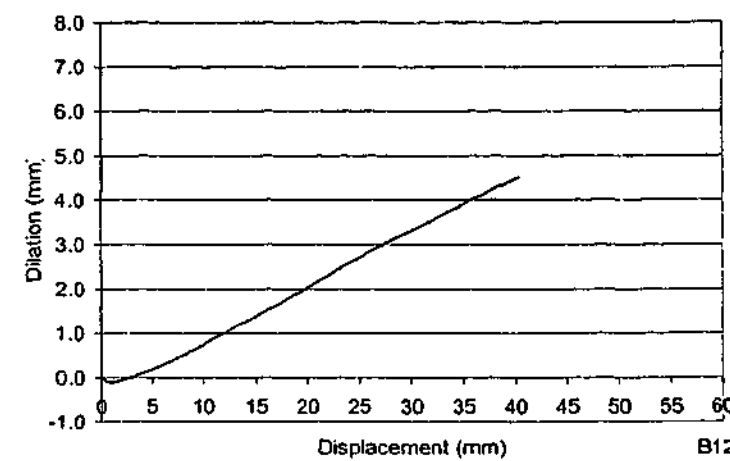
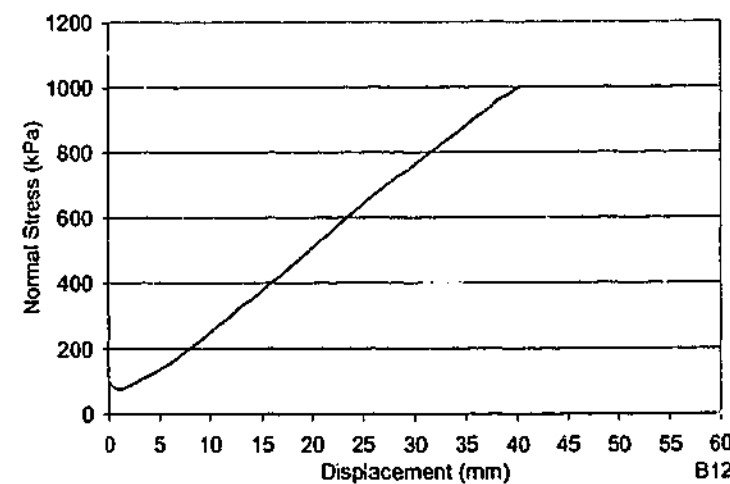
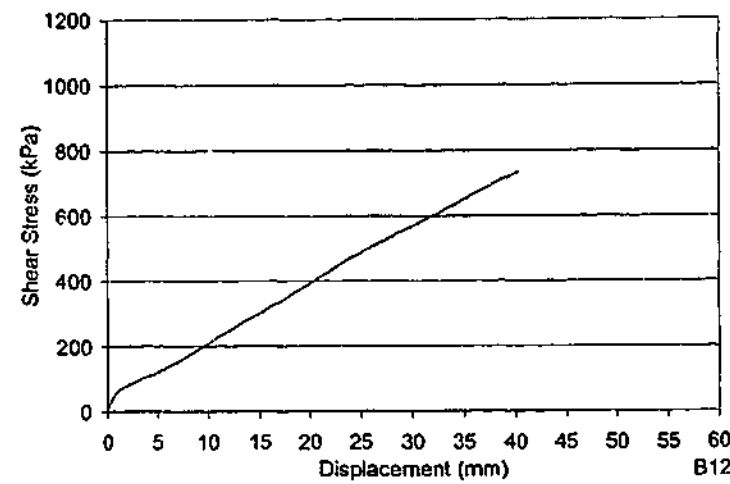


Test B11-6 – dx = 33 mm

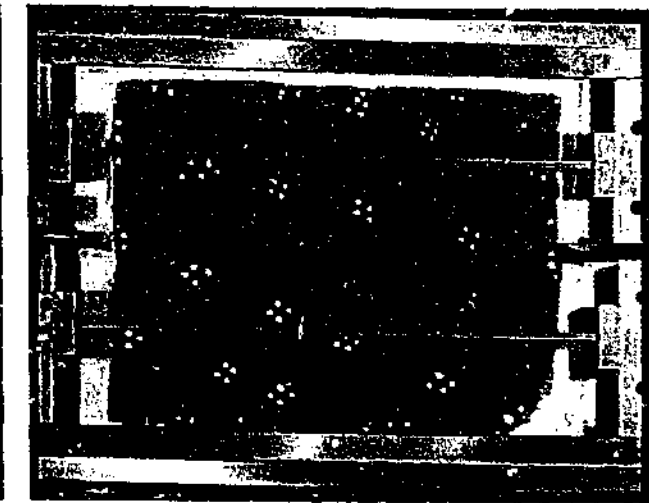
TEST B11
 $\theta_1 = -45 \pm 5^\circ$ $\theta_2 = 15 \pm 5^\circ$ $\theta_3 = n/a^\circ$ spacing = 70 mm (nom)
 $\sigma_{ni} = 100$ kPa $k_v = 200$ kPa/mm UCS = 2.59 MPa



Test Details B12	
θ_1	= $-13 \pm 5^\circ$
θ_2	= $43 \pm 5^\circ$
θ_3	= n/a°
spacing	= 70 mm (nom)
σ_{ni}	= 100 kPa
k_v	= 200 kPa/mm
UCS	= 2.73 MPa



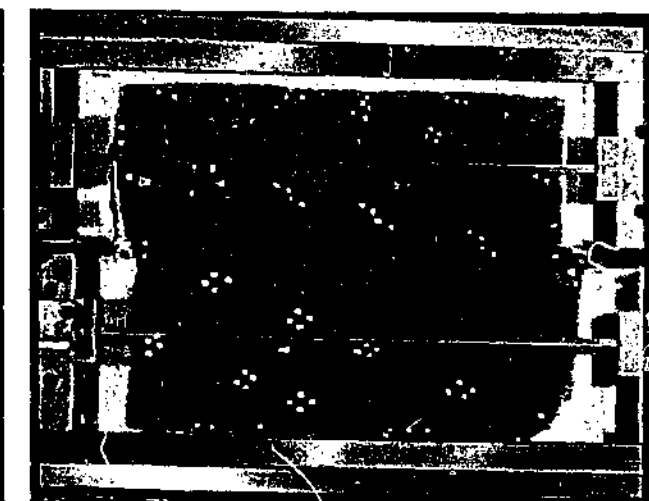
Test B12-1 – dx = 0 mm



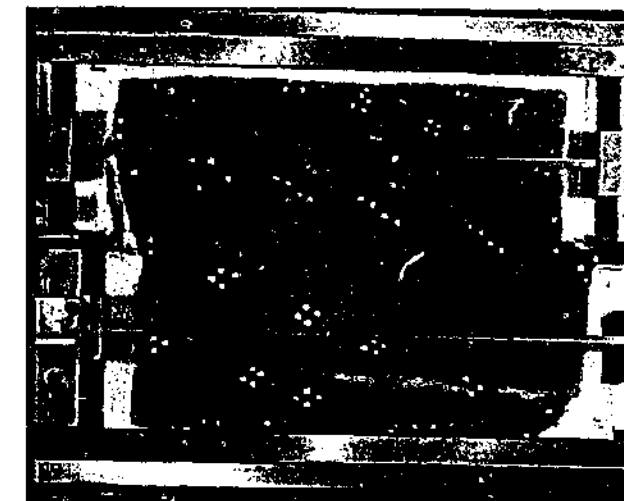
Test B12-2 – dx = 6 mm



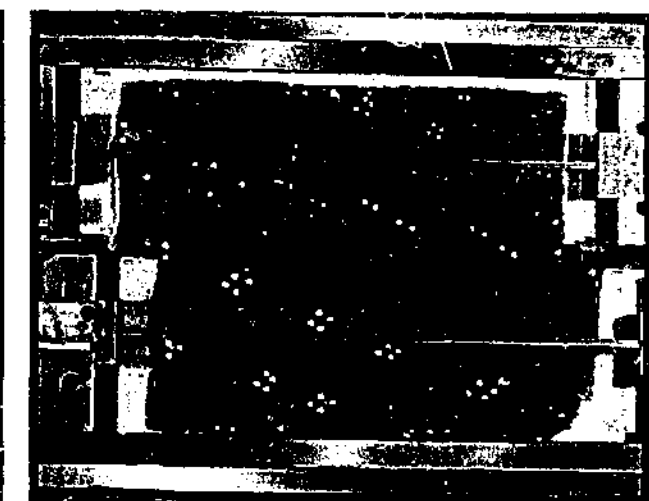
Test B12-3 – dx = 13 mm



Test B12-4 – dx = 21 mm

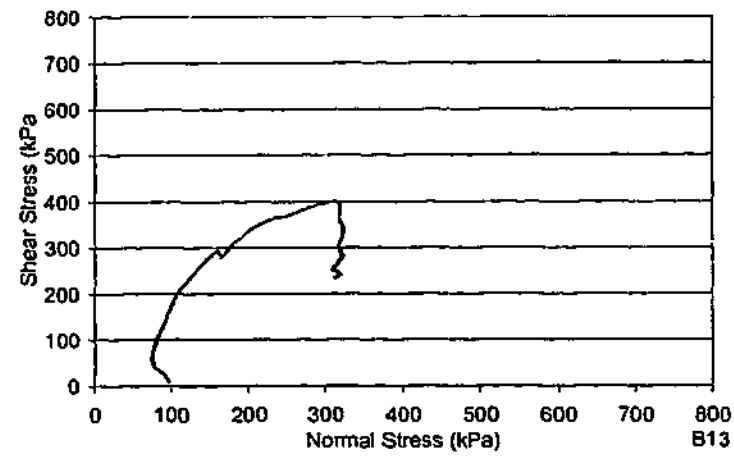


Test B12-5 – dx = 29 mm

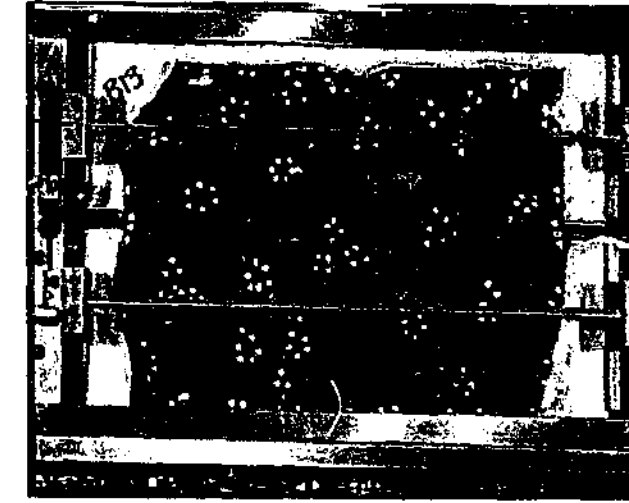
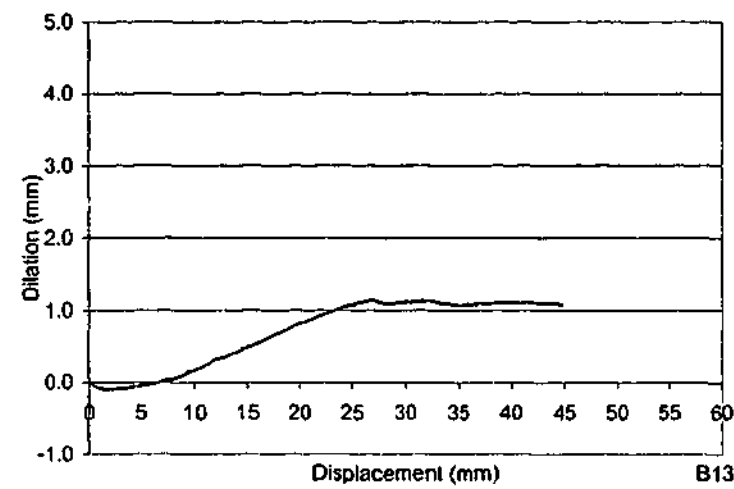
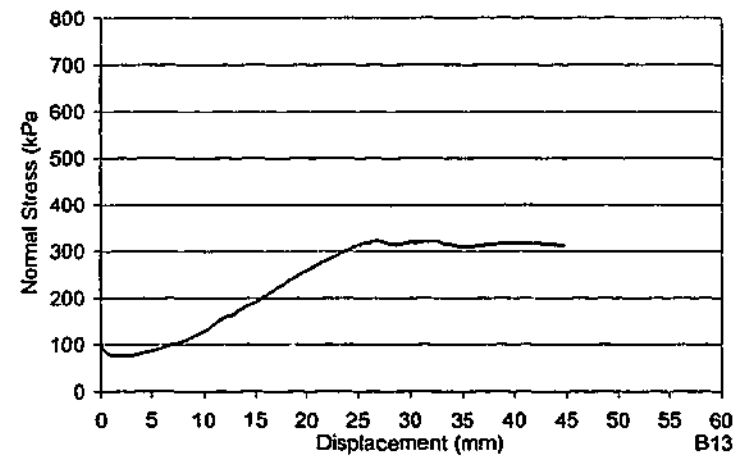
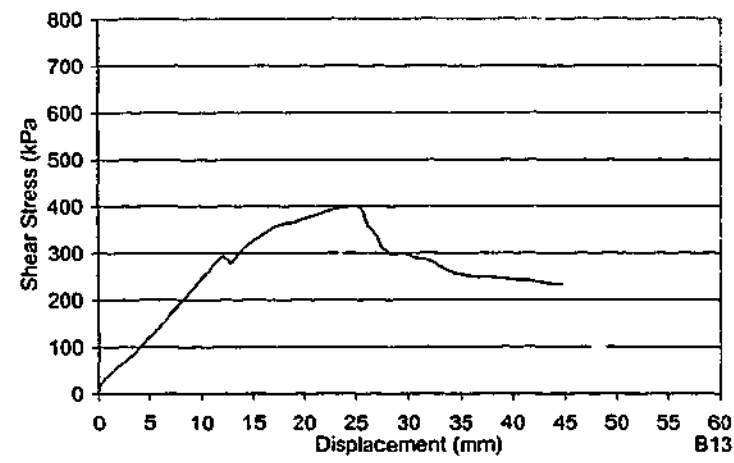


Test B12-6 – dx = 38 mm

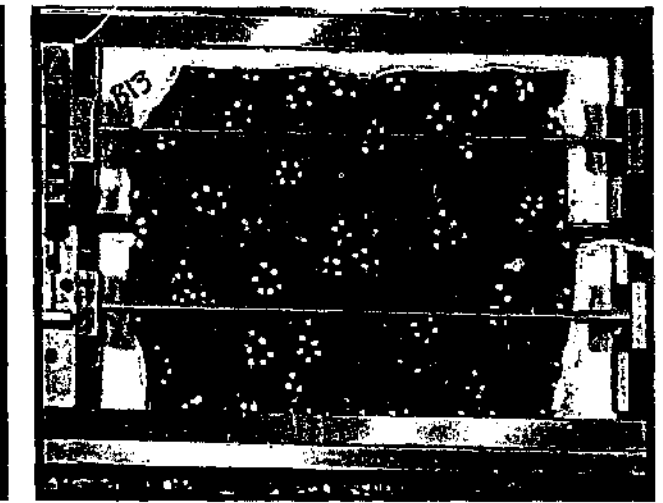
TEST B12			
$\theta_1 = -13 \pm 5^\circ$	$\theta_2 = 43 \pm 5^\circ$	$\theta_3 = n/2^\circ$	spacing = 70 mm (nom)
$\sigma_{ni} = 100 \text{ kPa}$	$k_v = 200 \text{ kPa/mm}$		UCS = 2.73 MPa



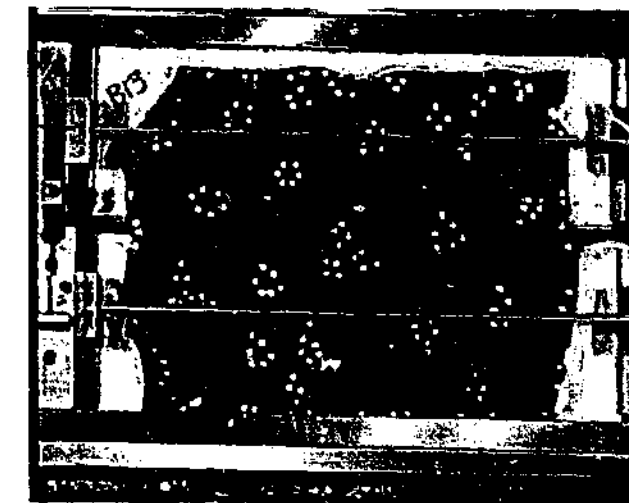
Test Details B13	
θ_1	= $-46 \pm 5^\circ$
θ_2	= $15 \pm 5^\circ$
θ_3	= $74 \pm 5^\circ$
spacing	= 70 mm (nom)
σ_{ni}	= 100 kPa
k_v	= 200 kPa/mm
UCS	= 2.82 MPa



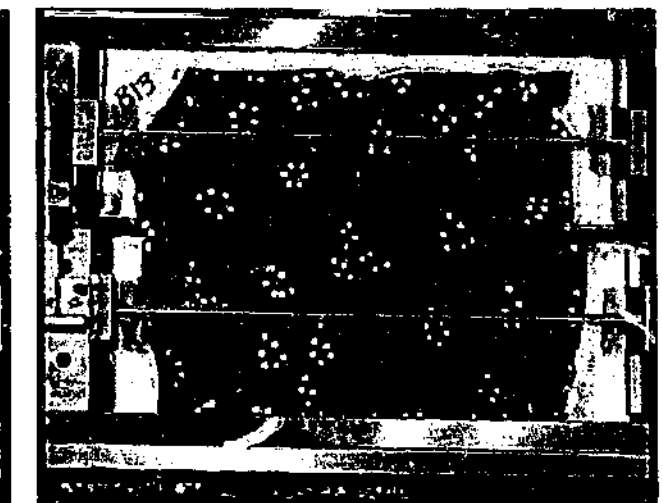
Test B13-1 – dx = 0 mm



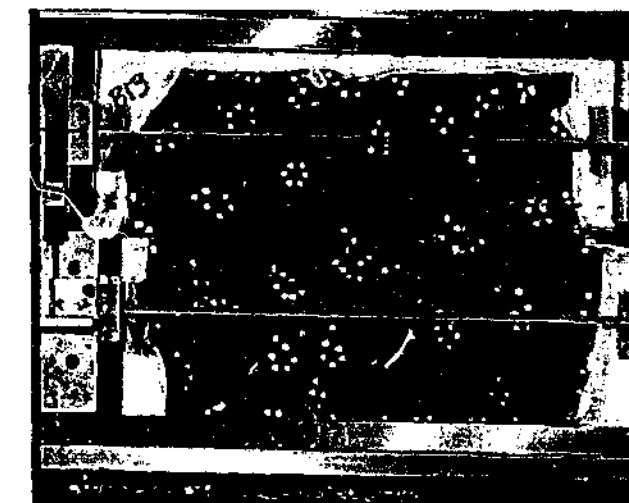
Test B13-2 – dx = 5 mm



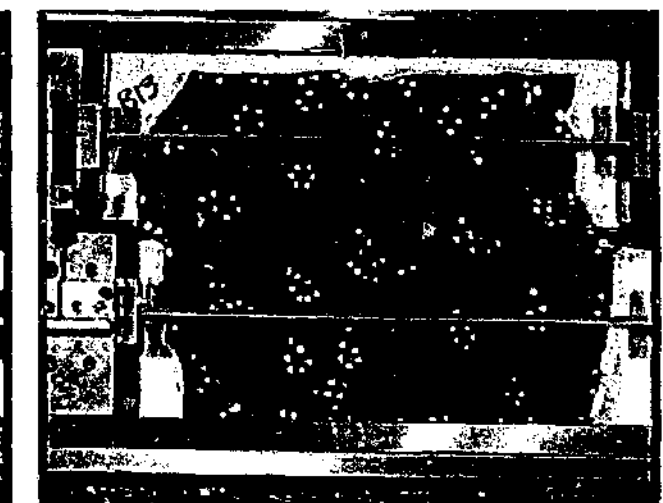
Test B13-3 – dx = 10 mm



Test B13-4 – dx = 15 mm

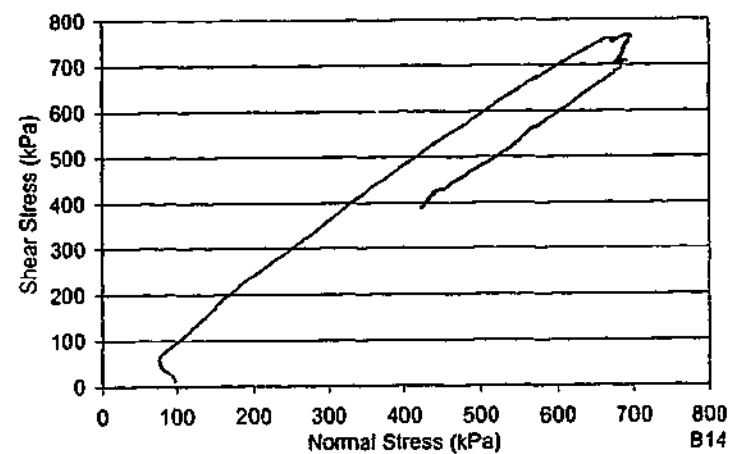


Test B13-5 – dx = 26 mm

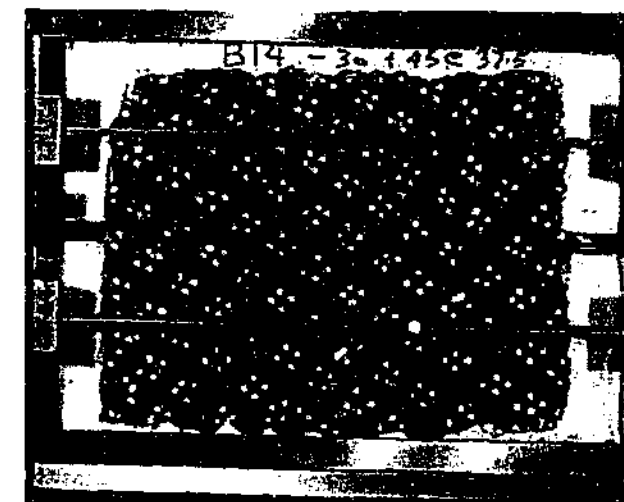
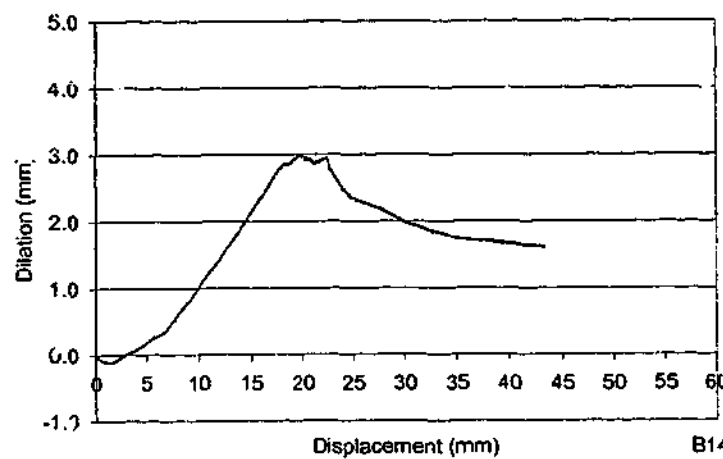
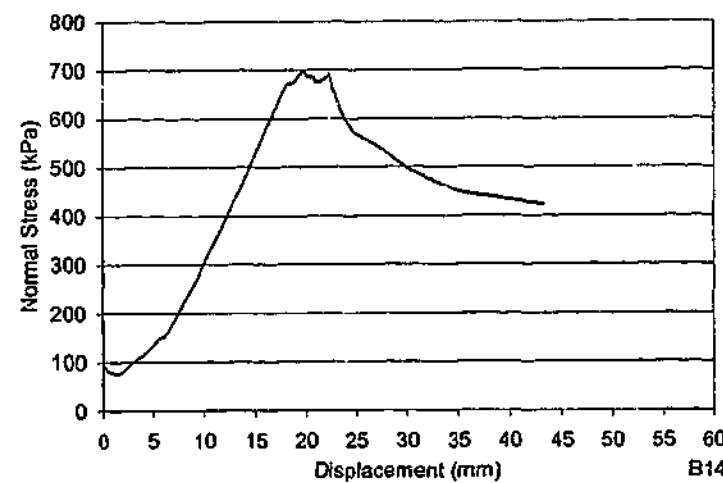
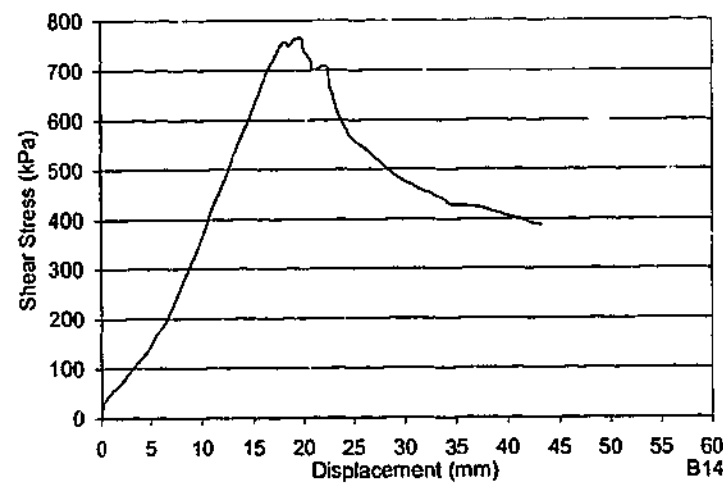


Test B13-6 – dx = 35 mm

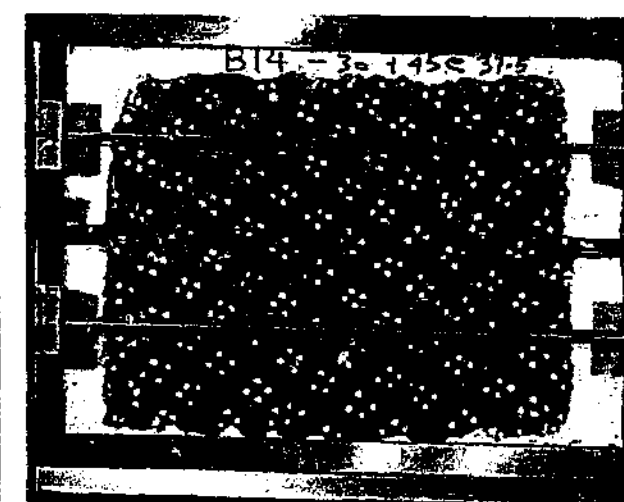
TEST B13			
$\theta_1 = -46 \pm 5^\circ$	$\theta_2 = 15 \pm 5^\circ$	$\theta_3 = 74 \pm 5^\circ$	spacing = 70 mm (nom)
$\sigma_{ni} = 100$ kPa	$k_v = 200$ kPa/mm		UCS = 2.82 MPa



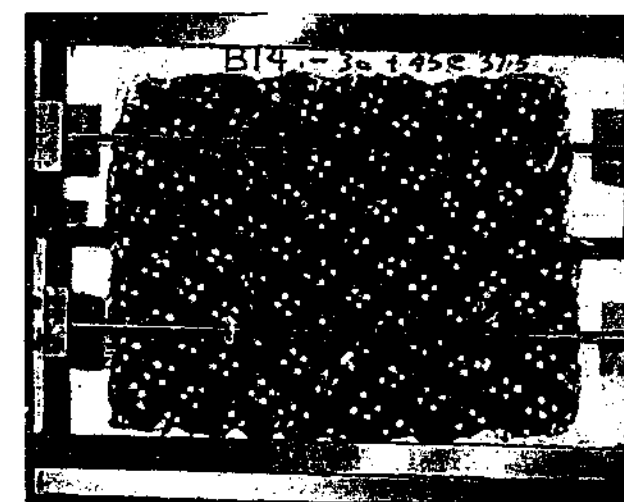
Test Details B14	
θ_1	= -31°
θ_2	= 44°
θ_3	= n/a°
spacing	= 30 mm
σ_{ni}	= 100 kPa
k_v	= 200 kPa/mm
UCS	= 4.52 MPa



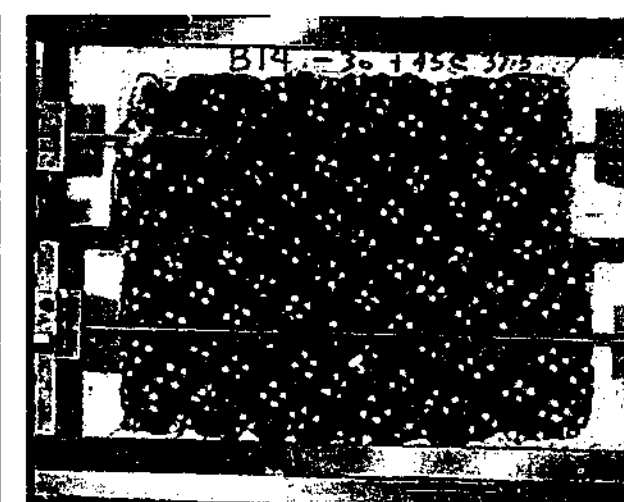
Test B14-1 – dx = 0 mm



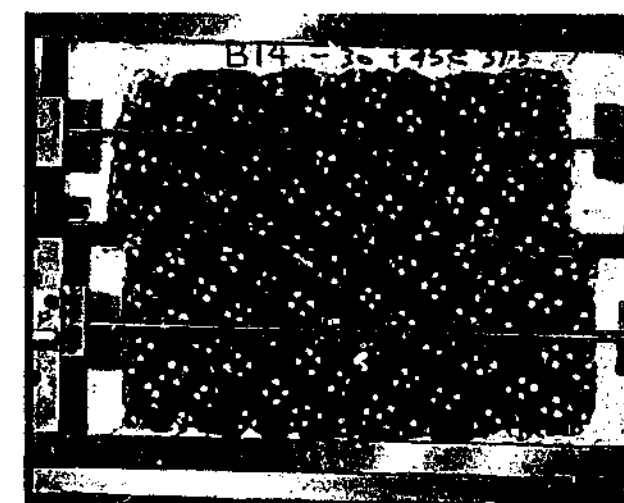
Test B14-2 – dx = 1 mm



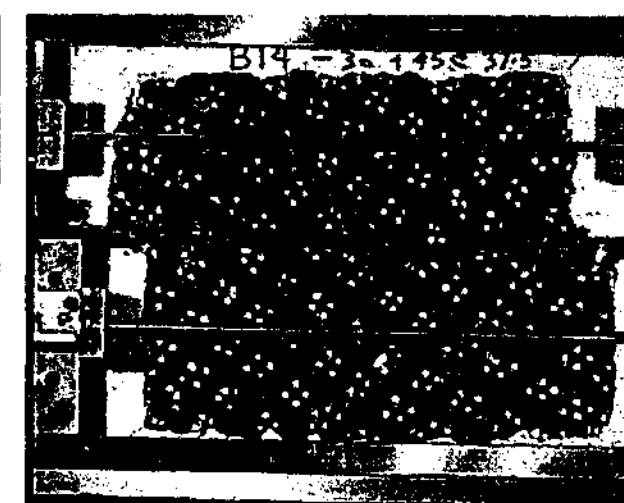
Test B14-3 – dx = 6 mm



Test B14-4 – dx = 15 mm

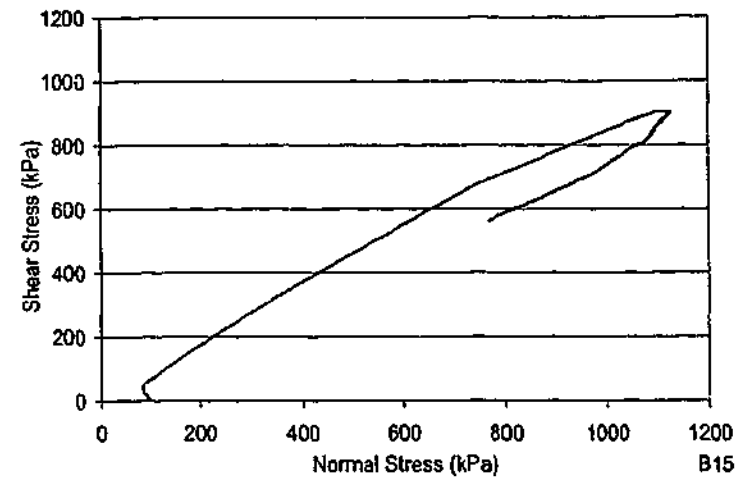


Test B14-5 – dx = 18 mm

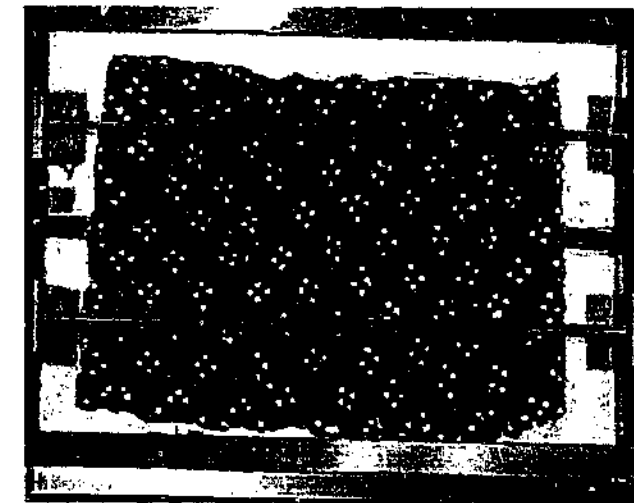
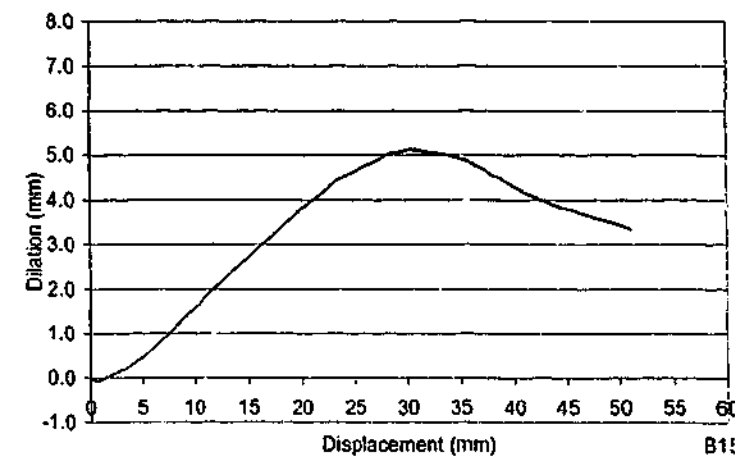
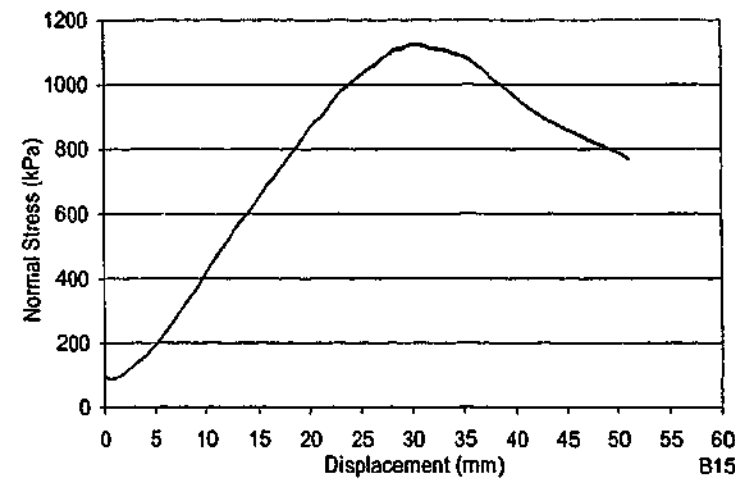
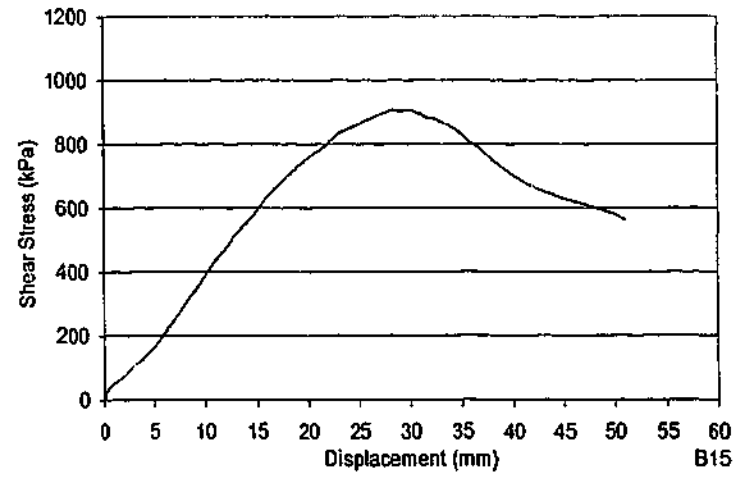


Test B14-6 – dx = 33 mm

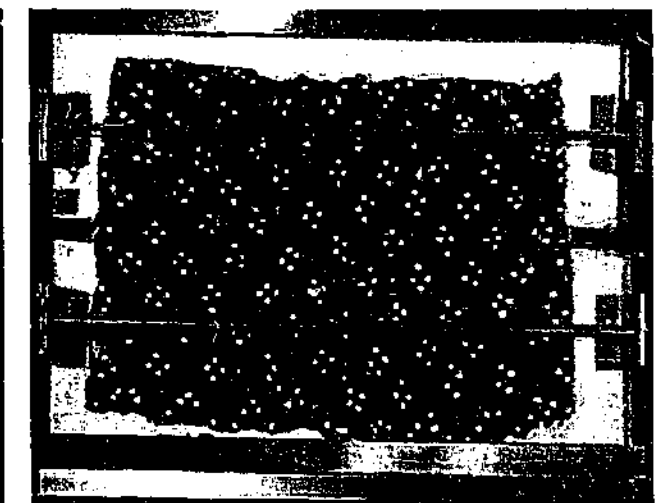
TEST B14			
$\theta_1 = -31^\circ$	$\theta_2 = 44^\circ$	$\theta_3 = n/a^\circ$	spacing = 30-32 mm
$\sigma_{ni} = 100 \text{ kPa}$	$k_v = 200 \text{ kPa/mm}$		UCS = 4.52 MPa



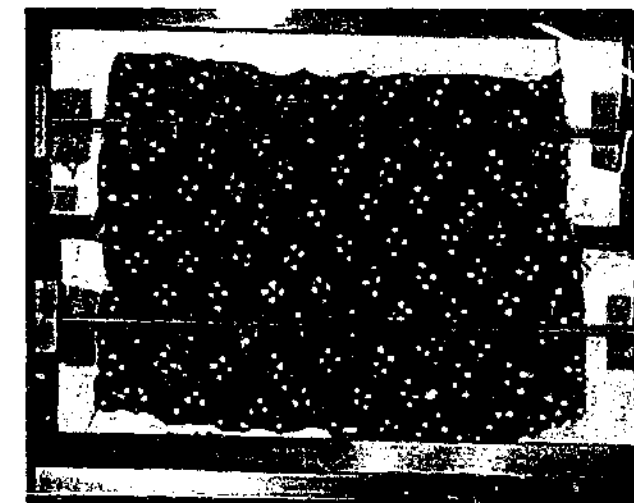
Test Details B15	
θ_1	= -47°
θ_2	= 57°
θ_3	= n/a°
spacing	= 30 mm
σ_{ni}	= 100 kPa
k_v	= 200 kPa/mm
UCS	= 3.22 MPa



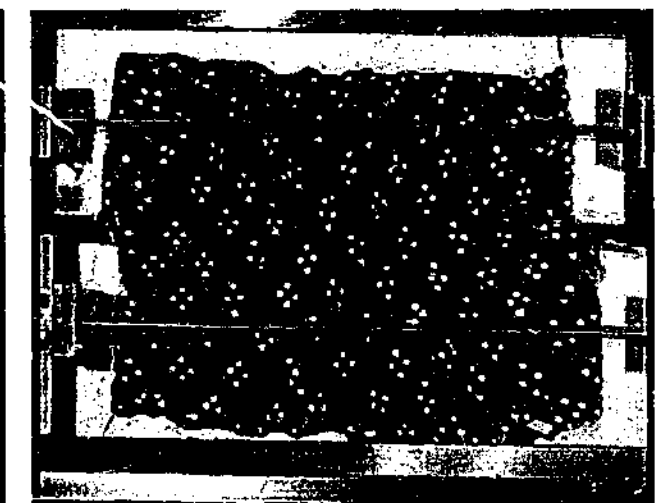
Test B15-1 – dx = 0 mm



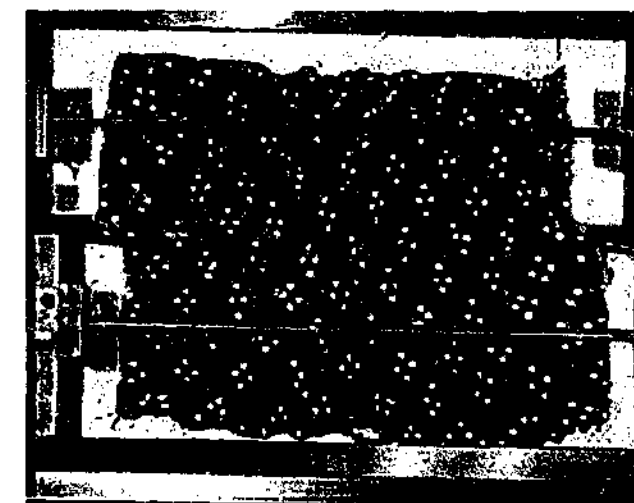
Test B15-2 – dx = 5 mm



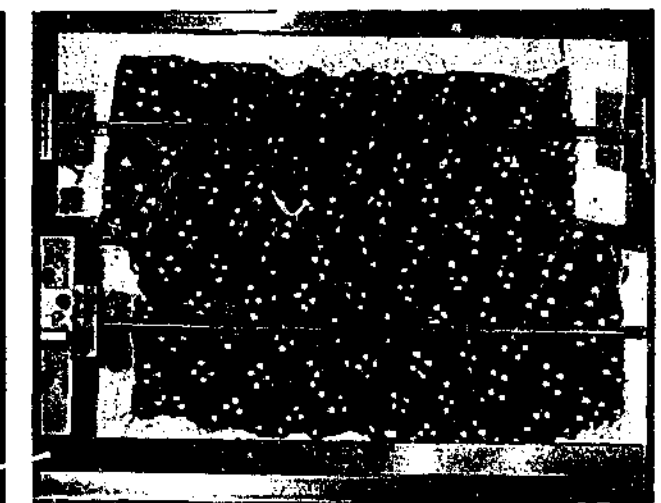
Test B15-3 – dx = 15 mm



Test B15-4 – dx = 25 mm



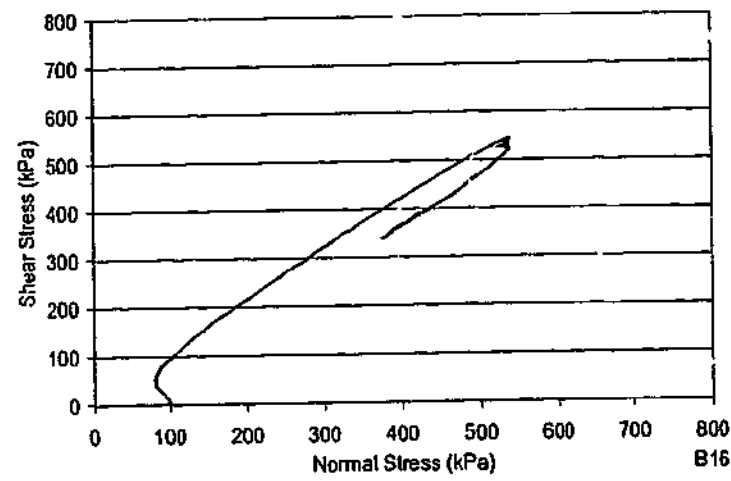
Test B15-5 – dx = 32 mm



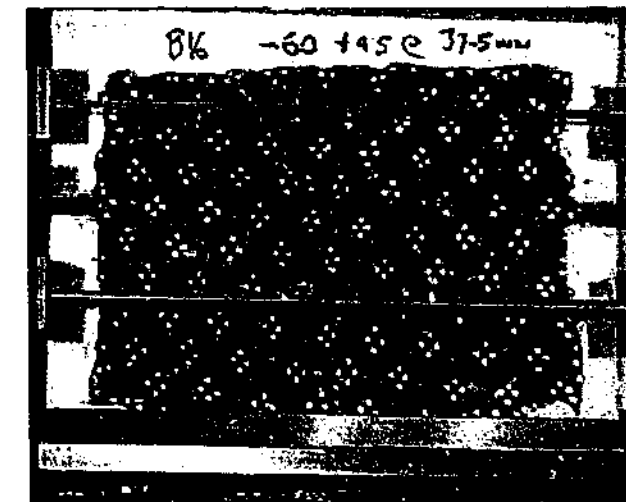
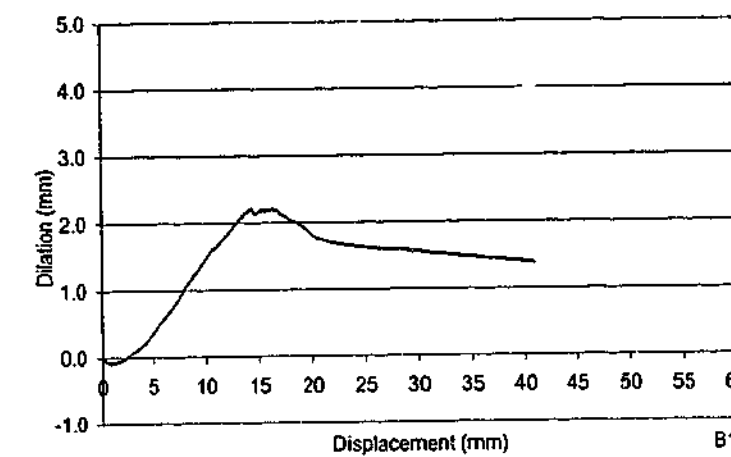
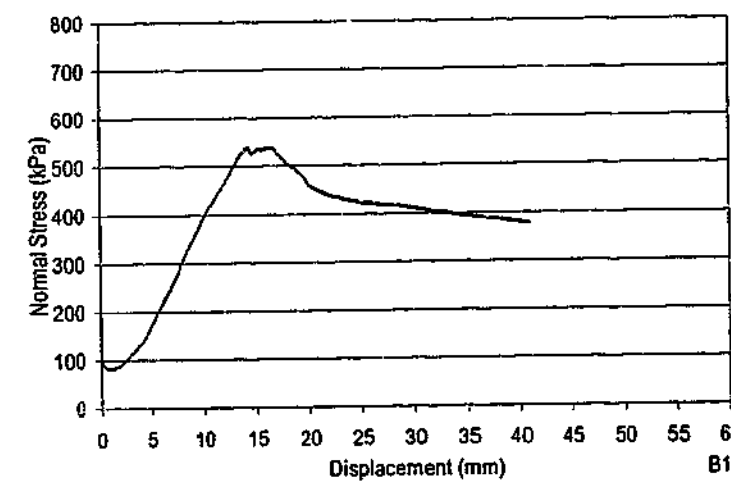
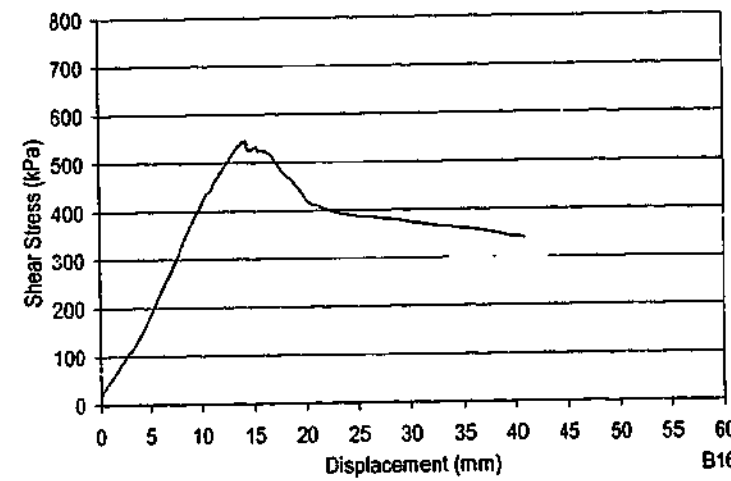
Test B15-6 – dx = 41 mm

TEST B15

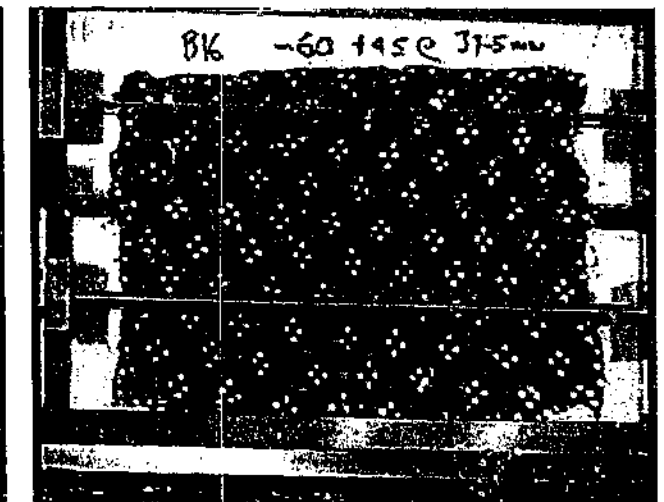
$\theta_1 = -47^\circ$ $\theta_2 = 57^\circ$ $\theta_3 = n/a^\circ$ spacing = 30-35 mm
 $\sigma_{ni} = 100 \text{ kPa}$ $k_v = 200 \text{ kPa/mm}$ UCS = 3.22 MPa



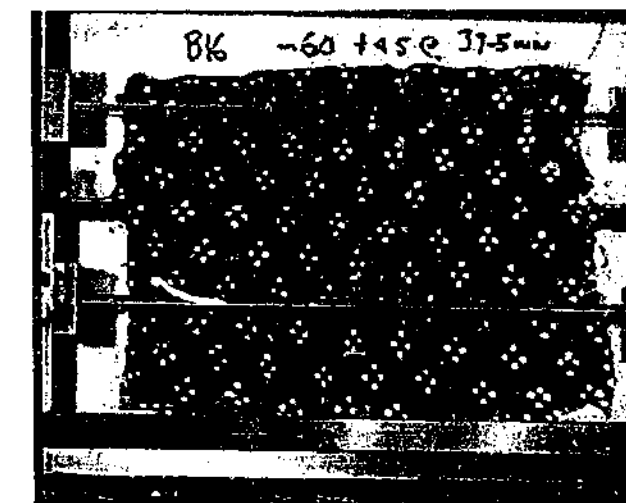
Test Details B16	
θ_1	= -58°
θ_2	= 47°
θ_3	= n/a°
spacing	= 30 mm
σ_{ni}	= 100 kPa
k_v	= 200 kPa/mm
UCS	= 2.66 MPa



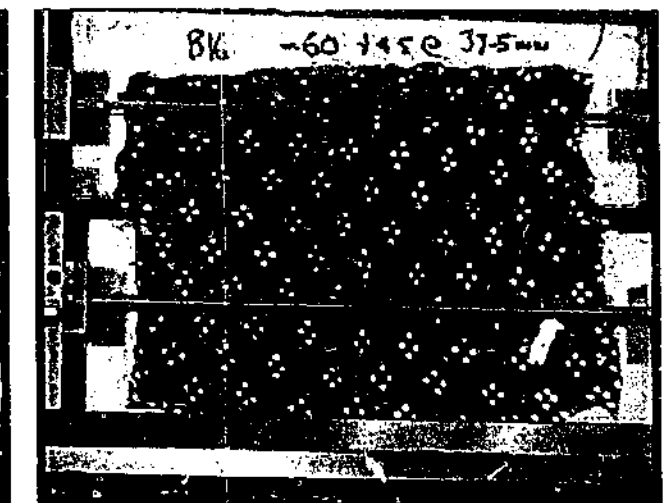
Test B16-1 – dx = 0 mm



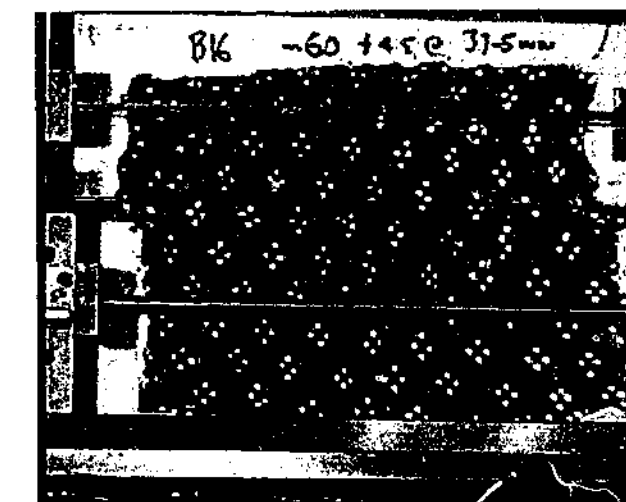
Test B16-2 – dx = 4 mm



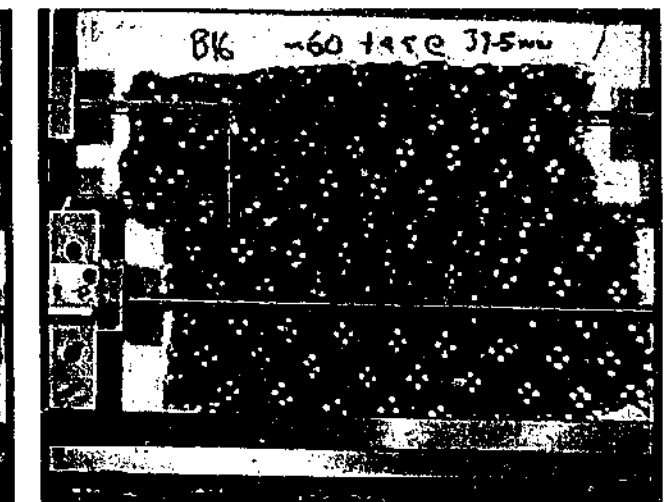
Test B16-3 – dx = 9 mm



Test B16-4 – dx = 17 mm

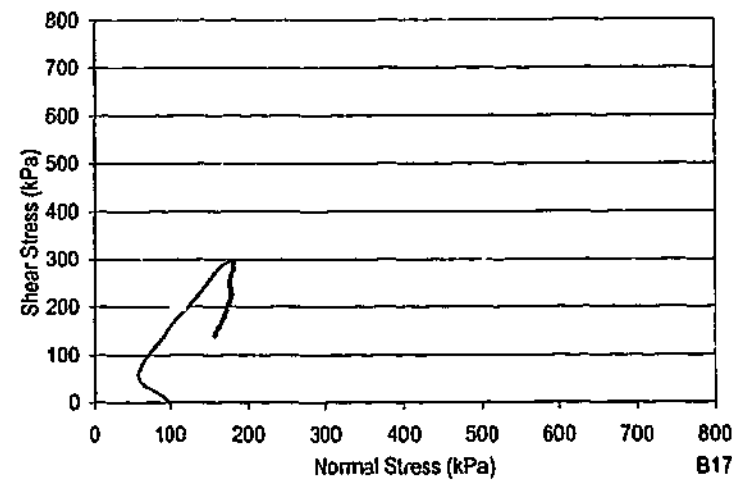


Test B16-5 – dx = 26 mm

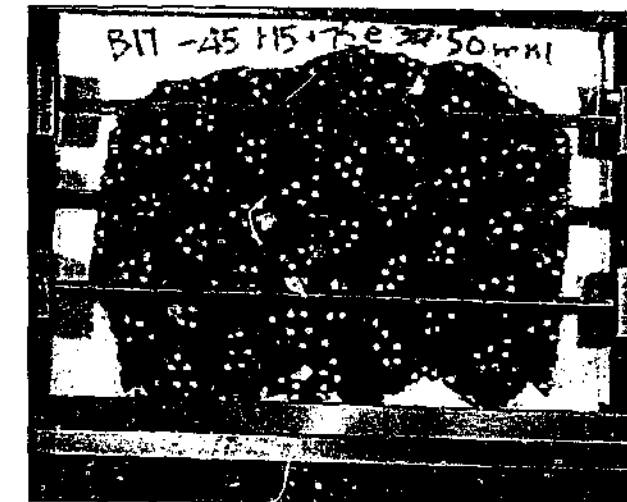
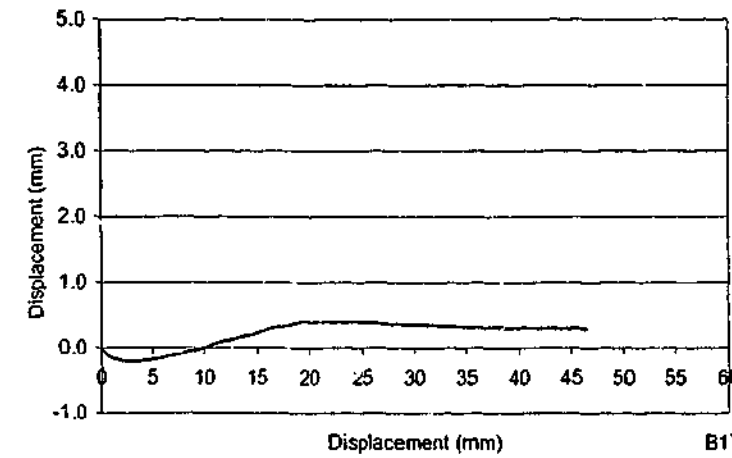
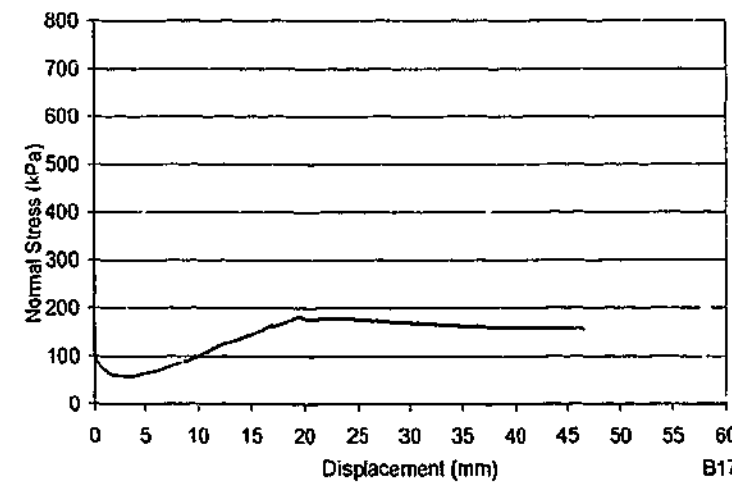
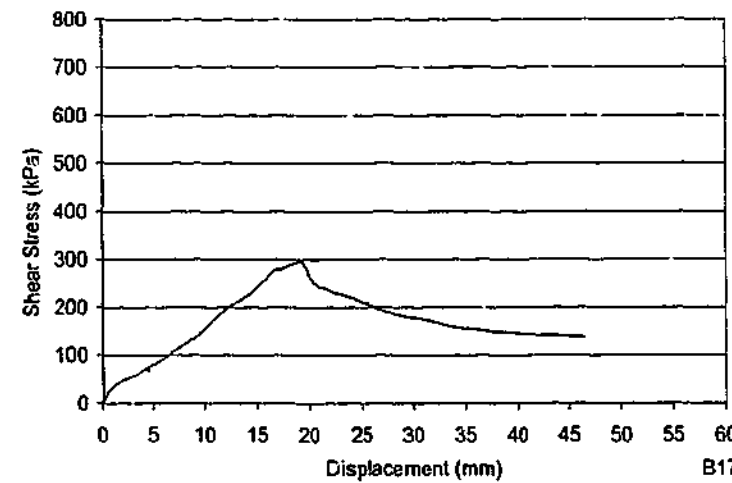


Test B16-6 – dx = 35 mm

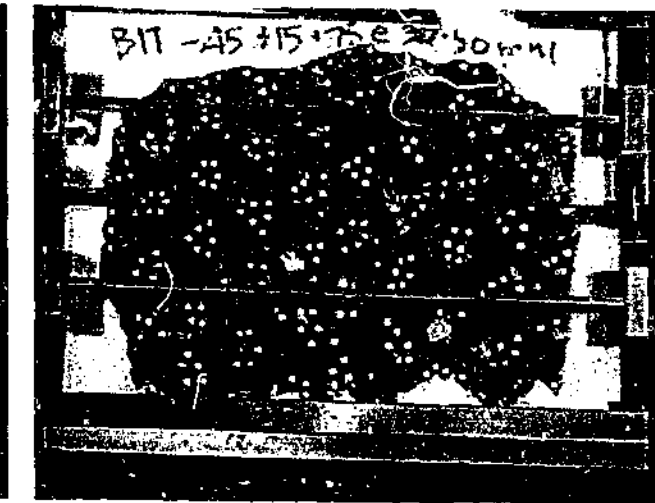
TEST B16			
$\theta_1 = -58^\circ$	$\theta_2 = 47^\circ$	$\theta_3 = n/a^\circ$	spacing = 30-35 mm
$\sigma_{ni} = 100 \text{ kPa}$	$k_v = 200 \text{ kPa/mm}$		UCS = 2.66 MPa



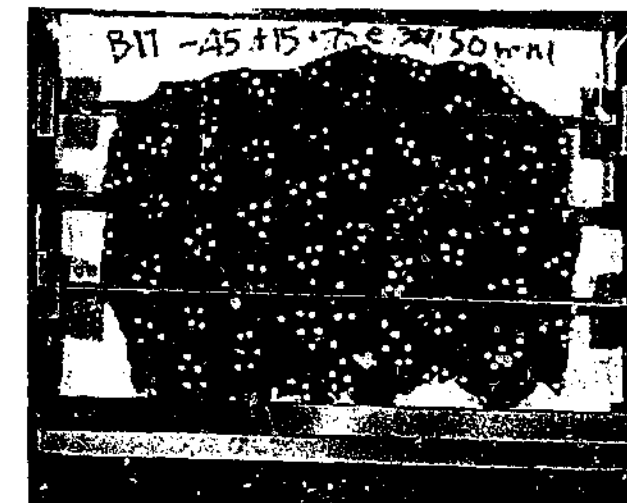
Test Details B17	
θ_1	= -38°
θ_2	= 27°
θ_3	= 84°
spacing	= 30 mm
σ_{ni}	= 100 kPa
k_v	= 200 kPa/mm
UCS	= 3.91 MPa



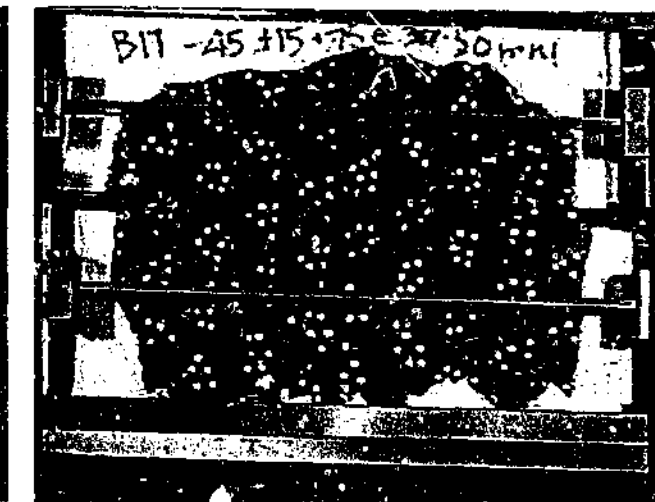
Test B17-1 – dx = 0 mm



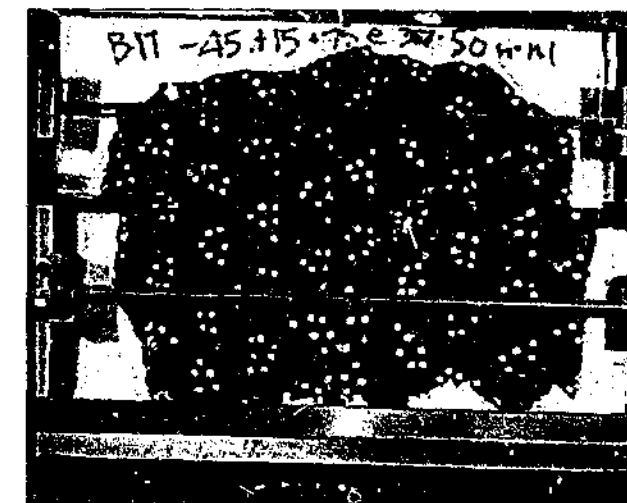
Test B17-2 – dx = 6 mm



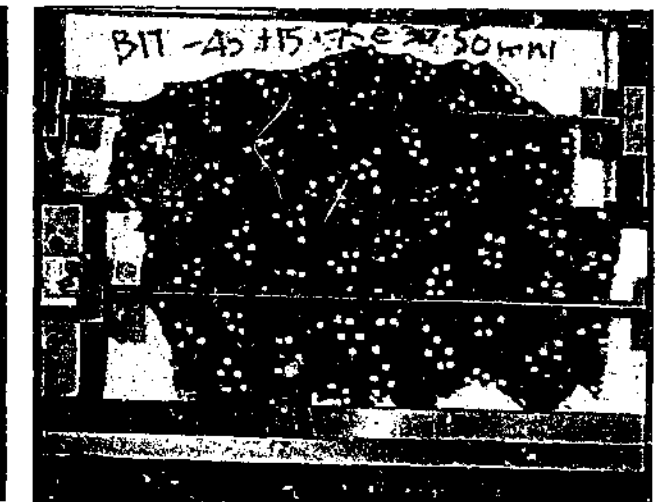
Test B17-3 – dx = 9 mm



Test B17-4 – dx = 13 mm

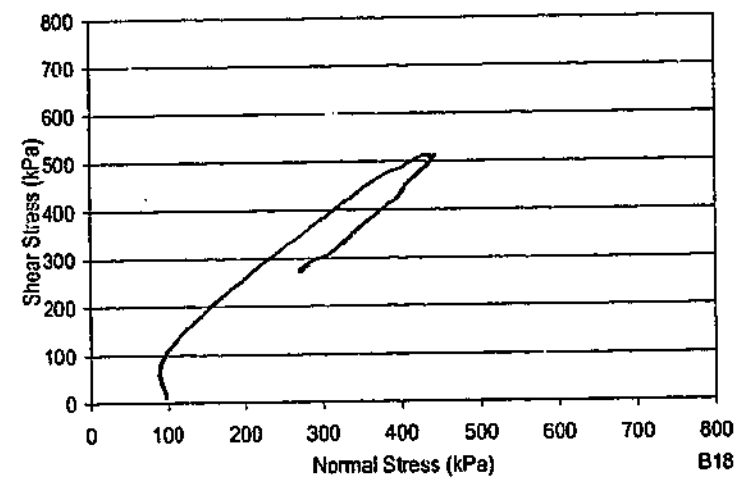


Test B17-5 – dx = 20 mm

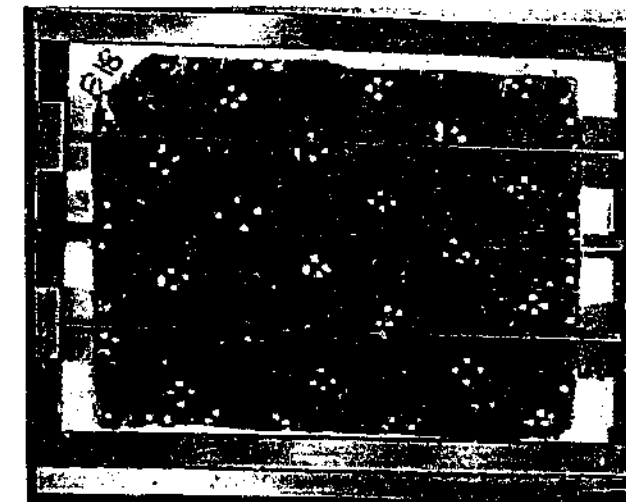
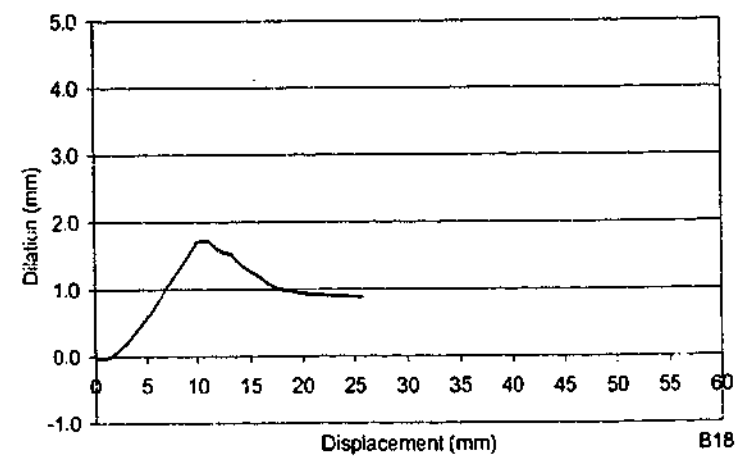
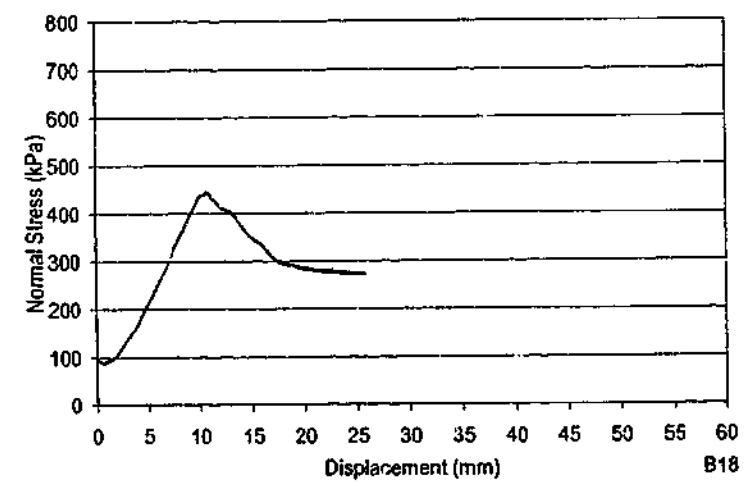
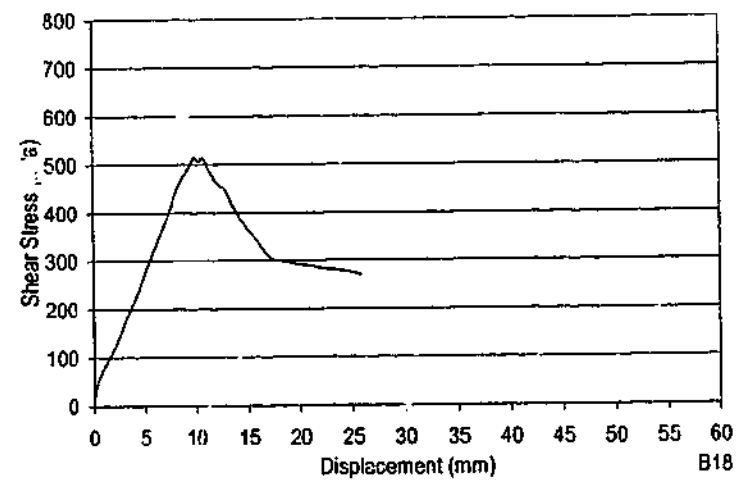


Test B17-6 – dx = 38 mm

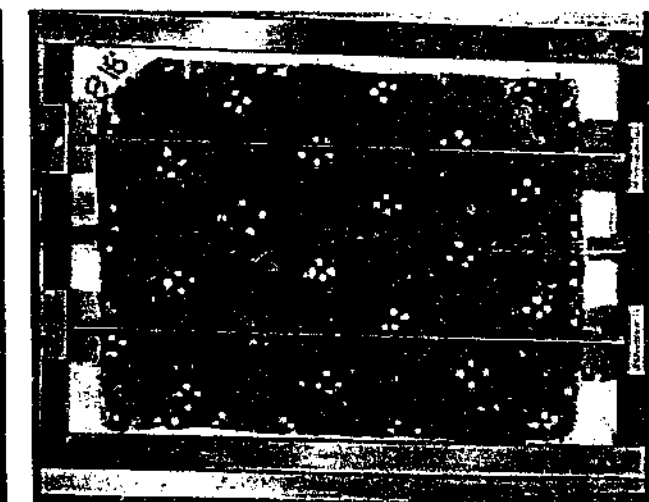
TEST B17			
$\theta_1 = -38^\circ$	$\theta_2 = 27^\circ$	$\theta_3 = 84^\circ$	spacing = 30-55 mm
$\sigma_{ni} = 100 \text{ kPa}$	$k_v = 200 \text{ kPa/mm}$		UCS = 3.91 MPa



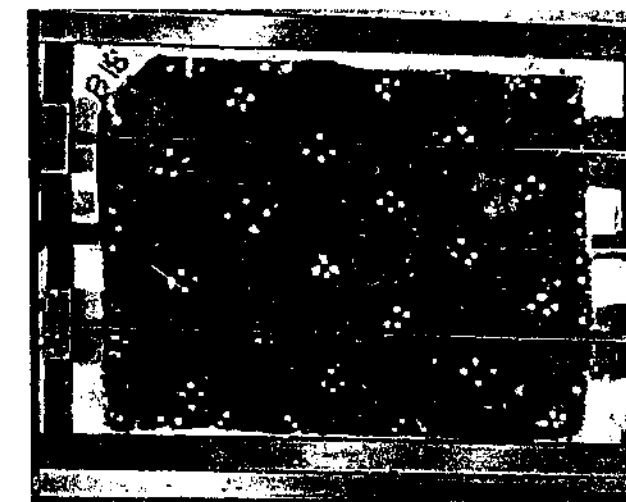
Test Details B18	
θ_1	= -31°
θ_2	= 43°
θ_3	= n/a $^\circ$
spacing	= 70 mm
σ_{ni}	= 100 kPa
k_v	= 200 kPa/mm
UCS	= 1.93 MPa



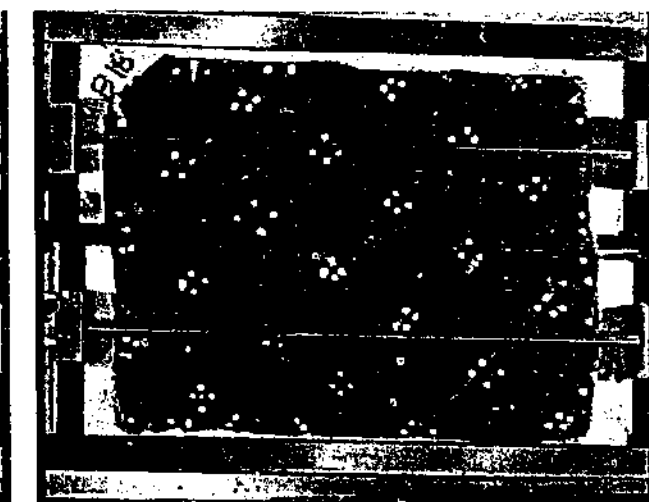
Test B18-1 – dx = 0 mm



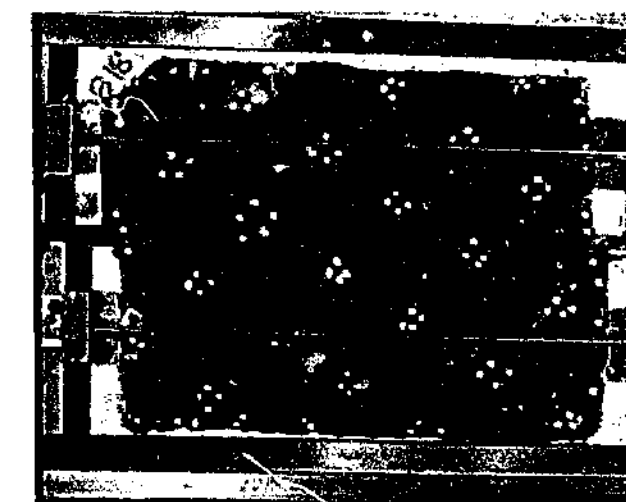
Test B18-2 – dx = 2 mm



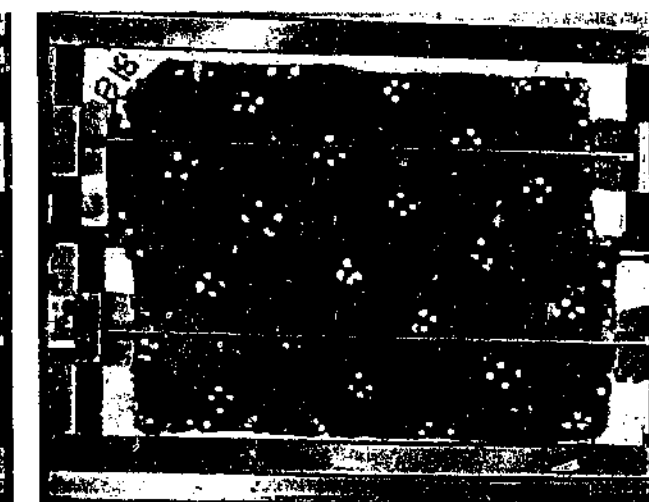
Test B18-3 – dx = 6 mm



Test B18-4 – dx = 9 mm

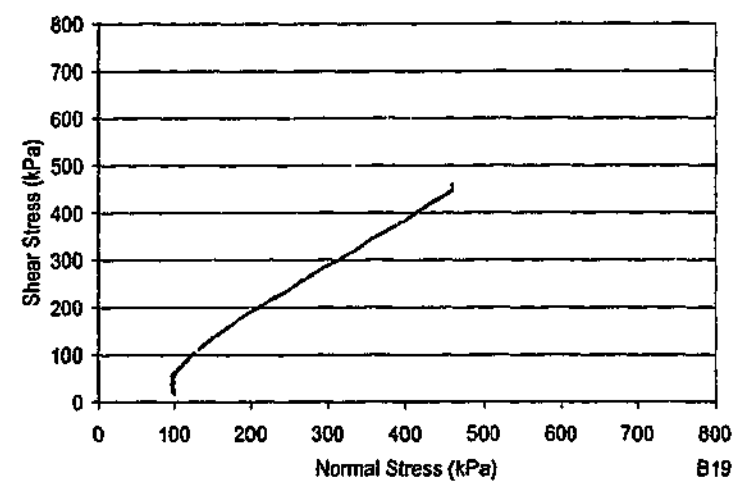


Test B18-5 – dx = 15 mm

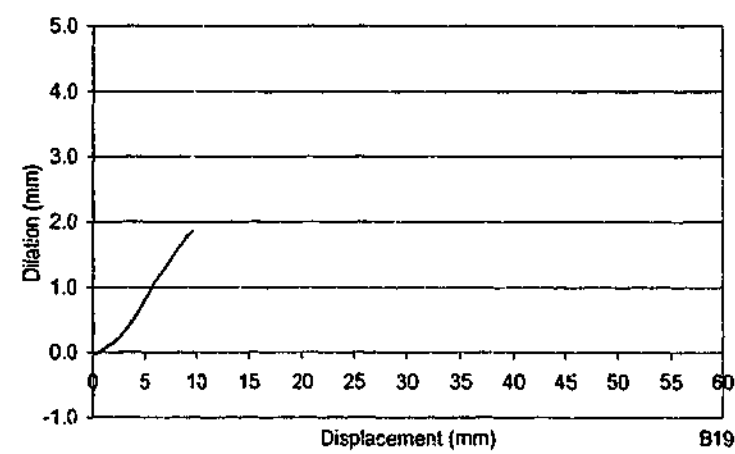
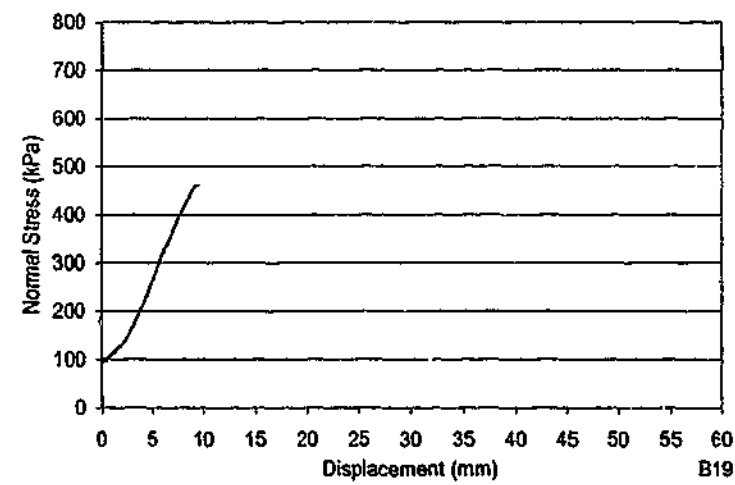
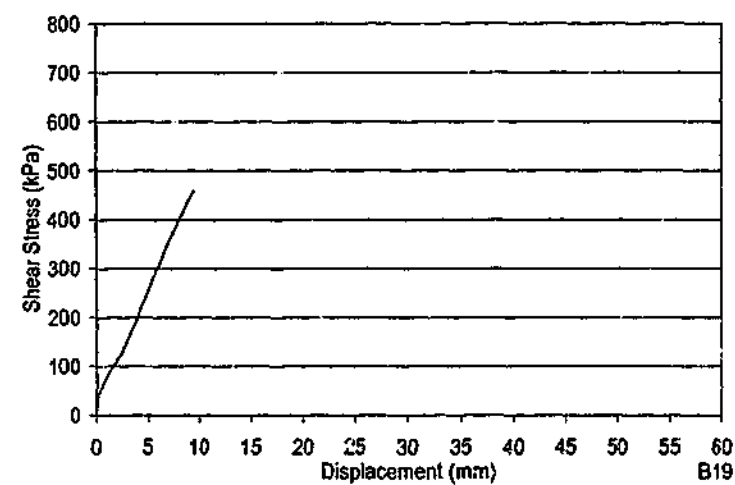


Test B18-6 – dx = 21 mm

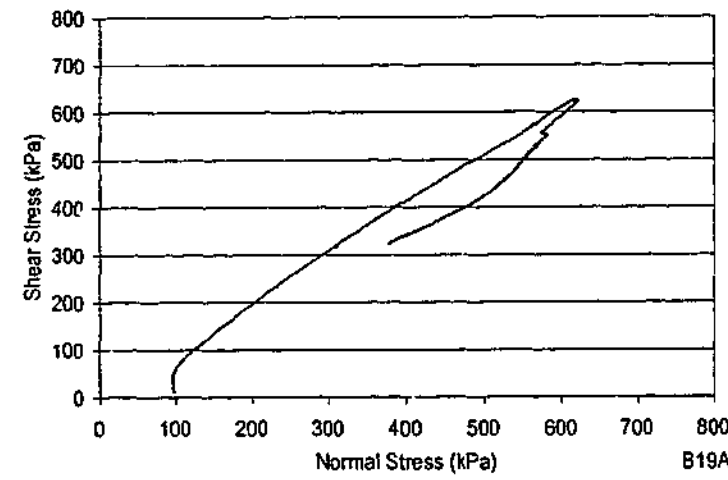
TEST B18			
$\theta_1 = -31^\circ$	$\theta_2 = 43^\circ$	$\theta_3 = n/a^\circ$	spacing = 70 mm
$\sigma_{ni} = 100$ kPa	$k_v = 200$ kPa/mm		UCS = 1.93 MPa



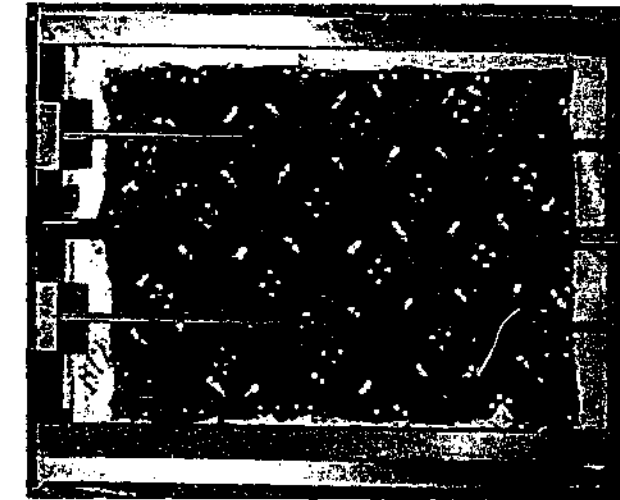
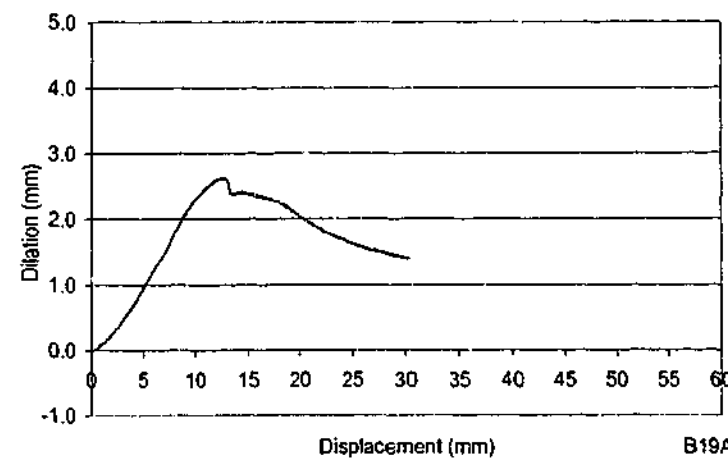
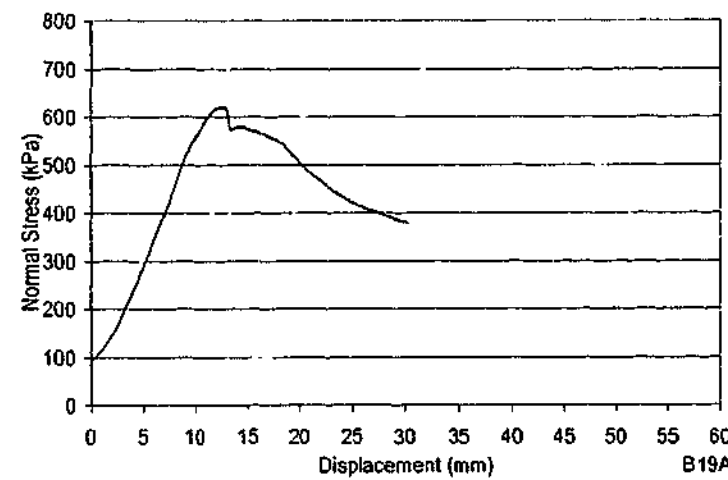
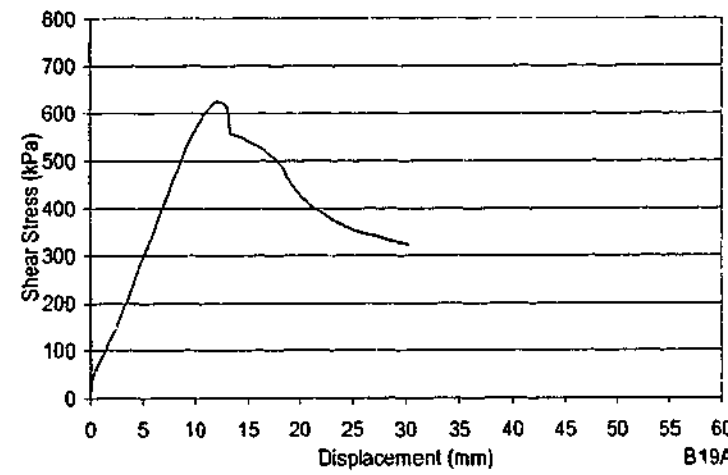
Test Details B19	
θ_1	= -45°
θ_2	= 59°
θ_3	= n/a $^\circ$
spacing	= 70 mm
σ_{ni}	= 100 kPa
k_v	= 200 kPa/mm
UCS	= 2.21 MPa



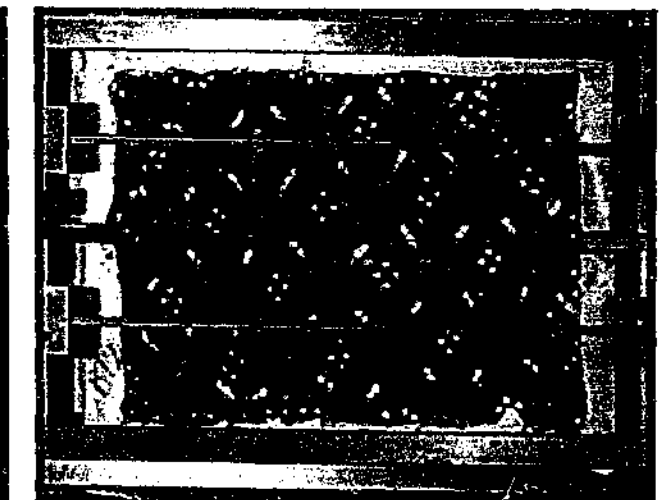
No video footage.



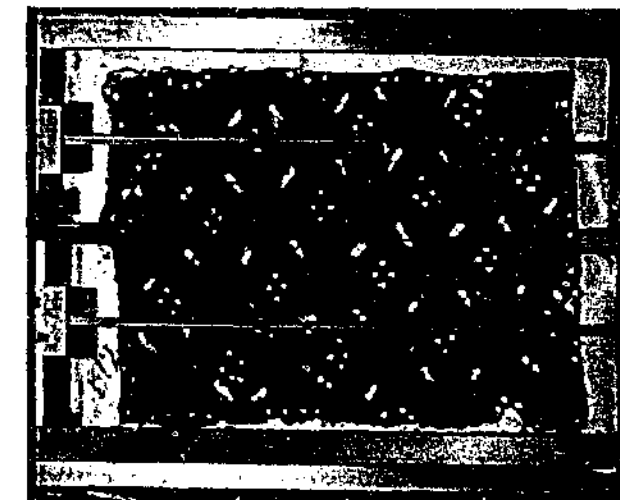
Test Details B19A
 $\theta_1 = -45^\circ$
 $\theta_2 = 59^\circ$
 $\theta_3 = n/a^\circ$
 spacing = 70 mm
 $\sigma_{ni} = 100$ kPa
 $k_v = 200$ kPa/mm
 UCS = 2.21 MPa



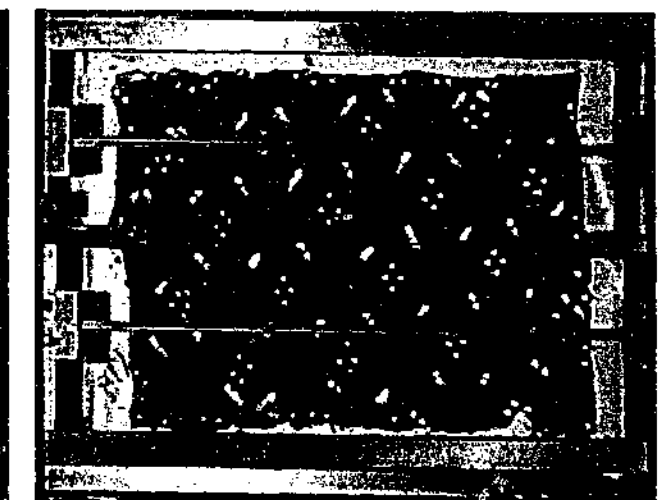
Test B19A-1 – dx = 0 mm



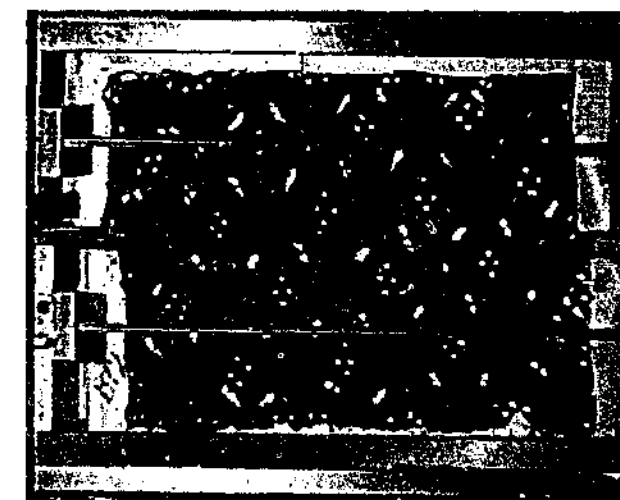
Test B19A-2 – dx = 3 mm



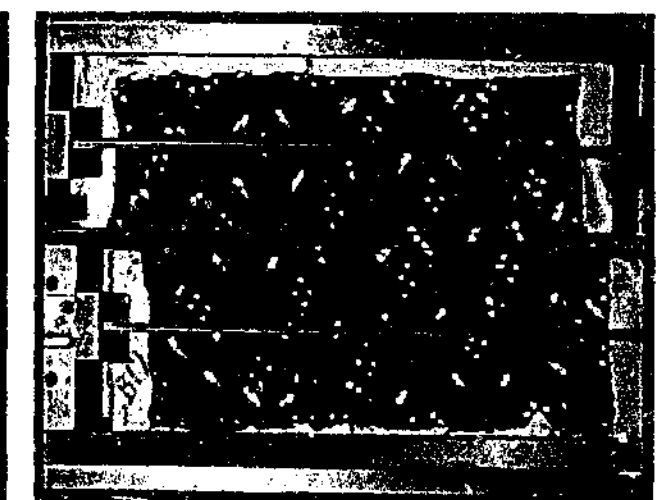
Test B19A-3 – dx = 6 mm



Test B19A-4 – dx = 8 mm

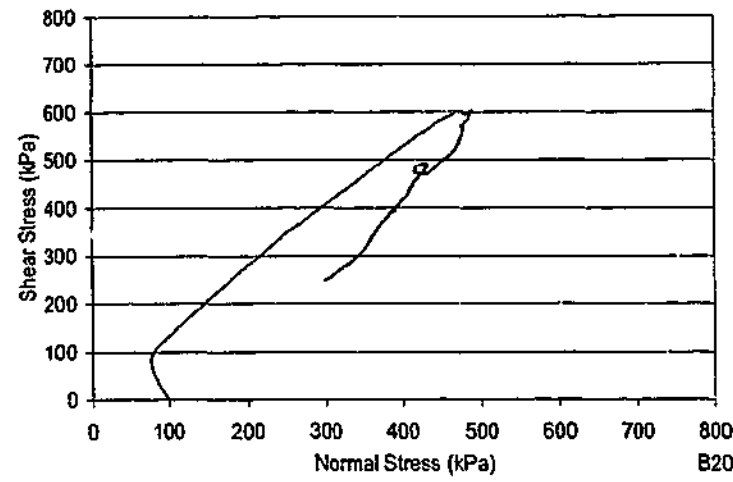


Test B19A-5 – dx = 13 mm

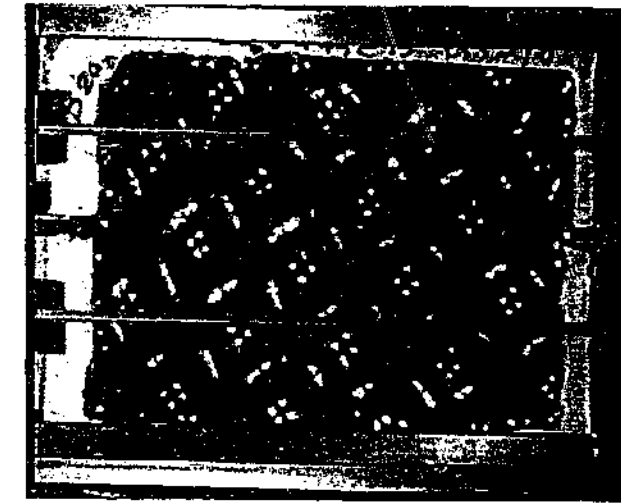
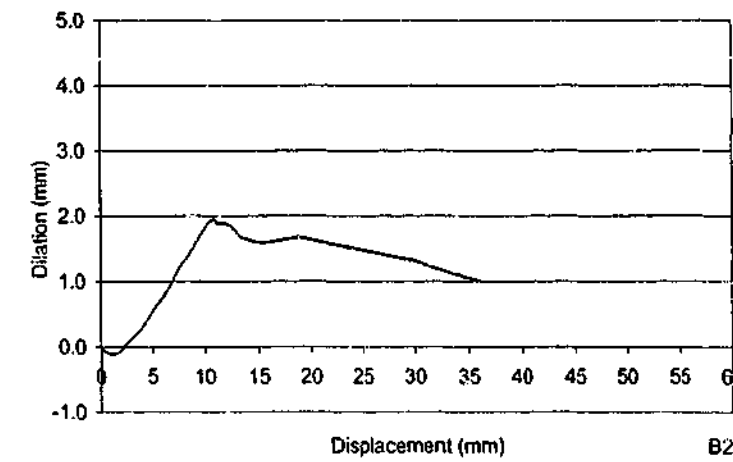
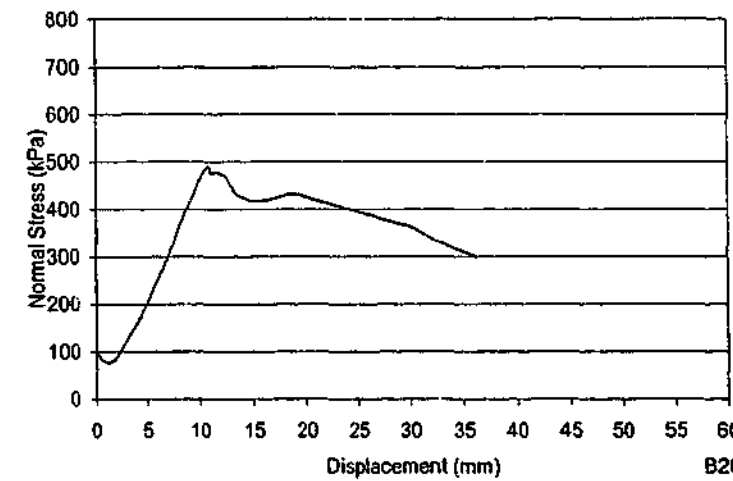
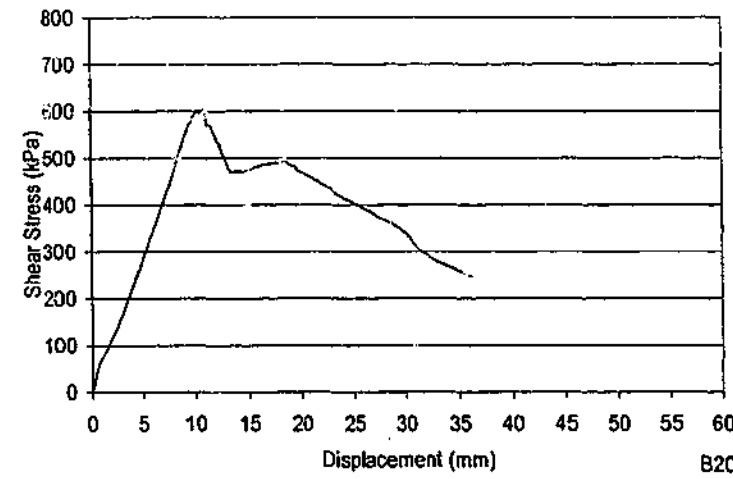


Test B19A-6 – dx = 27 mm

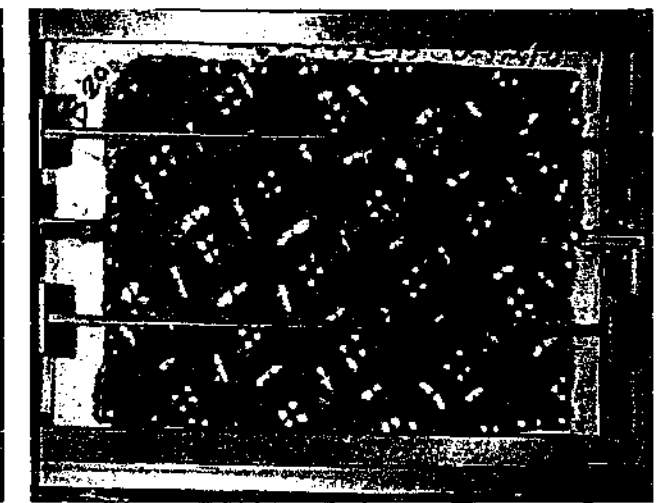
TEST B19A
 $\theta_1 = -45^\circ$ $\theta_2 = 60^\circ$ $\theta_3 = n/a^\circ$ spacing = 70 mm
 $\sigma_{ni} = 100$ kPa $k_v = 200$ kPa/mm UCS = 2.21 MPa



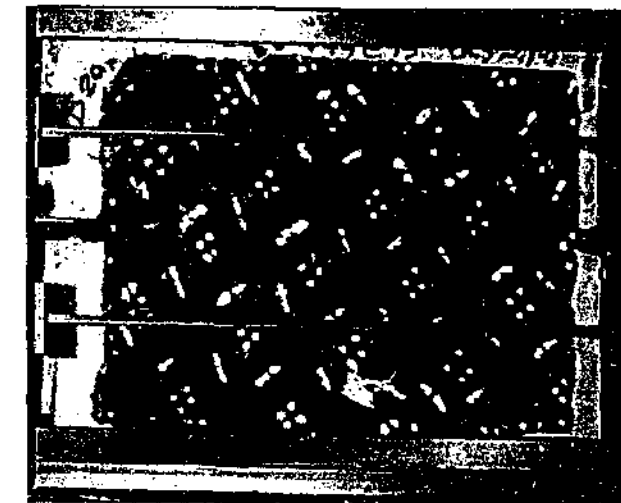
Test Details B20	
θ_1	= -61°
θ_2	= 45°
θ_3	= n/a°
spacing	= 70 mm
σ_{ni}	= 100 kPa
k_v	= 200 kPa/mm
UCS	= 2.38 MPa



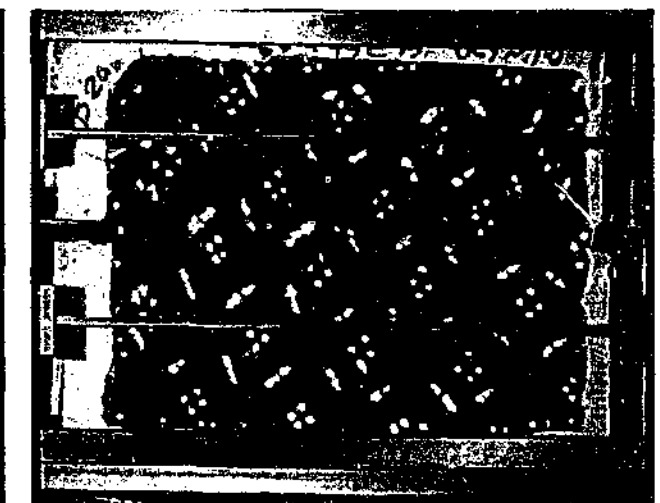
Test B20-1 – dx = 0 mm



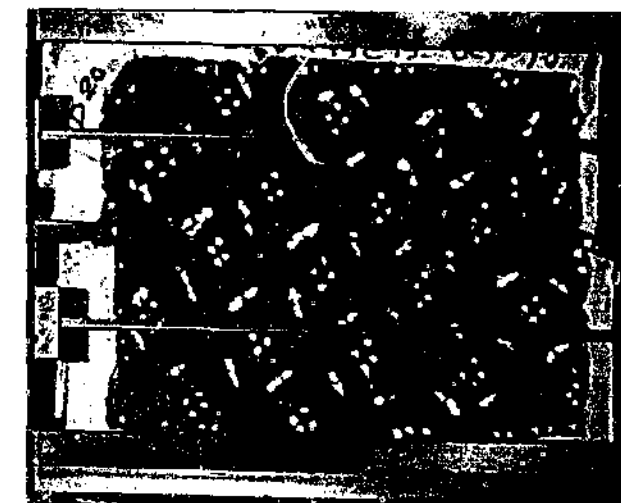
Test B20-2 – dx = 4 mm



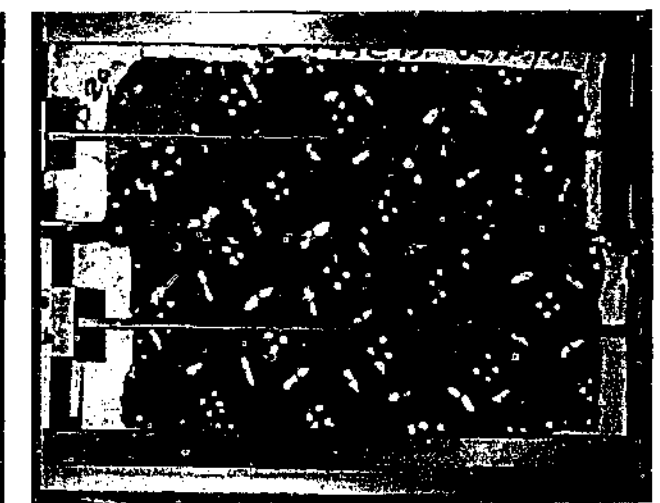
Test B20-3 – dx = 11 mm



Test B20-4 – dx = 18 mm

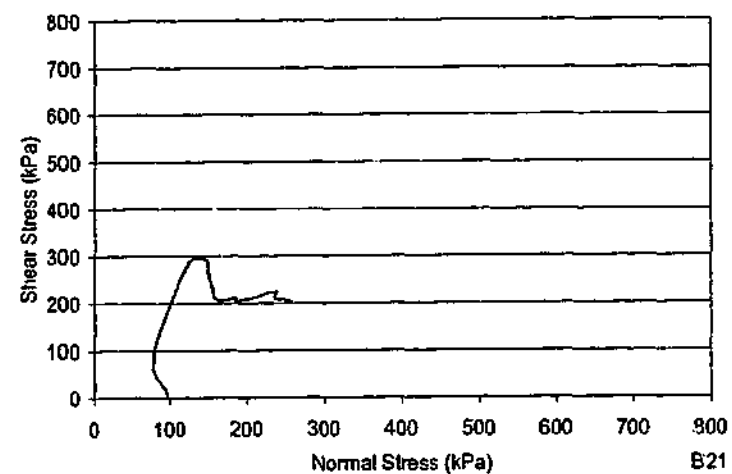


Test B20-5 – dx = 27 mm

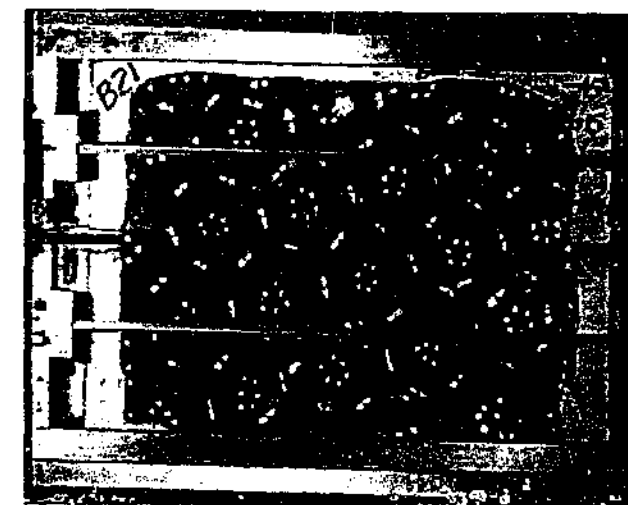
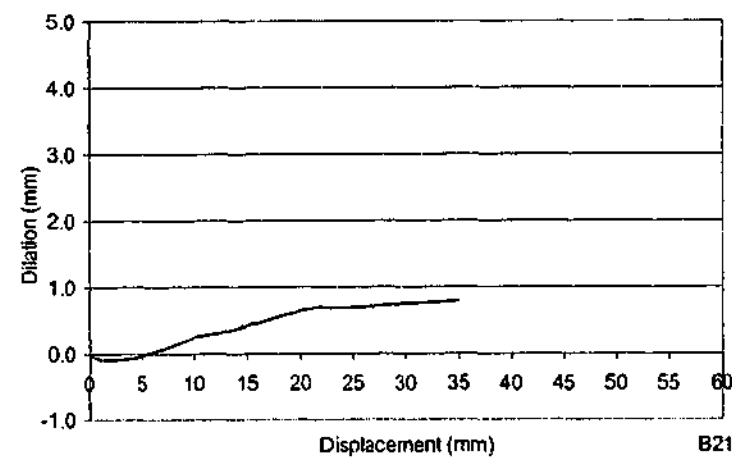
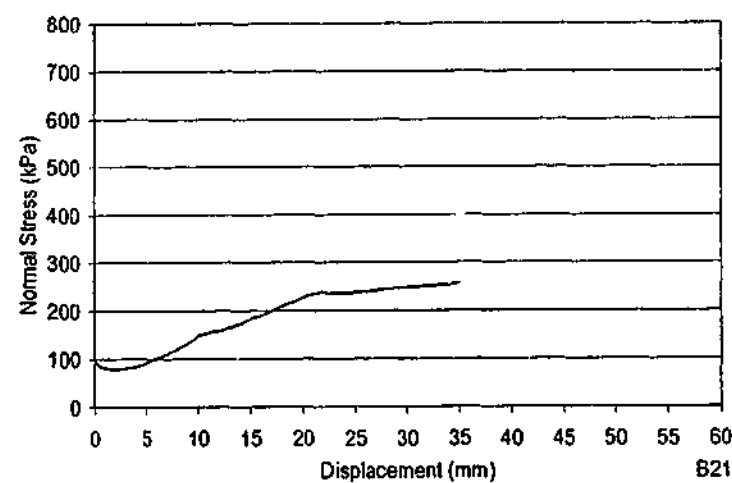
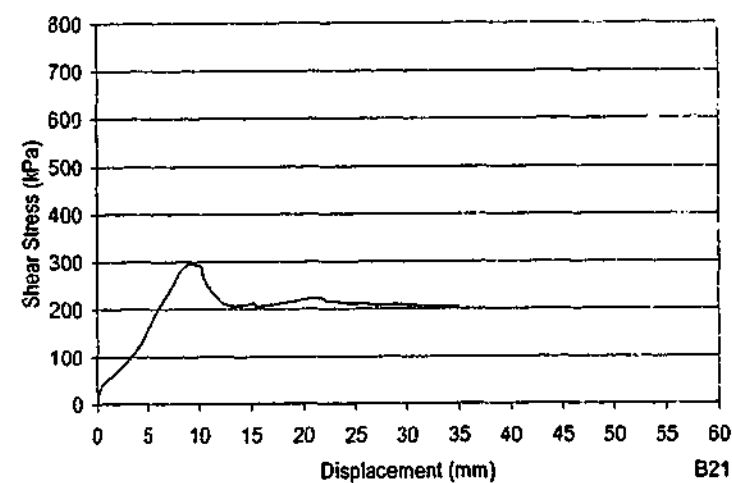


Test B20-6 – dx = 33 mm

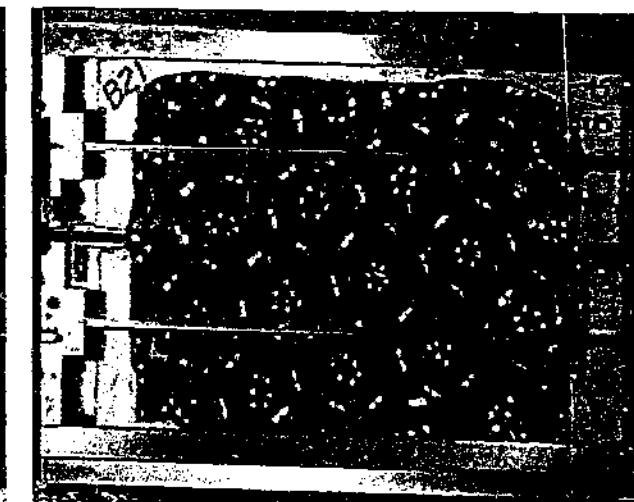
TEST B20			
$\theta_1 = -61^\circ$	$\theta_2 = 45^\circ$	$\theta_3 = n/a^\circ$	spacing = 70 mm
$\sigma_{ni} = 100$ kPa	$k_v = 200$ kPa/mm		UCS = 2.38 MPa



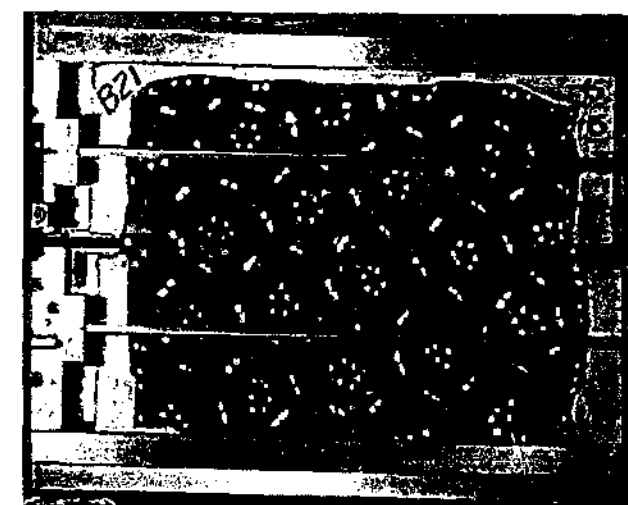
Test Details B21
 $\theta_1 = -45^\circ$
 $\theta_2 = 16^\circ$
 $\theta_3 = 74^\circ$
 spacing = 70 mm
 $\sigma_{ni} = 100$ kPa
 $k_v = 200$ kPa/mm
 UCS = 2.52 MPa



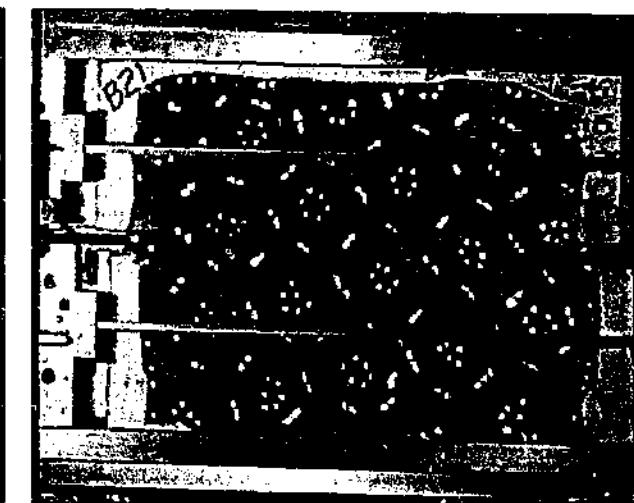
Test B21-1 – dx = 0 mm



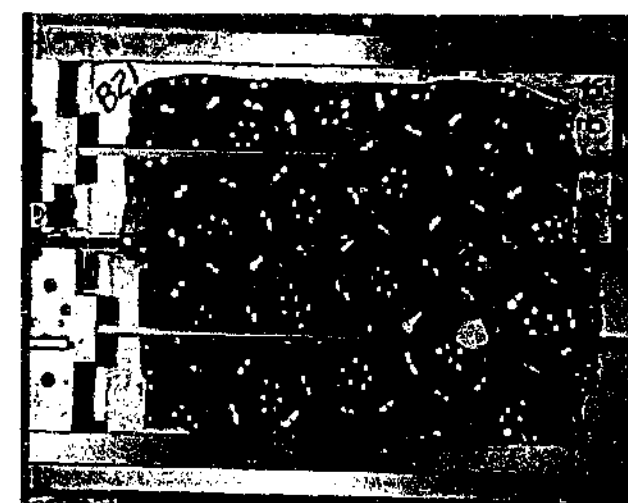
Test B21-2 – dx = 3 mm



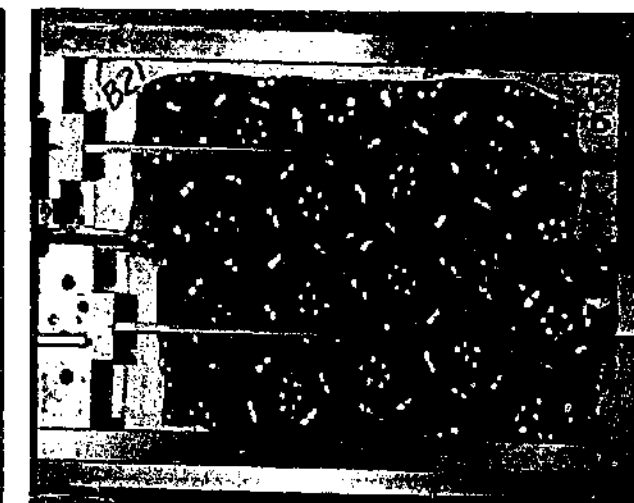
Test B21-3 – dx = 7 mm



Test B21-4 – dx = 11 mm

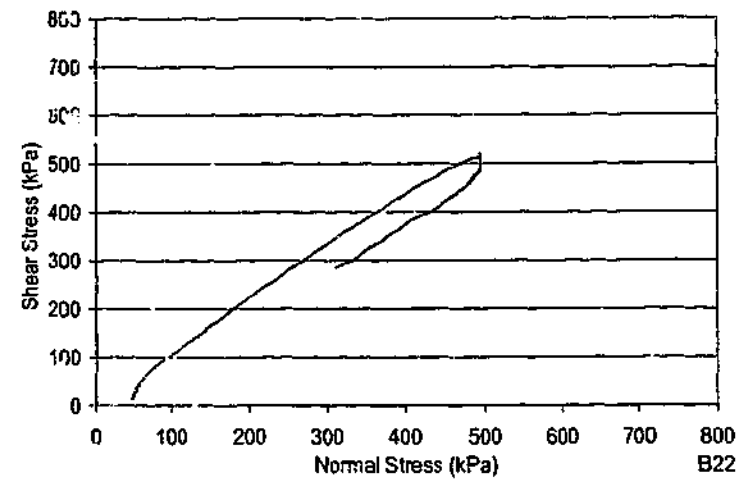


Test B21-5 – dx = 19 mm

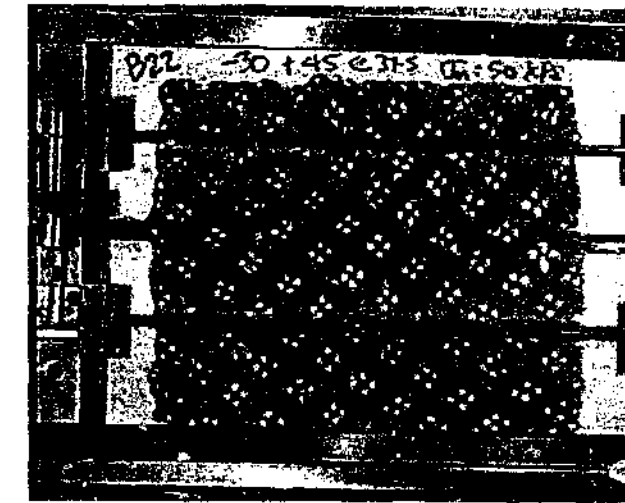
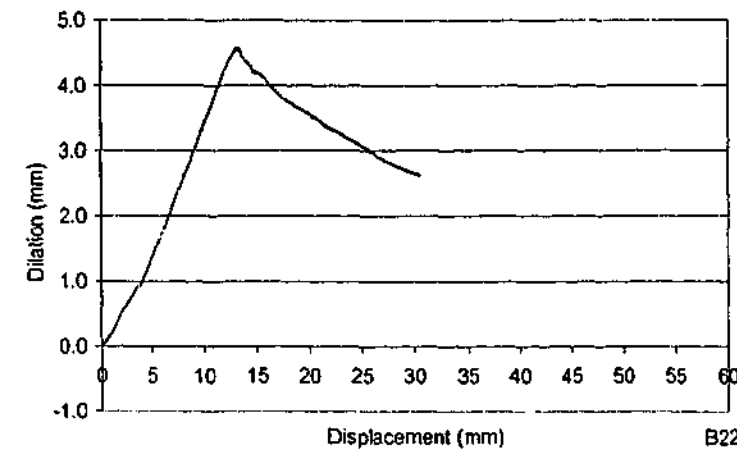
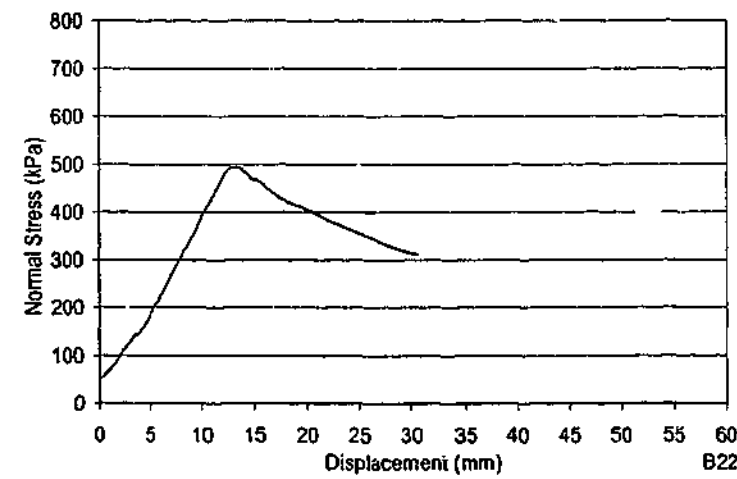
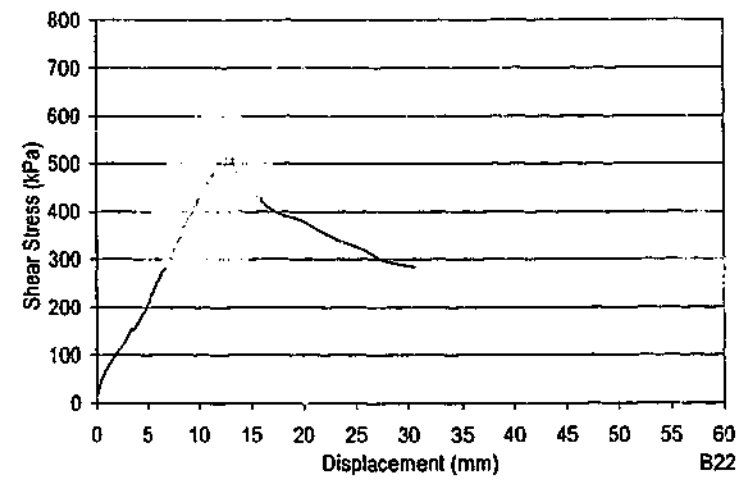


Test B21-6 – dx = 30 mm

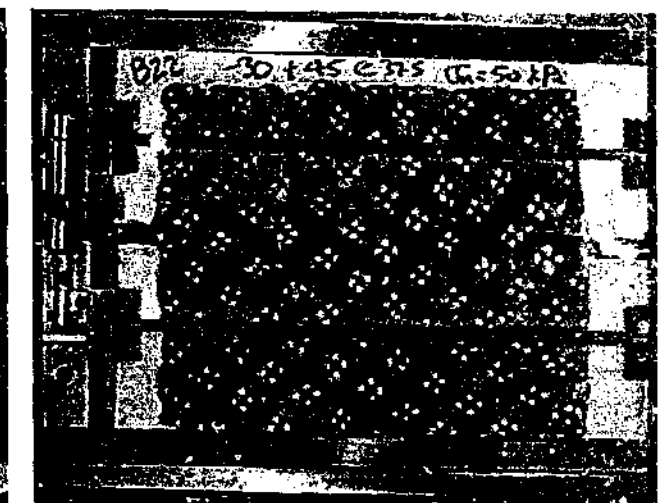
TEST B21
 $\theta_1 = -45^\circ$ $\theta_2 = 16^\circ$ $\theta_3 = 74^\circ$ spacing = 70 mm
 $\sigma_{ni} = 100$ kPa $k_v = 200$ kPa/mm UCS = 2.52 MPa



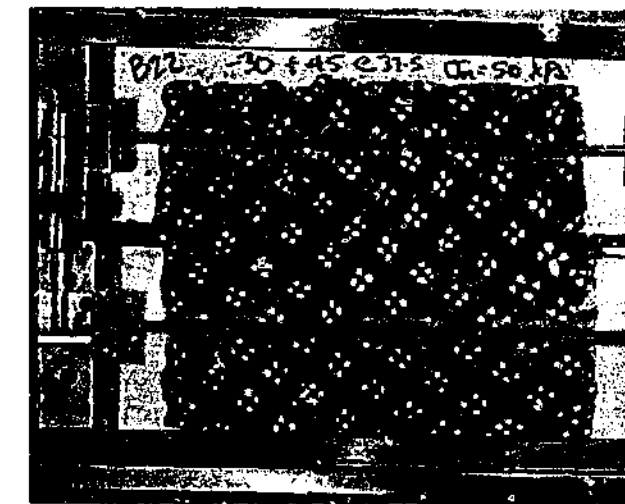
Test Details B22	
θ_1	= -30°
θ_2	= 46°
θ_3	= n/a°
spacing	= 32 mm
σ_{ni}	= 50 kPa
k_v	= 200 kPa/mm
UCS	= 3.40 MPa



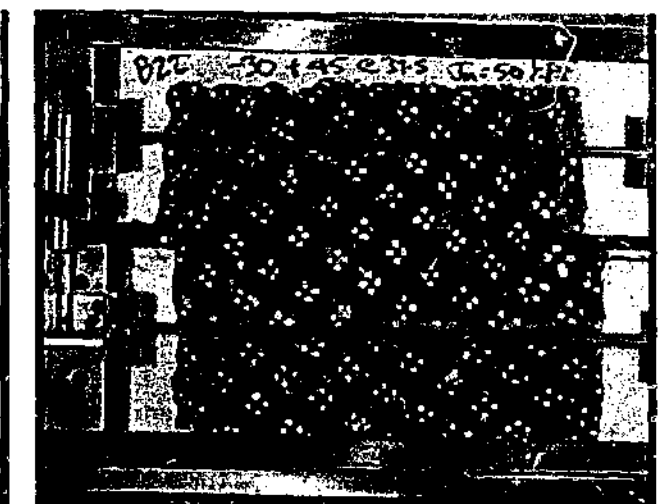
Test B22-1 – dx = 0 mm



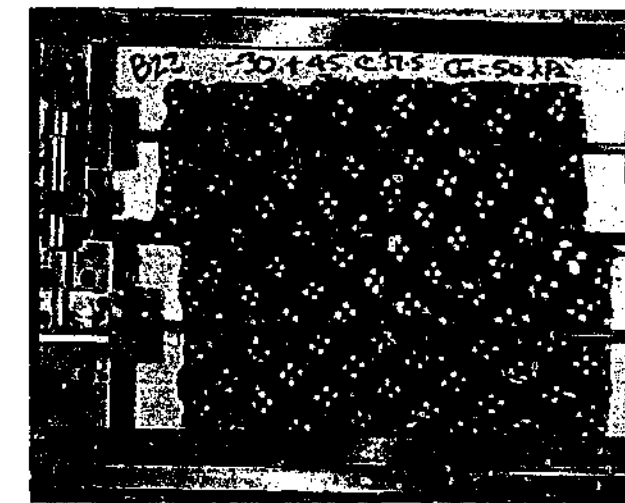
Test B22-2 – dx = 2 mm



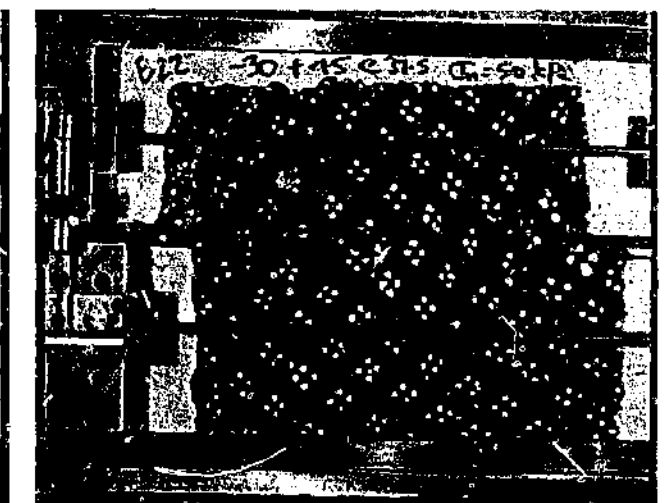
Test B22-3 – dx = 7 mm



Test B22-4 – dx = 13 mm

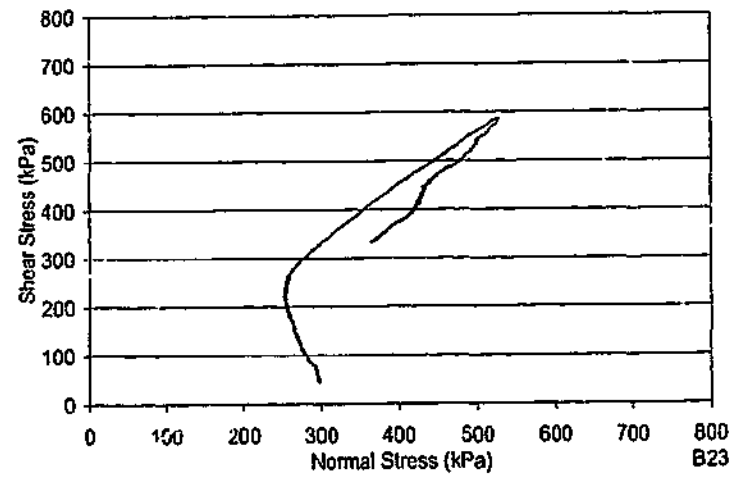


Test B22-5 – dx = 20 mm

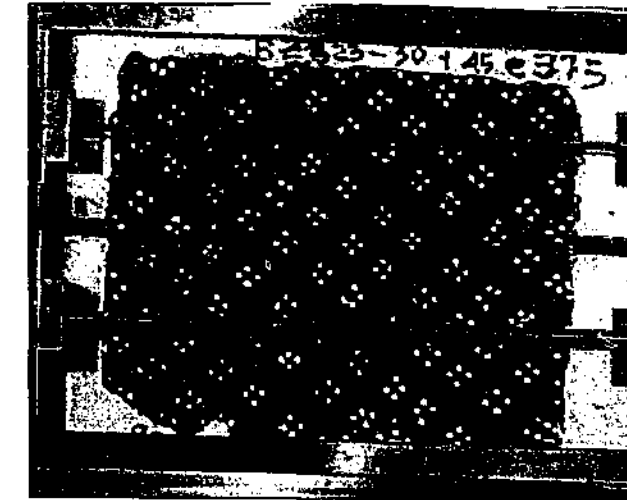
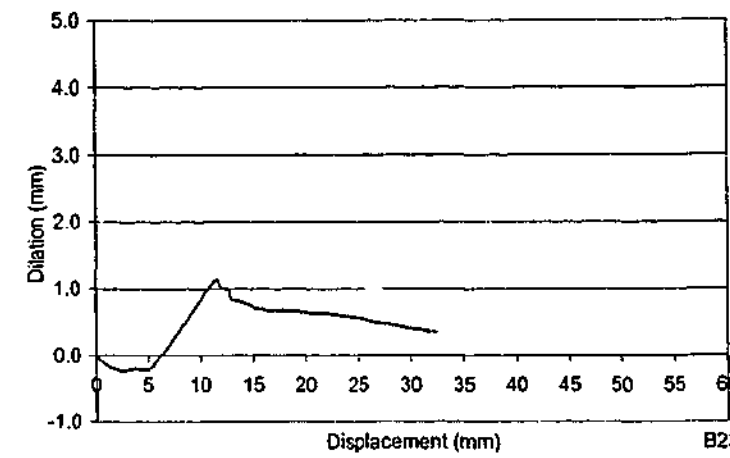
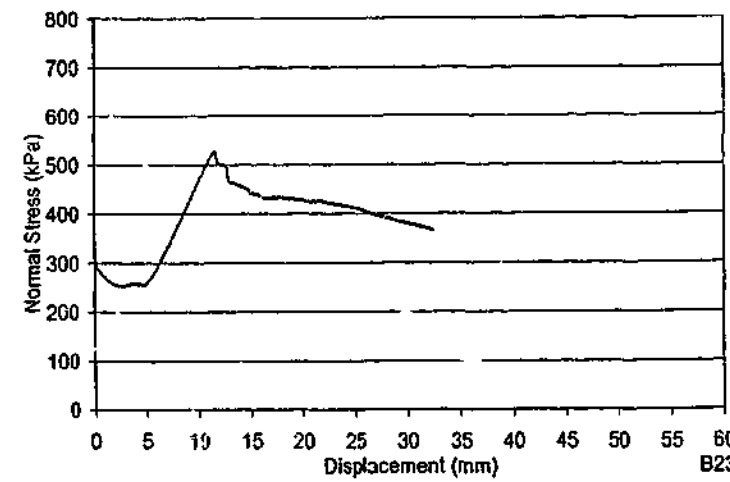
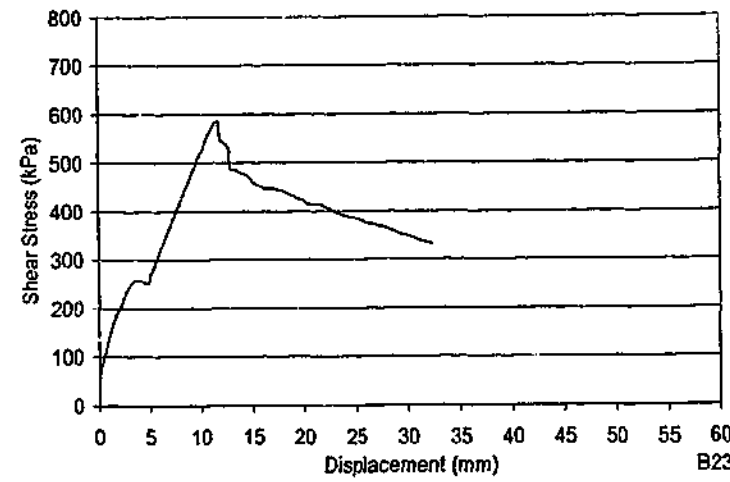


Test B22-6 – dx = 28 mm

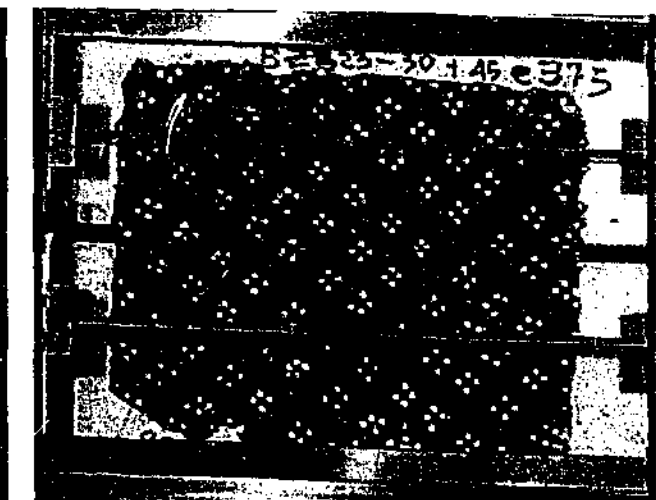
TEST B22			
$\theta_1 = -30^\circ$	$\theta_2 = 46^\circ$	$\theta_3 = n/a^\circ$	spacing = 32 mm
$\sigma_{ni} = 50$ kPa	$k_v = 200$ kPa/mm		UCS = 3.40 MPa



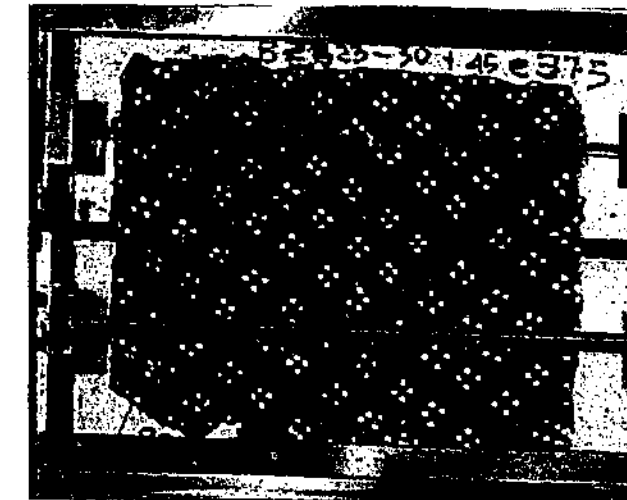
Test Details B23	
θ_1	= -33°
θ_2	= 43°
θ_3	= n/a $^\circ$
spacing	= 32 mm
σ_{ni}	= 300 kPa
k_v	= 200 kPa/mm
UCS	= 3.37 MPa



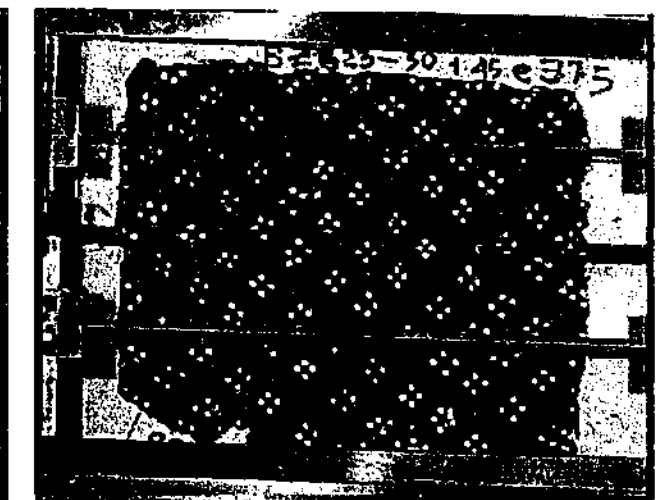
Test B23-1 – dx = 0 mm



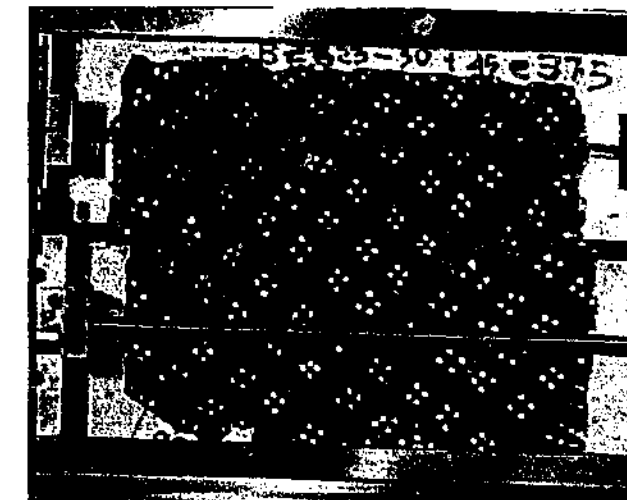
Test B23-2 – dx = 2 mm



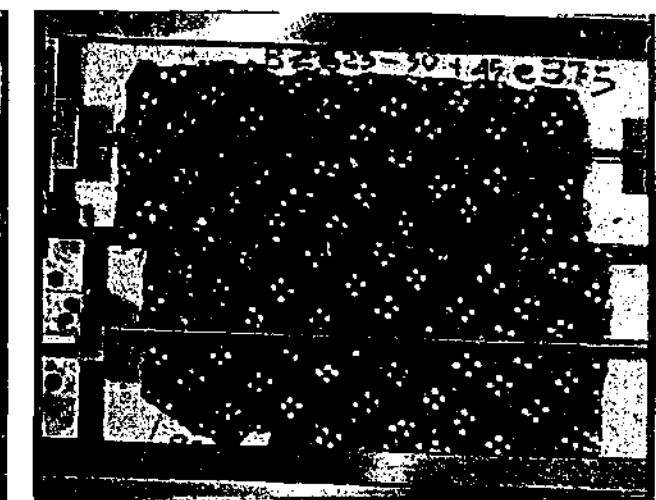
Test B23-3 – dx = 5 mm



Test B23-4 – dx = 7 mm

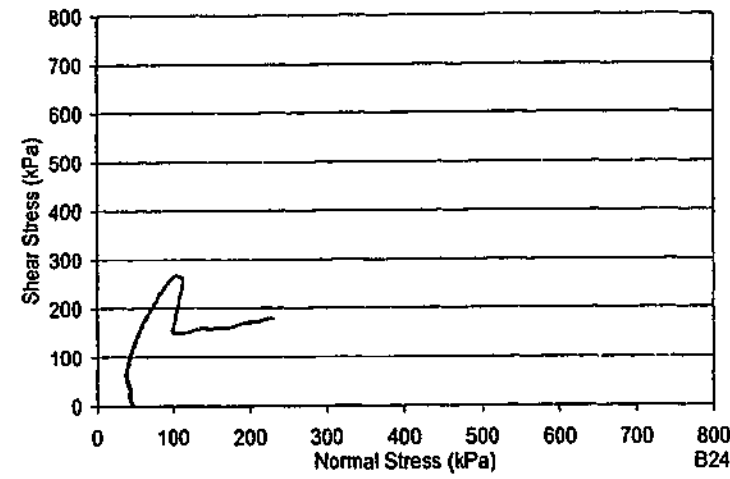


Test B23-5 – dx = 15 mm

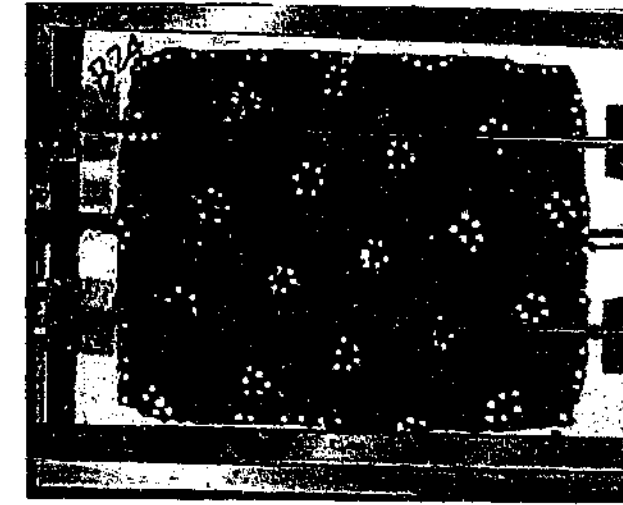
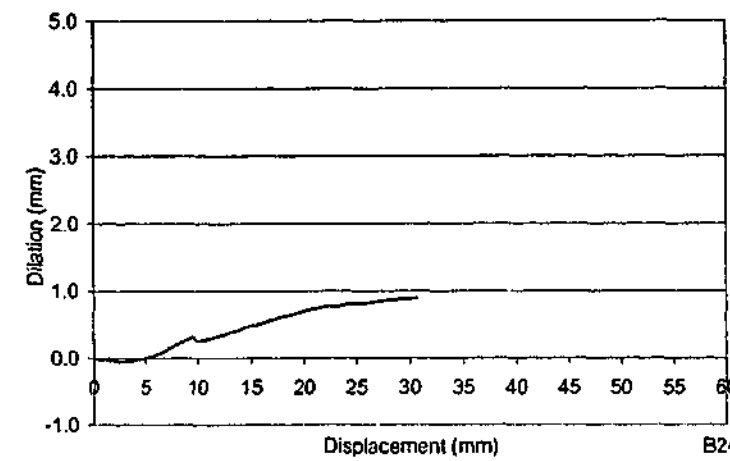
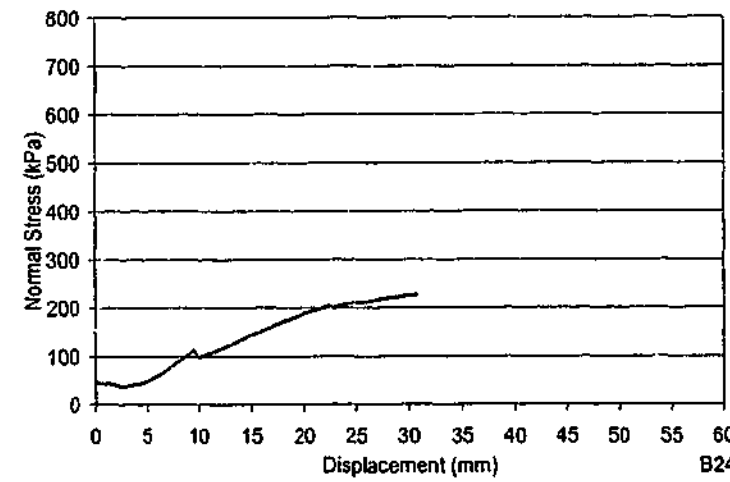
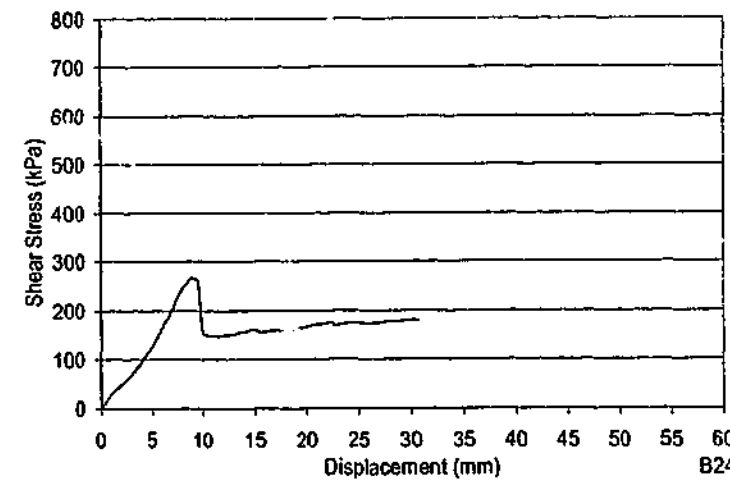


Test B23-6 – dx = 25 mm

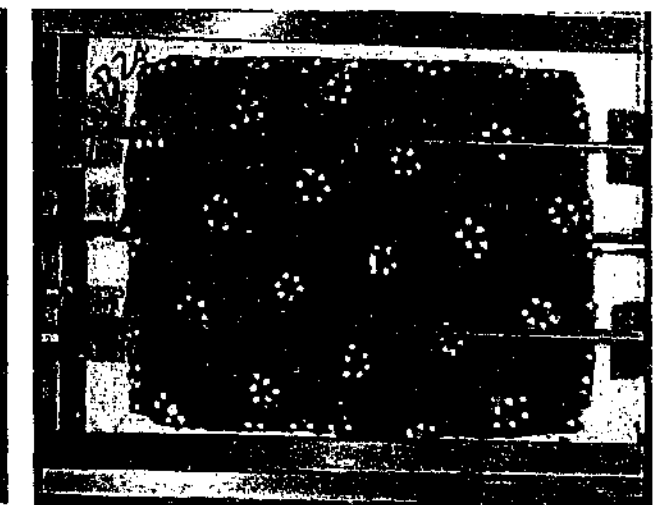
TEST B23			
$\theta_1 = -33^\circ$	$\theta_2 = 43^\circ$	$\theta_3 = n/a^\circ$	spacing = 30-37 mm
$\sigma_{ni} = 300$ kPa	$k_v = 200$ kPa/mm		UCS = 2.38 MPa



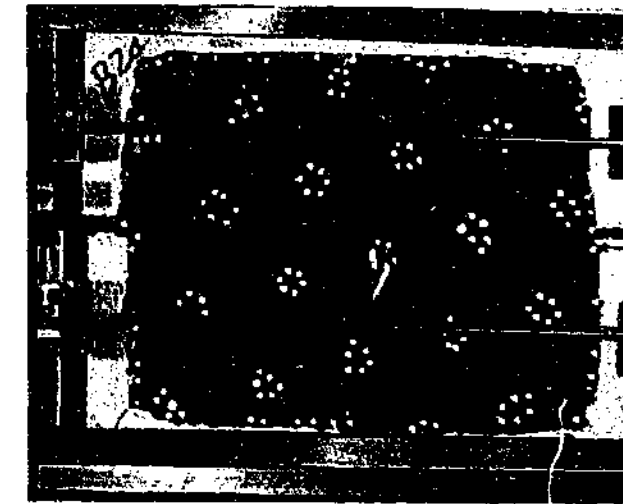
Test Details B24
 $\theta_1 = -45^\circ$
 $\theta_2 = 16^\circ$
 $\theta_3 = 74^\circ$
 spacing = 70 mm
 $\sigma_{ni} = 50$ kPa
 $k_v = 200$ kPa/mm
 UCS = 2.50 MPa



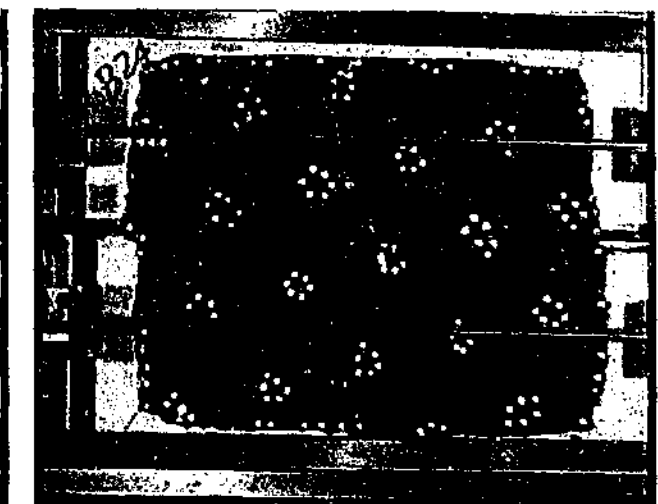
Test B24-1 – dx = 0 mm



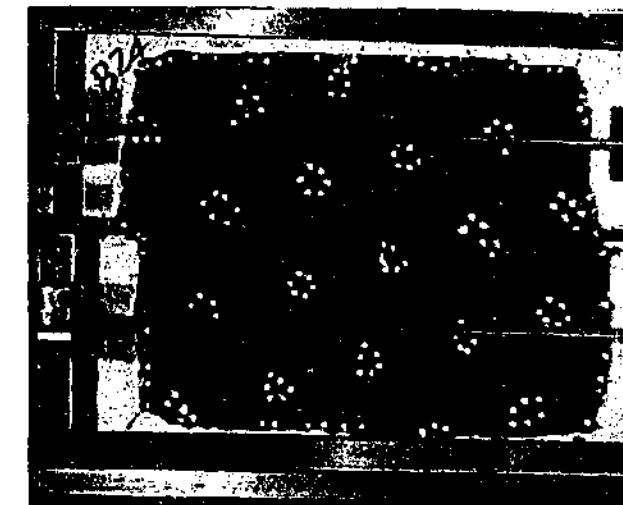
Test B24-2 – dx = 4 mm



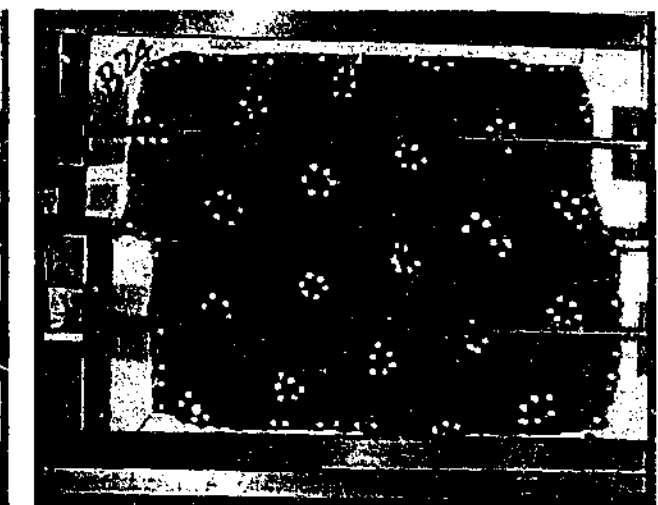
Test B24-3 – dx = 7 mm



Test B24-4 – dx = 10 mm

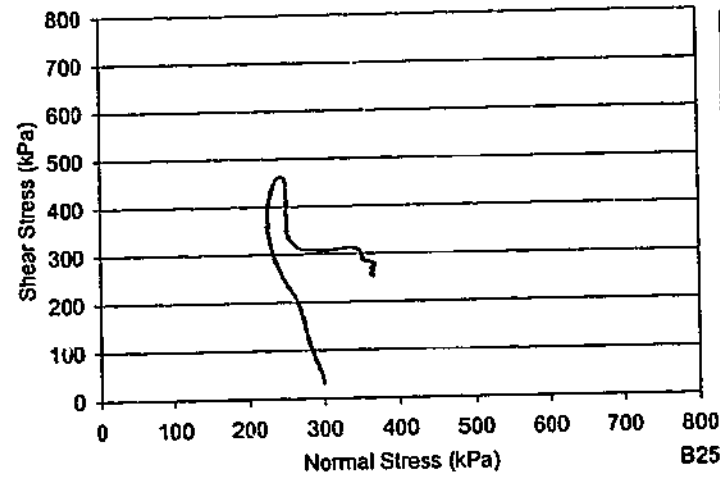


Test B24-5 – dx = 16 mm

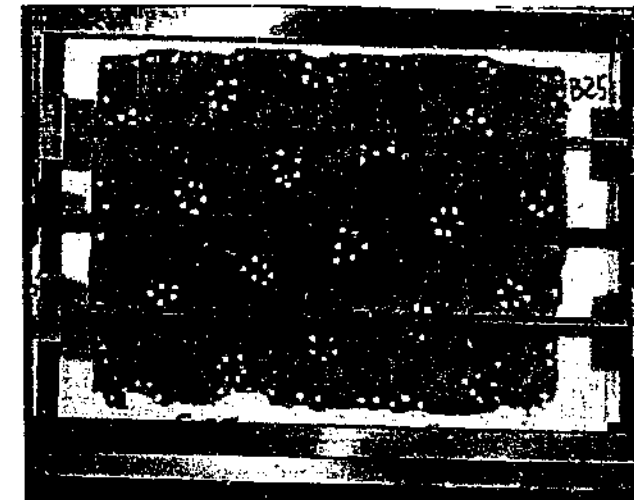
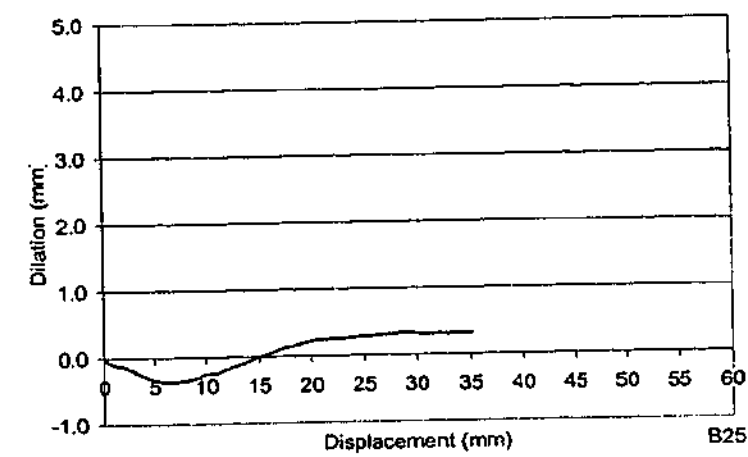
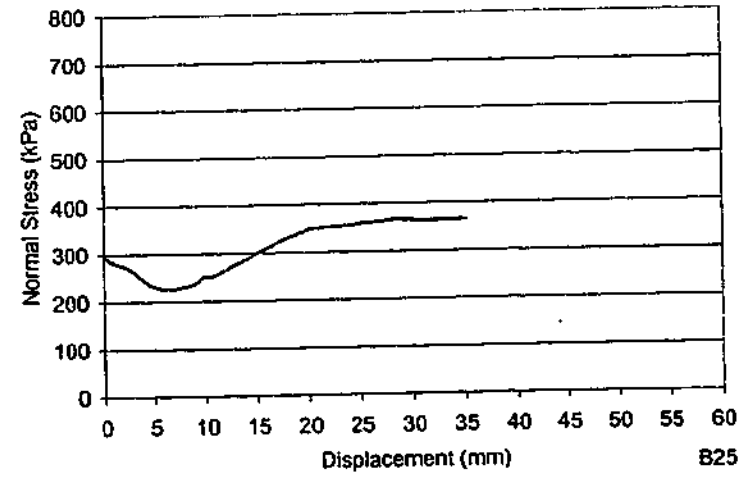
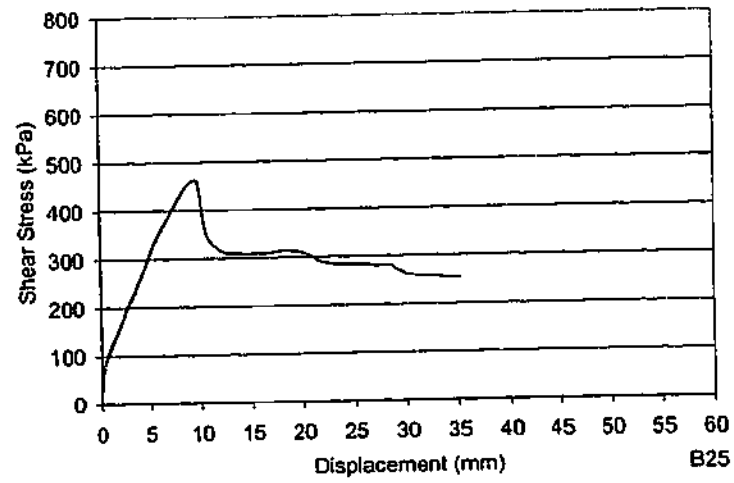


Test B24-6 – dx = 28 mm

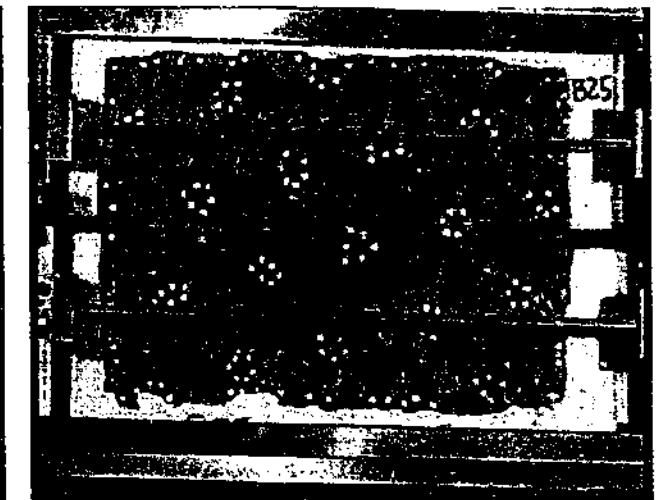
TEST B24
 $\theta_1 = -45^\circ$ $\theta_2 = 16^\circ$ $\theta_3 = 74^\circ$ spacing = 70 mm
 $\sigma_{ni} = 50$ kPa $k_v = 200$ kPa/mm UCS = 2.50 MPa



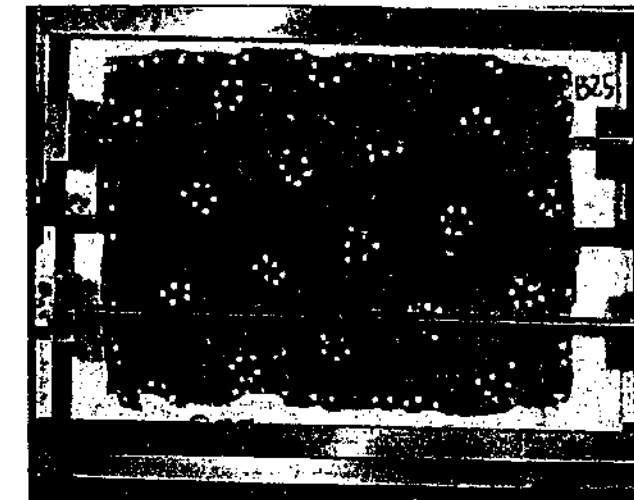
Test Details B25	
θ_1	= -45°
θ_2	= 15°
θ_3	= 75°
spacing	= 70 mm
σ_{ni}	= 300 kPa
k_v	= 200 kPa/mm
UCS	= 2.89 MPa



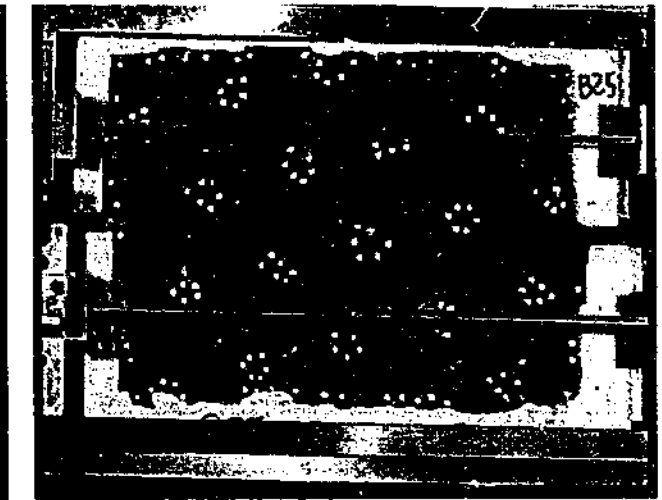
Test B25-1 – dx = 0 mm



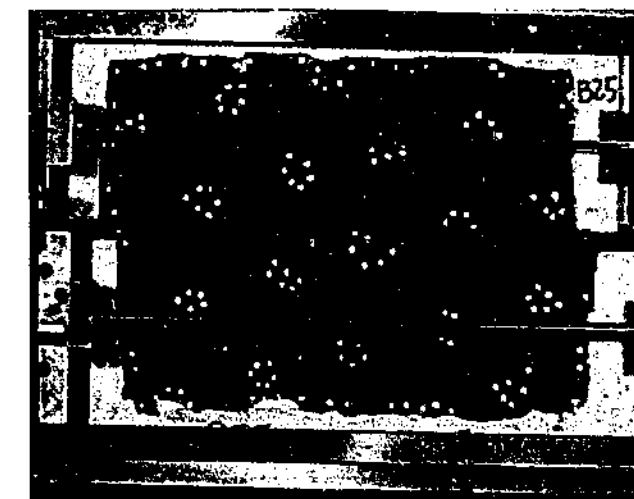
Test B25-2 – dx = 5 mm



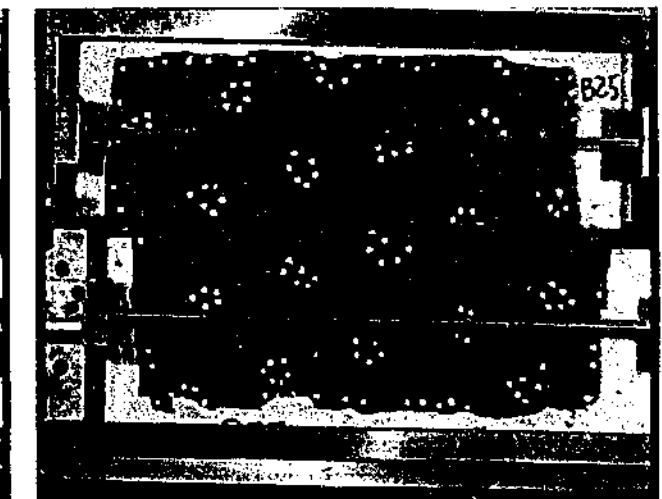
Test B25-3 – dx = 9 mm



Test B25-4 – dx = 13 mm

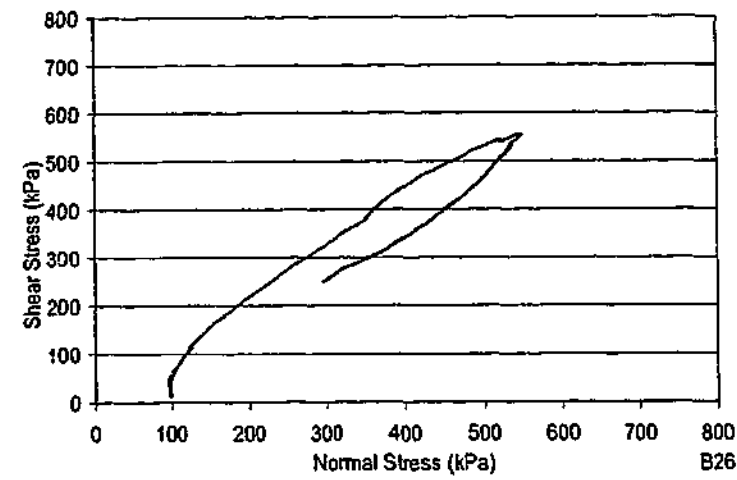


Test B25-5 – dx = 21 mm

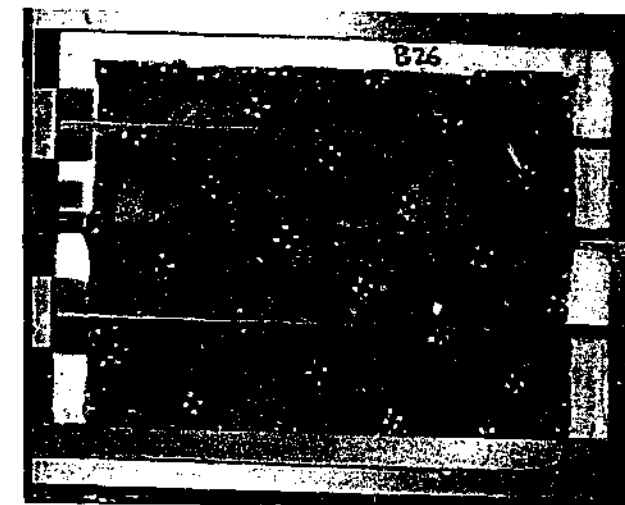
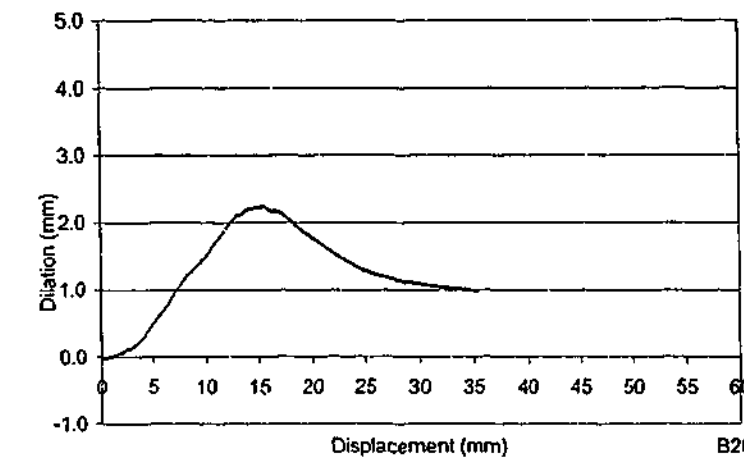
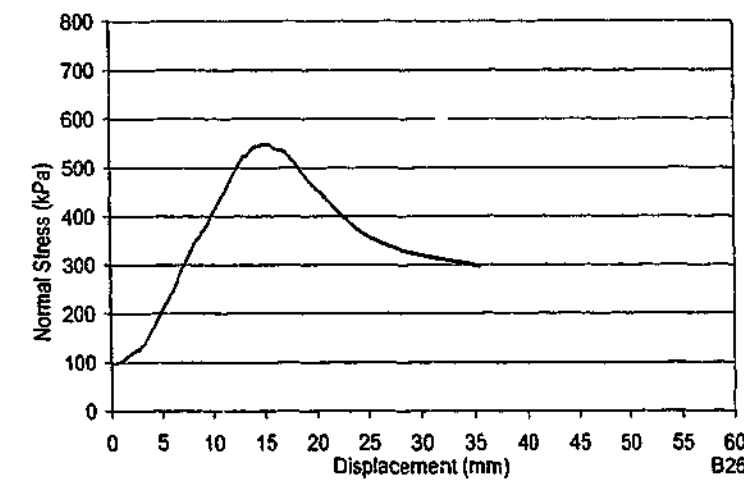
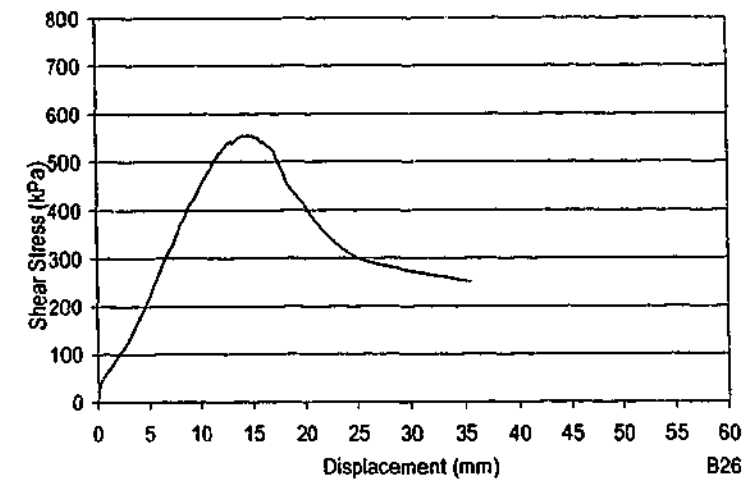


Test B25-6 – dx = 34 mm

TEST B25			
$\theta_1 = -45^\circ$	$\theta_2 = 15^\circ$	$\theta_3 = 75^\circ$	spacing = 60-70 mm
$\sigma_{ni} = 300$ kPa	$k_v = 200$ kPa/mm		UCS = 2.89 MPa



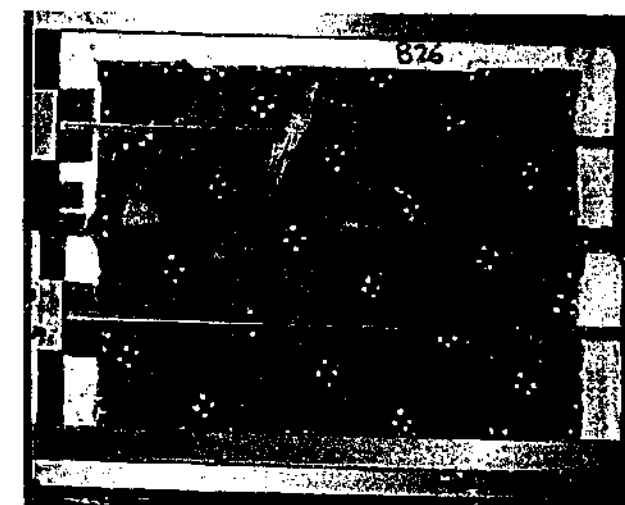
Test Details B26	
θ_1	= -29°
θ_2	= 61°
θ_3	= n/a°
spacing	= 70 mm
σ_{ni}	= 100 kPa
k_v	= 200 kPa/mm
UCS	= 2.04 MPa



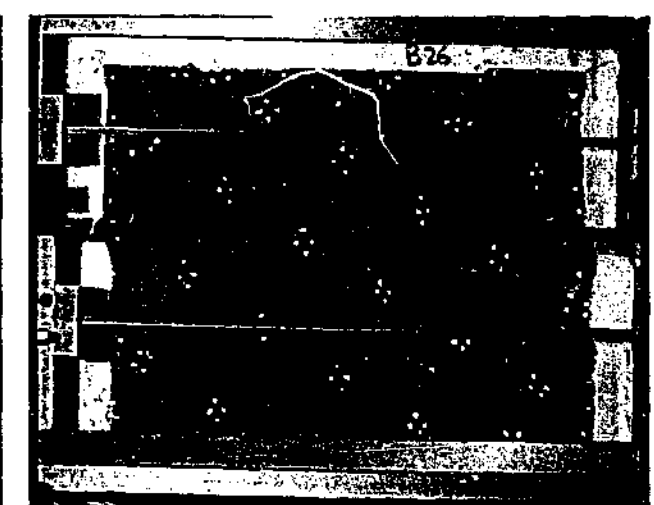
Test B26-1 – dx = 0 mm



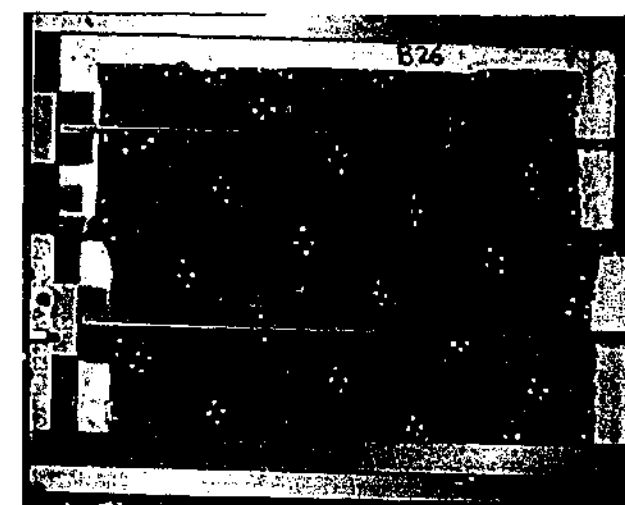
Test B26-2 – dx = 5 mm



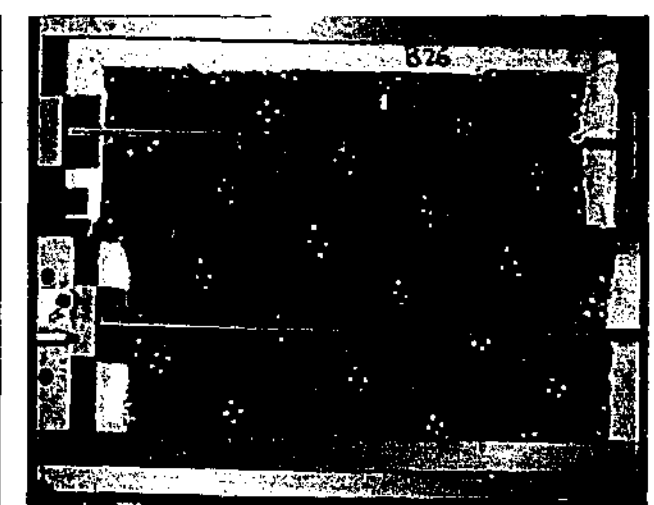
Test B26-3 – dx = 9 mm



Test B26-4 – dx = 15 mm

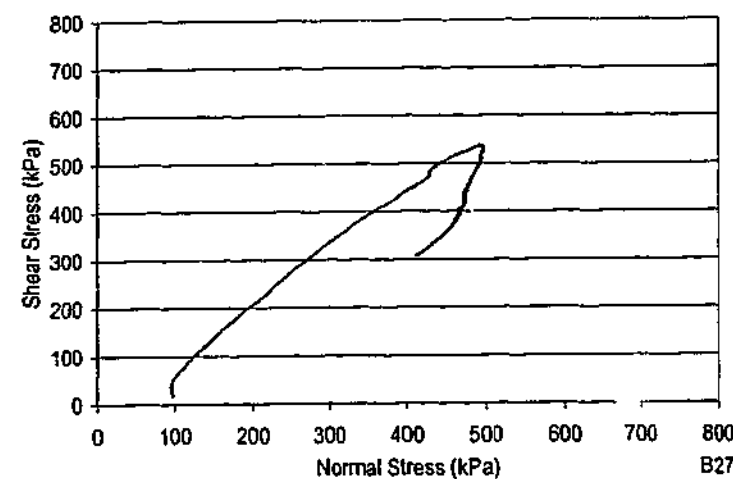


Test B26-5 – dx = 20 mm

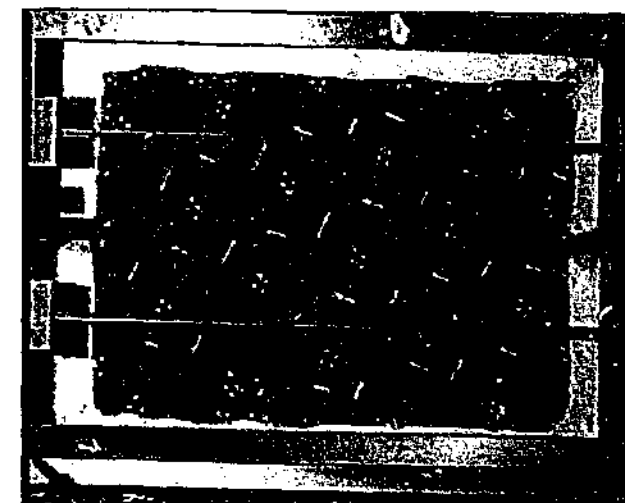
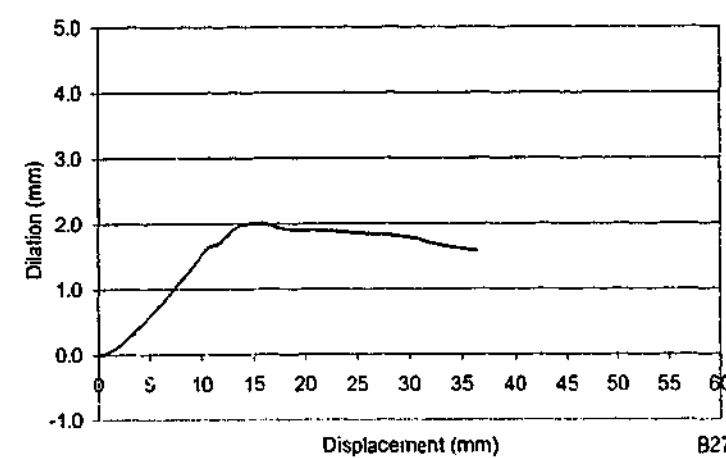
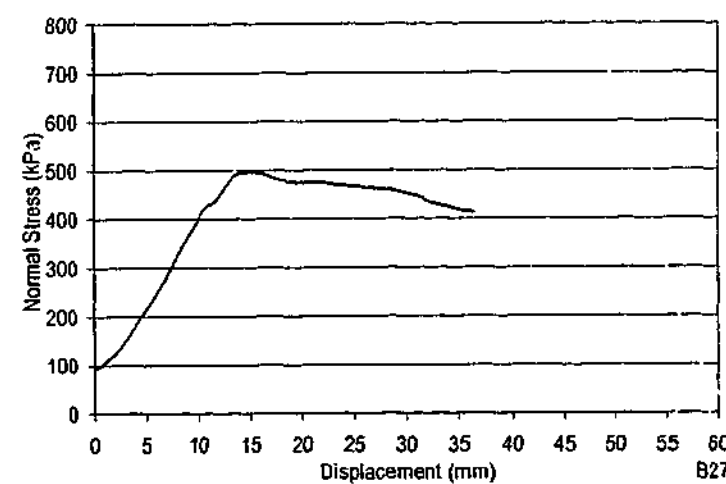
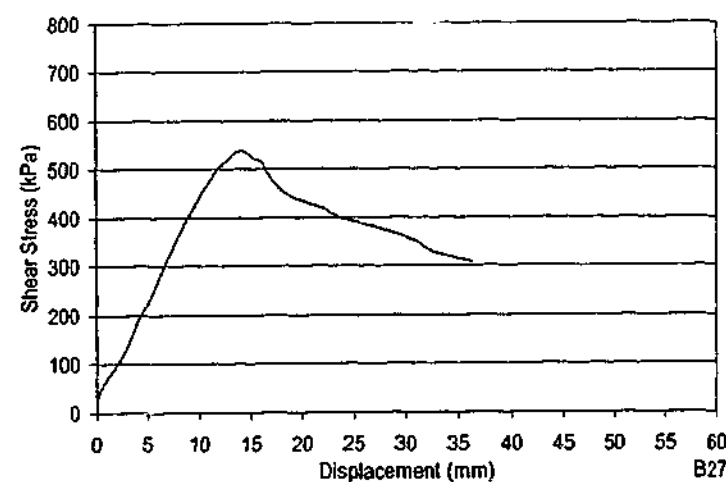


Test B26-6 – dx = 30 mm

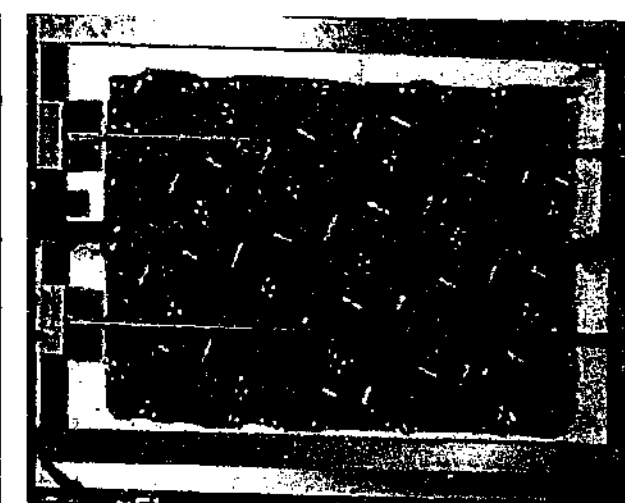
TEST B26			
$\theta_1 = -29^\circ$	$\theta_2 = 61^\circ$	$\theta_3 = n/a^\circ$	spacing = 70 mm
$\sigma_{ni} = 100$ kPa	$k_v = 200$ kPa/mm		UCS = 2.04 MPa



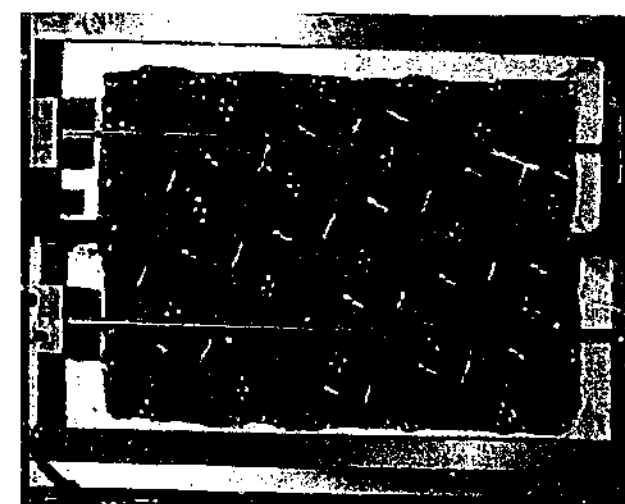
Test Details B27	
θ_1	= -45°
θ_2	= 75°
θ_3	= n/a $^\circ$
spacing	= 70 mm
σ_{ni}	= 100 kPa
k_v	= 200 kPa/mm
UCS	= 1.66 MPa



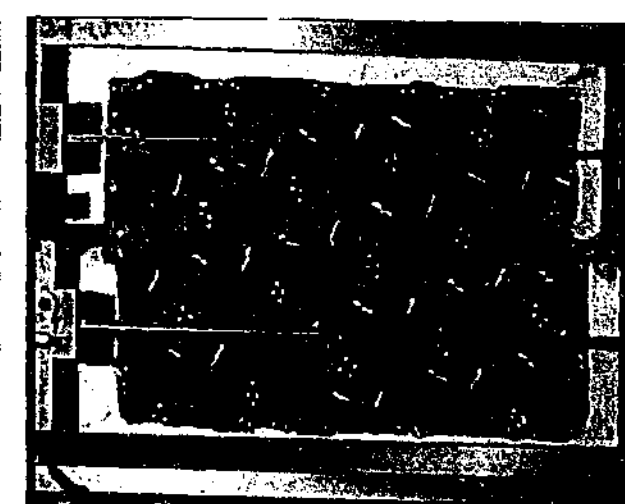
Test B27-1 – dx = 0 mm



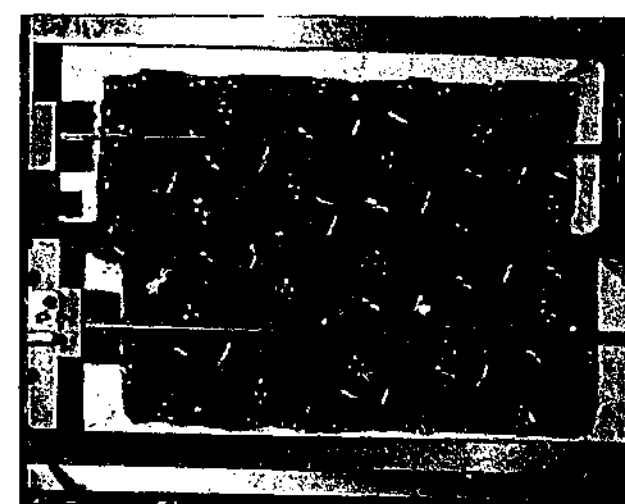
Test B27-2 – dx = 5 mm



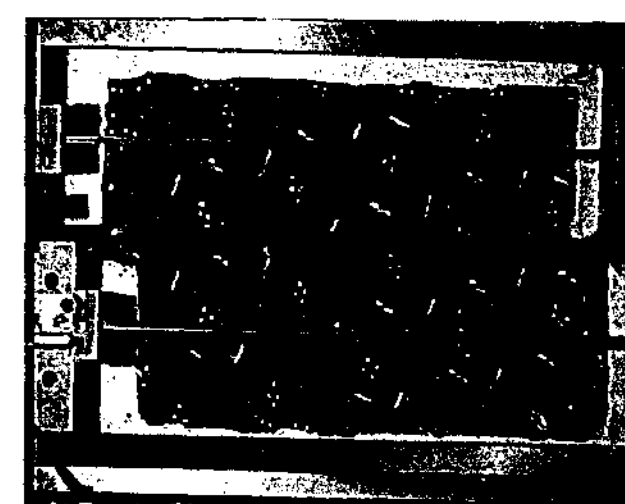
Test B27-3 – dx = 9 mm



Test B27-4 – dx = 15 mm

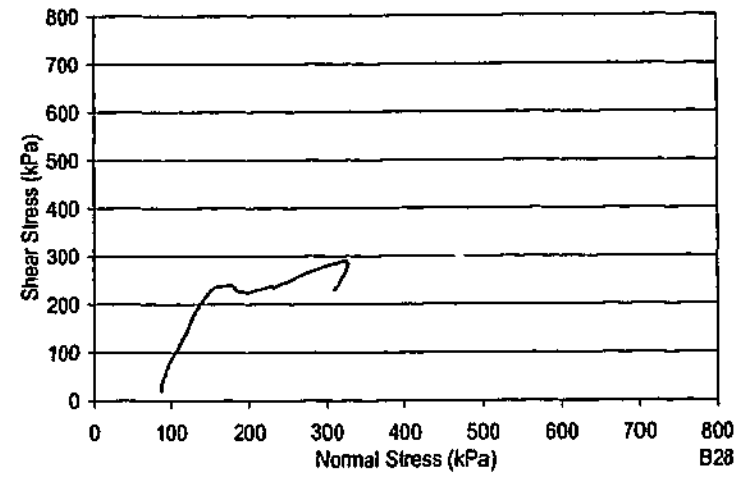


Test B27-5 – dx = 25 mm

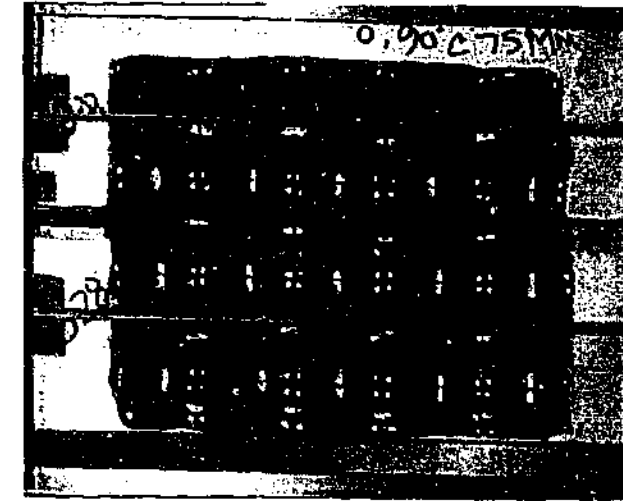
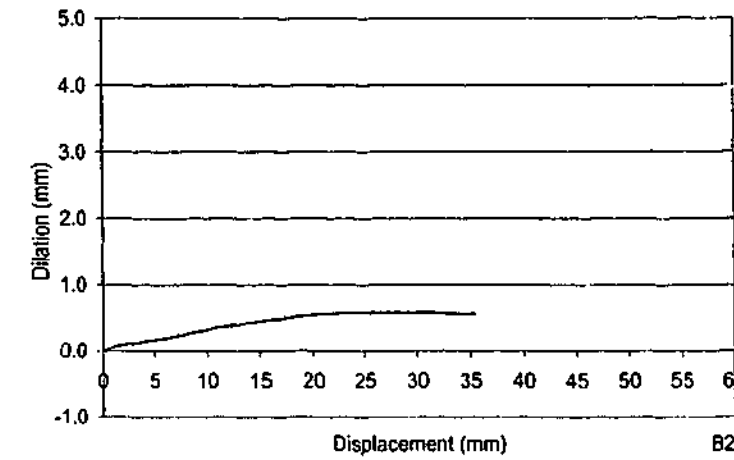
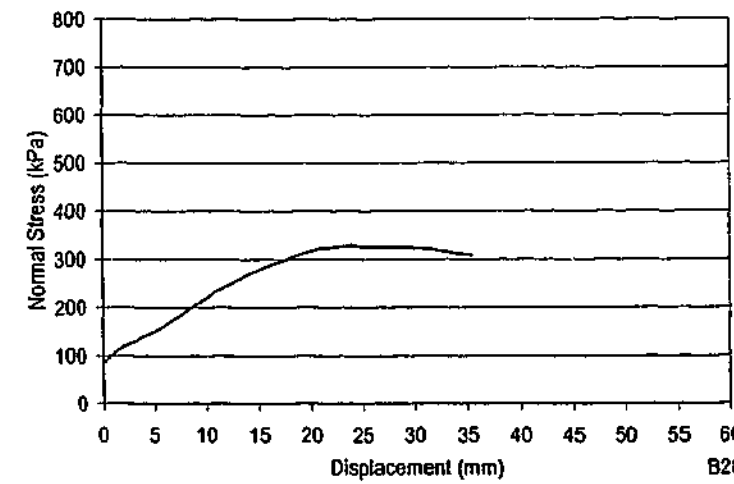
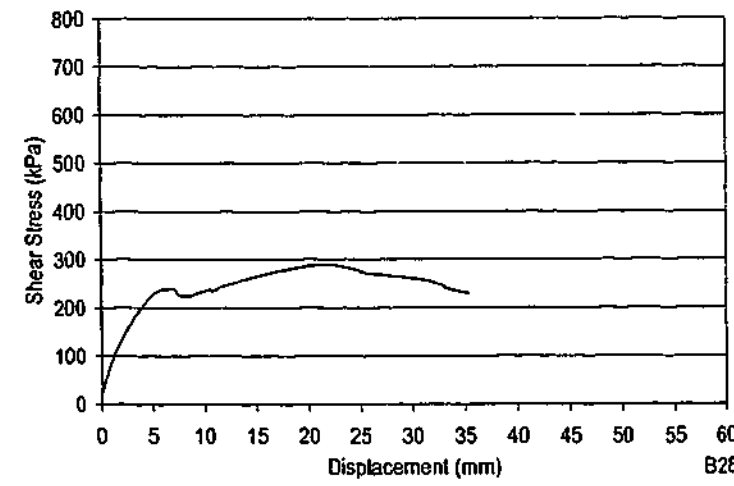


Test B27-6 – dx = 35 mm

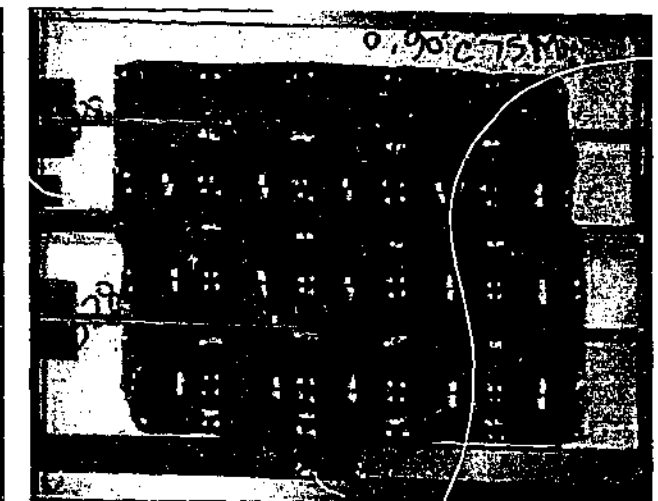
TEST B27			
$\theta_1 = -45^\circ$	$\theta_2 = 75^\circ$	$\theta_3 = n/a^\circ$	spacing = 70 mm
$\sigma_{ni} = 100$ kPa	$k_v = 200$ kPa/mm		UCS = 1.66 MPa



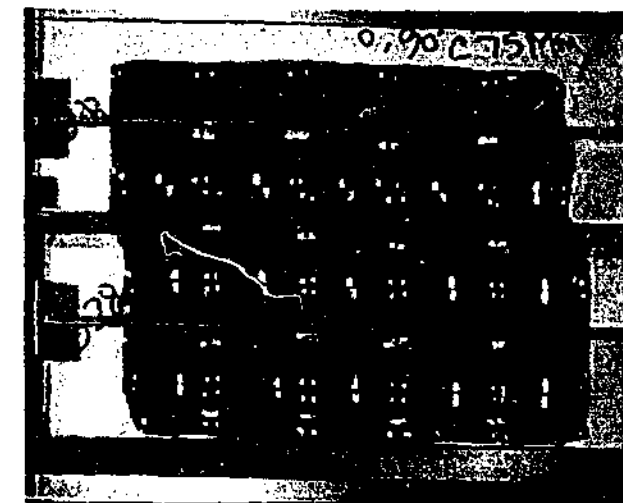
Test Details B28	
θ_1	= -90°
θ_2	= 0°
θ_3	= n/a°
spacing	= 70 mm
σ_{ni}	= 100 kPa
k_v	= 200 kPa/mm
UCS	= 1.15 MPa



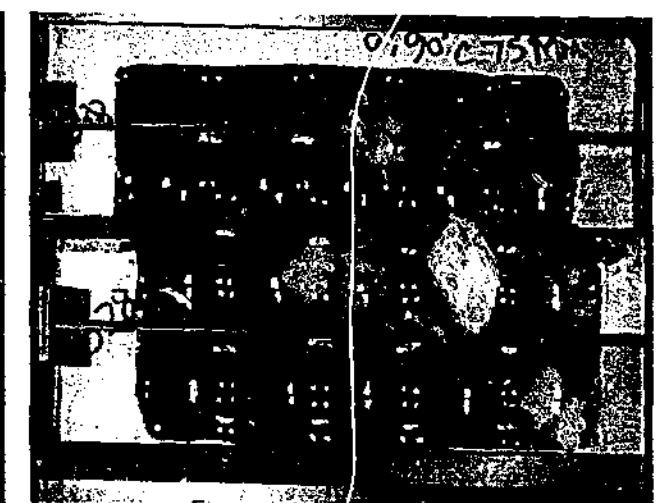
Test B28-1 – dx = 0 mm



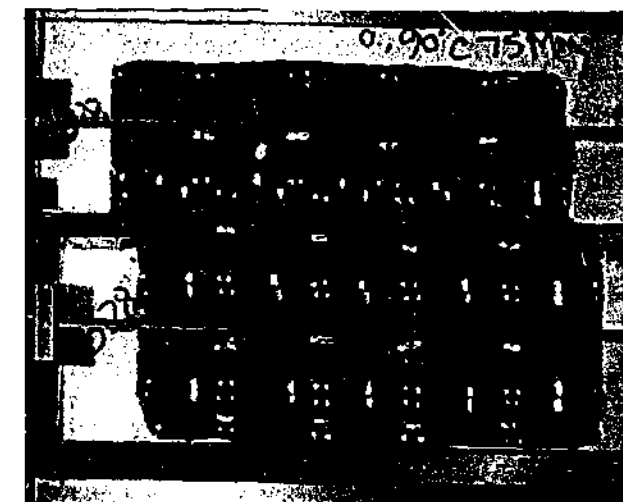
Test B28-2 – dx = 5 mm



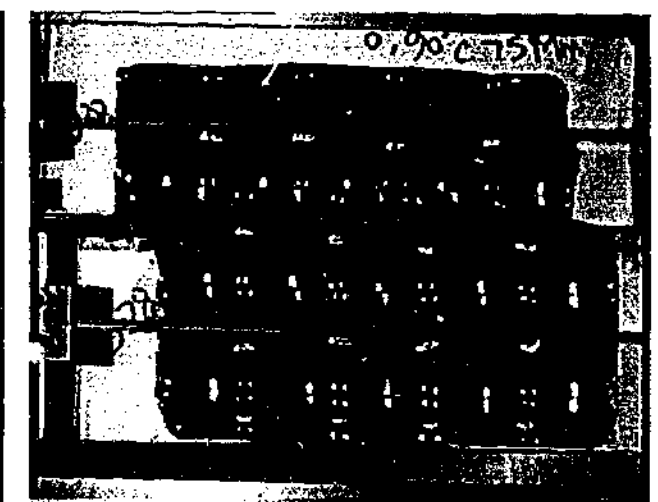
Test B28-3 – dx = 10 mm



Test B28-4 – dx = 15 mm

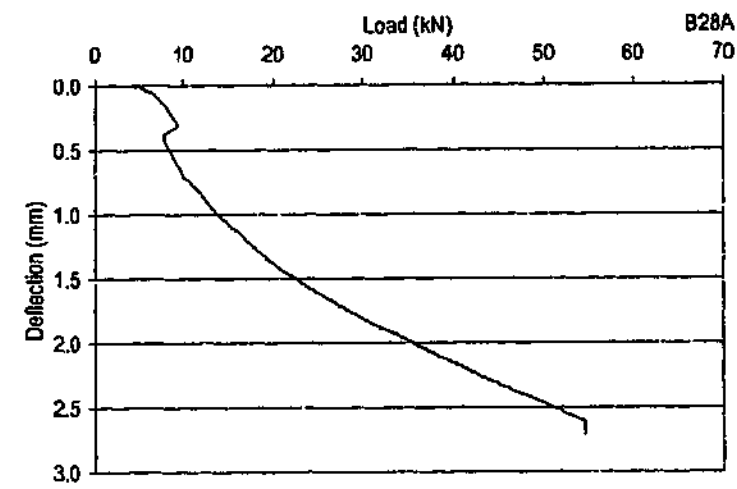


Test B28-5 – dx = 20 mm

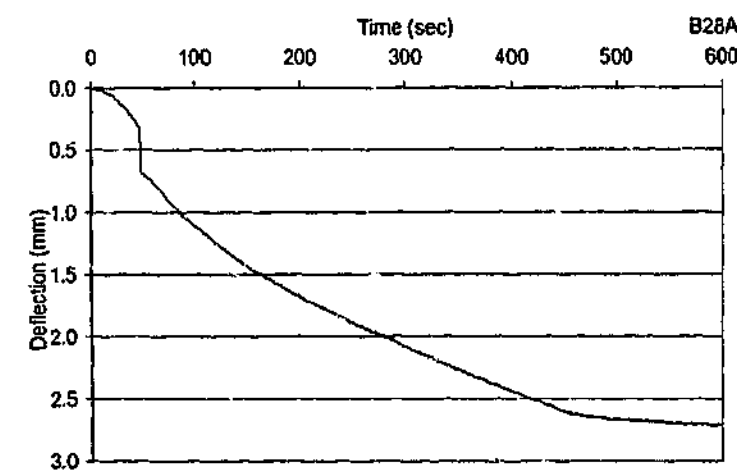
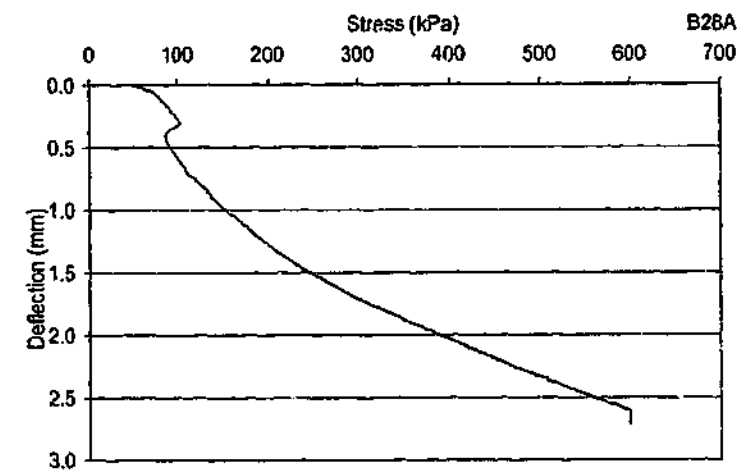


Test B28-6 – dx = 30 mm

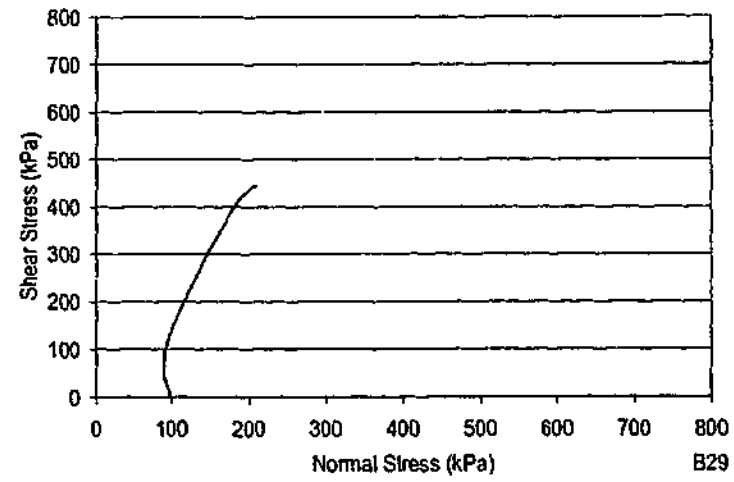
TEST B28			
$\theta_1 = -90^\circ$	$\theta_2 = 0^\circ$	$\theta_3 = n/a^\circ$	spacing = 70 mm
$\sigma_{ni} = 100$ kPa	$k_v = 200$ kPa/mm		UCS = 1.15 MPa



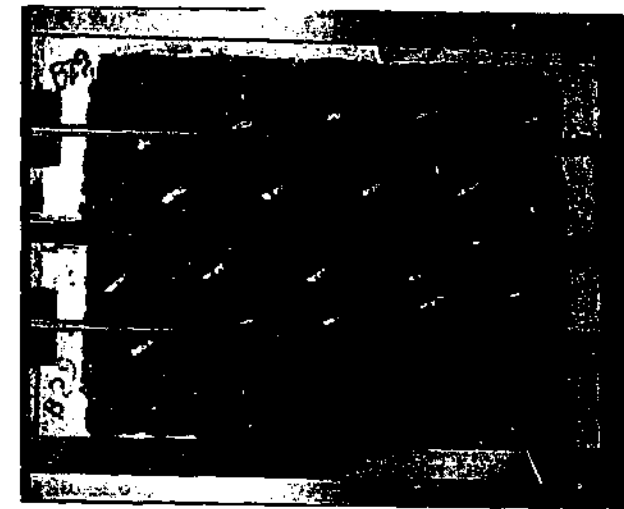
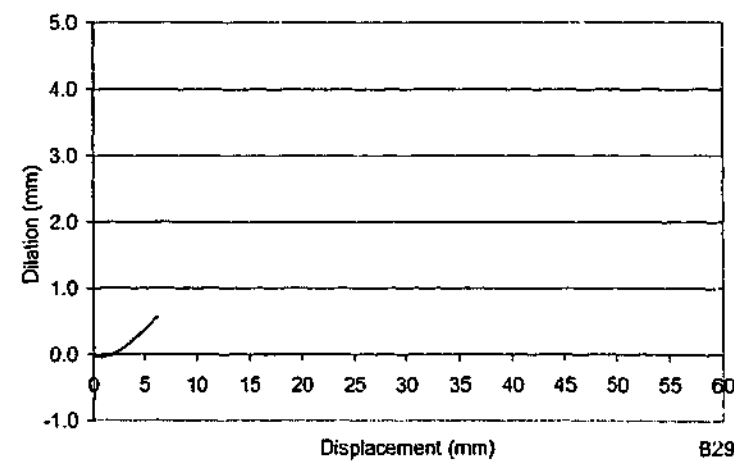
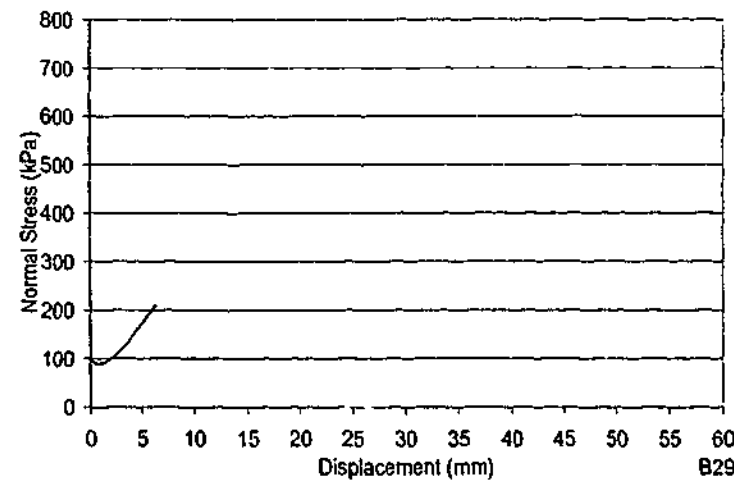
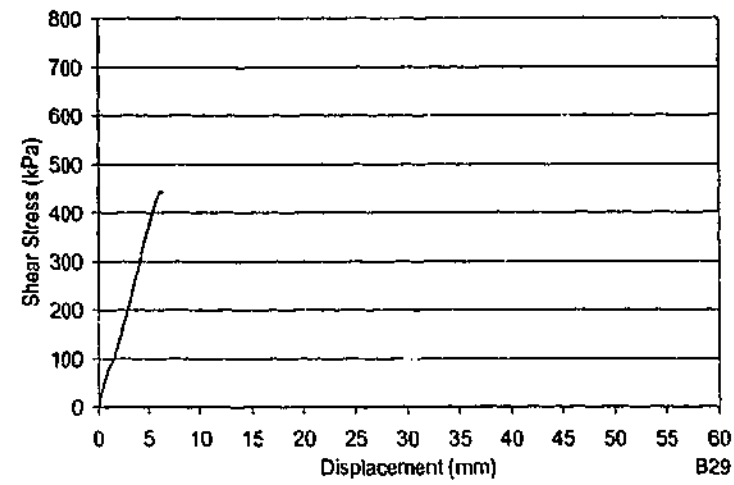
Test Details B28A	
Joint Compliance Test	
θ_1	= -90°
θ_2	= 0°
θ_3	= n/a°
spacing	= 70 mm
σ_{ni}	= 600 kPa
k_v	= 200 kPa/mm
UCS	= 1.15 MPa



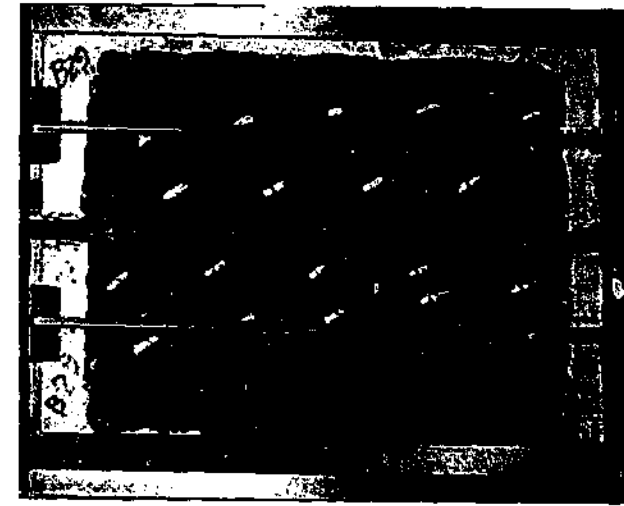
No video footage.



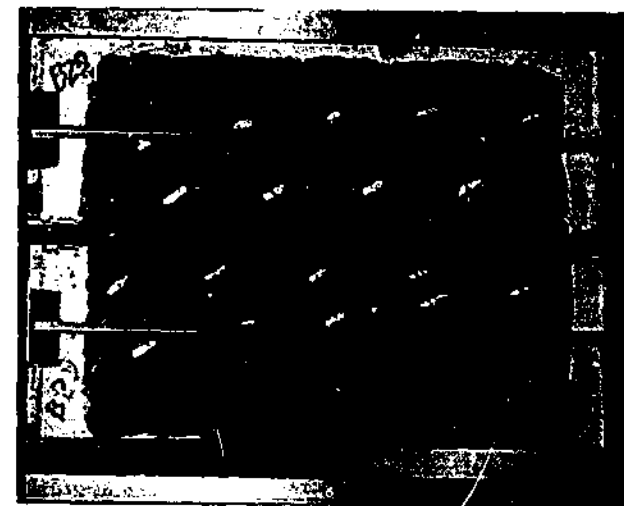
Test Details		B29
θ_1	=	-60°
θ_2	=	n/a $^\circ$
θ_3	=	n/a $^\circ$
spacing	=	70 mm
σ_{ni}	=	100 kPa
k_v	=	200 kPa/mm
UCS	=	1.80 MPa



Test B29-1 – dx = 0 mm

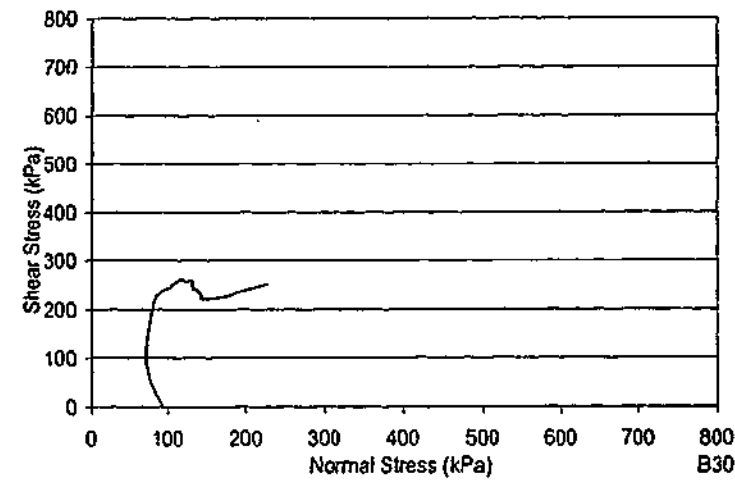


Test B29-2 – dx = 3 mm

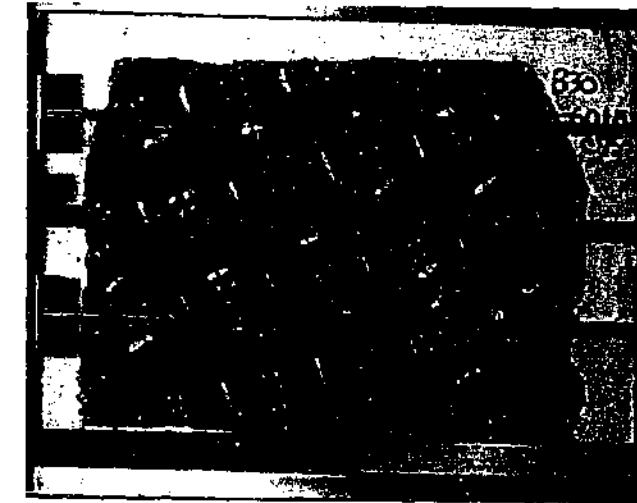
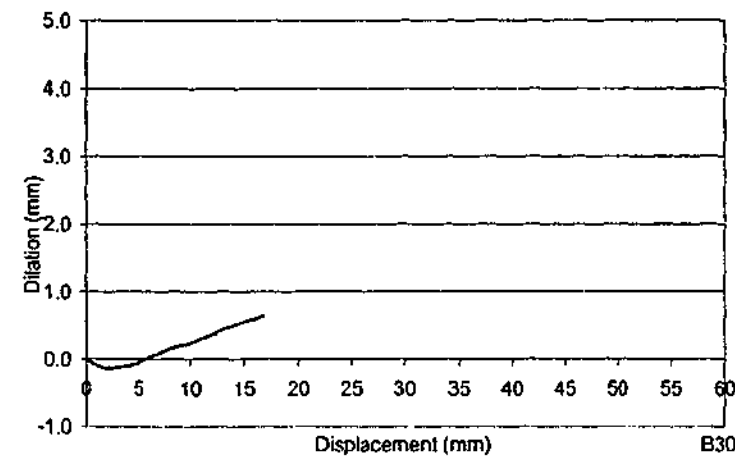
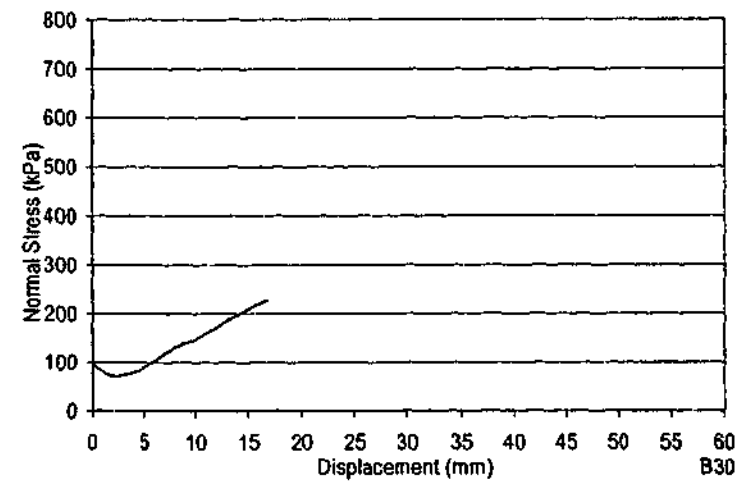
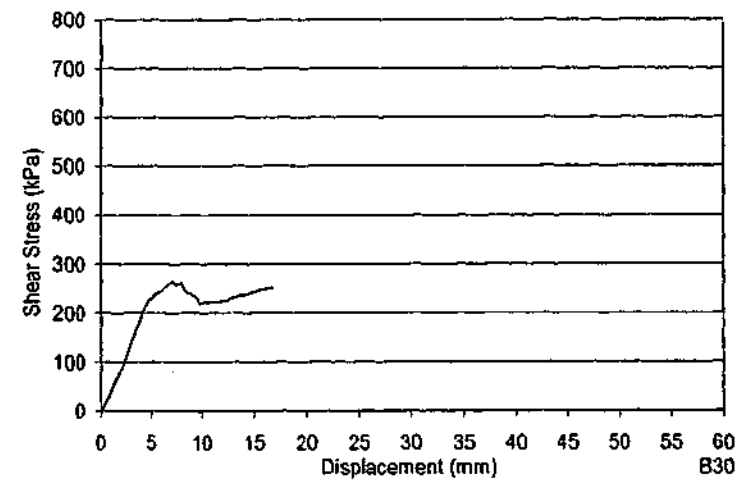


Test B29-3 – dx = 5 mm

TEST B29					
$\theta_1 = -60^\circ$	$\theta_2 = n/a^\circ$	$\theta_3 = n/a^\circ$	spacing = 70 mm	UCS = 1.80 MPa	
$\sigma_{ni} = 100$ kPa	$k_v = 200$ kPa/mm				



Test Details B30	
θ_1	= -62°
θ_2	= 15°
θ_3	= n/a $^\circ$
spacing	= 70 mm
σ_{ni}	= 100 kPa
k_v	= 200 kPa/mm
UCS	= 1.97 MPa



Test B30-1 – dx = 0 mm



Test B30-2 – dx = 4 mm

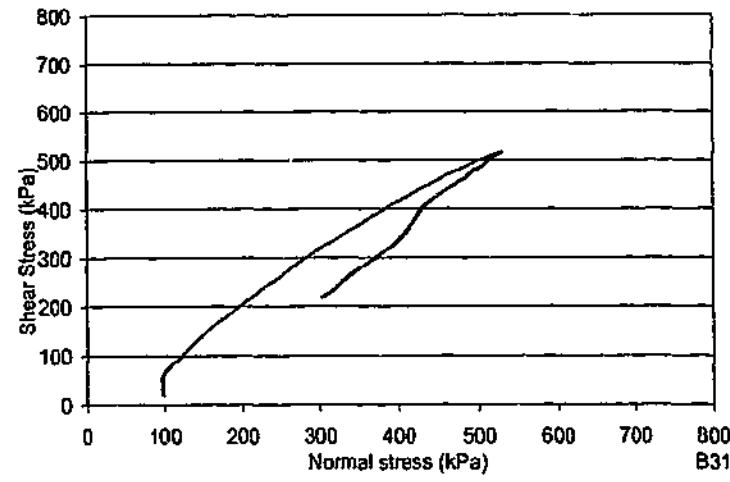


Test B30-3 – dx = 9 mm

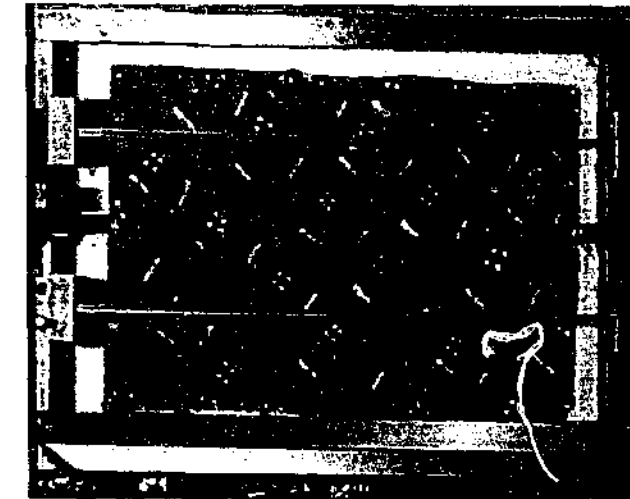
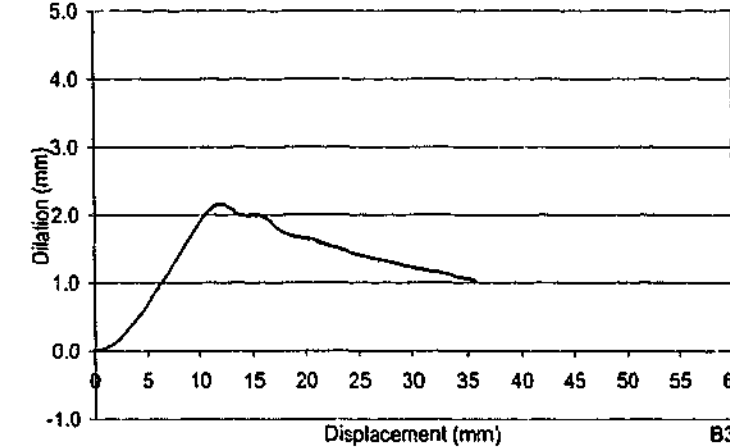
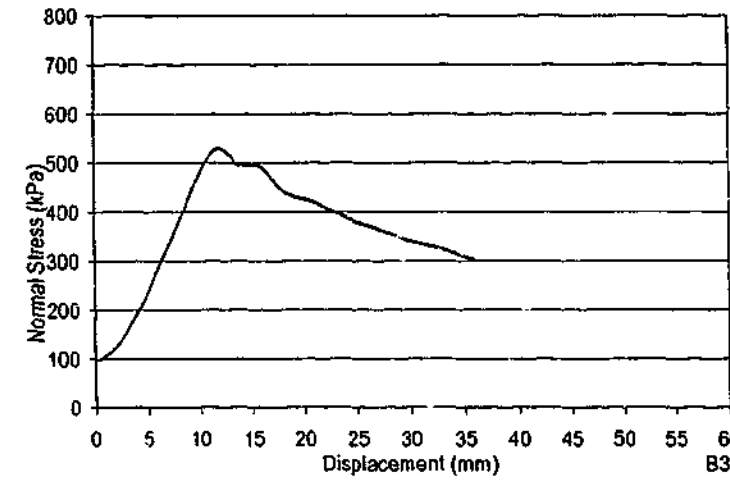
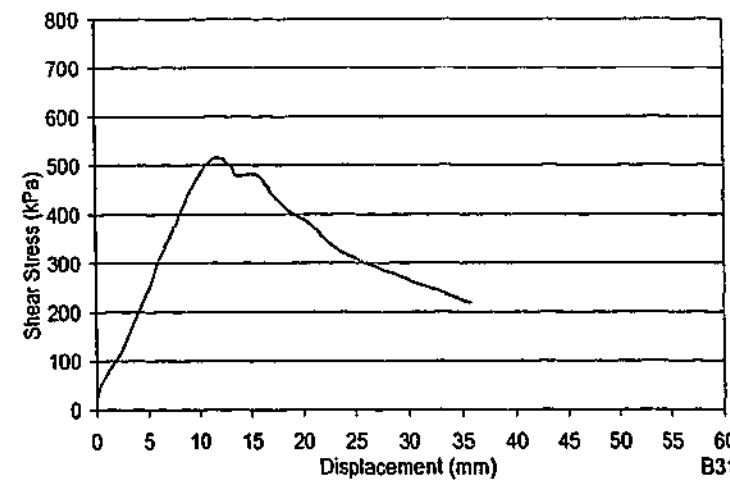


Test B30-4 – dx = 15 mm

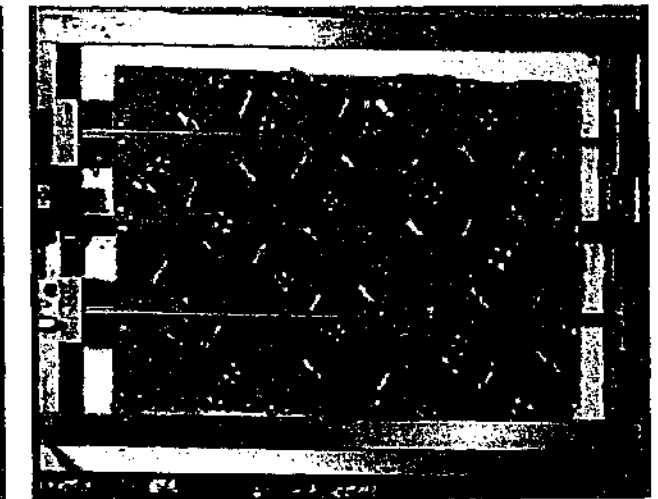
TEST B30			
$\theta_1 = -62^\circ$	$\theta_2 = 15^\circ$	$\theta_3 = n/a^\circ$	spacing = 70 mm
$\sigma_{ni} = 100$ kPa	$k_v = 200$ kPa/mm		UCS = 1.97 MPa



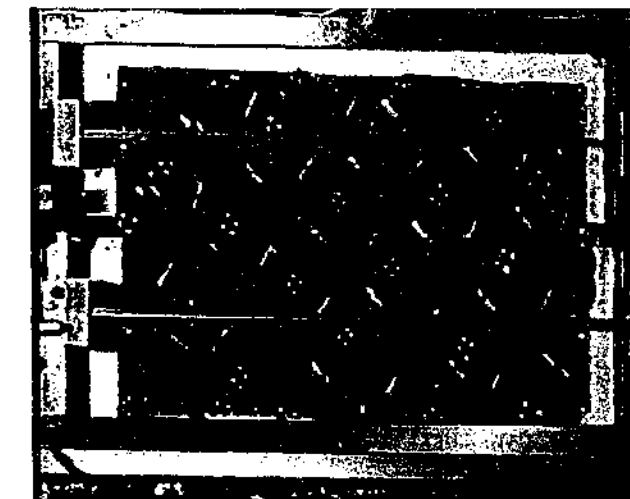
Test Details B31
 $\theta_1 = -45 \pm 5^\circ$
 $\theta_2 = 60 \pm 5^\circ$
 $\theta_3 = n/a^\circ$
 spacing = 70 mm (nom)
 $\sigma_{ni} = 100$ kPa
 $k_v = 200$ kPa/mm
 UCS = 1.72 MPa



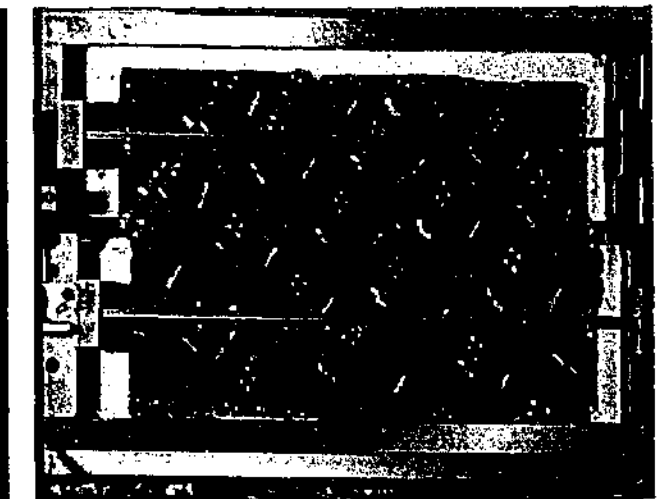
Test B31-1 – dx = 0 mm



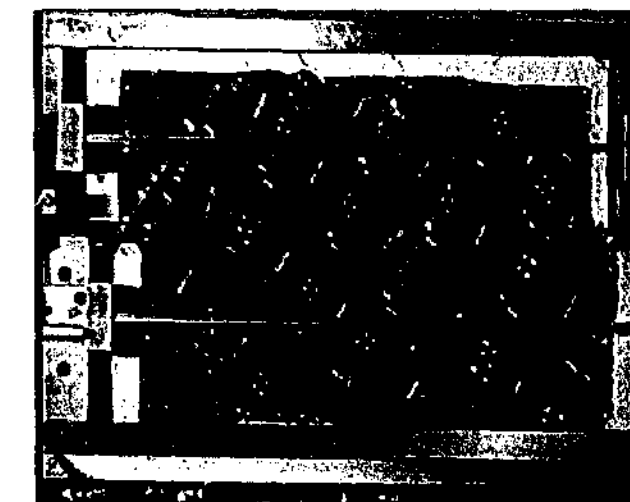
Test B31-2 – dx = 4 mm



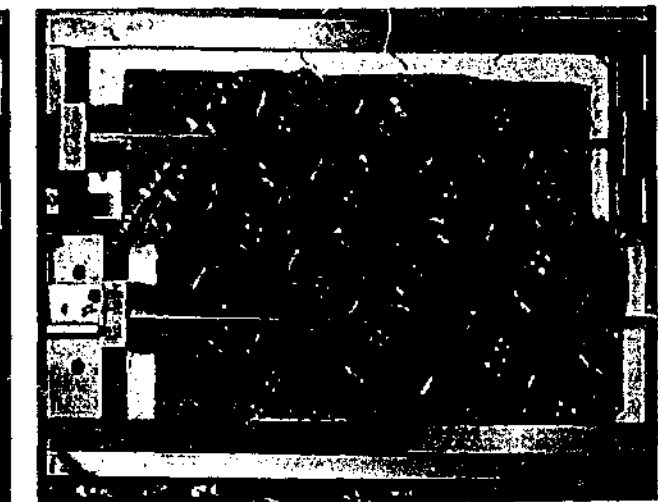
Test B31-3 – dx = 9 mm



Test B31-4 – dx = 15 mm

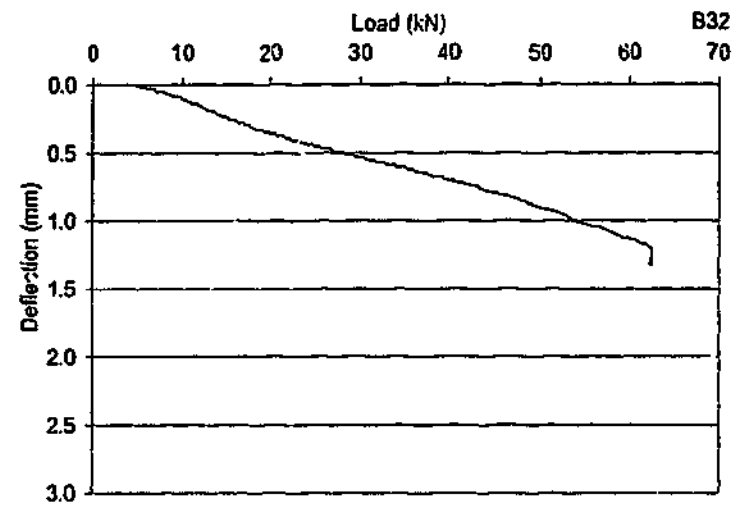


Test B31-5 – dx = 25 mm

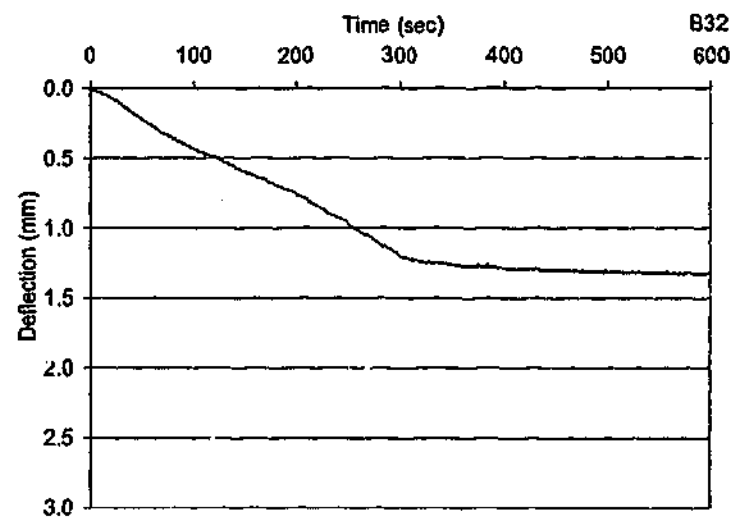
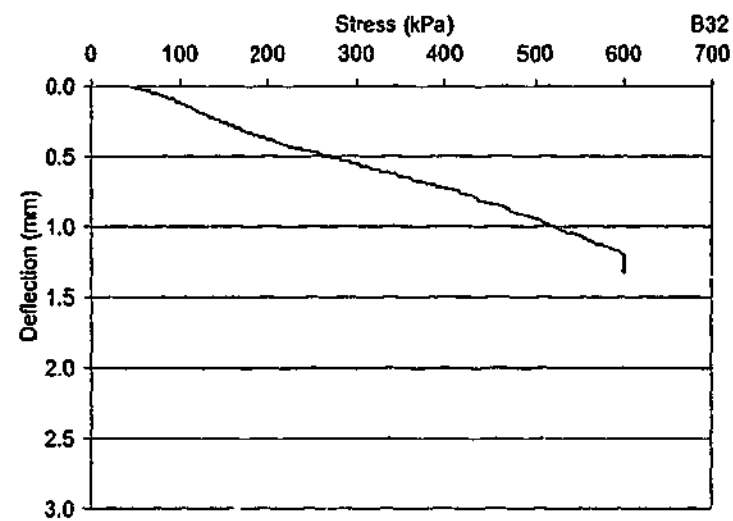


Test B31-6 – dx = 35 mm

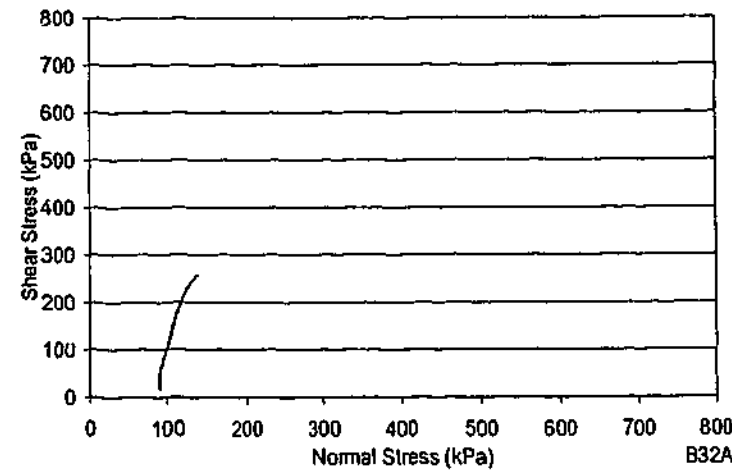
TEST B31
 $\theta_1 = -45 \pm 5^\circ$ $\theta_2 = 60 \pm 5^\circ$ $\theta_3 = n/a^\circ$ spacing = 70 mm
 $\sigma_{ni} = 100$ kPa $k_v = 200$ kPa/mm UCS = 1.72 MPa



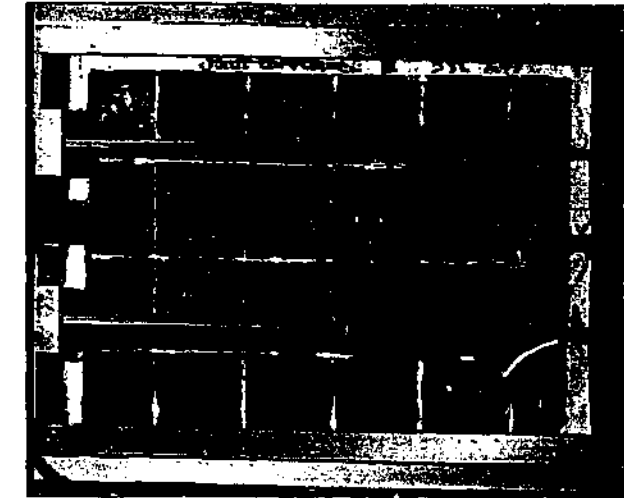
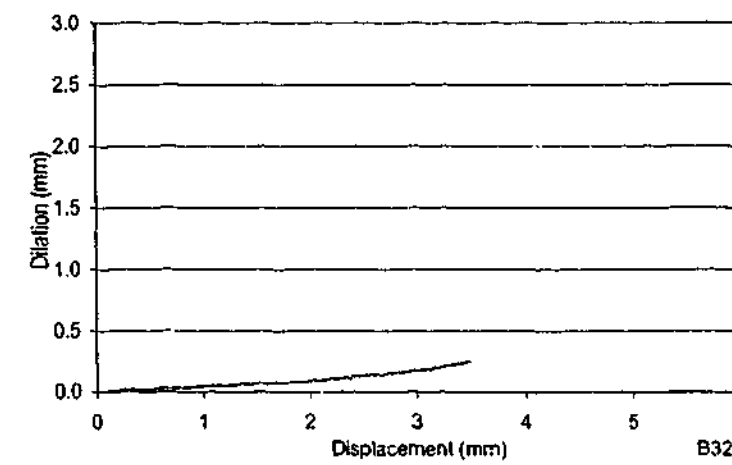
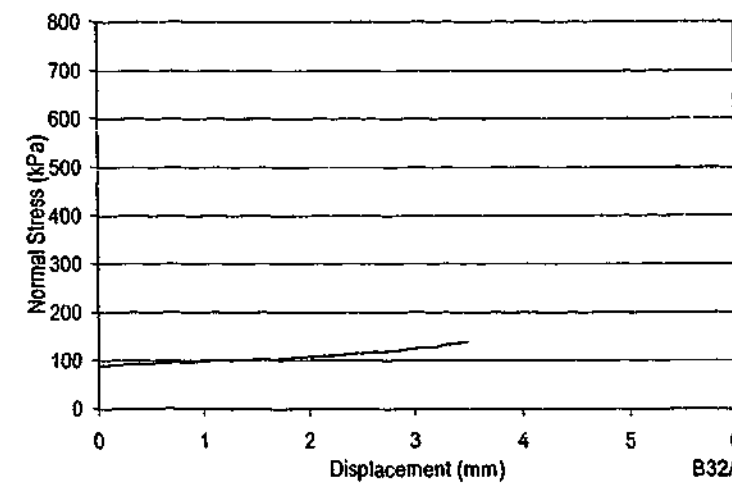
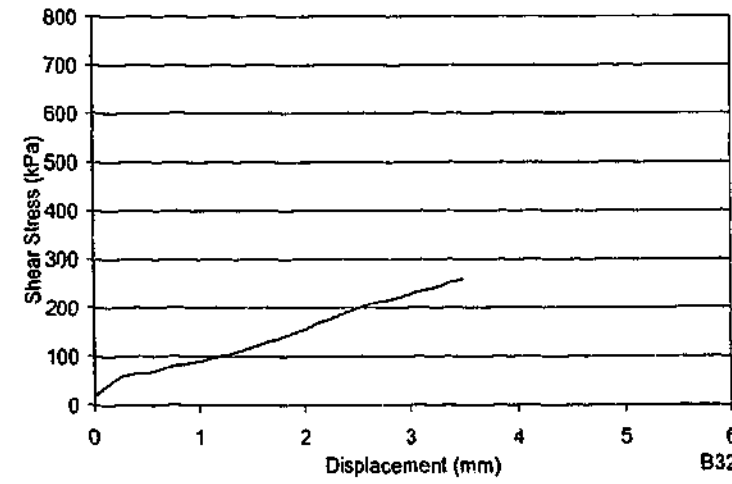
Test Details B32
 Johnstone - Intact Block
 σ_{ni} = 600 kPa
 k_v = 200 kPa/mm
 UCS = 1.15 MPa



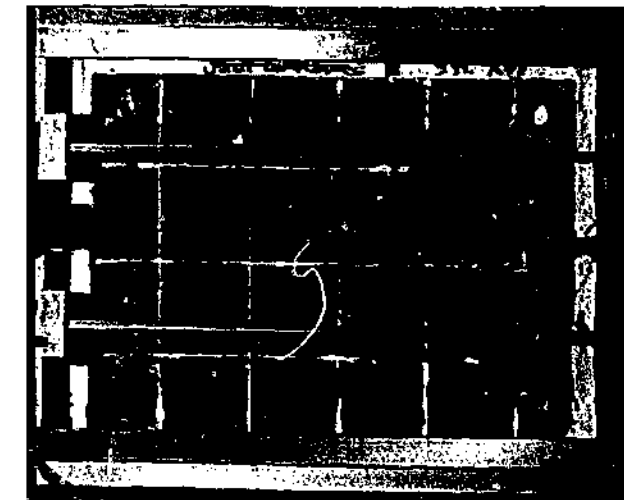
No video footage.



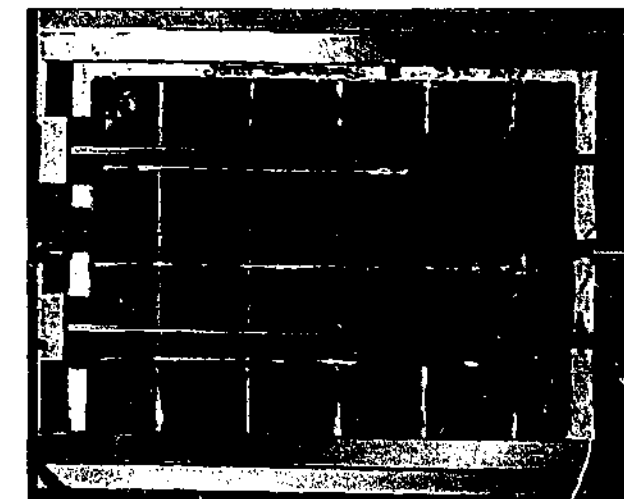
Test Details B32A
 Johnstone - Intact Block
 σ_{ni} = 100 kPa
 k_v = 200 kPa/mm
 UCS = 1.15 MPa



Test B32A-1 – dx = 0 mm

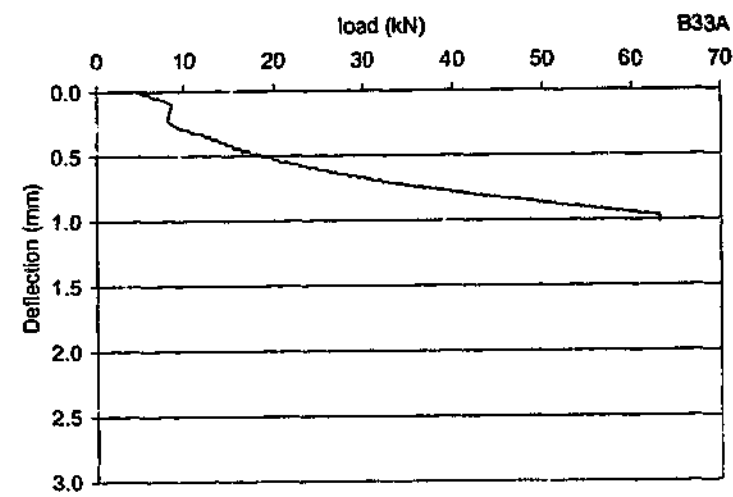


Test B32A-2 – dx = 2 mm

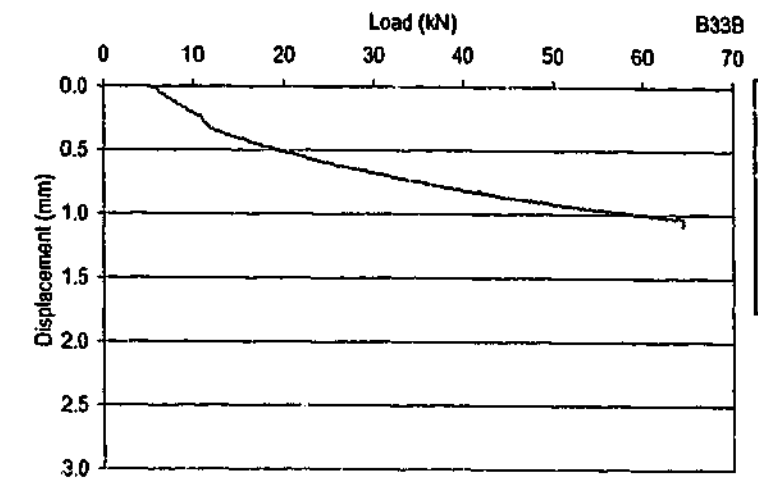
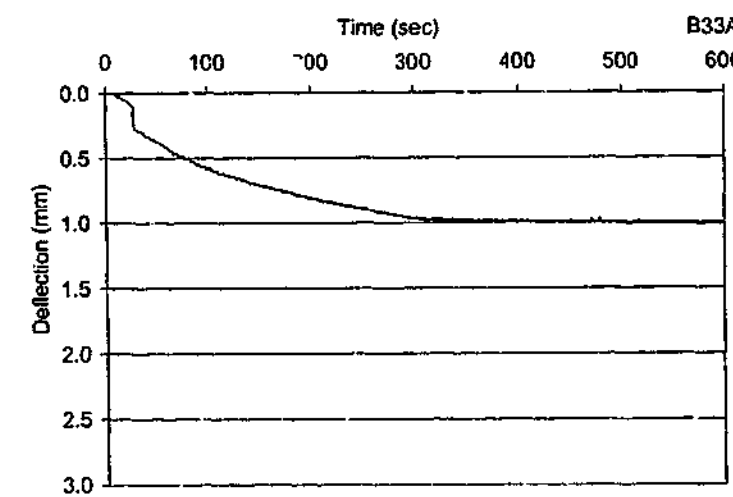
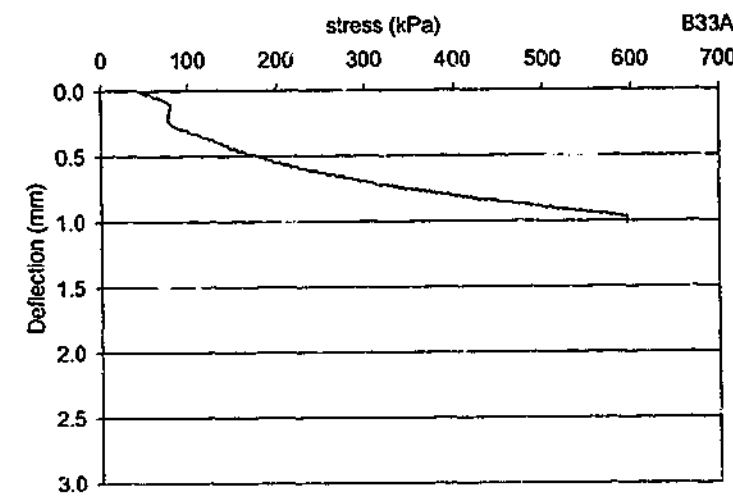


Test B32A-3 – dx = 3 mm

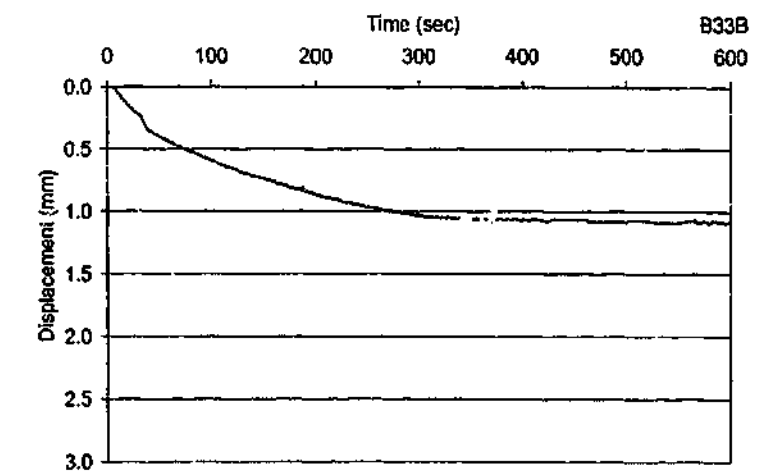
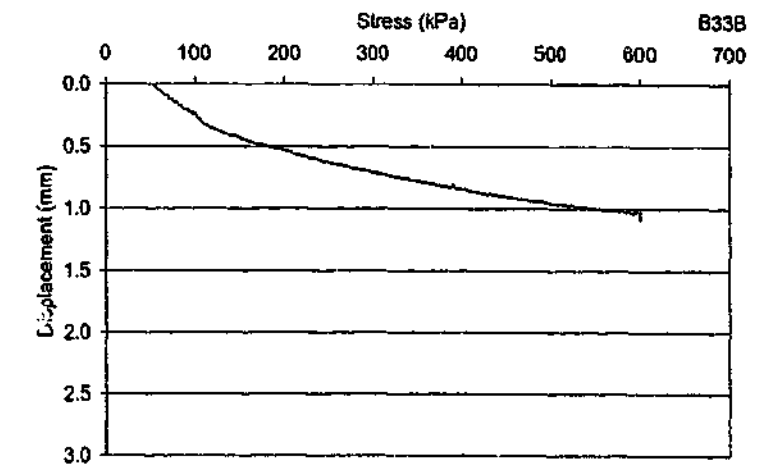
TEST B32A - Intact Johnstone with shear.
 $\theta_1 = n/a^\circ$ $\theta_2 = n/a^\circ$ $\theta_3 = n/a^\circ$ spacing = n/a
 $\sigma_{ni} = 100$ kPa $k_v = 200$ kPa/mm UCS = n/a

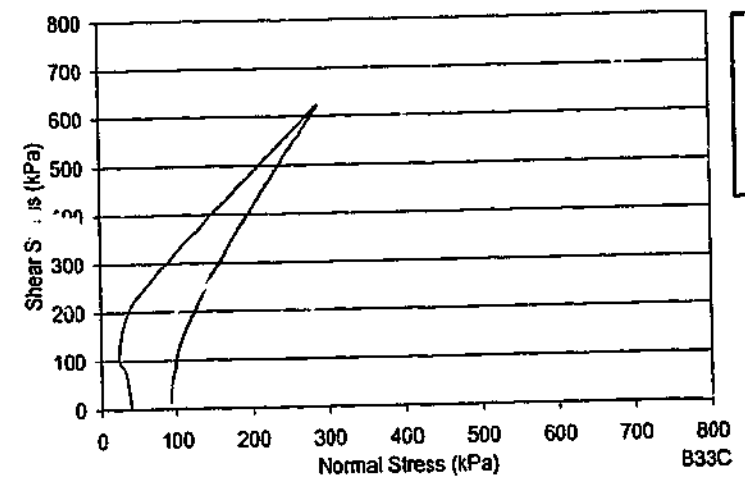


Test Details B33A
 System Compliance - Test 1
 Concrete - Intact Block
 σ_{ni} = 600 kPa
 k_v = 200 kPa/mm

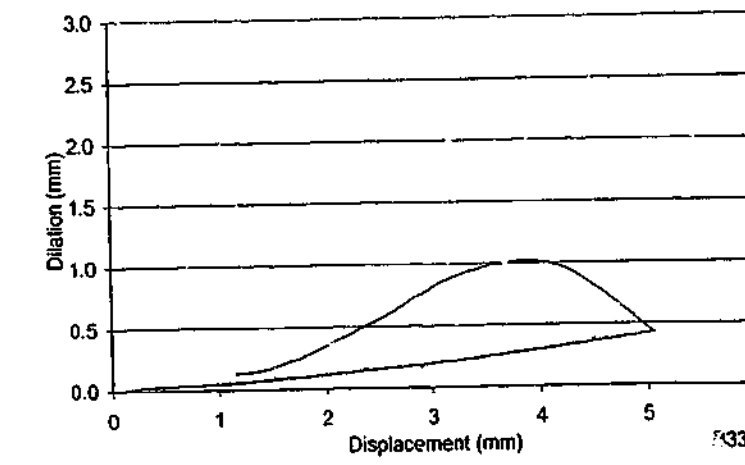
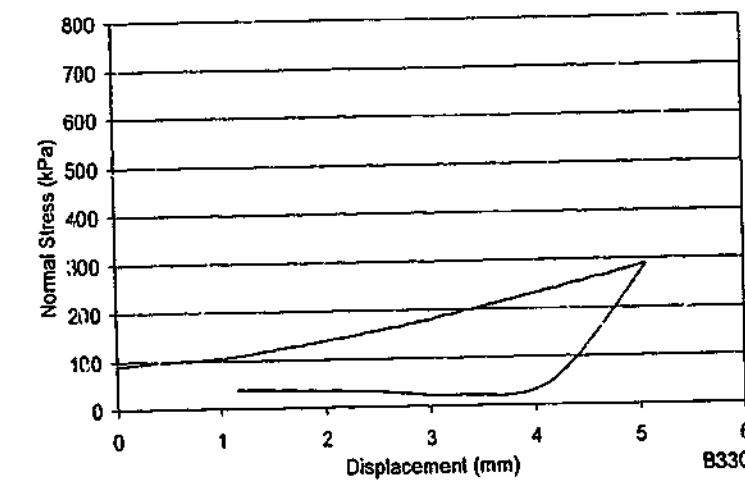
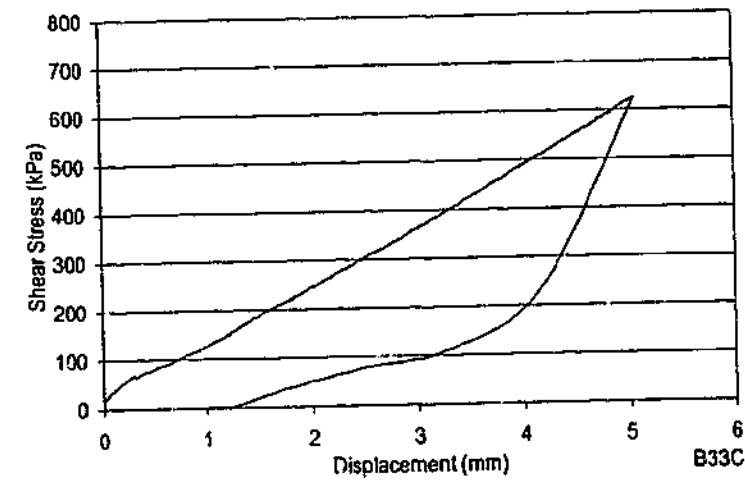


Test Details B33B
 System Compliance - Test 2
 Concrete - Intact Block
 σ_{ni} = 600 kPa
 k_v = 200 kPa/mm





Test Details B33C	
Concrete -	Intact Block
σ_{ni} =	100 kPa
k_v =	200 kPa/mm



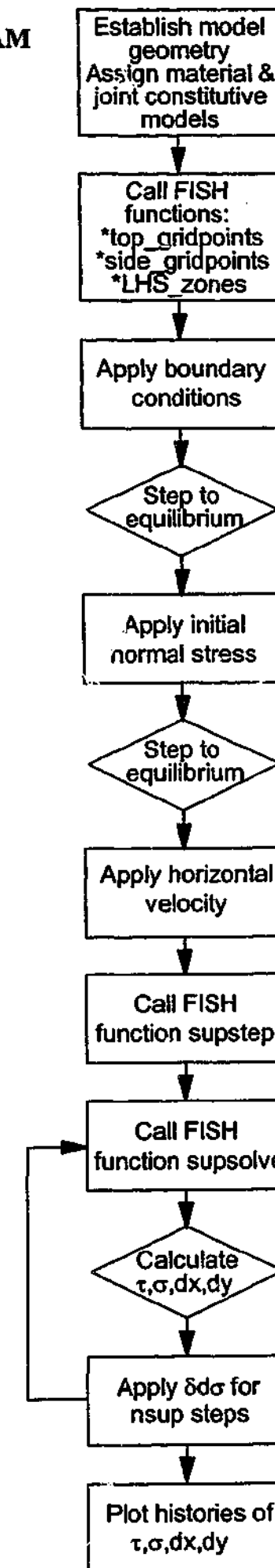
No video footage.

APPENDIX C

UDEC CODE AND OUTPUT

UDEC PROGRAM FLOW DIAGRAM.....	C-3
SAMPLE UDEC CODE (based on Test B18).....	C-5
CD-ROM CONTAINING UDEC MOVIE OUTPUT AND POWERPOINT SLIDESHOW FOR EACH TYPE "B" TEST	
	INSIDE BACK COVER

UDEC PROGRAM FLOW DIAGRAM



SAMPLE UDEC CODE (based on Test B18)

```

title
Shear Test Simulation-displacement control-CNS
head
Test B18
;
ro 0.001
;----plot outer box----
bl 0,0 0,0.34 0.44,0.34 0.44,0
;
;----plot top half of shear box
crack 0.00,0.18 0.02,0.18
crack 0.02,0.18 0.02,0.34
crack 0.02,0.32 0.42,0.32
crack 0.42,0.34 0.42,0.18
crack 0.42,0.18 0.44,0.18
;
;----plot bottom half of shear box
crack 0.00,0.17 0.02,0.17
crack 0.02,0.17 0.02,0.0
crack 0.02,0.02 0.42,0.02
crack 0.42,0.0 0.42,0.17
crack 0.42,0.17 0.44,0.17
crack 0.00,0.02 0.02,0.02
crack 0.01,0.02 0.01,0.17
;
;----plot gaps
crack 0.02,0.18 0.02,0.17
crack 0.42,0.18 0.42,0.17
;
;----assign material models----
;
;delete gaps
del range 0.00,0.02 0.17,0.18
del range 0.42,0.44 0.17,0.18
;
;----steel box - upper
ch cons=1 mat=6 range 0.0,0.02 0.18,0.34
ch cons=1 mat=6 range 0.02,0.42 0.32,0.34
ch cons=1 mat=6 range 0.42,0.44 0.18,0.34
;
;----steel box - lower
ch cons=1 mat=6 range 0.0,0.02 0.0,0.17
ch cons=1 mat=6 range 0.02,0.42 0.0,0.02
ch cons=1 mat=6 range 0.42,0.44 0.0,0.17
;
;----rock mass
ch cons=3 mat=4 range 0.02,0.42 0.02,0.32
;

```

```

;----plot joints in rock mass----
jset 43,0.5 0.70,0 0,0 0.07,0.002 0.02,0.175 range mat 4
jset -31,0.5 0.70,0 0,0 0.07,0.002 0.02,0.175 range mat 4
pl bl
;
gen.edge 0.015
;
;----assign material properties----
;----steel
prop mat=6 d=7800 bu=185e9 sh=110e9
;----rock
prop mat=4 d=2200 bu=185e6 sh=110e6 coh=600e3 fr=37 ten=350e3 dil=)
;----rock joints
prop jmat=4 jkn=1000e6 jks=100e6 jc=0 jf=27 jt=0
;----steel-steel joints
prop jmat=6 jkn=1000e9 jks=100e9 jc=10e6 jf=28 jt=10e9
;----steel-rock interface
prop jmat=8 jkn=1000e6 jks=100e6 jc=0 jf=28 jt=0
;
;----assign joint models
;----jmat=6 steel-steel, jmat=8 steel-rock jmat=4 rock-rock
ch jcons=2 jmat=6 range mint 6,6
ch jcons=2 jmat=8 range mint 6,4
ch jcons=2 jmat=4 range mint 4,4
;
;----fish routine to set up array of gridpoints in top----
def top_gridpoints
array gp_top(100)
ntop=0
bi=block_head
loop while bi#0
if b_y(bi)< 0.325 then
gi=b_gp(bi)
loop while gi#0
if gp_y(gi)>0.315 then
ntop=ntop+1
gp_top(ntop)=gi
endif
gi=gp_next(gi)
end_loop
endif
bi=b_next(bi)
end_loop
end
;

```

```

;----fish routine to set up array of gridpoints in side----
def side_gridpoints
array gp_side(100)
nside=0
bi=block_head
loop while bi#0
if b_y(bi)<0.175 then
if b_y(bi)>0.022 then
if b_x(bi)>0.015 then
gi=b_gp(bi)
loop while gi#0
if gp_x(gi)<0.025 then
nside=nside+1
gp_side(nside)=gi
endif
gi=gp_next(gi)
end_loop
endif
endif
bi=b_next(bi)
end_loop
end
;
;----fish routine to set up array of zones in LHS----
def LHS_zones
array z_LHS(100)
nLHS=0
bi=block_head
loop while bi#0
zi=b_zone(bi)
if z_y(zi)<0.17 then
if z_y(zi)>0.02 then
if z_x(zi)<0.02 then
loop while zi#0
if z_x(zi)>0.01 then
nLHS=nLHS+1
z_LHS(nLHS)=zi
endif
zi=z_next(zi)
end_loop
endif
endif
bi=b_next(bi)
end_loop
end
;

```

```

;----call fish function to set up top and side arrays of gridpoints
top_gridpoints
side_gridpoints
LHS_zones
;
save TestB18.sv0
;
;----apply initial boundary conditions----
;----bottom box
bound yvel=0 range -0.01,0.441 -0.01,0.01

;----top box
bound xvel=0 range 0.0,0.02 0.18,0.34
bound xvel=0 range 0.42,0.44 0.18,0.34

;----apply initial horizontal stress
insitu str -100e3,0,0 range mat=4
insitu szz -300e3 range mat=4
solve force =200 step 10000
pl bl sxx
;
;----apply initial vertical stress and step to equilibrium
bound str 0,0,-100e3 range -0.0,0.44 0.338,0.341
grav 0,-10
his unbal
his ydis 0.22,0.34
his xdis 0.0,0.09
solve force=200 step=10000
pl bl disp
pl bl syy
;
save TestB18.sv1

;----fish routine to measure stresses and displacements in top----
def top_disp
normal_area=0.1
y_dis=0.
y_load=0.
ini_nstress = -100e3
stiffness=200e6
inc_nstress=0.
loop nn (1,ntop)
gi=gp_top(nn)
y_dis=y_dis+gp_ydis(gi)
y_load=y_load + gp_yforce(gi)
end_loop
average_ydis= 4e-4 + y_dis/float(ntop)
normal_stress=ini_nstress - average_ydis*stiffness
inc_nstress=normal_stress-old_nstress
old_nstress=normal_stress
end
;

```

```

;----fish routine to measure displacements in side----
;
def side_disp
shear_area=0.1
x_dis=0.
average_xdis=0.
loop mm (1,nside)
gi=gp_side(mm)
x_dis=x_dis+gp_xdis(gi)
end_loop
average_xdis=x_dis/float(nside)
;
;----fish routine to measure stress in side----
;
def side_stress
shear_area=0.1
x_stress=0.
shear_stress=0.
loop tt (1,nLHS)
zi=z_LHS(tt)
x_stress=x_stress+z_sxx(zi)
end_loop
shear_stress=x_stress*0.375/float(nLHS)
end
;
def supstep
top_disp
side_disp
side_stress
dummy=ns ; need to make ns a FISH parameter, so can 'set' a value in UCSC
command
bou stress 0,0,inc_nstress range 0.02,0.42 0.32,0.40
step ns
print inc_nstress
endcommand
end
movie on file=TestB18.dcx
movie step on 5000
;
def supsolve
loop kk (1,nsup)
supstep
endloop
end
;

```

```
;----displace lower half----  
bou xvel=0.1 range -0.01,0.1 0.0,0.17  
bou xvel=0.1 range 0.43,0.45 0.0,0.17  
pl bl plas  
  
set ovtol=0.5  
;  
set ns=250 nsup=800 stiffness=200e6 old_nstress=-100e3 average_ydis=0.  
  
his normal_stress  
label hist 4  
Normal Stress  
;  
his average_ydis  
label hist 5  
Y Displacement  
;  
his shear_stress  
label hist 6  
Shear Stress  
;  
his average_xdis  
label hist 7  
X Displacement  
;  
his inc_nstress  
label hist 8  
Incremental Normal Stress  
;  
supsolve  
;  
save TestB18.sv2  
;  
pl his -6 vs -4  
pl his -4 vs 7  
pl his 5 vs 7  
pl his -6 vs 7  
movie off  
ret
```

**CD-ROM CONTAINING UDEC MOVIE OUTPUT AND POWERPOINT
SLIDESHOW FOR EACH TYPE "B" TEST INSIDE BACK COVER.**

**CR-ROM ALSO CONTAINS UDEC MOVIES OF VARIATION OF JOINT
SPACING AND INTACT ROCK STRENGTH.**